THÈSE

en vue de l'obtention du grade de Docteur, délivré par

l'ÉCOLE NORMALE SUPERIEURE DE LYON

École Doctorale N°206
Chimie de Lyon

Discipline : Chimie

Soutenance publique prévue le 10 mars 2025, par :

Justine DORIVAL

Ammonia as a hydrogen carrier: optimization study of its catalytic decomposition promoted by ruthenium and lithium amide according to a joint experimental and theoretical approach

L'ammoniac comme vecteur d'hydrogène : étude de l'optimisation de sa décomposition catalytique promue par le ruthénium et l'amidure de lithium suivant une approche mixte expérimentale et théorique

Devant le jury composé de :

Emilie GAUDRY, Professeur des universités, Université de Lorraine	Rapporteure
Nicolas BION, Directeur de recherche, Université de Poitiers	Rapporteur
Corinne LACAZE-DUFAURE, Professeur des universités, Université de Toulouse	Examinatrice
Sebastien ROYER, Professeur des universités, Université de Lille	Examinateur
Jérôme DELMAS, Chercheur, CEA	Examinateur
David LOFFREDA, Directeur de recherche, Ecole Normale Supérieure de Lyon	Directeur de thèse

Remerciements

Cette thèse marque l'aboutissement de plusieurs années de travail, d'apprentissages mais aussi de rencontres. Elle n'aurait jamais vu le jour sans le soutien, les conseils et l'inspiration de nombreuses personnes, que je souhaite remercier ici avec toute ma sincérité et ma reconnaissance.

Je tiens à exprimer ma profonde gratitude à David LOFFREDA, mon directeur de thèse, pour son accompagnement constant et sa bienveillance tout au long de ces années. Je lui suis particulièrement reconnaissante de m'avoir fait découvrir la chimie théorique, et la DFT, avec la plus grande pédagogie et patience, ce domaine dont j'ai pris grand plaisir à découvrir et contribuer. Je n'aurais pas pu espérer de meilleure direction pour cette thèse.

Je remercie chaleureusement le CEA ainsi que le Laboratoire de Chimie de l'ENS de Lyon pour m'avoir accueillie au sein de leurs équipes.

Je souhaite également remercier tout particulièrement Jérôme DELMAS pour son encadrement toutes ces années, pour sa disponibilité, ses conseils précieux et son soutien technique et scientifique, qui ont été d'une grande aide tout au long de ce projet.

Un grand merci également aux membres de mon jury de thèse, en particulier Émilie GAUDRY et Nicolas BION, pour le temps consacré à la lecture attentive de ce manuscrit, ainsi que pour leurs retours constructifs. Merci également à Sébastien ROYER pour la richesse de nos échanges le jour de la soutenance, et à Corinne LACAZE-DUFAURE d'avoir accepté de présider ma soutenance.

Une grande partie de cette thèse n'aurait jamais vu le jour sans l'aide inestimable d'Olivier BLANCHOT, qui m'a soutenue sans relâche et tant appris tout au long de ce travail. Sa présence, sa patience et ses conseils ont été des repères essentiels, et c'est en grande partie grâce à lui que j'ai su garder le cap malgré les nombreuses difficultés rencontrées. Pour tout cela, je lui suis profondément et sincèrement reconnaissante.

Je tiens également à remercier chaleureusement tous mes collègues qui m'ont accompagnée tout au long de ces trois années passées au sein du LITEN : Vincent Faucheux, Christophe Brouard, Corentin Chatelier, Isabelle Rougeau et Konstantin Tarasov, Jeanne SILVESTRE, Clément SAINT ANDRE, Manon BOUVET, Selya OUALI, pour leur soutien, leurs conseils et leur bonne humeur au quotidien.

Je souhaite adresser un merci tout particulier à Sandrine Barthélémy et Laura Belz pour leur aide précieuse

dans la réalisation des analyses ICP, ainsi qu'à Parviz Hajiyev pour son accompagnement attentif et toujours pertinent.

Un grand merci à tous les doctorants avec qui j'ai partagé cette aventure : Duc NGUYEN, Elijah UGADHAN, Florian D'AMBRA, Julia LEVY, Corentin BOURDIOL, Nora COLLAY, Agathe VACHE et Roberto BARBANO.

Une pensée toute particulière à Chloé GUILLOT, ma partenaire de galère, dont l'arrivée au laboratoire sur un sujet proche du mien m'a été d'un grand réconfort. Merci pour ton aide précieuse pour les analyses Raman, ta disponibilité, et le temps que tu m'as généreusement consacré.

Un merci tout spécial à l'open-space : Louis DUBRULLE, Ana-Carolina FERNANDEZ, Pierre JUDAIS, Kristina BELIAEVA, José VACHAUD, Hassan AMATERZ, Léa MARTY et Betsabé RODRIGUEZ. Merci pour toutes ces années passées à vos côtés, pour les goûters du jeudi, les minutes musicales, les discussions (parfois scientifiques, souvent beaucoup moins). Vous faites partie de mes plus beaux souvenirs de thèse, et je vous en suis profondément reconnaissante.

Enfin, je souhaite remercier du fond du cœur tous mes amis, que j'aime tant, ainsi que ma famille. À mes parents, à ma petite mémé, à ma sœur : merci pour votre soutien indéfectible et votre amour tout au long de ces années. Je ne serais jamais arrivée là sans vous.

Une pensée tendre également à mes compagnons à quatre pattes, dont l'amour inconditionnel et la présence rassurante ont souvent apaisé les moments les plus compliqués.

Merci à mon compagnon Edwin, pour son soutien constant tout au long de cette aventure. Ta présence a été une force précieuse, et sans toi, tout cela aurait été bien plus difficile.

Résumé

Dans le domaine de l'énergie et de l'environnement, il est devenu primordial de changer de sources d'énergie et d'accélérer une transition énergétique qui peine à progresser dans de nombreux secteurs industriels. La chaîne de production énergétique doit être repensée en étant la plus respectueuse possible de l'environnement. Le but est d'éliminer le carbone, point faible de notre économie actuelle. Parmi les solutions prometteuses, l'hydrogène apparaît comme un élément central dans la décarbonation. Il offre une alternative propre aux combustibles fossiles, en particulier pour l'industrie lourde et le secteur des transports. L'ammoniac représente une excellente option en tant que vecteur d'hydrogène, bien que ce stockage à coûts minimisés demeure un véritable défi. Son utilisation requiert une excellente connaissance des propriétés des matériaux, capables de promouvoir ces réactions catalytiques, dans des conditions de température de fonctionnement abaissée. Dans ce contexte, la thèse se propose d'étudier la synthèse, les performances et la caractérisation de matériaux mixtes à base de ruthénium, métal noble, et d'amidure de lithium, ayant des propriétés catalytiques intéressantes pour décomposer l'ammoniac et libérer l'hydrogène stocké.

Au niveau expérimental, la comparaison des performances catalytiques entre les divers systèmes sélectionnés (ruthénium seul, amidure de lithium seul et les deux matériaux en contact) a montré que l'amidure de lithium a un effet promoteur sur la cinétique de la décomposition de l'ammoniac dans le cas du matériau mixte.

Afin d'interpréter ce résultat, des modèles théoriques inédits ont été développés. Le premier objectif du travail théorique était d'étudier les interfaces catalytiques solide-solide entre les matériaux considérés dans le travail expérimental (ruthénium en contact avec amidure de lithium), d'un point de vue thermodynamique. Des calculs de type théorie de la fonctionnelle de la densité en condition périodique ont ainsi été menés pour modéliser ces interfaces complexes, qui étaient principalement non stœchiométriques, polaires et magnétiques. Compte tenu de la complexité des systèmes il a été nécessaires d'utiliser différentes fonctionnelles d'échange et de corrélation électronique, avec prise en compte des interactions faibles de type van der Waals.

L'étude théorique a montré que le contact entre le ruthénium et l'amidure de lithium est préférentiel lorsque ce sont les plans aminyles de l'amidure qui sont adsorbés sur la surface du ruthénium. Une analyse électronique détaillée de type Bader a montré qu'il existe un transfert de charges du métal vers l'amidure de lithium.

Le second objectif du volet théorique concernait l'étude mécanistique et cinétique de la décomposition de l'ammoniac aux interfaces catalytiques entre le ruthénium et l'amidure de lithium. Pour cela des modèles

plus sophistiqués entre l'amidure de lithium (hydrogénation totale), l'imidure de lithium (déshydrogénation partielle), le nitrure de lithium (déshydrogénation totale) et le ruthénium ont dû être développés. Les calculs ont montré que ces interfaces multiples sont plutôt favorables par comparaison aux interfaces précédentes.

La recherche de chemins réactionnels de recombinaison des atomes d'azote adsorbés en surface du ruthénium pour former la molécule de diazote a montré que le lithium du matériau nitrure n'est pas spectateur au cours de la réaction. Il joue un rôle promoteur en accompagnant le mouvement des atomes d'azote dans l'acte élémentaire du mécanisme, aboutissant ainsi à un abaissement de la barrière d'énergie d'activation. Ce résultat totalement original reproduit de manière remarquable la tendance observée dans les mesures expérimentales.

Ce travail expérimental et théorique a ainsi permis de progresser sur la compréhension du fonctionnement de ces catalyseurs au niveau fondamental. Il ouvre des perspectives prometteuses quant à l'utilisation future de l'ammoniac comme vecteur d'hydrogène.

Abstract

In the field of energy and environment, it has become essential to change energy sources and fasten an energy transition which fails to progress in many industrial sectors. The energy production must be redesigned to be as environmentally friendly as possible. The goal is to eliminate carbon, the weak point of our current economy. Among the promising solutions, hydrogen appears to be a central element in decarbonization. It offers a clean alternative to fossil fuels, particularly for heavy industry and transport sector. Ammonia represents an excellent option as a hydrogen carrier, although its storage at minimized costs remains a real challenge. Its use requires excellent knowledge of the properties of materials, able of promoting these catalytic reactions, under conditions of low operating temperature. In this context, the PhD thesis aims to study the synthesis, performance and characterization of mixed materials containing ruthenium, a noble metal, and lithium amide, with interesting catalytic properties for decomposing ammonia and releasing stored hydrogen.

At the experimental level, the comparison of the catalytic performances between the various selected systems (ruthenium alone, lithium amide alone and the two materials in contact) showed that lithium amide has a promoting effect on the kinetics of ammonia decomposition in the case of the mixed material.

In order to interpret this result, new theoretical models were developed. The first objective of the theoretical work was to study the solid-solid catalytic interfaces between the materials considered in the experimental work (ruthenium in contact with lithium amide), from a thermodynamic point of view. Density functional theory calculations in periodic boundary conditions were thus carried out to model these complex interfaces, which were mainly non-stoichiometric, polar and magnetic. Given the complexity of the systems, it was necessary to use different electronic exchange and correlation functionals, taking into account weak van der Waals interactions. The theoretical study showed that the contact between ruthenium and lithium amide is preferential when the aminyl planes of the amide are adsorbed on the ruthenium surface. A detailed Bader analysis showed that there is a charge transfer from the metal to the lithium amide.

The second objective of the theoretical part concerned the mechanistic and kinetic study of the decomposition of ammonia at the catalytic interfaces between ruthenium and lithium amide. For this, more sophisticated models between lithium amide (total hydrogenation), lithium imide (partial dehydrogenation), lithium nitride (total dehydrogenation) and ruthenium had to be developed. Calculations showed that these multiple interfaces are rather favorable compared to previous interfaces. The search for reaction pathways for the recombination of nitrogen atoms adsorbed on the ruthenium surface to form the dinitrogen molecule showed that the lithium in the nitride material is not spectator during the reaction. It plays a promoting role

by accompanying the movement of nitrogen atoms in the elementary act of the mechanism, thus leading to a lowering of the activation energy barrier. This totally original result remarkably reproduces the trend observed in experimental measurements. This experimental and theoretical work has thus made it possible to progress in understanding the functioning of these catalysts at the fundamental level. It opens promising perspectives for the future use of ammonia as a hydrogen carrier.

Introduction

In order to meet the pressing need to decarbonize our economy and lessen the effects of global, the energy transition is an essential first step.[1] In addition to lowering dependence on fossil fuels, diversifying energy sources and carriers also helps to ease economic, environmental, and geopolitical tensions.[2] As a result, the integration of renewable energy sources has far-reaching impacts across various levels of society. Among the promising solutions, hydrogen emerges as a versatile energy carrier and a pivotal element toward decarbonization. Hydrogen has potential in a number of areas, such as industrial, power generation, and transportation.[3, 4] Hydrogen can be produced sustainably through water electrolysis, and its reaction with oxygen produces only water and heat, making it a cleaner and environmentally friendly alternative to fossil fuels.[4] Its high energy density (120 $kJ.kg^{-1}$) and clean combustion properties, position hydrogen as a promising building block for a carbon-neutral energy economy.[5, 4]

However, unlike traditional liquid fuels, H_2 exists as a gas at room temperature and pressure, presenting significant practical challenges. Its extremely low density (0.09 g/L under standard conditions) requires substantial storage volumes, making efficient storage a major obstacle.[6] To address this issue, many hydrogen storage systems aim to densify H_2. To overcome the limitations associated with storing pure hydrogen, various hydrogen carriers—such as metal hydrides,[6, 4] liquid organic hydrogen carriers (LOHCs),[7] and ammonia[4, 8]—have been proposed.

Ammonia stands out among hydrogen carriers due to its relatively simple liquefaction process at moderate pressures, well-established worldwide production infrastructure, and high hydrogen content (17.6% by weight).[4, 8] Its effectiveness as a hydrogen carrier is intrinsically linked to its ability to decompose into nitrogen and hydrogen. However, the high-temperature conditions required for breakdown and the high-pressure needs for synthesis severely limit the energy efficiency of this process.[8, 9] This work focuses on optimizing ammonia decomposition through the development of advanced catalytic systems, with the aim of improving energy efficiency by lowering the reaction conditions.

An ideal catalyst for ammonia decomposition must be both highly efficient at the lowest possible operating temperatures and economically viable. Among the materials studied, ruthenium (Ru) has demonstrated exceptional catalytic performance for this process.[10] However, its high cost, limited availability, and the relatively demanding operating conditions associated with its use necessitate the exploration of alternatives.[11] Since other transition metals (TM) fail to match ruthenium's catalytic performance,[10], alternative catalytic systems are investigated, such as alkali and alkaline-earth metal amides.[12, 13, 14]

In particular, lithium amide ($LiNH_2$) coupled with transition metals (TM) has shown promising catalytic performance for ammonia decomposition.[15, 16, 17] Recent advancements have highlighted the potential of Ru-based catalysts enhanced with lithium amide, where the synergy between Ru and $LiNH_2$ significantly improves catalytic activity.[15] Despite the promising performance of TM-$LiNH_2$ catalysts, the underlying catalytic mechanisms remain poorly understood, limiting further advancements in efficiency and selectivity.

This thesis aims to address these challenges by investigating Ru-$LiNH_2$ catalytic system for ammonia decomposition, providing crucial mechanistic insights and paving the way for improved catalyst TM-$LiNH_2$ designs.

To address these challenges, this thesis adopts a combined theoretical and experimental approach. Density functional theory (DFT) calculations are used to investigate the electronic and structural properties of the Ru-$LiNH_2$ system and to simulate reaction pathways. Experimentally, the catalytic performance is evaluated through material synthesis, structural characterization, and performance testing under relevant reaction conditions.

The present manuscript is structured into seven main parts. The first chapter provides a comprehensive review of hydrogen as an energy carrier, focusing on the existing hydrogen storage technologies and their limitations, with an emphasis on ammonia. This chapter also explores the catalytic processes involved in the synthesis and decomposition of ammonia, along with the corresponding catalysts, highlighting the significance and potential of lithium amide-based catalysts.

The second chapter outlines the experimental methodology employed in this study. It includes the synthesis and characterization techniques for Ru-$LiNH_2$-based catalysts, as well as the evaluation of their catalytic performance for ammonia decomposition and the accompanying kinetic analysis.

The third chapter presents the fixed-bed reactor developed to evaluate the performance of the catalysts. This reactor was specifically designed to accommodate lithium amide properties, less common in heterogeneous catalysis. A commercial ruthenium catalyst supported on alumina was employed to validate the setup. Subsequently, this chapter focuses on the catalytic performance, material characterization, and detailed insights into the structural and chemical properties of Ru-$LiNH_2$-based materials when used as catalyst for ammonia decomposition.

The fourth chapter marks the beginning of the theoretical component of this work by presenting the theoretical methodology employed throughout the study. It discusses the principles of density functional theory (DFT), with particular attention to the exchange-correlation functionals used. Additionally, the chapter provides details on the implementation of periodic DFT calculations using a plane-wave basis set.

The fifth chapter begins with the selection of the most appropriate exchange-correlation functionals for DFT calculations. The development of interface models between Ru(0001) and $LiNH_2$(001) is then introduced, starting with an analysis of the different possible $LiNH_2$(001) surfaces. Various interface models were optimized, taking into account the effects of $LiNH_2$(100) thickness, stoichiometry, and polarity, as well as the inclusion of spin polarization and van der Waals interactions.

The sixth chapter focuses on developing a catalytic model to elucidate the reaction mechanism of ammonia decomposition. This model aims to enrich the interface with lithium through dehydrogenation processes. By predicting the bulk and surface properties of Li_3N and Li_2NH, a new partially hydrogenated interface model with Ru(0001) was developed as reactivity model.

The seventh chapter focuses on the recombinant desorption of nitrogen from Ru(0001)/Li_3N(001) interface, a dehydrogenated reactivity model. This is followed by an investigation into the adsorption and dehydrogenation of ammonia at the interface of the reactive model. To evaluate the influence of lithium on catalytic performance, an equivalent delithiated model is also analyzed for comparison.

The final section of the manuscript summarizes the conclusions and key findings of this work. Additionally, potential perspectives are proposed to further advance and deepen the understanding of the catalytic mechanism of Ru-$LiNH_2$-based catalysts.

Contents

Remerciments ii

Résumé v

Abstract viii

Introduction xi

I Bibliography 5
- I.1 Importance of energy vectors in the energy transition . . . 7
- I.2 Hydrogen as an energy carrier . . . 8
  - I.2.1 Physical and chemical properties . . . 9
  - I.2.2 Hydrogen production . . . 9
  - I.2.3 Energy recovery from hydrogen . . . 14
  - I.2.4 Hydrogen utilizations . . . 15
- I.3 Hydrogen Storage and Transport . . . 16
  - I.3.1 Physical-based hydrogen storage . . . 17
  - I.3.2 Chemical-based hydrogen storage . . . 20
  - I.3.3 Comparison of storage and transportation efficiency . . . 33
- I.4 Ammonia in the chemical industry . . . 37
  - I.4.1 History and role of ammonia . . . 37
  - I.4.2 Properties of ammonia . . . 37
  - I.4.3 Safety and precautions . . . 37
  - I.4.4 Ammonia synthesis . . . 38
  - I.4.5 Recent developments . . . 39
- I.5 Ammonia Decomposition Reaction . . . 43
  - I.5.1 Reaction thermodynamics . . . 43
  - I.5.2 Ammonia Decomposition Catalysts . . . 46
- I.6 Conclusion . . . 65

II Experimental approach 68
- II.1 Chemicals . . . 69
- II.2 Catalysts preparation methods . . . 71
  - II.2.1 Catalyst synthesis . . . 71
  - II.2.2 Catalyst purification . . . 74
- II.3 Measurement of catalytic activity . . . 76
  - II.3.1 Fixed bed reactor . . . 76

II.3.2 Quantification of ammonia decomposition . . . 79
II.3.3 Activation energy measurement . . . 81
II.4 Catalysts characterization . . . 81
II.4.1 X-Ray Diffraction (XRD) . . . 81
II.4.2 Inductively coupled plasma atomic emission spectroscopy (ICP-AES) . . . 82
II.4.3 Thermogravimetric Analysis (TGA) and Differential Scanning Calorimetry (DSC) . . . 84
II.4.4 Raman spectroscopy . . . 84
II.4.5 Fourier-Transfer InfraRed (FTIR) spectroscopy . . . 84
II.4.6 Scanning Electron Microscopy Energy-Dispersive X-Ray Spectroscopy (SEM-EDX) . . . 85
II.5 Key calculations . . . 85
II.6 Appendix . . . 87

III Evaluation of catalytic performance **88**
III.1 Experimental setup for catalytic activity measurement . . . 89
III.1.1 Prerequisite . . . 89
III.1.2 Catalyst bed: material and fastening . . . 90
III.1.3 Ammonia detection limit measurement . . . 95
III.1.4 Comparison of commercial Ru/Al_2O_3 catalyst performance to literature . . . 95
III.1.5 Implementation of the Ru dosage method by ICP-AES . . . 99
III.2 Lithium amide: catalytic activity and activation energy . . . 100
III.3 Ruthenium and lithium amide couple: catalytic activity and activation energy . . . 107
III.3.1 $Ru\text{-}LiNH_2$ . . . 107
III.3.2 $Ru\text{-}LiNH_2/MgO$ . . . 114
III.4 Lithium nitride: catalytic activity and activation energy . . . 120
III.5 Conclusion . . . 125
III.6 Appendix . . . 127

IV Theoretical approach **131**
IV.1 Schrödinger equation . . . 132
IV.2 Fundamental approximation . . . 132
IV.2.1 Born-Oppenheimer approximation . . . 132
IV.2.2 Hartree and Hartree-Fock methods . . . 133
IV.3 Density functional theory (DFT) . . . 134
IV.3.1 Hohenberg and Kohn theorems . . . 134
IV.3.2 Kohn and Sham equations . . . 135
IV.3.3 Approximations of the exchange-correlation functional . . . 136
IV.4 Plane-wave basis set . . . 139
IV.4.1 Interest . . . 139
IV.4.2 Pseudopotential: PAW method . . . 139
IV.5 Catalyst modeling and search of thermodynamic states . . . 140
IV.5.1 Valence electrons . . . 140
IV.5.2 Atoms and molecules . . . 140
IV.5.3 Bulks . . . 141
IV.5.4 Bulk-modulus calculation . . . 142
IV.5.5 Surface and adsorption models . . . 143
IV.5.6 Interface models . . . 144
IV.6 Search of transition states and kinetic study . . . 145
IV.6.1 Constrained geometry optimization . . . 145

IV.6.2 Improved dimer method . . . 145
IV.6.3 Geometry refinement and Quasi-Newton algorithm . . . 147
IV.6.4 Minimal energy pathway and Intrinsic-reaction-coordinate (IRC) . . . 147
IV.7 DFT software: VASP . . . 148
IV.7.1 Computational details . . . 148
IV.7.2 Computational tool and environment (PSMN mesocenter) . . . 148

V Solid-solid interface models of ruthenium and lithium amide 149
V.1 Bulk Materials and choice of exchange-correlation functional . . . 150
V.1.1 Ru bulk . . . 150
V.1.2 $LiNH_2$ bulk . . . 151
V.2 Clean Surfaces . . . 153
V.2.1 Ru(0001) surface . . . 153
V.2.2 $LiNH_2$ surfaces . . . 154
V.3 Adsorptions on Ru(0001) . . . 160
V.3.1 Li adsorption . . . 160
V.3.2 NH_2 adsorption . . . 161
V.4 Ruthenium-Lithium Amide Interfaces . . . 162
V.4.1 Prerequisites for interfacing the two solids . . . 162
V.4.2 Case of $LiNH_2$(001) reconstruction . . . 166
V.4.3 Ru(0001)-$LiNH_2$(001) interface energies results . . . 167
V.4.4 Bader charge analysis . . . 171
V.5 Conclusion . . . 173
V.6 Appendix . . . 175

VI DFT models of ruthenium and lithium amide catalytic interfaces for ammonia decomposition 185
VI.1 Hydrogenated and hollow interface model Ru(0001)/$LiNH_2$(001) . . . 187
VI.1.1 Plain and hydrogenated interface: Ab initio molecular dynamics simulations . . . 187
VI.1.2 Hollow and hydrogenated interface: static DFT model . . . 190
VI.1.3 Reactivity hypothesis: formation of N_2 via NLi_2 species adsorbed on Ru(0001) . . . 191
VI.1.4 Conclusion . . . 194
VI.2 Dehydrogenation of $LiNH_2$ at the Ru(0001) surface . . . 196
VI.2.1 Dehydrogenation Models and thermodynamic analysis . . . 196
VI.2.2 Hydrogen adsorption sites . . . 197
VI.2.3 Dihydrogen formation from $LiNH_2$ at the Ru(0001) surface . . . 199
VI.2.4 Conclusion . . . 204
VI.3 Partially hydrogenated interface model: Ru(0001)/Li_3N(001)/Li_2NH(001)/ $LiNH_2$(001)/Gas . . . 205
VI.3.1 Preliminary study of lithium nitride and lithium imide . . . 205
VI.3.2 Partially hydrogenated interface model . . . 216
VI.3.3 Conclusion . . . 220
VI.4 Conclusion . . . 221
VI.5 Appendix . . . 222

VII Catalytic DFT models of ruthenium and lithium nitride dehydrogenated catalytic interface 231
VII.1 Simplified catalyst model for reactivity study: dehydrogenated Ru(0001)/ Li_3N(001) interface 232
VII.1.1 Optimized structure of Ru(0001)/Li_3N(001) interface . . . 232
VII.1.2 Equivalent delithiated ruthenium surface model: Ru(0001)/8N . . . 234

VII.2 Transition states search and kinetic study . . . 235
VII.2.1 Atomic nitrogen coadsorption structures . . . 236
VII.2.2 Comparison: effect of lithium . . . 238
VII.2.3 Bader charge analysis . . . 246
VII.2.4 Conclusion . . . 248
VII.3 Catalyst regeneration and ammonia decomposition from thermodynamics . . . 249
VII.3.1 Successive ammonia adsorption and dissociation steps . . . 249
VII.3.2 Comparison: effect of lithium . . . 252
VII.3.3 Conclusion . . . 254
VII.4 Overall comparison of all studied reactivity models . . . 256
VII.5 Conclusion . . . 260
VII.6 Appendix . . . 262

Conclusion and perspectives **268**

References **271**

Chapter I

Bibliography

Contents

I.1 Importance of energy vectors in the energy transition . . . 7
I.2 Hydrogen as an energy carrier . . . 8
I.2.1 Physical and chemical properties . . . 9
I.2.2 Hydrogen production . . . 9
I.2.2.1 Thermochemical production . . . 10
I.2.2.2 Electrochemical production . . . 11
I.2.2.3 Hydrogen production from biomass . . . 11
I.2.2.4 Cost comparison of hydrogen gas production . . . 12
I.2.3 Energy recovery from hydrogen . . . 14
I.2.4 Hydrogen utilizations . . . 15
I.3 Hydrogen Storage and Transport . . . 16
I.3.1 Physical-based hydrogen storage . . . 17
I.3.1.1 Compressed hydrogen gas . . . 18
I.3.1.2 Underground hydrogen storage . . . 19
I.3.1.3 Liquid hydrogen . . . 19
I.3.1.4 Cryo-compressed hydrogen . . . 20
I.3.2 Chemical-based hydrogen storage . . . 20
I.3.2.1 Solid storage . . . 21
I.3.2.1.1 Hydrogen adsorption . . . 21
I.3.2.1.2 Metal hydrides . . . 23
I.3.2.1.2.a Binary hydrides . . . 24
I.3.2.1.2.b Interstitial metal hydrides . . . 25
I.3.2.1.3 Complex metal hydrides . . . 25
I.3.2.1.3.a Alanates . . . 25
I.3.2.1.3.b Borohydrides . . . 26
I.3.2.1.3.c Metal Amides . . . 26
I.3.2.1.4 Ammonia borane . . . 27
I.3.2.2 Liquid storage . . . 28
I.3.2.2.1 Liquid Organic Hydrogen Carriers (LOHC) . . . 28
I.3.2.2.2 Circular hydrogen carrier . . . 29
I.3.2.2.2.a Methanol . . . 29
I.3.2.2.2.b Formic acid . . . 30
I.3.2.2.2.c Ammonia . . . 31
I.3.3 Comparison of storage and transportation efficiency . . . 33

I.4 Ammonia in the chemical industry . . . 37
I.4.1 History and role of ammonia . . . 37
I.4.2 Properties of ammonia . . . 37
I.4.3 Safety and precautions . . . 37
I.4.4 Ammonia synthesis . . . 38
I.4.4.1 Reaction thermodynamics . . . 38
I.4.4.2 Haber-Bosh process . . . 39
I.4.5 Recent developments . . . 39
I.4.5.1 Electrochemical approach . . . 40
I.4.5.1.1 Direct nitrogen reduction . . . 40
I.4.5.1.2 Indirect nitrogen reduction . . . 41
I.4.5.2 Chemical-looping approaches . . . 42
I.5 Ammonia Decomposition Reaction . . . 43
I.5.1 Reaction thermodynamics . . . 43
I.5.1.1 Mechanism of catalyzed ammonia decomposition . . . 44
I.5.1.2 Similarities and differences with ammonia synthesis . . . 45
I.5.2 Ammonia Decomposition Catalysts . . . 46
I.5.2.1 Metal-based catalysts . . . 46
I.5.2.1.1 Active metals for ammonia decomposition . . . 46
I.5.2.1.2 Supports for metal catalysts . . . 48
I.5.2.1.3 Promoters for metal catalysts . . . 49
I.5.2.1.4 Deactivation of ruthenium catalysts . . . 50
I.5.2.1.5 Application limits of ruthenium . . . 50
I.5.2.2 Alternatives to ruthenium . . . 50
I.5.2.2.1 Challenges with alternative active metals . . . 50
I.5.2.2.2 Bimetallic catalysts . . . 51
I.5.2.2.3 Transition metal nitrides and carbides . . . 52
I.5.2.2.4 Alkaline or alkaline earth metal amides . . . 53
I.5.2.2.4.a Sodium amide . . . 53
I.5.2.2.4.b Lithium amide . . . 53
I.5.2.2.4.c Plasma treatments of lithium amide . . . 57
I.5.2.2.4.d Theoretical study of lithium amide . . . 57
I.5.2.2.4.e Impact of the reaction medium on the catalytic performance of lithium amide . . . 58
I.5.2.2.4.f Support for lithium amide-based catalyst . . . 58
I.5.2.2.5 Alkaline metal amide and transition metal pairs . . . 60
I.5.2.2.5.a Lithium amide and ruthenium . . . 60
I.5.2.2.5.b Theoretical study of lithium amide and ruthenium catalyst . . . 62
I.5.2.2.5.c Lithium amide and transition metal nitrides . . . 63
I.5.2.2.5.d Theoretical study of lithium amide and iron . . . 64
I.6 Conclusion . . . 65

I.1 Importance of energy vectors in the energy transition

Primary energies are forms of energy naturally found in the environment, including non-renewable energy resources (such as oil, coal and natural gas), nuclear energy and renewable energy resources (like wind, solar, geothermal, biomass and hydropower).[18, 19] While some primary energy sources can be used directly, they more often require conversion into secondary energy carriers (such as electricity, gasoline, or steam) to enhance usability and transportability. These energy carriers are ultimately consumed as final energy in various applications, providing mechanical work, heat, or powering chemical and physical processes.[19] The combination of various primary energy sources utilized to fulfill energy requirements is commonly known as the energy mix.[20] This composition fluctuates across countries or regions and over time. Depending on factors such as accessibility to resources, import potential, scale and nature of energy demands, and prevailing policies. These policies, shaped by historical, economic, social, demographic, environmental, and geopolitical dynamics, play a pivotal role in shaping the composition of the energy mix.[21] On a global scale, fossil fuels overwhelmingly dominate the energy mix, accounting for more than 81% of total energy consumption.[22]

The diversification of energy sources and vectors is crucial for ensuring energy security. Expanding the energy mix reduces dependence on a single source, thereby mitigating risks associated with geopolitical, environmental, and economic tensions. Integrating renewable energy into the mix promotes energy independence while significantly lowering greenhouse gas emissions. Moreover, diversification enhances system flexibility, allowing for dynamic adjustments to energy supply in response to evolving market demands and technological advancements.[2]

Energy diversification goes beyond sources to include energy carriers, which facilitate the transfer and utilization of energy across different times and locations from its original source.[19, 23] Exploring innovative and efficient energy carriers enhances the resilience of energy systems, optimizes resource utilization, and supports a more sustainable and comprehensive energy transition. Advancing research into new energy carriers is thus critical for accelerating progress in diversifying the energy mix and ensuring a safer, cleaner, and more adaptable energy future.[23]

Furthermore, the development of efficient energy vectors for storing intermittent energy is crucial in transitioning to a more sustainable energy system. The energy transition stands as a pivotal objective in this regard. Renewable energy sources like solar and wind are intermittent, operating only under specific weather conditions.[24] However, electricity demand doesn't always coincide with their production periods, resulting in excess energy being wasted.[25] Consequently, energy storage is imperative to balance electricity supply and demand, ensuring grid stability.

Energy storage can be achieved through various methods, each offering increasing potential for large-scale storage capacities: mechanical < thermal < electrochemical < chemical energy. Each approach presents distinct advantages and drawbacks, including factors such as energy density, capacity, price, and scalability.[3]

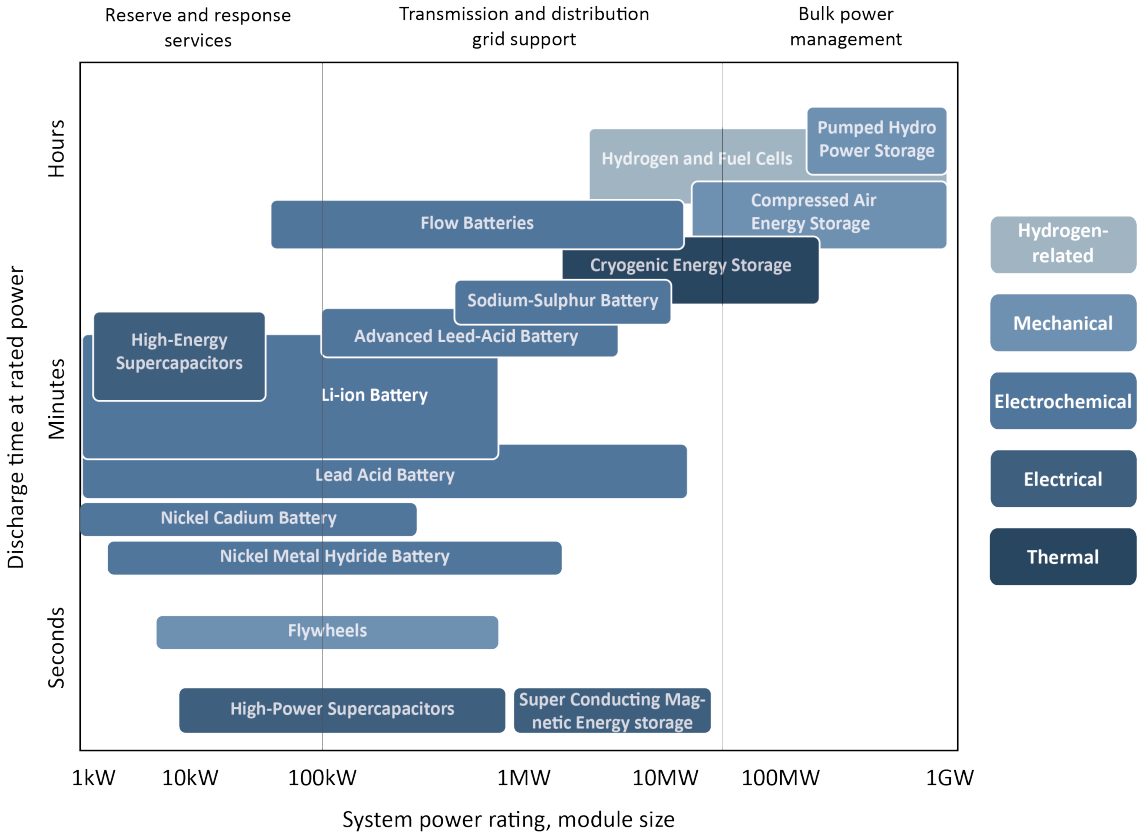

Figure I.1: Comparison of energy storage technologies in terms of storage capacity and discharge time (adapted from [26]).

Mechanical energy storage systems, such as pumped-hydro and compressed air energy storage, have the potential to achieve gigawatt-scale storage capacities, surpassing those of electrochemical and electrical energy storage methods like batteries and supercapacitors (see Figure I.1). However, the utilization of compressed air energy storage is constrained by geographical conditions, such as the availability of lakes in mountainous regions or suitable underground salt caverns.[27] Chemical energy storage, as hydrogen, holds the greatest potential for large-scale energy storage, surpassing even the scale depicted in Figure I.1.[3] Energy storage methods utilizing hydrogen include storing compressed hydrogen gas in large stationary tanks or underground cavities, as well as utilizing liquid hydrogen or liquid hydrogen carriers.[28]

I.2 Hydrogen as an energy carrier

Energy storage with hydrogen depends on the production of hydrogen, achievable through diverse synthesis methods like water electrolysis or steam reforming of methane. Once produced, hydrogen can be stored or transported to desired locations.[29] This principle allows hydrogen to serve as a flexible energy carrier. There are various methods to recover the energy stored in hydrogen, each tailored to the specific form of energy

desired. While combustion[30] and fuel cells (FC)[31] are the main pathways for energy conversion.

I.2.1 Physical and chemical properties

Hydrogen, with its unique physical and chemical properties, serves as a versatile resource across various industries. Occupying the primary position in the periodic table of chemical elements with atomic number 1 and electronic configuration $1s^1$, is predominantly composed of the stable isotope ^1H (one proton and zero neutron), known as protium. Additionally, a minor fraction of terrestrial hydrogen (0.015% on average) comprises deuterium ^2H (one proton and one neutron). Alongside these stable isotopes, there exists a third variant, tritium ^3H (characterized by one proton and two neutrons) which is unstable. Tritium is generated during nuclear fission reactions.[32]

The physicochemical properties of hydrogen make it exceptionally versatile and distinct among elements. In terms of its physical attributes, its lightness positions it *as the lightest element in the periodic table*.[33] Under standard conditions of room temperature and atmospheric pressure, it exists in a gaseous state, composed of diatomic molecules (H_2), devoid of color, odor and taste. It is highly flammable and burns with a clean flame, making it an ideal fuel for numerous applications.[32] The bond dissociation energy of H_2 is 436 $kJ.mol^{-1}$ (or 4.52 eV), and its equilibrium bond length is 0.074 nm (or 0.74 Å).[34] At standard temperature and pressure (STP) conditions, its density is measured at 0.0899 $g.L^{-1}$.[32] Hydrogen gas exhibits a melting point of −259.2°C, a boiling point of 252.9 °C, and solidifies at -259.3 °C and standard atmospheric pressure.[35] Chemically, hydrogen exhibits a diverse range of potential chemical bonds, encompassing both covalent and ionic interactions. It forms covalent H–H bonds through electron pairing between two hydrogen atoms, metallic bonds (H^0) by electron sharing with a group of atoms, hydride ions (H^-) by electron acceptance, and cations (H^+) through electron donation.[36]

On Earth, hydrogen gas is present in the atmosphere, albeit at a very low concentration of about 0.5 parts per million by volume.[32] The primary source of hydrogen is water, comprising two hydrogen atoms and one oxygen atom per molecule. The reaction between H_2 and O_2 to form water releases 241.826 $kJ.mol^{-1}$ of energy, making it a process known for environmentally clean energy release.[33] Hydrogen is also a fundamental element in all living matter, being closely associated with carbon in organic compounds. Nearly all biological molecules contain hydrogen, such as proteins and DNAs.[33] For instance, hydrogen constitutes 63% of the atoms and 10% of the mass in the human body.[37]

I.2.2 Hydrogen production

As previously mentioned, hydrogen is mostly found in organic compounds and water, making pure H_2 rare in nature. This is why pathways for H_2 production are essential. Presently, the global annual production of hydrogen exceeds 50 million tons. Regrettably, the vast majority, estimated at 95% or more, is derived from petrochemical feedstocks.[33, 38] Nearly half of the global hydrogen supply is derived from natural gas reforming[39] (see Figure I.2).

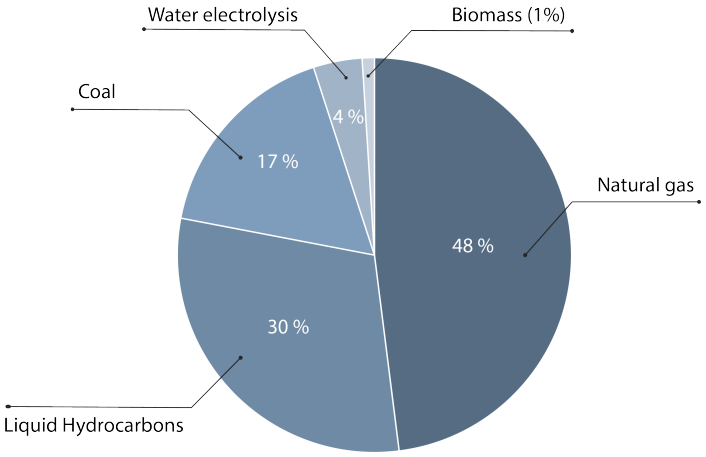

Figure I.2: Feedstock distribution for hydrogen gas production (adapted from [38] and [39]).

As hydrogen can obtained from different primary energy sources and process, hydrogen production technologies are often classified based on different colors. In scientific literature, grey hydrogen typically refers to methods that rely on fossil fuel inputs without carbon capture, utilization, and storage (CCUS).[40] However, for coal gasification, difference can be made, leading to terms like 'brown hydrogen' for brown coal and 'black hydrogen' for black coal.[41] It's worth noting that these terms are less common and are usually grouped under grey hydrogen.[40] When hydrogen is derived from fossil fuels but with CCUS technology, it is classified as blue hydrogen.[42] Turquoise hydrogen is produced from fossil fuels through methane pyrolysis, but unlike other methods, the by-product is solid carbon instead of CO_2.[43] Green hydrogen is produced through water electrolysis using electricity sourced from renewable energy. This form of hydrogen holds particular significance in the shift towards a more sustainable energy and transportation infrastructure.[40] While yellow hydrogen refers to hydrogen produced by water electrolysis using grid electricity.[40] Purple hydrogen is generated through electrolysis using electricity derived from nuclear power sources. While it attracts attention, particularly in regions like China[44] and Russia,[45] it is not commonly featured in European hydrogen strategies. The color classification system serves as a useful shorthand for understanding the carbon footprint and sustainability of different hydrogen production methods.

I.2.2.1 Thermochemical production

The thermochemical production of hydrogen encompasses diverse processes exploiting heat to drive chemical reactions, thereby liberating hydrogen gas. These methods commonly entail the generation of H_2 and carbon monoxide through the utilization of fossil fuels. Thermochemical production stands as the predominant method in the hydrogen market (96%). Fossil resources primarily originate from natural gas (48%), oil (30%), and coal (18%).[39] Among the prevalent industrial techniques are reactions involving hydrocarbons with water (such as steam reforming using liquid or gaseous fuel and steam-gasification using solid fuel), oxygen (like partial oxidation (POx) and gasification), and a sequence involving both oxygen and water (as seen in auto-thermal reforming).[46, 47] Each method offers distinct advantages and challenges in the produc-

tion of hydrogen for various industrial applications.

The challenges associated with thermocatalytic hydrogen production stem from both the use of fossil fuels as reactants and the high energy demand of these processes. Typically, these reactions occur at elevated temperatures and pressures. The prevalent method, steam methane reforming (SMR), involves the reaction of methane (CH_4) with water steam under high temperatures (700-1100°C) and pressures (between 3-25 atm),[46] facilitated by a Ni catalyst.[47] Finally, it's essential to note that the hydrogen generated requires purification downstream of the synthesis process.

I.2.2.2 Electrochemical production

Instead of relying on hydrocarbons for hydrogen production, water can serve as an alternative source. Through processes like electrolysis,[48] photo-reduction,[49] and thermolysis,[50] water molecules can be split into their constituent elements, oxygen (O_2) and hydrogen (H_2). The most promising method for water splitting is electrolysis, capable of producing high-purity hydrogen (>99.999%).[51] Despite its potential, the practical implementation of water electrolysis has faced significant challenges, including relatively low efficiency and high production costs compared to hydrocarbon reforming methods.[52]

Various technologies are employed for water electrolysis, including alkaline electrolyser,[46, 53] polymer electrolyte membrane (PEM),[54, 55] and solid oxide electrolyte (SOE) methods.[46, 52] Alkaline electrolysis is known for its simplicity and relatively lower capital costs. However, it exhibits lower efficiency and higher electrical energy consumption,[46] making it less suitable for large-scale applications where efficiency is needed. Nonetheless, it often boasts superior cost-effectiveness over its acidic counterpart.[50] On the other hand, PEM electrolysis offers higher efficiency and faster response times, making it more suitable for dynamic operation and integration with renewable energy sources like solar and wind. Additionally, PEM electrolyzers are compact and modular, allowing for easier scalability and deployment in various settings.[54] However, PEM technology tends to be more expensive due to the materials used, such as Nafion membranes and noble catalysts like platinum or platinum alloys.[55] SOE, while less common than the two previous technologies, offers higher efficiency. Operating at elevated temperatures, SOE systems can facilitate faster reaction kinetics and reduce the energy input required for water splitting.[46] However, SOE is a less mature technology, and there are still challenges related to material durability, regarding corrosion, seals, thermal cycling, and chrome migration.[52]

I.2.2.3 Hydrogen production from biomass

Unlike traditional methods reliant on fossil fuels, hydrogen can also be produced using biomass as a feedstock, presenting a more sustainable alternative. Biomass sources encompass a variety of materials, including energy crops, agricultural residues and waste, forestry residues and waste, as well as industrial and municipal wastes.[56] The production of hydrogen from biomass can be classified into two main categories: thermochemical and biological processes.

The thermochemical pathway for synthesizing hydrogen from biomass encompasses several processes, including pyrolysis,[57] gasification,[58] and supercritical water gasification.[58] These processes bear similarities to their petrochemical counterparts, underscoring the significance of their advancement.[56] However, these processes can yield both liquid and gaseous by-products, necessitating the use of purification systems. Additionally, their energy demands are considerable as high temperatures and pressures are needed.[59]

Biological production of hydrogen (biohydrogen) involves the metabolic processes of (micro)organisms, the different process are direct biophotolysis, indirect biophotolysis, biological water-gas shift (WGS) reaction, photo-fermentation and dark fermentation. These synthesis pathways hold promise as they enable the production of biohydrogen from water and biomass at standard operating temperatures and pressures. they are still in the early stages of development, with the primary objective being to improve their efficiency and significantly reduce costs to enhance the competitiveness of biohydrogen production.[59]

I.2.2.4 Cost comparison of hydrogen gas production

Assessing hydrogen production costs requires navigating a complex interplay of economic, environmental, and geopolitical factors. These costs depend not only on the chosen production method but also on variable factors such as raw material expenses, regulatory frameworks, and global resource distribution disparities. For instance, Russia, which holds the world's largest natural gas reserves (25%) and the second-largest coal reserves (18%), has experienced significant geopolitical disruptions since the onset of the Russia-Ukraine conflict in 2022. This conflict has led to a sharp increase in fossil resource prices, directly impacting the cost of hydrogen production. The cost of hydrogen produced from natural gas with Carbon Capture and Storage (CCS) has tripled compared to pre-crisis levels, now ranging between 5.3 and 8.6 USD/kg H_2, with natural gas contributing 75% of this cost.

While hydrogen derived from fossil fuels remains one of the most cost-effective options, it is also among the most environmentally harmful. Steam Methane Reforming (SMR) without CCS generates between 8 and 12 kg of CO_2 per kg of H_2 produced. Incorporating CCS technology to capture up to 93% of emissions can reduce this to 1.5–6.2 kg CO_2/kg H_2, but CCS certainly adds to the cost of the resulting hydrogen (see Figure I.3). Regional disparities further influence production economics; in the Middle East, where natural gas and coal are abundant, hydrogen production costs range from 0.6–1.0 USD/kg H_2 for unabated natural gas and 1.0–1.4 USD/kg H_2 with carbon capture.

In regions facing fluctuating natural gas prices, water electrolysis could emerge as a more economically viable alternative. However, this method requires substantial electrical energy, often derived from non-renewable sources, which can exacerbate carbon emissions depending on the electricity's origin. For example, using the 2021 global grid electricity mix, hydrogen production via electrolysis can result in up to 24 kg CO_2/kg H_2, comparable to coal gasification without CCS (see Figure I.3). In contrast, regions with low-emission electricity, such as Sweden, achieve significantly lower emissions—just 0.5 kg CO_2/kg H_2.

Nuclear electricity offers a promising avenue for powering electrolyzers, reducing emissions to 0.1–0.3 kg CO_2/kg H_2, even accounting for uranium mining, conversion, enrichment, and fuel fabrication. Similarly, renewable energy sources yield low emissions; onshore wind energy results in 0.4–0.8 kg CO_2/kg H_2, while solar energy emissions range from 0.9–2.5 kg CO_2/kg H_2, primarily due to the manufacturing of photovoltaic modules. Despite their environmental advantages, these renewable and nuclear options generally incur higher costs than traditional fossil-fuel-based methods, underscoring the economic challenges of transitioning to greener hydrogen production technologies.

Given the US Department of Energy's target price for hydrogen at 2.30 USD/kg established in 2020, the development of renewable hydrogen sources faces limitations.[60] Additionally, the initial investment costs vary across different technologies, with electrolysis-based methods notably more expensive than SMR. Furthermore, electrolysis plants generally have a shorter lifespan compared to SMR facilities. Both alkaline and PEM electrolyzers exhibit also lower efficiency rates than SMR. However, solid oxide electrolyzers are still in the developmental stage but show promising efficiency for hydrogen production.[61]

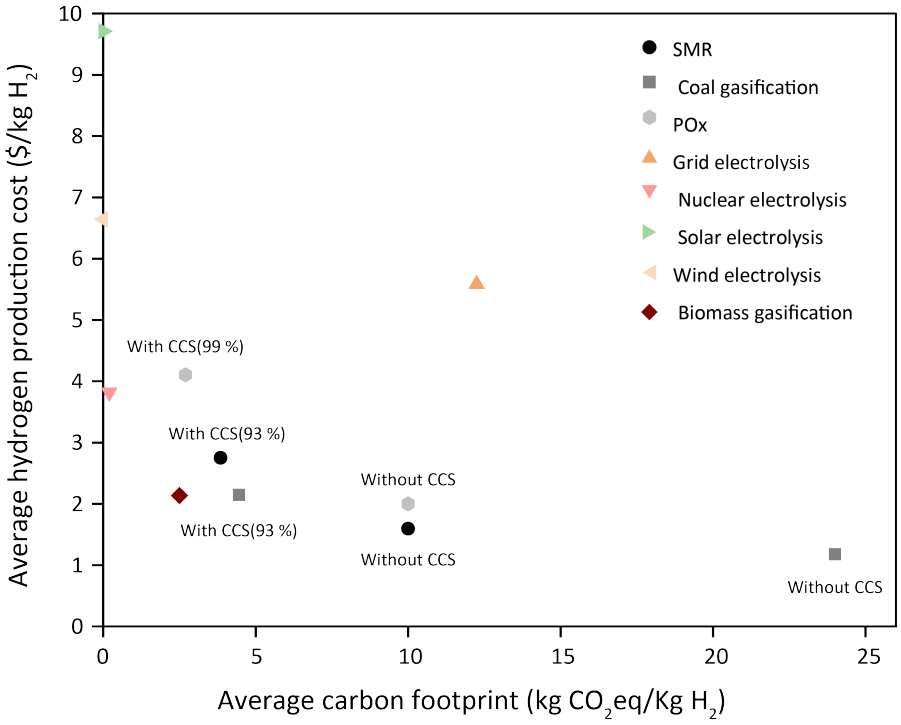

Figure I.3: Average hydrogen production costs (USD/kg H_2) are plotted against the average carbon footprint (kg CO_2/kg H2) of various technologies. With POx being partial oxidation of hydrocarbons; the average carbon footprint of grid electrolysis based on global grid average of 2021; the average carbon footprint of SMR-CCS based on 93% of carbon capture while the average price is based on SMR-CCS with 61% carbon capture. Adapted from[62, 63, 64, 65, 66, 67, 68, 69].

I.2.3 Energy recovery from hydrogen

Hydrogen combustion occurs when H_2 reacts with oxygen in the presence of heat or a flame, producing water and releasing energy.[30] This process can be utilized in gas turbines, which can be adapted to burn hydrogen for generating electricity or mechanical power.[35] Additionally, hydrogen combustion can also be performed with internal combustion engines (ICEs). These engines function similarly to their gasoline or diesel counterparts, with hydrogen replacing traditional fuels.[34] Hydrogen ICEs may use spark ignition, where a spark plug ignites the hydrogen-air mixture (as in gasoline engines),[70] or compression ignition, where the heat generated from compressing the hydrogen-air mixture triggers ignition (as in diesel engines).[71]

As mentioned earlier, the utilization of FC is another significant method of harnessing the energy stored through hydrogen formation. In FCs, a chemical reaction occurs between hydrogen and oxygen to produce electricity, water, and heat.[31] This direct transformation of chemical energy into electrical energy offers the potential for increased energy efficiency compared to traditional combustion-based power generation methods.[72]

Fuel cells can be classified into several types based on the electrolyte material used and the operating conditions (see Figure I.4). Solid oxide fuel cells (SOFCs) are a variant of fuel cell technology employing a solid ceramic material, such as yttria-stabilized zirconia, as the electrolyte. They operate at elevated temperatures ranging from 600 to 1000°C.[73] Molten carbonate fuel cells (MCFCs) utilize a mixture of molten carbonate salts, including lithium and potassium carbonates, as the electrolyte. They operate at high temperatures between 600 and 700°C.[74] SOFCs and MCFCs are well-suited for applications such as large-scale stationary power generation and combined heat and power systems.[73, 74] Phosphoric acid fuel cells (PAFCs) use liquid phosphoric acid as the electrolyte. Operating at moderate temperatures (between 150 and 220°C), PAFCs are well-suited for various applications, including stationary power generation and combined heat and power systems.[29] Proton exchange membrane fuel cells (PEMFC) use a polymer membrane (such as Nafion) as the electrolyte. Operating at relatively low temperatures (between 50 and 100°C), PEMFCs offer quick start-up times and versatility for various applications. Including transportation (fuel cell electric vehicles), portable power, and small-scale stationary power generation.[75] Alkaline fuel cells (AFC) utilize a liquid alkaline solution (such as KOH) as the electrolyte. Operating at moderate temperatures (from 60 to 250°C), AFC are well-suited for specialized applications such as spacecraft, submarines, and limited stationary power generation.[76]

While promising, the use of fuel cells is not without limitations. One key limitation is the high cost of FC technology, specially PEMFCs, primarily due to the expensive materials such as platinum used as catalysts.[29] Additionally, the durability and lifespan of FC remain a concern, as they can degrade over time. Particularly in harsh operating conditions (like high temperature), affecting their long-term reliability and cost-effectiveness.[78] Despite these limitations, FCs offer numerous advantages. They operate with minimal noise, can be designed in various sizes and capacities, making them suitable for a wide range of applications (from portable electronics to large-scale power generation). Additionally, they boast remarkable efficiency

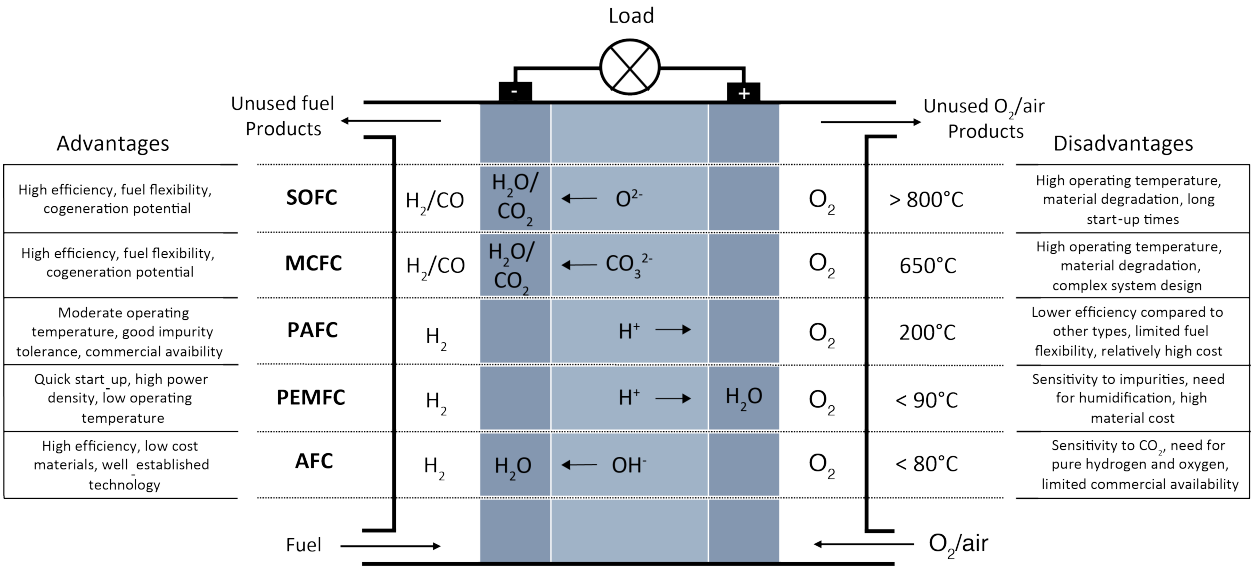

Figure I.4: Overview of different fuel cell types, temperature range, reactants, advantages and disadvantages (adapted from [29] and [77]).

and produce minimal CO_2 emissions, among other benefits.[29]

With such technologies available to convert stored energy through hydrogen formation, interest in this mode of energy storage is steadily rising. Indeed, hydrogen is increasingly acknowledged as a promising alternative to traditional fossil fuels across various sectors, with the highest gravimetric energy among all energy carriers (i.e., lower heating value (LHV) of roughly 120 $MJ.kg^{-1}$). Its potential application extends beyond transportation to include the storage of intermittent renewable energies.[3] Given that emissions from transportation are among the primary contributors to greenhouse gas emissions, hydrogen is envisioned as a key player in reducing such environmental impacts.[79] While hydrogen boasts high energy content, its gaseous state under normal temperature and pressure results in a low density of 0.09 $g.L^{-1}$. Consequently, both gaseous and liquid hydrogen exhibit a low volumetric density (0.16 $MJ.L^{-1}$ and 8.5 $MJ.L^{-1}$ respectively), making their storage and distribution challenging.[80] It's worth noting that hydrogen's small molecular size poses challenges for hydrogen storage reactors due to permeability issues.[81] Furthermore, hydrogen tends to react with the metals used in pipelines.[82]

I.2.4 Hydrogen utilizations

Hydrogen, as discussed in Section I.2, serves as an efficient energy carrier that can be converted into electricity using fuel cells without emitting air pollutants. Beyond energy conversion, hydrogen plays a pivotal role in various industrial processes, functioning as both a feedstock and a fuel.

In steel production, hydrogen is a valuable reducing agent, providing an environmentally friendly alternative to traditional carbon-based reductants like coke. By directly reducing iron ore with hydrogen, greenhouse

gas emissions are significantly reduced. For instance, hydrogen direct reduction—a process that uses hydrogen to produce direct reduced iron—substantially lowers emissions compared to conventional blast furnace methods.[83]

Hydrogen is also critical in ammonia production, an essential component of fertilizers. Through the Haber-Bosch process, nitrogen and hydrogen react under high pressure and temperature to synthesize ammonia.[84] Similarly, hydrogen is integral to methanol production, where it reacts with carbon dioxide (CO_2) or carbon monoxide. Utilizing hydrogen from renewable sources alongside captured CO_2 enables "green methanol" production, reducing greenhouse gas emissions.[85]

In the petrochemical industry, hydrogen is extensively used in refining processes such as hydrocracking, hydrotreating, and hydrodesulfurization. These treatments effectively remove impurities like sulfur and nitrogen, improving product quality and reducing harmful emissions.[86] Additionally, hydrogen acts as a reactant in the production of various chemicals, including hydrogen peroxide, hydrochloric acid, and other essential compounds.[87]

In the semiconductor industry, hydrogen serves as a carrier gas and cleaning agent, enabling the production of high-purity silicon wafers and eliminating contaminants during manufacturing processes.[88] Its versatility and utility in these and other industrial applications significantly enhance product quality and sustainability.[89]

However, hydrogen's use also introduces challenges, including safety concerns related to storage, handling, inherent flammability, and the risk of metal component degradation from hydrogen embrittlement.[90] Furthermore, the costs associated with hydrogen production, storage, and distribution can hinder its widespread industrial adoption, especially when inexpensive fossil fuels remain readily available.[91]

Despite these challenges, ongoing advancements in hydrogen production methods, storage technologies, and integration into industrial processes aim to enhance its efficiency and cost-effectiveness. These efforts are paving the way for broader utilization of hydrogen across industries, supporting cleaner and more sustainable manufacturing practices.[29]

I.3 Hydrogen Storage and Transport

As mentioned previously, hydrogen is regarded as a pivotal energy carrier in future energy systems worldwide. The development of safe, compact, lightweight, and cost-efficient hydrogen storage is paramount for establishing a hydrogen economy. This emerging hydrogen economy necessitates both mobile and stationary storage systems. While stationary storage systems are less constrained by volume and weight compared to their mobile counterparts, they can also operate at higher temperatures and pressures and occupy larger spaces. Nonetheless, the availability of suitable materials for stationary storage tanks remains a significant

challenge. Mobile hydrogen storage systems have distinct requirements to fulfil to be effective. Onboard hydrogen storage demands low-operating pressure and temperature, fast hydrogen uptake/release kinetics with minimal energy loss and multicycle reversibility, low formation heat to minimize the required energy for hydrogen release, high stability against oxygen and moisture, and high safety with public acceptance. Additionally, an overly heavy storage system can limit the vehicle's range, while excessive volume may reduce available luggage space.[92]

For mobile hydrogen applications, hydrogen carriers need to fulfil several key criteria. Firstly, they must exhibit a high gravimetric density of hydrogen. The U.S. Department of Energy (US DoE) has set a target for hydrogen gravimetric density at 6 wt%, while the European VII FP call has raised this objective to 8 wt%. Secondly, the selected carriers should have a low hydrogen release temperature under the operating conditions of a PEM fuel cell. Thirdly, they need to demonstrate high rates of hydrogen absorption and desorption. Lastly, hydrogen carriers should be economically viable.[93]

Hydrogen's stability enables long-term energy storage, with various available technologies aiming to densify hydrogen for practical use.[94] The primary methods of hydrogen storage include physical technologies, such as compressed gas, liquid hydrogen, and cold/cryo compressed storage, as well as chemical storage methods like physical absorbents, complex metal hydrides, interstitial hydrides, circular hydrogen carriers such as liquid organic hydrogen carriers (LOHC), and chemical hydrogen (see Figure I.5). The choice of hydrogen storage technology depends on their respective strengths and weaknesses, as well as the specific requirements of the application in terms of size and area.[92]

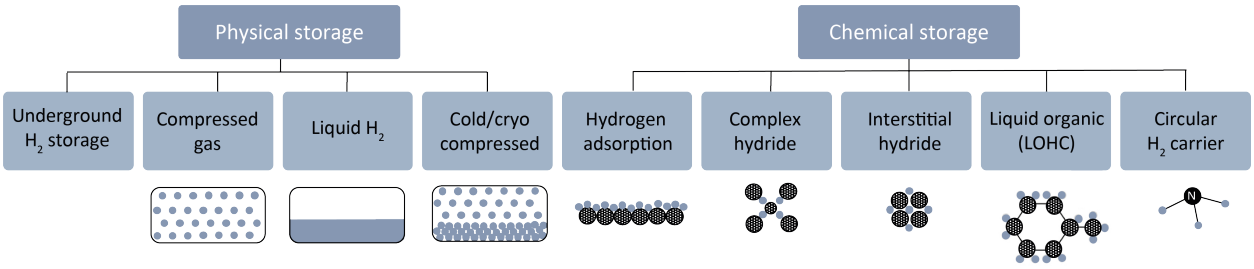

Figure I.5: Illustration of various hydrogen storage technologies.

I.3.1 Physical-based hydrogen storage

Among the possibilities, hydrogen physical-based storage technologies enable hydrogen to be stored in a more compact and efficient manner, facilitating its use as an energy carrier in various applications. These methods typically involve compressing hydrogen gas to high pressures or cooling it to very low temperatures to reduce its volume and increase its density, thereby enhancing transportability and storage capabilities.[94] In the following, several alternatives are introduced in this context.

This section will explore various physical-based hydrogen storage methods, including compressed hydrogen

gas, underground hydrogen storage, liquid hydrogen, and cryo-compressed hydrogen.

I.3.1.1 Compressed hydrogen gas

High-pressure compression is the most common method for storing hydrogen, offering notable advantages in terms of energy density and ease of setup. The technology allows for straightforward retrieval of hydrogen when needed. Additionally, this approach efficiently packs a significant amount of hydrogen into a compact volume, making it suitable for applications with space constraints, like vehicles and small-scale energy systems. Its widespread use in hydrogen FC electric vehicles, such as the Toyota Mirai,[95, 96] Honda Clarity, and Hyundai Nexo.[95] Moreover, current FCs typically require hydrogen compressed to specific pressures, typically ranging between 35 to 70 MPa.[92]

While increasing the compression of hydrogen might seem like a straightforward solution to enhance storage efficiency, the reality is more nuanced. Unlike some gases, the volumetric density of hydrogen doesn't increase linearly with pressure.[97] Therefore, a balance must be struck between the amount of stored hydrogen and the associated costs. Typically, hydrogen compression is maintained within the range of 350 to 700 bar. At the upper limit of this range, for instance, utilizing lightweight polymer fibber-reinforced vessels, the hydrogen storage system weighs approximately 125 kg. This translates to a hydrogen weight percentage of 5% and a volumetric density of 30 $g.L^{-1}$.[98]

Concerns surrounding hydrogen storage primarily center on the risk of leaks, especially given the high compression required for storage. Safety remains a top priority, particularly in embedded applications where the potential for container rupture or hydrogen accumulation in confined spaces, such as underground parking areas, poses significant hazards.[99] High-pressure storage vessels are categorized into four main types:[100]

- Type I vessels: The traditional choice, constructed entirely of steel. These containers are highly durable and offer excellent safety features but are significantly heavy.
- Type II vessels: Address weight concerns by integrating composite materials, such as carbon fibers, while retaining a thin metal inner liner (usually steel or aluminum) to maintain airtightness.
- Type III vessels: Further reduce weight by combining a carbon fiber-reinforced composite core with an aluminum liner. This design provides substantial strength while being lighter than Type II vessels.
- Type IV vessels: The lightest option, utilizing advanced composite materials like carbon fiber-reinforced plastic without requiring a metal liner. These containers boast the best weight-to-strength ratio but may involve higher manufacturing costs.

Each type offers unique trade-offs between weight, cost, and safety, tailored to meet the diverse demands of hydrogen storage applications. However, compressing hydrogen involves a significant energy cost and generates heat during the process. The associated costs with hydrogen compression can amount to 11-13% of the energy stored, adding to the overall expense of the storage process.[101]

I.3.1.2 Underground hydrogen storage

Underground hydrogen storage involves storing hydrogen in underground geological formations such as salt caverns, empty oil or gas reservoirs, or aquifers. A notable advantage of this approach is its scalability, offering significant potential for mid to long-term and large-scale storage of compressed hydrogen.[92] To ensure the integrity of the storage and prevent leaks, the chosen geological formation must feature solid rock structures and an inert layer, as hydrogen can react with certain minerals to form carbonates.[102]

Salt caverns emerge as particularly promising sites for underground hydrogen storage, although they currently constitute only 8% of the global capacity. Presently, only four artificial salt caverns are being utilized for this purpose.[103] Notably, the cavern located in Spindletop, USA, stands out with a volume of 906,000 m^3 and an operational pressure of 200 bar. It has the capacity to store up to 500 GWh of hydrogen, equivalent to approximately 0.02% of France's primary energy consumption in 2020.[104]

Nevertheless, underground hydrogen storage facilities face challenges associated with geological events such as earthquakes and can be complex to design and monitor effectively.[105] Furthermore, these geological formations are limited in availability, and competition for their use exists with other underground gas storage solutions like carbon dioxide.[106] Despite these challenges, ongoing research and technological advancements aim to address these limitations and optimize the utilization of underground hydrogen storage for enhanced energy security and sustainability.

I.3.1.3 Liquid hydrogen

Liquid hydrogen storage offers several advantages, primarily due to its high density of 70.8 $g.L^{-1}$. Cooling hydrogen to extremely low temperatures induce a phase transition into a liquid state, greatly reducing its volume and enabling higher storage densities, up to 1.5-2 times compared to compressed hydrogen.[107] However, hydrogen liquefaction is a challenging process due to its liquid phase existing within a narrow temperature range. Liquid hydrogen must be stored in cryogenic tanks at -253°C, its boiling point at atmospheric pressure.[108]

It's crucial to note that hydrogen has a low critical point, meaning it must be stored in an open system to prevent it from reverting to a gaseous state. Otherwise, in a closed vessel, the pressure could rise to 104 bar at ambient temperature.[108] In addition to these challenges, heat transfer from the surroundings to the liquefied hydrogen is inevitable, even with the most effective insulation.[109] This ongoing heat transfer, gradually warms the liquid hydrogen, leading to vaporization. Furthermore, hydrogen gas consists of 75 mol% orthohydrogen and 25 mol% parahydrogen (referring to nuclear spin isomers), while liquid hydrogen primarily exists in the para form. Consequently, liquefying hydrogen necessitates the conversion of orthohydrogen to parahydrogen,[110] a process that occurs slowly and releases heat (ΔH = 525 $kJ.kg^{-1}$). A catalyst is often incorporated into the heat exchanger to facilitate this conversion. As a result of these factors, hydrogen gas can form within the storage vessel. To maintain a constant pressure, this excess gas must be vented from the vessel, this essential step is known as "boil-off", as cryogenic vessels are not designed to withstand pressure.[109]

Liquid hydrogen has gained significant attention as a potential fuel for aircraft, presenting a promising alternative to mitigate emissions from the conventional fossil fuels used in the aviation industry.[111] The concept of cryoplanes capitalizes on the high energy density and environmentally friendly nature of liquid hydrogen, offering the potential for extended-range flights.[112] Airbus is spearheading efforts to introduce the world's first commercial flight utilizing zero-emission cryoplane technology, with potential deployment as early as 2035.[113] This initiative represents a significant step towards reducing the environmental impact of aviation and advancing sustainable air travel.

While liquid hydrogen offers a higher energy density than compressed hydrogen, the challenges of storing it in liquid form present significant drawbacks. Open storage systems present challenges for thermal efficiency. The current system experiences a loss of approximately 1.5 wt% of hydrogen per day.[114] Moreover, the hydrogen liquefaction process is highly energy-intensive, requiring roughly 10 to 15 kWh to liquefy 1 kg of H_2, equating to 30–40% of the energy contained in the stored hydrogen. Additionally, there is the issue of hydrogen loss via the boil-off process, further compounded by the cost of super-insulated cryogenic containers.[115] These factors collectively highlight the complex and costly nature of liquid hydrogen storage.

I.3.1.4 Cryo-compressed hydrogen

Cryogenic-compressed hydrogen storage, also known as cryo-compressed hydrogen storage, offers a hybrid solution that combines the advantages of both liquid and compressed hydrogen storage methods. This technology involves cooling hydrogen to cryogenic temperatures (-253°C) and then compressing it to pressures at least 30 MPa,[116] surpassing the hydrogen critical pressure of 13 bar.[107] By doing so, cryo-compressed hydrogen achieves high storage densities of approximately 80 $g.L^{-1}$, surpassing those of liquid hydrogen, while circumventing the challenges associated with storing hydrogen in its liquid form.[117] Moreover, this approach enhances safety by eliminating the need of hydrogen boil-off and for open storage systems.[117, 116] In dormancy period tests, cryo-compressed hydrogen vessels filled up to 85% of their capacity demonstrated the capability to retain hydrogen without any losses for up to 7 days.[118] However, challenges such as the energy requirements for cooling and compression,[116] as well as the complexity and cost of implementing specialized cryogenic equipment, as type III vessel is to be used,[117] remain significant considerations for widespread adoption.

I.3.2 Chemical-based hydrogen storage

To establish hydrogen as a viable energy carrier, achieving high energy density while minimizing production costs is essential. Physical hydrogen storage technologies, though effective, often demand substantial energy inputs, compromising their overall efficiency and economic viability. Chemical hydrogen storage, in contrast, offers a promising alternative for efficient and practical hydrogen utilization. By binding hydrogen within chemical compounds rather than relying on temperature and pressure modifications, chemical storage provides several advantages, including higher energy density, improved safety during handling, and

on-demand hydrogen release through reversible hydrogenation and dehydrogenation processes. However, challenges such as significant energy requirements for hydrogen release, slow reaction kinetics, and potential material degradation must be addressed for broader adoption.

This section explores various chemical-based hydrogen storage technologies, categorized into two main groups: solid storage, which includes hydrogen adsorption, metal hydrides, and ammonia borane, and liquid storage, which includes liquid organic hydrogen carriers (LOHCs) and circular hydrogen carriers. Each technology is presented and analyzed with a focus on its advantages, limitations, and potential for future development.

I.3.2.1 Solid storage

I.3.2.1.1 Hydrogen adsorption

Hydrogen adsorption is sometimes categorized as chemical and sometimes as physical hydrogen storage due to the dual nature of its interactions. Physical adsorption occurs when hydrogen molecules adhere to a solid material's surface via weak van der Waals forces, with enthalpies of adsorption/desorption typically ranging from 1 to 10 $kJ.mol^{-1}$.[119] While these weak interactions enable manageable heat transfer,[120] hydrogen storage capacity at room temperature is limited. Enhanced storage is achieved by lowering the temperature around -196 °C and applying pressures around 50-100 bar, improving adsorption significantly.[121]

A substance absorbed by another material is named the absorbate when it penetrates the bulk (sub-surface), or the adsorbate when it adheres to the surface. Conversely, the material that facilitates this process is referred to as the absorbent or adsorbent depending on the interaction. For hydrogen, certain materials feature pores and channels large enough to accommodate hydrogen molecules. Porous materials are commonly used as adsorbents, with their performance depending on key factors such as specific surface area, pore size, and structural morphology. These materials are categorized based on pore size into microporous (pore diameter < 2 nm), mesoporous (pore diameter between 2 and 50 nm), and macroporous (pore diameter > 50 nm).[122] Microporous materials with a high surface area are exceptionally well-suited for hydrogen adsorption. Given that adsorption primarily occurs at the material's surface, materials with extensive and accessible surface areas are ideal. Various materials have been explored as potential absorbents for hydrogen adsorption, including microporous carbon structures, zeolites, polymers of intrinsic microporosity (PIM), metal-organic frameworks (MOF),[94] and water clathrates. These materials offer diverse pore structures and surface chemistries.

- **Carbon nanomaterials**

Microporous carbon-based materials, including nanotubes, graphite nano-fibbers, solid foams, fullerenes, and activated carbon, have attracted significant interest as absorbents for hydrogen physisorption owing to their high specific surface area, microporosity, low mass, and strong adsorption capacity. Hydrogen adsorption tests conducted on carbon nanotubes (CNTs) have shown a hydrogen content of 1.7 wt% at room

temperature and 12 MPa.[123] Similarly, activated carbon demonstrates a hydrogen content of around 5 wt.% at 77K and 30-60 MPa.[124] Potential increases is observed when adsorption is conducted at cryogenic temperatures, reaching up to 6.5 wt.% of hydrogen for activated carbon.[125] However, some adsorption tests yield inconsistent results, such as those for K-doped CNTs, where hydrogen absorption can vary between 1.8[126, 127] to 14 wt% under the same operating conditions.[126] Such discrepancies have led to speculation that results beyond 1 wt%H_2 could be attributed to experimental errors, possibly due to leaks.[127] Furthermore, considering the high hydrogen desorption temperatures, typically around 400 K,[128] the collective findings have led to the conclusion that they fail to meet the necessary technical criteria to serve as effective storage solutions for hydrogen.[107]

- **Zeolites**

Another type of material considered as sorbent is zeolites. Also known as molecular sieves, zeolites are composed of an aluminosilicate negatively charged framework counterbalanced by exchangeable metal cations. Zeolites offer microporous structures with a high specific surface area and precise control over pore size. However, the heavier atoms in zeolites compared to carbon affect their gravimetric capacity for hydrogen storage.[129] The adsorption behavior of hydrogen on zeolites is temperature-dependent. At higher temperatures, zeolites become more activated, facilitating hydrogen adsorption. Nonetheless, the quantity of stored hydrogen is not significantly affected by high temperatures, with reported maximums of only 0.8 wt% of H_2 adsorbed.[130] At room temperature, achieving hydrogen storage in zeolites requires high pressures, resulting in less than 0.1 wt% of hydrogen stored.[131] The highest hydrogen storage capacity observed in zeolites, such as CaX, was obtained at cryogenic temperatures (77 K) at 15 bar, reaching only 2.19 wt% of H_2,[132] which is close to the theoretical maximal capacity of 2.86 wt%.[133] These low storage capacities render zeolites unsuitable for practical applications as a hydrogen vector.

- **Polymers of intrinsic microporosity (PIM)**

In the polymers domain, PIMs have emerged as candidates for hydrogen storage due to their unique structural characteristics. Their rigid framework forms a densely interconnected network of micropores, on the nanometre scale, offering a vast surface area for hydrogen adsorption.[134] Moreover, PIMs offer remarkable design versatility, enabling tailored modifications of their monomer structures to enhance hydrogen storage capabilities.[135] Additionally, these materials are lightweight, cost-effective, and ease of processing. Despite these advantages, PIMs, like carbon-based materials, require cryogenic temperatures and high pressures to achieve adequate hydrogen storage capacities. The quantity of hydrogen stored by adsorption by PIMs remains insufficient, with a gravimetric capacity 1.7 wt% of hydrogen at -196°C and 10 bar.[135] Nevertheless, ongoing research activities aim to enhance the storage properties of PIMs by incorporating additional physical sorbents, indicating a promising pathway for advancing their efficacy in hydrogen storage applications.[136]

- **Metal-Organic Frameworks (MOF)**

Among the most promising materials, MOFs have attracted considerable attention for hydrogen storage applications due to their distinctive structural properties. MOFs consist of metal atoms or clusters coordinated with organic ligands, forming highly porous crystalline structures with large surface area. Notably, they feature adjustable and uniform pore sizes, along with well-defined sites for hydrogen occupancy.[137] One of the key advantages of MOFs is their structural versatility, enabling precise customization by selecting metal ions and organic linkers. This versatility allows MOFs to serve various purposes, including catalysis, gas storage, separation, biomedical imaging, and more.[138] This opens up possibilities for organic linkers and metals combinations to tailor pore size and specific surface area to enhance hydrogen adsorption capacities. At cryogenic temperatures, DUT-32 exhibits a gravimetric density of 14.21 wt% of H_2 at 88 bar,[139] comparable to NU-1501-Al, which achieves 14.5 wt% of hydrogen at 100 bar.[140] The gravimetric densities of MOFs are notably high, positioning them as promising candidates for hydrogen storage via physisorption. However, at room temperature, the hydrogen storage capacity of MOFs typically hovers around 1 wt%.[141] Ongoing research efforts continue to explore novel MOF formulations and functionalization aimed at overcoming these limitations and realizing the full potential of MOFs for hydrogen storage.

Water clathrates have attracted considerable attention as potential candidates for hydrogen storage due to their unique lattice-like structure formed by water molecules. Within this structure, small gas molecules such as H_2, CH_4, and CO_2 can be trapped inside cavities created by water molecules bound via hydrogen bonds.[142] Hydrogen water clathrates has demonstrated the capability to store a significant quantity of hydrogen, up to 11.2 wt% for the stoichiometric H_2:H_2O.[143] However, the formation of these clathrates typically occurs under cryogenic temperatures or extreme pressures ranging from 2500 to 6000 bar.[144] The addition of promoters like tetrahydrofuran (THF) can stabilize clathrate formation and reduce the required temperature and pressure. Nonetheless, this comes at the cost of reduced gravimetric hydrogen storage capacity, often dropping to around 1-2 % or less depending on the applied pressure.[145] The demanding formation conditions required for water clathrates pose challenges to their efficient use as hydrogen storage media.

In conclusion, absorbents offer advantages such as high specific surface areas, adjustable pore sizes, and well-defined hydrogen adsorption sites, which contribute to their ability to store hydrogen efficiently. But challenges remain, particularly regarding achieving high storage capacities at ambient temperatures and pressures. While cryogenic temperatures and high pressures can enhance hydrogen adsorption, they also introduce practical limitations and energy costs.

I.3.2.1.2 Metal hydrides

In the solid phase, metal hydrides present an interesting option for hydrogen storage, presenting several advantages over alternative methods. These compounds are formed when hydrogen molecules dissociate on the surface of metals or metal alloys, leading to the formation of stable compounds where hydrogen atoms are chemically bound.[117] This process, known as chemisorption, causes the lattice structure to expand by

20-30%, enabling the storage of hydrogen within the bulk of the material.[146] Hydrides are formed through direct hydrogenation of the metal (as depicted in Equation I.1).

$$M + \frac{x}{2} H_2 \leftrightarrow MH_x \quad \text{(I.1)}$$

where M is the metal or alloys. The dehydrogenation of hydrides requires a decrease in pressure or an increase in temperature to reform the metallic phase and release H_2.[147] Metal hydrides offer enhanced safety and higher hydrogen storage capabilities compared to hydrogen compression and liquefaction, all achieved under more moderate temperature and pressure conditions.[107] Metal hydrides demonstrate excellent cyclability, with the loading and release of hydrogen capable of being repeated extensively. For instance, magnesium-based metal composite hydrides have been shown to maintain their performance for up to 2000 cycles.[148] However, their reversibility can be disrupted by impurities.[107] On the other hand, metal hydrides exhibit low sorption and desorption kinetics, requiring relatively more time for hydrogen absorption and release. Additionally, they often require high temperatures for hydrogen release and can produce undesirable gases during dehydrogenation.[147, 149] It's essential to note that metal hydrides are sensitive to both water and air. Exposure to oxygen initiates the gradual formation of a passivation layer composed of oxides, hydroxides, and carbon-oxygen compounds. Consequently, removing this layer becomes necessary to enhance the hydrogenation kinetics.[150]

The classification of hydrides depends on the bonding mechanism between hydrogen and the metallic material: ionic hydrides (characterized by ionic bonding); covalent hydrides (exhibiting covalent bonding); and interstitial metal hydrides (demonstrating metallic bonding). Ionic and covalent hydrides are referred to as complex metal hydrides.[117]

I.3.2.1.2.a Binary hydrides

Ionic hydrides, also known as binary hydrides, are salt with a high degree of ionic character, such as LiH and NaH.[117] These compounds offer high volumetric and gravimetric energy densities,[107] but they require harsh conditions of temperature and pressure for hydrogenation and dehydrogenation. For instance, LiH provides a high gravimetric energy density of 7.7 wt%, but its hydrogen release requires temperatures above 900°C.[151] While typical ionic hydrides are thermally stable toward dehydrogenation, magnesium hydride (MgH_2) stands out as an exception. This is attributed to the partially ionic and partially covalent interaction between hydrogen and magnesium in MgH_2,[117] which enables hydrogen release at a moderate temperature range of 350-400 °C with a reaction enthalpy of 75 $kJ.mol^{-1}$.[152] With a gravimetric energy density of 7.6 wt% and a volumetric density twice that of liquid hydrogen (110 $g.L^{-1}$), MgH_2 is extensively studied among binary hydrides.[153] Added to this, magnesium is an inexpensive and abundant metal. However, MgH_2 formation requires a high temperature of approximately 300 °C and pressures exceeding 30 bar.[46] Micro and nano-structuring, achieved through particle size reduction via ball-milling, has been extensively researched to enhance the hydrogenation and dehydrogenation properties of binary hydrides.[154] This approach seeks to enhance their thermal and mechanical stability while also optimizing their thermodynamic and kinetic

properties.[155] Alloying binary hydrides with transition metals such as Ti, V, Mn, Ni, and Fe enhance thermodynamics, hydrogenation and dehydrogenation kinetics, and stability.[156] For example, Mg_2NiH_4 exhibits improved kinetics and can be formed at 280°C under 1 bar pressure. However, alloying often results in a reduction in gravimetric density; for Mg_2NiH_4, it decreases to 3.6 wt% of hydrogen.[157] Carbon-based materials, mesoporous silica, zeolites, and MOFs can be incorporated into binary hydrides to enhance hydrogen physisorption, H_2 dissociation, stability by mitigating metal hydride agglomeration, and improving desorption thermodynamics and kinetics.[158] For instance, mixing graphite with MgH_2 enables hydrogen loading at around 200°C.[159] Finally, metallic catalysts can also enhance the kinetics of hydriding. The presence of a Pd catalyst, for instance, can reduce the hydrogenation time by half.[152]

I.3.2.1.2.b Interstitial metal hydrides

Interstitial metal hydrides, also known as intermetallic hydrides, are compounds formed by combining two metals with hydrogen, wherein the hydrogen atoms occupy interstitial sites within the metallic lattice structure.[150] The intermetallic hydride system ($A_mB_nH_x$) typically involves an element with a strong affinity for hydrogen (A), such as Mg,[160, 161] Ti, and La,[161] coupled with an element with a lower affinity for hydrogen (B), as Mn, Fe, Co, and Ni.[160] Variations in the hydride's composition from the partial substitution of elements A, B, or both (e.g., AB_5, AB_2, A_2B and so forth) alter the crystal structure. These modifications influence the size of the interstitial sites, thereby affecting the properties related to hydrogen absorption.[162] The primary appeal of such compounds lies in their close to normal temperature and pressure operating conditions.[107] However, this characteristic also raises safety concerns, particularly regarding the potential hazards associated with unintended hydrogen release.[163]

I.3.2.1.3 Complex metal hydrides

Complex metal hydrides consist of metal cations, such as Li,[147, 164] Na,[164] Mg or Zn,[147] bonded with complex anions containing hydride ions, such as $[AlH_6]^{-3}$, $[AlH_4]^{-1}$, $[BH_4]^{-1}$,[164, 6] $[NH_2]^{-1}$.[164] As complex metal are primarily formed from light elements in Groups I, II et III of the periodic table, they offer higher storage density.[165] The main types of complex hydrides for hydrogen storage include alanates and borohydrides.

I.3.2.1.3.a Alanates

Alanates are complex hydrides containing aluminium, with hydrogen atoms octahedrally or tetrahedrally coordinated.[147] Sodium alanate ($NaAlH_4$) is a well-studied complex hydride, containing 7.4 wt% of hydrogen.[166] Its dehydrogenation process occurs in two steps until the formation of sodium hydride (NaH). Since NaH is a binary hydride, it exhibits a high dehydrogenation temperature of 425°C.[46] Consequently, the dehydrogenation of NaH is not considered in this process, resulting in a total dehydrogenation of only 5.6 wt% of H_2.[116] The release of hydrogen from complex hydrides like alanates exhibits slow kinetics,[166] often requiring high temperatures ranging from 185 to 260°C.[167] Rehydrogenation happens at temperatures of 200 to 400°C and pressures between 10 and 40 MPa, presenting challenges in achieving full reversibility of the process.[166]

I.3.2.1.3.b Borohydrides

Borohydrides are complex hydrides containing boron and are more stable than alanates,[107] they can content up to 10[162] to 18 wt%[168] of hydrogen. Among these materials, $LiBH_4$ has been extensively studied and offers an exceptionally high hydrogen storage capacity of 18.5 wt%. However, it is challenging to dehydrogenate, as only 13.5 wt% of hydrogen can be released above 380°C.[147] $LiBH_4$ also dehydrogenizes until its binary hydride form (LiH), which is also considered the final stage of dehydrogenation due to the high temperature required to continue. $LiBH_4$ formation occurs at a high temperature of 650 °C and a hydrogen pressure of 150 bar.[169] Likewise, $NaBH_4$ is also a well-known borohydride with a hydrogen content of 10.8 wt%. Its dehydrogenation temperature (400°C) to form NaH is similar to $LiBH_4$. The formation of alkali metal amidoborane, $LiNH_2BH_3$ and $NaNH_2BH_3$ can help reduce the dehydrogenation temperature around 90°C, however they are irreversible.

I.3.2.1.3.c Metal Amides

Another type of complex hydride used for hydrogen storage is the metal imide/amide pair. In these compounds, metal cations are bonded to amide ions $[NH_2]^-$ or imide ions $[NH]_{-2}$. The general formula for metallic amides is $M(NH_2)_x$, while for metallic imides it is $M(NH)_x$. These materials have been extensively studied for hydrogen storage due to their high gravimetric density and relatively low hydrogen release temperature.[46] However, the direct decomposition of the metallic amide form into its metallic imide form generate ammonia.[170] This ammonia formation is undesirable as it reduces cycling ability due to nitrogen loss and poses a potential risk of FCs poisoning. To mitigate this issue, metallic amides are often combined with metallic hydrides. The combination of a protic hydrogen (H^+) with hydridic hydrogen (H^-) promote the hydrogen release instead of ammonia upon heating.[171] The resulting hydride mixtures, known as reactive hydride composites (RHCs), is what is referred to in the literature on hydrogen storage via metal amides.[172]

One of the most extensively studied hydride composites is the combination of $LiNH_2$ and LiH in a molar ratio of 1:2, providing a total hydrogen content of 10.4 wt%. The initial step of hydrogen release involves the decomposition of $LiNH_2$ in the presence of LiH, yielding Li_2NH and hydrogen, resulting in the liberation of 5.5 wt% of H_2 (see Equation I.2).[173] The decomposition of the amide occurs gradually at 180°C,[3] exhibiting slow kinetics, with an enthalpy change of 44.5 $kJ.mol^{-1}$.[174] The subsequent step in the dehydrogenation process involves the formation of Li_3N from Li_2NH (see Equation I.3), achieving complete conversion above 400°C, with an enthalpy of 165 $kJ.mol^{-1}$.[147]

$$LiNH_2 + LiH \leftrightarrow Li_2NH + H_2 \qquad \Delta H^0_{298K} = 75\ kJ.mol^{-1} \tag{I.2}$$

$$Li_2NH + LiH \leftrightarrow Li_3N + H_2 \qquad \Delta H^0_{298K} = 92\ kJ.mol^{-1} \tag{I.3}$$

Given the elevated temperature requirements of the second step, only the initial one is considered reversible. However, by employing an equimolar mixture of $LiNH_2$ and LiH, the gravimetric density of the system is enhanced to 6.5 wt% of H_2, with a hydrogen release temperature below 300°C.[174] The proposed mechanisms for dehydrogenation and H_2 formation involve either the interaction between protic and hydridic hydrogen,[175] or the reaction of LiH with ammonia, stemming from its generation as a reaction intermediate,[176] or potentially both pathways.[177] Regarding the cyclic performance of these compounds, after 200 cycles, the gravimetric density decreases from 5 wt% to 2 wt%, likely due to nitrogen loss attributed to ammonia formation.[178]

The replacement of $LiNH_2$ with $Mg(NH_2)_2$ or LiH with MgH_2 has been shown to enhance the hydrogen storage capabilities. For example, the $Mg(NH_2)_2$-LiH composite can reversibly store 5.6 wt% of hydrogen, with a desorption temperature ranging between 150-200 °C, corresponding to an enthalpy of 54 kJ/mol.[179] Likewise, its counterpart, $2LiNH_2$-$1.1MgH_2$, exhibits a hydrogen release of 4.5 wt% at approximately 100°C, characterized by a low dehydrogenation enthalpy of 34 $kJ.mol^{-1}$.[180]

As discussed, substituting Li amide-hydride composite with Mg can improve their thermodynamic properties. However, the dehydrogenation kinetics of these mixtures tend to be slower compared to other hydrides.[181] Moreover, metallic amides are sensitive to water,[107] and the possibility of ammonia emissions further restricts the application of amide hydride composites, particularly for embedded applications.

I.3.2.1.4 Ammonia borane

In the last class of solid storage, ammonia borane (AB), NH_3BH_3, stands out as a promising candidate for hydrogen storage owing to its impressive hydrogen content by weight (19.6 wt%, 145 $kg_{H_2}.m^{-3}$), deriving from both protic hydrogen (from its bond with N) and hydridic hydrogen (from its bond with B).[182] AB demonstrates excellent stability under ambient conditions, is non-toxic, and exhibits high solubility in common solvents like water and methanol.[183] The release of hydrogen from AB occurs in three steps, each contributing 6.5 wt% of hydrogen. The initial dehydrogenation step, moderately exothermic (−21 $kJ.mol^{-1}$), takes place at temperatures between 100 and 120 °C, forming polyaminoborane $(BH_2NH_2)_x$. Subsequently, at around 150 °C, polyiminoborane $(BHNH)_x$ is formed,[184] while the first step remains incomplete.[185] Complete dehydrogenation requires high temperatures, typically in the range of 800-900 °C, to form boron nitride.[186] Despite its incomplete dehydrogenation, AB boasts a considerable hydrogen capacity of 14.3 wt%.[185] However, challenges remain in the utilization of AB for hydrogen storage, including its susceptibility to hydrolysis in acidic environments, complex synthesis procedures,[187] slow kinetics below 100°C, and the potential generation of byproducts such as borazine, ammonia, and diborane during decomposition, which pose concerns for fuel cell applications.[188]

I.3.2.2 Liquid storage

I.3.2.2.1 Liquid Organic Hydrogen Carriers (LOHC)

Liquid organic hydrogen carriers (LOHCs) are molecules capable of storing and releasing hydrogen through covalent bonds. The use of organic compounds for hydrogen storage offers several advantages. Firstly, it provides a volumetric density comparable to physical storage methods while enhancing the handling and safety of the storage system by eliminating the need for heavy gas tanks or complex cooling devices.[189] Additionally, many LOHCs share similarities with conventional oils, facilitating their integration into existing oil and gas infrastructure with minimal adjustments. This inherent compatibility not only mitigates implementation costs but also promotes public acceptance due to the familiarity with current fuel technologies.[190]

The storage principle of LOHCs revolves around the reversibility of unsaturated carbon bonds. Hydrogen storage begins with the catalytic hydrogenation of a lean-hydrogen molecule, during which its unsaturated bonds become saturated with hydrogen. This storage process is exothermic and occurs at high temperatures and pressures. Subsequently, hydrogen recovery takes place through the catalytic dehydrogenation of the hydrogen-rich form (see Figure I.6). Dehydrogenation is an endothermic process, meaning it is favored at atmospheric pressure and high temperatures.[190]

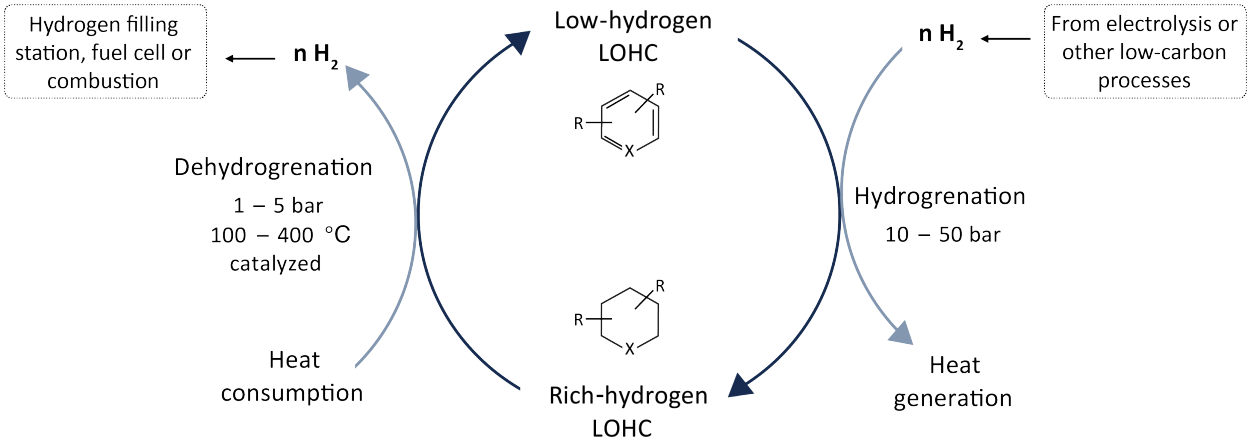

Figure I.6: Schematic diagram of the use of LOHCs to store hydrogen (adapted from [191, 192]).

Cycloalkanes, including cyclohexane, methylcyclohexane, and decalin, have been among the earliest investigated LOHCs, offering a hydrogen capacity ranging from 6.2 to 7.3 wt%.[193] However, cyclohexane dehydrogenation yields benzene, a carcinogenic compound, while decalin produces naphthalene, a solid at room temperature. Conversely, methylcyclohexane dehydrogenation leads to toluene, a non-carcinogenic liquid readily available due to its established bulk production. Moreover, methylcyclohexane exhibits density and viscosity akin to gasoline, making it a promising candidate for hydrogen storage. Despite its gravimetric energy density of 6.2 wt% hydrogen, the methylcyclohexane/toluene system, also known as MTH (Methylcyclohexane-Toluene-Hydrogen), faces challenges such as high dehydrogenation enthalpy (68.3 $kJ.mol^{-1}$ H_2) and the elevated temperature (325°C) required to achieve 100% conversion at 1 bar.[107] The incorpora-

tion of heteroatoms, such as N or O, into the cycloalkane ring has been suggested to mitigate the high dehydrogenation enthalpy associated with traditional cycloalkanes. While this modification indeed enhances their thermodynamic and kinetic properties, studies indicate that N-based heterocycles are prone to decomposition, resulting in the formation of undesired degradation products.[191]

One of the primary challenges hindering the widespread adoption of LOHCs lies in their high dehydrogenation enthalpies, typically ranging between 50 to 70 kJ.mol^{-1} H_2. This corresponds to approximately 25% of the higher heating value (HHV) of hydrogen, meaning that around a quarter of the hydrogen produced is required to sustain the reaction. Consequently, a significant area of research focuses on developing LOHCs with lower dehydrogenation enthalpies, coupled with the use of non-PGM (Platinum Group Metal) catalysts to enhance efficiency and reduce costs.

Since rich-hydrogen LOHC forms require elevated temperatures to release hydrogen, they add complexity to the storage and retrieval processes.[194] Additionally, the kinetics of both hydrogenation and dehydrogenation steps present significant challenges, often requiring catalysts from the platinum group metals (PGM), which are both scarce and costly.[108] Another critical consideration is the stability of LOHCs across multiple hydrogenation/dehydrogenation cycles.[195] Despite these challenges, ongoing research aims to identify LOHC systems with lower enthalpies, enhanced stability, combine with the utilization of more cost-effective catalysts.[108]

I.3.2.2.2 Circular hydrogen carrier

Circular hydrogen carriers, akin to LOHCs, operate through two reversible reaction steps: the hydrogenation of hydrogen-lean molecules, which can exist in either gaseous or liquid form, and the subsequent dehydrogenation of hydrogen-rich molecules. However, in contrast to LOHCs, circular hydrogen carriers are not inherently organic, and the dehydrogenated molecules are released back into the atmosphere following hydrogen recovery.[196]

I.3.2.2.2.a Methanol

The pair formed by CO_2 and methanol can effectively store hydrogen, offering a high hydrogen capacity of 12.1 wt% and an energy density of 3.3 kWh/L.[197] During the CO_2 hydrogenation process, two possible reactions may occur, resulting in either methanol and water (see Equation I.4) or CO and water.[198] However, to optimize hydrogen storage, it's essential to prevent the formation of CO. This hydrogenation reaction, catalyzed by Cu, typically occurs at temperatures ranging from 220 to 270 °C and pressures between 20 to 80 bar, with a relatively low conversion rate. While methanol is not a LOHC by definition, some studies occasionally categorize it as such.[197]

$$CO_2 + 3\ H_2 \leftrightarrow CH_3OH + H_2O \qquad \Delta H^0_{298K} = \text{-}49.5\ \text{kJ.mol}^{-1} \tag{I.4}$$

$$CH_3OH \leftrightarrow CO + H_2 \qquad \Delta H^0_{298K} = 90.7\,\text{kJ.mol}^{-1} \tag{I.5}$$

The dehydrogenation of methanol leads to the formation of carbon monoxide (CO) (see Equation I.5), a toxic byproduct that is also harmful for PEM,[94] and its production should be avoided. Hydrogen recovery can occur at either high or low temperatures. High-temperature dehydrogenation, or steam reforming of methanol, is catalysed by metals such as Cu, and metal from group 8 to 10 (such as Ni, Rh, Pd, Pt or Ir), at temperatures exceeding 200 °C,[199] albeit with the production of CO as a by-product.[197, 199] The hydrogen capacity is around 10 wt% via this process. Conversely, low-temperature dehydrogenation (<100 °C) of methanol occurs in an aqueous medium, employing water or other solvents like tetrahydrofuran (THF) or triglyme. Dehydrogenation yields vary from 15 to 84%, depending on the catalyst used, with reaction times spanning from 10 to 24 hours. Importantly, only a minimal amount of CO is generated in this process, but the hydrogen capacity drops to 4 wt%.[197]

While methanol remains stable up to temperatures of 320°C,[200] and research indicates that even after 200 hours of high-temperature dehydrogenation, only minimal impact on methanol conversion has been observed.[201] Methanol presents handling challenges due to its flammability and toxicity. Additionally, its high vapor pressure presents storage difficulties. Furthermore, capturing CO_2 from the atmosphere for use in methanol formation and hydrogen storage presents significant energetic challenges.[197]

I.3.2.2.2.b Formic acid

Formic acid, also known as methanoic acid, is a promising candidate for hydrogen storage applications, similar to methanol, as it can be produced via CO_2 hydrogenation (see Equation I.6). It offers a theoretical hydrogen storage capacity of 4.4 wt%[197, 202] and an energy density of 1.8 kWh.L^{-1},[197] demonstrating significant storage potential.

$$CO_2 + H_2 \leftrightarrow HCOOH \qquad \Delta H^0_{298K} = -32.5\,\text{kJ.mol}^{-1} \tag{I.6}$$

The formation of formic acid involves CO_2 hydrogenation, an exothermic and endergonic reaction. To shift the reaction equilibrium favorably, additives such as water and/or bases like ammonia are often incorporated. Hydrogenation is typically carried out using homogeneous catalysts at temperatures between 50 to 100 °C and pressures ranging from 1 to 100 bar. However, the low solubilities of CO_2 and H_2 in the reaction medium limit formic acid production,[203] reducing the effective hydrogen capacity to 0.3 wt% and 0.1 kWh/L.[197]

The dehydrogenation of formic acid occurs at temperatures below 100 °C,[197] leading either to the formation of CO_2 and H_2 (the reverse of Equation I.6, an endothermic reaction with ΔH= 31.2 kJ.mol^{-1}), or CO and

water.[204] Same as methanol, it is crucial to prevent the formation of CO during dehydrogenation. Dehydrogenation is catalyzed by homogeneous catalysts. To simplify the process and avoid the need for separation, the same catalyst is often used for both hydrogenation and dehydrogenation, though this may compromise efficiency compared to using specialized catalysts for each step.[197]

In the same way as for methanol, capturing CO_2 from the atmosphere for the production of formic acid presents significant energy challenges. Additionally, there are practical difficulties associated with handling formic acid, including its flammability and corrosiveness. Furthermore, its high vapor pressure complicates storage. The use of solvents in the hydrogen storage process requires the implementation of hydrogen purification measures. While formic acid, when dissolved in water, exhibits thermal stability, the same may not hold true for the catalysts utilized in the hydrogenation and dehydrogenation steps.[197]

I.3.2.2.2.c Ammonia

Ammonia is an essential molecule mainly used for producing nitrogen-based fertilizers through the well-established Haber-Bosch (HB) process. Beyond its vital role in fertilizer synthesis, ammonia is gaining recognition as a highly promising hydrogen carrier due to its substantial hydrogen content (17.75% by weight)[205] and the ease of its liquefaction at -33.35 °C at atmospheric pressure, or compressed to liquid at a mild pressure of 8.6 bar at 20 °C,[206] making it a dense and efficient option for hydrogen transport.

Here, hydrogen produced via electrolysis can be stored by hydrogenating nitrogen extracted from the air to form ammonia. When the stored energy is required, ammonia can be dehydrogenated, releasing hydrogen for use while returning nitrogen to the atmosphere(see Figure I.7).[8] Alternatively, the energy stored in ammonia can be recovered by burning it (up to 80-90%) in diesel engines, with the use of a pilot fuel such as fuel oil or hydrogen. However, this method results in high emissions of nitrous oxides, implying the purification of exhaust gases to mitigate environmental impact.[207]

Its extensive presence in the industrial sector means that the global infrastructure for ammonia storage and transportation is already in place, facilitating rapid large-scale deployment as a hydrogen carrier.[208] Ammonia can be transported by ships or pipelines, with the USA operating an extensive network of 3,057 km of ammonia pipelines, and a notable 2,417 km pipeline linking Russia and Ukraine.[209] Currently, there are 38 ports worldwide dedicated to ammonia exportation, 88 for importation, and 6 capable of both,[210] highlighting the widespread use of cargo tankers for ammonia marine transport.[9]

Ammonia synthesis currently utilizes the (HB) process (see Equation I.7),[9] where ammonia is produced by the catalytic reaction of hydrogen and nitrogen at temperatures between 450–600°C and pressures of 10–25 MPa.[211] This process consumes approximately 1.8–3% of global energy.[212]

$$N_2 + 3\ H_2 \leftrightarrow 2\ NH_3 \qquad \Delta H^0_{298K} = \text{-}46\ \text{kJ.mol}^{\text{-}1} \tag{I.7}$$

Given that the hydrogen feedstock is predominantly derived from fossil fuels, current ammonia synthesis generates around 2.4 t CO_2 per tonne of ammonia produced.[213] To reduce the carbon footprint of ammonia production, it is crucial to source hydrogen from low-carbon methods, such as water electrolysis,[214] and to implement CCS technologies.

Hydrogen storage via ammonia faces energy efficiency challenges due to the significant energy required for hydrogen regeneration. Without a catalyst, ammonia decomposition requires temperatures above 677 °C,[215] and as an endothermic reaction, it demands substantial energy input to maintain these conditions.[216] The introduction of metallic heterogeneous catalysts, such as Ru, significantly lowers the reaction temperature to approximately 400 °C, improving the overall efficiency of hydrogen release.[217]

The U.S. Department of Energy (DoE) has highlighted key barriers to using ammonia as an onboard hydrogen carrier, primarily concerning safety and efficiency.[218] Ammonia's toxicity raises concerns about accidental release,[219] and its corrosivity presents additional risks.[220] However, ammonia is non-flammable and has a relatively narrow explosion limit (16–25% in air), making it less prone to combustion and explosion compared to other gases and liquid fuels.[221] Many argue that safety concerns should not hinder ammonia's development as an energy carrier, given the century of accumulated safety expertise in its production and handling. The associated risks and hazards are now well-understood and manageable.[211] Developing lightweight, "indestructible" tanks, cost-effective ammonia sensors, and comprehensive assessments of both short- and long-term health effects will be crucial to addressing these concerns.[218]

For onboard applications, efficiency depends heavily on the performance, cost, and size of ammonia crackers. Current catalyst technologies suggest that reactors will need to operate at temperatures exceeding 500 °C.[217, 218] Moreover, PEM fuel cells are highly sensitive to ammonia contamination, being poisoned at concentrations above 0.1 ppm. This necessitates sophisticated ammonia decomposition reactors and robust purification systems.[218, 219]

These challenges led the U.S. DoE to exclude funding for research on ammonia as an onboard hydrogen storage option in their 2006 report. However, they acknowledged its potential as a hydrogen carrier for delivery and off-board storage, such as at refueling stations or in stationary power applications.[218]

Despite facing challenges, there has been a notable increase in research and publications focusing on the use of ammonia as a hydrogen carrier. This interest is largely due to ammonia's advantageous properties for energy storage.[211, 219, 9] Notably, ammonia's decomposition yields only 75% H_2 and 25% N_2,[211] with no CO_x by-products,[219] offering a significant advantage over some LOHCs that produce carbon oxides during dehydrogenation. In addition, ammonia demonstrates considerable versatility, serving not only as a hydrogen carrier but also as a direct fuel for combustion engines,[222, 223] and as a feedstock for fertilizer production. Recent models suggest that ammonia produced using renewable energy sources is now cost-competitive with that produced through traditional methods.[224, 225] This economic feasibility, combined with its multi-

functional uses, positions ammonia as a particularly attractive option in the transition towards sustainable energy solutions.

Ammonia is seriously considered for hydrogen transport between Australia and Japan. In 2016, the Japanese Ministry of Economy, Trade and Industry (METI) released the ”Strategic Roadmap for Hydrogen and Fuel Cells,” aimed at addressing technical challenges and ensuring the economic viability of hydrogen technologies. This roadmap is structured around three key phases: initially, the deployment of fuel cells; followed by the development of hydrogen power plants and a mass supply chain; and ultimately, the production of carbon-free hydrogen.[226] Concurrently, Australia has been proactive in establishing ammonia production facilities that utilize solar energy for the synthesis process. This ”green ammonia” is then intended for export to countries where renewable energy projects are economically challenging, such as Japan and Germany, thereby supporting global clean energy initiatives.[227, 228]

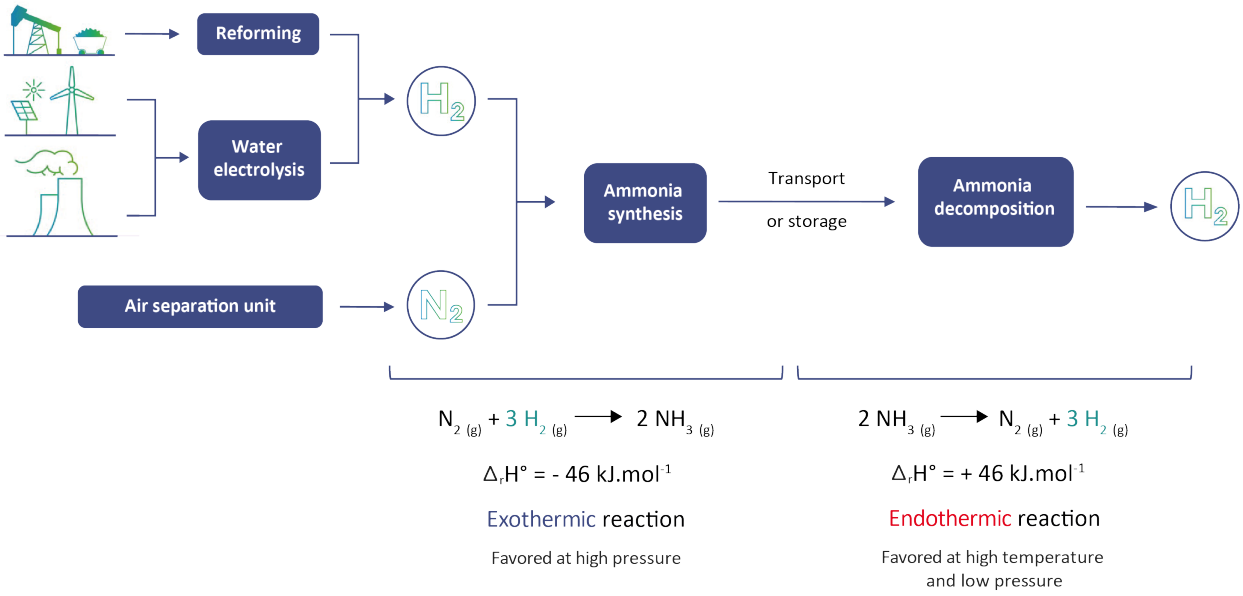

Figure I.7: Principle of using ammonia as a hydrogen vector.

I.3.3 Comparison of storage and transportation efficiency

In summary, hydrogen stands out as a highly promising energy carrier with a wide range of applications. These include mitigating the intermittent nature of renewable energy sources, enabling seasonal and long-duration energy storage, facilitating global energy trade and export, and supporting the decarbonization of industries and transportation. Each of these applications comes with unique challenges and requirements, necessitating hydrogen carriers to adapt and meet their specific demands effectively.

To advance hydrogen storage solutions for transportation, the U.S. Department of Energy (DOE), in collaboration with automotive industry partners, has established specific technical targets for onboard hydrogen

storage systems.[229] These targets aim to focus research and development efforts, fostering innovation in hydrogen storage technologies to address the critical requirements of hydrogen-powered vehicles:

(i) **High Storage Capacity:** The system should achieve a usable gravimetric capacity of 2.2 kWh/kg (approximately 6.5 wt%) and a volumetric capacity of 1.7 kWh/L (approximately 50 g H_2/L).

(ii) **Cost-Effectiveness:** The storage system cost target is $8 per kWh net, equating to about $266 per kg of hydrogen.

(iii) **Temperature and Pressure Requirements:** The system should operate within an ambient temperature range of -40°C to 60°C (with solar loading), with a hydrogen delivery temperature between -40°C and 85°C, and a maximum delivery pressure suitable for the fuel cell system.

(iv) **Efficiency in Operation:** The system should enable refueling of 5 kg of hydrogen within 3-5 minutes, aligning with the DOE's refueling time targets.

(v) **Minimal Hydrogen Loss:** The system should have a dormancy time (the time before venting occurs) of at least 5 days under worst-case conditions, minimizing hydrogen loss.

(vi) **Safety and Environmental Concerns:** The storage system should comply with applicable safety standards, ensuring non-toxicity, non-flammability, and environmental compatibility.

Despite the variety of hydrogen storage technologies discussed before, no single technology currently satisfies all these demanding criteria simultaneously. Consequently, the selection of a hydrogen storage vector remains a complex decision, influenced by a trade-off between performance metrics, safety standards, environmental considerations, hydrogenation and dehydrogenation conditions, and economic factors. This underscores the ongoing need for innovation and development in hydrogen storage technologies.

From the hydrogen content perspective, few compounds achieve the minimum target of 6.5 wt% of hydrogen as specified by the US DoE (see Table I.3.3). Among the most researched systems, notable examples include lithium borohydride (18.5 wt%), ammonia borane (19.6 wt%), methanol (12.1 wt%), ammonia (17.8 wt%), and liquid hydrogen (approximately 12 wt%). However, liquid hydrogen is often discounted due to the substantial energy demands required for its liquefaction.

Among these hydrogen vectors, one of the primary challenges is meeting the required dehydrogenation temperature standards. Ammonia borane and methanol have the lowest dehydrogenation temperatures even if they remain higher than the maximum set at 80 °C (see Table I.3.3). However, ammonia borane, while rich in hydrogen content, does not form directly from a reaction with hydrogen. Methanol faces issues related to the potential formation of CO and challenges in capturing the CO_2 to form methanol and store hydrogen. However, there is a discrepancy of tenfold (almost a factor 10) between the dehydrogenation temperature limit set by the US DoE and those exhibited by ammonia and lithium borohydride (see Table I.3.3). Additionally, lithium borohydride reacts upon contact with water, which contravenes the DoE's guidelines stipulating that an ideal storage medium should be inert to both water and oxygen. Thus, if not

for its dehydrogenation temperature, ammonia has strong potential as hydrogen carrier.

Ammonia economically distinguishes itself due to its well-established global synthesis infrastructure. In 2023, production reached approximately 150 million tons,[230] with costs averaging $1.09 per kg in Europe.[231] Initiatives to produce 'green' ammonia from renewable energy sources are expected to significantly enhance its economic viability. Additionally, the processes for transporting and storing ammonia are well-established, which enhances its financial attractiveness as a hydrogen carrier. When compared to other hydrogen storage methods, such as liquid organic hydrogen carriers (LOHC) and liquefied hydrogen, ammonia consistently proves more cost-effective than LOHC regardless of transport distance. Compared to liquefied hydrogen, ammonia becomes more cost-effective at distances exceeding 5000 km (see Figure 8).[210]

Given these substantial advantages, ammonia stands out as a serious candidate for use as a hydrogen carrier. The primary challenge hindering its broader application is the high temperature required for its dehydrogenation. Reducing this temperature would make ammonia one of the most suitable systems for hydrogen storage, enhancing its practicality and efficiency in energy applications.

Achieving a moderate temperature for hydrogen recovery from ammonia requires enhancements of the catalytic system. This improvement is crucial for increasing the efficiency and feasibility of using ammonia as a hydrogen carrier.

Table I.1: Comparison of hydrogen vector properties against US DoE recommendations (with values displayed in green when the criteria are met and in red when they are not), for physical-based hydrogen storage (compressed hydrogen gas,[146, 98, 101, 232] liquid hydrogen,[146, 232, 108, 107] and cryo-compresses hydrogen[233]), solid chemical-based hydrogen storage (hydrogen adsorption, binary hydrides,[232, 234, 46] sodium alanates,[116, 166, 167] lithium borohydrides,[235, 147, 169] lithium amide and lithium hydride (1:1),[236, 174, 178] and ammonia borane[182, 184, 185]) and liquid chemical-based hydrogen storage (LOHC (here dibenzyltoluene as an example),[232, 237] methanol, acid formic,[238, 197, 203] and ammonia[232, 239, 214, 240]).

Hydrogen storage type	Hydrogen storage system	Storage conditions	Theoretical gravimetric density (wt % H_2)	Volumetric (g_{H_2}/L)	Energy density (kWh/L)	Hydrogenation conditions	Dehydrogenation conditions	Advantages	Drawbacks
Physical-based hydrogen storage	Compressed hydrogen gas	350 - 700 bar	5 - 7	42	1.3	Compression	Pressure reduction	Simple and mature technology	High energy cost for compression (11-13 % of total energy stored), potential leaks
	Liquid hydrogen	- 253 °C	7 - 12	70.8	2.4	Evaporation	Liquefaction at low temperature	Simple and mature technology	High energy for cooling (30-40 % of the total energy stored), boil-off losses
	Cryo-compressed hydrogen	- 253 °C and 300 bar	7.5	80	2.7	Compression and cooling	Warming and decompression	Higher density than simple compression	Complex handling, costly technology
Solid chemical-based hydrogen storage	Hydrogen adsorption	Atmospheric up to about -253°C ≈1 (for carbon based, zeolites, PIMs) Atmospheric up to about 100 bars ≈14 (MOFs at -253°C and 80 - 100 bar)		15 - 35	0.5 - 1.2	Adsorption at low temperature and and under pressure	Heating or pressure reduction	Fast adsorption	Low capacity, storage (low temperature pressure), conditions and desorption kinetics
	Binary hydrides	Ambient and anhydrous	2.5 - 12.6 (7.6 % for MgH_2)	36–110 (110 g/L for MgH_2)	1.2 - 3.7 (3.7 for MgH_2)	300°C and 30 bar	Decomposition at high temperatures (350-400 °C for MgH_2)	High hydrogen content	High temperature and slow hydrogen-release
	Sodium alanates	Ambient and anhydrous	7.4	93	3.1	200 - 400 °C 100 - 400 bar	185 - 260 °C	Reversible storage, proper hydrogen content	High temperatures needed for release (NaH formation = H_2 capacity reduced to 5.6 wt%), slow kinetics
	Lithium borohydrides	Ambient and anhydrous	18.5	123	4.1	650 °C and 150 bar	> 380 °C	High hydrogen content	High temperatures needed for release (LiH formation = H_2 capacity reduced to 13.5 wt%)
	Lithium amide and hydride (1:1)	Ambient and anhydrous	6.5	75		Ball milling under 20 bar or 200 - 300 °C and 50 bar	< 300 °C	Proper hydrogen content	High temperatures for H_2 release, slow kinetics, decline of gravimetric density
	Ammonia borane	Ambient	19.6	146	4.8	Dehydrogenation of ammonium borohydride or reaction between ammonia and diborane	150 °C	High hydrogen content, non toxic	800-900°C for total dehydrogenation, hydrolyzation, difficult synthesis, by-products formation
Liquid chemical-based hydrogen storage	LOHC (here dibenzyltoluene)	Ambient	6.2	57	1.9	150 °C and 50 bar (depends on the catalyst used)	> 300°C (catalyzed)	Non-flammable	High dehydrogenation enthalpy and temperature
	Methanol	Ambient	12.1	96	3.3	220 - 270 °C 20 - 80 bar	< 100°C in THF (yield = 15-84 %) °< 200°C (catalyzed)	Safe and convenient handling	Formation of CO, CO_2 capture, H_2 content depend on catalyst (from 4 to 10 wt%)
	Acid Formic	Ambient	4.4	53	1.7	50 - 100 °C and 1 - 100 bar (with homogeneous catalyst)	< 100 °C	Safe and convenient handling	Formation of CO, CO_2 capture and low solubilities of CO_2 and H_2 in the reaction medium
	Ammonia	- 33.5 °C at P_{atm} 8.6 bar at 20 °C	17.75	121	4.0	450 - 600 °C and 100 - 250 bar (catalyzed)	> 400 °C (catalyzed)	High H_2 density, no CO_x by-products, infrastructure	Toxicity, handling risks, high temperature for dehydrogenation, poison for PEM

I.4 Ammonia in the chemical industry

I.4.1 History and role of ammonia

Ammonia is a major product of the chemical industry, primarily used in the production of fertilizers, explosives, and polymers. It is a crucial component of nitrogen fertilizers, with 80% of global ammonia production dedicated to soil fertilization. Over the past century, this application has significantly contributed to increasing the number of humans supported per hectare of arable land, rising from 1.9 to 4.3 persons.[241] Ammonia ranks as the second most produced synthetic chemical, just behind sulfuric acid.[242]

The global annual production of ammonia reached 183 million tonnes (Mt) in 2020. Driven by population growth and the increasing need for fertilizers, ammonia demand is projected to rise significantly, reaching 223 Mt by 2030 and 333 Mt by 2050, under a scenario aligned with limiting global warming to 1.5°C.[243] China leads global production, accounting for 30%, followed the United States, the European Union, India, Russia, and the Middle East each account for about 8-10% of global production.[244]

I.4.2 Properties of ammonia

Ammonia consists of one nitrogen atom bonded to three hydrogen atoms. The nitrogen, serving as the central atom, initially has the ground state electronic configuration of 1s2 2s2 2p3. In the formation of ammonia, nitrogen undergoes sp^3 hybridization, where one 2s orbital and three 2p orbitals combine to create four sp^3 hybrid orbitals of equivalent energy. Three of these sp^3 orbitals, each containing one electron, overlap with the 1s orbital of a hydrogen atom, forming three sigma (σ) bonds. The fourth sp^3 orbital retains a lone pair of electrons. This specific configuration of one lone pair and three sigma bonds gives ammonia its trigonal pyramidal geometry, which is a slightly distorted form of a tetrahedral structure.[245]

At standard temperature and pressure, ammonia is a colourless gas, highly soluble in water, forming a corrosive solution known as ammonium hydroxide (NH_4OH). It boils at -33.34°C and freezes at -77.7°C, properties that are particularly advantageous for its use as a hydrogen carrier since it can be easily liquefied.

Ammonia gas, with a density of 0.769 $kg.m^3$, is less dense than air, which has a density of 1.225 $kg.m^3$ under normal conditions. This lower density allows ammonia to dissipate quickly, thereby reducing the risk of fire or explosion in the event of a leak. Additionally, ammonia has a relatively narrow flammability range, spanning from 15.15% to 27.35% in dry air and from 15.95% to 26.55% in air at 100% relative humidity. Ammonia has a higher ignition temperature of 650°C compared to hydrogen (520 °C).[246]

I.4.3 Safety and precautions

Ammonia is highly useful but requires strict precautions due to its toxicity, which is significantly greater, approximately three orders of magnitude, than that of methanol or gasoline.[246] Inhalation of ammonia at

concentrations between 2000 and 3000 ppm in the air can be potentially fatal, while levels exceeding 5,000 ppm are extremely dangerous and can lead to rapid death (see Table I.2). Ammonia is also corrosive and has a pungent smell that is easily recognizable at low concentrations, typically detectable between 20-50 ppm,[212] some sources suggest it can be noticed even at levels as low as 5 ppm.[247] Making ammonia far more perceptible than odourless hydrogen. The recommended exposure limits for ammonia are set below 100 ppm to ensure safety.[220] However, ammonia's potential to cause combustion and explosion is lower compared to other gases and liquid fuels.[211]

To ensure safety when handling ammonia, facilities must be equipped with effective ventilation systems[211] and sensitive sensors that can trigger alarms for prompt response.[220] Specialized containers are essential for the storage and transportation of ammonia, designed to resist its corrosive properties and prevent accidental releases.[211] These measures are critical to maintaining a safe environment when handling this hazardous chemical.

Table I.2: Exposure effects of ammonia in air.[212]

Effect	Ammonia concentration in air (by volume)
Readily detectable odor	20–50 ppm
No impairment of health for prolonged exposure	50–100 ppm
Severe irritation of eyes, ears, nose and throat. No lasting effect on short exposure	40 0–70 0 ppm
Dangerous, less than ½ hours of exposure may be fatal	2000–3000 ppm
Serious edema, strangulation, asphyxia, rapidly fatal	5000–10000 ppm

I.4.4 Ammonia synthesis

I.4.4.1 Reaction thermodynamics

The synthesis of ammonia from N_2 and H_2, in a ratio of 1:3, is exothermic and reversible (see Equation I.7).[248] The synthesis of ammonia is constrained by chemical equilibrium. As the volume of gas decreases during the formation of ammonia, according to Le Châtelier's principle, increasing pressure shifts the equilibrium toward the formation of ammonia. Similarly, lowering the temperature also favors the formation of ammonia by shifting the equilibrium in a favorable direction. However, lower temperatures slow down the synthesis process. From a manufacturing perspective, selecting the temperature for ammonia synthesis represents a compromise between achieving a sufficient concentration of ammonia in the equilibrium mixture, typically around 15%, and maintaining a rapid production rate. Similarly, the choice of pressure conditions represents a balance between efficiency and cost.[249] Likewise, removing ammonia from the reaction medium shifts the equilibrium toward ammonia production. Typically, ammonia is extracted from the gas stream through condensation by cooling. The unreacted components are then recycled back to the inlet of the chemical reactor, enhancing overall process efficiency.[248]

I.4.4.2 Haber-Bosh process

The HB process was developed at the beginning of the 20th century. Synthesizing ammonia from N_2 is challenging due to its chemical inertness with its strong triple covalent bond. However, in 1908, chemists Fritz Haber and Robert Le Rossignol demonstrated that producing ammonia from N_2 and H_2 was industrially feasible, by the application of Le Châtelier's principle. The industrial synthesis of ammonia was developed by a team from BASF, including Carl Bosch. The first production facility, established in 1913, had a capacity of 30 ton of NH_3 per day.[250] The process involves several stages: first, the production of H_2 through SMR and its subsequent purification. Next, in a chemical reactor, H_2 and N_2 undergo catalytic synthesis to form ammonia. This is followed by the separation of products and reactants through liquefaction, with the recycling of unreacted molecules. Finally, the process includes the recycling of released thermal energy. To achieve acceptable profitability, the synthesis operates under conditions of approximately 200 bar pressure and around 500°C temperature, utilizing a continuous process and efficient thermal energy recycling.[251]

The catalysts used in the HB process have seen little change since the early 20th century. They are primarily Fe-based[251, 252, 253] and are enhanced with structural promoters like Al_2O_3,[251, 252, 253] CaO,[251] MgO,[251] and SiO_2[252, 253] to improve stability, as well as electronic promoters such as K_2O[251, 252, 253] to boost activity. The development of these catalysts focuses on maximizing their efficiency and ensuring high thermal and chemical stability, which is crucial given the extremely high temperatures and the presence of various oxygen species in the process. Before use, the catalyst is activated by reducing Fe oxide to metallic Fe, while promoters remain in their oxide forms.[251]

Ru-based catalysts have also been explored for ammonia synthesis, offering higher activity at lower pressures and enabling high conversion rates. In the Kellogg Ammonia Process (KAAP), a ruthenium catalyst supported on activated carbon and combined with multiple promoters is used, achieving an energy saving of approximately 1.17 GJ/ton of NH_3 compared to Fe-catalyzed processes. These catalysts also function effectively at lower H_2:N_2 ratios. However, the industrial application of ruthenium-based catalysts is limited by their rarity and high cost.[251]

To be economically viable, the SMR-HB process requires operation at a large scale, typically between 2000 to 3000 tons per day, with a capital investment amounting to billions of dollars and a long-term commissioning phase that usually spans several years.[254] The synthesis of ammonia, to support global food production contribute to around 1% of global CO_2 emissions,[211] with 1.6–1.8[255] and 2.5–3.8[256] tonnes of CO_2 for every ton of NH_3 produced, when hydrogen is derived from SMR and coal gasification respectively.

I.4.5 Recent developments

Currently, ammonia is predominantly produced from fossil resources such as natural gas, naphtha, heavy fuel oil, or coal, and is referred to as "brown ammonia." When ammonia production from fossil resources is combined with CCS systems, it is termed "blue ammonia." In contrast, "green ammonia" is derived from

hydrogen obtained through electrolysis powered by renewable energy sources or from biomass, offering a pathway with minimal carbon emissions.[250]

Recent advancements in ammonia synthesis are primarily focused on enhancing efficiency and reducing the environmental impact associated with the Haber-Bosch (HB) process. As global demand for ammonia continues to rise, particularly with its potential as a hydrogen carrier, efforts are being made to transition toward more sustainable production methods. Key innovations include integrating HB with Carbon Capture and Storage (HB + CCS) to capture and store CO_2 emissions, significantly reducing the carbon footprint of ammonia production. Similarly, HB using hydrogen produced via electrolysis (HB + H_2 from electrolysis) leverages renewable energy to produce green hydrogen, enabling a low-carbon ammonia synthesis route.

Beyond HB, alternative approaches such as electrochemical, and chemical looping synthesis methods are being explored. These methods aim to further improve sustainability and efficiency by bypassing the high-pressure and high-temperature requirements of traditional HB. Additionally, there is considerable interest in developing advanced catalysts to lower energy consumption and emissions.

I.4.5.1 Electrochemical approach

Electrochemical ammonia synthesis reduces atmospheric nitrogen to ammonia using electricity, offering advantages over the Haber-Bosch process such as milder conditions, modular scalability, and compatibility with renewable energy. This method eliminates the need for a separate hydrogen source, as protons are generated in situ at the anode, simplifying the process and enhancing efficiency.[251]

The process begins with hydrogen or water oxidation at the anode, producing protons and electrons. Protons travel through an electrolyte while electrons flow via an external circuit to the cathode, where nitrogen is reduced to ammonia.[251] Current research focuses on two routes: direct nitrogen reduction using electrocatalysts and indirect reduction with chemical mediators.[250]

I.4.5.1.1 Direct nitrogen reduction

Electrochemical systems for ammonia synthesis are broadly categorized into high-temperature (HT, 300–750°C) and low-temperature (LT, 20–100°C) systems. HT systems include solid-state electrolyte reactors, molten salt reactors, and composite membrane reactors, while LT systems utilize liquid or solid-state electrolytes.[251, 257] Solid-state electrolytes show promise for enhancing purity and efficiency by separating hydrogen from ammonia,[258] though HT variants face material degradation issues and low Faradaic efficiency (<50%),[259] dropping to 1% with water as the proton source.[258, 260]

LT electrochemical systems often employ aqueous, organic,[261] or ionic liquid electrolytes.[262] Aqueous electrolytes can directly provide protons,[259] with acidic electrolytes enhancing efficiency and alkaline solutions reducing parasitic hydrogen evolution.[263] However, global efficiency remains low, with ammonia production

rates at room temperature ranging from 10^{-12} to 10^{-9} mol.s^{-1}.cm^{-2} and Faradaic efficiencies under 10%. A major challenge lies in the lack of suitable catalysts, as those effective for nitrogen reduction often promote hydrogen evolution, blocking nitrogen adsorption on catalytic surfaces, especially in aqueous media.[264]

I.4.5.1.2 Indirect nitrogen reduction

Lithium-mediated ammonia synthesis represents a novel electrochemical approach that strategically separates the nitrogen activation from the hydrogenation step. This separation effectively eliminates the interference from the competing hydrogen evolution reaction. The process begins with the electrochemical reduction of Li^+ ions to metallic lithium, deposited on an electrode. This is followed by exposing the metallic lithium to a nitrogen atmosphere at room temperature and atmospheric pressure, facilitating the formation of Li_3N. The final step involves reacting Li_3N with water or another proton source to produce ammonia and regenerate the Li^+ salt, thus completing the cycle. This sequential approach ensures a more efficient and targeted synthesis of ammonia (see Figure I.8.a).[265, 266] To improve the efficiency and scalability of ammonia production, a continuous process has been developed, involving nitrogen gas bubbled through an electrolyte solution comprised of tetrahydrofuran (THF), ethanol, and lithium (see Figure I.8.b).[267, 268] This approach ensures a steady flow of reactants, which is crucial for consistent production. Current research is also exploring systems that incorporate various metals, aiming to further reduce energy consumption and optimize the process.

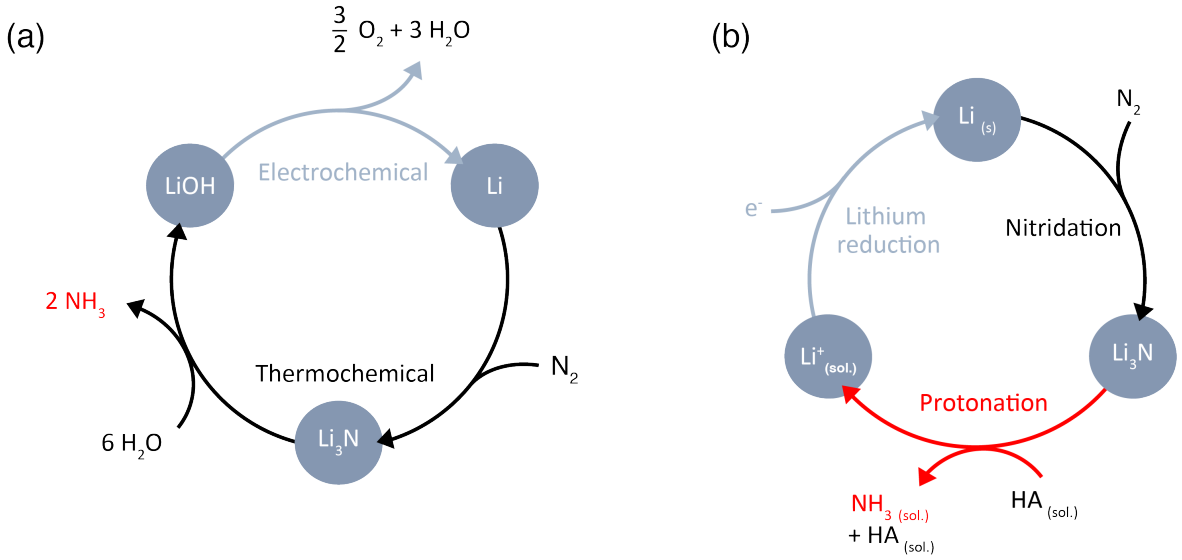

Figure I.8: Schematic representation of lithium-mediated ammonia synthesis: (a) electrochemical/thermochemical cycling (adapted from [265]); and (b) continuous cycling process (adapted from [269]).

Despite considerable theoretical and experimental efforts, a suitable catalyst for electrochemical nitrogen reduction has yet to be discovered.[270] LT electrochemical ammonia production is hindered by slow kinetics, the inert nature of N_2, and its low solubility. As a result, electrochemical ammonia production cannot currently be considered a replacement for the HB process. However, it holds potential as a technology for

small-scale, intermittent ammonia production.[251]

I.4.5.2 Chemical-looping approaches

Chemical looping (CL) approaches involve the separation of thermodynamically stable reaction intermediates, which enhances control over reaction dynamics. In the context of ammonia synthesis, CL offers the advantage of independently controlling nitrogen activation and ammonia formation, enabling the reaction to occur at more moderate pressures (1-10 bar).[251] Three types of chemical looping have been considered for ammonia synthesis: hydrogen CL,[271] water CL,[272] and alkali or alkali earth metal hydride CL.[273]

Hydrogen CL involves the nitridation of metal in a nitrogen stream, which then serves as a nitrogen source for ammonia synthesis. Subsequently, the metal nitride is reduced back to its metallic form in the presence of hydrogen, with ammonia being formed during the process. (see Figure I.9) For ammonia synthesis via hydrogen CL, compounds such as Mo_2N,[271] Ca_3N_2,[271] Sr_2N,[271] and Mn_xN_y[271, 274] have been considered. However, a significant challenge in this method is the high temperature required to reduce the metal nitride, typically exceeding 500°C,[251] which can impact the overall energy efficiency and feasibility of the process.

The water CL process involves a cyclic sequence of nitridation, oxidation, and reduction of a metal (see Figure I.9). Initially, metal nitride is formed, which is then hydrolysed with steam to produce ammonia along with metal oxide. Finally, the metal oxide is reduced back to its metallic form.[266] One of the main advantages of this process is the direct hydrogenation of nitrogen through the metallic nitride, eliminating the need for a separate hydrogen production step. However, a significant drawback is that the reduction of the metal oxide requires temperatures above 1000°C, and involves the use of methane.[251]

For alkali earth metal hydride CL, nitridation occurs on a metal hydride forming a metal amide, then reduced back to its hydride from in presence of hydrogen, forming ammonia alongside (see Figure I.9).[266, 275] With Ni-BaH_2/Al_2O_3, ammonia was formed at atmospheric pressure below 100°C.[273]

Chemical looping for ammonia synthesis, although promising due to its ability to operate at moderate pressures, remains in the early stages of development. Additionally, this method is characterized by the intermittency of its ammonia production. These factors highlight the need for further research and development to address these limitations and enhance the feasibility of chemical looping as a viable industrial process for ammonia synthesis.

Although new technologies and catalysts are being investigated to enable ammonia synthesis under milder conditions, this objective still presents a significant technological challenge that has yet to be resolved.

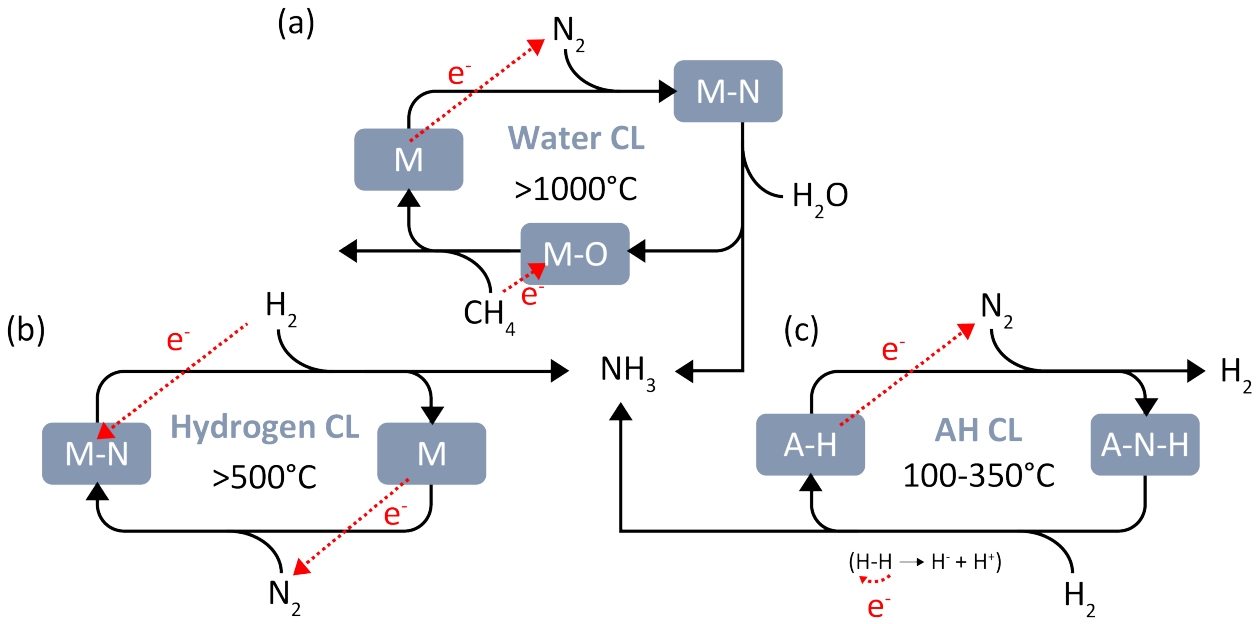

Figure I.9: Catalytic mechanisms of ammonia synthesis via CL : (a) water CL ; (b) hydrogen CL ; and (c) akali or alkaline earth metal CL. (adapted from [273]).

I.5 Ammonia Decomposition Reaction

I.5.1 Reaction thermodynamics

The decomposition of ammonia is the reverse of its formation (see Equation I.7); it is an endothermic reaction where the volume of the gaseous products exceeds that of the reactants. Therefore, in accordance with Le Châtelier's principle, and in contrast to synthesis, this reaction is favored under high temperature and low pressure conditions.[276]

Similar to its synthesis, the equilibrium of ammonia decomposition is influenced by reaction conditions, although the shift in equilibrium depends on temperature rather than pressure. While the conversion of ammonia is never entirely complete, it can approach near-total decomposition under optimal conditions (see Table I.3).[277]

Therefore, it is crucial to integrate ammonia decomposition with hydrogen purification systems, particularly for use with PEM fuel cells, to ensure the hydrogen's purity is sufficient for optimal performance.[240, 219]

Table I.3: Equilibrium conversion of ammonia according to temperature at atmospheric pressure.[277]

Temperature (°C)	250	300	350	370	400	420	450	470	500
Conversion (%)	89.21	95.69	98.12	98.61	99.11	99.31	99.53	99.63	99.74

I.5.1.1 Mechanism of catalyzed ammonia decomposition

The decomposition of ammonia has been thoroughly investigated by Ertl et al., who utilized well-defined Fe single crystal surfaces in conjunction with surface spectroscopic techniques. This approach enabled them to identify the nature of the surface species involved and elucidate the mechanism of the decomposition reaction as follows[278]:

$$NH_3 \leftrightarrow NH_{3,\,ads} \tag{I.8}$$

$$NH_{3,\,ads} \rightarrow NH_{2,\,ads} + H_{ads} \tag{I.9}$$

$$NH_{2,\,ads} \rightarrow NH_{ads} + H_{ads} \tag{I.10}$$

$$NH_{ads} \rightarrow N_{ads} + H_{ads} \tag{I.11}$$

$$2\,H_{ads} \rightarrow H_2 \tag{I.12}$$

$$2\,N_{ads} \rightarrow N_2 \tag{I.13}$$

Initially, an ammonia molecule adsorbs onto the catalyst surface (Equation I.8). Subsequently, hydrogen atoms are sequentially cleaved from the ammonia molecule and also adsorb onto the catalyst surface (Equation I.9-I.11). Finally, pairs of adsorbed hydrogen atoms combine to form H_2 and desorb from the surface (Equation I.12). Similarly, pairs of nitrogen atoms combine to form N_2, which then also desorbs from the catalyst surface (Equation I.13). This sequential process efficiently breaks down ammonia into its constituent gases. Under these conditions, it was determined that the associative recombinative desorption of nitrogen atoms to form N_2 (Equation I.13) is the rate-determining step (RDS).[278]

Tsai and *al.* investigated the catalytic decomposition of ammonia on the Ru(0001) surface at temperatures ranging from approximately 500 to 1250 K and pressures between 10^{-6} and 2 x 10^{-6} Torr. They observed that for temperatures above 750 K, the reaction rate approaches first-order dependence on ammonia pressure, with an apparent activation energy of 5.0 $\pm$ 0.3 kcal.mol^{-1}. This apparent activation energy is attributed to the difference between the activation energies for the cleavage of N-H bonds in chemisorbed ammonia and the desorption of molecularly chemisorbed ammonia. However, at lower temperatures, the reaction rate becomes independent of ammonia pressure, exhibiting an apparent activation energy of 43 $\pm$3 kcal.mol^{-1}, which is linked to the recombinative desorption of nitrogen.[279]

Theoretical modeling has become a powerful tool for advancing our understanding of catalytic systems at the atomic scale, with methodologies like density functional theory (DFT) demonstrating strong predictive capabilities.[280, 281, 282, 283, 284, 285, 286] This approach has been extensively applied to ammonia synthesis[280, 281, 283, 287, 288, 289] and decomposition,[284, 285, 290] particularly on Ru extended surfaces and clusters modeled under ideal conditions (vacuum). For ammonia synthesis on Ru(0001), DFT calculations reveal that nitrogen dissociation is the RDS of the reaction mechanism.[280] Recent studies have highlighted the potential

of small Ru clusters to facilitate ammonia synthesis under mild conditions, emphasizing the importance of their structural dynamics.[289]

In the context of ammonia decomposition on Ru(0001), the RDS is the recombination of adsorbed atomic nitrogen into N_2, with the activation energy being sensitive to nitrogen surface coverage (E_a = 51.0 - 43.8 × θ_N kcal.mol^{-1}).[284] These findings are supported by a recent DFT-based investigation comparing simulated temperature-programmed desorption (TPD) spectra with experimental measurements for Ru(0001), Ru(111), and Ir(111) surfaces.[286] Additionally, a theoretical study of Ru clusters (1–13 atoms) supported on carbon nanotubes highlights the influence of cluster size on reducing activation barriers and underscores the critical role of interfacial active sites between ruthenium and the carbon support in enhancing catalytic performance.[290]

I.5.1.2 Similarities and differences with ammonia synthesis

Research on ammonia decomposition is traditionally strongly related to research on ammonia synthesis, as both processes share fundamental principles. Developments in the synthesis of ammonia, particularly in the realm of catalyst innovation, are directly applicable to its decomposition.[291] This cross-utilization of advancements aids significantly in optimizing catalysts for both reactions. The synthesis and decomposition of ammonia follows Sabatier's law: the chemisorption energy of reactants and products on the catalyst surface should not be too high or too low (but within a "just right" range).[292] Catalysts must effectively activate the reactants, N_2 and H_2, while ensuring minimal adsorption of intermediate species and products to prevent surface poisoning.[224] Catalyst activity thus represents a balance between having sufficient adsorption energy to facilitate reactant coverage on the surface and maintaining enough unoccupied sites to allow the reaction to proceed efficiently.[292]

Despite the similarities between the decomposition and synthesis of ammonia, it has been demonstrated that the optimal catalyst for ammonia decomposition is not the same as for its synthesis. Specifically, the most effective catalyst for decomposition is one that binds nitrogen less strongly. Moreover, the optimal nitrogen binding energy changes depending on the ammonia concentration, a factor that varies between the synthesis and decomposition processes (see Figure I.10).[291]

This distinction underscores the subtle yet significant differences in catalytic requirements between these two closely related chemical reactions. Consequently, there is a crucial need to intensively study catalysts specifically for the ammonia decomposition reaction, particularly to identify a catalyst capable of facilitating this reaction at low temperatures. This focus is essential for enhancing the efficiency and applicability of ammonia as a hydrogen carrier in various energy applications.

The viability of ammonia-based hydrogen storage systems depends on the efficient release of hydrogen from ammonia at moderate reaction temperatures (below 500°C). Furthermore, the application of ammonia, whether it is for on-site decomposition at fueling stations or on-board hydrogen production in vehicles,

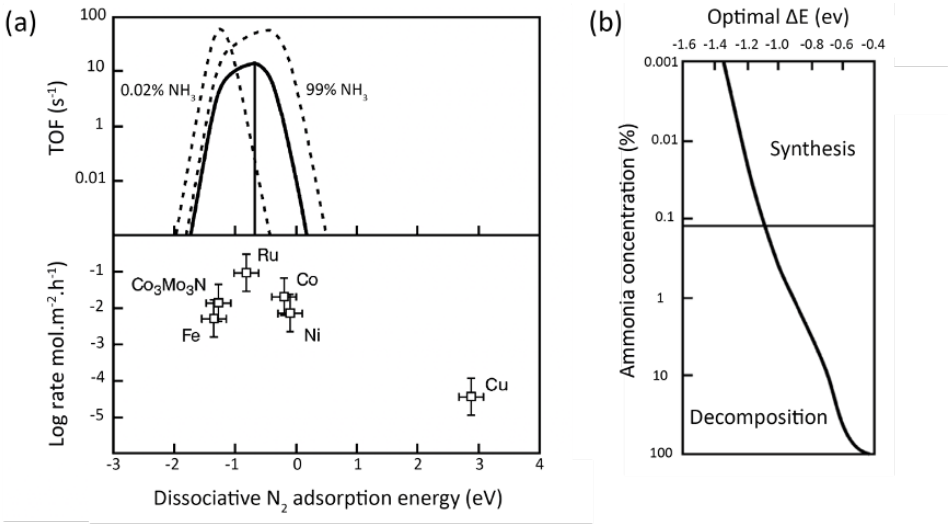

Figure I.10: (a) Calculated turnover frequencies (TOF) for ammonia synthesis and decomposition as a function of the reaction energy associated with dissociative N_2 adsorption at 500°C and 1 bar, evaluated for ammonia concentrations of 0.02% and 99%. The optimal catalytic performance for ammonia decomposition is indicated by a vertical line, corresponding to an ammonia concentration of 20% (top); (b) Dissociative N_2 adsorption energy of optimal catalyst for ammonia synthesis/decomposition at 500°C and 1 bar.[291]

determines the specific extent of ammonia decomposition needed (see Figure I.11). This situation underscores the critical importance of developing a wide array of catalyst materials, each specifically engineered to meet these diverse operational requirements effectively.[224]

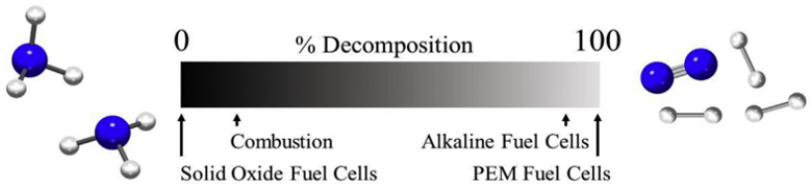

Figure I.11: (a) Calculated turnover frequencies (TOF) of ammonia synthesis/decomposition as a function of the reaction energy of dissociative N_2 adsorption, at 500 °C and 1 bar, for 0.02 and 99% of NH_3. The optimal ammonia decomposition catalysis represents by vertical, for an ammonia concentration of 20% (top). Experimental rates of ammonia decomposition (20%) over various catalysts at 500 and 1 bar (bottom). (b) Dissociative N_2 adsorption energy of optimal catalyst for ammonia synthesis/decomposition at 500°C and 1 bar.[291]

I.5.2 Ammonia Decomposition Catalysts

I.5.2.1 Metal-based catalysts

I.5.2.1.1 Active metals for ammonia decomposition

Regarding ammonia decomposition catalysts, Ru demonstrates the highest catalytic activity among all metals, following the activity order Ru > Ni > Rh > Co > Ir > Fe $\gg$Pt > Cr > Pd > Cu $\gg$Te (see Figure I.11).[10] The decomposition of ammonia on metal surfaces involves several sequential steps, beginning with the ad-

sorption of ammonia onto the metal surface, followed by gradual dehydrogenation of NH_3 and subsequent desorption of H_2 and N_2. In the case of precious metals, the Rate Determining Step (RDS) is commonly associated with the breakage of N–H bonds, whereas for non-precious metals, it is the desorption of N_2 that serves as the RDS (see Figure 13.a).

Ru stands out as the most extensively studied metal for ammonia decomposition, owing to its remarkable catalytic activity. Through ongoing research, a deeper understanding of its catalytic mechanisms has been achieved, leading to advancements and refinements in its performance. These insights into Ru behavior serve as a cornerstone for the development of non-noble catalysts. An essential consideration in evaluating metal catalysts is the size of their particles, crucial for optimizing their specific surface area while ensuring adequate recombination of nitrogen atoms.[224] Achieving an optimal balance is key: particles must be sufficiently small to maximize surface area yet large enough to facilitate nitrogen recombination.[293] The ideal particle size for Ru is determined by the concentration of B5 sites, a structural arrangement crucial for catalytic activity (see Figure I.13.a). Typically, particles ranging from 3 to 5 nm in size are considered optimal, with maximum B5 site concentration observed between 1.8 and 2.5 nm. These sites play a pivotal role in facilitating N_2 desorption due to their favorable adsorption energy (see Figure I.13.b).[294]

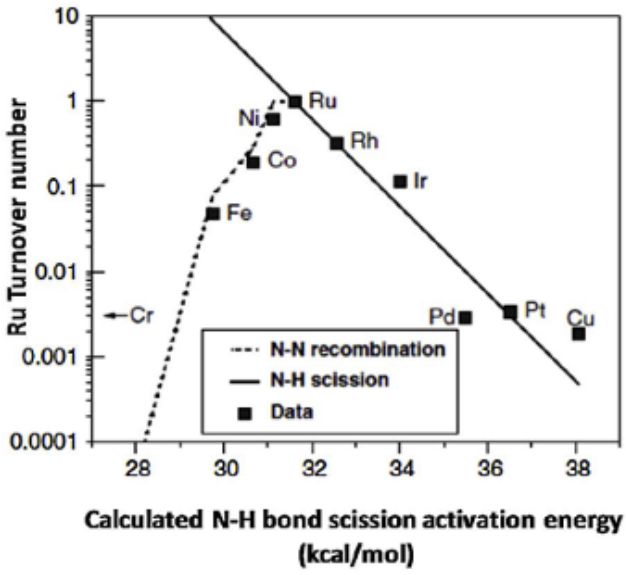

Figure I.12: TOF variation of various transition metals plotted against activation energy for N–H bond breaking estimated using Blowers-Masel correlation.[295]

Additionally, the shape of Ru particles influences their catalytic efficiency, with hemispherical particles exhibiting the highest Turnover Frequency (TOF) within the 1.8 to 3 nm size range. Conversely, elongated and flat particles achieve peak TOF at a larger size of around 7 nm. These findings underscore the intricate relationship between particle size, shape, and catalytic performance, offering valuable insights for optimizing ruthenium catalysts for ammonia decomposition applications.[296]

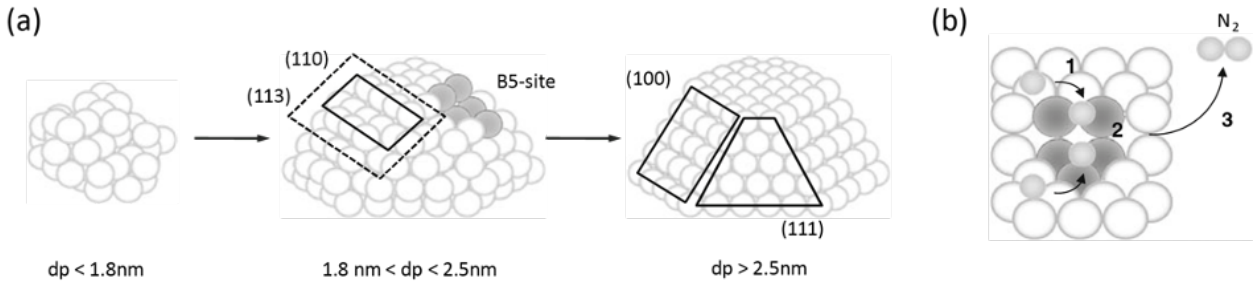

Figure I.13: (a) The three stages of Ru particle growth; (b) Schematic illustrating the associative adsorption of two N atoms to produce N_2 at a B5 type site: (1) Diffusion of N atoms toward the B5 type site, (2) Association of N atoms to form N_2, and (3) Desorption of N_2.[294]

I.5.2.1.2 Supports for metal catalysts

The beneficial influence of a support on the activity of metal catalysts is intricately linked to its inherent characteristics. Thus, the support should enable effective dispersion of active particles, thereby promoting enhanced catalytic activity while minimizing metal particle agglomeration. However, excessive dispersion must be avoided, as overly small catalyst particles may impede nitrogen atom recombination into N_2 due to limited space on active sites.[224] Once optimal dispersion is achieved, the support must also exhibit conductivity to facilitate electron transfer among the support, promoter, and metal (see Figure I.14).[297] Additionally, employing a basic support can promote the recombinant desorption of N_2 from the catalyst surface. It is the synergistic combination of these factors that culminates in a support exerting a tangible impact on catalytic activity.[224]

Carbon nanotubes (CNTs) have proven to be effective supports for Ru catalysts in ammonia decomposition. As members of the fullerene family, CNTs consist of graphene layers rolled into hollow cylindrical tubes, with single-walled (SWCNTs) and multi-walled (MWCNTs) variants. MWCNTs maintain their interlayer spacing through van der Waals forces (see Figure I.15). CNTs possess high specific strength, low weight, exceptional elasticity, thermal stability, and superior electrical and thermal conductivity.[298] Their electron-conductive nature facilitates optimal Ru dispersion.[299] Nitrogen modification of CNTs can double catalytic activity by increasing basicity, though this performance still lags behind CNTs combined with potassium.[299]

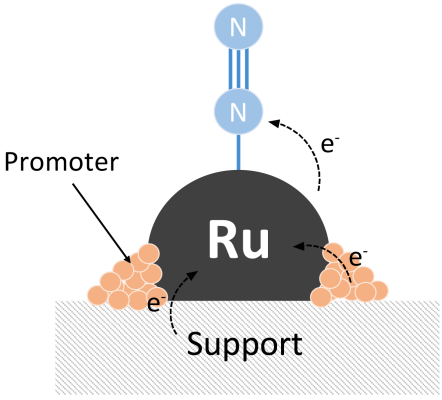

Figure I.14: Illustration of electron transfer from the support to the promoter then to the B5 sites of Ru and finally to the π^* orbital of N_2.[23]

Nevertheless, CNTs do not offer the highest catalytic activity based on the number of accessible metallic active sites. Magnesium oxide (MgO) outperforms CNTs in this aspect.[299] J. Zhang et al. succeeded in synthesizing a Ru/MgO catalyst with metal particles measuring approximately 2 nm, all supported on a sub-

strate with a high specific surface area.[300] When these two supports are combined with a promoter, like K, their catalytic activities become comparable.[277] In the literature, Ru catalysts supported on MgO or CNTs are considered benchmarks in terms of performance.

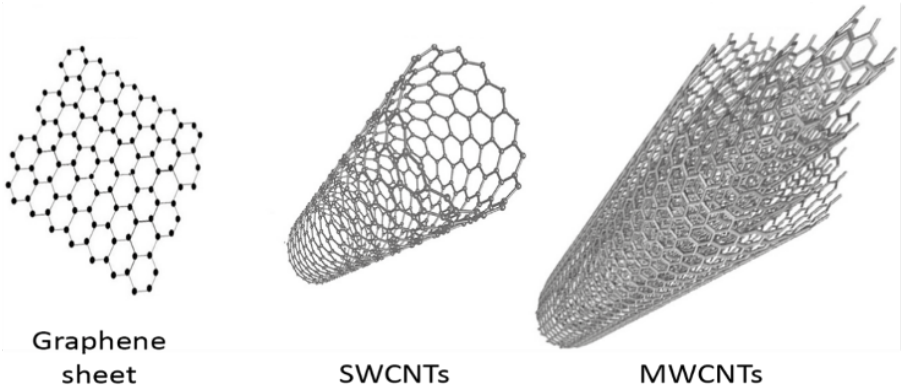

Figure I.15: Graphene sheet, single-walled carbon nanotubes and multi-walled carbon nanotubes.[298]

I.5.2.1.3 Promoters for metal catalysts

Promoters can significantly enhance the catalytic activity of metals. Alkaline, alkaline earth, or rare earth ions are commonly employed as promoters in the ammonia decomposition process.[224] The beneficial effect of promoters in this context is attributed to their ability to donate electrons, thereby facilitating electron transfer from the support to the metal catalyst. This, in turn, simplifies the recombinant desorption of N on the catalyst surface.[301] Additionally, promoters can help mitigate the sintering of metal catalysts.[224] However, it's important to note that not all compounds serving as promoters have the same impact on catalytic activity. Among these promoters, K, Cs, and Ba have received significant attention due to their effectiveness. The order of promoter efficiency is as follows: K > Na > Li > Ba > Ca (see Figure I.16).[302]

Modification of metal catalysts with metal salts leads to a reduction in pore volume and specific surface area, yet enhances the catalyst's thermal stability. Although this modification doesn't alter the particle size and morphology of metallic Ru, it does impact its electronic properties, consequently affecting the kinetics of N atoms recombinant desorption.[302]

The incorporation of promoters onto supported catalysts has been explored through various methods. Typically, supports are doped with precursors of different promoters. A novel approach involves nanoscale alkaline supports like $K_2Ti_6O_{13}$ and $Cs_2Ti_6O_{13}$, where alkali metal is atomically dispersed. Again, the same order in the promoter effect, Cs > K > Na, was observed. Despite their promising properties, these supports decompose above 750 K, rendering them unsuitable for NH_3 decomposition catalysts.[303]

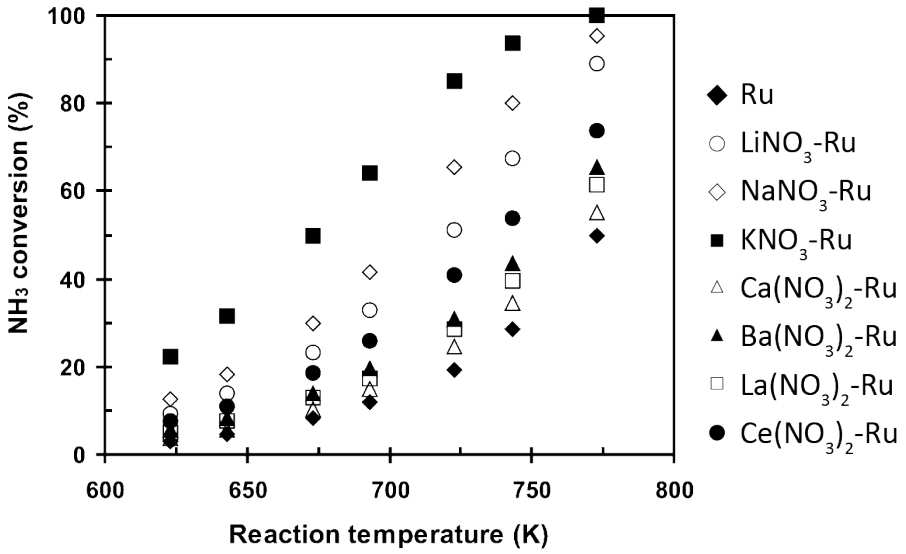

Figure I.16: Conversion of ammonia as a function of temperature on the Ru/CNTs catalyst modified by different metal nitrates; with a Weight Hourly Space Velocity (WHSV) of 60,000 ml.h^{-1}.g_{cat}^{-1}).[302]

I.5.2.1.4 Deactivation of ruthenium catalysts

The deactivation mechanisms of Ru catalysts in ammonia decomposition have received comparatively less attention despite the extensive research on this metal. Much of our understanding regarding its deactivation stems from studies on Fischer-Tropsch-type hydrocarbon synthesis, where Ru-based catalysts are prevalent. Reported deactivation pathways include the formation of RuO_x and RuC_xO_2, metal sintering, and diffusion into the surrounding medium. While Ru sintering predominantly occurs at high temperatures, it can also take place at lower temperatures. A potential remedy to mitigate catalyst deactivation involves employing Fe_2O_3 as a support, facilitating the formation of Fe-Ru complexes that impede the volatilization of the active metal.[292]

I.5.2.1.5 Application limits of ruthenium

Despite the promising performance of Ru-based catalysts, their high costs and limited availability present substantial obstacles to large-scale industrial applications. Currently, annual production remains limited, amounting to only 25 tonnes per year.[304] As a result, there is a pressing need to explore more economically viable alternatives. Ongoing research aims to develop catalysts capable of achieving complete ammonia conversion at lower temperatures, ideally between 450 and 500°C.

I.5.2.2 Alternatives to ruthenium

I.5.2.2.1 Challenges with alternative active metals

Extensive research has been conducted on metals that serve as catalysts for ammonia decomposition, providing valuable insights into their catalytic properties and potential applications. However, the suitability of

each metal for this application may vary, and their limitations need to be carefully considered. For example, iron (Fe), widely used as a catalyst in ammonia synthesis, has also attracted interest for its potential application in ammonia decomposition. However, under the reaction conditions of ammonia decomposition, Fe tends to form stable nitrides. Ammonia itself is utilized in Fe nitriding processes. While traditional nitriding temperatures exceed 500°C, nanocrystalline Fe surfaces can form nitrides at temperatures below 300°C.[305] Consequently, in ammonia decomposition, the active species expected for Fe is predominantly its nitride form. Nevertheless, depending on the specific reaction conditions, Fe may exist in various forms including metallic, oxides, oxynitrides, or carbides.[299] Despite these variations, metallic Fe appears to exhibit greater activity for decomposition compared to Fe4N nitride.[306, 307]

Ni emerges as a compelling alternative to Ru. For instance, at 500°C, for Ru/CNT (5 wt% of Ru) the NH_3 formation rate was 19 $kg_{NH_3}.kg_{cat}^{-1}.h^{-1}$ for Ru/CNT (5 wt% of Ru), compared to 2 $kg_{NH_3}.kg_{cat}^{-1}.h^{-1}$ for Ni/CNT (5 wt% of Ni).[308] However, carbon nanotubes (CNTs) may not fully exploit the catalytic potential of Ni. The use of mesoporous supports allows for improved Ni dispersion. For example, incorporating ceria into the Ni/SBA-15 catalyst achieved a rate of 14.8 $kg_{NH_3}.kg_{cat}^{-1}.h^{-1}$.[309] The benefits of ceria include facilitating nitrogen recombination, stabilizing Ni particles, and enlarging the pore size of the support. With its excellent catalytic performance and lower cost, Ni stands out as a strong candidate to replace Ru.

While metallic catalysts have been extensively studied and substantial progress has been made in improving their catalytic activity, ammonia decomposition generally begins at temperatures exceeding 300°C. Even at 400°C, under a space velocity of 30,000 $mL_{NH_3}.kg_{cat}^{-1}\cdot h^{-1}$, the ammonia conversion rate remains below 90%.[285, 299] These findings suggest there is still potential for improvement to further enhance catalytic performance and efficiency.

I.5.2.2.2 Bimetallic catalysts

A proposed solution to develop more efficient catalysts at lower temperatures involves the use of bimetallic catalysts. D. A. Hansgen et al. have identified the optimal binding energy between N and metal in ammonia decomposition, which is approximately 561 $kJ.mol^{-1}$. As previously said, A metal-nitrogen bond that is too weak prevents full NH_3 dehydrogenation, while a bond that is too strong hinders N_2 desorption. For example, bond energy values are approximately 148 $kcal.mol^{-1}$ for Fe, 142 $kcal.mol^{-1}$ for Ru, 125 $kcal.mol^{-1}$ for Co, and 122 $kcal.mol^{-1}$ for Ni. Therefore, the development of bimetallic catalysts with intermediate metal/nitrogen bond energies shows promise in addressing this challenge.[310]

In ammonia decomposition, bimetallic catalysts generally exhibit higher activity than monometallic catalysts, even when their metal-nitrogen bond energy is below 134 $kcal.mol^{-1}$. The synergistic interaction between the two metals enhances catalytic performance. For example, nickel-cobalt bimetallic catalysts outperform their monometallic counterparts, demonstrating superior efficiency (see Figure I.17).[311]

Despite their significant synergistic advantages, the development of bi-metallic catalysts presents consid-

erable challenges. Identifying the optimal ratio of the two metals to maximize catalytic performance is complex and critical. The interactions between the metals can vary extensively based on their atomic ratios, the methods used for their preparation, and the specific reaction conditions employed. Furthermore, bi-metallic catalysts are still susceptible to issues such as deactivation and thermal stability.

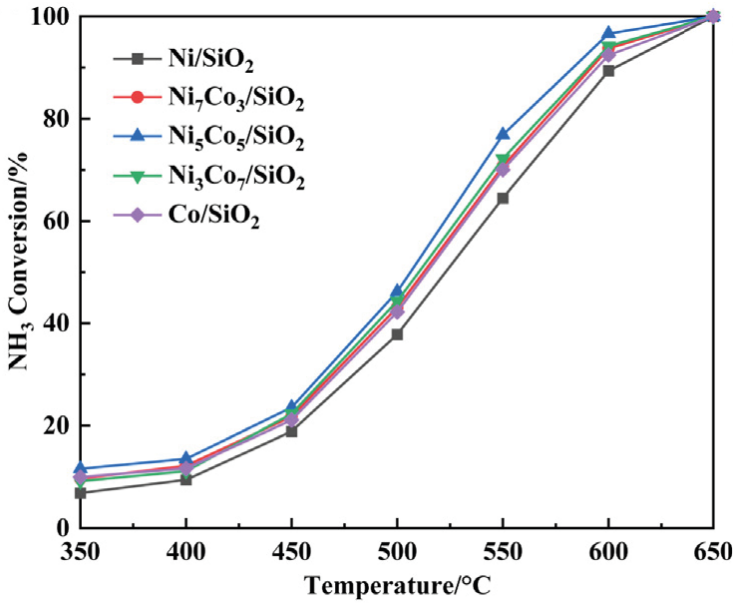

Figure I.17: Conversion of ammonia as a function of reaction temperature with monometallic and bimetallic catalysts (GHSV 30,000 mL.h_i^{-1}.$g_{cat,\,i}^{-1}$).[311]

I.5.2.2.3 Transition metal nitrides and carbides

Nitrides have been a subject of extensive study in catalysis ever since the discovery of Mo_2N catalytic activity, which was found to be similar to that of Pt.[299] The exploration of metallic nitrides (M_xN) and carbides (M_xC) is particularly relevant because these compounds naturally form under the reaction conditions of ammonia decomposition. Therefore, nitrides and carbides of metals such as Fe, Co, Ni, Ti, V, Mn, and Cr can serve as catalysts for ammonia decomposition.

Metal carbides and nitrides are characterized by the incorporation of C and N atoms into the interstitial sites of larger metal atoms, thereby modifying the electronic properties of the catalyst surface. This alteration results in a reduction of the activation energy necessary for ammonia decomposition on the surface of nitrides and carbides. The process is believed to involve successive dehydrogenation steps followed by nitrogen desorption, resembling the mechanism observed on Fe(110) and Ni(111) surfaces.[295]

Beyond the transition metals commonly explored for their interaction with ammonia, W[312] and V[313] carbides have been studied for hydrogen generation with promising outcomes. To elucidate the catalytic activity of vanadium carbides (VC), it is hypothesized that the 3d orbitals of the metal strongly interact with the 2p orbitals of carbon, thereby altering the electron density of the Fermi level and consequently, the electronic

structure of the compound. This electronic structure resembles that of precious metals. Moreover, there is no partial pressure dependency observed for either ammonia or hydrogen. The mechanism mirrors that of W, with nitrogen desorption being the RDS.[295]

Oxy-nitrides represent another intriguing category of materials stemming from nitrides. Zr oxy-nitrides, for instance, have demonstrated catalytic activity in ammonia decomposition. They exhibit reactivity with nitrogen and resist reduction, presenting a distinctive property.[314]

I.5.2.2.4 Alkaline or alkaline earth metal amides

I.5.2.2.4.a Sodium amide

Among the alternative solutions to Ru, alkali metal amides, such as sodium amide ($NaNH_2$), have been explored as a catalyst for ammonia decomposition. Initially, the catalytic activity of these compounds was unreported until 2014, when a detailed study revealed a mechanism involving the transition of sodium amide to its metallic form, producing N_2 and H_2. The metal then reacts with ammonia to regenerate the metal amide (Step 2), establishing an equilibrium that favors ammonia decomposition. This catalytic mechanism is observed for Na, K, and Rb.[12]

Wood *et al.* performed isotopic studies using ND_3 and confirmed that H_2 production originates exclusively from ammonia. When tested under argon without ammonia, no kinetic isotope effects were observed, ruling out $NaNH_2$ as the source. These findings establish sodium amide not merely as a promoter but as an independent catalyst, supporting the proposed ammonia decomposition mechanism via $NaNH_2$ (Equations I.14 and I.15).[315]

$$MNH_{2\,(s)} \rightarrow M_{(s)} + \frac{1}{2} N_{2\,(g)} + H_{2\,(g)} \tag{I.14}$$

$$M_{(s)} + NH_{3\,(g)} \rightarrow MNH_{2\,(s)} + \frac{1}{2} H_{2\,(g)} \tag{I.15}$$

Despite the promising results regarding the performance of $NaNH_2$ (see Table I.4), its high volatility limits its practical application. Consequently, there has been a broader exploration of light metal amides and imides.[316]

I.5.2.2.4.b Lithium amide

Among alkali metal amides, and unlike sodium amide, lithium amide ($LiNH_2$) undergoes a different decomposition mechanism. $LiNH_2$ melts at 360°C, and upon further heating, it decomposes to form solid lithium imide (Li_2NH) and ammonia (see Equation I.18). Li_2NH decomposes around 600 °C (see Equation I.17).[12, 317] It's worth noting that potassium and sodium do not have an imide form. Unlike lithium and magnesium

Table I.4: Comparison of catalytic activity for Ni-SiO_2/Al_2O_3, Ru-Al_2O_3, $NaNH_2$, and $LiNH_2$, evaluated at 450 °C in a 46.9 cm^3 stainless steel reactor under an ammonia flow rate of 60 sccm (WHSV = 7200 $mL_{NH_3} \cdot g_{cat}^{-1} \cdot min^{-1}$), with 0.5 g of catalyst.[12]

Catalyst	NH_3 conversion (%)	Reaction rate ($kg_{NH_3}.kg_{cat}^{-1}$)	TOF (h^{-1})
Ni-SiO_2/Al_2O_3	34.0	1.78	9.31
Ru/Al_2O_3	53.7	2.81	334
$NaNH_2$	54.9	2.88	6.59
$LiNH_2$	90.7	4.75	6.42

(MgNH). However, for magnesium, its nitride form Mg_3N_2 is thermodynamically more stable.[318]

$$2\,LiNH_{2\,(s)} \rightarrow Li_2NH_{\,(s)} + NH_{3\,(g)} \qquad \Delta H = 84.1\ kJ.mol^{-1}\ NH_3 \tag{I.16}$$

$$2\,Li_2NH_{\,(s)} \rightarrow 4\,Li_{\,(s)} + H_{2\,(g)} + N_{2\,(g)} \qquad \Delta H = 444\ kJ.mol^{-1}\ kJ.mol^{-1}\ H_2 \tag{I.17}$$

The industrial production of $LiNH_2$ involves heating Li metal or LiH in the presence of ammonia (NH_3), as depicted in Equations I.18 and I.19. Additionally, $LiNH_2$ can be synthesized by dissolving metallic lithium in liquid ammonia, with the presence of metallic chloride often accelerating this process.[319]

$$2\,Li_{\,(s)} + 2\,NH_{3\,(s)} \rightarrow 2\,LiNH_{2\,(s)} + H_{2\,(g)} \qquad \Delta H^0_{298K} = -135.1\ kJ.mol^{-1} \tag{I.18}$$

$$LiH_{\,(s)} + NH_{3\,(s)} \rightarrow LiNH_{2\,(s)} + H_{2\,(g)} \qquad \Delta H^0_{298K} = -135.1\ kJ.mol^{-1} \tag{I.19}$$

Li amides and their derivatives, such as Li imides and nitrides, have shown relevant properties to store hydrogen and has even been considered for this purpose.[320] $LiNH_2$ can store up to 6.5 wt.% of hydrogen, which it releases upon decomposition into imide (see Equation I.18). However, this compound is not particularly favorable for this application due to the high temperature (350°C) required to release the stored hydrogen and the formation of ammonia during the decomposition of $LiNH_2$.[12] These materials have been studied and characterized with various experimental techniques, from X-Ray powder[321, 322] and neutron powder[322] diffractions, to Raman[322, 323], and Infrared[323, 324] spectroscopies. The typical size distributions of $LiNH_2$ particles correspond to median and mean nanoparticle diameters of 36 and 42 nm, respectively.[321] From Raman spectroscopy, amide and imide groups can be differentiated by the N–H stretching frequency, with distinct bands observed for both amide and imide materials.[322]

The utilization of such compounds in the realm of ammonia synthesis and decomposition is closely linked to the analysis of products derived from the thermal breakdown of $LiNH_2$. In 2003, the observation of N_2 and H_2 post-decomposition were observed after its decomposition, therefore when ammonia was present. However, it took six years before experimental investigations began to explore the potential catalytic activity of the solid residue Li_2NH and/or the non-stoichiometric $Li_{3-x}NHx$ residue ($0 < x < 2$) in ammonia decomposition.

Li imide-containing species have emerged as the effective catalysts for the thermocatalytic decomposition of ammonia (see Figure I.18.a), thus attracting significant attention in research.[108] Metallic Li has previously been explored as a promoter for the metal catalysts mentioned above. Typically regarded as one of the less electron-donating alkali metals, Li is often considered less effective as a promoter compared to Cs and K. However, in the form of a metal imide, Li exhibits a remarkable enhancement in its electron-donating character. Given that Li_2NH is only formed following the decomposition of $LiNH_2$, the decomposition temperature of NH_3 must necessarily exceed 350°C.[325]

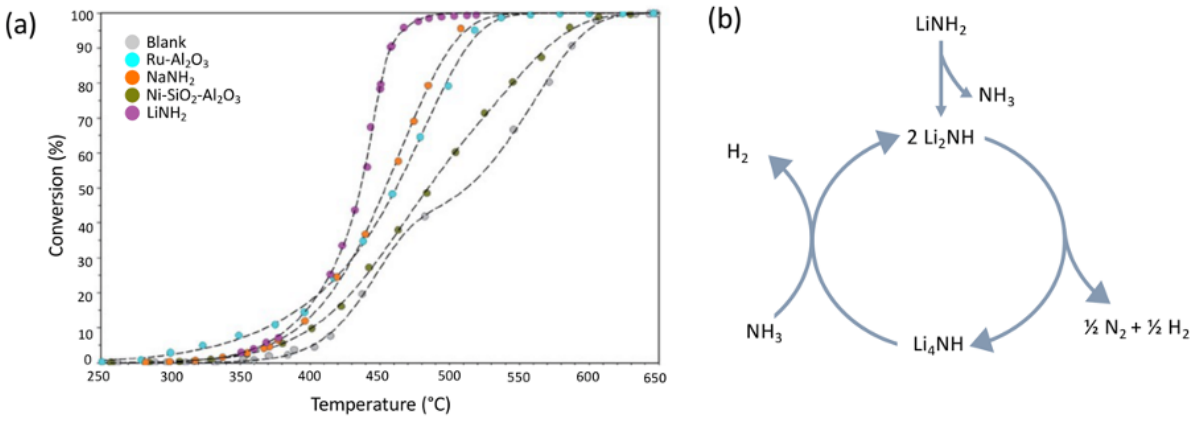

Figure I.18: Possible conversions among lithium metal (Li), hydride (LiH), nitride (Li_3N), amide ($LiNH_2$), imide (Li_2NH), and lithium nitride-hydride (Li_4NH).[326]

In situ neutron and X-ray powder diffraction experiments revealed that the active state of Li_2NH is a solid solution of $LiNH_2$ and Li_2NH, with the exact stoichiometry being contingent on the reaction conditions (Equation I.20). It's worth noting that the lithium amide/imide pair is recognized for forming non-stoichiometric intermediates, which share the same cubic structure as Li_2NH.[325] The catalytic mechanism proposed for this couple differs from that of "conventional" metallic catalysts. The mechanism involving transition metal nanoparticles aligns more closely with the Mars-van Krevelen mechanism. In this scenario, it is hypothesized that both the hydrogen and nitrogen of Li_2NH can be interchanged with those of ammonia under the conditions of the ammonia decomposition reaction.[108]

$$(1\text{-}x)\ Li_2NH + x\ NH_3 \rightarrow Li_{2-2x}NH_{1+2x} \tag{I.20}$$

After a thorough investigation of the decomposition kinetics of Li_2NH, findings indicated its decomposition into another solid complex, Li_4NH. Subsequent isotope studies validated that the ammonia decomposition correlates with the breakdown of Li_2NH into Li_4NH, and it is the latter that would interact with ammonia (see Figure I.18.b), thereby regenerating lithium imide.[13]

In situ neutron diffraction were conducted to determine the nature of the active species when employing lithium imide as a catalyst (see Figure I.19.a and I.19.b). Initially, an isotope exchange was performed. To achieve this, a deuterated lithium amide ($LiND_2$) sample was synthesized through the reaction of lithium nitride (Li_3N) with deuterated ammonia (ND_3). Following heat treatment and the formation of Li_2ND, the deuterated ammonia flow was replaced by an ammonia flow. Subsequently, HD was produced (see Figure I.19.c). Three potential explanations could account for this observation. Firstly, the decomposition of ammonia on the Li_2ND surface could lead to the formation of Li_2NH, N_2, HD, and H_2. The second hypothesis suggests the formation of HD through interaction between NH_3 and residual ND_3 present in the reactor or with the Li_2ND catalyst, resulting in an ND_xH_{3-x} species, which then decomposes. Finally, the third possibility involves the interaction between H_2 and residual D_2.[12]

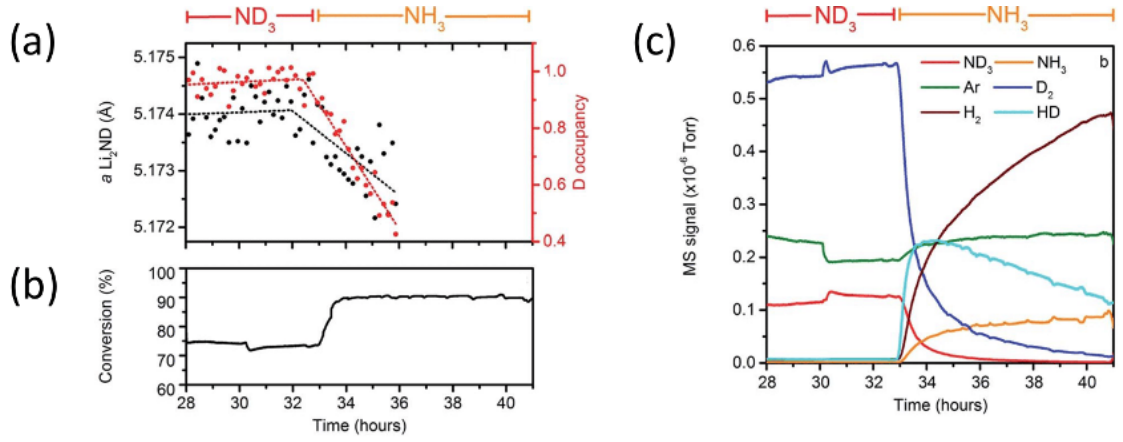

Figure I.19: Isotope exchange experiment, with the gaseous species flowing through the sample during the experiment (ND_3 and NH_3) are shown at the top with: (a) the refined deuterium occupancy (in red) and lattice parameter (in black) in the Li_2ND sample; (b) the ammonia conversion percentage; and (c) the QGA (Quadrupole Gas Analyzer) data recorded during the experiment.[12]

The reaction equation proposed by the authors is $2\ Li_2ND + 2\ NH_3 \rightarrow 2\ Li_2NH + 2\ HD + H_2 + N_2$. This equation aligns with the high rate of HD formed initially (see Figure I.19.c) and is also consistent with the results of ammonia conversion. However, it is unlikely that this reaction is stoichiometric, despite a slope linked to the change of deuterium by hydrogen corresponding to a linear function. The authors note that this phenomenon may be a consequence of the low precision of the refined data.

Stoichiometry is no longer respected when the Li_2ND sample is brought into contact with ammonia. This indicates the formation of lithium amide, consistent with the catalytic mechanism proposed by the authors. Consequently, hydrogen is incorporated into the imide, causing it to transition to its amide form. This hydro-

gen originates from ammonia, involving the cleavage of the N-H bond. Hence, this process can reasonably be considered the decomposition reaction of NH_3 on the surface of the lithium imide/amide mixture.[12]

Moreover, the conversion of ND_3 was 73% compared to 91% for NH_3, suggesting a potential role for hydrogen or deuterium atoms in the RDS of ammonia decomposition. The isotope exchange experiment conducted suggests that the rate of diffusion of H in the lithium imide structure (Equation I.21) is faster than the recombinant desorption of H on the surface of a catalyst. Thus, the RDS might involve the breakdown of N–H/D bonds, the diffusion of H/D, or the formation of H_2/D_2.[12]

$$Li_2ND + NH_3 \leftrightarrow LiNDH + LiNH_2 \tag{I.21}$$

I.5.2.2.4.c Plasma treatments of lithium amide

Wen *et al.* have explored the effects of plasma treatments on $LiNH_2$ under ambient temperature and pressure in an argon flow. Their findings indicate that plasma treatment results in the formation of metallic Li colloids, observable with and without color changes. Unlike the thermal decomposition of $LiNH_2$, which predominantly produces NH_3 as the main gaseous product and Li_2NH as a solid product, the plasma treatment uniquely yields N_2 and H_2 without generating NH_3.[327]

The authors propose that the key distinction between plasma and thermal decomposition of $LiNH_2$ lies in the formation of NH_2-vacancies during the plasma process. These vacancies facilitate the creation and migration of metallic Li colloids on the surface of lithium amide. This alteration leads to an electron-rich $LiNH_2$ surface, thereby creating a chemically favorable environment for the activation and transformation of molecules. This research paves the way for plasma-driven ammonia decomposition using $LiNH_2$, potentially offering a novel method for producing N_2 and H_2.[327]

I.5.2.2.4.d Theoretical study of lithium amide

Lithium amide has been studied in the DFT literature as bulk materials with various computational conditions.[328, 329, 330, 331, 332, 333, 334] The ambient temperature and pressure α phase of $LiNH_2$ is a cubic anti-fluorite-like crystal structure with space group $\Gamma 4$ (corresponding to a tetragonal lattice with 32 atoms per unit cell).[335, 336] The surfaces and possible terminations of $LiNH_2$ have not been studied in the literature to date, although interesting theoretical models have been proposed for its interface with Li_2NH compound.[337]

DFT studies of $LiNH_2$ and Li_2NH have revealed a low energy barrier for proton migration between imide/amide groups. This indicates that hydrogen can move within the amide structure, likely via the Frenkel mechanism, previously studied in the context of hydrogen storage in the Li-N-H system. In every DFT study of $LiNH_2$ decomposition, hydrogen plays a crucial role in the RDS. Hoang et al. proposed two distinct mechanisms depending on the size of the $LiNH_2$ particles. For large particles, the RDS involves the cleavage of the N–H bond, whereas for small particles, it entails the diffusion of H+ to the surface of the particles.[332]

I.5.2.2.4.e Impact of the reaction medium on the catalytic performance of lithium amide

Despite progress, concerns persist regarding the stability of the $LiNH_2/Li_2NH$ couple, particularly due to the compound's liquefaction with temperature. Additionally, lithium amide and imide react with water, leading to the formation of lithium hydroxides (LiOH). Consequently, an anhydrous ammonia source is required to prevent any degradation in catalyst reactivity. Despite this, in tests of ammonia decomposition catalyzed by $LiNH_2$, the decomposition rate remained similar even after 15 hours of reactions.

One of the challenges encountered during tests to evaluate the catalytic activity of this compound was the inconsistency of the results obtained. One explanation proposed is the significant influence of the reactor material. It was found that a stainless-steel reactor yields better results compared to a copper or nickel reactor (see Figure I.20.a).[338] This observation highlights the critical role of transition metals in lithium amide/imide catalysis, driving research efforts to enhance the performance of these compounds through the incorporation of transition metals.[13] It is crucial that catalytic tests of lithium amide/imide pairs be conducted in stainless steel reactors. This is because the NH_2^- and NH^{2-} anions are highly basic and can react with conventional quartz or glass reactors (see Figure I.20.b).[13] The inability to conduct catalytic tests of imides or amides in a quartz reactor was only realized later, well after the publication of initial articles on the performance of this compound.[338] Tests involving this material yield vastly different performance results depending on the reaction conditions, making comparisons complex.

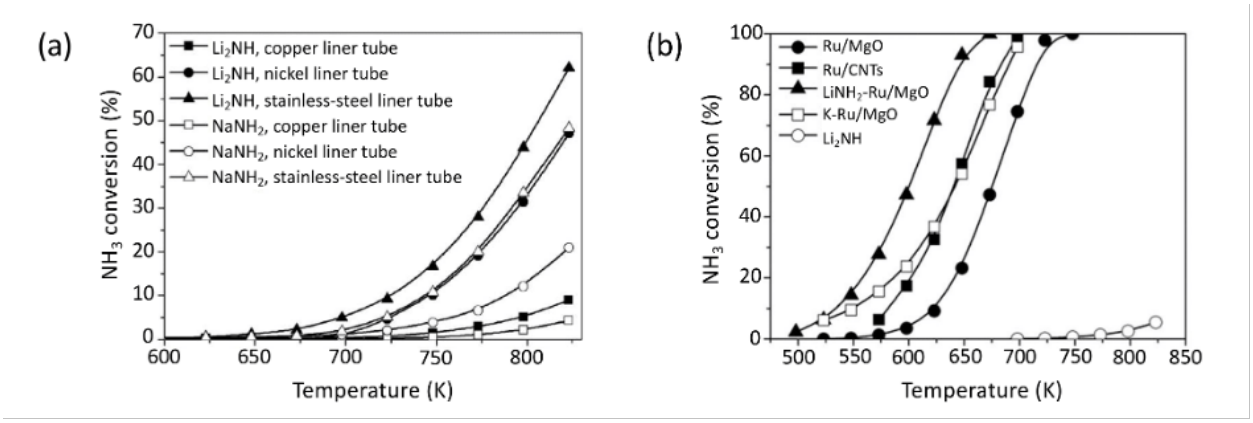

Figure I.20: Temperature-dependent ammonia conversion for (a) Li_2NH (0.06 g, 30 mL.min-1) in a tank reactor with Cu, Ni, or stainless-steel liner tubes;[339] (b) Li_2NH, Ru, and Li_2NH–Ru (30 mg, flow rate 5% vol NH_3/Ar, 30 ml.min-1) in a quartz reactor.[340]

I.5.2.2.4.f Support for lithium amide-based catalyst

To enhance the catalytic performance of $LiNH_2$, Bramwell *et al.* deposited $LiNH_2$ onto carbon supports (CX27). This nano-scaling approach has been successfully applied to other systems such as $LiBH_4$,[341] MgH_2,[342, 343] and $NaAlH_4$[344, 345] supported on carbon. The $LiNH_2$/C nanocomposite was prepared by impregnating carbon

with a butyllithium solution to generate LiH particles. Subsequently, after treatment with gaseous ammonia, LiH transforms into $LiNH_2$ supported on carbon. Butyllithium was selected due to the low solubility of $LiNH_2$, enabling direct impregnation. This material represents a potential solution for solid-state ammonia storage. Specifically, lithium hydride reacts with NH_3, capturing it in a solid form (see Figure I.21).[325]

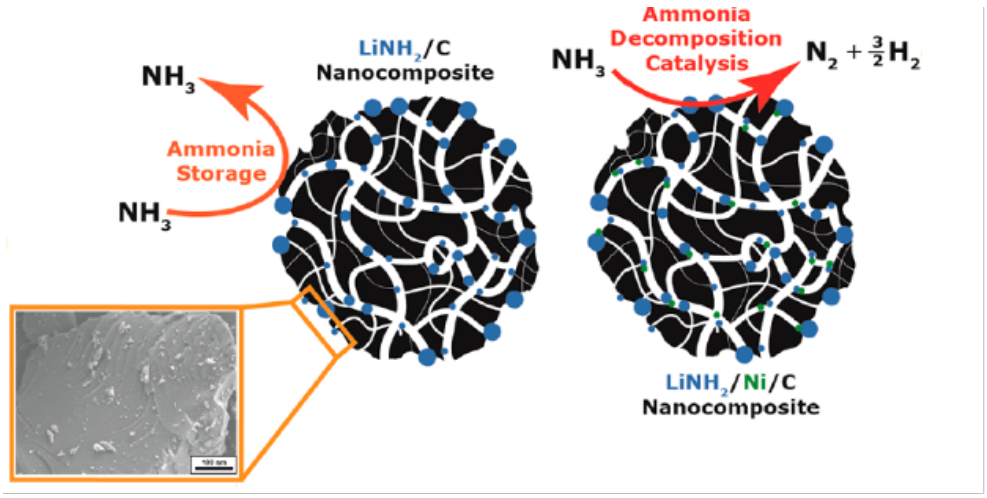

Figure I.21: Schematic representation of the $LiNH_2$-Carbon nanocomposite and the $LiNH_2$–Ni/Carbon nanocomposite.[325]

The decision to utilize a carbon support might seem unconventional, given that lithium amide reacts with carbon to form Li_2CN_2 at elevated temperatures. This information could explain the relatively lower performance of the $LiNH_2$/C nanocomposite compared to macrocrystalline lithium amide (see Figure I.22). Additionally, a hybrid compound comprising Ni and $LiNH_2$ was supported on the same carbon support. Although initially efficient, a significant decline in ammonia conversion occurred upon raising the temperature. This decline in performance could potentially be attributed to the reaction between $LiNH_2$ and the carbonaceous support at high temperatures. Consequently, combining $LiNH_2$ with Ni resulted in higher ammonia conversion compared to nickel alone; this nanoscale approach could prove beneficial for replication on a non-carbon support, thereby avoiding $LiNH_2$ deactivation.[325]

T. J. Wood et al. have investigated the effects of various supports on the catalytic performance of $LiNH_2$, including activated carbon, SiO_2, Al_2O_3, and MgO. In the cases of carbon, SiO_2, and Al_2O_3, there is a reaction between these supports and the catalysts, these materials cannot therefore be used as support of $LiNH_2$-based catalysts.

However, for MgO, the interaction with lithium amide-imide leads to the formation of a ternary nitride (LiMgN) instead of a ternary oxide. And this ternary nitride is unstable in the presence of ammonia, reverting back to the $LiNH_2$ catalyst. Consequently, MgO emerges as a potentially viable support for the $LiNH_2$-based catalyst in ammonia decomposition. This conclusion is supported by the consistent catalytic performance of lithium amide when combined with magnesium oxide, unlike the other tested supports (see Figure I.23).[13]

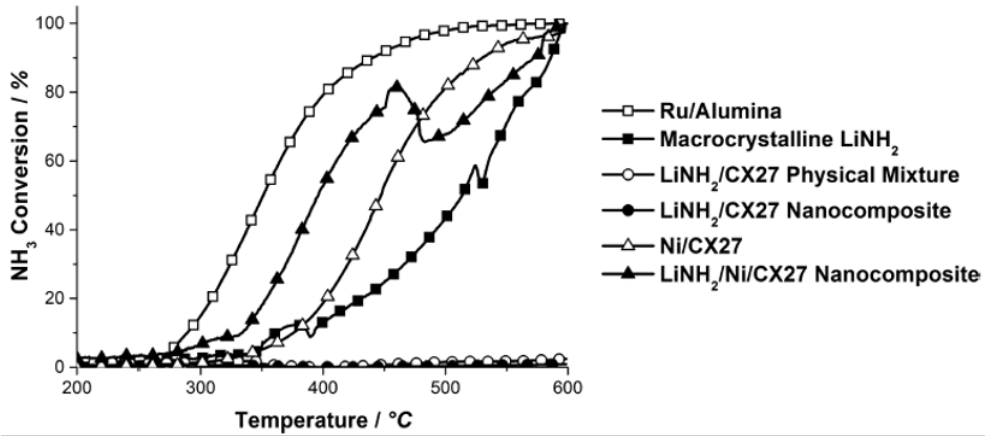

Figure I.22: Ammonia conversion rates were measured for various catalysts, including Ru/alumina, macrocrystalline $LiNH_2$, $LiNH_2$/CX27 physical mixtures and nanocomposites, Ni/CX27, and $LiNH_2$/Ni/CX27. The measurements were based on the nitrogen concentration in the gas flow. Experiments were performed with catalyst quantities ranging from 100 to 250 mg, under a 10% NH_3 flow in helium at a rate of 50 $mL.min^{-1}$, corresponding to a gas hourly space velocity (GHSV) of 13,000 $mL.h^{-1}.g_{cat}^{-1}$.[325]

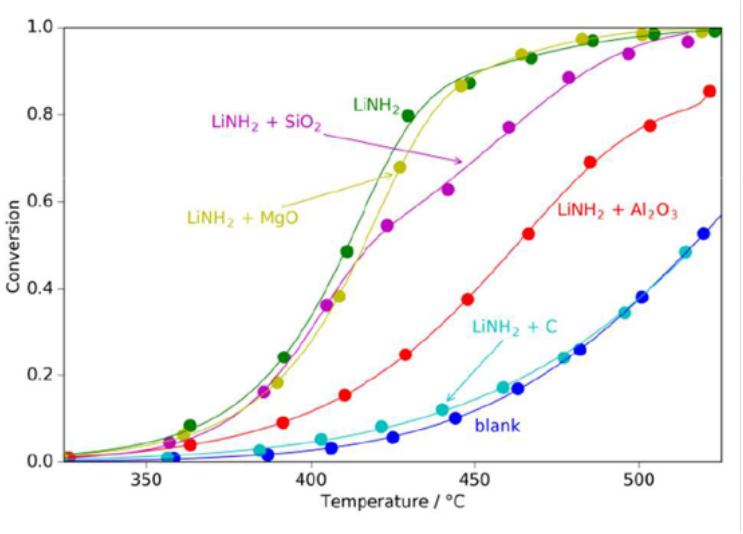

Figure I.23: Ammonia conversion catalyzed by $LiNH_2$ supported on activated carbon, SiO_2, Al_2O_3, and MgO. Measurements were conducted in a stainless steel reactor using 0.5 g of lithium amide hand-ground with 0.5 g of support, under a flow of 30 $mL.min^{-1}$ NH_3.[13]

I.5.2.2.5 Alkaline metal amide and transition metal pairs

I.5.2.2.5.a Lithium amide and ruthenium

To enhance the catalytic activity of $LiNH_2$, the addition of transition metals has been investigated, leading to significantly higher rates of ammonia decomposition. This improvement suggests a potential interaction between transition metals and $LiNH_2$.[338]

Notably, the $LiNH_2$-Ru/MgO catalyst outperformed benchmarks catalysts such as Ru/MgO, Ru/CNT, and K-Ru/MgO systems for ammonia decomposition in the 500–700 K range (see Figure I.24.a).[340] The temperature-dependent catalytic activity revealed an apparent activation energy of 53.2 ± 1.5 $kJ.mol^{-1}$ for $LiNH_2$-Ru/MgO. In contrast, the pure Li_2NH catalyst demonstrated significantly lower activity, requiring a minimum operating temperature of 700 K and exhibiting a much higher apparent activation energy of 150 ± 2.9 $kJ.mol^{-1}$.[340] This reduced catalytic performance is likely due to the catalytic tests being conducted in a quartz reactor, as quartz reacts with $LiNH_2$.

X-ray absorption near edge structure (XANES) and extended X-ray absorption fine structure (EXAFS) analyses confirmed that the $LiNH_2$-Ru interfaces consisted of metallic ruthenium in direct contact with $LiNH_2$ materials. FTIR spectroscopy further identified the presence of both $LiNH_2$ and Li_2NH, as indicated by characteristic N–H stretching frequencies. The proposed mechanism suggests that $LiNH_2$ partially decomposes into $Li_2NH(Li_{3-x}NH_x)$ species at the ruthenium interface, enhancing ammonia dissociation more effectively than ruthenium alone. This bifunctional mechanism likely involves lithium amide/imide materials facilitating the partial dissociation of NH_3 into NH_x intermediates, while ruthenium catalyzes the subsequent formation of nitrogen and hydrogen products (see Figure I.24.b).

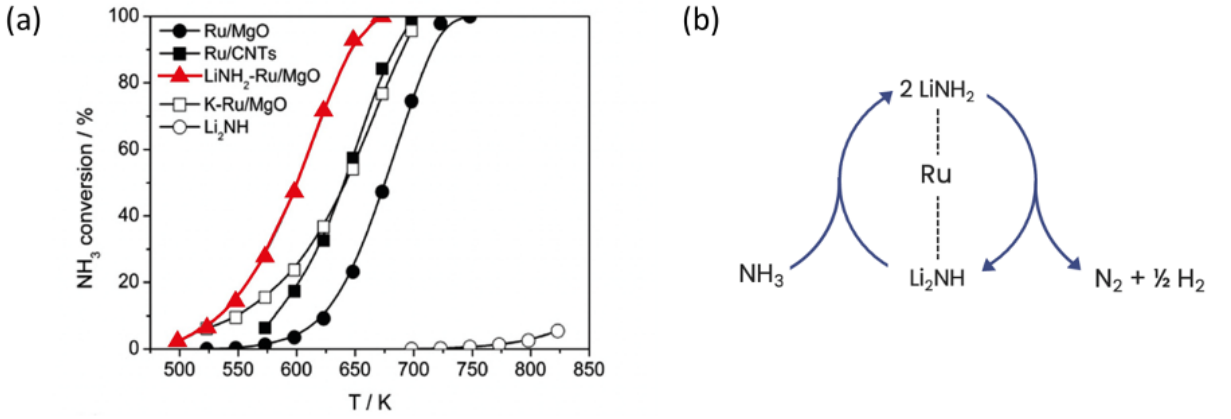

Figure I.24: (a) Conversion of ammonia catalyzed by Ru-$LiNH_2$/MgO (red), Ru/CNTs, Ru/MgO, K-Ru/MgO and Li_2NH (black), for catalyst precursor mass of 30 mg, flow rate 30 $ml.min^{-1}$ for 5 vol% NH_3 in Ar in a quartz reactor (adapted from[15]) ; (b) Assumed catalytic mechanism for Li_2NH–Ru (adapted from [340]).

Although extensive experimental efforts have been dedicated to evaluating the catalytic performance of ruthenium-based lithium amide catalysts for ammonia decomposition, the structure (size, geometry, chemical composition) and energetics of the interfacial region between the metal and the amide remain unknown. This gap in understanding is largely due to a lack of in situ and operando characterization. Furthermore, as the catalytic site has not yet been clearly identified, the reaction mechanism requires further elucidation, particularly through the detection and analysis of reaction intermediate species.

I.5.2.2.5.b Theoretical study of lithium amide and ruthenium catalyst

Given the complexity of characterizing the interfacial region between the metal and the amide, a DFT investigation was conducted using a $Li_2NH(110)$ extended surface model doped with a single Ru atom. This approach aimed to simulate ammonia decomposition on a Ru-$LiNH_2$-based catalyst.

The model demonstrated a strong capacity to adsorb and dissociate ammonia into NH_2 surface species, suggesting potential for regenerating $LiNH_2$ from Li_2NH. However, when exploring NH_2–NH and NH–NH coupling to produce N_2, the final product of ammonia decomposition, significant activation barriers were predicted, ranging from 1.68 to 1.99 eV. These barriers arise from the strong repulsive interactions between the negatively charged NH_x species. Notably, these values are comparable to or exceed the activation barrier for a pure Ru(0001) surface at a nitrogen surface coverage of 0.25 ML (1.70 eV). Consequently, the study concluded that Li_2NH alone is not an efficient catalyst for NH_3 decomposition due to the kinetically hindered recombination step of nitrogen atoms. This theoretical finding aligns well with experimental observations, which also indicate the inefficacy of Li_2NH as a standalone catalyst for this reaction.[340]

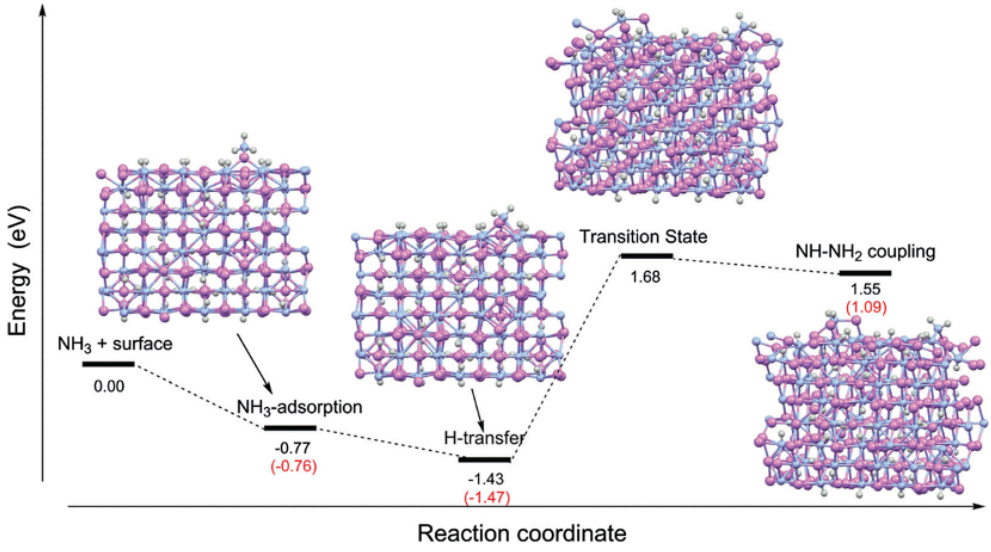

Figure I.25: Energetic profile of ammonia adsorption on $Li_2NH(110)$ surface (values in black), and $Li_2NH(110)$ surface dopped by one Ru atom (values in red); with Li, N and H atoms being purple, light blue and grey spheres, respectively.[340]

The inability to achieve ammonia decomposition may arise from limitations in the DFT model employed. Specifically, the model likely does not accurately represent experimental reality. For instance, experimental data indicate the presence of metallic Ru–Ru bonds within the catalyst, whereas the model used a single Ru atom on a lithium imide surface. These findings suggest a more complex interfacial structure, involving a ruthenium surface in contact with lithium amide/imide, which this model fails to capture.

I.5.2.2.5.c Lithium amide and transition metal nitrides

Building on the promising results obtained with ruthenium, other transition metals in contact with $LiNH_2$ have been tested for ammonia decomposition. Transition metals from the fourth row of the periodic table, including Ti, V, Cr, Fe, and Mg, form stable nitrides (TMN) and are generally less active for ammonia decomposition.[339] However, when these transition metals are combined with $LiNH_2$ under typical ammonia decomposition temperatures, they lead to the formation of ternary lithium nitrides accompanied by the release of H_2. The interaction of these ternary nitrides with ammonia results in the production of N_2 while regenerating the initial TMN-Li_2NH composite. It is hypothesized that reaction intermediates [A-NH_x-TM] (where x = 0, 1, or 2) modify the reaction and energy pathways of ammonia decomposition, thereby enhancing the catalytic activity of these transition metals (see Figure I.26).

The formation of ternary nitrides was confirmed through TPD-MS, XRD, and XANES analyses. Specifically, for iron nitride, these techniques reveal that it reacts with Li_2NH at temperatures above 500 K to form Li_3FeN_2. It is proposed that Li_3FeN_2 subsequently decomposes, releasing N_2 at approximately 350 K and NH_3 at 500 K, which leads to the regeneration of Fe_2N and Li_2NH. At higher temperatures, the catalytic activity is attributed to the interaction of Li_3FeN_2 with NH_3, resulting in the release of N_2 while simultaneously reforming Fe_2N and Li_2NH (see Figure I.26.b).[339]

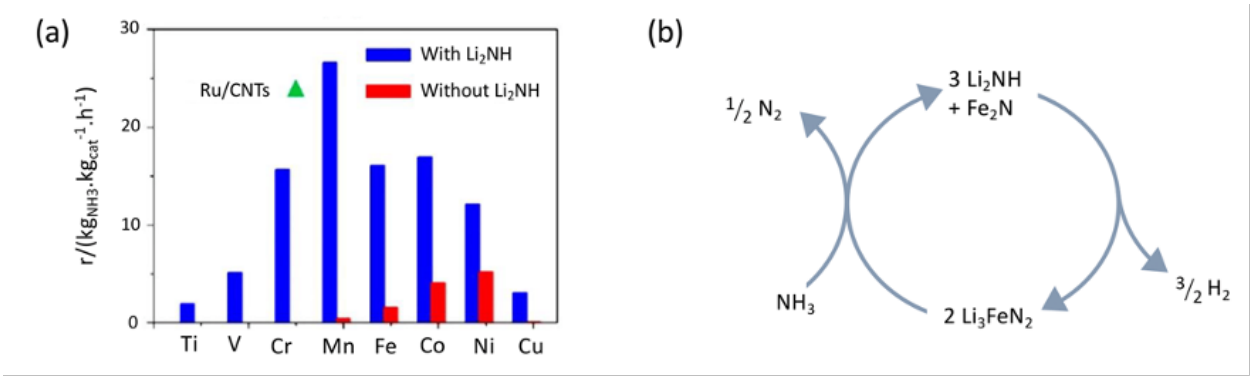

Figure I.26: (a) Decomposition rate of ammonia catalyzed by different 3d metal nitrides with and without Li_2NH at 500 °C (reaction conditions: 30 mg catalyst mass and WHSV = 60000 mLNH_3.g_{cat}-1.min-1)[338] ; (b) Catalytic diagram proposed to explain the performance of Li_2NH-Fe_2N composites.[108]

3D transition metals can form a range of stable or unstable low-nitrogen interstitial nitrides. The introduction of lithium facilitates the formation of ternary nitrides that boast a higher nitrogen content and enhanced stability. Consequently, these compounds are likely to surpass the catalytic activities of pure 3D transition metals in the decomposition of ammonia. The catalytic mechanisms for these systems consistently involve the formation of a ternary nitride, underscoring the pivotal role of lithium in improving the catalytic properties.[339]

Regarding performances, all tested transition metal nitrides exhibit catalytic activity in ammonia decomposition when combined with lithium amide. The activity of the Li_2NH-TM(N) compounds follows a volcano

trend, with Li_2NH-MnN emerging as the most efficient catalyst. Notably, the Li_2NH-MnN compound outperforms even the Ru/CNT catalyst containing 5 wt% Ru (see Figure I.26.a). This result is particularly surprising given that nickel is typically considered the most active transition metal for ammonia decomposition. A "reversal" in performance is observed when metal nitrides are paired with lithium imide, indicating a significant enhancement in their catalytic properties.[339]

I.5.2.2.5.d Theoretical study of lithium amide and iron

In the same way as for ruthenium, a DFT investigation was conducted using a $Li_2NH(110)$ extended surface model doped with a single Fe atom. This study also aimed to simulate the ammonia decomposition process on a Fe-$LiNH_2$-based catalyst.

DFT calculations of the Fe–Li_2NH system suggest that hydrogen atoms from the N–H bonds in ammonia are captured by lithium atoms within the system. This interaction is believed to enhance catalytic activity, particularly in the Fe–N–Li configuration. Hydrogen gas (H_2) formation is facilitated by the recombination of hydrogen atoms associated with lithium (H(Li)) and those bonded to nitrogen (H(N)) (see Figure I.27). This process highlights the synergistic effect between Fe and Li_2NH, enabling efficient hydrogen extraction and ammonia decomposition.[339] However, the investigation halted at this intermediate step, leaving the RDS unexamined.

Despite this brief theoretical study, the experimental results clearly demonstrate that the role of the alkali or alkaline earth metal imide extends beyond merely acting as a promoter; it functions as an ammonia transmission agent with an activated N-H bond. Additionally, the presence of a second cation linked to nitrogen contributes a positive inductive effect, which helps stabilize the covalent bond between nitrogen and the transition metal. This interaction significantly enhances the stability of the nitrogen-rich LiTMN intermediate, showcasing the complex interplay of elements that improves the overall efficiency of the catalytic process.[339]

Despite the limited theoretical scope, experimental results underscore that alkali or alkaline earth metal imides do more than act as promoters—they serve as ammonia transmission agents by activating the N–H bond. Additionally, the presence of a secondary cation bound to nitrogen introduces a positive inductive effect that stabilizes the covalent bond between nitrogen and the transition metal. This interaction significantly enhances the stability of the nitrogen-rich LiTMN intermediate, demonstrating the sophisticated interplay of components that optimizes catalytic performance.[339]

In summary, when coupled with transition metals, two catalytic pathways become possible. If the metal is capable of forming a nitride, the formation of a ternary nitride is typically observed (e.g., Li_7MnN_4, Li_3FeN_2, Ca_6MnN_5).[339, 346, 347] In the case of metals that do not form nitrides, such as Ru, an electronic interaction between the metal and the NH_x species from the amide/imide pair facilitates the cleavage of N–H bonds.[340, 348] The activation energies for these reactions are generally lower than those observed with metal catalysts

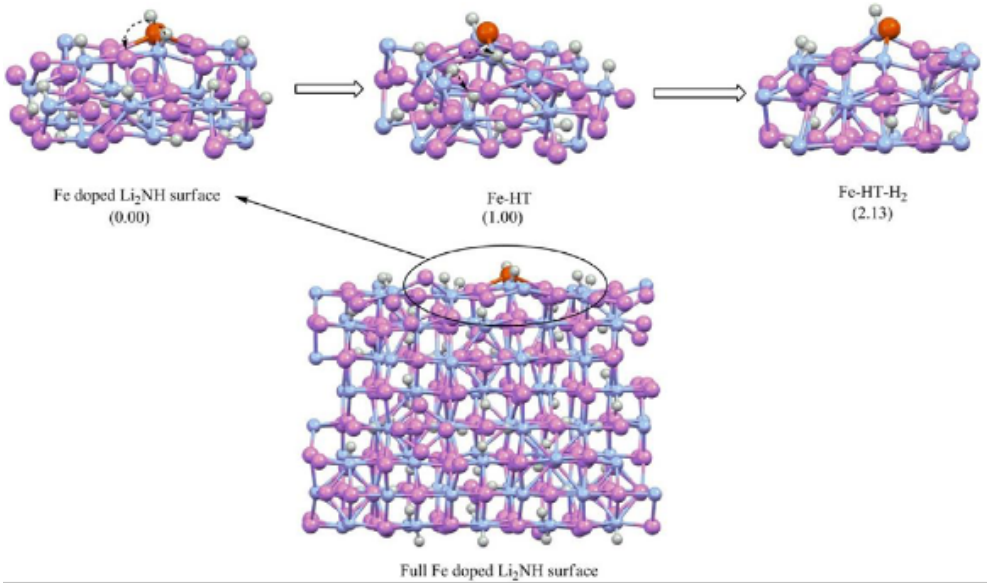

Figure I.27: DFT model of $Li_2NH(110)$ surface doped with one atom of Fe, and the reaction path of H_2 release simulated, the different steps increased energies are marked in parentheses. Fe, Li, N and H atoms are represented as red, purple, light blue and grey spheres, respectively.[339]

alone, highlighting the efficiency of these hybrid catalytic systems. While the potential of this type of catalysts is significant, the structure and energetics of the interfacial region between the metal and the lithium amide remain unknown. The reaction mechanism, as well as the intermediate species involved, must be elucidated. These knowledge gaps hinder the development of an efficient and cost-effective catalyst for ammonia decomposition, as a thorough understanding of these aspects is crucial for advancing catalyst design and optimizing performance.

I.6 Conclusion

Ammonia, with its advantageous properties, holds significant potential as a hydrogen carrier. While its synthesis has been extensively researched for over a century, this is not the case with its decomposition. Successfully extracting hydrogen from ammonia at lower temperatures would undoubtedly enhance its viability as a hydrogen carrier.

A variety of strategies can be employed to reduce the decomposition temperature of ammonia, including optimizing reactor design, improving heat transfer characteristics, and implementing a hydrogen extraction system. Central to these efforts is the development of catalyst that operates efficiently at low temperatures.

While ruthenium is one of the most efficient catalysts for ammonia decomposition, its high cost limits its widespread use. Consequently, research is focused on finding catalysts that are as effective as, or even superior to, ruthenium but at a more reasonable cost. Lithium amide paired with transition metals, particularly

the $LiNH_2$-Mn combination, has shown remarkable catalytic activity. This pairing competes effectively with the benchmark catalyst for this reaction, Ru/CNTs, demonstrating both high efficiency and potential cost advantages.

While $LiNH_2$ paired with transition metals have shown high activity for ammonia decomposition, the underlying catalytic mechanisms remain unclear. Several theories have been proposed to explain this effectiveness. One suggestion is the phase change from Li_2NH to Li_4NH that might occur upon interaction with Ru, and which would be the cause of the decomposition of ammonia. Another possibility is the formation of lithium-enriched ternary nitride when in contact with initial transition metals from the fourth row of the periodic table. Further research is needed to clarify these mechanisms and understand how they contribute to the catalytic performance.

Alkali and alkaline earth metals can form a diverse family of compounds, including nitrides, amides, imides, hydrides, and nitride-hydrides, all within a relatively narrow range of temperatures and pressures (see Figure I.28). The potential structural transformations of the lithium amide precursor under ammonia exposure are numerous, and non-stoichiometric $Li_xN_yH_z$ phases may also form. This complexity adds significant challenges to the study and understanding of these types of catalysts.

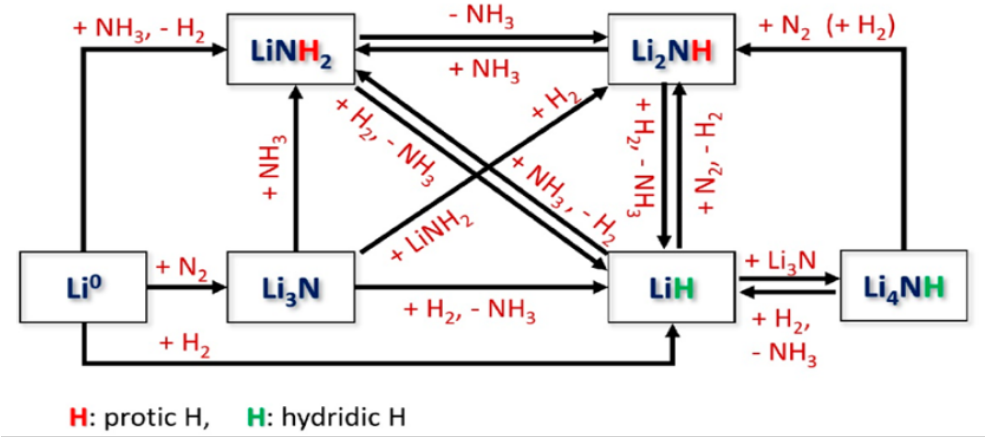

Figure I.28: Possible conversions among lithium metal (Li), hydride (LiH), nitride (Li_3N), amide ($LiNH_2$), imide (Li_2NH), and lithium nitride-hydride (Li_4NH).[326]

The approach in this work involves a joint experimental and theoretical study of this specified type of catalyst. The chosen catalytic system for this investigation is Ru-$LiNH_2$. Despite the inclusion of Ru, which is highly active in conjunction with $LiNH_2$, the long-term goal is to substitute Ru with another metal or a combination of metals that are not only efficient but also more cost-effective. This substitution strategy will be guided by the comprehensive insights derived from the detailed analysis of the Ru-$LiNH_2$ system.

Experimentally, the aim is to synthesize, characterize, and verify the catalytic performance of Ru-$LiNH_2$ catalyst for ammonia decomposition at atmospheric pressure. On the theoretical part, DFT studies will be em-

ployed to model $LiNH_2$ surfaces and $Ru/LiNH_2$ interfaces in the context of ammonia decomposition, building on previous measurements and characterizations of this catalyst. These studies will explore the mechanisms by which the solid-solid interface catalyses the formation of N_2 and H_2 from $LiNH_2$ material with the assistance of Ru, and how the catalyst is subsequently regenerated by decomposing ammonia.

Chapter II

Experimental approach

This chapter presents all the reactants used, along with a detailed description of the experimental setup for measuring the catalytic performance and apparent activation energies of Ru and $LiNH_2$ based catalysts. It also outlines the analytical techniques employed to quantify ammonia, nitrogen, and hydrogen. Finally, it covers all the methods used for the characterization of the catalysts.

Contents

II.1 Chemicals . . . 69
II.2 Catalysts preparation methods . . . 71
II.2.1 Catalyst synthesis . . . 71
II.2.1.1 Mechanochemistry . . . 71
II.2.1.2 Impregnation in liquid ammonia . . . 72
II.2.2 Catalyst purification . . . 74
II.3 Measurement of catalytic activity . . . 76
II.3.1 Fixed bed reactor . . . 76
II.3.2 Quantification of ammonia decomposition . . . 79
II.3.3 Activation energy measurement . . . 81
II.4 Catalysts characterization . . . 81
II.4.1 X-Ray Diffraction (XRD) . . . 81
II.4.2 Inductively coupled plasma atomic emission spectroscopy (ICP-AES) . . . 82
II.4.3 Thermogravimetric Analysis (TGA) and Differential Scanning Calorimetry (DSC) . 84
II.4.4 Raman spectroscopy . . . 84
II.4.5 Fourier-Transfer InfraRed (FTIR) spectroscopy . . . 84
II.4.6 Scanning Electron Microscopy Energy-Dispersive X-Ray Spectroscopy (SEM-EDX) . 85
II.5 Key calculations . . . 85
II.6 Appendix . . . 87

II.1 Chemicals

This section lists all the reactants, catalyst and gases used in this work. All chemicals were used as received, without any purification done.

- **Synthesis and purification of catalysts**

Details of the reactants used for catalyst synthesis—including $LiNH_2$, Li_3N, $RuCl_3$, and MgO—are provided in Table II.1. Information on the thermal diluent SiC, employed during catalytic performance measurements, and the solvent (THF) used for catalyst purification are also included.

All anhydrous reactants were stored in an MBraun 10 compact glovebox filled with argon (O_2 < 1 ppm, H_2O < 1 ppm).

Table II.1: Reactants name and formula used in the synthesis and purification of catalysts, as well as purity grade (%), supplier and various remarks (such as impurities and composition).

Reactant name	Reactant formula	Purity grade	Supplier	Remark
Lithium amide	$LiNH_2$	95	Sigma-Aldrich	unspecified impurities
Lithium nitride	Li_3N	$\geq$ 99.5	Sigma-Aldrich	80 mesh particle size
Ruthenium(III) chloride	$RuCl_3$	99.99	Sigma-Aldrich	Anhydrous
Magnesium oxyde	MgO	98	Sigma-Aldrich	–
Silicon carbide	SiC	$\geq$ 97.5	Sigma-Aldrich	400 mesh particle size
Tetrahydrofuran (THF)	C_4H_8O	$\geq$ 99.9	Sigma-Aldrich	Anhydrous, inhibitor free

- **Gases**

Details of the gases used for various applications—including inerting and diluting agents (Ar), carrier gases (Ar and He), reactants and solvents (NH_3), reducing agents (H_2), and calibration standards for ammonia decomposition quantification (NH_3, H_2, and N_2)—are presented in Table II.2. Hydrogen gas was generated using a ZOH electrolyzer supplied by UnityLab Services, operating at a delivery pressure of 2 bar.

All gases were used without further purification, expect for hydrogen and ammonia. Desiccants were employed upstream to ensure additional drying of these gases, as they were introduced to water-sensitive catalysts.

- **Ammonia and hydrogen gases desiccant**

Details regarding ammonia desiccant (soda lime) and hydrogen desiccant (drierite) can be found in Table II.3. Drierite offers the advantage of changing color (from blue to pink) when saturated with water, providing a clear indication of its state. However, it cannot be used with ammonia due to a reactive incompatibility.

Table II.2: Details of gases used for various applications—such as inerting and diluting agents (Ar), as carrier gases (Ar and He), as reactants and solvent (NH_3), as reducing agents (H_2), and as calibration standards for quantifying ammonia decomposition (NH_3, H_2, and N_2)—are provided, including their chemical formulas, purity grades (%), suppliers, and specific impurities.

Gas name	Gas formula	Purity grade	Supplier	Impurities
Argon	Ar	$\geq$ 99.998	Air-liquide	H_2O < 2 ppm, O_2 < 3 ppm, H_2 < 5 ppm, CO_2 < 1 ppm, N_2 < 1 ppm, C_nH_m < 1 ppm
Helium	He	$\geq$ 99.999	Air-liquide	$H_2O \leq$ 3 ppm, $O_2 \leq$ 2 ppm and C_nH_m < 0.5 ppm
Ammonia	NH_3	$\leq$ 99.999	Air-liquide	$H_2O \leq$ 1 ppm, $O_2 \leq$ 1 ppm, $N_2 \leq$ 4 ppm, $CO \leq$ 1 ppm, $CO_2 \leq$ 1 ppm and HC $\leq$ 1 ppm
Nitrogen	N_2	$\geq$ 99.9999	Air-liquide	H_2O < 0.8 ppm, O_2 < 0.5 ppm, H_2 < 0.1 ppm, CO + CO_2 < 0.15 ppm and C_nH_m < 0.020 ppm
Hydrogen	H_2	$\geq$ 99.9	Water electrolysis	Not specified

Table II.3: Reactant names and formulas used as ammonia and hydrogen desiccants, as well as composition (wt%), supplier and specifications.

Dessicant name	Dessicant formula	Composition	Supplier	Specifications
Drierite	$CaSO_4$, $CoCl_2$	$\geq$ 98% $CaCO_4$, < 2% $CoCl_2$	Fisher Scientific	300 mL.min^{-1} of maximum flow rate and water capacity of 3 grams 10-20 mesh granules
Soda Lime	CaO, NaOH	$\geq$ 75% CaO_4, $\leq$ 3% NaOH, and $\leq$ 20% H_2O	Sigma aldrich	Pellets

- **Commercial catalyst**

The commercial catalyst used to evaluate the performance of the catalytic bench, perform comparisons with synthesized catalysts, and establish the ruthenium digestion method for ICP analysis was ruthenium on alumina (Ru/Al_2O_3), with a 5 wt% Ru loading, supplied by Sigma Aldrich.

- **Ammonia quantification**

Details regarding the reactants used for ammonia colorimetric titration via ultraviolet-visible spectroscopy can be found in Table II.4. Note that the reference ammonia for producing the calibration curves comes from the solubilization of $LiNH_2$ (see Table II.1) and the bubbling of ammonia gas (see Table II.2).

Table II.4: Reactant name and formula used for ammonia colorimetric titration by ultraviolet-visible spectroscopy, as well as purity grade (%), supplier and various remarks.

Reactant name	Reactant formula	Purity grade	Supplier	Remark
Citric acid	$C_6H_8O_7$	$\geq$ 99.5	Sigma-Aldrich	–
Sodium hydroxyde	NaOH	$\geq$ 99.5	Sigma-Aldrich	–
Sodium nitroferricyanide(III) dihydrate	$Na_2[Fe(CN)_5NO]\cdot 2H_2O$	$\geq$ 99	Sigma-Aldrich	also known as sodium nitroprusside dihydrate
Salicylic acid	$C_7H_6O_3$	$\geq$ 99	Sigma-Aldrich	–
Sulfuric acid	H_2SO_4	$\geq$ 98	Sigma-Aldrich	–
Sodium hypochlorite	NaClO	$\geq$ 99.9	Sigma-Aldrich	Stored between 2 and 8°C

- **Digestion of catalysts**

Details of the reactants used in the development of digestion process of ruthenium-based catalysts for quantification by ICP-AES are provided in Table II.5.

Table II.5: Reactant name and formula used for catalysts digestion, as well as purity grade (%), supplier and various remarks (such as impurities and composition).

Digestion type	Reactant name	Reactant formula	Purity grade	Supplier	Remark
Acid wet digestion	Hypochloric acid (37 %)	HCl			–
	Nitric acid (69.5 %)	HNO_3		Carlo Erba	–
Alkaline fusion	Potassium hydroxyde	KOH	99.99	Sigma-Aldrich	Trace metals basis (purity grade exclude sodium content, which is < 500.0 ppm)
	Potassium nitrate	KNO_3	99.99	Sigma-Aldrich	–
	Sodium hydroxyde	NaOH	97	Sigma-Aldrich	–
	Sodium nitrate	$NaNO_3$	$\geq$ 99.0	Sigma-Aldrich	–
	Sodium peroxide	Na_2O_2	$\geq$ 99.0	Sigma-Aldrich	–

II.2 Catalysts preparation methods

II.2.1 Catalyst synthesis

II.2.1.1 Mechanochemistry

Following the process developed by Guo et al., $Ru(NH_2)_3$-$LiNH_2$ precursor for the Ru-Li_2NH catalyst, was synthesized via mechanochemistry,[15] with a ruthenium loading of 5% by mass. Typically, 0.40 g of $RuCl_3$ and 4.52 g of $LiNH_2$ were placed in a 25 mL zirconium oxide milling jar. Ten zirconium oxide balls, each with a diameter of 1 cm, were added to the jar. The milling jar was filled in a glove box, then hermetically sealed with a metal clamp between the jar and its lid. In mechanochemistry, it is generally recommended to fill the grinding jar with one third balls, one third reactants, and to leave one third free space. However, in

this work, the amount of reactants was reduced, filling only 1/6 of the jar, to avoid producing an excessive quantity of catalyst.

For the mechanochemical synthesis, a Retsch planetary ball mill (PM 100) was used. The milling process was carried out at room temperature under inert atmosphere (Ar). The rotation speed of the planetary mill was set to 150 rpm, with a grinding duration of 3 hours. Intervals of 5 minutes of milling were followed by 1-minute pauses to prevent overheating. After each pause, the direction of rotation was reversed to ensure uniform grinding. The milling jar is opened in a glove box at the end of the reaction.

II.2.1.2 Impregnation in liquid ammonia

Mechanochemistry offers several advantages: it eliminates the need for solvents, enables reactions to proceed more quickly with higher yields, and often operates under milder conditions. However, scaling up mechanochemical processes to industrial levels presents challenges, particularly due to the high centrifugal forces involved. As the scale increases, efficiency may decrease, and energy consumption can become significant.[349]

Given the limitations of mechanochemistry for potential scale-up (e.g., pilot-scale tests), a solvent-based synthesis route was also explored. While only a few solvents are suitable for $LiNH_2$, ammonia had previously been employed for incorporating a Ru/MgO catalyst (prepared in an aqueous KNO_3 solution) as well as metallic lithium into liquid ammonia.[16] However, no data regarding the solubility of $RuCl_3$ in ammonia was available.

To assess the feasibility of the reaction between $LiNH_2$ and $RuCl_3$ for the formation of $Ru(NH_2)_3$, stoichiometric proportions were initially tested, confirming the viability of this route (see Equation III.S3). The synthesis of $Ru(NH_2)_3$-$LiNH_2$ and $Ru(NH_2)_3$-$LiNH_2$/MgO precursors was then performed using $RuCl_3$, $LiNH_2$, and MgO in liquid ammonia.

$$3LiNH_2 + RuCl_3 \rightarrow 3LiCl + Ru(NH_2)_3 \quad \text{(II.1)}$$

To enable the transfer of liquid ammonia in an inert environment, a 316 stainless steel transfer manifold was developed from stainless-steel Swagelok fittings, connecting the ammonia storage reactor to a second reactor containing reactants, which had been filled in a glove box. This setup, depicted in Figures II.1 and II.2, was inspired by the one developed by Hajiyev.[350] Once the synthesis reactor is connected to the transfer manifold, the system is inerted using a Schlenk line by performing three Ar/vacuum cycles, each consisting of 2 minutes of argon flow followed by 2 minutes of vacuum. The Schlenk line is connected to an oil bubbler, which serves as a one-way pressure release valve, allowing excess Ar gas to escape. After the cycles are completed, the transfer line is left under vacuum and isolated from the Schlenk line by a valve.

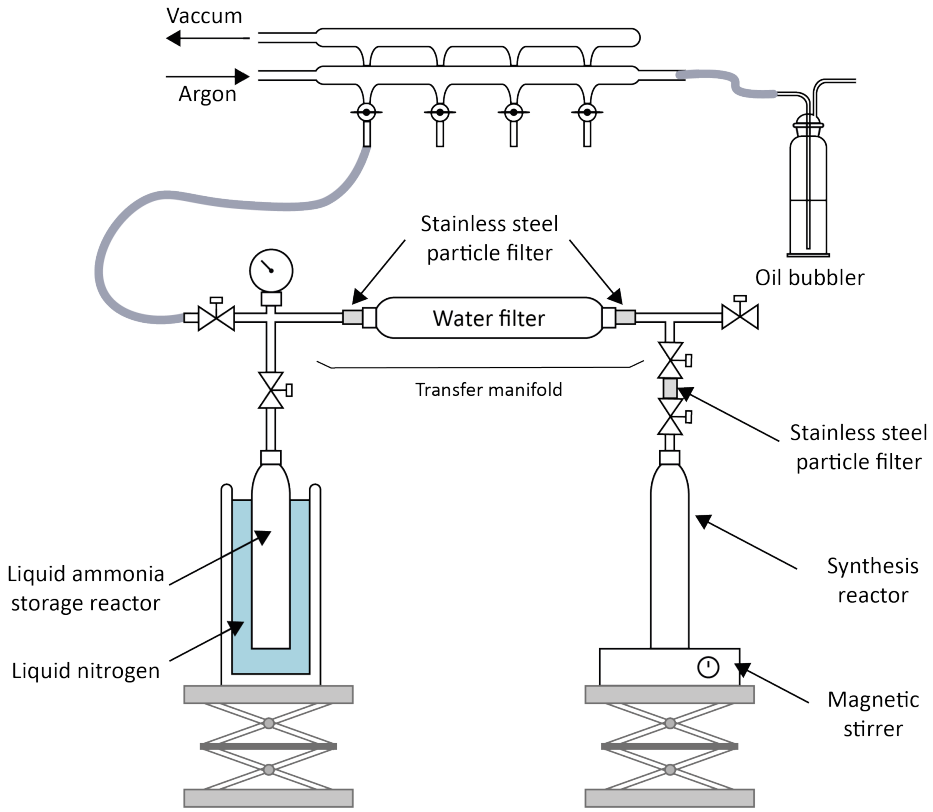

Figure II.1: Diagram of the transfer manifold setup for catalyst synthesis using ammonia as the solvent. The diagram illustrates the system in ammonia transfer mode, showing the flow from the synthesis reactor to the storage reactor.

In a closed system, ammonia exists in equilibrium between its liquid and vapor phases, with the saturation vapor pressure dependent on temperature. At 20°C, the saturation vapor pressure of ammonia is 8.6 bar.[351] When the valve of the ammonia storage reactor is opened, the entire transfer manifold becomes pressurized to 8.6 bar with ammonia. Simultaneously, the synthesis reactor is immersed in liquid nitrogen to lower its temperature (-196 °C). Once the reactor is sufficiently cooled, the valve of the storage reactor is closed, and the valve of the synthesis reactor is opened, leading all the ammonia gas in the transfer line to solidify into the synthesis reactor. This process is repeated until the desired amount of ammonia has been transferred from the storage reactor. The synthesis reactor can then be removed from the liquid nitrogen. Once it warms up and the ammonia liquefies, the reactor can be stirred to initiate and facilitate the reaction. The volume of liquefied ammonia in the synthesis reactor is determined based on the total pressure of the transferred ammonia, and the known volume of the transfer system (measured at 75 mL using a Pressure-Composition-Temperature (PCT) apparatus). On average, 0.028 mol of NH_3 was transferred per transfer cycle. Once the reaction is complete, the solvent is removed from the synthesis reactor by cooling the storage reactor and reversing the transfer process.

Typically, 0.20 g of $RuCl_3$, 1.90 g of $LiNH_2$, with or without 1.85 g of MgO, were placed into a 25 mL 316 stainless steel reactor and sealed in glove box. The reactor was then connected to the ammonia transfer manifold, and 5–10 mL of ammonia was introduced, depending on the type of reaction done, either

Ru(NH2)3, Ru(NH2)3-LiNH2 or Ru(NH2)3-LiNH2/MgO. The synthesis reactor was left at room temperature and with stirring for 2 days to allow the reaction to proceed.

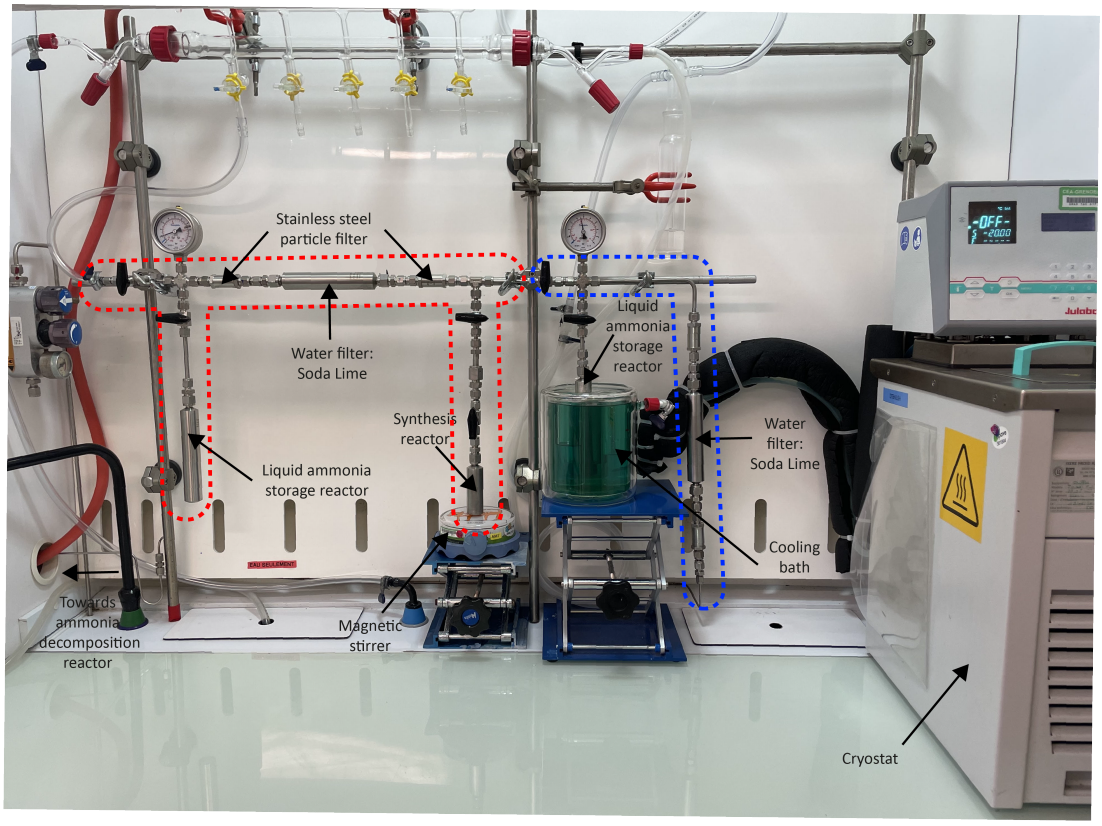

Figure II.2: Image of the inert catalyst synthesis setup, outlined with a red dotted line, and the ammonia source for catalyst performance evaluation, outlined with a blue dotted line.

II.2.2 Catalyst purification

The $Ru(NH_2)_3$-$LiNH_2$ and $Ru(NH_2)_3$-$LiNH_2$/MgO catalysts were purified using Soxhlet extraction with anhydrous THF as the solvent to remove residual LiCl formed during catalyst synthesis (see Equation III.S3).

The purification setup consists of a 30 mL Soxhlet extractor connected at one end to a two-neck round-bottom flask, and at the other end to a condenser. The entire setup is connected to the Schlenk line via the condenser (see Figure II.3). Prior to purification, the Soxhlet extractor and round-bottom flask are placed in a drying oven to ensure an optimal moisture-free environment (for 2h at 80°C). Vacuum tightness of the glassware components is maintained with Teflon seals, as vacuum grease is incompatible with THF. Once assembled, the system is inerted by performing three cycles of argon/vacuum, of 2 minutes each.

Meanwhile, 1 to 4 g of catalyst is placed in a cellulose cartridge inside the glovebox, containing theoretically between 3.1 and 7.2 wt% of LiCl, depending on the specific catalyst. The cartridge is then transferred to the Soxhlet extractor. During installation, the purification setup is kept under a higher argon pressure to mini-

mize the entry of air. The cellulose cartridge is exposed to air for only a few seconds during its installation in the Soxhlet extractor. Although the $LiNH_2$ is not in a protected environment during this brief period, the risk of degradation remains minimal due to the short exposure time and the enclosed nature of the cartridge. Once the cellulose cartridge is installed in the Soxhlet extractor and then reconnected to the condenser, the system is inerted by performing three argon/vacuum cycles, each lasting 5 minutes.

Once the purification setup inerted, it is maintained under higher argon pressure, preventing air from entering when the cap of the second inlet of round-bottom flask will be removed. In the glove box, 120 mL of THF is drawn using a syringe and transferred into the round-bottom flask through its second inlet. Since the volume of the Soxhlet extractor is 100 mL, at least this volume must condense in the Soxhlet to enable a cycle of filling and emptying. Once the solvent is added, the cap is replaced, and the argon flow to the purification setup is reduced. The catalyst is left for at least 6 hours, with Soxhlet extraction cycles of filling and emptying lasting approximately 30 to 45 minutes each.

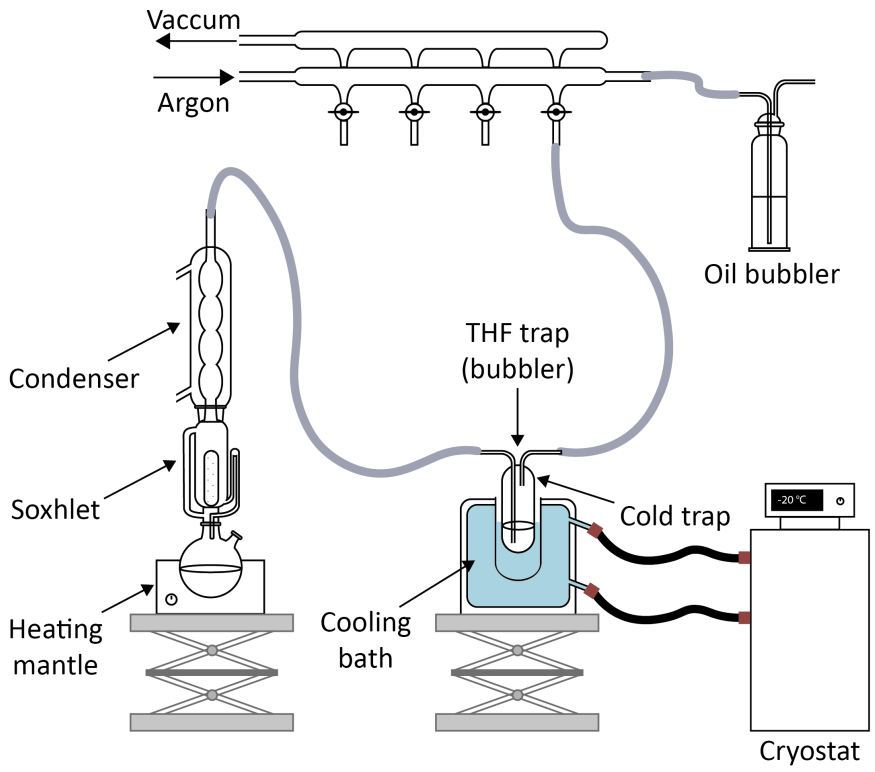

Figure II.3: Diagram of the inert catalyst purification setup, using Soxhlet extraction with anhydrous THF as the solvent.

At the end of the purification process, the argon pressure is increased once again, and when the Soxhlet extractor has just emptied, the round-bottom flask containing the extractor solvent is removed. It is replaced by a Schlenk flask, a glass vessel equipped with a stopcock. The system is then kept under a flow of argon to purge as much air as possible from the Schlenk flask. Subsequently, the argon is turned off and vacuum is applied to dry the cartridge. A bubbler, installed before the Schlenk line, is placed in a cooling bath chilled by a circulating ethylene-glycol solution, cooled to -20°C using a Julabo F25 cryostat. The tubes connecting

the cryostat to the cooling bath are insulated to prevent heat loss. This setup condenses the evaporated THF in the cooled bubbler, protecting the pump. Once dry, the cellulose cartridge containing the purified catalyst is put back in the glove box.

II.3 Measurement of catalytic activity

II.3.1 Fixed bed reactor

The catalytic decomposition of ammonia involves gaseous reactant and products, as well as a solid catalyst. This reaction is typically carried out in a fixed-bed reactor. As the name suggests, the catalyst is immobilized in a fixed position, while the reactants, whether in gas or liquid form, flow through the catalytic bed, where the reaction takes place. This type of reactor offers relatively simple installation and ease of operation.[352]

In this work, the performance of the catalysts was evaluated using a horizontal stainless steel (316) fixed-bed reactor. The setup consists of a Carbolite TS1 tube furnace, which houses a quartz or metal tube measuring 600 mm in length, with an outer diameter (OD) of 32 mm and an inner diameter (ID) of 29 mm. Inside this tube is placed the stainless steel catalytic reactor, with an OD of 6 mm and an ID of 4 mm (see Figures II.5 and II.6.a). The outer tube is designed to protect the metallic reactor from the high temperatures during catalytic tests by utilizing argon circulation through a dedicated gas inlet. The reactor exhaust consists of several meters of tubing to prevent air intake during gas analysis.

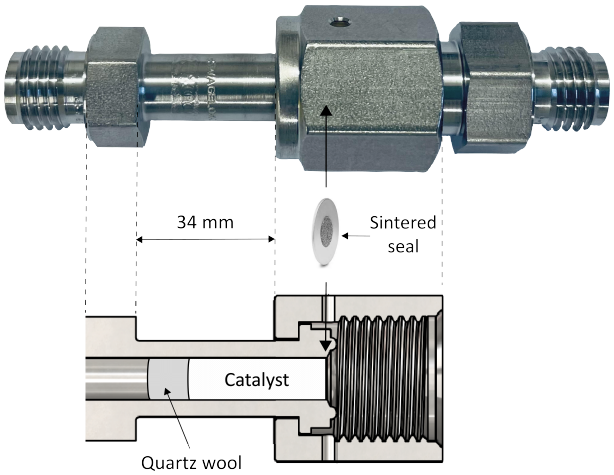

Figure II.4: (a) Picture and (b) diagram of Swagelok VCR fitting system used as catalyst bed. This system consists of two fittings connected by a VCR joint, sealed with a sinter stainless steel.

Fixed-bed catalytic reactors are typically positioned vertically, allowing gravity to naturally compact the catalytic bed. However, in this thesis, the reactor was positioned horizontally to accommodate space constraints, as the oven was placed under a fume hood. This orientation made achieving a compact catalytic bed more challenging. Faced with this, a Swagelok fitting system was used as the catalyst bed (see Figures II.4 and II.6.c). This system consists of two stainless-steel fittings, connect together by a Variable Compres-

sion Ratio (VCR) seal, also made of stainless steel. The spherical seal in its center is sintered, with a porosity of 20 µm, also made of stainless-steel, allowing gas mixtures to pass through while retaining solids. Once the catalyst is placed against the metal sinter, it is maintained at the end with quartz wool. The entire assembly process is conducted vertically to ensure a compact catalyst bed, which is then rotated horizontally for installation in the furnace's heating zone. The compact size of the fitting assembly allows for easy introduction into the glove box, providing a significant handling advantage for lithium amide based catalysts.

The catalytic reactor is connected to four mass flow controllers (MFCs), enabling the supply of various gas mixtures. Argon and hydrogen are regulated using Brooks MFCs (SLA850), with two dedicated MFCs for argon: one connected to the outer tube for inerting, and the other to the reactor for diluting hydrogen and ammonia gases. For ammonia, an Allicat MFC (MC Series) was used (see Figure II.6.b). Previously, Brooks MFCs (SLA850) calibrated specifically for ammonia were tested, but they had a limited service life of only a few weeks to a few months when in contact with pure ammonia gas. All MFCs are analogically controlled by a Brooks 0254 controller. A non-return valve is installed at each MCF outlet. Lastly, a soda lime water filter is installed before the furnace entrance to protect the lithium amide catalysts.

To monitor the temperature of the catalyst bed, a type N thermocouple (with a theoretical accuracy of ±1.5°C) was positioned directly against the metal sinter. This allows precise monitoring of the catalyst temperature and ensures consistent temperature measurements across the different catalysts studied. The furnace temperature is regulated based on the catalyst bed thermocouple.

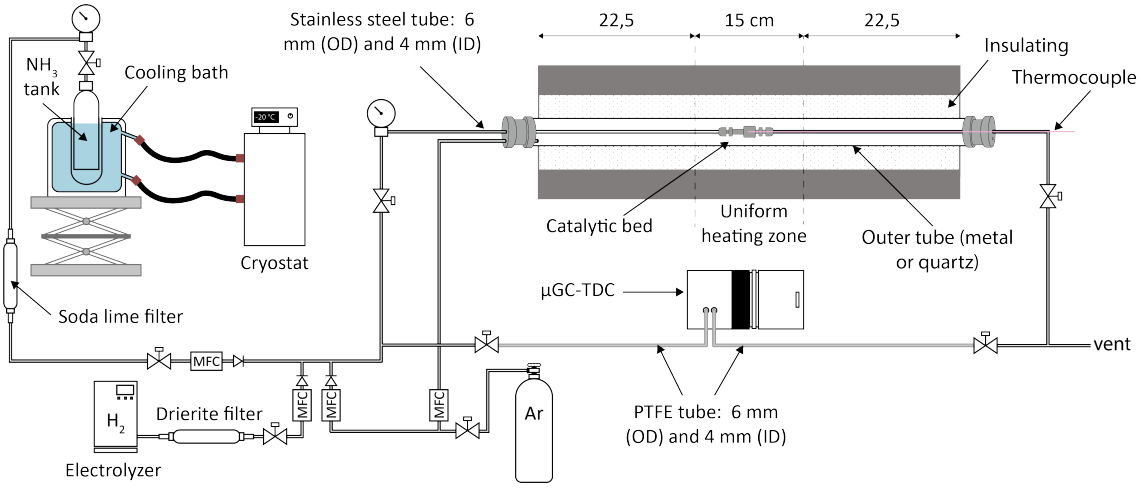

Figure II.5: Diagram of the horizontal fixed-bed catalytic reactor developed for measuring the performance of catalysts in ammonia decomposition.

Our reactant (NH_3) is gaseous, and the use of gas cylinders was prohibited in the laboratory where the fixed-bed catalytic reactor was installed. To supply the catalytic reactor, custom reactor tanks (50 mL) were prepared and filled in a dedicated facility designed for handling NH_3. Since these tanks were not equipped with built-in pressure regulators, their pressure was controlled by cooling (see Figure II.5). During ammonia

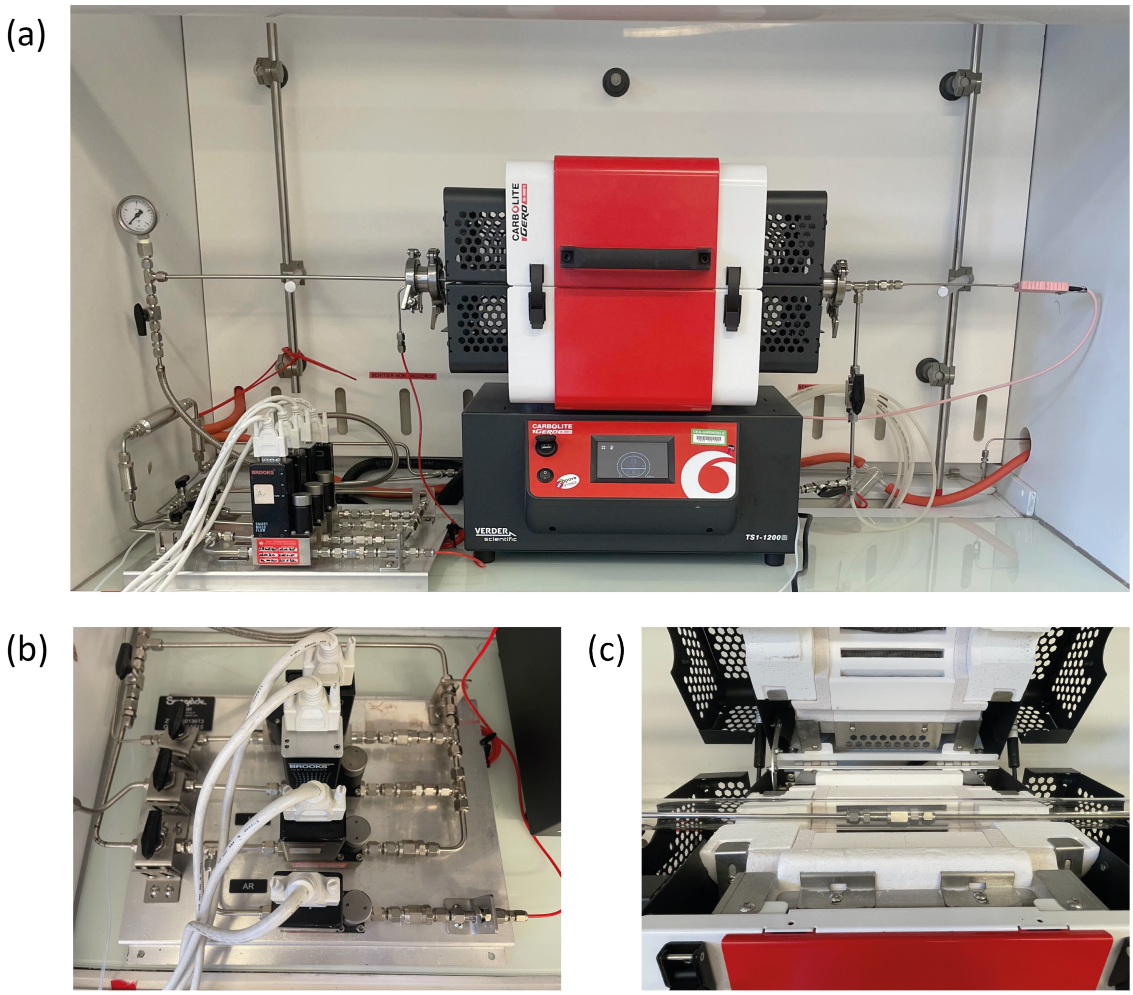

Figure II.6: (a) Picture of the fixed-bed catalytic reactor developed for ammonia decomposition, showing the oven and the MFCs mounting plate on the left.. The µGC-TDC, the Brooks controller for the MFCs and the ammonia source do not appear; (b) Close-up of the mounting plate, with the ammonia MFC at the top, followed by the hydrogen MFC, and finally the two argon MFCs; and (c) The two stainless steel Swagelok fittings serving as the catalytic bed, installed within the outer quartz tube, positioned in the homogeneous heating zone of the furnace.

decomposition experiments, the tank was maintained at approximately -20°C to ensure a system pressure between 2 and 2.5 bar. For the other gases, dedicated gas lines already installed in the laboratory were utilized, with the exception of hydrogen, which was generated on-site using an electrolyzer.

The catalyst masses ranging from 100 mg for Ru/Al_2O_3, $LiNH_2$, $Ru\text{-}LiNH_2$ and Li_3N, and up to 200 mg for $Ru\text{-}LiNH_2/MgO$ catalysts. Lithium amide based catalysts were mixed (1:1 wt%) with silicon carbide (SiC) with a particle diameter bellow 38 µm. Once the catalyst bed is positioned, the catalysts are reduced under a flow of hydrogenated argon (10% H_2 by volume) with a total flow rate of 20 $mL.min^{-1}$, for one hour at 600 °C. Before the reduction process, while the system is under 10% hydrogen, a leak test is systematically performed using the Adixen H2000 Plus hydrogen leak detector. This highly sensitive instrument can detect leaks as small as 5×10^{-7} $mbar.L.s^{-1}$, ensuring system integrity. After the catalyst reduction, the reactor is then purged with argon (20 $mL.min^{-1}$) for one hour as the temperature decreases to 300 °C. The catalyst

evaluation begins once a stable flow of dilute ammonia (5% NH_3 by volume) with a total flow rate of 20 $mL.min^{-1}$, so 1 $mL.min^{-1}$ of NH_3 and 19 $mL.min^{-1}$ of Ar, is established in the system (stability checked by sampling and analysis the input flow by μGC-TDC). The temperature during the catalytic evaluation is varied between 300 and 600 °C in increments of 50 °C, with each step maintained for 45 minutes to one hour. The catalytic performance evaluation was conducted three times for each catalyst. The average of the three measurements is reported as ammonia conversion and H_2 production rate for each catalyst, and the standard deviation between the three measurements is given as error. During evaluation, at each temperature, the concentrations of NH_3, N_2, and H_2 were determined by averaging the results from four μGC-TCD analyses.

II.3.2 Quantification of ammonia decomposition

- **Micro gas chromatography (μGC)**

Micro Gas Chromatography with Thermal Conductivity Detection (μGC-TCD) was used to quantify ammonia decomposition, enabling the evaluation of catalyst performance through the direct measurement of NH_3, N_2, and H_2 concentrations (see Figures VII.S1.a–c in the appendices for the corresponding calibration curves). The μGC-TCD system is directly connected to both the reactor inlet and outlet, ensuring real-time and accurate analysis.

This technique operates on the same principles as traditional gas chromatography, separating gases based on their interactions with a chromatographic column under controlled temperature conditions. The separated gases are then detected using TCD, which measures each gas's ability to conduct heat (a property that varies among different gases). The advantages of μGC-TCD include its straightforward setup and rapid analysis capabilities, typically completing within minutes. These features make it suitable for monitoring of ammonia decomposition.

In this study, we employed an Agilent 990 μGC-TCD equipped with two distinct columns. The first one, a MolSieve 5 Å (MS5A) of 10 meters long, utilizes Ar as the carrier gas for quantifying H_2, O_2, and N_2. The second column, a 15-meter Volamine, uses He as the carrier gas and is used specifically for ammonia quantification. The optimized column parameters for analyzing H_2, N_2, and NH_3 are provided in Table II.6. According to the manufacturer, the detection limit for ammonia is set at 100 ppm.[353]

As the MS5A column is a molecular sieve, heavy components can accumulate in the column, leading to longer retention times and potential column degradation. To prevent this, the carrier gas flow direction is reversed for a specific duration to flush out unwanted components—a process known as backflush. In this study, the backflush was set at 23 seconds, which is the maximum time allowed to minimize the entry of unwanted gases while still permitting the separation and detection of H_2 and N_2 in the column.

Table II.6: Column name, gas species detected and quantified, along with operational parameters such as injector and column temperatures, injection time, column pressure, and backflush duration for MS5A.

Column	Quantifiable compounds	Injector temperature (°C)	Column temperature (°C)	Injection time (ms)	Column pressure (Psi)	Backflush time (s)
MS5A	N_2 and H_2	80	80	50	25	23
Volamine	NH_3	90	50	100	15	-

- **Ultraviolet-visible spectroscopy**

Colorimetric titration, following the method proposed by Bower *et al.*, was used to verify the detection limit of ammonia by µGC-TCD. Under alkaline conditions, ammonia reacts with sodium hypochlorite in the presence of salicylic acid to form chloramine (see Equation II.2). This reaction produces a blue quinone-imine derivative with a characteristic absorption band at approximately 650 nm.

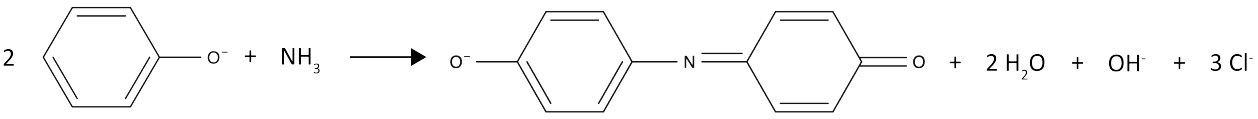

(II.2)

This colorimetric titration involves the preparation of three solutions. The first solution is prepared by dissolving 7 mg of sodium nitroprusside dihydrate, 2.75 g of sodium hydroxide, and 9.5 g of salicylic acid in 25 mL of water. The second solution is prepared by dissolving 5.85 g of sodium hydroxide and 6.53 g of citric acid in 100 mL of water. Finally, the third solution is prepared by mixing 9.5 mL of the second solution with 0.5 mL of sodium hypochlorite solution.

A concentration-absorbance calibration curve was established by diluting the commercial 13.3 M NH_4OH sample to achieve concentrations within the detection range of 0 to 10 ppm for known NH_4^+ concentrations (see Figure VII.S1.d). To analyze the samples, the bubbling efficiency was verified using ammonia gas in Ar at a known concentration of 5000 ppm. This verification involved measuring the NH_3 flow rate and analyzing the gas with µGC-TCD, followed by bubbling the ammonia into 30 mL of 5 M sulfuric acid for 2 minutes. For the detection limit verification, ammonia at a stabilized concentration of approximately 100 ppm (as indicated by µGC-TCD) was bubbled into 10 mL of 5 M sulfuric acid for 3 hours. Finally, 2 mL of the resulting solution was neutralized with 2 mL of 1 M sodium hydroxide.

Typically, 0.5 mL of the neutralized sample was mixed with 100 µL of the first solution, followed by 200 µL of the third solution. The resulting solution should exhibit a blue color. A yellow solution indicates that the ammonia concentration in the sample is too low to be detected, while a dark blue color suggests an excessively high concentration. Prior to measurement, the samples were allowed to stand for two hours in the dark at room temperature to ensure color stabilization. Finally, the UV-Vis absorbance spectrum was

recorded at a wavelength of 655 nm.

II.3.3 Activation energy measurement

The relationship between temperature and the rate of a chemical reaction is described by the Arrhenius equation. Assuming that the activation energy E_a is independent of temperature—a reasonable assumption over a limited temperature range—the Arrhenius equation can be integrated as follows:

$$r = A \cdot e^{-\frac{E_a}{RT}} \tag{II.3}$$

where r is the reaction rate (mol.kg^{-1}.s^{-1}), A is the pre-exponential factor, and E_a (kJ.mol^{-1}) is the apparent activation energy of the reaction. By plotting the natural logarithm of the reaction rate against the inverse of the temperature, the Arrhenius equation can be linearized, allowing for the calculation of the apparent activation energy.

Since the rate of reactant diffusion via the pores and boundary layer is faster than that of surface reactions at lower temperatures, it is crucial to quantify the apparent activation energy at these temperatures. This guarantees that the intrinsic reaction kinetics govern the observed rate of reaction utilized to determine the apparent activation energy.

In this study activation energies were calculated in 5% NH_3 for a total gas flow of 20 mL.min^{-1} between 300 and 450 °C, using the reaction rate each 25°C. The activation energy test were performed twice for each catalyst. The average of the two measurements is reported as the apparent activation energy for each catalyst, and the standard deviation between the two measurements is given as error.

II.4 Catalysts characterization

II.4.1 X-Ray Diffraction (XRD)

X-Ray Diffraction (XRD) is an analytical technique that utilizes the diffraction of X-rays by matter to investigate the crystallographic structure of crystals. The atoms in the crystal lattice scatter X-rays, which results in a diffraction pattern unique to the material's atomic structure. The constructive interferences that results from diffraction can be explicit from the Bragg's Law:

$$2d \sin\theta = n\lambda \tag{II.4}$$

where d is the distance between two crystallographic planes (in Å), θ is the angle of incidence (in degrees), n is the order of diffraction, and λ is the wavelength of the X-ray beam (in Å).

In this thesis, XRD patterns of the catalysts were acquired on a BRÜKER D8 ADVANCE A25 spectrometer equipped with a LYNXEYE XE-T detector. The X-rays source was a copper tube, radiation Cu K_α = 1.5406 Å, operating at 40 kV and 40 mA. XRD patterns were collected using a 1mm divergence slit, in the 2θ range of 10–90°, with a step size of 0.0237° and an acquisition time of 1 second per step.

The samples were prepared in the glovebox using a silicon zero diffraction plate with cavity, cut at special orientation as sample holder. To avoid air exposure, the sample were coated with thin Kapton (polyimide) films. The sample holder for the analysis of air-sensitive compounds is shown in Figure II.7.

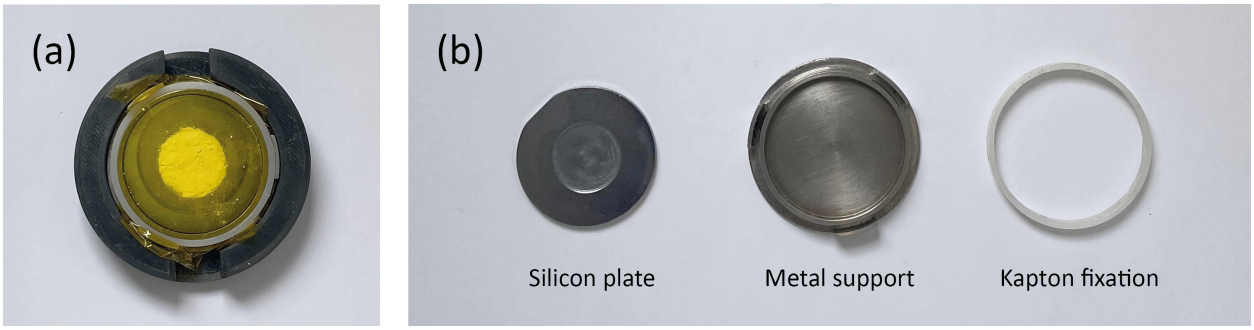

Figure II.7: (a) Assembled XRD sample holder placed in a black plastic adapter, the sample is visible through the Kapton film; (b) Detailed view of the components of the XRD sample holder: on the left, the silicon zero-diffraction plate with a central cavity for the sample; in the center, the metal support for the silicon plate and the Kapton plastic holder; and on the right, the Kapton plastic holder.

II.4.2 Inductively coupled plasma atomic emission spectroscopy (ICP-AES)

Inductive Coupled Plasma optical emission spectroscopy (ICP-AES) is an analytical technique used for the detection and quantification of elements. The sample are mineralized prior to the analyses, usually by using strong acid. Then a high-temperature plasma, typically generated by an argon gas flow, is used to excites atoms and ions in the sample. After excitation, return to their ground state emits light with at characteristic wavelengths of the element. The emitted light is then analyzed by a spectrometer, allowing for the identification and quantification of the present elements based on their emission spectra.

This technique is highly sensitive, providing results with a measurement uncertainty of 5%, and is capable of detecting a broad range of elements, with the exception of hydrogen, noble gases, carbon, oxygen, nitrogen, and unstable or volatile elements like mercury. However, a significant challenge of this method lies in achieving effective mineralization of the samples to be analyzed.

- **Digestion of catalysts**

Despite the fact that ruthenium is extremely resistant to wet acid treatments, some reports indicate that aqua regia—a solution of nitric acid and hydrochloric acid, usually in a 1:3 molar ratio—can be used to

successfully digest the metal.[354, 355] It is commonly known that alkaline fusion is a successful process for dissolving ruthenium.[356] By combining the solid sample with a flux, this approach reduces the sample's melting point and makes it easier for a high-temperature "glass bead" to form, which may then be dissolved after.

For acid wet digestion techniques, 10 mL of aqua regia was used to digest approximately 100 mg of sample. Three methods were explored to achieve ruthenium catalyst mineralization: the hot block digestion system, microwave digestion, and agitation, with or without temperature assistance. During sample preparation, the sample was initially placed with HCl for a few minutes before HNO_3 was added.

- **Hot Block Digestion System:** The sample in aqua regia solution was refluxed for 16 hours at 175°C in a 50 mL plastic mineralization flask.
- **Microwave Digestion:** The sample in aqua regia solution was placed in 50 mL Teflon microwave reactors and processed in a Microwave T3000 system from PerkinElmer Anton Paar for 45 minutes at 800 W. This corresponds to a temperature range of 170–220°C and an average pressure of 47 bar.
- **Agitation with and without Temperature Assistance:**
  - For agitation without heating, the sample and aqua regia solution were placed in a glass flask with a magnetic stirrer and stirred at room temperature for 7 days. Degassing was performed twice—6 hours after stirring began and again 16 hours later.
  - For agitation with heating, the sample and aqua regia solution were placed in a glass flask and heated in an oil bath at 60°C during the day, with the bath switched off overnight. Degassing was performed daily.

For alkaline fusion techniques, the type of flux used varied, with three types being tested: a mixture of KOH and KNO_3, of NaOH and $NaNO_3$, or Na_2O_2. For each flux combination, two types of crucibles were tested: nickel and zirconium. Typically, 100 mg of sample were placed in the crucible along with 2 g of KOH, NaOH, or Na_2O_2, and 200 mg of KNO_3 or $NaNO_3$ (or none, when Na_2O_2 was used). The contents were homogenized using a vortex mixer. The crucible, with its lid, was placed in a furnace under an argon atmosphere and heated to 550°C (5°C/min) for 1 hour when KOH/KNO_3 or NaOH/$NaNO_3$ was used as the flux. For Na_2O_2 as the flux, the heating was conducted at 700°C (5°C/min) for 1 hour. After the crucible cooled to room temperature, its contents were mixed with 5 mL of distilled water. Additionally, 10 mL of hydrochloric acid were used to rinse the zirconium crucible and lid (distilled water was used for nickel crucibles).

Following mineralization, whether by alkaline fusion or acid wet digestion, a 2% vol. solution of HNO_3 was added to each sample to dilute it to the appropriate concentration for ICP-AES analysis.

II.4.3 Thermogravimetric Analysis (TGA) and Differential Scanning Calorimetry (DSC)

Thermogravimetric Analysis (TGA) and Differential Scanning Calorimetry (DSC) are two complementary thermal analysis techniques. TGA is a destructive method that measures a sample's mass change as a function of temperature and time, providing insights on oxidation, decomposition, or even moisture loss. This analysis can be conducted in different gas atmospheres to assess their impact on the material's behavior. In contrast, DSC measures the heat flow into or out of a sample as the temperature changes, offering information on the energetics of thermal transitions such as melting, crystallization, glass transitions, and variations in specific heat capacity.

For the TGA-DSC analysis, all samples were analyzed under an argon atmosphere (100 $mL.min^{-1}$) with a heating ramp of 5 °C/min up to 450 °C, using a Labsys Evo Setaram instrument. The samples, weighing between 15 and 30 mg, were prepared in a glovebox using aluminum crucibles sealed with perforated aluminum caps. The cap minimize exposure during installation in the TGA-DSC instrument and the hole prevent overpressure during thermal decomposition.

II.4.4 Raman spectroscopy

Raman spectroscopy is an analytical technique that that provides information about molecular vibrations and crystal lattice dynamics. The majority of photons scattered by a laser beam when it interacts with a material scatter elastically, but a tiny percentage scatter inelastically, producing an energy shift known as Raman scattering. This shift shows the sample's vibrational modes, including the phonons—the vibrations of the crystal lattice. FTIR-ATR provides similar, yet complementary, information; however, in both techniques, not all vibrational modes are detectable.

Raman spectroscopy analyses were conducted using a confocal Raman microscope (Renishaw InVia) with a 532 nm excitation laser at low power (< 0.2 mW) in a micro-Raman backscattering configuration with a long working distance (LWD) 50x objective. To prevent air exposure during the analysis, the samples were transferred directly from the glovebox into a custom airtight optical sample holder.

II.4.5 Fourier-Transfer InfraRed (FTIR) spectroscopy

Fourier-Transform Infrared Spectroscopy (FTIR) is an analytical technique used to measure the absorption of infrared (IR) light by a sample, providing detailed information about its chemical bonds and functional groups. Unlike dispersion spectrometers, FTIR simultaneously captures a broad range of frequencies, enabling rapid and comprehensive spectral analysis. In transmission mode, it measures the amount of infrared light that passes through a sample.

For this study, the samples were prepared as pressed pellets by thoroughly mixing 2 mg of sample with 400 mg of potassium bromide (KBr) in an agate mortar to ensure homogeneity. The mixture was then compressed into thin, uniform 10 mm discs under high pressure (8 tons) for 15 minutes using a hydraulic press. All spectra were recorded in the mid-IR region (4000–400 cm^{-1}) using a Bruker Vertex 70 spectrometer.

II.4.6 Scanning Electron Microscopy Energy-Dispersive X-Ray Spectroscopy (SEM-EDX)

Scanning Electron Microscopy (SEM) is a technique that uses a focused beam of electrons to scan the surface of a sample, producing detailed images of its topography and morphology at the micro- and nanoscale. When combined with Energy-Dispersive X-Ray Spectroscopy (EDX), which detects X-rays emitted from the sample, it enables the identification and mapping of the sample's elemental composition.

In this thesis, SEM-EDX was employed to evaluate the size and distribution of the supported ruthenium and $LiNH_2$ particles. The samples were prepared in a glovebox and placed on a carbon sample holder. A transfer box was utilized between the glovebox and the SEM to minimize exposure to air. The SEM-EDX analysis was performed using a FEG-SEM LEO 1530 equipped with Ray-EDS. The accelerating voltage applied to the electron beam was set between 3 and 15 kV.

II.5 Key calculations

- **Weight Hourly Space Velocity (WHSV)**

In catalytic processes, the Weight Hourly Space Velocity (WHSV), expressed in $mL_{NH_3}.min^{-1}.g_{cat}^{-1}$, is a parameter that expresses the flow rate of a gas or liquid reactant relative to the mass of the catalyst. For ammonia decomposition, it is expressed as follows:

$$WHSV = \frac{F_{NH_3}}{m_{cat}} \tag{II.5}$$

where F_{NH_3} is the mass flow rate of ammonia gas (in $mL.min^{-1}$), and m_{cat} the mass of the catalyst in the reactor is measured in grams. The catalyst can consist of lithium amide, ruthenium, or a combination of both compounds supported on MgO.

- **Ammonia conversion**

The conversion of ammonia (X_{NH_3}) in our catalytic process can be expressed using the inlet and outlet flow rates of ammonia. The equation for ammonia conversion is given by:

$$X_{\mathrm{NH_3}} = \frac{F_{\mathrm{NH_3,in}} - F_{\mathrm{NH_3,out}}}{F_{\mathrm{NH_3,in}}} \times 100 \tag{II.6}$$

where $F_{\mathrm{NH_3,in}}$ (mL.min^{-1}) is the ammonia flow rate at the inlet of the catalytic reactor, and $F_{\mathrm{NH_3,out}}$ (mL.min^{-1}) is the ammonia flow rate at the outlet. $F_{\mathrm{NH_3,in}}$ is the value indicated by MFCs and verified by µGC-TCD. $F_{\mathrm{NH_3,out}}$ is measured by µGC-TCD.

- **Rate of hydrogen production**

The hydrogen formation rate (rate $_{\mathrm{H_2}}$), expressed in mmol$_{\mathrm{H_2}}$.min^{-1}.g$_{\mathrm{cat}}^{-1}$, is given by:

$$\mathrm{H_2\ formation\ rate} = \frac{\frac{F_{\mathrm{NH_3,in}}}{V_m} \times X_{\mathrm{NH_3}} \times 1.5}{m_{\mathrm{cat}}} \tag{II.7}$$

where $F_{\mathrm{NH_3,in}}$ (mL.min^{-1}) is the ammonia flow rate at the inlet of the catalytic reactor, V_m is the molar volume of the gas (22.4 mL.mmol^{-1}), and m_{cat} (g) is the mass of the catalyst.

II.6 Appendix

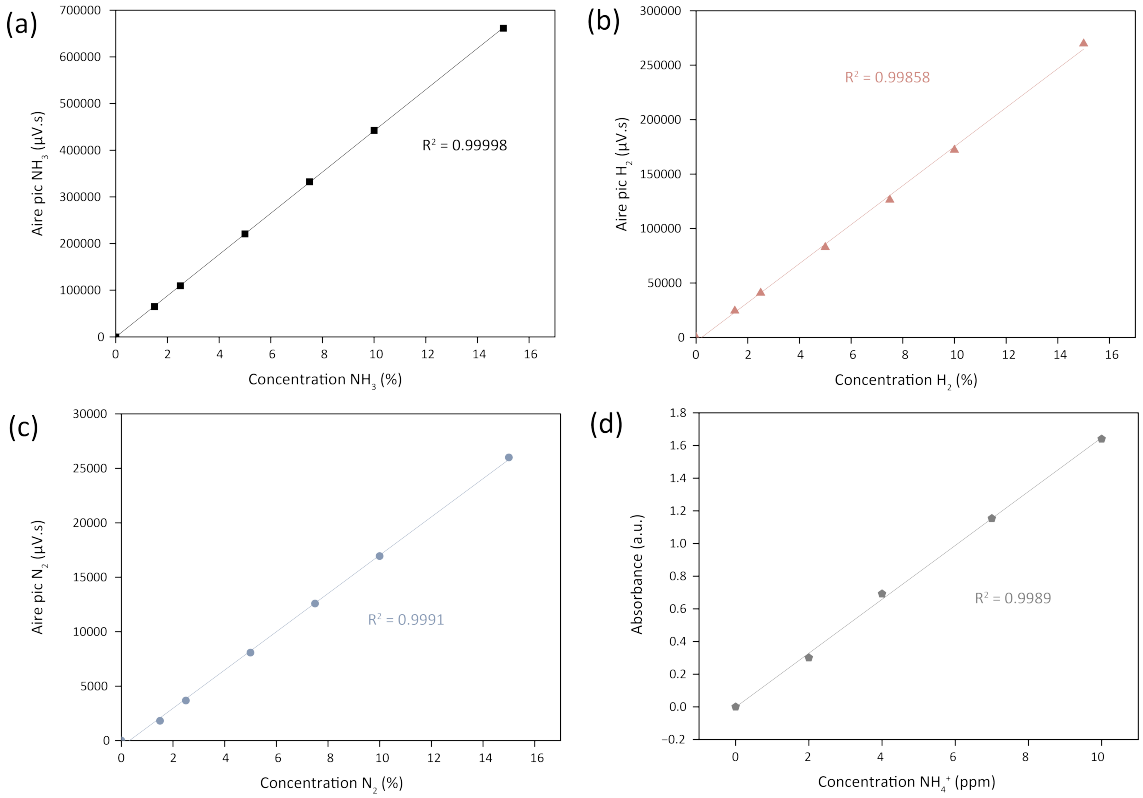

Figure VII.S1: Calibration curves obtained using µGC-TCD for the quantification of (a) NH_3, (b) H_2, and (c) N_2 at varying concentrations (%) in Ar, measured at a constant total gas flow rate of 20 mL/min. (d) Calibration curves for NH_4^+ concentrations ranging from 1 to 10 ppm, obtained via colorimetric titration. Data points represent experimental values, while the lines correspond to the respective linear fits.

Chapter III

Evaluation of catalytic performance

This chapter presents the fixed-bed reactor developed to evaluate the performance of the catalysts. This reactor was specifically designed to accommodate lithium amide properties, less common in heterogeneous catalysis. A commercial ruthenium catalyst supported on alumina was employed to validate the setup. Subsequently, this chapter focuses on the catalytic performance, material characterization, and detailed insights into the structural and chemical properties of Ru-$LiNH_2$-based materials when used as catalyst for ammonia decomposition.

Contents

III.1 Experimental setup for catalytic activity measurement . . . 89
III.1.1 Prerequisite . . . 89
III.1.2 Catalyst bed: material and fastening . . . 90
III.1.3 Ammonia detection limit measurement . . . 95
III.1.4 Comparison of commercial Ru/Al_2O_3 catalyst performance to literature . . . 95
III.1.5 Implementation of the Ru dosage method by ICP-AES . . . 99
III.2 Lithium amide: catalytic activity and activation energy . . . 100
III.3 Ruthenium and lithium amide couple: catalytic activity and activation energy . . . 107
III.3.1 Ru-$LiNH_2$ . . . 107
III.3.2 Ru-$LiNH_2$/MgO . . . 114
III.4 Lithium nitride: catalytic activity and activation energy . . . 120
III.5 Conclusion . . . 125
III.6 Appendix . . . 127

III.1 Experimental setup for catalytic activity measurement

III.1.1 Prerequisite

This experimental study began with the development of a test bench specifically designed to evaluate the performance of catalysts for ammonia decomposition. A key challenge in heterogeneous catalysis, for a given reaction, lies in the wide variety of experimental conditions and catalytic reactor designs, which often complicates direct comparison of catalytic performances. These differences typically arise from a combination of technical, economic, and safety constraints, which vary across institutions. This work is no exception; the proposed fixed-bed reactor setup reflects a balance between these considerations, alongside the unique properties of lithium amide. This section provides a comprehensive overview of the development process of a setup adapted to lithium amide based materials, and in this chapter we will explore potential optimizations for the test bench. The proposed improvements with respect to classical configurations aim to refine the current setup while serving as a blueprint for future installations dedicated to studying lithium amide-based catalysts.

To address the safety constraints associated with ammonia handling, the used reactive medium was diluted to 5% by volume in argon. This concentration was imposed by additional safety restrictions prohibiting the use of ammonia gas cylinders within the laboratory. The only alternative—installing a dedicated ammonia gas line with the gas source located outside the building—would have required extensive and costly construction works, hence making it unachievable in the timescales of the PhD works.

Instead, the chosen solution was to use custom-built storage reactors, filled via the transfer method described in the previous chapter, at an external facility equipped with an ammonia gas line. These stainless steel (316) reactors, with a volume of 50 mL, can store between 20 and 25 g of ammonia, providing an operational autonomy of one to two months per reactor. Unlike commercial gas cylinders, these reactors do not include built-in pressure regulators; instead, cooling them around -20°C achieves a comparable effect. At this temperature the ammonia pressure in the system is maintain between 2 and 2.5 bar, depending on the cooling efficiency of the reactor.

The ammonia flow rate (20 $mL.min^{-1}$) during measurements was carefully selected to extend the autonomy of the storage reactors while maintaining sufficient flow for effective analysis using µGC-TDC. Operating at a low ammonia flow rate minimizes the impact of the increased gas volume resulting from ammonia decomposition. Under these conditions, the combined effects of temperature and gas volume expansion lead to a relatively small change in total flow rate. At the maximum ammonia decomposition rate coupled with the highest temperature of the study (600°C), the flow rate changes by only 2 $mL.min^{-1}$ (from 20 to 18 $mL.min^{-1}$). This stability allows the same calibration curve to be used throughout all ammonia decomposition tests. In our continuous system, the total gas flow rate analyzed by the µGC-TDC influences the peak area of the detected compounds and, consequently, the measured concentrations. Maintaining a consistent flow ensures reliable and comparable results. This approach balances safety, efficiency, and practicality, ensuring reliable

operation without the need for costly infrastructure modifications.

Compared to the conditions found in the literature, the reaction parameters vary significantly, with gas flow rates ranging from 25 to 200 $mL.min^{-1}$, and containing from 10% ammonia by volume to 100%.[325, 12, 13, 296] Although low flow rates and low ammonia concentrations are reported (such as 25 $mL.min^{-1}$ of 10% NH_3),[325] our operating conditions fall within the lower end of the studied range. Consequently, our setup operates with a WHSV of 600 $mL_{NH_3} \cdot g_{cat}^{-1} \cdot h^{-1}$, which is relatively low compared to other studies. This reduced WHSV implies a lower flow rate of reactant per unit mass of catalyst, resulting in an increased contact time between the reactant and the catalyst. This prolonged contact time can enhance the conversion efficiency.

Another constraint imposed on our fixed-bed reactor was the requirement for a horizontal configuration. At first glance, this may seem unconventional for heterogeneous catalysis, where reactors are typically oriented vertically to take advantage of gravity for maintaining a compact catalytic bed. However, spatial limitations within the fume hood designated for this setup imposed a horizontal installation.

To address this challenge, the catalytic bed needs to be specifically designed to accommodate this orientation, while also meeting the unique demands of working with a $LiNH_2$-based catalyst. This material requires handling in an inert atmosphere due to its high reactivity and has the additional complication of liquefying under the reaction conditions, further influencing the design considerations.

III.1.2 Catalyst bed: material and fastening

- **Selection of catalytic reactor materials**

Setting up a fixed-bed reactor begins with selecting an appropriate material. For ammonia decomposition, quartz is one of the most commonly used materials due to its numerous advantages. First, quartz has high thermal resistance, capable of withstanding temperatures up to 1100°C,[357] according to the manufacturer, which far exceeds the typical conditions required for ammonia decomposition. Additionally, quartz exhibits excellent chemical inertness, making it resistant to most gases and catalysts, including ammonia and the metal catalysts commonly used for its decomposition. Furthermore, its optical transparency allows for visual monitoring of the catalysts, which is particularly valuable during different testing stages, such as reduction and evaluations at working temperatures.

Despite these benefits, quartz also has notable drawbacks. Its mechanical fragility makes it prone to breaking under stress or sudden temperature changes. Its high cost can be a limiting factor for some applications, and its low thermal conductivity can lead to significant temperature gradients within the reactor, potentially affecting the reaction uniformity.

However, while quartz is commonly used for ammonia decomposition, its suitability for evaluating the catalytic performance of $LiNH_2$-based materials is not guaranteed. At elevated temperatures, lithium amide

can react with quartz, potentially forming lithium oxide and lithium silicates.[13] However, no precise data are available in the literature regarding the specific temperature at which this reaction occurs. If this reaction only takes place at temperatures significantly above 600°C, a quartz fixed-bed reactor could still be suitable for our tests. Notably, Guo *et al.* conducted several studies evaluating the catalytic performance of $LiNH_2$ and TM-$LiNH_2$, from 230 to 550°C, using quartz reactors, without reporting on any formation of lithium silicates in their conclusions.[15, 16] This suggests that the use of quartz remains a viable option, and further tests with this material are justified to confirm its applicability.

For this experiment, a quartz tube measuring 800 mm in length, with an outer diameter (OD) of 6 mm and an inner diameter (ID) of 4 mm, was used (see section II.3.1. of the Chapter II for details on the reactor setup). A sample of 100 mg of $LiNH_2$ was placed in the center of the tube's heating zone (which is 15 cm long in the center of the tube furnace) and secured using quartz wool. A thermocouple was positioned against the quartz wool, as close as possible to the catalyst bed, to monitor its temperature accurately.

Before initiating ammonia decomposition, the lithium amide powder was pre-treated at 600°C under a 20 $mL.min^{-1}$ argon flow to ensure its complete decomposition. The system was then cooled to 300°C under the same argon flow, and the reactor's effluent was analyzed using μGC-TDC to confirm the absence of residual ammonia from the $LiNH_2$ decomposition before starting the ammonia decomposition reaction (the detection limit of ammonia being 100 ppm).

However, during the catalytic activity measurements, an unexpected increase in ammonia concentration was observed in the reactor's effluent at 350°C and 400°C (see Figure III.1). This suggests that ammonia was being released due to a reaction between lithium amide or lithium imide and the SiO_2 in the quartz reactor,[358] providing a preliminary indication of an undesired interaction between the material and the reactor.

This suspicion of a reaction between $LiNH_2$ and the reactor material is confirmed by XRD analysis, as illustrated in Figure III.S1 in the appendices. The diffraction pattern clearly displays peaks associated with lithium silicates (Li_xSiO_y), providing strong evidence of their formation. These results highlight the incompatibility of quartz as a material for catalytic reactors in this context.

The second material option considered is stainless steel, which offers several advantages. It has good thermal conductivity, facilitating uniform heat distribution within the reactor, and provides significantly greater mechanical resistance compared to quartz. However, stainless steel is not completely inert during the decomposition of ammonia. In particular, the stainless steel used in this case (grade 316) is composed in mass of approximately 50% iron, 10–14% nickel, 16–18% chromium, 2–3% molybdenum, and trace amounts of other elements, each present at concentrations below 1%. These transition metals can act as catalysts for the decomposition of ammonia.[359]

While stainless steel offers superior mechanical strength, its thermal resistance is not comparable to that of quartz. The manufacturer specifies a maximum operating temperature of 537°C.[360] However, our exper-

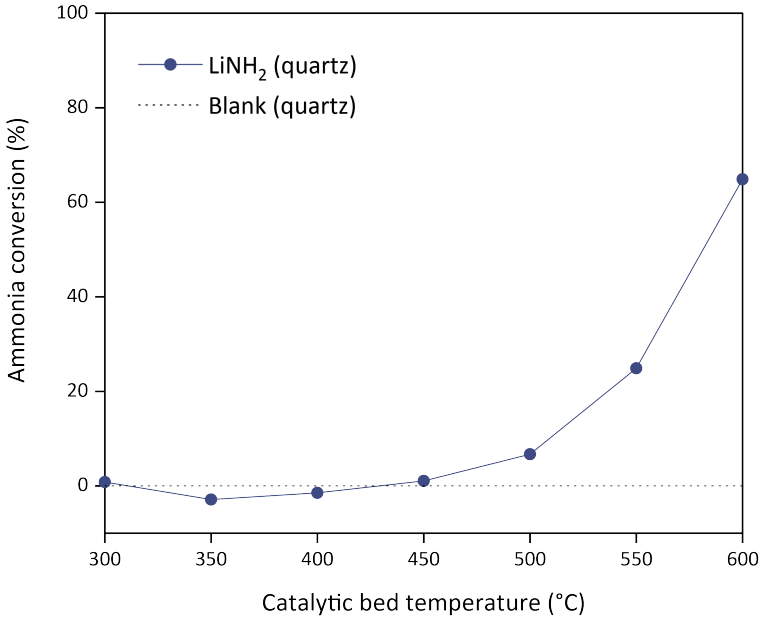

Figure III.1: Temperature dependences of the activities of $LiNH_2$ in a quartz catalytic reactor. Reaction conditions: catalyst loading of 100 mg, with a 20 $mL \cdot min^{-1}$ flow rate of diluted ammonia in argon (5% vol).

imental conditions require temperatures as high as 600°C. Notably, several studies involving $LiNH_2$-based catalysts have successfully utilized stainless steel reactors (grade 316),[358, 361, 12] including one operating at temperatures up to 650°C.[12] Unfortunately, all these findings suggest the potential suitability of stainless steel for this application, even under elevated thermal conditions.

Since stainless steel (316) is catalytically active in the decomposition of ammonia, performing a blank test is essential. For this purpose, the entire system was assembled, consisting of a stainless steel (316) tube with an outer diameter (OD) of 6 mm and an inner diameter (ID) of 4 mm, the two fittings used for the catalytic bed, and the sinter seal, also made of stainless steel (316), as detailed in Section II.3.1 of the previous chapter.

Before testing, the set-up was subjected to the same reduction conditions applied to the catalysts. The temperature dependence of the stainless steel catalytic reactor indicates no significant catalytic activity below 450°C, with an ammonia conversion rate of only 1.44% at this temperature. However, at 500°C, the conversion increases notably to 7.99% (see Figure III.2). This suggests that for conventional catalysts, the activity up to 450°C can be attributed almost entirely to the catalyst itself, not to the stainless-steel reactor. However, for $LiNH_2$-based catalysts, as $LiNH_2$ interact with transition metals, this assumption cannot be directly applied.

Unfortunately, as anticipated, the metallic fixed-bed reactor material undergoes significant expansion under our reaction conditions. Despite this, it is still possible to disassemble the fitting system and recover the catalyst after the reaction. However, collecting the catalyst inside the glove box proved to be challenging,

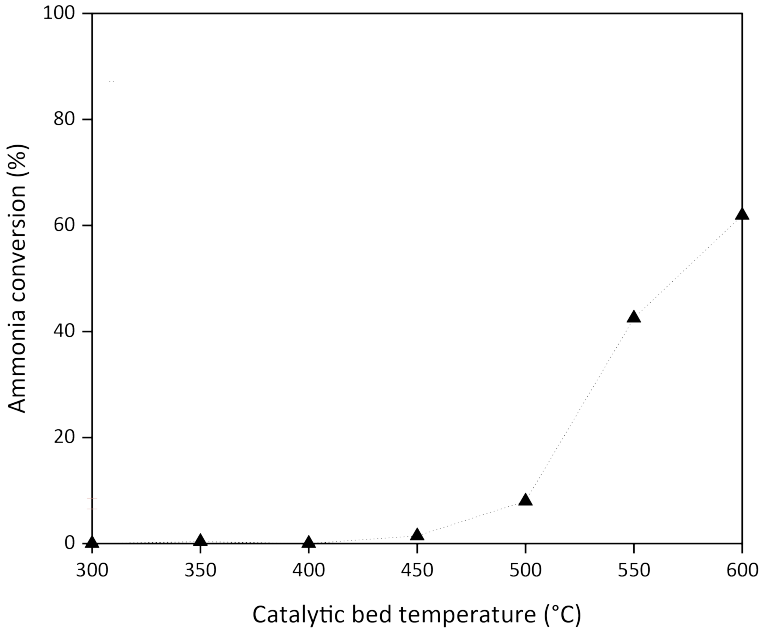

Figure III.2: Temperature dependences of the stainless-steel catalytic reactor. Reaction conditions: 20 mL.min^{-1} flow rate of diluted ammonia in argon (5% vol).

requiring the use of a vise for disassembly outside the controlled environment. While the catalyst can be retrieved, the thermal expansion of the reactor's metal components renders them unsuitable for reuse. As a result, the tube and connection system for the catalytic bed are single-use.

From a cost perspective, the reactor tube is relatively affordable around 10 euros, but the catalytic bed components—including the two fittings and the metal seal—is clearly more expensive (around 125 euros). Although this solution is not the most cost-effective, it facilitates the straightforward preparation of the catalyst within a glove box, which is crucial for ensuring airtight handling of the sample during experiments.

To secure the catalyst in the heated zone and maintain a compact catalytic bed, quartz wool is commonly used for the reasons previously outlined. However, as demonstrated earlier, this material is not inert with respect to our materials. An alternative in the form of ceramic felt was tested, but it failed to resist our reaction conditions, and it is unlikely that it would have been more inert.

Quartz wool was therefore retained for this study, although this solution is not ideal. The surface of $LiNH_2$-based catalysts in contact with the quartz wool is prone to react, potentially losing its activity. Stainless steel wool could eventually replace quartz wool, but due to its inherent activity, standardization of experimental protocol and the use of precise amounts will be required to avoid introducing bias into the catalyst performance measurements.

- **Effect of thermal diluent**

When setting up the catalytic bed of the reactor, the use of a thermal diluent became a key consideration. In catalytic processes, thermal diluents not only help distribute the heat evenly but also homogenize temperatures during exothermic or endothermic reactions.[362]

For ammonia decomposition, many studies incorporate thermal diluents, with silicon carbide (SiC) being the main choice.[363, 364, 365, 366] SiC is renowned for its exceptional thermal conductivity (146–270 $W.m^{-1}.K^{-1}$) and its high thermal (up to 1700°C) and chemical stability.[367] Consequently, we evaluated the impact of incorporating SiC on the performance of our reference catalyst. The catalyst-to-thermal diluent ratio varies significantly across different studies, ranging from 0.2:1[364] to 1:2[366] by mass between the catalyst and SiC. Regarding the particle size of the diluent, most studies use particles ranging from 300 to 400 µm.[363, 365, 366] In contrast, our study employed a thermal diluent with particles approximately 10 times smaller, between 30 and 40 µm. This choice was made as a compromise. In the literature, a high catalyst-to-thermal diluent ratio is commonly achieved by using a significant amount of diluent.[364, 366] However, due to the limited volume of our catalytic bed, a ratio of 0.2:1 was not feasible while maintaining a catalyst mass of 100 mg. Although the direct comparison of the quantity and particle size of SiC has not been specifically studied or evaluated here, smaller diluent particles offer potential benefits. They can increase the available surface area, thereby enhancing heat and mass transfer efficiency within the catalytic bed, even when used in smaller quantities.

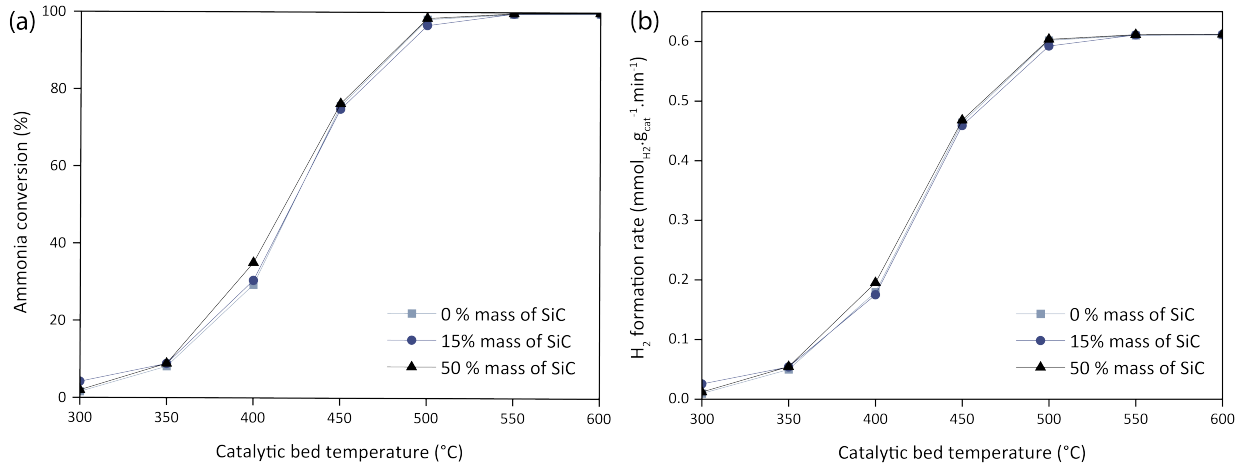

Figure III.3: Impact of thermal diluent on Ru/Al_2O_3: comparison without diluent, with 15%, and with 50% diluent. (a) Temperature dependence of catalytic activities; (b) temperature dependences of H_2 formation rate. Reaction conditions: catalyst loading of 100 mg, with a 20 $mL.min^{-1}$ flow of ammonia diluted in argon (5% vol).

The influence of thermal diluents was assessed by adjusting their mass fractions to 0%, 15%, and 50% relative to the total catalyst mass. A mixture of 100 mg of Ru/Al_2O_3 and the corresponding mass of SiC for each specified percentage was prepared by weighing the components into a mortar. The mixture was then blended with pestle thoroughly for several minutes to ensure homogeneity before placement into the catalytic bed.

As depicted in Figure III.3, the presence of SiC did not significantly affect the catalytic performance. Although a slight deviation is observed at 300°C and 400°C, its origin does not appear to be linked to the presence of the thermal diluent. Based on these findings, we conclude that incorporating a thermal diluent is unnecessary for Ru/Al_2O_3 catalytic performance measurements.

III.1.3 Ammonia detection limit measurement

The detection limit of µGC-TDC was validated at 600°C, where the ammonia concentration stabilized around 100 ppm at the catalytic reactor outlet. At this point, several samples were collected by bubbling the outgoing gas mixture into 5M of H_2SO_4 solution. The bubbling system was designed to ensure complete solubilization of the ammonia gas. To verify this, the solubilization efficiency was tested using a gas flow with a known concentration of 5% ammonia by volume in argon.

Subsequently, the dissolved ammonia concentration was determined using a salicylate-hypochlorite colorimetric titration method. The average concentration from three samples was determined to be 164 $\pm$29 ppm, which aligns closely with the concentration measured by µGC-TDC, confirming the accuracy of the detection method.

III.1.4 Comparison of commercial Ru/Al_2O_3 catalyst performance to literature

To validate our setup, we selected a commercial ruthenium-based catalyst supported on alumina. This catalyst was chosen for several key reasons:

(i) **High activity:** Ru/Al_2O_3 is among the most active catalysts for ammonia decomposition, particularly within the temperature range of our study (300–600°C).[363, 368]

(ii) **Well-documented performance:** The behavior of Ru/Al_2O_3 in ammonia decomposition, especially the commercial version, is extensively studied in the literature, providing reliable and reproducible benchmarks for comparison.[12, 369]

(iii) **Commercial availability:** Ru/Al_2O_3 is widely available from numerous commercial suppliers, ensuring consistent accessibility.

For all these reasons, this catalyst was selected as a reference. This choice ensures that the performance measurements obtained with our setup can be directly compared to other studies where the catalytic performance of fixed-bed reactors was evaluated using the same commercial catalyst.

The decomposition of Ru/Al_2O_3 catalyst was performed under argon at 500°C for 1 hour, with an argon flow rate of 20 $mL.min^{-1}$. For the reduction, it was conducted using a 10 vol% of H_2 in Ar mixture at 500°C, also with a total flow rate of 20 $mL.min^{-1}$. These conditions are consistently applied throughout this chapter for

all catalysts.

The XRD patterns of the Ru/Al_2O_3 catalyst as supplied reveal the presence of ruthenium oxide (RuO_2) and aluminum phases, specifically $Al_2(OOH)_2$ (bohmite) and $Al(OH)_3$ (gibbsite), resulting from the hydration of Al_2O_3. After decomposition under argon, the peaks corresponding to $Al_2(OOH)_2$ and $Al(OH)_3$ disappear, likely due to water loss, as suggested by the observed mass loss (3.6%) during TGA analysis of the as-supplied catalyst.

However, the material undergoes a loss of crystallinity following this heat treatment, indicating the formation of an amorphous alumina phase (see Figure III.4). This amorphous phase may have two possible origins. First, it could result from a rapid cooling process, which prevents the formation of crystalline phases.[370] Alternatively, the aluminum hydroxides present in the catalyst may transform directly into an amorphous alumina phase during thermal treatment.[371]

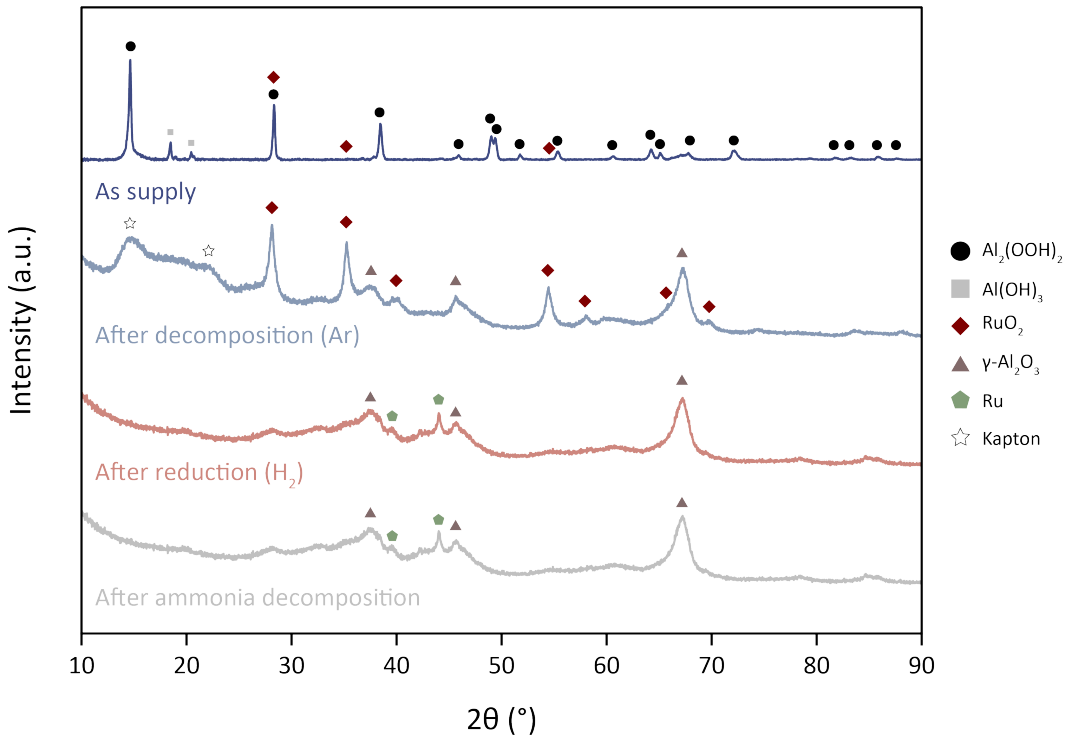

Figure III.4: XRD patterns of Ru/Al_2O_3 catalyst as supply, after thermal treatment under Ar gas at 500°C, after reduction under 10 vol% of H_2 at 500°C and after ammonia decomposition experiment.

Decomposition under argon facilitates the transformation of $Al_2(OOH)_2$ and $Al(OH)_3$ into alumina (amorphous and γ-Al_2O_3); however, it does not result in the formation of metallic ruthenium, as the peaks corresponding to ruthenium oxide (RuO_2) remain present. Following the reduction under hydrogen, the RuO_2 peaks disappear, indicating the formation of the metallic ruthenium phase, as evidenced by the appearance of diffraction peaks corresponding to metallic Ru. This highlights the necessity of the reduction step prior to measuring the catalytic performance of Ru/Al_2O_3. Regarding the XRD patterns of the catalyst after ammonia

decomposition, no changes observed compared to the one obtained after the reduction step under H_2.

The distribution of ruthenium on alumina and the size of the Ru and Al_2O_3 particles were analyzed using SEM (see Figure III.5). SEM images of the catalyst after the reduction step revealed an uneven distribution of ruthenium across the alumina particles (see Figure III.S2). This irregular dispersion of ruthenium may be attributed to the reduction conditions, particularly the after the temperature drop, as the catalyst undergoes amorphization because of these treatments. However, further analyses prior to the reduction step would be required to confirm this hypothesis. Regarding the alumina particles, their size ranges between 30 and 40 µm.

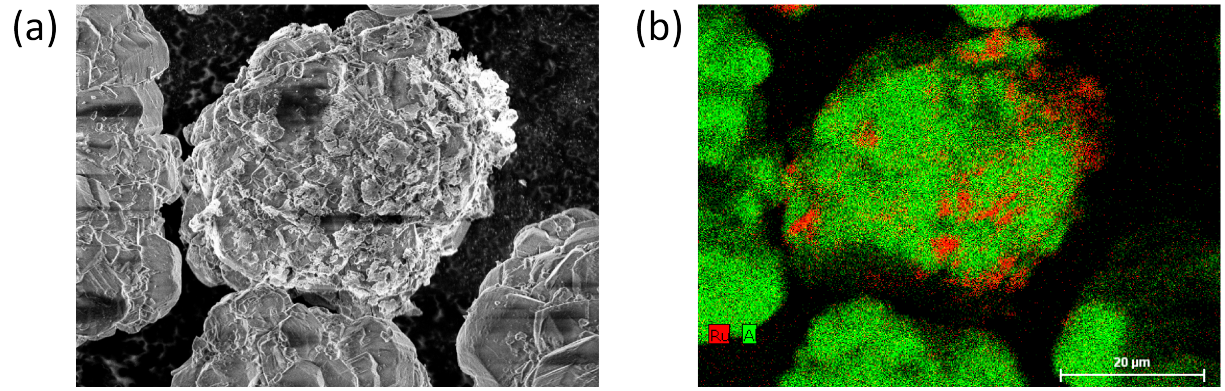

Figure III.5: (a) SEM image of Al_2O_3 particles with metallic Ru after reduction of the catalyst (10 vol% of H_2 at 500°C); and (b) EDX mapping of Al (green) and Ru (red) elements.

Despite the apparent agglomeration of the catalyst, the performance of Ru/Al_2O_3 for ammonia decomposition in the fixed-bed reactor setup is highly satisfactory (see Figure III.6.a). At 450°C, an average of 97.6 % of the ammonia was converted, significantly exceeding the 1.4 % contribution from the metal reactor at the same temperature.

The reproducibility tests of the catalytic performance measurements confirmed consistent results. This reproducibility can be attributed to the catalytic bed setup, which ensures that the thermocouple is placed in a similar position across different tests, despite the limited visibility provided by the stainless-steel reactor compared to a quartz reactor. Additionally, the catalyst is easily recoverable after ammonia decomposition, and no issues were observed regarding the stabilization of the concentrations of the various gaseous species at the reactor outlet following each temperature change.

The impact of the ammonia decomposition conditions used in this study becomes obvious when comparing the performance of this commercial catalyst with other investigations. Notably, when tested in stainless steel reactors, as reported by Makepeace *et al.*, their results showed significant differences. However, they used five times more catalyst than we did and operated with a flow rate of 60 $mL.min^{-1}$ of pure ammonia, whereas in this study, the flow rate was 20 $mL.min^{-1}$ of diluted NH_3 (5 vol% in argon). Consequently, the WHSV in their experiments was 7200 $mL_{NH_3}.g_{cat}^{-1}.h^{-1}$, compared to only 600 $mL_{NH_3}.g_{cat}^{-1}.h^{-1}$ in this study.

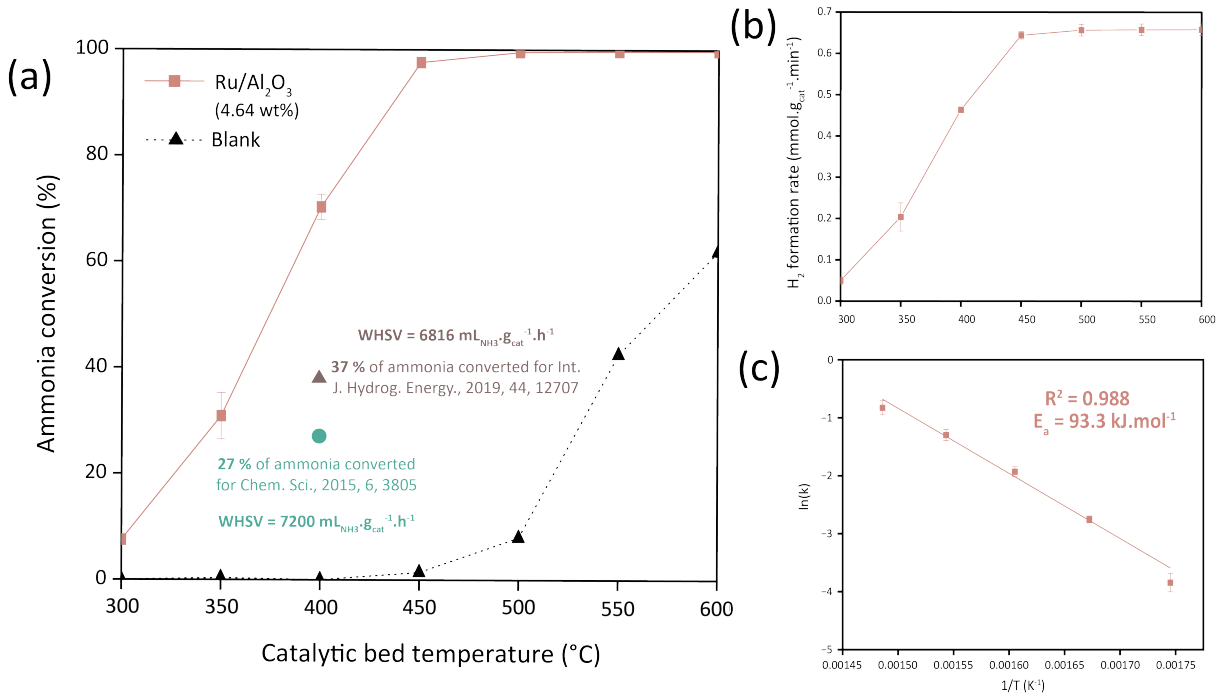

Figure III.6: (a) Temperature dependences of the activities of Ru/Al_2O_3 and the equivalent without any catalyst; (b) temperature dependences H_2 formation rate for Ru/Al_2O_3; and (c) the corresponding Arrhenius plot for the temperature range of 300–450°C. Reaction conditions: catalyst loading of 100 mg, with a 20 $mL.min^{-1}$ flow of ammonia diluted in argon (5 vol%), and a WHSV of 600 $mL_{NH_3}.g_{cat}^{-1}.h^{-1}$. Comparative ammonia conversion performances are extracted from sources [12] and [363].

Therefore, at 400°C, their ammonia conversion was only about 27%, whereas our tests achieved an average conversion of 70.3 ± 2.4%.[12]

Similarly, Lucentini *et al.* reported a conversion of 37% at 400°C, with a WHSV of 6800 $mL_{NH_3}.g_{cat}^{-1}.h^{-1}$,[363] which lies between the WHSV values of this study and those of Makepeace *et al.*, though closer to their value. This intermediate WHSV may explain why their conversion rate is also intermediate, though also closer to the value reported by Makepeace et *al.*.

Regarding the apparent activation energy reported in literature, there is again significant variation reported for commercial Ru/Al_2O_3, ranging from 67 ± 10[12] $kJ.mol^{-1}$ to 117 $kJ.mol^{-1}$.[369] All these disparities arise not only from differences in reaction conditions but also from variations in standardized commercial catalysts, where slight differences between batches can lead to variations in catalytic performance. Nevertheless, the apparent activation energy measured for Ru/Al_2O_3 in this study, 93.3 $kJ.mol^{-1}$, remains within the same order of magnitude. This relatively high apparent barrier is really consistent with the intrinsic difficulty of decomposing ammonia.

III.1.5 Implementation of the Ru dosage method by ICP-AES

Comparing the efficiency of Ru catalysts with and without lithium amide requires precise knowledge of their initial catalyst loading. However, ruthenium's chemical inertness poses significant challenges during digestion. This difficulty is linked to the unequal effectiveness of digestion methods in solubilizing the various ruthenium phases. Additionally during the digestion process, a ruthenium tetroxide (RuO_4) phase may form, leading to potential material loss. Ruthenium digestion methods generally fall into two main categories: alkaline oxidative fusion and acid wet digestion.

The two main digestion pathways were tested on the commercial Ru/Al_2O_3 catalyst, with several methods explored for each. For the alkaline fusion pathway, three types of flux were evaluated: NaOH-$NaNO_3$, KOH-KNO_3, and Na_2O_2. For the acid wet digestion pathway, aqua regia was consistently employed, using five different digestion techniques: microwave-assisted (MW), autoclave reactor, digester, stirring, and heating-assisted stirring. All digestion conditions are described in section II.4.2 of Chapter 2. Among these, only the MW and autoclave methods were conducted in a closed environment. For the other three techniques, regular degassing was required to prevent damage to the container, which introduced a potential risk of ruthenium loss due to the formation of volatile RuO_4.

The results of the various digestion protocols applied to Ru/Al_2O_3 were unexpected. Alkaline fusion, widely cited in the literature as a reliable method for determining ruthenium, yielded results significantly lower than the theoretical (from the synthesis conditions) Ru mass loading of Ru/Al_2O_3, with measured values ranging between 1.52 and 2.55 wt% (see Table III.1). Several factors could explain this discrepancy. Despite conducting the fusion under argon, the formation of RuO_4, a volatile species, may still have occurred. Additionally, impurities were detected during the Ru determination by ICP-AES, notably nickel and zirconium, depending on the crucible used. These impurities could have interfered with the accuracy of the ruthenium measurement. Although alkaline fusion is advantageous due to its simplicity and its speed for the digestion of samples, these limitations led us to exclude it as a viable method for this study.

The results of acid wet digestion were also unexpected. The two techniques anticipated to be the most effective—MW-assisted digestion and the one using an autoclave reactor—failed to fully solubilize all the ruthenium present (see Table III.1). However, the reasons for this inefficiency differ between the two methods. For MW-assisted digestion, the issue lies in the significant temperature variation observed within the reactors during the process, ranging from 170°C to 220°C across different reactors in the same MW digestion experiment. Even in reactors that reached the highest temperatures, complete digestion was not achieved. In contrast, the autoclave reactor allowed for better temperature control, but its tightness was frequently compromised during digestion, under normal conditions of use of the autoclave reactor.

Surprisingly, prolonged stirring yielded the best results for the digestion of Ru/Al_2O_3. However, the average value obtained remains slightly below the reported ruthenium content by commercial provider (see Table III.1). This discrepancy could be attributed to measurement uncertainties inherent to ICP-AES (5%), but it

may also result from the potential loss of RuO_4 during the degassing process of the flask used for digestion.

Table III.1: Results for various techniques used to mineralize 100 mg of Ru/Al_2O_3, a commercial catalyst with a 5 wt% Ru loading. For alkaline fusion, the results are presented for three different fluxes applied under identical conditions. For digestion in aqua regia, five techniques were employed, including microwaves (MW), autoclave reactor, stirring, and heating-assisted stirring. Only the last two techniques were applied over an extended period of one week.

Fusion			Digestion with aqua regia				
$NaOH\text{-}NaNO_3$	$KOH\text{-}KNO_3$	Na_2O_2	MW	Digester	Autoclave reactor	Agitation	Heating assisted agitation
1.94 ± 0.10	2.55 ± 0.13	1.52 ± 0.08	2.88 ± 0.14	3.29 ± 0.14	3.95 ± 0.20	4.64 ± 0.23	1.80 ± 0.09

Based on these results, prolonged agitation in aqua regia (with sample degassing) was selected for the digestion of all ruthenium-based catalysts. However, all future comparative performance results will be interpreted with caution, as the digestion of ruthenium remains a challenging process.

This method was specifically optimized for the commercial Ru/Al_2O_3 catalysts used as supplied, which, as confirmed by XRD, contain RuO_2 phases. In contrast, the synthesized catalysts feature ruthenium amide phases ($Ru(NH_2)_3$), whose solubilization properties are currently unknown. Moreover, while the digestion protocol could be tested during this study, its efficiency could not be fully verified due to the lack of reference $Ru(NH_2)_3$ material with a precisely known ruthenium concentration.

III.2 Lithium amide: catalytic activity and activation energy

The catalytic activity of lithium amide alone was evaluated under our experimental conditions (see Section II.3.1 of Chapter 2 for details) before testing the Ru-$LiNH_2$ catalysts. Characterization techniques—including Raman and IR spectroscopy, XRD, and TGA-DSC (refer to Section II.4 of Chapter for details)—confirmed the presence of $LiNH_2$ (refer to Figures III.7, III.10, III.8, and III.9). Additionally, LiOH was detected in some analyses (see Figures III.7 and III.8).

- **Characterization of $LiNH_2$**

Spectroscopic analysis consistently reveals the presence of $LiNH_2$ and LiOH. In the IR spectrum (Figure III.7.a and III.7.b, as well as Table III.2), characteristic vibrations of the NH_2 group in $LiNH_2$ are clearly identified. These include symmetric stretching vibrations of the N–H bonds at 3263 cm^{-1} and asymmetric stretching vibrations at 3325 cm^{-1}, values closely aligned with literature reports for this compound (3260 and 3313 cm^{-1}, respectively).[324] Additionally, two angular deformation vibrations of the N–H bond are present in the IR spectrum of $LiNH_2$, observed at 1537 cm^{-1} and 1564 cm^{-1}. These values also align with literature findings, which report two closely spaced peaks near 1560 cm^{-1}.[372] Moreover, vibrational bands characteristic of O–H bond stretching are detected at 3450 cm^{-1} and 3676 cm^{-1}, likely arising from the presence of LiOH,

initially present in the commercial $LiNH_2$ and consistently found in all analyzed samples. These frequencies correspond well to literature values for LiOH, reported at 3438 cm^{-1} and 3678 cm^{-1}, respectively.[373]

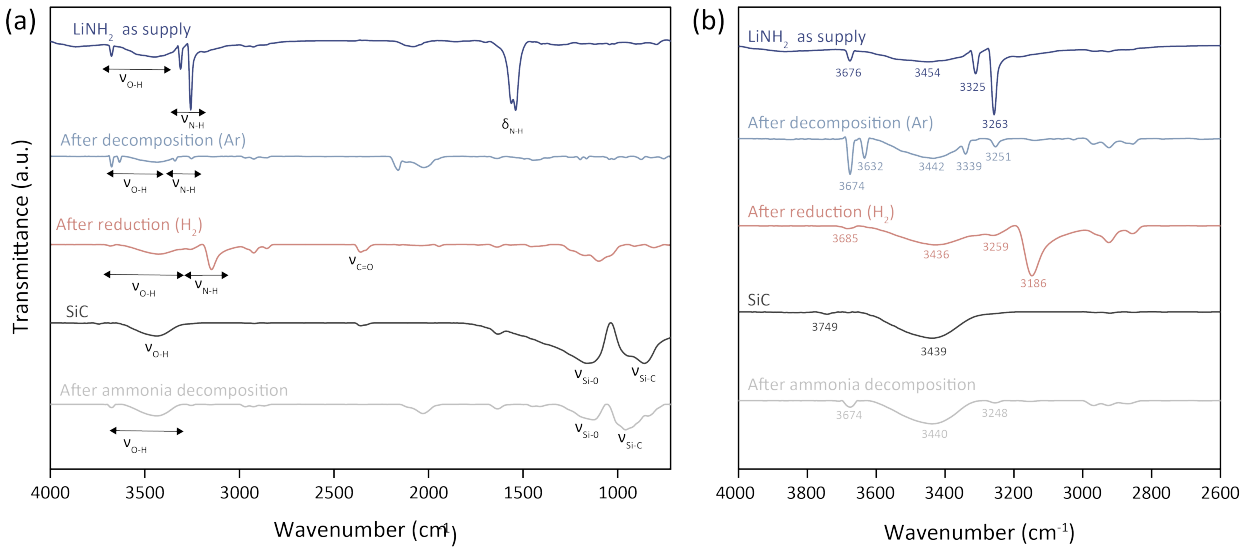

Figure III.7: (a) Infrared (IR) spectra of lithium amide ($LiNH_2$) as supplied, after decomposition under Ar at 500°C, after reduction with 10 vol% H_2 at 500°C, and of silicon carbide (SiC) as received, along with the residues from the ammonia decomposition experiment using $LiNH_2$-SiC (1:1 wt%) as the precursor, and (b) zoom view of the same IR spectra in the range of 4000–2600 cm^{-1}.

Table III.2: Vibrational bands of $LiNH_2$ as supply, after decomposition under Ar, after reduction (10% H_2), and after ammonia decomposition, as well as those of SiC as supply, obtained through IR analyses. Comparative reference spectra for SiC, $LiNH_2$,[324, 372] Li_2NH,[324, 372] and LiOH[374] are also included.

		N-H bending	N-H stretch		O-H stretch	C≡N stretch	Si-C stretch	Si-O stretch	unknown
			symmetric	antisymmetric					
$LiNH_2$	As supply	1539; 1562	3263	3325	34548; 3676	-			2083
	After decomposition (Ar)	-	3251	3396	3442; 3632; 3674	-			2160; 2025
	After reduction (H_2)	-	3186	3259	3436; 3685	-			1039
	After NH_3 decomposition	-	-	3248	3440; 3674	2027	835	1119	-
SiC	As supply	-	-	-	-	-	842	1148	-
Experimental references	SiC [375]	-	-	-	-	-	~800	~1200	-
	$LiNH_2$ [324, 372]	1564; 1582	3260	3315	-	-	-	-	-
	Li_2NH [324, 372]	~ 1500	3180	3250	-		-	-	-
	LiOH [374]	-	-	-	3438; 3565; 3678	-	-	-	-

Similarly, in the Raman spectrum of commercial $LiNH_2$, characteristic vibrations of the NH_2 groups are observed (see Figure III.8). These include one band corresponding to the symmetric stretching of N–H bonds at 3263 cm^{-1} and two bands corresponding to the asymmetric stretching of N–H bonds at 3315 and 3325 cm^{-1}. These values align well with those reported in the literature: 3260 cm^{-1} for the symmetric stretching and 3313 and 3323 cm^{-1} for the asymmetric stretching of N–H bonds.[322] Additionally, a band at 3666 cm^{-1} is observed, characteristic of the stretching vibrations of O–H bonds, likely due to the presence of LiOH. This feature matches the Raman spectra of LiOH reported in the literature, where the same vibration is identified at 3664 cm^{-1}.[374]

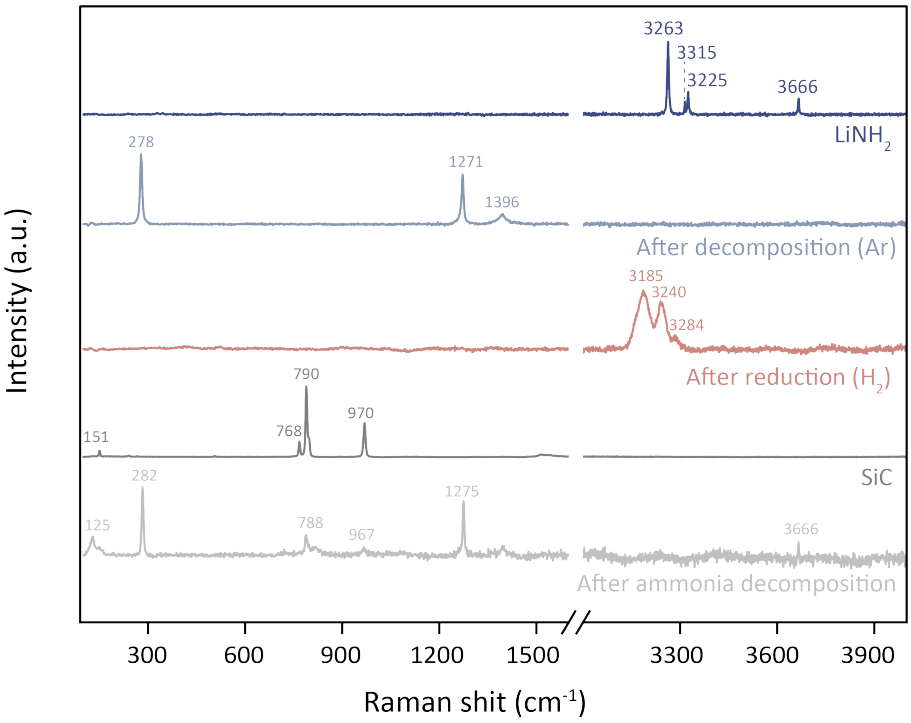

Figure III.8: Raman spectra of the lithium amide ($LiNH_2$) as supply, after decomposition under Ar at 500°C, after reduction with 10 vol% H_2 in Ar at 500 °C, of silicon carbide (SiC) as received, and of the residues from ammonia decomposition experiment, using $LiNH_2$-SiC (1:1 wt%) as the precursor.

Although LiOH is detected through IR and Raman spectroscopy, its diffraction peaks are not fully observed in the XRD patterns of commercial lithium amide. This discrepancy is likely due to the higher sensitivity of spectroscopic methods to hydroxyl groups, whereas XRD is less effective at detecting LiOH when present in small quantities. While one diffraction peak could potentially be associated with LiOH (see the peak marked with an asterisk in the XRD pattern of $LiNH_2$ in Figure III.10), it is insufficient for definitive identification. This highlights the importance of employing multiple complementary characterization techniques when analyzing such compounds.

Finally, the TGA analysis of commercial $LiNH_2$ under argon reveals a mass loss attributed to the decomposition of the amide phase by its decomposition into the imide phase, and DSC analysis reveals its liquefaction (see Figures III.9.a and III.9.b, respectively). During the heating phase at a rate of 5°C/min, the mass loss begins around 365°C and stabilizes at 30.1% following a one-hour isothermal hold at 500°C. For a sample composed purely of lithium amide, the expected mass loss would be 37.1%, corresponding to the formation of Li_2NH and the release of ammonia gas. The observed difference could stem from several factors, such as the presence of impurities in the sample or insufficient decomposition kinetics due to an isothermal hold that was not long enough, even though the mass loss appeared stable at 500°C. If $LiNH_2$ were completely decomposed into Li_2NH under the chosen experimental conditions, TGA analysis would suggest a significantly higher impurity content, estimated at 18.9%, with possible impurities being lithium oxides or hydroxides. This contrasts with the manufacturer's specified purity level of 95%. Furthermore, DSC mea-

surements identify the melting point of $LiNH_2$ at 370°C, compared to 375°C in the literature,[376] with a calculated liquefaction enthalpy of 24.3 kJ.mol^{-1}. However, there is significant uncertainty in this value due to the simultaneous occurrence of fusion and decomposition of $LiNH_2$, which complicates the accurate measurement of its enthalpy of fusion.

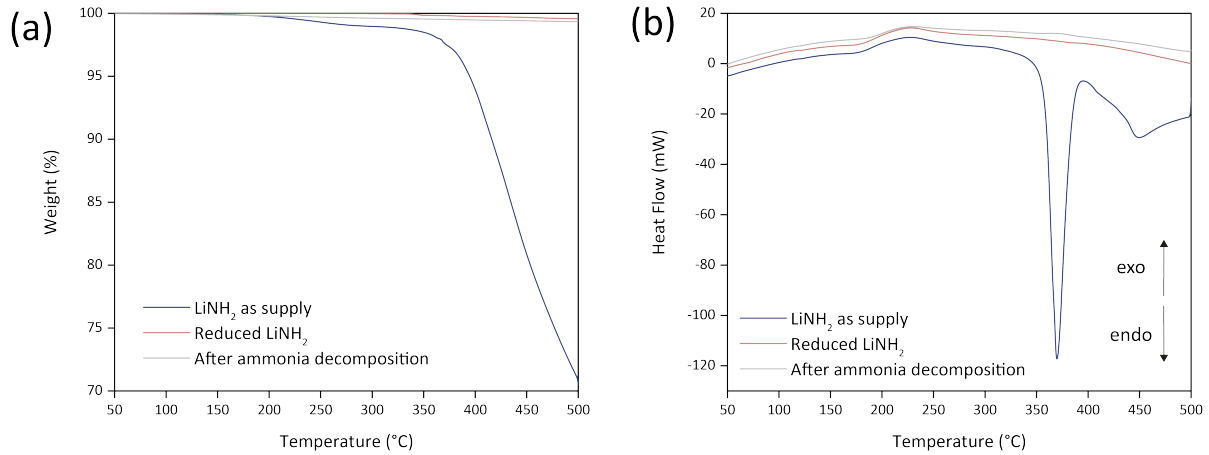

Figure III.9: (a) Thermal Gravimetric Analysis (TGA) and (b) Differential Scanning Calorimetry (DSC) under argon of the $LiNH_2$, as supplied, after reduction (10 vol% H_2 in Ar at 50 °C) and after ammonia decomposition.

Lithium amide after decomposition under Ar was also analyzed, yielding mixed results. XRD analysis confirmed the formation of a lithium imide (Li_2NH) phase, accompanied by Li_2O, as shown in Figure III.10. However, spectroscopic analyses did not detect the characteristic vibrations of Li_2NH: the broad NH stretching vibration at 3180 cm^{-1} in Raman spectroscopy,[377] nor the two characteristic bands at 3180 cm^{-1} and 3250 cm^{-1} in IR spectroscopy.[324] The absence of these signals in Figures III.7 and III.8, in IR and Raman spectra respectively, along with the lack of NH stretching vibrations around 3200 cm^{-1} present in the more dehydrogenated phases, may indicate a greater extent of dehydrogenation of $LiNH_2$. However, no sharp phonon modes around 500 cm^{-1}, which are characteristic of phases such as Li_3NH, Li_4NH,[377] or other dehydrogenated intermediates, were observed, suggesting the absence of these specific forms. Instead, the two vibrations observed in IR spectroscopy at 3249 cm^{-1} and 3342 cm^{-1} are more closely aligned with NH_2 stretching, as found in $LiNH_2$, rather than Li_2NH. Although no $LiNH_2$ related decomposition or liquefaction is present in TGA-DSC analysis after reduction under hydrogen and after ammonia decomposition experiment (see Figure III.9). All these results, which fail to converge on a single structural interpretation, prevent us from drawing a definitive conclusion about the form of $LiNH_2$ obtained after decomposition under argon under our specific conditions (see above in Section III.1.4 for details).

Regarding ammonia decomposition test, and to enable a meaningful comparison with the reference catalyst Ru/Al_2O_3, $LiNH_2$ was first subjected to a reduction process. This reduction step was applied to ensure comparable performance within the catalytic reactor, which may benefit from such a pretreatment. However, these reduction conditions can alter the initial lithium phase present at the beginning of ammonia decomposition. To assess this impact of our reduction condition on lithium amide, the same characteriza-

tion techniques were used.

After reduction, the XRD analysis and the Raman spectrum converge towards the same conclusion: the presence of a lithium amide-imide phase. Indeed, as shown in Figure III.8 of the Raman spectra, there are characteristic vibrations of the NH_2 group of $LiNH_2$ (also present in $LiNH_2$ as supplied): symmetric stretching vibrations of the N–H bonds (3263 cm^{-1}) and asymmetric stretching vibrations of the N–H bonds (3325 cm^{-1}). Additionally, there is a characteristic N–H stretch of imide at 3186 cm^{-1}, close to the known value for this vibration (3185 cm^{-1}).[322] The XRD patterns (Figure III.10) further confirmed the presence of a lithium amide-imide phase, accompanied by Li_2O. Yet, in IR spectroscopy after reduction, both vibrations are characteristic—by their values and the shape of the peaks—of lithium imide, as depicted in Figure III.7 measured at 3147 and 3253 cm^{-1} (in good agreement with the lithium imide vibrations reported by Kojima *et al.* at 3180 cm^{-1} and 3250 cm^{-1}).[324]

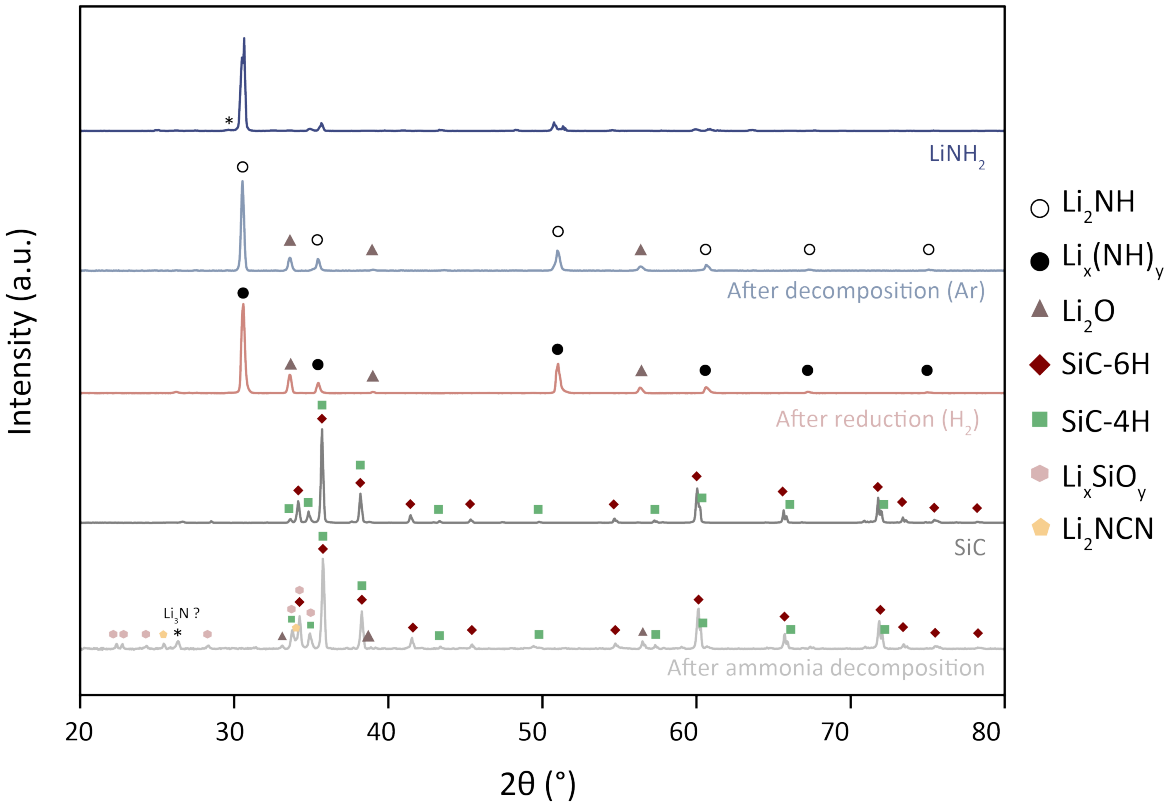

Figure III.10: XRD patterns of lithium amide ($LiNH_2$) as supply, of lithium imide (Li_2NH) obtained after the decomposition of $LiNH_2$ under argon at 500°C, of lithium amide-imide formed by the reduction of $LiNH_2$ with 10 vol% H_2 at 500°C, of silicon carbide (SiC) as received, and of the residues from ammonia decomposition experiment, using $LiNH_2$-SiC (1:1 wt%) as the precursor.

For clarity, the catalysts will be labeled according to their precursor lithium phase in the activity comparison figures, even though this may not represent the actual phase present at the start of the ammonia decomposition tests.

- **$LiNH_2$ performance as a NH_3 decomposition catalyst**

During preliminary tests, it was frequently observed that the material, during the heating phase (whether under Ar or H_2), resolidified within the metallic frit, causing a blockage. This blockage was evidenced by an increase in system pressure upstream of the catalytic bed, accompanied by a halt in mass flow, as the flow controllers are not designed to operate under back-pressure conditions. To prevent this, the thermal diluent (SiC) was mixed with $LiNH_2$, which had previously shown no benefit with Ru/Al_2O_3, was considered as a solution to prevent blockage. While this approach proved effective in avoiding blockages, interactions between $LiNH_2$ and SiC under our operating conditions were identified at a later stage. Specifically, in the residue after ammonia decomposition, the presence of Li_2NCN was detected, likely resulting from contact between $LiNH_2$ and SiC (see Figure III.10).

After the reduction phase, lithium amide exhibited activity for ammonia decomposition under our reaction conditions. As anticipated, its activity is significantly lower than that of Ru/Al_2O_3, particularly in the 300–450°C range. However, as shown in Figure III.11.a, its performance becomes comparable at 500°C. The apparent activation energy for $LiNH_2$ was measured at 132.5 $kJ.mol^{-1}$, which is higher than that of Ru/Al_2O_3 (93.3 $kJ.mol^{-1}$). This observation aligns with the ammonia conversion trends, as a higher activation energy generally results in greater sensitivity to temperature increases, consistent with the Arrhenius equation.

Our conversion value at 450°C (83.3 ± 3.3%) is comparable to that reported by Makepeace *et al.* (90.7%), despite the presence of SiC in contact with our catalyst. Similarly, the measured apparent activation energy (132.5 $kJ.mol^{-1}$) closely matches theirs (133 ± 4 $kJ.mol^{-1}$).[12] This agreement is notable given the substantial differences in reaction conditions. Their experiments employed five times more lithium amide, a non-diluted ammonia flow rate of 60 $mL.min^{-1}$, and a different reactor design. Additionally, their WHSV was 7200 $mL_{NH_3}.g_{cat}^{-1}.h^{-1}$, compared to 600$mL_{NH_3}.g_{cat}^{-1}.h^{-1}$ here.

However, it is important to highlight that, despite the similarities to the Makepeace *et al.* study, our ammonia decomposition conversion values are significantly higher than those reported by Bramwell *et al.*.[325] This is notable given that our reaction conditions are more closely aligned with theirs, including a flow rate of 25 $mL.min^{-1}$ of 10% NH_3 in He and a comparable amount of $LiNH_2$, conducted in a stainless steel reactor. Even their WHSV is similar, ranging from 600 to 1500 $mL_{NH_3}.g_{cat}^{-1}.h^{-1}$. These discrepancies highlight the variability in catalytic performance observed across different studies, even when reaction conditions seem comparable at first glance.

A challenge encountered was the recovery of the catalyst after ammonia decomposition. During the process, the $LiNH_2$ catalyst installed in the fixed bed liquefies before resolidifying, resulting in a significant alteration of its initial powder-like appearance. The residue takes on a ”concrete-like” texture, making extraction extremely difficult. It requires forceful manipulation with a rod to separate it from the catalytic bed. This recovery process is particularly delicate, as it is almost impossible to extract the residue without also dislodg-

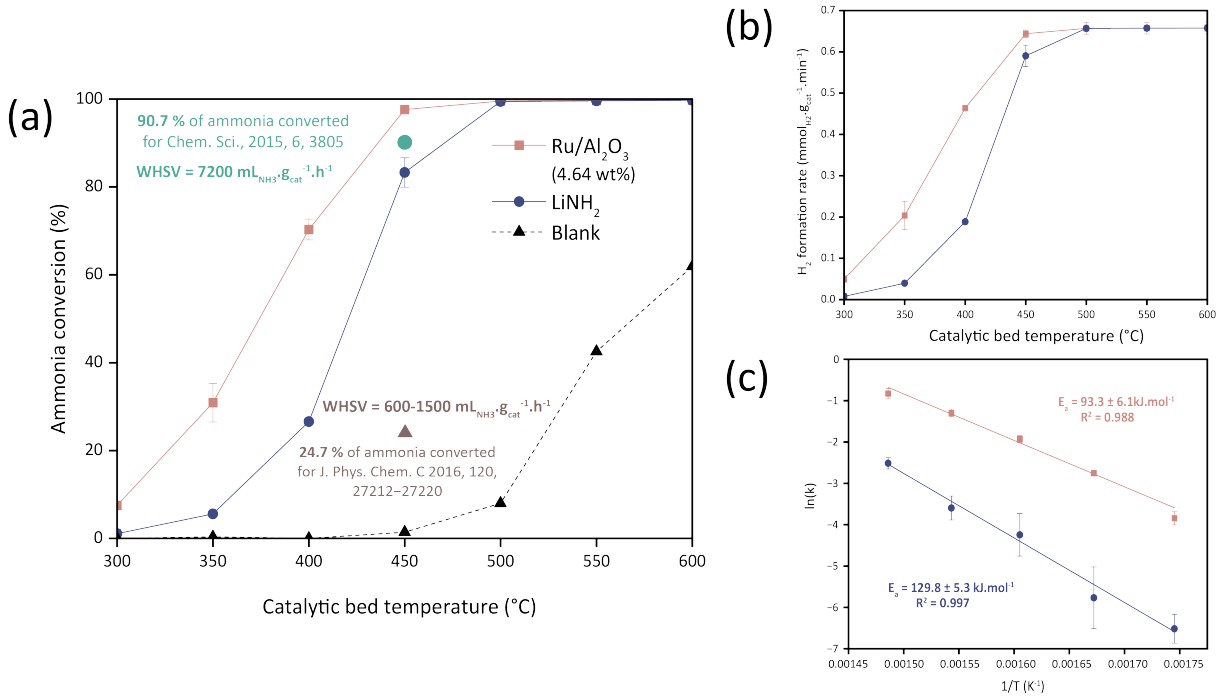

Figure III.11: (a) Temperature dependences of the activities of $LiNH_2$, Ru/Al_2O_3 and the equivalent without any catalyst; (b) temperature dependences H_2 formation rate for $LiNH_2$ and Ru/Al_2O_3; and (c) the corresponding Arrhenius plot for the temperature range of 300–450°C. Reaction conditions: catalyst loading of 100 mg, with a 20 mL.min^{-1} flow of ammonia diluted in argon (5% vol), and a WHSV of 600 $mL_{NH_3}.g_{cat}^{-1}.h^{-1}$. Comparative performances of ammonia conversion, using $LiNH_2$ as catalyst, are extracted from sources [325] and [12].

ing the quartz wool that holds the catalyst in place. Furthermore, the quartz wool itself tends to crumble very easily, complicating the operation further.

As for the residue after decomposition, interpreting the different phases by XRD is challenging due to the presence of SiC diffraction peaks (see Figure III.10). However, the presence of Li_xSiO_y can be confirmed, likely resulting from a parasitic reaction caused by the interaction of $LiNH_2$ with quartz wool. The confirmation of these phases by IR analysis is challenging because their vibrational bands overlap with those of SiC. Specifically, the asymmetric stretching vibrations of Si-O typically appear between 900 and 1100 cm^{-1}, while the symmetric stretching vibrations are observed between 600 and 850 cm^{-1}.[378]

Regarding Li_2NCN, from previously mentioned reaction with SiC, diffraction peaks corresponding to Li_2NCN are present in XRD analysis, as shown in Figure III.10). The presence of Li_2NCN can also be inferred from IR analysis by the vibrational band observed at 2027 cm^{-1}, which may correspond to the stretching vibrations of the nitrile group (C≡N). However, to the best of my knowledge, the IR spectrum of Li_2NCN is not available in the literature, making it impossible to confirm this peak assignment with certainty. In contrast, the IR spectrum of MgNCN is available and includes a vibrational band around 2000 cm^{-1}, attributed to the nitrile group, supporting a possible similarity in spectral features.[379] No peaks corresponding to the carbodiimide anion (NCN^{2-}) are observed in the Raman spectrum. Symmetric stretching vibrations are typically expected

around 1200 cm^{-1}, while bending vibrations are anticipated near 1300 cm^{-1}.[380, 381]

No diffraction peaks, in the recovered $LiNH_2$ catalyst after NH_3 decomposition tests, corresponding to $LiNH_2$ or Li_2NH are observed. Additionally, no vibrations associated with their NH or NH_2 groups are detected in Raman or IR spectroscopies (see Figures III.8 and III.7, respectively). However, the Raman spectrum does reveal two unknown peaks (283 and 1275 cm^{-1}), which were also observed in the catalyst after the decomposition of $LiNH_2$.

One diffraction peak could potentially be associated with Li_3N, marked with a star on the XRD pattern of the post-reaction catalyst (see Figure III.10). However, a single peak is insufficient to conclusively confirm its presence. Furthermore, IR analysis of Li_3N does not reveal any identifiable vibrational bands,[382] limiting the applicability of this characterization method. Similarly, no evidence of Li_3N is observed in the Raman spectrum, as the characteristic peak expected around 600 cm^{-1} is absent.[383]

III.3 Ruthenium and lithium amide couple: catalytic activity and activation energy

III.3.1 Ru-$LiNH_2$

Given that ruthenium is the most active metal for ammonia decomposition, it was the first transition metal tested in combination with $LiNH_2$ to evaluate its effect on the activity of $LiNH_2$. To further investigate the influence of Ru on the catalytic activity of $LiNH_2$ under our experimental conditions (see Section II.3.1 of Chapter 2 for details), two catalysts were synthesized via two distinct methods, then characterized, and evaluated in terms of their catalytic performance and activation energy.

The two synthesis routes employed for the preparation of Ru-$LiNH_2$ catalysts are: mechanochemistry, as described in the literature for TM-$LiNH_2$ synthesis,[16] and impregnation using anhydrous ammonia as a solvent. Since the use of anhydrous ammonia for the reaction between $LiNH_2$ and $RuCl_3$ has not been previously reported, it was necessary to verify the feasibility of this approach. Initial tests were conducted using stoichiometric proportions to ensure that all $LiNH_2$ could be converted into $Ru(NH_2)_3$ under the chosen reaction conditions.

The success of the reaction was confirmed by XRD and TGA-DSC analysis (see Figure III.S3 in the appendix). The XRD pattern of $Ru(NH_2)_3$ after decomposition under argon shows only the peaks corresponding to metallic ruthenium and impurities, including lithium oxides and LiCl. Furthermore, the TGA-DSC curves of $Ru(NH_2)_3$ showed no evidence of liquefaction or decomposition of $LiNH_2$ within the expected temperature range. These findings demonstrate the feasibility of forming $Ru(NH_2)_3$-$LiNH_2$ using anhydrous ammonia as a solvent.

- **Characterization of catalysts**

Ru-$LiNH_2$ was synthesized with a ruthenium loading of 5 wt% to match the loading of the commercial Ru/Al_2O_3 catalyst and because this value is commonly used for Ru-based catalysts in the literature. The ruthenium content was subsequently analyzed using ICP. While the measured lithium mass percentages were consistent with the theoretical value of 28%, yielding 27.93 $\pm$1.40% and 29.47 $\pm$1.47% for Ru-$LiNH_2$ synthesized via mechanochemistry and using ammonia as a solvent, respectively, the same consistency was not observed for ruthenium. Specifically, the mass percentages of Ru were measured at 2.75 $\pm$0.14% and 3.01 $\pm$0.15% for the respective synthesis routes. This discrepancy could be attributed to the loss of ruthenium during the synthesis process or to experimental conditions that were not optimal for achieving the expected amount of $Ru(NH_2)_3$. However, it is more likely due to incomplete solubilization of $Ru(NH_2)_3$ or formation of RuO_4 during the digestion step of the ICP analysis.

The ruthenium percentage can also be estimated through the decomposition of $Ru(NH_2)_3$ using TGA. However, the mass losses observed during decomposition—6% for the sample synthesized with NH_3 as a solvent (see Figure III.12) and 5% for the sample obtained via mechanochemistry (see Figure III.S5) around 250°C—correspond to calculated ruthenium mass percentages of 14% and 11%, respectively. These values are significantly higher than the expected ruthenium loading of 5 wt%. This apparent discrepancy can be attributed to the simultaneous mass losses of $LiNH_2$ and $Ru(NH_2)_3$, making it impossible to independently determine their concentrations during TGA analysis. Measuring the fusion enthalpy of $LiNH_2$ is inherently challenging due to the simultaneous occurrence of decomposition and fusion. Introducing a third contribution to the mass loss, with the decomposition of $Ru(NH_2)_3$, further complicates the analysis, which is why no calculation of the fusion enthalpy was attempted in this study.

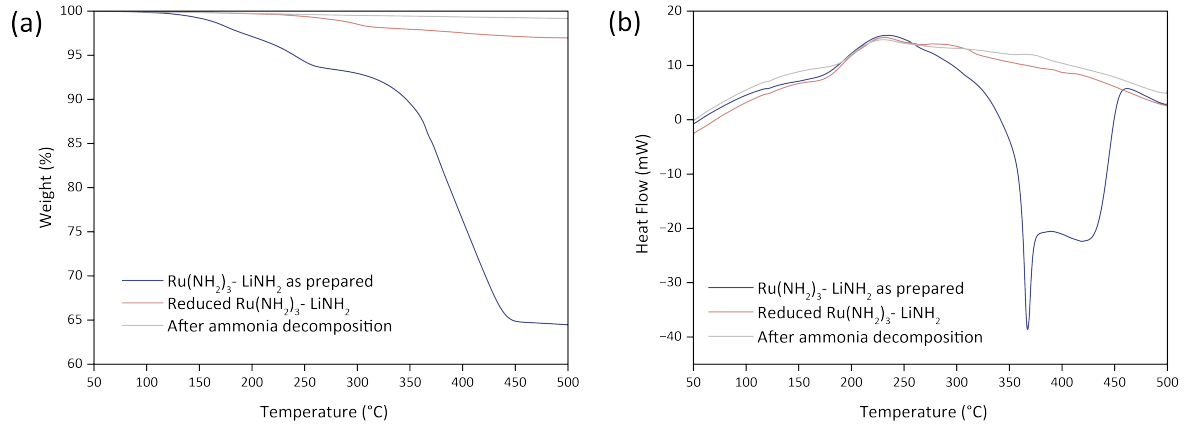

Figure III.12: (a) Thermal Gravimetric Analysis (TGA) and (b) Differential Scanning Calorimetry (DSC) under argon of the $Ru(NH_2)_3$-$LiNH_2$ as prepared from impregnation in liquid ammonia, after reduction with 10% vol of H_2 at 500°C, and after ammonia decomposition.

Given this uncertainty in the actual loading rate, all catalytic performance results will be presented with caution. While these results will help assess whether the addition of Ru enhances the catalytic performance of $LiNH_2$, particular attention will be paid to the limitations in quantifying ruthenium's exact contribution to

this improvement. In this chapter, all catalytic performance results are presented based on the ruthenium loading determined by ICP-EAS measurements.

For the synthesized catalysts, the presence of lithium amide was confirmed through XRD (Figures III.13 and III.S4), IR spectroscopy (Figures III.14 and III.S6), and Raman spectroscopy (Figures III.15 and III.S7). A detailed summary of the vibrational frequencies observed in the IR and Raman spectra, along with comparisons to the literature, is presented in Table III.3.

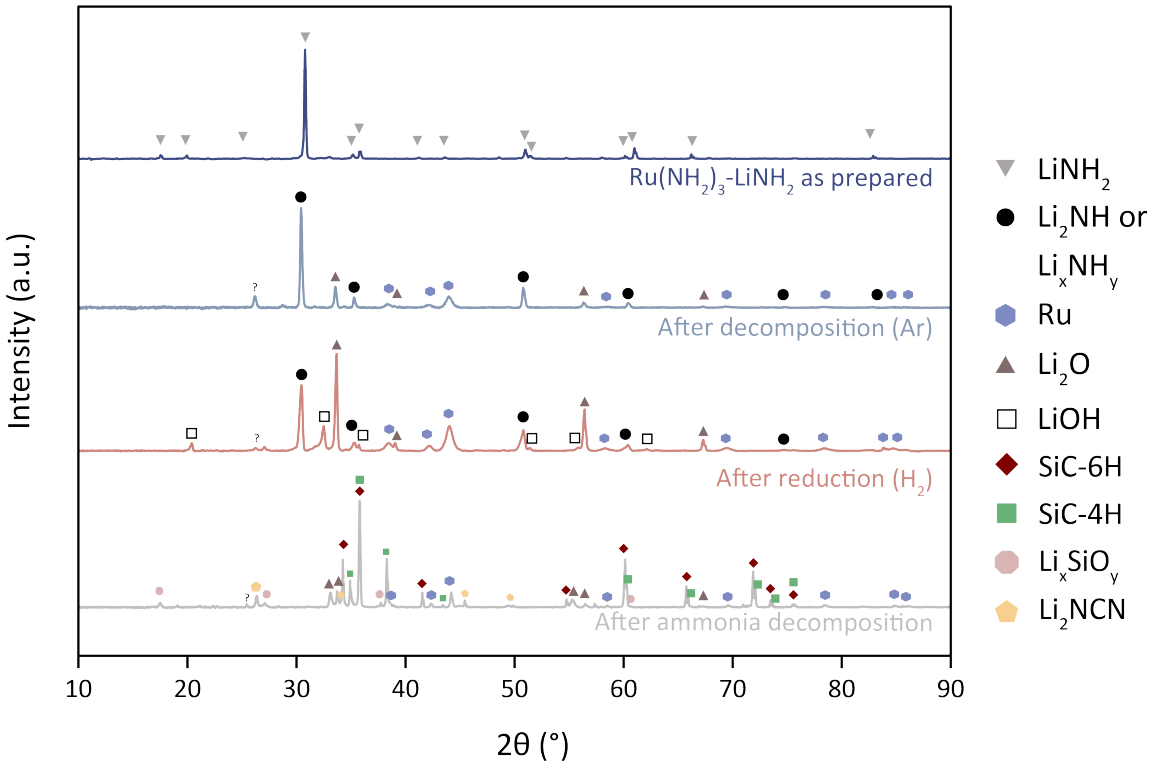

Figure III.13: XRD patterns of $Ru(NH_2)_3$-$LiNH_2$ as prepared from impregnation in liquid ammonia, after decomposition under Ar at 500°C, after reduction with 10 vol% H_2 at 500°C, and after ammonia decomposition experiment, using $Ru(NH_2)_3$-$LiNH_2$-SiC (1:1 wt%) as the precursor.

The presence of $Ru(NH_2)_3$ could not be confirmed by XRD due to its amorphous nature. However, its formation can be deduced, as peaks corresponding to metallic Ru are observed in the XRD patterns after decomposition under argon (see Figures III.13 and III.S4). No distinction is observed between $LiNH_2$ and $Ru(NH_2)_3$-$LiNH_2$ in the Raman spectra.

In contrast, the IR spectra show differences in the N-H stretching region for $Ru(NH_2)_3$-$LiNH_2$, where a shoulder at 3159 cm^{-1} is present (indicated with a star in the zoom view of the IR spectrum for $Ru(NH_2)_3$-$LiNH_2$ in Figure D0300_IR.b). However, this shoulder cannot be unequivocally attributed to $Ru(NH_2)_3$, as this vibrational band (3159 cm^{-1}) closely resembles that of Li_2NH (3180 cm^{-1}).[324] As for $Ru(NH_2)_3$, to the best of my knowledge, its IR spectrum is not reported in the literature. However, the spectrum of $Ru(NH_3)_3$ is available

and indicates a Ru–N stretching vibration in the range of 450–470 cm^{-1}.[384] Unfortunately, this range is near the detection limit of our IR setup, preventing verification of the Ru–N stretching mode.

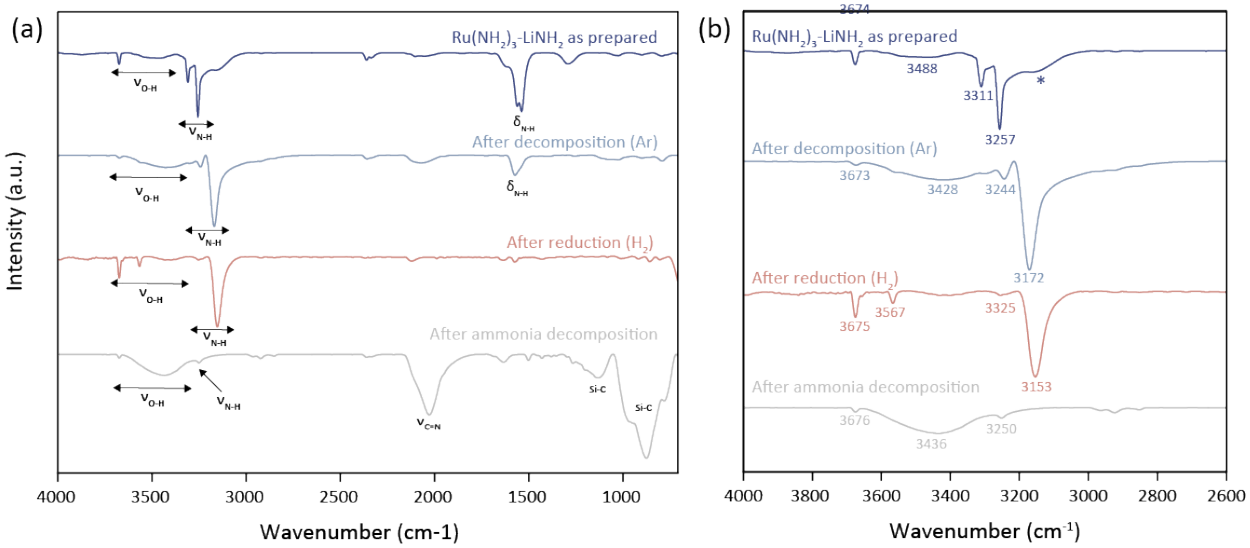

Figure III.14: (a) Infrared (IR) spectra of $Ru(NH_2)_3$-$LiNH_2$ as prepared from impregnation in liquid ammonia, after decomposition under Ar at 500°C, after reduction with 10 vol% H_2 at 500°C, and after ammonia decomposition experiment, using $Ru(NH_2)_3$-$LiNH_2$-SiC (1:1 wt%) as the precursor, and (b) zoom view of the same IR spectra in the range of 4000–2600 cm^{-1}.

Table III.3: Vibrational bands of $Ru(NH_2)_3$-$LiNH_2$ as prepared from impregnation in anhydrous ammonia, after decomposition under Ar, after reduction (10% H_2), and after ammonia decomposition, as well as $Ru(NH_2)_3$-$LiNH_2$ as prepared from ball-milling, after decomposition under Ar, after reduction (10% H_2), and after ammonia decomposition, obtained through IR analyses. Comparative reference spectra for $LiNH_2$,[324, 372] Li_2NH,[324, 372] and LiOH[374] are also included.

		N-H bending	N-H stretch		O-H stretch	C≡N stretch
			symmetric	antisymmetric		
Prepared in ammonia	As prepared	1540; 1536	3257	3311	3488; 3674	-
	After decomposition (Ar)	1575	3172	3244	3428; 3673	-
	After reduction (H_2)	-	3153	3252	3567; 3675	-
	After NH_3 decomposition	1503; 1635	-	3250	3436; 3676	2027
Prepared by ball-milling	As prepared	1550	3256	3312	3456; 3562; 3678	-
	After decomposition (Ar)	-	3142	3248	3440; 3672	-
	After reduction (H_2)	-	3152	3258	3431; 3674	-
	After NH_3 decomposition	-	-	3250	3439; 3674	2023
Experimental references	$LiNH_2$ [324, 372]	1564; 1582	3260	3315	-	-
	Li_2NH [324, 372]	~ 1500	3180	3250	-	-
	LiOH [374]	-	-	-	3438; 3565; 3678	-

After decomposition under argon, the IR spectra results (Figures III.14 and III.S6) consistently indicate the presence of Li_2NH in both types of samples. This is also confirmed by the TGA-DSC analysis since no liquefaction and decomposition of $LiNH_2$ is shown there (see Figures III.12 and III.S5). However, the Raman spectra reveal the coexistence of peaks corresponding to both lithium amide and lithium imide phases, as shown in Figure III.15.

According to the literature, during the heat treatment of $LiNH_2$ to form Li_2NH, intermediate phases such as $Li_{3-x}NH_x$ can form.[174] This suggests that in our samples, the decomposition of $LiNH_2$ may not be complete.

Based on the XRD results shown in Figures III.13 and III.S4, it is not possible to definitively identify the exact lithium phase, as Li_2NH and $Li_{3-x}NH_x$ exhibit very similar diffraction patterns, it is also possible that both phases are present. The discrepancies observed across XRD, IR, and Raman analyses, which do not consistently align regarding the lithium phases present, may also suggest an issue with sample homogeneity following the heat treatments.

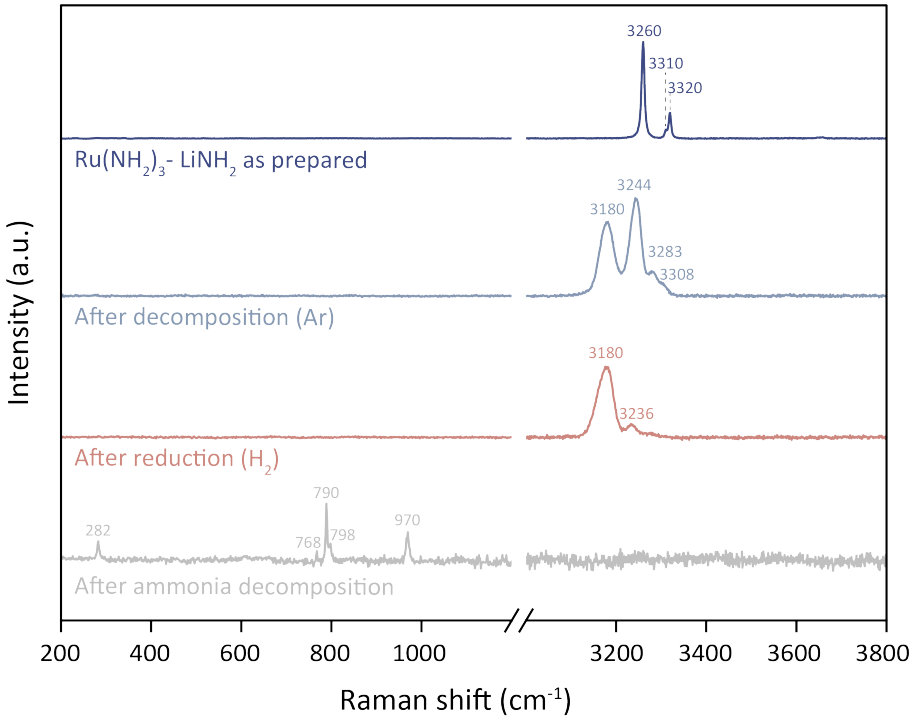

Figure III.15: Raman spectra of $Ru(NH_2)_3$-$LiNH_2$ as prepared from impregnation in liquid ammonia, after decomposition under Ar at 500°C, after reduction with 10 vol% H_2 at 500°C, and after ammonia decomposition experiment, using $Ru(NH_2)_3$-$LiNH_2$-SiC (1:1 wt%) as the precursor.

The characterization of the catalysts after reduction under hydrogen shows results similar to those observed following decomposition under argon. IR analysis reveals characteristic vibrations of Li_2NH (see Figures III.14 and III.S6), while Raman spectra exhibit a peak corresponding to Li_2NH and another that could correspond to $LiNH_2$, although the latter is less pronounced compared to the samples decomposed under argon (see Figure III.15). Regarding the XRD results, the diffraction peaks do not allow for a definitive identification of Li_2NH, $Li_{3-x}NH_x$, or a combination of both, as suggested by the Raman data (see Figures III.13 and III.S4). For the catalyst prepared via ball milling, the Raman peaks associated with $LiNH_2$ are less pronounced, which could reflect either variations in the results due to different heat treatments or still a lack of homogeneity in the analyzed samples.

Similarly to $LiNH_2$, the catalysts will be referred to as Ru-$LiNH_2$ throughout this section for simplicity. However, based on characterizations conducted after catalyst reduction, the actual form at the start of the ammonia decomposition tests is closer to Ru-$Li_{3-x}NH_x$.

- **Catalysts performance**

Finally, regarding catalytic performance, the addition of Ru enhances the activity of $LiNH_2$, as shown in Figures III.16.a and III.16.b. However, the activation energies measured for Ru-$LiNH_2$-based catalysts show significant variation. The catalyst synthesized via solubilization in anhydrous NH_3 exhibits an activation energy of 84.3 ± 5.5 kJ.mol^{-1}, compared to 125.5 ± 6.8 kJ.mol^{-1} for its counterpart prepared by ball-milling (Figure III.16.c).

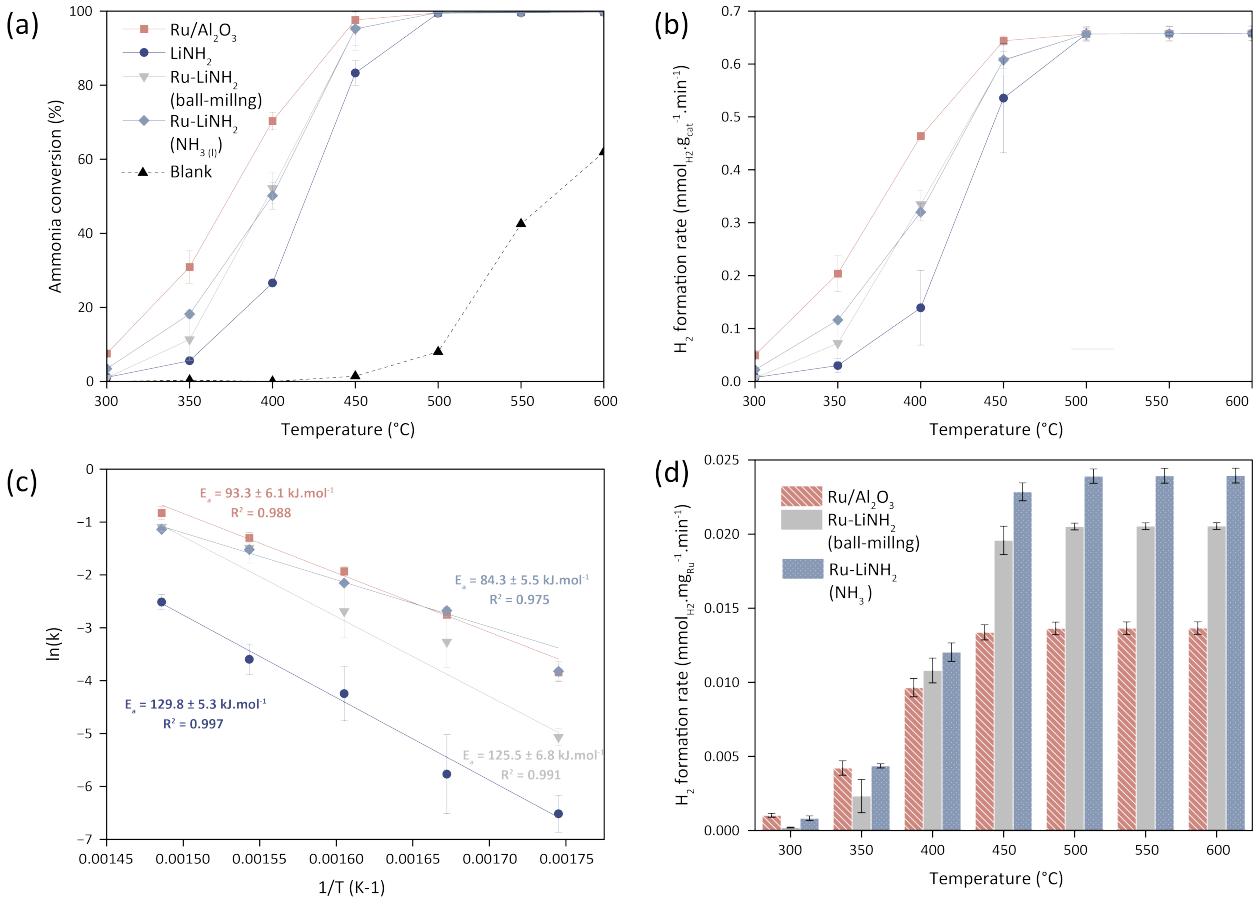

Figure III.16: (a) Temperature dependences of the activities of $LiNH_2$, Ru/Al_2O_3, Ru-$LiNH_2$ obtained from impregnation in ammonia, Ru-$LiNH_2$ obtained from ball-milling and the equivalent without any catalyst; (b) temperature dependences H_2 formation rate taking into account the total mass of the catalyst for $LiNH_2$, Ru/Al_2O_3, Ru-$LiNH_2$ obtained from impregnation in ammonia and the one obtained from ball-milling; (c) the corresponding Arrhenius plot for the temperature range of 300–450°C; and (d) temperature dependences H_2 formation rate taking into account the mass of Ru for Ru/Al_2O_3, Ru-$LiNH_2$ obtained from impregnation in ammonia and the one obtained from ball-milling. Reaction conditions: catalyst loading of 100 mg, and (1:1 wt%) with SiC as precursor for $LiNH_2$-based catalyst, with a 20 mL.min^{-1} flow of ammonia diluted in argon (5% vol), and a WHSV of $mL_{NH_3}.g_{cat}^{-1}.h^{-1}$.

These results are still preliminary, and the origin of this discrepancy remains unclear. Especially since neither the catalytic performance nor the activation energy of Ru-$LiNH_2$ is reported in the literature. However, the synthesis method may have a significant impact on the catalytic performance of $LiNH_2$-based catalysts. This could be related to differences in chemical composition, particularly as the measured ruthenium loading rates have varied between samples. Additionally, the influence of the catalyst's environment during measurements must be considered, as two materials (SiO_2 and SiC) are known to interact with the catalyst during performance evaluations. Even if the catalyst bed is prepared identically, there is no guarantee that these parasitic reactions occur to the same extent across all samples.

Based on the Ru mass percentages in the catalysts obtained through ICP analysis, and a comparison of the catalytic performance between Ru-$LiNH_2$ and Ru/Al_2O_3, the latter demonstrates higher activity than Ru-$LiNH_2$ in the temperature range of 300–350 °C. However, this trend reverses at 400 °C, where Ru-$LiNH_2$ becomes more active (see Figure III.16.d). These results, however, require further validation, particularly regarding the precise ruthenium concentrations in the synthesized catalysts.

Following ammonia decomposition, the identification of phases in both catalysts using XRD proves challenging due to overlapping diffraction peaks from SiC (see Figures III.13 and III.S4). Nevertheless, the same by-products of parasitic reactions with the catalytic environment—Li_xSiO_y and Li_2NCN—are detectable and confirmed by XRD. This assignment is further supported by the available IR spectrum of MgNCN, which features a vibrational band around 2000 cm^{-1} attributed to the nitrile group.[379]

A recurring issue across all our samples, particularly with the catalyst residues obtained after ammonia decomposition, is the lack of homogeneity of samples. This inconsistency makes it challenging to achieve reproducible results, especially in Raman spectroscopy, both within the same sample and between different samples. For the catalyst impregnated with anhydrous ammonia, the Raman spectrum closely resembles that of $LiNH_2$ following ammonia decomposition (see Figure III.15). A peak at 282 cm^{-1} may be associated with the phonons of the Ru(0001) surface, which typically span the range 0–242 cm^{-1},[385] and the characteristic SiC peaks observed between 768 and 970 cm^{-1}. In contrast, for the catalyst residues obtained after ammonia decomposition using the ball-milled catalyst, only the SiC peaks are observed (see Figure III.S7).

In conclusion, Ru-$LiNH_2$ catalysts can be synthesized using various methods, including mechanochemistry and impregnation in anhydrous ammonia. Ruthenium, recognized as the most active metal for ammonia decomposition, significantly enhances the catalytic activity of $LiNH_2$. However, the exact mechanism and magnitude of this enhancement remain uncertain, due to challenges in characterizing Ru-$LiNH_2$ catalysts and doubt about measured Ru loading. Furthermore, critical issues such as sample homogeneity and parasitic reactions with environmental components, such as SiO_2 and SiC, emphasize the need for improved catalyst preparation and evaluation techniques.

Additionally, the impact of reaction conditions on the structural evolution of the catalyst, including particle size and Ru dispersion with regard to $LiNH_2$, was not addressed in this preliminary study. Before focusing

on optimizing synthesis methods, it is essential to evaluate how phase transitions in the lithium-based material—whether involving solid-to-liquid changes or fluctuations in chemical composition—affect the morphology of the catalytic phases. Addressing these factors will be key to realizing the full potential of this catalytic system for ammonia decomposition.

III.3.2 Ru-$LiNH_2$/MgO

Supported catalysts can significantly enhance their performance by increasing surface area, preventing sintering, and maintaining consistent gas flow through the catalyst bed, and can even directly influence catalytic activity. This latter aspect is particularly critical for systems involving $LiNH_2$, which undergoes state changes with temperature. Additionally, as seen previously, conventional thermal diluents are unsuitable for $LiNH_2$, further emphasizing the need for an effective support material.

Identifying a suitable support for $LiNH_2$ is particularly challenging due to its high reactivity with conventional heterogeneous catalyst supports. In literature, MgO was the first support investigated for the Ru-$LiNH_2$ catalyst and demonstrated highly promising catalytic performance, surpassing that of the reference Ru/CNTs catalyst in terms of activity.[15] A subsequent study on potential supports for $LiNH_2$ also identified MgO as the most viable option, despite Rietveld analysis of XRD patterns revealing the formation of the ternary nitride LiMgN in two crystalline phases (face-centered cubic and primitive orthorhombic).[358] This ternary nitride, however, is unstable in the presence of ammonia and decomposes back into the lithium amide catalyst. Nevertheless, Wood *et al.* concluded that the catalytic performance of lithium amide with MgO remains comparable to unsupported $LiNH_2$, confirming the feasibility of using MgO as a support for $LiNH_2$-based catalysts.[358]

Guo *et al.* synthesized the Ru-$LiNH_2$/MgO catalyst through a two-step process. First, a Ru/MgO catalyst containing 5 wt% of Ru was prepared via incipient wetness impregnation of MgO with an acetone solution of $RuCl_3 \cdot xH_2O$. Subsequently, the prepared Ru/MgO was impregnated in a lithium-ammonia solution, where lithium metal was converted to $LiNH_2$ in the presence of Ru, while maintaining a Li:Ru weight ratio of 2.7:1.[15]

Building on our previous results for synthesizing $Ru(NH_2)_3$-$LiNH_2$ in anhydrous ammonia, the Ru-$LiNH_2$/MgO catalyst was directly synthesized from $RuCl_3$, $LiNH_2$, and MgO via impregnation in ammonia. The synthesis was carried out with equal mass ratios of Ru to MgO and Ru to $LiNH_2$ (5 wt%), resulting in a total Ru content of 2.5 wt%, to enable comparison with unsupported Ru-$LiNH_2$ (5 wt%).

- **Characterization of catalysts**

The measured composition of our catalyst, by ICP-AES, after synthesis showed a ruthenium content of 2.26 ± 0.11%, lithium at 20.24 ± 1.01% (compared to the theoretical value of 13.6%), and magnesium at 19.23 ± 0.96% (compared to the theoretical value of 30.1%). These results indicate that the catalyst is slightly richer in lithium and poorer in MgO than anticipated, while the amount of ruthenium aligns with the expected value.

For the synthesized $Ru(NH_2)_3$-$LiNH_2$/MgO catalyst, the presence of MgO was confirmed through XRD analysis (see Figure III.20). Similarly, the presence of $LiNH_2$ was also confirmed, and also through IR spectroscopy (see Figure III.18) and Raman spectroscopy (see Figure III.19). A detailed summary of the vibrational frequencies observed in the IR spectra, along with comparisons to literature data, is provided in Table III.4. Further confirmation was obtained through TGA-DSC analysis, which revealed the decomposition of $Ru(NH_2)_3$ and $LiNH_2$ beginning at approximately 150°C (see Figure III.17.a). Additionally, the liquefaction of $LiNH_2$ was indicated by an endothermic peak around 370°C (see Figure III.17.b).

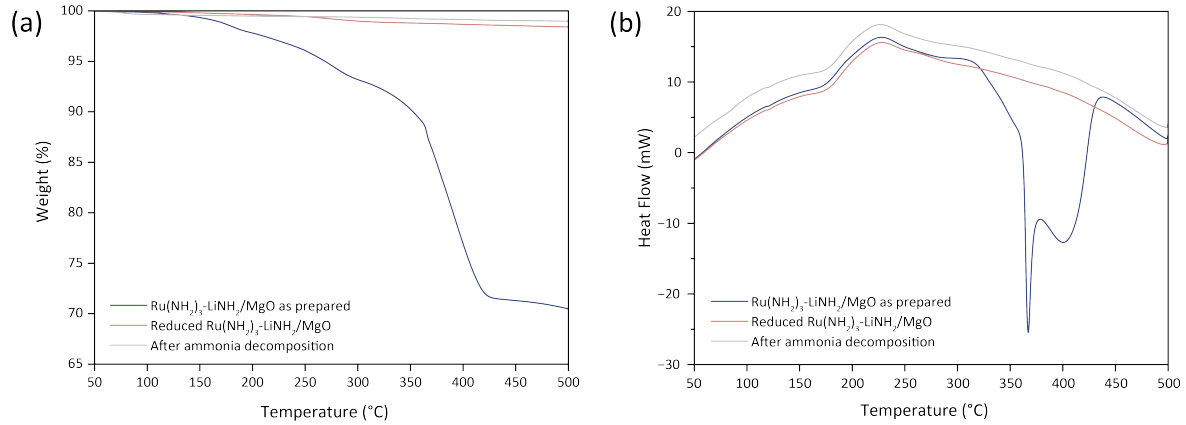

Figure III.17: (a) Thermal Gravimetric Analysis (TGA) and (b) Differential Scanning Calorimetry (DSC) under argon of the $Ru(NH_2)_3$-$LiNH_2$/MgO as prepared from impregnation in liquid ammonia, after reduction (H_2) at 500°C, and after ammonia decomposition.

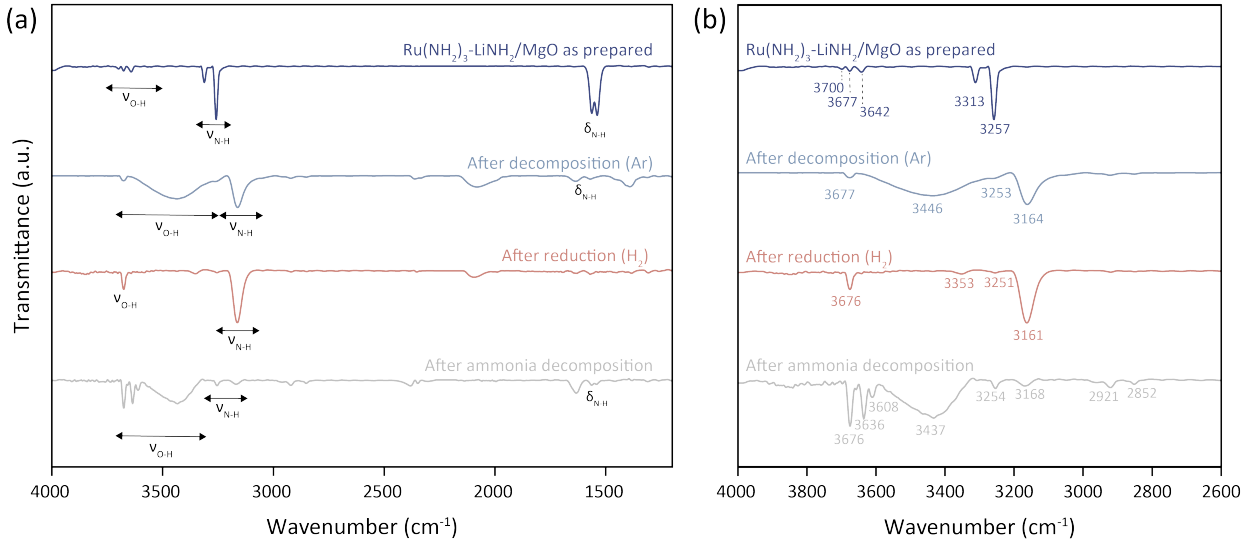

Figure III.18: (a) Infrared (IR) spectra of $Ru(NH_2)_3$-$LiNH_2$/MgO as prepared from impregnation in liquid ammonia, after decomposition under Ar at 500°C, after reduction with 10 vol% H_2 at 500°C, and of the residues from ammonia decomposition experiment, using $Ru(NH_2)_3$-$LiNH_2$ as the precursor, and (b) zoom view of the same IR spectra in the range of 4000–2600 cm^{-1}.

Table III.4: Vibrational bands of $Ru(NH_2)_3$-$LiNH_2$/MgO as prepared from impregnation in anhydrous ammonia, after decomposition under Ar, after reduction (10% H_2), and after ammonia decomposition, obtained through IR analyses. Comparative reference spectra for $LiNH_2$,[324, 372] Li_2NH,[324, 372] and LiOH[374] are also included.

		N-H bending	N-H stretch		O-H stretch
			symmetric	antisymmetric	
Ru-$LiNH_2$/MgO	As prepared	1537; 1564	3257	3313	3642; 3677
	After decomposition (Ar)	-	3164	3253	3446; 3677
	After reduction (H_2)	-	3161	3251	3676
	After NH_3 decomposition	1541; 1563	3168	3254	3437; 3676
Experimental references	$LiNH_2$ [324, 372]	1564; 1582	3260	3315	-
	Li_2NH [324, 372]	~ 1500	3180	3250	-
	LiOH [374]	-	-	-	3438; 3565; 3678

The decomposition under argon and the reduction of $Ru(NH_2)_3$-$LiNH_2$/MgO yielded comparable results. The Raman spectra for both processes display N-H stretching vibrations characteristic of Li_2NH, with a slight shoulder observed in the sample decomposed under argon (see Figure III.19). Similarly, the N-H stretching vibrations in the IR spectra are consistent with those of Li_2NH. However, for the sample after decomposition, two distinct peaks characteristic of N-H stretching are visible, as shown in Figure III.18 and detailed in Table III.18.

XRD analyses do not allow for a clear distinction between Li_2NH and $Li_{3-x}NH_x$. Nevertheless, based on the vibrational data, it can be inferred that the peaks correspond to Li_2NH in the reduced catalyst and to a mixture of Li_2NH and $Li_{3-x}NH_x$ in the decomposed version.

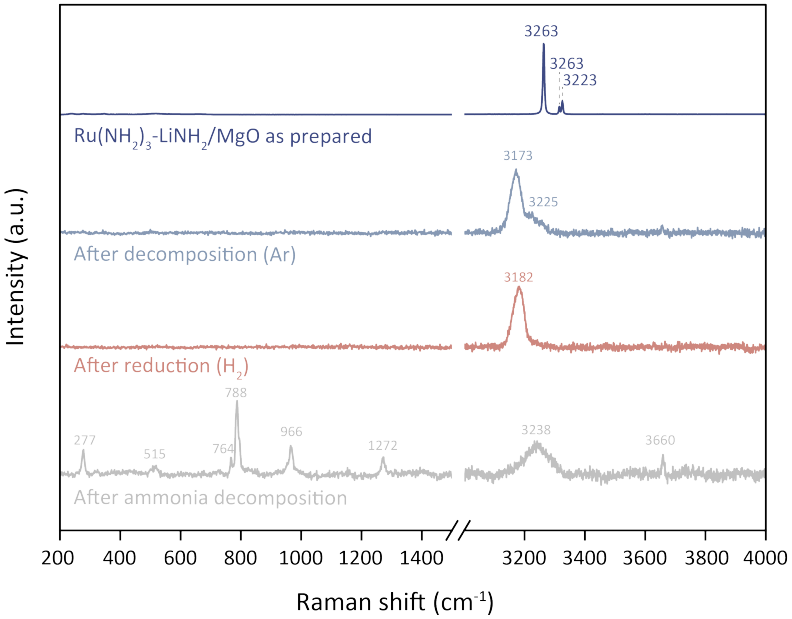

Figure III.19: Raman spectra of $Ru(NH_2)_3$-$LiNH_2$/MgO as prepared from impregnation in liquid ammonia, after decomposition under Ar at 500°C, after reduction with 10 vol% H_2 at 500°C, and after ammonia decomposition experiment, using $Ru(NH_2)_3$-$LiNH_2$ as the precursor.

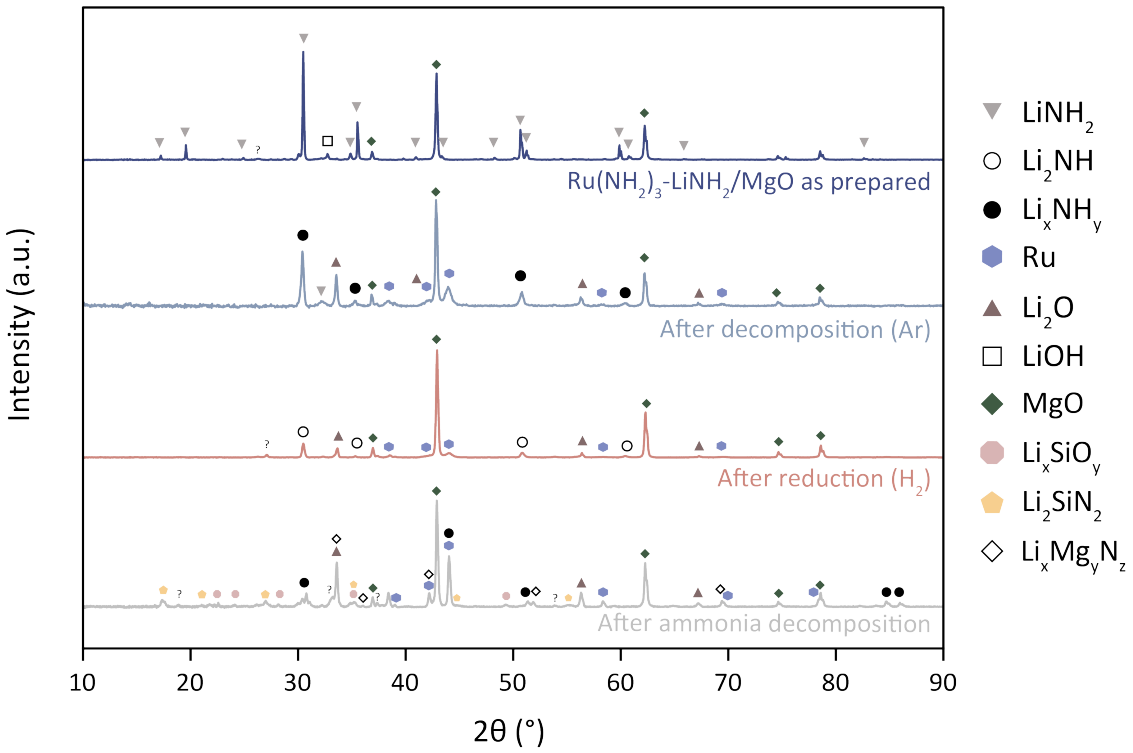

Figure III.20: XRD patterns of $Ru(NH_2)_3$-$LiNH_2$/MgO as prepared from impregnation in liquid ammonia, after decomposition under Ar at 500°C, after reduction with 10 vol% H_2 at 500°C, and after ammonia decomposition experiment, using $Ru(NH_2)_3$-$LiNH_2$ as the precursor.

- **Catalysts performance**

The catalytic tests of Ru-$LiNH_2$/MgO were conducted under the same conditions as the previous catalysts, with the same WHSV, but without the need for SiC. This corresponds to a Ru content of 2.26 wt% during the tests. Despite containing twice less ruthenium than Ru/Al_2O_3, the catalytic activities of the two catalysts are comparable (as shown in Figures III.21.a and III.21.b). Moreover, the activity of Ru-$LiNH_2$/MgO is even slightly higher than that of Ru/Al_2O_3 at 300°C when normalized to the Ru mass (see Figure III.21.d).

The activation energy of Ru-$LiNH_2$/MgO was measured at 74.6 ± 6.6 kJ.mol^{-1} (see Figure III.20.c), which is lower than that of Ru-$LiNH_2$, where the Ru content was measured by ICP at 2.75 wt%, as determined by ICP, or 0.49% difference Ru-$LiNH_2$/MgO. These results align with the observations of Makepeace *et al.* and Guo *et al.*, who noted the beneficial role of MgO as a support for $LiNH_2$-based catalysts. However, the presence of SiC in Ru-$LiNH_2$ catalyst could also influence its catalytic activity. For their Ru-$LiNH_2$/MgO catalyst, Guo *et al.* reported an activation energy of 53 ± 1.5 kJ.mol^{-1}, significantly lower than the value obtained in this study. This discrepancy could stems from differences in reaction conditions; Guo's catalyst contained twice as much Ru, and their WHSV was 60,000 $mL_{NH_3}.g_{cat}^{-1}.h^{-1}$, 100 times greater than the value here. While this may seem contradictory, it highlights the ongoing challenge of establishing a clear relationship between catalytic performance and reaction conditions across different studies.

Despite these differences, the activity measurements for Ru-$LiNH_2$/MgO in this study are highly promising, especially considering that no optimization were made to the synthesis procedure or the ammonia decomposition reactor. This leaves significant room for improvement, particularly at low temperatures.

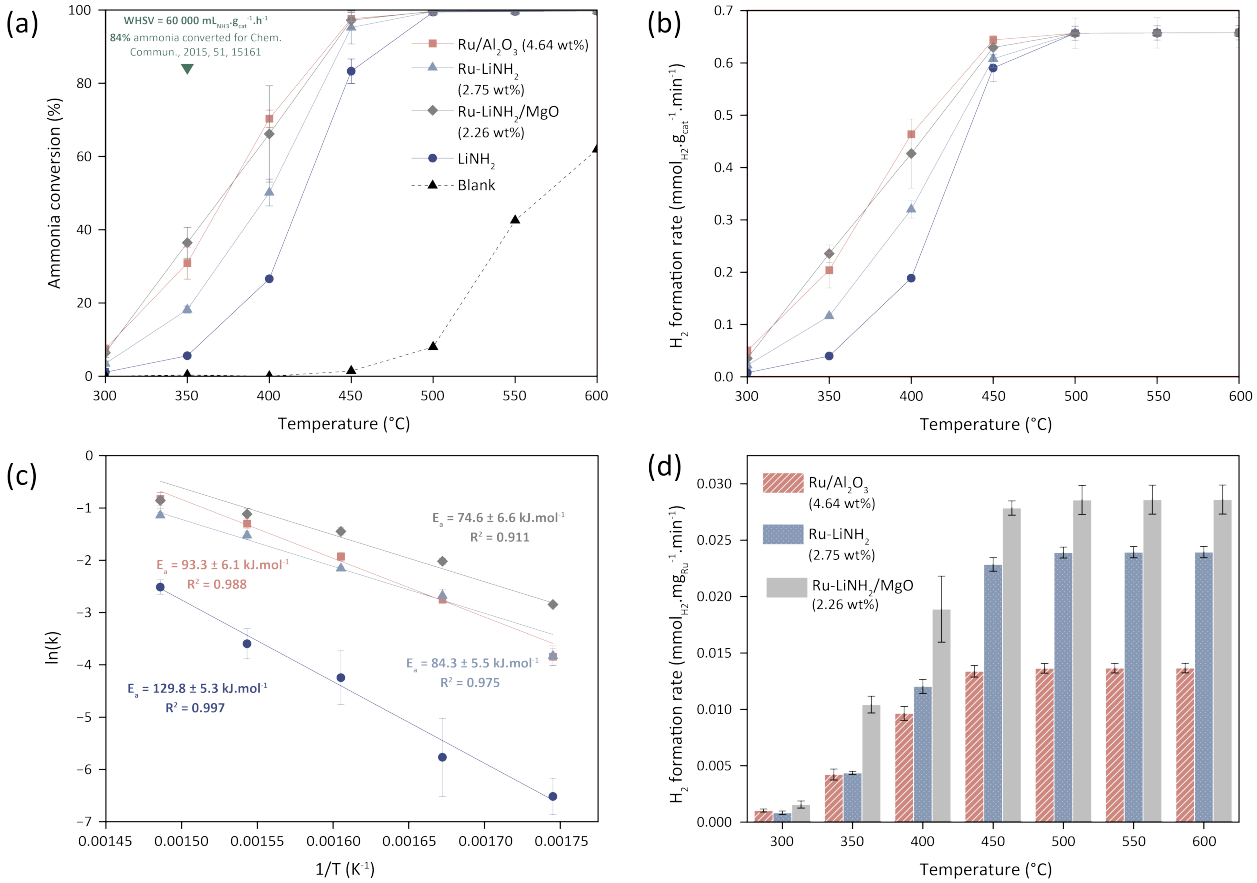

Figure III.21: (a) Temperature dependences of the activities of $LiNH_2$, Ru/Al_2O_3, Ru-$LiNH_2$ obtained from impregnation in ammonia, Ru-$LiNH_2$/MgO and the equivalent without any catalyst; (b) temperature dependences H_2 formation rate for $LiNH_2$, Ru/Al_2O_3, Ru-$LiNH_2$ obtained from impregnation in ammonia and Ru-$LiNH_2$/MgO; and (c) the corresponding Arrhenius plot for the temperature range of 300–450°C. Reaction conditions: catalyst loading of 100 mg, with a 20 mL.min^{-1} flow of ammonia diluted in argon (5% vol), and a WHSV of 600 $mL_{NH3}{\cdot}g_{cat}^{-1}{\cdot}h^{-1}$. Comparative performances of ammonia conversion, using Ru-$LiNH_2$/MgO as catalyst, are extracted from sources [15].

As all $LiNH_2$-based catalysts, recovering the catalyst from the reactor after ammonia decomposition process is challenging. Its extraction is quite impossible without also dislodging the quartz wool. This results in a significant presence of quartz wool in the samples, as demonstrated in the SEM image of Ru-$LiNH_2$/MgO post-reaction, shown in Figure III.22. Nevertheless, the lithium-based material and ruthenium remain relatively well dispersed on the support, with no observable agglomerates formed after ammonia decomposition.

Although the performances shown in Figure III.21 were achieved without the use of thermal diluents (only for Ru/Al_2O_3 and Ru-$LiNH_2$/MgO), Raman analyses of the post-reduction samples were inconclusive. Preliminary tests conducted to establish the performance measurement for Ru-$LiNH_2$/MgO, which included SiC,

yielded Raman spectra similar to those of $LiNH_2$. However, this is insufficient to conclude that the observed peaks are linked to by-products formed during reactions between $LiNH_2$ and SiC or SiO_2. These inconsistencies may instead stem from the persistent challenge of obtaining reproducible Raman results.

The Raman spectrum of the catalyst after ammonia decomposition shows bands at 277 and 515 cm^{-1}, which could be attributed to the Si-O-Si stretching vibrations of Li_2SiO_3, as this compound exhibits bands at 292 and 523 cm^{-1}.[386] However, this attribution remains uncertain due to the absence of Si-O stretching bands typically observed between 800 and 1000 cm^{-1}.[386] These bands might also be associated with a more dehydrogenated phase of the lithium material, though this seems unlikely, given that the sharp phonon modes of Li_4NH are located at 452, 584, and 775 cm^{-1}. The SiC-related bands are clearly present between 764 and 966 cm^{-1}, while a peak at 1272 cm^{-1} remains unidentified. Finally, two additional bands are observed: one at 3238 cm^{-1}, which likely corresponds to a lithium imide phase in the sample, and another at 3660 cm^{-1}, attributed to LiOH.

As for the IR analysis of the catalyst after ammonia decomposition; the LiOH bands are present, along with two N-H stretching vibrations comparable to those of Li_2NH, although they are not very intense. A band at 1631 cm^{-1} is attributed to the bending mode of the N-H bond in Li_2NH, while two additional N-H stretching bands comparable to those of $LiNH_2$ are also observed. For more details, refer to Figure III.18 and Table III.4. The spectrum also shows a band at 2346 cm^{-1}, associated with the asymmetric stretching of the C=O bond, attributed to the presence of CO_2 during the analysis. In the OH stretching region, two additional bands at 3610 and 3634 cm^{-1}, not related to LiOH, are also observed.

Finally, for the XRD patterns of the catalyst post-reaction, the absence of SiC simplifies the interpretation of the results. Several peaks corresponding to Li_xNH_y phases are observed, although their precise identification cannot be achieved with this standard XRD analysis alone. Peaks associated with lithium magnesium nitride are also present, indicating a reaction between $LiNH_2$ and MgO, as reported in the literature.[358] Additionally, diffraction peaks potentially corresponding to Li_xSiO_y and Li_2SiN_2 are observed, from reaction with quartz wool. However, these species are only detected in XRD, as no evidence of their presence has been identified through IR or Raman spectroscopy.

In conclusion, the synthesis of Ru-$LiNH_2$/MgO directly from the reaction of $RuCl_3$ and $LiNH_2$ in ammonia, in the presence of the support, is feasible. Although the dispersion and particle size of the catalyst from the reaction conditions were not investigated in detail, this limitation stems from the focus on evaluating the impact of phase transitions of $LiNH_2$ during reduction and ammonia decomposition.

Despite this, the catalytic performance of Ru-$LiNH_2$/MgO is really promising, and optimizing its synthesis would likely enhance its activity further. However, the catalytic reaction mechanism remains unclear within the framework of this study, particularly due to the incomplete characterization of the post-reaction phases, which still needs to be addressed.

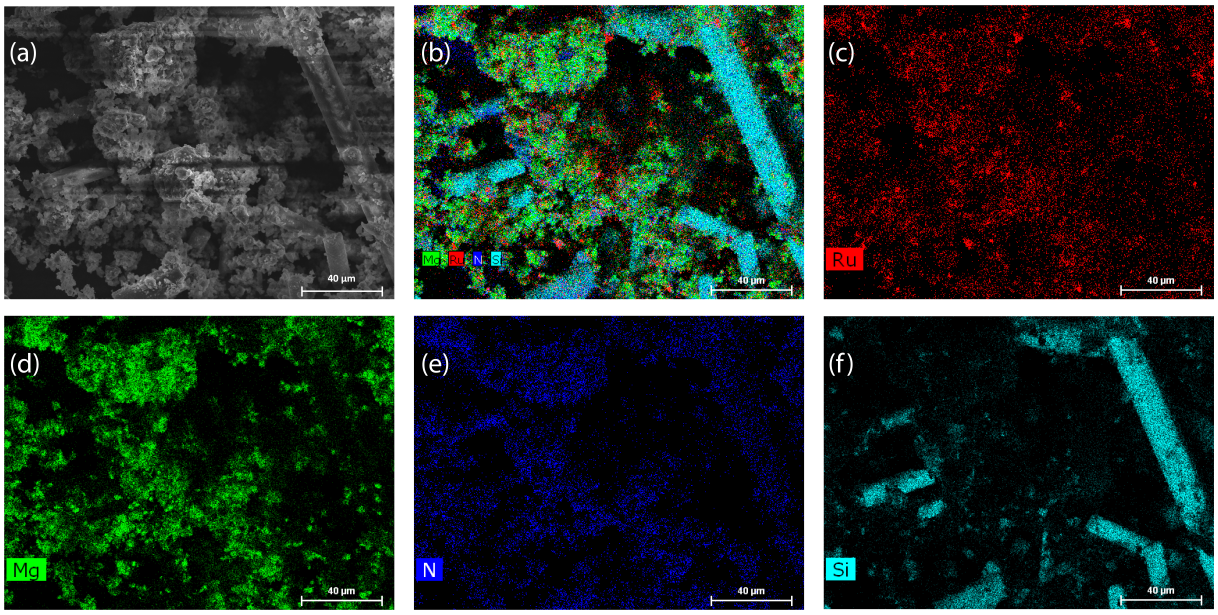

Figure III.22: (a) SEM image of Ru-$LiNH_2$/MgO after ammonia decomposition; (b) EDX mapping of Ru (red), Mg (green), N (dark blue) and Si (light blue) elements; (c) EDX mapping of Ru (red); (d) EDX mapping of Mg (green); (e) EDX mapping of N (dark blue); and (f) EDX mapping of Si (light blue).

While the inclusion of MgO as a support enables the study of $LiNH_2$-based catalysts without interference from SiC, parasitic reactions with quartz wool continue to be a challenge. Addressing these limitations will be key to evaluate precisely the catalytic activity.

III.4 Lithium nitride: catalytic activity and activation energy

In this study, lithium nitride (Li_3N) was also tested as a catalyst for ammonia decomposition to evaluate the catalytic activity of Li-based catalysts. The selection of Li_3N as a potential catalyst is inspired by its role in electrochemical ammonia synthesis, where lithium nitride acts as a reactive intermediate for the reduction of N_2.[387]

One potential advantage of Li_3N the absence of liquefaction with temperature like $LiNH_2$. This may prevent the catalyst from resolidifying into the stainless-steel sintered, while also possibly facilitates its recovery from the catalyst bed at the end of the ammonia decomposition tests.

- **Characterization of Li_3N**

The commercial lithium nitride used is composed of both α-Li_3N and β-Li_3N phases, as indicated by its XRD pattern (see Figure III.24). After heat treatment under argon, the XRD analysis shows only the α-Li_3N phase is present with Li_2O (see Figure III.24). The lithium content in the commercial Li_3N was measured by ICP at 59.76 ± 2.99%, which aligns with the theoretical lithium mass percentage of 59.8%.

O-H stretching bands are observed in the IR spectrum of commercial Li_3N, potentially corresponding to LiOH. However, no diffraction peaks associated with LiOH is present neither the XRD pattern of the commercial Li_3N, nor present in the Raman spectra. These O-H stretching bands also appear in the IR spectrum after the reduction process, and, as suggested by the XRD pattern of the post-reduction sample, LiOH is present in the sample. Hence, these vibrational bands in all sample are likely associated with the presence of LiOH.

The Raman spectra of Li_3N, after heat treatment under Ar, exhibit characteristic peaks for this phase at 509 cm^{-1}, 667 cm^{-1}, and a prominent peak at 595 cm^{-1}. These values are in good agreement with data from literature, where several peaks around 500 cm^{-1}, 580 cm^{-1}, and 600 cm^{-1} were previously registered.[383] However, after heat treatment, an additional Raman peak is observed at 333 cm^{-1}. According to a previous Raman study on Li_3N, peaks in the 250–460 cm^{-1} range may also appear, attributed to resonant conditions established during laser irradiation.[383]

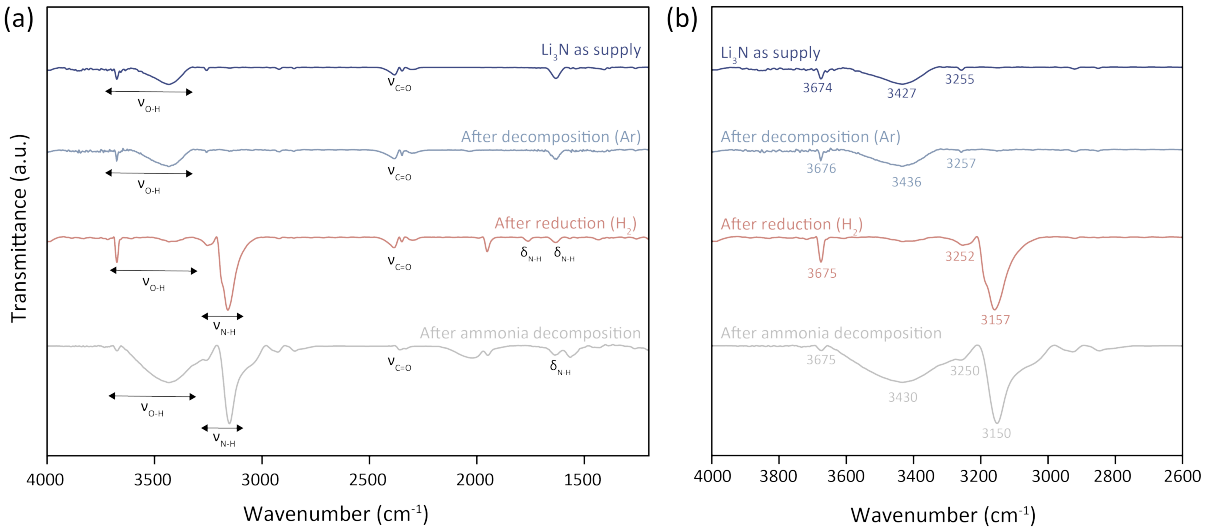

Figure III.23: (a) Infrared (IR) spectra of Li_3N as supply, after heat treatment under argon at 500°C, after reduction under 10 vol% H_2 at 500°C, and of the residues from the ammonia decomposition experiment, , and (b) zoom view of the same IR spectra in the range of 4000–2600 cm^{-1}.

Table III.5: Vibrational bands of Li_3N as supply, after decomposition under Ar, after reduction (10% H_2), and after ammonia decomposition, obtained through IR analyses. Comparative reference spectra for SiC, $LiNH_2$,[324, 372] Li_2NH,[324, 372] and LiOH[374] are also included.

		N-H bending	N-H stretch		O-H stretch	C≡N stretch	unknown
			symmetric	antisymmetric			
Li_3N	As supply	1633	3255	-	3427; 3674	-	-
	After decomposition (Ar)	1633; 1762	3257	-	3676	-	-
	After reduction (H_2)	1364	3157	3252	3567; 3675	-	1950
	After NH_3 decomposition	1565; 1638	3150	3250	3436; 3675	2018; 1944	
Experimental references	$LiNH_2$ [324, 372]	1564; 1582	3260	3315	-	-	
	Li_2NH [324, 372]	~ 1500	3180	3250	-	-	
	LiOH [374]	-	-	-	3438; 3565; 3678	-	

The heat treatment under argon had little impact on the nature of Li_3N. However, after reduction under H_2, the coexistence of multiple Li_xNH_y phases becomes evident, as confirmed by the XRD pattern and IR spectra (see Figure III.24 and Figure III.5, respectively). No characteristic decomposition or liquefaction indicative of $LiNH_2$ is observed via TGA-DSC after this reduction (see Figure III.S8 in the appendix).

The Raman spectrum after reduction, however, shows no vibrational peaks associated with N-H bonds, as depicted in Figure III.25. Only peaks corresponding to Li_3N are present, along with an additional peak at 454 cm^{-1}, which may also be related to resonant conditions induced by laser irradiation.[383] The presence of Li_3N is further confirmed by XRD analysis. However, it also underscores a potential issue with sample homogeneity following the reduction process.

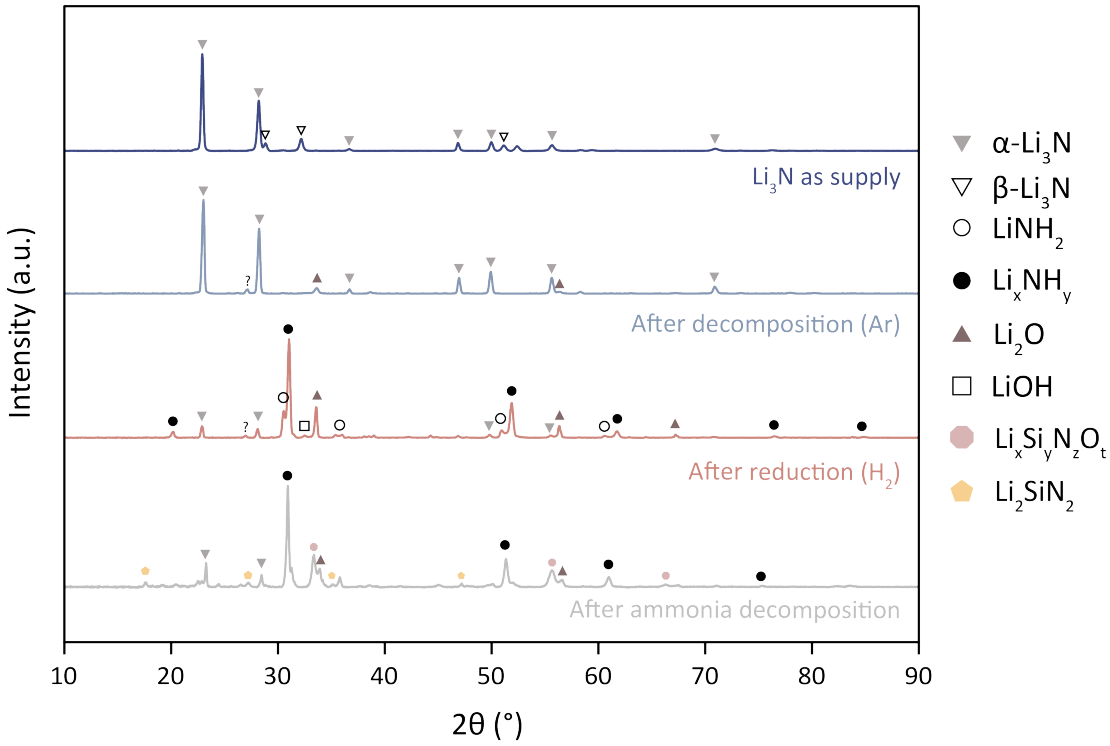

Figure III.24: XRD patterns of Li_3N as supply, after heat treatment under argon at 500°C, after reduction under 10 vol% H_2 at 500°C, and ammonia decomposition experiment.

Based on these characterization results, the catalyst used at the start of the ammonia decomposition reaction consists of a mixture of lithium nitride and a more hydrogenated fraction. For clarity, and as in previous discussions, the catalyst will be referred to simply as Li_3N, although its composition more accurately corresponds to Li_3N-Li_xNH_y.

The catalytic performance tests of Li_3N were conducted without SiC. However, quartz wool was placed before the metallic sintered seal to prevent potential obstruction. The measured performance of Li_3N was promising, as it appeared more active than $LiNH_2$. However, a potential discrepancy may exist between these catalytic results. On one hand, $LiNH_2$ is in contact with both quartz and SiC, which may negatively

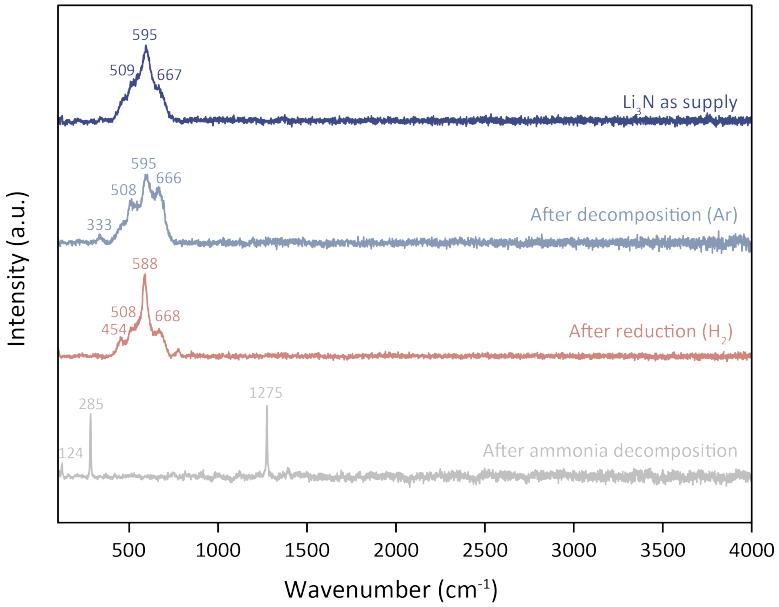

Figure III.25: Raman spectra of Li_3N as supply, after heat treatment under argon, after reduction under 10 vol% H_2, and of the residues from the ammonia decomposition experiment.

impact its activity. On the other hand, Li_3N avoids contact with SiC but interacts with a larger amount of quartz wool. To draw definitive conclusions about their exact catalytic performances, both materials need to be evaluated under conditions free from potential deactivating elements.

Additionally, this study is still in its early stage, and no definitive conclusion can yet be drawn regarding the intrinsic catalytic activity of Li_3N. The observed activity could be attributed to the presence of mixed Li_xNH_y phases generated during the reduction step, which are present at the beginning of the ammonia decomposition tests.

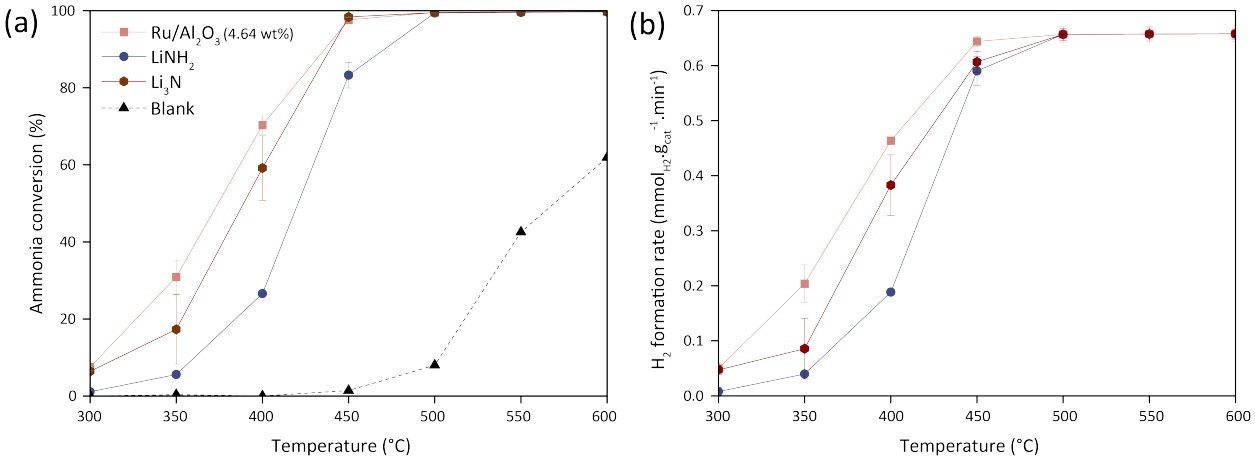

Figure III.26: (a) Temperature dependences of the activities of Li_3N, $LiNH_2$, Ru/Al_2O_3 and the equivalent without any catalyst; (b) temperature dependences H_2 formation rate for Li_3N, $LiNH_2$ and Ru/Al_2O_3. Reaction conditions: catalyst loading of 100 mg, with a 20 $mL.min^{-1}$ flow of ammonia diluted in argon (5% vol).

A notable particularity of Li_3N, not observed with $LiNH_2$-based catalysts, is the stabilization issue between 350 and 400°C, as illustrated in Figure III.27 (before and after this temperature range, this phenomenon disappears). At these temperatures, the ammonia concentration, continuously monitored using µGC-TDC, progressively decreases over several hours, with nearly the same proportional decrease observed in each subsequent analysis. This is in contrast to the typical stabilization period of just a few minutes. Concurrently, the concentrations of hydrogen and nitrogen increase proportionally.

This stabilization process was only observed for a few hours and did not reach completion, which explains the large error margins in the conversion values at these temperatures (see Figure III.26). While activation energy measurements are yet to be conducted, it is clear that accurate conversion values in this temperature range can only be obtained once stabilization has been fully achieved.

Regardless, after ammonia decomposition, the characterization results obtained from XRD and IR are similar to those observed after reduction under hydrogen. Specifically, the XRD pattern shows diffraction peaks corresponding to Li_3N and Li_xNH_y, with some diffraction peaks that could results from the impurities formation of contact with quartz. While the IR spectrum reveals bands associated with less defined N-H bond vibrations (see Figures III.24 and III.5, respectively). However, none of the characteristic peaks of Li_3N are detected in the Raman spectrum, as shown in Figure III.25. However, peaks are observed at 124, 285, and 1275 cm^{-1}, with the latter two frequently appearing in Raman analyses of post-reaction catalysts. It is unlikely that these peaks are associated with impurities from SiC, as no SiC was used in this case. Regarding the peak at 1275 cm^{-1}, it may be linked to Li_3N, as a Raman peak is observed around 1000 cm^{-1} for this compound.[388]

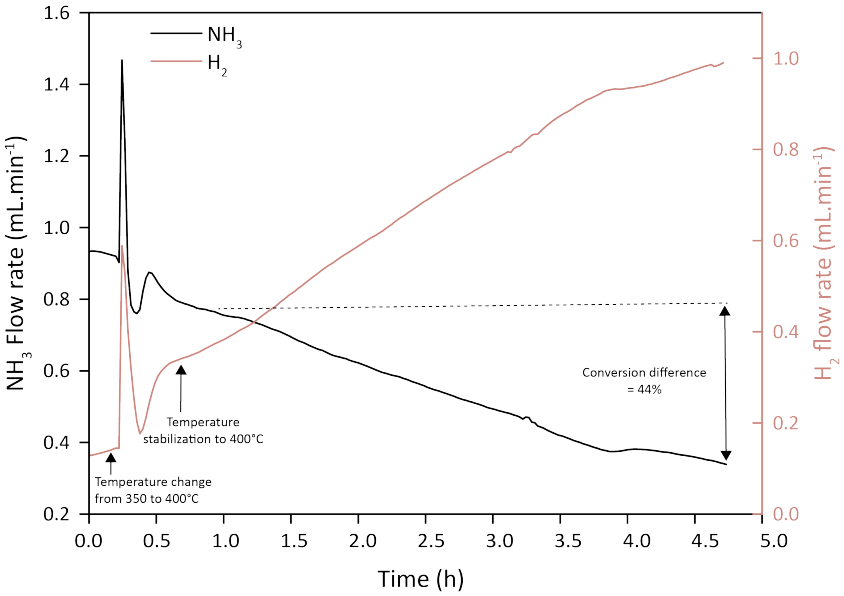

Figure III.27: Stabilization over time of ammonia and hydrogen concentrations in the gas mixture at the catalytic reactor outlet, with sampling and analysis performed every 80 seconds using µGC-TDC.

In conclusion, the use of Li_3N as a catalyst for ammonia decomposition appears promising. However, further testing is required to determine whether the observed activity is attributable to mixed Li_xNH_y phases generated during the reduction step, which are present at the start of the ammonia decomposition tests. Additionally, prolonged stabilization periods were observed at 350°C and 400°C, potentially linked to a phase change in the lithium material at these temperatures. A more detailed study of this phenomenon is essential to understand its origin and to accurately determine ammonia conversion values under these conditions.

III.5 Conclusion

A catalytic performance measurement bench has been developed to quantify the catalytic performance of $LiNH_2$-based catalysts. However, the system still requires significant adjustments to address the specific challenges posed by $LiNH_2$. Notably, it is crucial to eliminate the reliance on quartz wool for catalyst fixation or to identify an alternative material that is inert to lithium-based materials and ammonia decomposition ideally.

After attempting to optimize a fixed-bed tubular reactor for this type of catalyst, it became evident that this configuration is not well-suited for $LiNH_2$-based systems. Conversely, the reactor design developed by Makepeace *et al.* appears to be more appropriate. This setup involves a cylindrical stainless steel reactor where the catalyst is deposited at the bottom, eliminating the need for a fixing system or diluent under operating conditions.

In this design, $LiNH_2$ is free to liquefy, and the reactor's geometry ensures the catalyst remains contained. A gas inlet pipe extends to approximately 10 mm above the reactor base, allowing for efficient gas flow, while a gas outlet pipe facilitates the evacuation of reaction products. Although this configuration may not align with traditional recommendations for heterogeneous (as the ammonia flux does not necessarily "flow through" the catalytic bed)—particularly considering their catalytic performance results with the commercial Ru/Al_2O_3 catalyst—it appears to be the most suitable approach for studying $LiNH_2$.

Nonetheless, this developed setup, despite its limitations, successfully confirmed the catalytic activity of $LiNH_2$, with an apparent activation energy measured at 132.5 ± 5.3 $kJ{\cdot}mol^{-1}$, even in the presence of SiC and SiO_2. The addition of ruthenium, introduced via mechanochemistry and via impregnation in anhydrous ammonia, enhanced this catalytic activity. However, the precise degree of improvement remains to be determined, as doubts about the measurement of the Ru fraction in the catalysts remain. The apparent activation energy ranged between 84.3 ± 5.5 $kJ.mol^{-1}$ for the catalyst synthesized in anhydrous ammonia and 125.5 ± 6.8 $kJ.mol^{-1}$ for the one prepared by ball-milling.

The origin of this discrepancy has not yet been identified. It could stem from differences in Ru content, variations in operating conditions (such as the differing parasitic interactions of SiC and SiO_2 with the catalysts), or the impact of synthesis conditions. Furthermore, this preliminary study did not address the influence of

reaction conditions on the structural evolution of the catalyst, including particle size and Ru dispersion with respect to $LiNH_2$.

Then, the synthesis of Ru-$LiNH_2$/MgO was successfully achieved through the direct reaction of $RuCl_3$ and $LiNH_2$ in ammonia in the presence of the support. The catalyst demonstrated catalytic performance comparable to that of Ru/Al_2O_3, despite using only half the amount of Ru in the case of Ru-$LiNH_2$/MgO in the catalytic test. Its apparent activation energy was measured at 74.6 ± 6.6 kJ.mol^{-1}.

For Ru-$LiNH_2$ based catalysts, a critical aspect of optimization will involve understanding the morphological changes induced by $LiNH_2$ transformations and their subsequent impact on catalytic reactivity. Gaining this insight will provide the foundation for refining and improving synthesis methods.

Finally, the catalytic performance of Li_3N as a precursor was tested, yielding promising results. However, further studies are required to determine whether Li_3N is more efficient than $LiNH_2$, particularly under strictly identical experimental conditions. Prolonged stabilization periods between 400 and 450°C have been observed for Li_3N, and extended tests lasting only a few hours have not yet been sufficient to complete this stabilization process. The exact cause of this challenging stabilization remains unclear, but it is likely that the lithium phase undergoes significant structural changes in the presence of ammonia at these temperatures.

Looking ahead, it would be valuable to evaluate the catalytic performance of both $LiNH_2$ and Li_3N under varying thermal pretreatments prior to ammonia decomposition. While reduction was systematically applied in this study, exploring the performance of these materials without reduction could provide additional insights, especially for Li_3N, whose activity might only be accurately assessed in the absence of other Li_xNH_y phases.

Characterizing the catalysts after ammonia decomposition proved challenging, primarily due to the presence of unwanted by-products resulting from the reaction of $LiNH_2$ or Li_3N, with Si-based compounds. Furthermore, issues related to sample homogeneity following the various tests were not addressed, adding to the complexity of the analysis. Lastly, the intrinsic difficulties in identifying specific Li phases—whose similarities are likely pivotal to their reactivity but render their characterization highly complex—further added to the challenges.

The challenges associated with characterizing catalysts after ammonia decomposition highlight the current limitations of this experimental study in fully elucidating the nature of the active phases. Faced with this difficulty, DFT modeling emerges as a powerful complementary tool, to try to investigate the electronic structure, energetics, and reaction pathways of $LiNH_2$-based catalysts for ammonia decomposition. Such a theoretical approach will thus be developed in the following chapters of the PhD thesis.

III.6 Appendix

- **Selection of catalytic reactor materials: impact of quartz reactor on lithium amide**

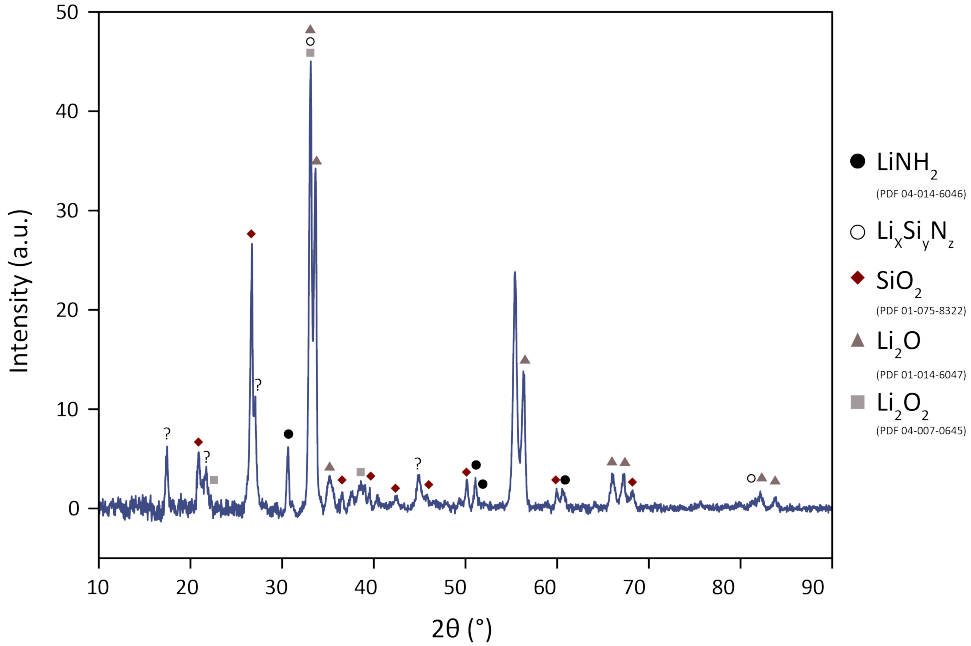

Figure III.S1: Temperature dependences of the activities of LiNH2 in a quartz catalytic reactor. Reaction conditions: catalyst loading of 100 mg, with a 20 mL·min^{-1} flow rate of diluted ammonia in argon (5% vol).

- **Performance comparison with a commercial catalyst: Ru/Al2O3**

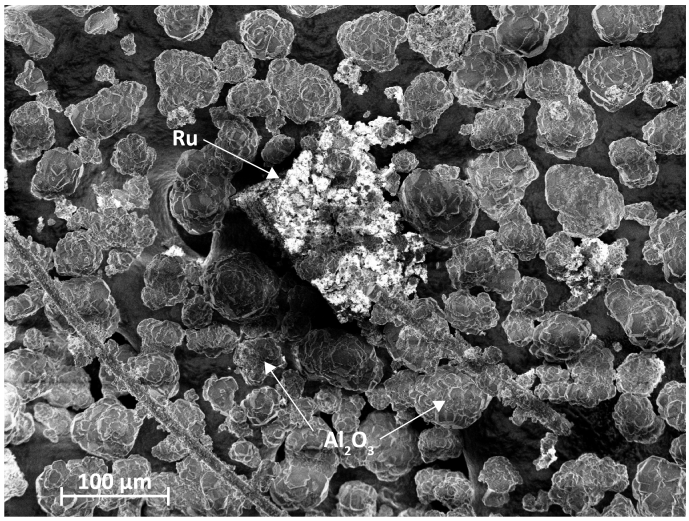

Figure III.S2: SEM image of Al_2O_3 particles with metallic Ru after reduction of the catalyst;

- **Verification of the feasibility of the reaction between $RuCl_3$ and $LiNH_2$ using anhydrous ammonia as a solvent: synthesis under stoichiometric conditions.**

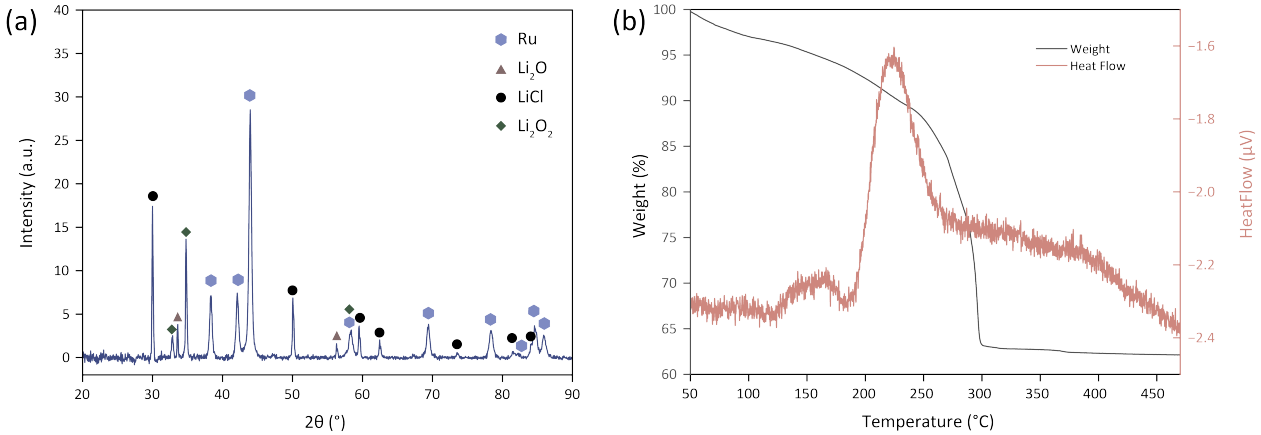

Figure III.S3: (a) XRD pattern after the decomposition of $Ru(NH_2)_3$ under argon and (b) Thermogravimetric Analysis (TGA) coupled with Differential Scanning Calorimetry (DSC) of $Ru(NH_2)_3$.

- **Characterizations of $Ru(NH_2)_3$-$LiNH_2$ synthesized by ball-milling**

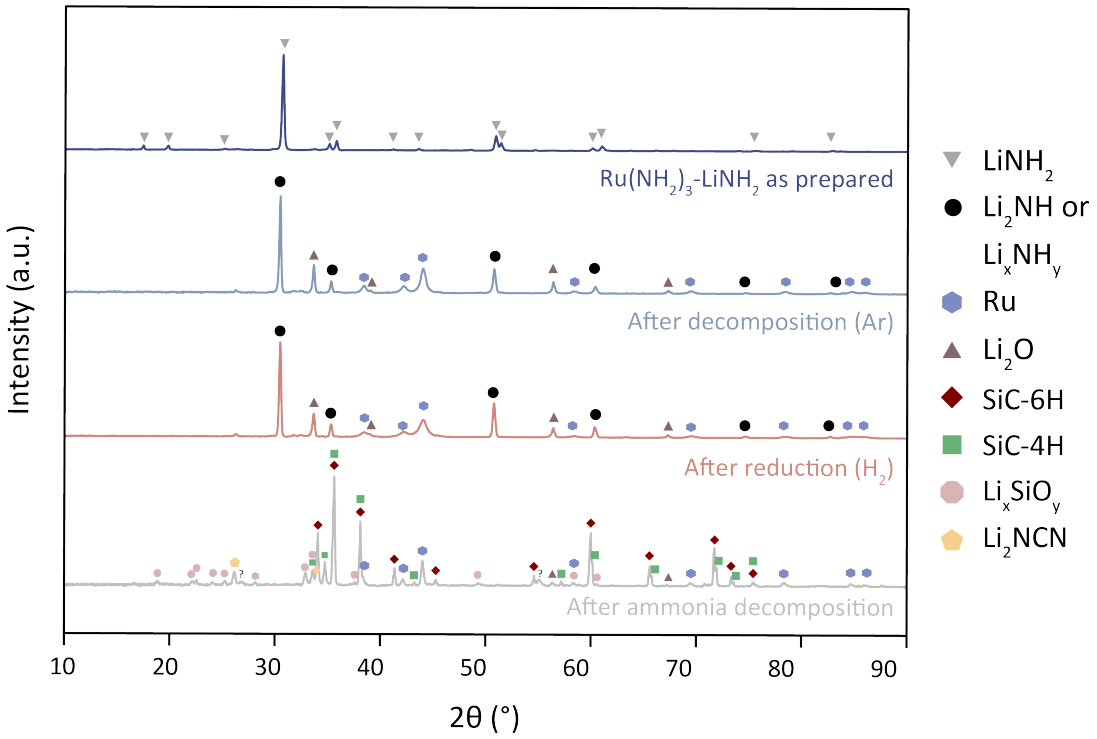

Figure III.S4: XRD patterns of $Ru(NH_2)_3$-$LiNH_2$ as prepared from ball-milling, after decomposition under Ar, after reduction with 10 vol% H_2, and of the residues from ammonia decomposition experiment, using $Ru(NH_2)_3$-$LiNH_2$-SiC (1:1 wt%) as the precursor.

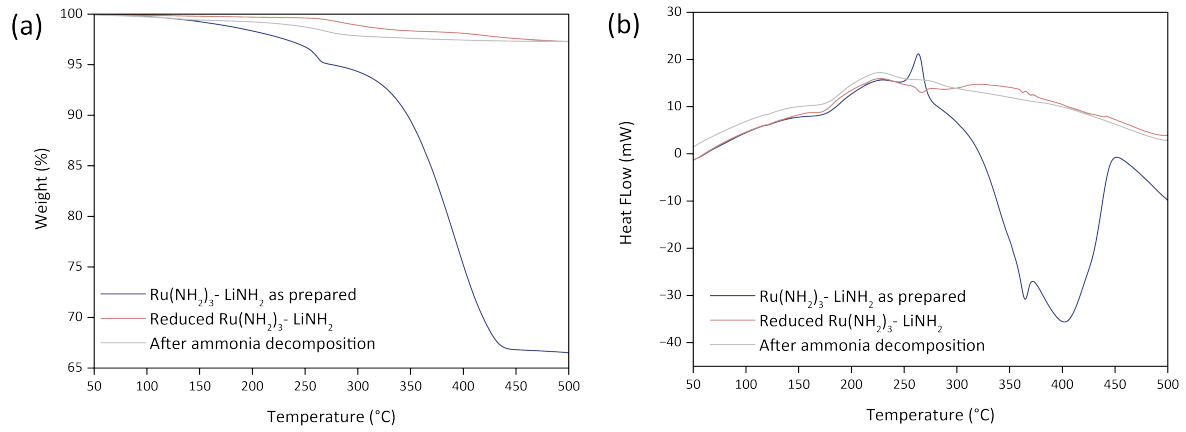

Figure III.S5: (a) Thermal Gravimetric Analysis (TGA) and (b) Differential Scanning Calorimetry (DSC) under argon of the $Ru(NH_2)_3$-$LiNH_2$ as prepared from ball-milling, after reduction (H_2) and after ammonia decomposition.

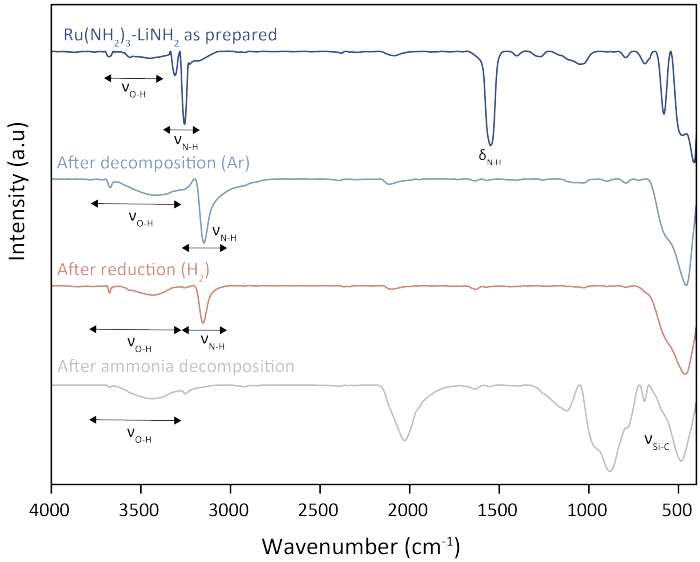

Figure III.S6: Infrared (IR) spectra of $Ru(NH_2)_3$-$LiNH_2$ as prepared from ball-milling, after decomposition under Ar, after reduction with 10 vol% H_2, and of the residues from ammonia decomposition experiment, using $Ru(NH_2)_3$-$LiNH_2$-SiC (1:1 wt%) as the precursor.

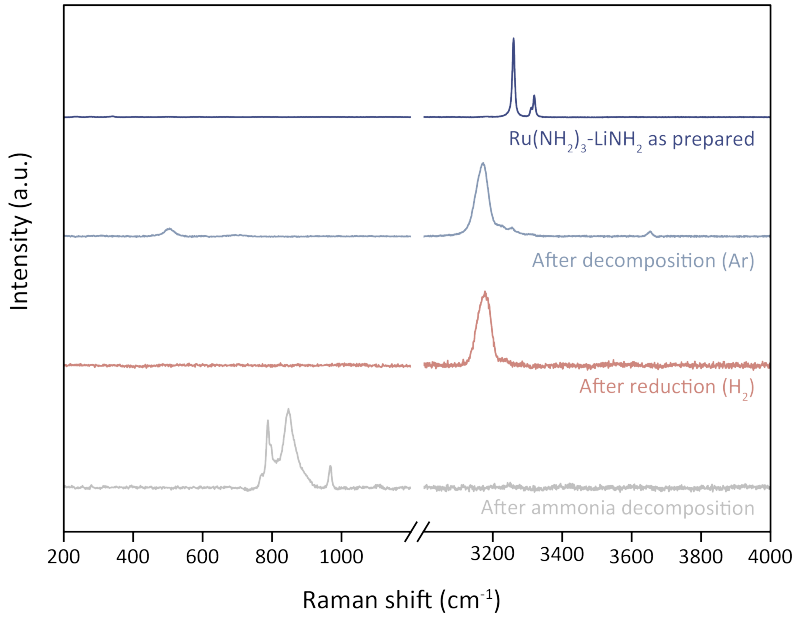

Figure III.S7: Raman spectra of $Ru(NH_2)_3$-$LiNH_2$ as prepared from ball-milling, after decomposition under Ar, after reduction with 10 vol% H_2, and of the residues from ammonia decomposition experiment, using $Ru(NH_2)_3$-$LiNH_2$-SiC (1:1 wt%) as the precursor.

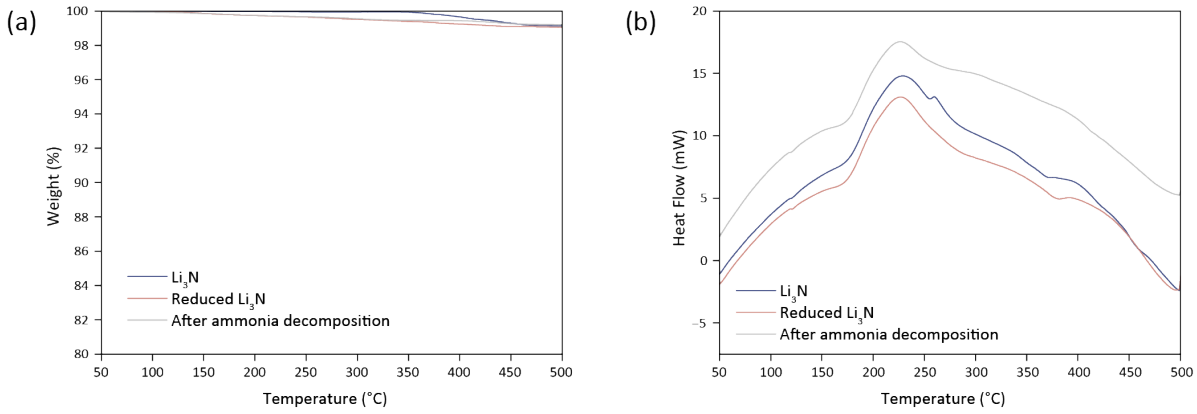

Figure III.S8: (a) Thermal Gravimetric Analysis (TGA) and (b) Differential Scanning Calorimetry (DSC) under argon of the Li_3N as supply, after reduction (H_2) and after ammonia decomposition.

Chapter IV

Theoretical approach

This chapter marks the beginning of the theoretical component of this work by introducing the theoretical methodology employed throughout the study. It explores the principles of density functional theory (DFT), with a particular focus on the exchange-correlation functionals utilized. Furthermore, it details the implementation of periodic DFT calculations using a plane-wave basis set.

Contents

IV.1 Schrödinger equation . . . 132
IV.2 Fundamental approximation . . . 132
IV.2.1 Born-Oppenheimer approximation . . . 132
IV.2.2 Hartree and Hartree-Fock methods . . . 133
IV.3 Density functional theory (DFT) . . . 134
IV.3.1 Hohenberg and Kohn theorems . . . 134
IV.3.2 Kohn and Sham equations . . . 135
IV.3.3 Approximations of the exchange-correlation functional . . . 136
IV.4 Plane-wave basis set . . . 139
IV.4.1 Interest . . . 139
IV.4.2 Pseudopotential: PAW method . . . 139
IV.5 Catalyst modeling and search of thermodynamic states . . . 140
IV.5.1 Valence electrons . . . 140
IV.5.2 Atoms and molecules . . . 140
IV.5.3 Bulks . . . 141
IV.5.4 Bulk-modulus calculation . . . 142
IV.5.5 Surface and adsorption models . . . 143
IV.5.6 Interface models . . . 144
IV.6 Search of transition states and kinetic study . . . 145
IV.6.1 Constrained geometry optimization . . . 145
IV.6.2 Improved dimer method . . . 145
IV.6.3 Geometry refinement and Quasi-Newton algorithm . . . 147
IV.6.4 Minimal energy pathway and Intrinsic-reaction-coordinate (IRC) . . . 147
IV.7 DFT software: VASP . . . 148
IV.7.1 Computational details . . . 148
IV.7.2 Computational tool and environment (PSMN mesocenter) . . . 148

IV.1 Schrödinger equation

The fundamental principle underlying *ab initio* quantum mechanical simulations is the Schrödinger equation (see Equation IV.1). By solving this equation the electronic structure of a system can be described by minimizing the required empirical parameters. The time-independent form of the Schrödinger equation can be expressed as follows

$$\hat{H}\Psi = E\Psi \tag{IV.1}$$

where $\hat{H}$ is the Hamiltonian operator, representing the total energy of the system, Ψ is the multi-electron wave function of the system, also known as the many-body wave function, and E total energy as an eigenvalue associated with the wave function.

The Hamiltonian describing the interactions of N_e electrons in the field of N_n nuclei is composed of different energy terms describing the system, including the total kinetic energy of the electrons ($\hat{T}_e$), of the nuclei ($\hat{T}_n$), the attractive interaction potential between electrons and nuclei ($\hat{V}_{e\text{-}n}$), as well as the repulsive electron-electron ($\hat{V}_{e\text{-}e}$) and nuclei-nuclei ($\hat{V}_{n\text{-}n}$) interaction potentials. The Hamiltonian operator is given by:

$$\hat{H} = \hat{T}_e(\vec{p}) + \hat{T}_n(\vec{P}) + \hat{V}_{e-n}(\vec{r},\vec{R}) + \hat{V}_{e-e}(\vec{r}) + \hat{V}_{n-n}(\vec{R}) \tag{IV.2}$$

where $\vec{p}$ and $\vec{P}$ represent the momentum of the electrons and nuclei, respectively, while the position vectors of N_e and N_n are denoted as $\vec{r}$ and $\vec{R}$, respectively.

This many-body equation cannot be solved analytically for a polyatomic and thus poly-electronic system due to the complexity of the many-body problem (only one equation for solving the movement of N_e+N_n particles). However, numerical solutions are achievable through some approximations aiming to scale down the many-body problem into a two-body system (one electron evolving in the mean field of a cloud of electrons, at frozen positions of the nuclei).

IV.2 Fundamental approximation

IV.2.1 Born-Oppenheimer approximation

The first approximation consists of decoupling the movement of electrons from that of the nuclei, known as the Born-Oppenheimer approximation.[389] Given the significant mass disparity between nuclei and electrons, this approximation posits that the much heavier nuclei move considerably slower than the electrons, effectively appearing stationary from the electronic perspective. Given the significant mass difference between nuclei and electrons, this approximation considers that the much heavier nuclei move considerably

slower than the electrons, effectively appearing stationary from the electronic perspective. Thus, the wavefunction of the complete system can be expressed as the product of electronic (Ψ_e) and nuclear (Ψ_n) components. The nuclei are treated as fixed points, creating an electrostatic potential in which the electrons move. Consequently, the kinetic energy of the nuclei is neglected in the electronic Hamiltonian, and the nuclear-nuclear repulsion potential ($\hat{V}_{n\text{-}n}$) is treated as a constant:

$$\hat{H} = \hat{H}_e + \hat{H}_n \tag{IV.3}$$

Hence, the resolution of the Schrödinger equation is now simply reduced to solving the electronic part:

$$\hat{H}_e \Psi_e = E_e \Psi_e \tag{IV.4}$$

where the electronic Hamiltonian contains three terms (electronic kinetic energy, electron-electron interactions and electron-nuclei interactions) and is parametrized by the frozen positions of the nuclei.

The separation of electronic and nuclear movements reduces the complexity of the initial many-body problem. However, N_e electrons are described by $3N_e$ cartesian coordinates in 3D space which need to be described to predict the movement of electrons, so we still have a $3N_e$ manybody quantum problem. The three energetic components are difficult to handle whatever the basis set describing the electrons in the electronic wavefunction, consequently, several approaches have been developed to solve the Schrödinger equation for polyatomic and poly-electronic systems. Among them, one can quote the Wavefunction Theory and related Hartree-Fock methods and the more recent Density Functional Theory. .

IV.2.2 Hartree and Hartree-Fock methods

Hartree-Fock (HF) theory is an approximate method for solving the Schrödinger equation and serves as the foundational introductory approach for most *ab initio* quantum chemistry calculations.[390, 391] At the heart of the HF method is to approximate the many-electron wave function of a system by a single Slater determinant which results from an antisymmetrized product of one-electron orbitals.[392] This reduces the complex many-body problem into simpler, single-electron problems while accounting for the average effects of electron-electron interactions. In this method, the electrons (core and/or valence) are described by atomic orbitals (of which the choice of the mathematical formulation is not unique) and the electronic basis set can be extended by the inclusion of polarization and diffuse functions aiming to improve the description of the electronic structure of the system. Among the advantages of Hartree-Fock theory, one can quote the exact treatment of the electronic exchange energy. Among the drawbacks, the computational cost and the non-consideration of the electronic correlation (which can be pictured as the instantaneous repulsion of electrons) are the most significant restrictions, which limit its predictive power and its use.

The neglect of electronic correlation can result in significant inaccuracies for describing the electronic structure of specific classes of systems such as materials (oxydes, metals etc) involving heavy elements with a large number of valence electrons. This can impact directly key properties in these systems such as equilibrium structures and energetics of chemical bondings (reaction energies and activation barriers for instance). More sophisticated methods aiming to evaluate the correlation energy through perturbation theory have been developed in the context of Hartree-Fock theory leading to the so-called, post-Hartree-Fock methods (such as Møller-Plesset "MP"). Although much more accurate, their computational power increases drastically. In addition, due to their formulation (perturbation theory), closed-band-gap systems such as metals, cannot be described unfortunately. During the sixties, an alternative theory using the total electronic density as a key variable (instead of the wavefunction) has emerged and is referenced as Density Functional Theory (DFT). Its interesting predictive power for describing thermodynamic properties of molecules and materials has allowed its use at the international level within a few decades.

IV.3 Density functional theory (DFT)

Density Functional Theory (DFT) is a powerful computational quantum mechanical modeling method. Unlike methods that are based on wave functions, DFT considers the electron density $\rho(\mathbf{r})$, a physical observable, as the primary quantity rather than the wave function. Thus, the quantum many-body problem is reformulate into a one-body problem quantum many-body problem is reformulated into a one-body problem (if spin is ignored):

$$\rho(\mathbf{r}) = \int_{\mathbf{r}_2} ... \int_{\mathbf{r}_N} |\psi(\mathbf{r}_1, \mathbf{r}_2 ... \mathbf{r}_N)|^2 \mathbf{r}_N \tag{IV.5}$$

The Thomas-Fermi model was the first attempt to use electron density to derive the properties of a system.[393, 394] Dirac later refined the model by incorporating an exchange energy term dependent on the electron density, ρ.[395] Building on these concepts, Hohenberg and Kohn mathematically demonstrated that the ground state properties of a system are a functional of its electron density. This initial principle led to the development of DFT, that allows for the study of electronic structures in an exact theoretical framework.

IV.3.1 Hohenberg and Kohn theorems

Thus, the DFT is based on two main theorems established by Hohenberg and Kohn:[396]

- **Existence theorem**

The first theorem assets that every observable of a system in its ground state, its energy E_0 in particular, is a unique functional of the electron density. Therefore, the Born-Oppenheimer approximation, for a multi-electron system system can be written as:

$$E[\rho(\mathbf{r})] = T_e[\rho(\mathbf{r})] + V_{e-e}[\rho(\mathbf{r})] + \int \rho(\mathbf{r}) v_{ext}(\mathbf{r}) d\mathbf{r} \tag{IV.6}$$

where T_e is the kinetic energy of the electrons, $V_{e\text{-}e}$ is the energy corresponding to to the electron-electron interaction (called the Hartree potential) and the last term is the nuclei-electron interaction $V_{n\text{-}e}$ (called the external potential) . In the absence of other external potentials, Equation IV.6 can be generalized as follows:

$$E[\rho(\mathbf{r})] = F_{HK}[\rho(\mathbf{r})] + \int \rho(\mathbf{r}) v_{ext}(\mathbf{r}) d\mathbf{r} \tag{IV.7}$$

where F_{HK} is universal functional, including just the kinetic and the electron-electron repulsion terms, and does not not depend on any external potential (meaning not parametrized by the frozen structure of the nuclei).

- **Variational principle**

According to the second theorem, the exact ground state density minimizes the ground state energy. This means that the energy functional E[ρ(**r**)] reaches its minimum when ρ(**r**) equals ρ_0(**r**), where ρ_0 is the ground state density. Thus, the ground state energy E_0 can be determined by minimizing the energy functional E[ρ] across all possible electron densities ρ.

The electron density, ρ(**r**), is not initially known, and the two theorems alone are not sufficient for determining it, because terms of the universal functional F_{HK} (T_e) the kinetic energy of the electrons and $V_{e\text{-}e}$ the electron-electron interaction) remain analytically unknown. If the exact form of this universal functional were known, it would enable the precise determination of the energy functional for the ground state, thereby allowing for an analytical solution to the multi-electron problem starting from F_{HK} and the electron density.

IV.3.2 Kohn and Sham equations

Kohn and Sham introduced a method to estimate the universal functional F_{HK} by treating the N_e electrons system not as interacting, but rather as a collection of non-interacting electrons moving in an effective potential composed of a mean-field of ($N_{e\text{-}1}$) electrons.[396] This approach simplifies the complex many-body problem into a set of n single-electron equivalent equations. The Kohn-Sham Hamiltonian ($\hat{H}_{KS}$) can be written as:

$$\hat{H}_{KS} = -\frac{1}{2}\nabla_i^2 + v_{KS}(\mathbf{r}_i) \tag{IV.8}$$

where

$$v_{KS}(\mathbf{r}_i) = J[p] + v_{XC}[p] + v_{ext}[\mathbf{r}] \tag{IV.9}$$

where $v_{ext}(\mathbf{r})$ represents the external potential, and $J[\rho]$ denotes the classical Coulomb repulsion energy and $v_{XC}(\mathbf{r})$ the exchange and correlation potential to be determined. This leads to a new expression for

Equations IV.4 and IV.5 :

$$\hat{H}_{KS}\,\psi_i(\mathbf{r}) = \epsilon_i\,\psi_i(\mathbf{r}) \tag{IV.10}$$

and for the electronic density of the system :

$$\rho(\mathbf{r}) = \sum_{i=1}^{n} |\psi_i(\mathbf{r})|^2 \quad \text{with i} \in 1, ..., \text{n} \tag{IV.11}$$

where $\psi_i(\mathbf{r})$ are the Kohn-Sham wavefunctions, and ϵ_i are the corresponding eigenvalues representing the energies of the eigenstates of the electronic Halmitonian. By applying the Hohenberg-Kohn theorems, an expression for the ground state energy of the system can be derived:

$$E_0[\rho] = T[\rho] + J[\rho] + V_q[\rho] + E_{xc}[\rho] + \int v_{ext}(\mathbf{r})\rho(\mathbf{r})d\mathbf{r} \tag{IV.12}$$

where $T[\rho]$ is the kinetic energy of the non-interacting electron system, E_{xc} denotes the exchange-correlation energy, $\int v_{ext}(\mathbf{r})\rho(\mathbf{r})\,d\mathbf{r}$ represents the interaction energy related to the external potential, and $V_q[\rho]$ accounts for the non-classical corrections to electron-electron repulsion.

However, E_{xc} remains unknown, and the determination of this exchange-correlation energy is the principal challenge in DFT-based methods. If E_{xc} was known, one could precisely calculate the exact ground state energy of the system through the resolution of the Kohn-Sham equations. So, to solve these equations numerically, it is necessary to approximate the exchange-correlation energy.

IV.3.3 Approximations of the exchange-correlation functional

- **Local density approximation (LDA)**

The first approximation for the exchange-correlation energy (E_{xc}) was introduced by Kohn and Sham themselves.[396] They proposed the Local Density Approximation (LDA meaning that the exchange and correlation functional depends only on the electron density and not its derivatives), as the electron density varies slowly, E_{xc} is approximated as that of a uniform electron gas with homogeneous density n. Thus, E_{xc}^{LDA} is separated linearly into an exchange term and a correlation term, each defined by:

$$E_{xc}^{LDA}[\rho] = \int \rho(\mathbf{r})\epsilon_{xc}[\rho(\mathbf{r})]d\mathbf{r} \tag{IV.13}$$

where ϵ_{xc} represents the exchange-correlation energy per particle for a homogeneous electron gas with a charge density ρ. LDA functional is exact for systems where electron density is uniform and constant. This makes LDA particularly effective for closed band gap systems with delocalized electrons. Structures are also

predicted at an interesting level of accuracy for various classes of systems. However, it fails to accurately describe the energy of strongly correlated systems where the electronic correlation is more complex (for instance in materials). Similarly, it struggles to properly account for systems characterized by weak interactions, such as hydrogen bonds and long-range van der Waals forces.

- **Generalized gradient approximation (GGA)**

Given that most real systems do not exhibit homogeneous electron density, advancements have been made to develop functionals that capture local and semi-local density information. The Generalized Gradient Approximation (GGA) incorporates dependency on the density gradient ($\nabla\rho$), making it a semi-local functional.[397] The exchange and correlation energy in GGA is then expressed as:

$$E_{xc}^{GGA}[\rho] = \int \epsilon_{xc}[\rho(\mathbf{r}), \nabla\rho(\mathbf{r})]\rho(\mathbf{r})d\mathbf{r} \tag{IV.14}$$

GGA-type functionals generally yield more accurate energetic results compared to the LDA approach, although the prediction of structures is sometimes less probative (such as for metals). Among the most used functionals, the ones developed by Lee, Yang, and Parr (LYP),[398] by Perdew-Wang (PW91),[399] by Perdew-Burke-Ernzerhof (PBE)[400] are the most famous for materials in particular. The GGA-PBE, in particular, is well-suited for studying the properties of metals, both in bulk and on surfaces, as well as adsorption properties in surface chemistry, thus justifying this choice for our study.

However, while GGA functionals address some shortcomings of the LDA approach, they still have notable limitations. Firstly, they fail to account for weak and long-range interactions such as van der Waals forces, but also for treating correctly the dynamic electronic correlation. Secondly, unlike wave function methods, they do not eliminate self-interaction errors (the so-called SICs or self-interaction corrections are missing), where an electron interacts with its own density via the Hartree potential.

- **Dispersion corrected functionals**

These neglected weak interactions are often crucial for accurately representing chemical systems. In scenarios like catalytic ammonia decomposition within a metallic environment, dispersion-corrected functionals may become essential to properly model the adsorption behaviors of NH_3, N_2, and H_2 onto metallic surfaces, as well as.

A typical method to address these interactions involves augmenting existing functionals with empirical corrections. Within this context, PBE dispersion-corrected functionals serve as enhancements to the GGA-PBE functionals, aimed at improving their handling of dispersion interactions. In our study, we have selected and evaluated three semi-empirical dispersion-corrected functionals within the framework of Grimme's DFT-D3, which includes PBE-D3 with zero damping (0D)[401, 402] and with Becke-Johnson (BJ)[401, 402] damping functions,

as well as Steinmann's formalism (PBE-dDsC).[403, 404]

The computational approach to solving the Kohn-Sham equations requires the use of self-consistent loops, as depicted in Figure IV.1. To handle these calculations, several software packages employ iterative methods that continually adjust the electron density and potential until changes between successive iterations are minimized, ensuring convergence to a stable electronic state. Crucially, these computations require a basis set—a collection of functions used to describe the electronic wave functions of the involved atoms. This basis set choice is crucial as it directly influences the accuracy and efficiency of the calculations.

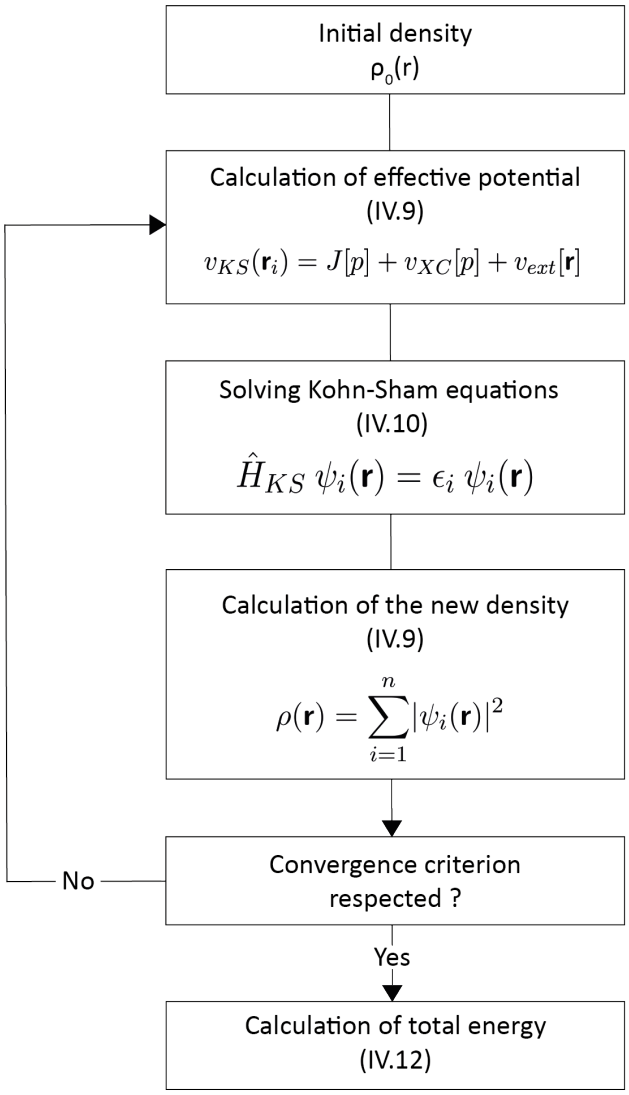

Figure IV.1: Illustration of self-consistent method used in the Density Functional Theory framework for solving Kohn-Sham equations.

IV.4 Plane-wave basis set

IV.4.1 Interest

In the Kohn-Sham equations, wavefunctions can be represented by using a basis set, with two primary function types being prevalent: localized basis functions (such as Gaussian or Slater Type Orbitals) and periodic basis functions such as plane waves (PWs). PWs are especially beneficial for modeling systems with crystalline or periodic symmetry.

Modeling infinite periodic systems using PWs can be computationally intensive due to the need for a large number of PWs to ensure convergence, particularly when accurately describing localized features within the wavefunctions. To address this computational challenge, Bloch's theorem is frequently utilized.[405] Bloch's theorem capitalizes on the inherent periodicity of wavefunctions in crystalline materials, asserting that each electronic wavefunction in a periodic solid can be expressed as a product of a cell-periodic function, the wave function can therefore be written:

$$\Psi_{nk}(\mathbf{r}) = u_{nk}(\mathbf{r})e^{ik\cdot\mathbf{r}} \quad \text{with} \quad u_{nk}(\mathbf{r}+\mathbf{R}) = u_{nk}(\mathbf{r}) \quad \text{and} \quad \Psi_{nk}(\mathbf{r}+\mathbf{R}) = \Psi_{nk}(\mathbf{r})e^{ik\cdot\mathbf{r}} \tag{IV.15}$$

where **R** is a translation vector, **k** is the Bloch wavevector located within the first Brillouin zone, n an index used to enumerate the the wavefunction, and $u_{nk}(\mathbf{r})$ represents the part of the wavefunction that is periodic due to the lattice structure.

The PWs basis set is typically extended across a finite grid of k-points to sample the first Brillouin zone effectively. Ideally, the mesh should be uniformly spaced to ensure both computational efficiency and precision. This balance is crucial to maintain reasonable computational costs. In practice, a general rule of thumb for selecting a k-points grid is to use a ($N_1 \times N_2 \times N_3$) format, where each dimension is tailored to the periodicity and symmetry of the system under study.

The number of PWs used to expand the wave function is determined by a parameter known as the cutoff energy, denoted by E_{cut}. The plane wave basis set for describing the valence electrons in this study is defined with a cutoff energy of 500 eV (E_{cut} = 499.034 eV for the plane wave basis set and E_{aug} = 628.945 eV for the plane wave representation of the augmentation charges).

IV.4.2 Pseudopotential: PAW method

In PWs calculations, the frozen core approximation is typically employed,[406] where core electrons are assumed to be frozen and are incorporated into the atomic nuclei through a pseudopotential. This approach explicitly treats only the valence electrons, simplifying the wavefunctions. The Projector Augmented Wave (PAW)[407] method addresses this challenge by converting the rapidly oscillating wavefunctions into smooth,

computationally manageable forms. The PAW method simplifies calculations and combines the efficiency of pseudopotentials with the accuracy of an all-electron method, providing a highly accurate description of the electronic structure without the need to explicitly include all electron states in the calculations. This method is particularly effective in studying materials where the core electrons have a significant effect on the chemical properties, such as transition metals and their compounds.

IV.5 Catalyst modeling and search of thermodynamic states

IV.5.1 Valence electrons

In our study, all ruthenium atoms have been described with 8 valence electrons and related PAW PBE pseudopotential (electronic configuration $4d^7 5s^1$), while Li atoms have been described with 3 valence electrons ($1s^2 2s^1$), N and H atoms with 5 ($2s^2 2p^3$) and 1 valence electrons, respectively.

IV.5.2 Atoms and molecules

To accurately assess our DFT models, it is essential to evaluate certain parameters, such as the calculation of formation, cohesion and interfaces energies, among others. Consequently, it is crucial to precisely determine the energies of the various 'building blocks' that constitute the materials under investigation.

For instance, to calculate the total cohesive energy of $LiNH_2$, Li_2NH, and Li_3N, it is necessary to determine the individual energies of the Li, N, and H atoms. Additionally, calculating the formation energies of these compounds requires the bulk energy of lithium and the molecular energies of N_2 and H_2. This approach ensures a thorough understanding of the energetic profiles of these materials. The energies of the N_2, H_2, and NH_3 molecules were also utilized during the calculations of interface energies. This information is crucial for comparing with the catalytic models during the adsorption and desorption processes of these molecules. All the equations using these 'building blocks' are detailed in the results chapters.

There is also the case of the evaluation of non-stoichiometric bulks set up for $LiNH_2$, Li_2NH, and Li_3N. To evaluate the non-stoichiometric bulks, an additive model is employed, applicable to all models that include lithium components, without this part having to correspond exactly to a multiple of the bulk. This approach involves segmenting the bulks into their constituent elements: lithium atoms and nitrogen-based groups (with or without hydrogen, depending on the material's hydrogenation level). For instance, a $LiNH_2$ bulk, which typically comprises equal numbers of Li and NH_2 (8 each), is dissected by systematically removing all Li atoms to isolate the NH_2 groups in the crystal structure. The reverse—removing all NH_2 to isolate Li—is similarly considered. The final step involves computing the energy of the isolated NH_2 moieties. The energy of an isolated Li atom, already determined in prior calculations, complements this data. Then, a term that corresponds to the non-additivity of the model, calculated with respect to the bulk and the different components of $LiNH_2$ calculated, is added. The non-stoichiometric bulk equation of $LiNH_2$ is detailed in Chapter

V, Section V.2.2.1. The same process is applied to the components of Li_2NH, which includes 8 Li atoms and 4 NH fragments, as well as to the structure of Li_3N, comprising 12 Li atoms and 4 N atoms.

All isolated atoms, as well as the crystalline structures $LiNH_2$, Li_2NH, and Li_3N, containing only Li atoms, NH_2, NH fragments or N atoms, are computed using spin-polarized geometry optimizations. These computations employ the blocked-Davidson and RMM-DIIS algorithms, setting the energy convergence criterion to 10^{-7} eV. For the calculations used to develop additive bulk properties, two distinct approaches are implemented: Methfessel-Paxton smearing and Gaussian-type smearing. This dual approach enables the generation of additive bulks that are consistent across scenarios involving the presence or absence of Ru, as Methfessel-Paxton smearing is specifically required for metals.

Geometry optimizations for molecules (NH_3, N_2, and H_2) were carried out without spin polarization, while for isolated NH and NH_2 spin polarization was included. The optimizations were guided by: an energy criterion of 10^{-7} eV and a force convergence criterion of ± 0.005 eV/Å. The same smearing treatment as previously utilized was applied to these calculations.

IV.5.3 Bulks

The theoretical study of Ru-$LiNH_2$ catalysts began with the individual study of the crystal structures of ruthenium, lithium amide, lithium imide, and lithium nitride bulks. This preliminary investigation helps in selecting the most appropriate functionals to accurately represent these materials. The decision is influenced by volume relaxations performed on each bulk material and their subsequent comparison with experimental crystalline parameters, ensuring the chosen functionals align closely with observed physical properties. It is important to note that the choice of the functional represents a compromise among the best-performing functionals for these four bulk materials.

Table IV.1: Space group, space group number, and crystal structure of Ru, $LiNH_2$, Li_2NH, and α-Li_3N bulks are detailed, alongside their respective cutoff energies (E_{cut}) in eV, k-point grids, and counts of irreducible k-points used in the calculations.

Bulks	Space group	Space group number	Structure	E_{cut} (eV)	K-points grid	Irreducible k-points
Ru	P63/mmc	194	Hexagonal close-packed (HCP)	499.034	(35 × 35 × 35)	1320
Li	Im-3m	229	Body centered cubic (BCC)	499.034	(15 × 15 × 15)	788
$LiNH_2$	I4	82	Tetragonal	499.034	(15 × 15 × 7)	228
Li_2NH	Fm3m	225	Cubic	499.034	(23 × 23 × 23)	6084
α-Li_3N	Fm3m	225	Cubic	499.034	(23 × 23 × 23)	364

To ensure converged total electronic energies with respect to Brillouin zone integration, systematic studies were developed by progressively increasing the density of k-point meshes for ruthenium, lithium amide, lithium imide and lithium nitride bulks. These 'golden rules' for k-point mesh density are crucial for obtaining accurate and reliable DFT results, as they directly affect the precision of the electronic structure calculations in the materials studied (see Table IV.1).

Single-point energy calculations were conducted using a combination of the blocked-Davidson and RMM-DIIS algorithms, for determining the golden rule, with an energy convergence criterion of 10^{-6} eV. Subsequent geometry optimizations were performed with the same algorithms but employed a more stringent energy convergence criterion of 10^{-7} eV, alongside a force convergence criterion set at $\pm$0.005 eV/Å. Both calculation types utilized Methfessel-Paxton smearing, and for materials containing lithium, Gaussian-type smearing was also applied. This rigorous approach ensures accurate and reliable optimization and energy assessments.

IV.5.4 Bulk-modulus calculation

The bulk modulus (B_0) is a fundamental property of materials, quantifying their resistance to uniform compression. It is defined as the ratio of an increase in pressure (P) to the corresponding relative decrease in volume (V), expressed as:

$$B = -V\frac{dP}{dV} \tag{IV.16}$$

A high bulk modulus indicates that a material strongly resists deformation under pressure, reflecting high rigidity. Conversely, materials with a low bulk modulus are more readily compressible. The bulk modulus can be measured experimentally or calculated through DFT by varying the material's volume (V) and fitting the corresponding energy values (E(V)), see Equation IV.17. Comparing experimental and theoretical bulk modulus values offers valuable guidance in selecting DFT functionals for more accurate and reliable modeling.

$$E(V) = E_0 + \frac{9V_0B_0}{16}\left\{\left[\left(\frac{V_0}{V}\right)^{\frac{2}{3}} - 1\right]^3 B_0' + \left[\left(\frac{V_0}{V}\right)^{\frac{2}{3}} - 1\right]^2 \left[6 - 4\left(\frac{V_0}{V}\right)^{\frac{2}{3}}\right]\right\} \tag{IV.17}$$

where E_0 is the equilibrium energy, V_0 the equilibrium volume, B_0 the bulk modulus, and B_0' the derivative of the bulk modulus with respect to pressure.

Starting from the fully optimized bulk structure (relaxed volume), modifications to the lattice vectors of the unit cell were made incrementally, ranging from $\pm$0.01 Å to $\pm$0.15 Å. For the $LiNH_2$ bulk, these modifications were extended to +0.35 Å to achieve uniform deformation across both directions. Following these adjustments, single-point energy calculations were performed on each volume ans related

structure. These calculations utilized a combination of the blocked-Davidson and RMM-DIIS algorithms, with an energy convergence criterion set at 10^{-7} eV.

IV.5.5 Surface and adsorption models

To facilitate the development of interface models between two solids, it is crucial to examine various crystallographic planes to identify surfaces that are thermodynamically favorable. In the case of Ru, since the (0001) surface is the natural termination and the most stable one, it has been selected in my works and only the impact of the Ru slab thickness has been studied. For $LiNH_2$, the (001) plane has been exclusively studied since this surface is the only one presenting lattice parameters minimizing the structure mismatch with those of Ru(0001). For Li_3N and Li_2NH, with cubic structures, several surface planes exhibit lattice parameters compatible with those of Ru. Specifically, the (100) and (111) surface planes of Li_2NH were considered. Likewise, for Li_3N, three potential cutting planes—(100), (111), and (110)—were investigated. The surface terminations for $LiNH_2$, Li_2NH, and Li_3N were explored based on the nature of their constituent atoms.

Table IV.2: Overview of surface models for Ru, $LiNH_2$, Li_2NH, and Li_3N, detailing supercell dimensions, crystallographic planes, atomic layer thickness, and K-point grid specifications.

Material	Surface planes	Supercell	Atomic layers	K-points grid	Irreducible k-points
Ru	(0001)	(1 ×1)	5,7,9 and 11	(35 ×35 ×1)	120
		(2 ×2)	7	(17 ×17 ×1)	33
		(4 ×2$\sqrt{3}$)	7	(11 ×11 ×1)	61
$LiNH_2$	(001)	(1 ×1)	10-17	(15 ×15 ×1)	113
Li_2NH	(100)	(1 ×1)	15-17	(7 ×7 ×1)	25
	(111)		8-10		
Li_3N	(100)	(1 ×1)	13, 15 and 16	(7 ×7 ×1)	10
	(111)				
	(110)		12		

The findings for the Ru and $LiNH_2$ surfaces are detailed in Section 2 of Chapter V. Results for Li_2NH and Li_3N terminations are discussed in Section VI.3.1.2 of Chapter VI. Information on models for surface studies is given in Table IV.2.

Concerning the generation of interface models between Ru(0001) and $LiNH_2$(001) systems, the adsorption behaviors of Li, NH_2, and N on the Ru(0001) surface were investigated. The findings from these studies are detailed in Sections V.3 and VI.3.2.1.

Surface energies were analyzed through spin-polarized geometry optimization (without for Ru surface and and adsorption studies), using the Davidson algorithm. The criteria for energy convergence were

set to 10^{-6} eV, with the force convergence criterion established at $\pm$0.01 eV/Å.

IV.5.6 Interface models

The interfaces between the Ru(0001) and the different lithiated materials were designed to align with the dimensions of the previously optimized Ru bulk supercell, obtained from the bulk geometry optimisation with different functionals. It is more feasible to adapt Li-containing materials to Ru due to Ru's significantly higher bulk modulus (or larger rigidity), as adapting ruthenium to the lattice parameters of other materials would lead to excessive energy costs. A key working principle was applied in constructing these interfaces by adapting the golden rule of the Ru bulk to match the size of the supercell used in the interface model (see Table IV.3).

Table IV.3: Overview of different interfaces models, for Ru(0001)/$LiNH_2$(001) and Ru(0001)/Li_3N(001)/Li_2NH(001)/$LiNH_2$(001) and Ru(0001)/Li_3N(001) detailing supercell dimensions, and K-point grid specifications.

Interface	Supercell	K-points grid	Irreducible k-points
Ru(0001)/$LiNH_2$(001)	(2 $\times\sqrt{3}$)	(17 $\times$ 21 $\times$ 1)	179
	(4 $\times$2$\sqrt{3}$)	(7 $\times$ 7 $\times$ 1)	25
Ru(0001)/$LiNH_2$(001) defective	(8 $\times\sqrt{3}$)	(3 $\times$ 21 $\times$ 1)	32
Ru(0001)/Li_2N(001)/Li_2NH(001)/$LiNH_2$(001)	(2 $\times\sqrt{3}$)	(19 $\times$ 23 $\times$ 1)	219
Ru(0001)/Li_3N(001)/Li_2NH(001)/$LiNH_2$(001) defective	(8 $\times$2$\sqrt{3}$)	(3 $\times$ 7 $\times$ 1)	11
	(8 $\times\sqrt{3}$)	(3 $\times$ 7 $\times$ 1)	11
	(8 $\times\sqrt{3}$)	(1 $\times$ 1 $\times$ 1)	11
Ru(0001)/Li_3N(001)	(4 $\times$2$\sqrt{3}$)	(11 $\times$ 11 $\times$ 1)	61

All interface results are found in section V.4 for Ru(0001)/$LiNH_2$(001), in section VI.3.2. for the partially hydrogenated interface model (Ru(0001)/Li_3N(001)/Li_2NH(001)/$LiNH_2$(001)), and in section VII.1 for Ru(0001)/Li_3N(001) interface model.

For all interfaces, spin-polarized geometry optimizations were conducted using the Davidson algorithm coupled with Methfessel-Paxton smearing. The criteria for energy convergence were set to 10^{-6} eV, with the force convergence criterion established at $\pm$0.01 eV/Å.

IV.6 Search of transition states and kinetic study

IV.6.1 Constrained geometry optimization

Understanding a reaction mechanism requires identifying the relevant intermediates involved in the elementary steps, determining the transition state (TS) structures, and estimating their stabilities based on total electronic energies. For ammonia decomposition, the rate-determining step—the recombinant desorption of N_2—was studied through TS searches and kinetic analyses, initiated with constrained geometry optimization.

Potential TS geometries were constructed, varying only in the adsorption sites of the two nitrogen atoms involved in N_2 formation. This initial phase involves a constrained geometry optimization where all atoms that are allowed to relax always have this possibility (just like in standard geometry optimization), but with the two N atoms fixed in guessed adsorption positions. This method ensures that while the rest of the structure adjusts dynamically, the key positions of interest for coadsorbed N atoms are maintained.

The constrained geometry optimization employed the Davidson algorithm, setting the energy convergence criterion to 10^{-6} eV and the energy convergence criterion at $\pm$0.01 eV/Å. To verify the nature of the model's geometry as a TS, a harmonic vibrational analysis is computed on the two 'frozen' N atoms only. Validation of the transition state was confirmed by the presence of one imaginary vibrational mode, linked to the reactive mode. The initial geometry was modified each time no imaginary frequency was found, specifically by adjusting the N-N distance thus redesigning the geometry of the adsorbates.

IV.6.2 Improved dimer method

The dimer method, introduced by Henkelman et al.,[408] is a sophisticated algorithm used for identifying saddle points and minimum energy paths (MEPs) in quantum chemistry calculations. In our study, we used the Improved Dimer Method (IDM), an enhancement developed by Heyden et al.,[409] which is more efficient as it requires fewer evaluations of gradients.

Similar in purpose to the nudged elastic band (NEB) method,[410, 411] IDM offers computational advantages as it does not require multiple replicas of the system between the presumed initial and final states of the elementary step and related reaction pathway . IDM utilizes the first derivatives of the potential energy surface, employing a "dimer"—two closely spaced images on this surface—to effectively probe its curvature and gradient, by moving the dimer uphill on the potential energy surface which progressively closes up as the dimer approaches the region of a local maximum or a saddle-point.

From the initial image, two dimer configurations will be generated around their common midpoint, denoted as **R**, by displacing them by a distance ΔR. The vector $\hat{N}$, derived from the vibrational calculations, is a unit

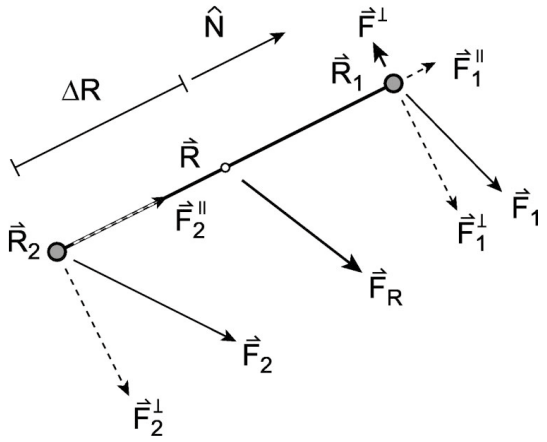

Figure IV.2: Diagram illustration of the dimer method, depicting the positions and force vectors associated with the dimer configuration.[408]

vector that dictates the orientation of the dimer. The energy of the dimer, E, is calculated as the sum of the energies of the two images, expressed as $E = E_1 + E_2$. The force of the common midpoint ($\mathbf{F}_R$) is the average force of the two dimer $\mathbf{F}_1$ and $\mathbf{F}_2$. The energy of the midpoint (E_0), s expressed as follows:

$$E_0 = \frac{E}{2} + \frac{\Delta R}{4}(\mathbf{F}_1 - \mathbf{F}_2) \cdot \hat{N} \tag{IV.18}$$

The IDM involves minimizing the energy at each displacement and calculating the forces and energy of the two images; however, this does not extend to the energy and force at the midpoint. The dimer is then rotated to identify the direction with the lowest curvature mode. The midpoint remains fixed until the lowest curvature mode is successfully identified.

At each displacement of the midpoint, the energy and forces for the updated position are recalculated to determine if the required convergence for the calculation has been achieved. If convergence has not been reached, another iteration is done.

The IDM calculations are carried out using the constrained TS geometry previously obtained. Prior to initiating the IDM calculations, a harmonic vibrational analysis is performed. The purpose of this vibrational study, in addition to checking the accuracy of the constrained TS geometry by ensuring the presence of one imaginary frequency (corresponding to the reactive mode of N_2 formation), is to obtained the first derivatives of the potential energy surface. This calculation employs the Davidson algorithm with an energy convergence criterion set to 10^{-6} eV. The IDM calculations are conducted using the same algorithm and energy convergence criterion as previously established, with the convergence criterion for geometry optimization set at $\pm$0.01 eV/Åfor residual forces.

IV.6.3 Geometry refinement and Quasi-Newton algorithm

In DFT calculations, the Quasi-Newton algorithm is commonly employed to optimize the geometry of molecular and crystalline systems. It efficiently finds the minimum energy configurations by determining the most favorable search directions based on the forces and stress tensor, without directly utilizing the total electronic energy. However, its effectiveness is contingent upon the initial guesses provided; if these initial positions are poorly chosen, the Quasi-Newton method can struggle significantly to converge to the correct minimum, leading to suboptimal or incorrect results. Reason why in our case, this algorithm is used to refine a transition state after an IDM calculation, when previously exposed methods were not enough to complete the geometry optimizations.

The refinement of the TS geometry, following the IDM calculation, utilized the quasi-Newton method paired with the Davidson algorithm. Convergence criteria were rigorously defined: with an energy convergence criterion was set at 10^{-6} eV, and with a convergence criterion $\pm$0.01 eV/Å for geometry optimization. This stringent set of parameters ensures precise and reliable optimization results, crucial for accurate TS characterization

IV.6.4 Minimal energy pathway and Intrinsic-reaction-coordinate (IRC)

Once a TS of interest has been identified by a refined geometry optimized followed by a vibrational analysis showing a single imaginary frequency related to the reaction mode, the Intrinsic reaction coordinate (IRC) method is used to predict the minimum energy pathway (MEP) between reactants and products on a potential energy surface.[412, 413] The IRC approach is based on the classical equations of motion, consider movement of the nuclei from a given point with an infinitesimal velocity. The velocity of nuclei is given for the coordinate X of atom α by:

$$m_\alpha X_\alpha = -\frac{\partial V}{\partial X_\alpha} t + \text{constant} \tag{IV.19}$$

where m_α represents the mass of atom α, and V denotes the potential energy function. The IRC equations, when expressed in terms of mass-weighted Cartesian coordinates, can be reformulated as follows:

$$d_x = -g_x t dt \quad \text{with} \quad g_x = \left(\frac{\partial V}{\partial x_1}, \frac{\partial V}{\partial x_2}, ..., \frac{\partial V}{\partial x_{3N}} \right)^T \tag{IV.20}$$

where $\mathbf{x} = (x_1, x_2, \ldots, x_{3N})^T$ represents the the mass-weighted cartesian coordinates. The common intrinsic reaction coordinate (IRC) equation incorporates the introduction of the infinitesimal distance ds, such that $ds^2 = dx \cdot dx$:

$$\frac{dx}{ds} = -\frac{g_x}{\|g_x\|} \tag{IV.21}$$

The equations yield an infinite number of solutions known as 'meta-IRC', with the IRC being the specific path that connects both the initial (or final) state and the TS. Plotting the IRC for a chemical reaction, a process

referred to as reaction ergodography,[412] provides a detailed visualization of the energy profile along the reaction pathway.

In this work, starting from TS optimized with Quasi-Newton, a two N restraint harmonic vibrational analysis is performed by restricting the degrees of freedom to those of the involved N atoms in the recombinant desoprtion. Then, the first derivatives of the potential energy surface obtained are used to perform IRC calculations. This analysis employs a damped velocity Verlet algorithm, as developed by Hratchian et al. and the damped-velocity-Verlet algorithm. From the TS, two parallel calculations are initiated in the +1 and -1 directions. The energy convergence criteria are set at 10^{-6} eV and with a geometric optimization tolerance of $\pm$0.01 eV eV/Å. The initial velocity v_0 is chosen as 0.02 Å/fs; a smaller value ensures the calculated trajectory remain close to the true IRC path, although it necessitates a higher number of ionic steps.

IV.7 DFT software: VASP

IV.7.1 Computational details

All calculations were performed in my PhD works by using the Vienna Ab initio Simulation Package (VASP) software, developped by Kresse et al.,[414, 415, 416] specifically versions 6.2.1 for all materials except Li_2NH bulk, which was calculated with the 6.4.2 version. These computations were performed under the guidance of the PAW method as the pseudopotential approach.[417]

IV.7.2 Computational tool and environment (PSMN mesocenter)

Computational resources were provided by computational cluster of the PSMN and Centre Blaise Pascal at école normale supérieure de Lyon (Lyon, France).[418]

Typical calculations were running on servers composed of 32 cores and a RAM of 384 Gb. Depending on the size of the systems (supercells, number of valence electrons, number of plane waves, number of irreducible k-points, etc), geometry optimizations have lasted from a few days to more than a year. The geometry optimizations involving dispersion-corrected van-der-Waals functionals are generally extremely long and the additional complexity of spin-polarized systems has also increased the required computational CPU time for the majority of my DFT systems.

Chapter V

Solid-solid interface models of ruthenium and lithium amide

Before considering interfaces between ruthenium and lithium amide materials, the most suitable DFT functionals have to be selected on the basis of the theoretical predictions of lithium amide and ruthenium bulks. The investigation progresses with an analysis of the various possible $LiNH_2$(001) surfaces, as well as the one of the most abundant Ru(0001) surface. Following this, the development of interface models between Ru(0001) and $LiNH_2$(001) surfaces starts with a preliminary study on the isolated adsorption of Li atom and NH_2 fragment on Ru(0001). The competitive adsorption of these species results in different possibilities to interface Ru and $LiNH_2$ materials, thanks to a contact either through Li or NH2. Various interface models have been optimized, considering the influences of $LiNH_2$(100) thickness, stoichiometry, and polarity, including spin polarization and van der Waals interactions. The stability of the interface is then interpreted with a Bader charge transfer analysis. The corresponding results of Ru(0001) and $LiNH_2$(001) solid-solid interfaces are detailed in an article published in The Journal of Physical Chemistry C in 2023.

Contents

V.1 Bulk Materials and choice of exchange-correlation functional . . . 150
V.1.1 Ru bulk . . . 150
V.1.2 $LiNH_2$ bulk . . . 151
V.2 Clean Surfaces . . . 153
V.2.1 Ru(0001) surface . . . 153
V.2.2 $LiNH_2$ surfaces . . . 154
V.2.2.1 Non stoichiometric $LiNH_2$ bulk energetic model . . . 156
V.2.2.2 $LiNH_2$(001) stoichiometric and non-stoichiometric surfaces energies . 158
V.3 Adsorptions on Ru(0001) . . . 160
V.3.1 Li adsorption . . . 160
V.3.2 NH_2 adsorption . . . 161
V.4 Ruthenium-Lithium Amide Interfaces . . . 162
V.4.1 Prerequisites for interfacing the two solids . . . 162
V.4.2 Case of $LiNH_2$(001) reconstruction . . . 166
V.4.3 Ru(0001)-$LiNH_2$(001) interface energies results . . . 167
V.4.3.1 Effect of $LiNH_2$ thickness on interface energy . . . 167
V.4.3.2 Sum of surface energies and adhesion energy analyses . . . 169
V.4.4 Bader charge analysis . . . 171
V.5 Conclusion . . . 173
V.6 Appendix . . . 175

V.1 Bulk Materials and choice of exchange-correlation functional

Before considering the interfaces between ruthenium and $LiNH_2$ materials, the choice of the electronic exchange and correla- tion functional is examined thanks to the predictions on the corresponding pure bulk materials and their relevance with respect to available measurements. Four functionals have been selected: standard GGA PBE, and three DFT-D functionals including van der Waals interactions through a semi-empirical correction, PBE-D3 (zero damping, noted 0D), PBE-D3 (Becke-Johnson, noted BJ) and PBE-dDsC.

V.1.1 Ru bulk

Regarding crystalline structures, Ru bulk is hexagonal close-packed (HCP),[419] see Figure V.1 and Table VII.4 for details of the measured lattice parameters. In the case of Ru bulk, the predictions of lattice parameters, cohesion energy and bulk modulus are quite satisfactory at the GGA PBE standard level (see Table VII.4), with +0.3% and -0.02% of systematic errors from measurements for a and c parameters, respectively, +6.7% for the total cohesive energy in the bulk and +2.3 % for the bulk modulus. Those theoretical results providing a reasonable model for describing the electronic properties in Ru bulk do not suggest the use of a dispersion-corrected functional, since both cohesion energy and bulk modulus are already overestimated with respect to experimental values. In fact, dispersion-corrected functionals are expected to further increase electronic correlation and the binding energy in metals through the inclusion of additional interactions. In addition, the theoretical predictions provided by the GGA PBE functional are known to be much better than those of the hyper-GGA functionals available in VASP such as HSE06 and PBE0 for Ru bulk, as already demonstrated previously.[420] This has justified our choice not to consider hybrid functionals, at the level of Ru bulk and for the theoretical study.

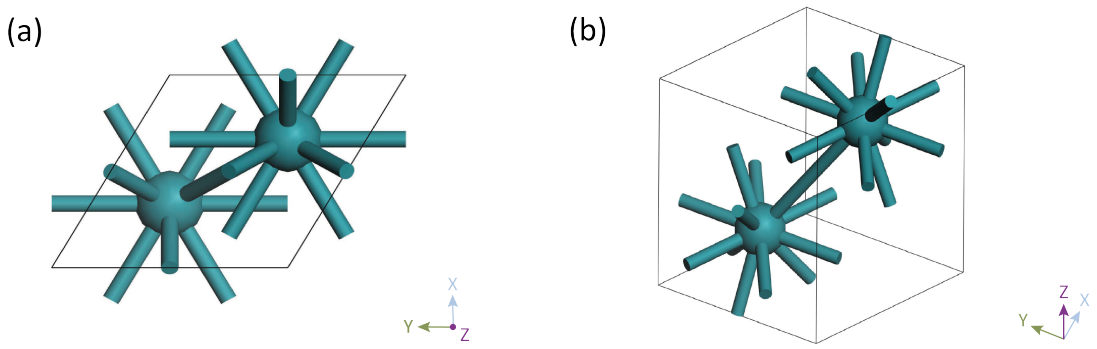

Figure V.1: HCP bulk structure of Ru (a) along the [001] direction and (b) perspective projection.[420]

At the level of van der Waals dispersion-corrected functionals (see Table VII.4), one can conclude that PBE-D3 (with zero damping and Becke-Johnson damping functions) functionals do slightly worse for predicting the lattice parameters than standard GGA PBE (-0.5 % for a for both functionals by comparison with measurements, while -0.8 %, -0.7 % for c for both functionals, respectively). The PBE-dDsC functional does not

behave similarly, since the prediction on a is slightly improved (-0.2 %) compared to GGA PBE, whereas the one on c is significantly worse (-0.4 %). Regarding cohesion energy, as expected, the three dispersion-corrected functionals do significantly worse than GGA PBE, to a lesser extent for PBE-dDsC (+12.2 %). For bulk modulus, the impact of van der Waals interactions is negligible. Therefore, if the use of a dispersion-corrected functional is imposed by $LiNH_2$ materials, PBE-dDsC appears as an acceptable compromise for describing Ru bulk properties.

Table V.1: Structural and energetic properties of optimized ruthenium and lithium amide bulks predicted by DFT calculations with various exchange and correlation functionals : standard GGA PBE, and dispersion-corrected PBE-D3(0D), PBE-D3(BJ), PBE-dDsC. Those optimized bulks are non magnetic. Lattice parameters (a, c, Å), cohesion energy (E_{coh}, eV/at.), formation energy (E_{form}, eV/$LiNH_2$), bulk modulus (B_0, GPa) and its derivative (B_0, dimensionless). Experimental crystallographic and energetic data are also reported.

System	Ru Bulk					$LiNH_2$				
Functional	GGA PBE	DFT-D3 PBE(0D)	DFT-D3 PBE(BJ)	dDsC PBE	Exp.	GGA PBE	DFT-D3 PBE(0D)	DFT-D3 PBE(BJ)	dDsC PBE	Exp.
a (Å)	2.71(5)	2.69(2)	2.69(2)	2.70(1)	2.7059[419]	5.00(4)	4.89(8)	4.85(1)	4.85(2)	5.0344[421]
c (Å)	4.28(0)	4.24(8)	4.25(0)	4.26(2)	4.2815[419]	10.32(5)	10.13(1)	10.07(6)	10.13(4)	10.2556[421]
E_{coh} (eV/$LiNH_2$)	-7.19(4)	-7.75(3)	-7.75(0)	-7.56(4)	-6.74[420]	-3.36(0)	-3.38(0)	-3.40(7)	-3.36(9)	
E_{form} (eV)						-2.07(4)	-2.05(8)	-2.09(3)	-2.07(0)	-1.82[422]
B_0 (GPa)	310	311	312	311	303[420]	24	30	31	30	
B'_0	4.8	4.7	4.6	4.7		4.8	4.9	4.9	4.1	

V.1.2 $LiNH_2$ bulk

$LiNH_2$ adopts a body-centered tetragonal structure, with its low-temperature phase exhibiting a cubic anti-fluorite-like crystal structure characterized by the space group $I\bar{4}$.[423, 421, 335, 170] The crystallographic details of $LiNH_2$ are presented in Figure V.2 and Table VII.4. In describing the bulk properties of $LiNH_2$, the role of long-range van der Waals interactions becomes significant, particularly between the fragments composing the crystalline structure. While the equilibrium distances between the NH_2^- fragments and Li^+ ions are relatively long (2.0508 and 2.2406 Å), these non-covalent interactions contribute to the overall structural cohesion alongside the electrostatic forces arising from the charges carried by the atoms.

For $LiNH_2$ bulk, the cohesion E_{coh} and formation E_{form} energies, which are addressed in Table VII.4, have been defined as follows:

$$E_{coh} = \frac{E_{LiNH_2(s)} - N_{Li} \times E_{Li} - N_N * E_N - N_H \times E_H}{N_{at,\, LiNH_2(s)}} \tag{V.1}$$

where $E_{LiNH_2(s)}$, E_{Li}, E_N and E_H being total electronic energies of $LiNH_2$ stoichiometric bulk, gas phase isolated Li, N and H atoms, respectively; N_{Li}, N_N and N_H being the total numbers of Li , N and H atoms in the $LiNH_2$ stoichiometric bulk, respectively; $N_{at,\, LiNH_2(s)}$ being the total number of atoms in the $LiNH_2$ stoichiometric bulk.

$$E_{form} = \frac{E_{LiNH_2(s)} - N_{Li} \times E_{Li,\,bulk} + N \times E_{N_2} + N_H \times E_{H_2}/2}{N_{unit,\,LiNH_2(s)}} \quad \text{(V.2)}$$

where $E_{\text{Li, bulk}}$, E_{N_2} and E_{H_2} being the total electronic energies of Li *BCC* bulk, gas phase N_2 and H_2 isolated molecules, respectively; N_{N}, N_{H} and $N_{\text{unit, LiNH}_2\text{(s)}}$, being the total numbers of N atoms, H atoms and $LiNH_2$ units in the $LiNH_2$ stoichiometric bulk, respectively.

Now let us examine the DFT predictions for $LiNH_2$ bulk materials. Concerning the optimal values of the lattice parameters, the standard GGA PBE functional offers a good description with systematic errors of -0.6 % for a and +0.7 % for c, respectively by comparison with measurements (see Table VII.4). Moreover, our GGA PBE results are in fair agreement with previous theoretical studies using various codes and computational conditions (LDA, GGA PW91, PBE, PAW, ultrasoft pseudopotentials) where van der Waals interactions were systematically neglected.[328, 329, 330, 424, 425, 426, 334] Those reasonable predictions of the crystal structure get worse when dispersion-corrected functionals are considered in the calculations, with a systematic decrease of a and c parameters, compared to GGA PBE. One can conclude that PBE-D3(0D) offers the smallest decrease for a with an error of -2.7 %, whereas PBE-dDsC provides a reasonable compromise for c with an error of -1.2 %. Hence, not to consider van der Waals interactions in the description of $LiNH_2$ bulk would be better regarding its crystalline structure, just like Ru bulk.

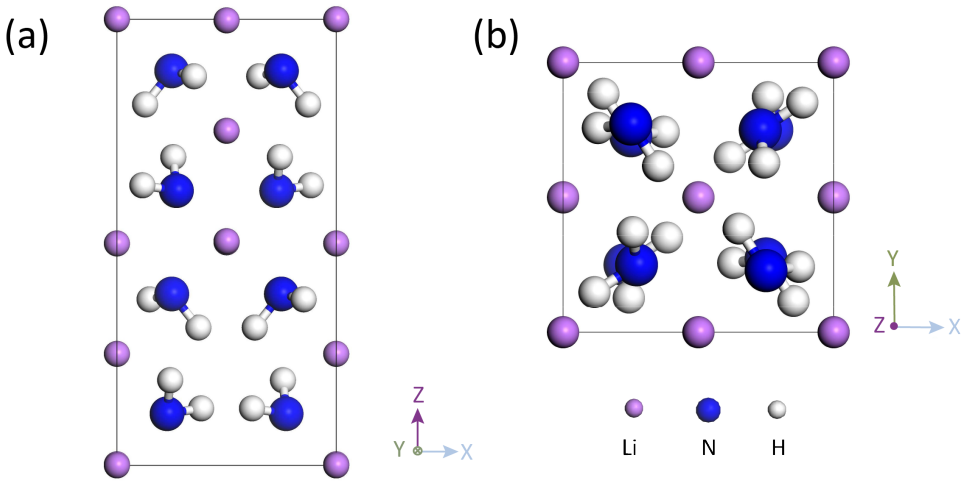

Figure V.2: Bulk structure of low-temperature $LiNH_2$ phase $I\bar{4}$ (a) along the [100] direction and (b) along the [001] direction.[423, 421, 335, 170]

At the level of energetics, a direct comparison with measurements can not be achieved neither for cohesion energy nor for bulk modulus, due to the lack of experimental data for $LiNH_2$. However previous theoretical studies have reported on cohesion energies of -3.08 eV/at,[329] and 12.086 eV.[334] The first value is compatible with our DFT results from -3.36 eV/at (GGA PBE) to -3.41 eV/at (PBE-D3(BJ)), as reported on Table VII.4. The second previously reported value also agrees with our computed cohesion energies, when a different normalization is considered (total number of NH_2 fragments or Li atoms, instead of the total number of atoms).

As one could expect, the cohesion energy increases when the dispersion correction is considered. PBE-dDsC registers the smallest increase (-3.37 eV/at) compared to GGA PBE (-3.36 eV/at).

For $LiNH_2$ bulk modulus, our predicted values in the range 24-30 GPa depending on the functional are in fair agreement with a previous study addressing a value of 33 GPa,[329] while being two times lower than another result reported more recently (77.9 GPa).[334] The bulk modulus derivative is quite similar for both Ru and $LiNH_2$ bulk (4.8) and agrees with previous DFT calculations (3.6).[334] The evaluated formation energy of $LiNH_2$ bulk varies from -2.07 to -2.35 eV/$LiNH_2$ (corresponding to -199.6 to -226.6 kJ.mol^{-1}/$LiNH_2$, respectively), depending on the functional (see Table VII.4). These values agree fairly well with formation enthalpy measurements at 298 K (-1.82 eV or -176 kJ.mol^{-1})[422] and with previous theoretical predictions at the GGA level (-196.5 kJ.mol^{-1};[328] -212.5 kJ.mol^{-1};[329] -199.2 kJ.mol^{-1};[424] -212.3 kJ.mol^{-1}).[426]

To conclude this analysis concerning the calibration of the DFT approach, we have then decided to keep two functionals for investigating the surfaces and the interfaces of both Ru and $LiNH_2$ materials: GGA PBE offering a good predictive power, both on structure and energetics, and PBE-dDsC as the dispersion-corrected functional exhibiting the smallest deviations with respect to the standard GGA PBE level. Note in passing that the inclusion of van der Waals long-range interactions may be required for interface reaction intermediates and especially for NH_3 adsorption and N_2 desorption.

V.2 Clean Surfaces

V.2.1 Ru(0001) surface

The next important step before generating interfaces between the two materials is the investigation of the DFT models for the clean Ru and $LiNH_2$ surfaces. On the basis of the two previously selected functionals, we have first examined the most abundant Ru(0001) surface, as the most stable Ru surface. In order to evaluate the convergence of the surface energy with respect to the slab thickness, symmetric slabs have been considered with various thicknesses in the range 5-13 atomic layers by using the smallest (1×1) supercell.

In these models, the three central atomic planes have been kept frozen to the ideal relaxed bulk geometry, while the remaining surface layers have been symmetrically optimized on both sides of the slabs. The vacuum space used to separate two equivalent Ru(0001) slabs along the z axis is 15 Å. Such a vacuum space is enough to avoid spurious interactions between equivalent periodic slabs along the z axis. By examining the convergence of the surface energy (see Equation V.3) as a function of the slab thickness, an absolute systematic error below $\pm$0.007 J.m^{-2} is obtained for models with a minimal thickness of 13 layers (see Figure V.3). For such thick model, the calculated surface energy of 2.59 J.m^{-2} is in very good agreement with available measurements (2.65 J.m^{-2} as reported in Table V.4). In the case of PBE-dDsC, the predicted surface energy of 3.02 J.m^{-2} is larger than the GGA PBE value, in line with the larger bulk cohesion energy discussed previously. This validates once again the choice of the GGA PBE functional. Since a 13-layer symmetric slab

can be effectively represented by a non-symmetric slab of half thickness (7 layers), later parts of this study will consider non-symmetric Ru(0001) slabs with a minimal equivalent thickness of 7 layers.

The stability of the clean Ru(0001) surface have been determined by evaluating the surface energy as follows. For Ru(0001), the surface energy $\gamma(Ru(0001))$ is calculated by considering the HCP bulk as the reference:

$$\gamma_{Ru(0001)} = \frac{E_{Ru(0001)} - N_{Ru(0001)} \times E_{Ru}/2}{2 \times \mathcal{A}_{Ru(0001)}} \tag{V.3}$$

where $E_{\text{Ru(0001)}}$ is the total electronic energy of the relaxed clean Ru(0001) surface, E_{Ru} being the total electronic energy of the HCP Ru Bulk (containing 2 atoms in the unit cell), $N_{\text{Ru(0001)}}$ being the total number of Ru atoms in the Ru(0001) slab and $\mathcal{A}_{\text{Ru(0001)}}$ being the surface area of the Ru(0001) model slab.

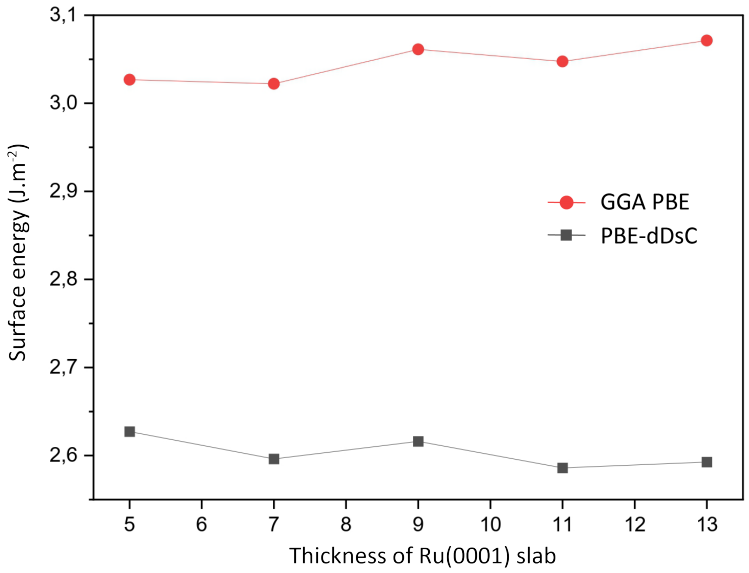

Figure V.3: Convergence of surface energy for Ru(0001) as a function of the slab thickness.

V.2.2 $LiNH_2$ surfaces

In the case of $LiNH_2$ materials, the choice of the clean surface in our study has been based on structural mismatch considerations between the HCP stacking of Ru and BCT crystallinity of $LiNH_2$. The (001) surface selected in this work offers the smallest supercell and minimal structural mismatch when the latter is interfaced with Ru(0001). In fact, $LiNH_2$(001) surface can be modeled with a square (1×1) supercell of length a (5.03 Å from experiments), while Ru(0001) hexagonal structure can be modeled by a rectangular $(2 \times \sqrt{3})$ supercell of lengths 5.40 Å (2×2.70) and 4.68 Å $(\sqrt{3} \times 2.70)$. With structural mismatches of -6.8% and 7.5% along a and c at the interface between Ru(0001) and $LiNH_2$(001), $LiNH_2$(001) is thus a reasonable compromise to elaborate interface models with Ru(0001).

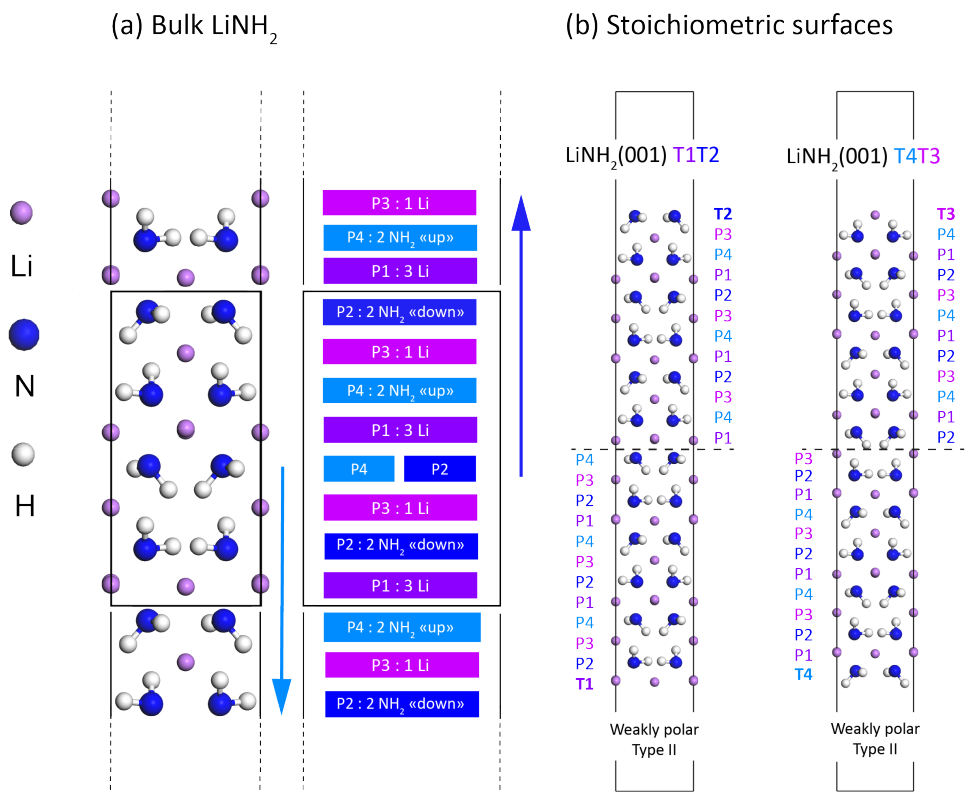

Figure V.4: (a) Definitions and notations related to the four planes (P_i, i=1,...,4) in the bulk of $LiNH_2$ materials leading to the generation of four surface terminations for $LiNH_2$(001) (noted T_i, i=1,...,4, respectively). Please note that in our lateral view, two of the three Li atoms of P1 plane are superposed. In the bulk, the notations of the Li and NH_2 planes are symmetrized starting from a hypothetic central NH_2 plane, in order to be able to define the equivalent planes in the symmetric slabs of $LiNH_2$(001), by following the blue arrows. (b) Bulk truncated structures of the two possible stoichiometric, neutral and pristine terminations for the $LiNH_2$(001) surface (see Figures VI.S2 and S2 in the Appendix for the optimized structures). According to our notations, the T2 termination corresponds to a surface composed of NH_2 fragments pointing toward $LiNH_2$ materials ("NH_2 down"), whereas, in T4 termination, the surface NH_2 moieties are pointing toward vacuum ("NH_2 up"). The notations of the different planes are following the definitions of the bulk exposed in (a). Labels and colors of atoms are depicted.

In $LiNH_2$(001), the layer stacking offers four different possible terminations (when the materials is cut perpendicularly to the [001] row), noted T1, T2, T3 and T4, which correspond respectively to the P1, P2, P3 and P4 planes of the bulk structure along the [001] row, as illustrated in Figure V.4. According to these notations, T1 termination leads to slabs composed of terminal planes presenting 3 Li atoms, while T3 termination generates slabs with terminal layers composed of 1 Li atom. In addition, T2 termination leads to slabs with surfaces exhibiting NH_2 fragments oriented toward the materials (the hydrogen atoms defining the convention of orientation and leading to the notation "NH_2 down"), whereas T4 termination leads to slabs with surfaces presenting NH_2 fragments pointing toward vacuum (noted "NH_2 up").

To evaluate the stability of the four possible terminations for $LiNH_2$(001), their surface energies must be determined. The surface models of $LiNH_2$(001) intrinsically have two terminal planes. When these terminal planes have the same composition, the surface energy obtained from DFT calculations will correspond to twice the surface energy the terminal plane, as both termination contribute equally to the total energy.

However, calculating surface energies require to subtract the bulk energy from the calculated surface energy, the model must represent an integer multiple (x) of the bulk unit.

Unfortunately, to respect the stoichiometry of $LiNH_2$ bulk in the surface models, the terminations of $LiNH_2$(001) must consist of different termination types (e.g., T1T2 or T3T4), as illustrated in Figure V.5. As a result, it is not possible to directly determine the surface energies of individual terminations (T1, T2, T3, and T4). Instead, only the combined surface energies of paired terminations (T1+T2 and T3+T4) can be calculated. To obtain the surface energy of each termination individually, surface models must be constructed with identical terminations on both sides, such as T1T1, T2T2, T3T3, or T4T4.

This requirement introduces an additional complication: slabs with identical terminations consist either of Li planes (positively charged) or NH_2 planes (negatively charged), making them fully polar (Type III). In contrast, stoichiometric slabs, such as T1T2 and T3T4, are weakly polar (Type II) because the charge is compensated by having one positively charged termination and one negatively charged one. However, by working with symmetrical slabs for the non-stoichiometric $LiNH_2$(001) surface models, the dipole moment is compensated and close to zero (see Figure V.5.b).

Therefore, to determine the surface energies of the four possible $LiNH_2$ terminations, it is necessary to develop an adapted bulk model that can accurately predict the total electronic energy of any bulk $LiNH_2$ composition, whether stoichiometric or non-stoichiometric. This model will be essential not only for analyzing $LiNH_2$(001) surfaces but also for studying interfaces between Ru(0001) and $LiNH_2$(001). Hence, the surface energies $\gamma_{LiNH_2(001)(\sigma,T_i)}$ and $\gamma(LiNH_2(001)(\sigma,T_j))$ of the two terminations T_i and T_j of the stoichiometric ($\sigma = s$) or non-stoichiometric ($\sigma = ns$) slab model are derived as follows:

$$\gamma_{LiNH_2(001)(\sigma,\,T_i)} + \gamma_{LiNH_2(001)(\sigma,\,Tj)} = \frac{E_{LiNH_2(001)(\sigma,\,T_iT_j)} - E_{LiNH_2(\sigma)}}{\mathcal{A}_{LiNH_2(001)}} \tag{V.4}$$

where $E_{LiNH_2(001)(\sigma,\ T_iT_j)}$ is the total electronic energy of the stoichiometric or non-stoichiometric slab of $LiNH_2$(001) containing the terminations T_i and T_j, $E_{LiNH_2(\sigma)}$ being the total electronic energy of the stoichiometric or non-stoichiometric lithium amide bulk and $\mathcal{A}_{LiNH_2(001)}$ being the surface area of the $LiNH_2$(001) surface model.

Examples of mixed T1T2 and T3T4 and pristine T1T1, T2T2, T3T3 and T4T4 $LiNH_2$(001) slabs are presented in Figures V.4 and V.8.In all our DFT symmetric models of clean $LiNH_2$(001), the retained supercell is then the (1×1) with a vacuum space of 15 Å. Regarding the thickness of the six considered models, it depends on the considered terminations.

V.2.2.1 Non stoichiometric $LiNH_2$ bulk energetic model

The calculation of total electronic energy of the lithium amide bulk (stoichiometric or non-stoichiometric) $E_{LiNH_2(\sigma)}$ is based on the determination of the elementary interaction pairs between Li atoms $E_{Li–Li}$, NH_2

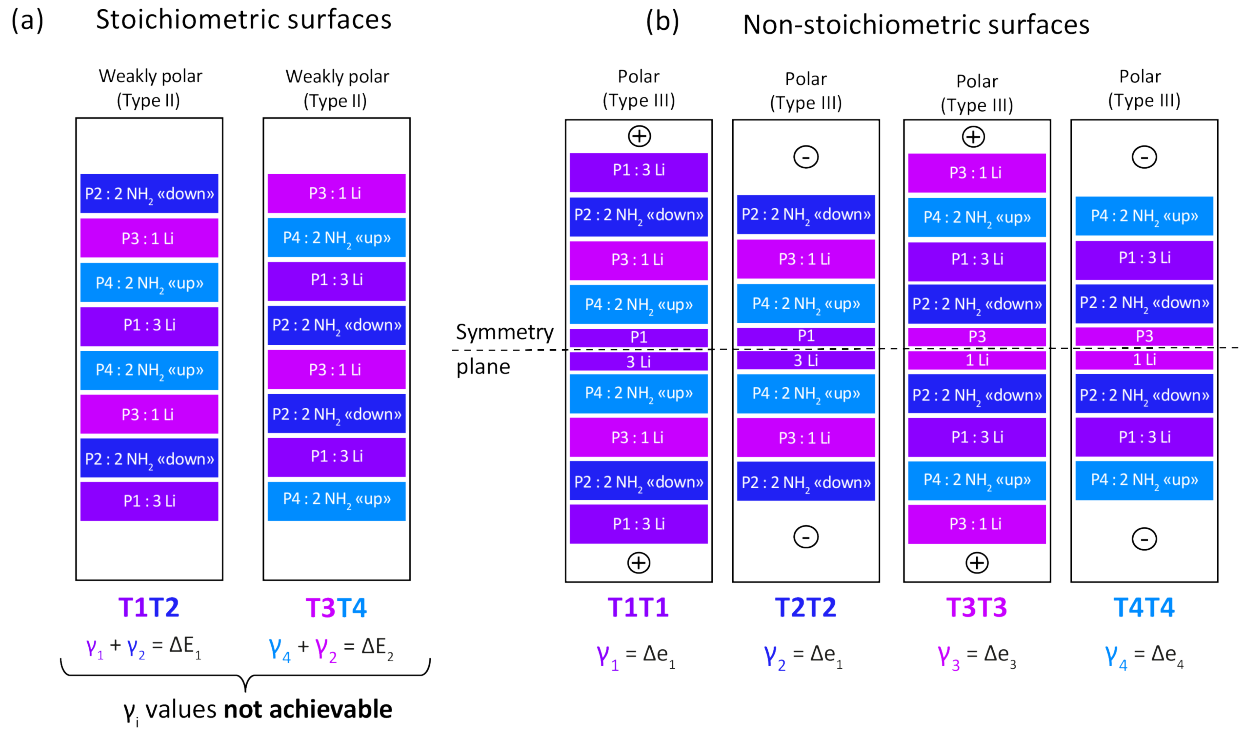

Figure V.5: Schematic representation of the different possible surface terminations: (a) stoichiometric and weakly polar T1T2 and T3T4 slabs; (b) non-stoichiometric and polar T1T1, T2T2, T3T3, and T4T4 slabs, where the symmetric construction compensates for the dipole moment of the system.

fragments $E_{NH_2–NH_2}$ and, Li and NH_2 fragments $\tilde{E}_{Li–NH_2}$, obtained on the basis of an energy decomposition analysis (EDA).

The Li–Li and NH_2–NH_2 two-body interaction terms are evaluated by calculating separately the total electronic energies of the corresponding frozen isolated fragments "Li" and "NH_2" resulting from the optimized structure of the complete and stoichiometric $LiNH_2$ bulk at both GGA PBE and PBE-dDsC levels. The non-additivity of the model is thus derived by subtracting the DFT total electronic energies of the complete bulk and the isolated atoms from Equation V.1 and the two-by interaction terms Li–Li and NH_2–NH_2, which are exposed in Table V.2. This EDA model has been derived as follows and can be compared to previous theoretical developments[329]:

$$E_{LiNH_2(\sigma)} = N_{Li} \times E_{Li-Li} + E_{Li} + N_{NH_2} \times E_{NH_2-NH_2} + E_{NH_2} + N_{Li-NH_2} \times \tilde{E}_{Li-NH_2} \quad \text{(V.5)}$$

where N_{Li}, N_{NH_2}, $N_{Li–NH_2}$ are the number of Li atoms, NH_2 fragments and of Li–NH_2 chemical bonds, respectively, E_{Li} and E_{NH_2} being the total electronic energy of Li atom and NH_2 fragments, respectively.

Table V.2: Energetic contributions in the additive model predicting the total electronic energy of $LiNH_2$ bulk: two-body interaction energy terms (Li-Li, NH_2-NH_2, Li-NH_2 at the GGA PBE and PBE-dDsC levels in (eV).

	Two-body interaction energy terms	
Functional	GGA PBE	PBE-dDsC
Li - Li	-0.52(2)	-0.56(6)
NH_2 - NH_2	0.07(3)	-0.09(5)
Li - NH_2-NH_2	-1.19(8)	-1.15(5)

V.2.2.2 $LiNH_2$(001) stoichiometric and non-stoichiometric surfaces energies

For the mixed T1T2 and T3T4 non symmetric slabs, the chosen thickness of our models is 24 planes, as shown in Figure V.4 for the initial geometries and Figures VI.S2-S2 in the appendix for optimized structures at both GGA PBE and PBE-dDsC levels. For the T1T1, T2T2, T3T3 and T4T4 pristine and symmetric slabs, the thickness varies from 23 to 25 planes, as illustrated in Figure V.6 for starting geometries and Figures S3-S6 for optimized structures at GGA PBE and PBE-dDsC levels.

During the geometry optimizations, the models containing T2 terminations (especially T1T2 and T2T2 slabs) with "NH_2 down" configurations at the surfaces, have undergone a surface reconstruction corresponding to a rotation of the NH_2 terminal fragments from a "down" configuration to a "up" position (thus leading to a reconstructed termination noted T4'), as illustrated in the appendix in Figures VI.S2 and S4. Hence, to ensure the optimization of T2 terminations in these cases (non reconstructed systems) and allow the evaluation of their surface energies, we had to freeze the positions of terminal NH_2 fragments in their initial configurations ("NH_2 down"). Similar geometric constraints have also been considered for three other T1T1, T3T4, T4T4 systems, especially to keep the orientation of the NH_2 fragments close to the surfaces. The only system which could be completely relaxed without losing the bulk crystallinity is T3T3. Apart from the necessary geometrical constraints at the terminal planes, all the degrees of freedom of all the other atoms belonging to internal planes have been systematically relaxed in the 5 DFT models of $LiNH_2$(001) surfaces (T1T2, T3T4, T1T1, T2T2, T4T4). In the appendix, the constrained optimized geometries and the fully relaxed structures presenting reconstructions have been reported in the Figures VI.S2-S6. The relative stability between the four possible terminations of $LiNH_2$(001) is then determined by calculating the surface energies as introduced in Equation V.4. Conversely to Ru(0001) model, the terminations of $LiNH_2$(001) models can be either identical (T_iT_i) or different (T_iT_j) in the slabs. This explains the generalization of the equation related to the calculation of surface energies. The symmetric slabs related to the T_iT_i non stoichiometric models allow the evaluation of the surface energy $\gamma(\sigma, t_i)$ of each termination T_i, as soon as the total electronic energy of the non stoichiometric equivalent bulk system ($E_{LiNH_2(\sigma)}$) is known.

In Table V.3, the predicted surface energies of the four terminations of $LiNH_2$(001) have been reported for both GGA PBE and PBE-dDsC functionals. Three terminations (T1, T2 and T4) are magnetic (from 1 to 3 μ_B) while T3 is diamagnetic. We conclude that the lithium terminated slabs T1 and T3 (4.77 J.m^{-2} and 1.53 J.m^{-2}, respectively) are less stable than the NH_2 terminated surfaces T2 and T4 (0.35 J.m^{-2} and 0.01 J.m^{-2},

respectively) with the GGA PBE functional. This trend is identical at the PBE-dDsC level, as exposed in Table V.3. According to these weakly polar symmetric model slabs, the "NH_2 up" terminated surface of $LiNH_2$(001) is the most stable one with a very weak surface energy for both functionals. Due to the weak polarity of the four symmetric non stoichiometric models of $LiNH_2$(001), the relevance of the predicted surface energies can be determined from the two other stoichiometric and neutral non symmetric slabs T1T2 and T3T4. Those two systems allow the evaluation of the sum of two surface energies : $\gamma(\sigma, t_1) + \gamma(\sigma, t_2)$ or $\gamma(\sigma, t_3) + \gamma(\sigma, t_4)$. The calculated values are reported in Table V.3. By summing the previously calculated surfaces energies of the four terminations predicted from the symmetric slabs, we calculate the systematic error between the models: 2% (1%) for T1T2 and 6% (5%) for T3T4 at the GGA PBE (PBE-dDsC) level. Since these systematic errors are reasonable with both functionals, the predicted surface energies of $LiNH_2$(001) terminations are thus validated.

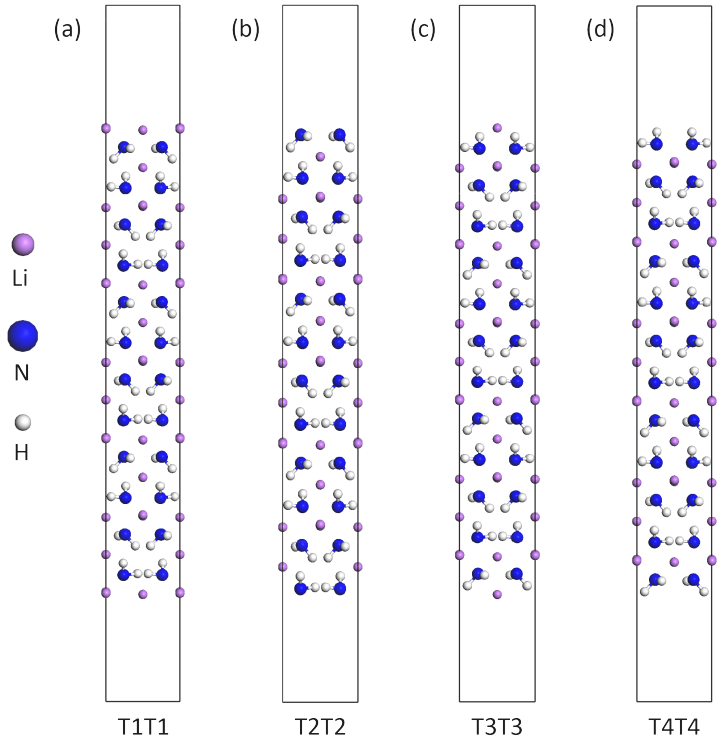

Figure V.6: Lateral views of the four possible bulk truncated symmetric and unrelaxed models of non stoichiometric, polar and pristine $LiNH_2$(001) surfaces: (a) T1T1, (b) T2T2, (c) T3T3, (d) T4T4 terminations. See Figures S3-S6 of the Appendix for the optimized structures.Labels and colors of atoms are depicted.

By the light of this analysis, the interfaces between $LiNH_2$(001) and Ru(0001) exhibiting a termination T4 not in contact with Ru is thus expected to be preferential from the energetic standpoint. This being said, the best choice among the four $LiNH_2$(001) terminations to generate an interface and a contact with Ru cannot be easily guessed. To advance on this question, the adsorption properties of Li atom and NH_2 fragment on Ru(0001) have to be investigated in preamble.

Table V.3: Surface energies (J.m^{-2}) and magnetization (μ_B) of optimized Ru(0001) (7 atomic layers) and $LiNH_2$(001) (from 23 to 25 planes) clean slabs according to pure GGA PBE and dispersion-corrected PBE-dDsC functionals. For $LiNH_2$(001), the four possible terminations (T_i) can be combined into two stoichiometric, neutral and pristine mixed slabs (T1T3 and T3T4) or four non stoichiometric, polar and pristine symmetric systems (T1T1, T2T2, T3T3 and T4T4).

System	Terminations	Surface energy			Magnetization	
Functional		GGA PBE	PBE-dDsC	Refs.	GGA PBE	PBE-dDsC
Ru(0001)	-	2.59(6)	3.02(2)	2.65[427]	-	-
$LiNH_2$(001)	T1T2	5.00(7)	5.57(4)		2.73(5)	1.64(6)
	T3T4	1.45(6)	1.83(0)		0.37(7)	0.37(9)
	T1T1	4.77(3)	5.17(7)		2.77(2)	1.64(5)
	T2T2	0.35(4)	0.48(9)		-3.00(0)	3.00(0)
	T3T3	1.53(5)	1.73(1)		0	0
	T4T4	0.01(5)	0.20(8)		0.99(8)	0.99(8)

V.3 Adsorptions on Ru(0001)

V.3.1 Li adsorption

For the adsorption studies of a Li atom and NH_2 fragment on the clean Ru(0001) surface, a non-symmetric slab model was employed, consisting of seven atomic layers with 4 Ru atoms per layer and a (2×2) supercell. This choice was guided by the results from the thickness convergence study of Ru(0001) (see Section V.2.1). A vacuum space of 15 Å was introduced along the z-axis to avoid spurious interactions between periodic replicas of the slab. In the Ru(0001) slab model, the three bottommost atomic layers were kept fixed at the ideal relaxed geometry of Ru HCP bulk, as determined by the selected functional, to simulate bulk-like behavior. Meanwhile, the four topmost atomic layers were fully relaxed to capture surface-specific atomic and electronic rearrangements.

Regarding now the definition of the adsorption energy E^A_{ads} of a Li atom or a NH_2 fragment on Ru(0001), the usual formula has been derived:

$$E^A_{ads} = E_{A/Ru(0001)} - E_{Ru(0001)} - E_A \tag{V.6}$$

where $E_{\text{A/Ru(0001)}}$ is the total electronic energy of the adsorbate A (being Li or NH_2) on a non symmetric Ru(0001) slab, $E_{\text{Ru(0001)}}$ being the total electronic energy of the clean Ru(0001) surface and E_{A} being the total electronic energy of an isolated A species in the gas phase (atom for Li and relaxed fragment for NH_2).

For atomic adsorption of one Li atom, four classical adsorption sites have been considered : onefold top, twofold bridge, threefold hollow HCP and threefold hollow free. The optimized structures have been presented in Figure V.7 and adsorption energetics (see Eq. V.6 for definition) and optimal distances in Table V.4 at the GGA PBE level. Based on the adsorption energy of Li on Ru(0001), a slight preference is observed for the two hollow sites (-2.53 eV), followed by the bridge site (-2.50 eV). The predicted adsorption energy for the best sites is in fair agreement with heat of adsorption measurements[428] (see Table V.4), while the

calculated Ru–Li distances at our GGA PBE level are larger than those obtained previously from LDA calculations,[429, 430] as expected.

Table V.4: Adsorption properties of Li atom and NH_2 fragment on Ru(0001) (GGA PBE, coverage 0.25 ML): adsorption site, energy E_{ads} (eV), key distances (Å).

System	Li					NH_2	
Site	Top	Bridge	Hollow HCP	Hollow free	Refs.	Bridge	Refs.
E_{ads} (eV)	-2.33	-2.50	-2.53	-2.53	-2.5 [a]	-2.97	-2.95 [d]; -3.01 [e]
Ru-Li (Å)	2.42	2.62	2.71	2.71	2.22 [b]; 2.13 [c]		
Ru-N (Å)						2.12(2)	2.13 [d,f]
N-H (Å)						1.02(1)	1.015 [d,f]

[a] Experimental for a surface coverage of 0.020 ML[428], [b] LDA calculation at a coverage of 0.25 ML[429], [c] LDA calculation at a coverage of 0.25 ML[430], [d] GGA B88XP86C calculation at a coverage of 1/6 ML[431], [e] GGA PW91 at a coverage of 0.25 ML[282], [f] GGA rPBE at a coverage of 1/16 ML[432]

V.3.2 NH_2 adsorption

For the adsorption of one NH_2 fragment on Ru(0001), only one structure is found stable (see Table V.4 and Figure V.7): a twofold bridge position with NH_2 fragment oriented perpendicularly with respect to the Ru-Ru bridge site, in agreement with previous theoretical studies.[281, 431, 282, 432] The top adsorption form is not stable and the NH_2 fragment diffuses spontaneously toward a bridge position during the geometry optimization. The adsorption energy of NH_2 fragment with respect to radical NH_2 gas phase reference is -2.97 eV, thus more exothermic than the energy gain for the best adsorption site for Li atom. The adsorption energetics and optimized geometry are in close agreement with previous DFT calculations performed with various GGA functionals and surface coverage, as shown in Table V.4.[431, 282, 432]

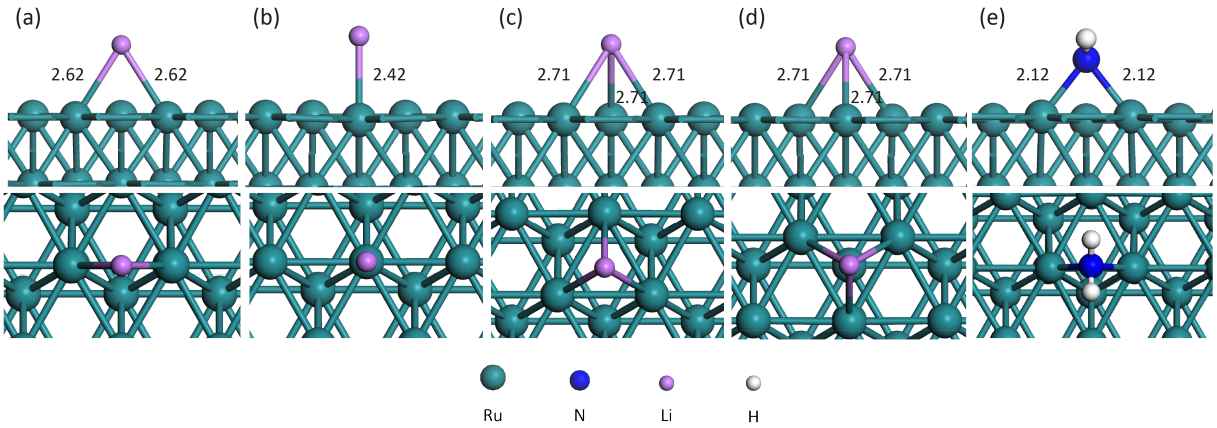

Figure V.7: Lateral and top views of optimized adsorption structures of a Li atom on Ru(0001): (a) bridge, (b) top, (c) hollow free and (d) hollow hcp positions. (e) Lateral and top views of the optimal adsorption structure of a bridge-bonded NH_2 fragment on Ru(0001). Distances are addressed in Å. Labels and colors of atoms are depicted.

Hence, in the perspective of the elaboration of Ru/$LiNH_2$ interface models, the choice of the best termination of $LiNH_2$(001) to be in contact with Ru(0001) is not clear cut at this stage due to the competition between adsorption strengths of Li and NH_2 on Ru(0001). As a consequence, in the following section devoted to those interfaces, the two possible contacts between materials (through either Li or NH_2) will be addressed and compared.

V.4 Ruthenium-Lithium Amide Interfaces

V.4.1 Prerequisites for interfacing the two solids

In the following section, the DFT models of interfaces between Ru(0001) and $LiNH_2$(001) surfaces will be developed by using the previous results obtained from bulk materials, clean surfaces and adsorption properties. Regarding the calibration of the Ru(0001) slab, we have minimized the computational effort by choosing:

- the smallest supercell which can be interfaced with $LiNH_2$(001) slabs with a minimal structural mismatch : $(2 \times \sqrt{3})$
- the minimal thickness required to have converged surface energy for Ru(0001) : 7 layers (the three bottom most atomic planes being frozen, while the four upmost layers being totally relaxed, such as the adsorption models exposed in the previous section).
- the vacuum space considered in the interface models is in the range 10-20 Å.
- in all the DFT interface models, the volume of the 3D boxes have not been further relaxed after having set both materials in contact; the optimal parameters of Ru bulk of each functional imposing the size of the 3D boxes due to the much larger rigidity of Ru bulk than the one of LiNHtextsubscript2 material (see the computed bulk moduli in Table VII.4).

Concerning now the working principles for generating interfaces between materials (see Figure V.8 for examples), we have ensured that:

- the $LiNH_2$(001) slabs are interfaced with Ru(0001) by considering both contacts with terminations maximizing the interface energy: either the $LiNH_2$(001) surface is composed of Li atoms (3 atoms in T1, cf. Figure V.8 a and b) and of NH_2 fragments (2 fragments in "NH_2 down" configuration in T2, cf. Figure V.8(c) and (d)). The notation of interfaces will thus be Ru@T_iT_j, where T_i is in direct contact with Ru(0001) slab.
- the contacts between $LiNH_2$(001) and Ru(0001) slabs have been chosen to reproduce as much as possible the most stable adsorption forms of Li atom and NH_2 fragment, as reported in the previous section.

- for the $LiNH_2$(001) slabs, there are four possible terminations to stop the interface models toward vacuum. For each case, two different $LiNH_2$(001) thicknesses have been considered to probe the convergence of interface properties. In our interface models, the $LiNH_2$(001) slab thickness ranges from 9 to 17 (Li or NH_2) planes. At this stage, this leads to 16 possible interface models.
- the $LiNH_2$(001) slab in the interface can be stoichiometric ($\sigma = s$) (cf. Figure V.8 a) or non-stoichiometric ($\sigma = ns$) (cf. Figure V.8 b, c and d) as previously evoked for $LiNH_2$(001) surfaces. This slab can be also neutral (n) (cf. Figure V.8 a), polar (p) and neutralized (nz) either by the adsorption of Li or NH_2 at the contact between materials (cf. Figure V.8 b) or by generating defects such as one or several vacancies (v) related to Li atoms (vLi) (cf. Figure V.8 c) or NH_2 fragments (vNH_2) (cf. Figure V.8 d). When there is no defect or vacancy, the $LiNH_2$(001) slab is pristine (ps) (cf. Figure V.8 a and b).
- to take into account all these possibilities in the notation, we introduce a general name for all our interfaces : Ru@T_iT_j(N_l,σ,p,v), where N_l is the number of layers in $LiNH_2$(001), σ the stoichiometry of $LiNH_2$(001), p its polarity and v its defect degree.
- the spin polarization is considered in all the interface models.

The interface energy between Ru(0001) and $LiNH_2$(001) slabs (composed of terminations T_i and T_j) noted $\Gamma_{LiNH_2(001)(\sigma,\ T_iT_j)/Ru(0001)}$ is derived by generalizing the concept of surface energy of these materials. It has thus been calculated by considering Ru and $LiNH_2$ bulks as references, as follows:

$$\Gamma_{LiNH_2(001)(\sigma,\ T_iT_j)/Ru(0001)} = \frac{E_{LiNH_2(001)(\sigma,\ T_iT_j)/Ru(0001)} - (E_{LiNH_2(\sigma)} + E_{Ru})}{\mathcal{A}_{LiNH_2/Ru}} \tag{V.7}$$

where $E_{LiNH_2(001)(\sigma,\ T_iT_j))/Ru(0001)}$ is the total electronic energy of the interface model between Ru(0001) and $LiNH_2$(001) slabs ($LiNH_2$(001) slab being either stoichiometric or non-stoichiometric with two T_i and T_j terminations) and $\mathcal{A}_{LiNH_2/Ru}$ being the surface area of the interface model.

By using these working principles and corresponding notation, we could have created 25 interface models, of which interface energetics has been addressed in Table V.5 and in Figure V.9, and of which the optimized structures of the most stable systems have been illustrated in Figure V.10. All the illustrations of the optimized interface structures, at both GGA PBE and PBE-dDsC levels, have been reported in appendix (Figures S7-S18).

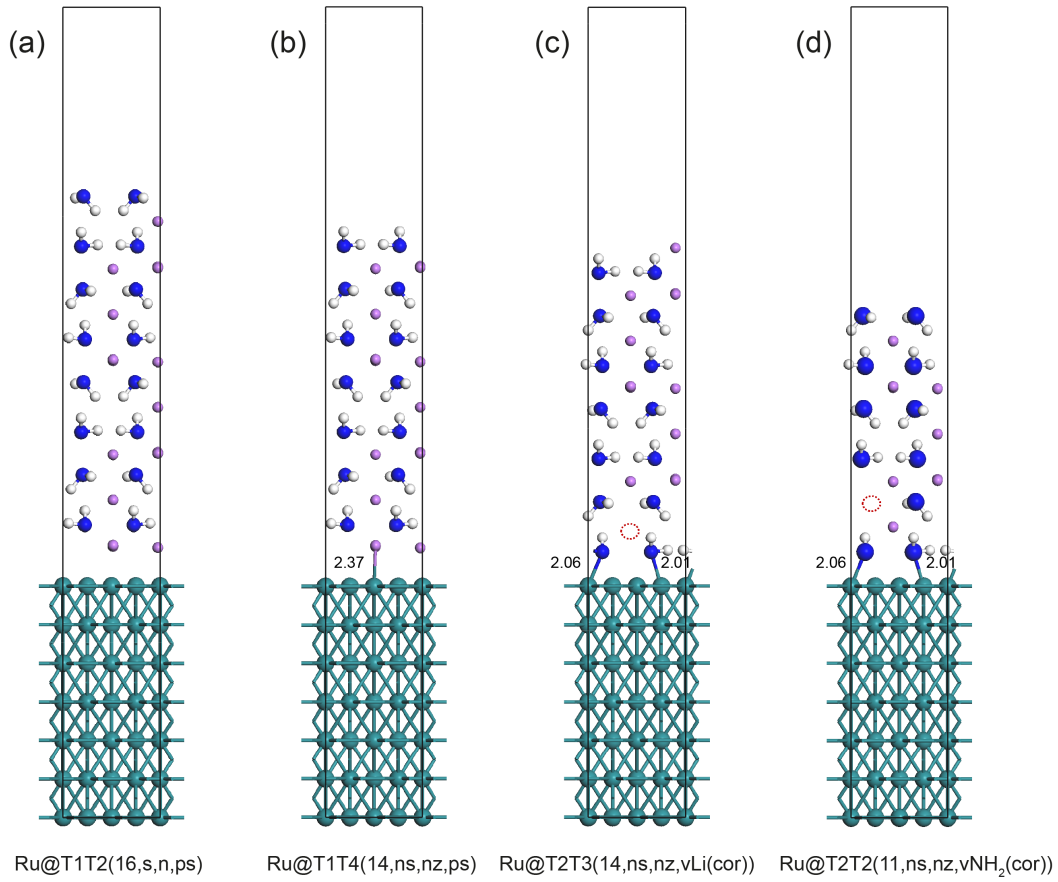

Figure V.8: Lateral views of starting geometries of Ru(0001)/$LiNH_2$(001) typical interfaces. A $(2 \times \sqrt{3})$ supercell is chosen to minimize the materials structural mismatch: (a) stoichiometric (s), neutral (n) and pristine (ps) Ru@T1T2(16,s,n,ps) interface (composed of 16 layers of $LiNH_2$); (b) non-stoichiometric (ns), neutralized (nz) and pristine Ru@T1T4(14,ns,nz,ps) interface (composed of 14 layers of $LiNH_2$); (c) non-stoichiometric, neutralized and defective Ru@T2T3(14,ns,nz,vLi(cor)) interface (with a single Li vacancy in the core, noted vLi(cor), of 14 layers of $LiNH_2$); (d) stoichiometric, neutralized and defective Ru@T2T2(11,ns,nz,vNH_2(cor)) interface (with a single NH_2 vacancy in the core, noted vNH_2(cor), of 11 layers of $LiNH_2$). Single vacancies are marked by red dotted line circles. Distances are expressed in Å. The colors and atom labels are those depicted in previous Figures V.8-V.7.

Table V.5: Interface name, interface energy (J.m$_2$), total magnetization (μB) and energy decomposition analysis (sum of surface energies of separated materials and adhesion energies between them, all expressed in J.m$_2$) for all the DFT models of Ru(0001)/LiNH$_2$(001) system (GGA PBE and PBE-dDsC functionals). Reconstructions of the LiNH$_2$(001) structure are mentioned with the corresponding transformations for terminal planes, when they occurred during the geometry optimizations.

Interface	Structure	Interface energy		Magnetization		Sum of surface energies		Adhesion energy	
Functional	Reconstruction	GGA PBE	PBE-dDsC	GGA PBE	PBE-dDsC	GGA PBE	PBE-dDsC	GGA PBE	PBE-dDsC
Ru@T1T4(10,ns,nz,ps)	none	7.36(6)	-	0.32(0)	-	10.06(7)	-	-2.70(1)	-
Ru@T1T4(14,ns,nz,ps)	none	7.50(1)	-	0	-	10.06(7)	-	-2.56(7)	-
Ru@T1T3(11,ns,p,ps)	none	9.14(5)	-	0	-	11.58(8)	-	-2.44(2)	-
Ru@T1T3(15,ns,p,ps)	none	9.21(7)	-	0	-	11.58(8)	-	-2.37(1)	-
Ru@T1T2(12,s,n,ps)	$T1T2 \rightarrow T1T4'$	7.09(8)	-	1.34(1)	-	10.40(6)	-	-3.30(8)	-
Ru@T1T2(16,s,n,ps)	$T1T2 \rightarrow T1T4'$	7.21(4)	-	1.39(0)	-	10.40(6)	-	-3.19(2)	-
Ru@T1T1(13,ns,p,ps)	none	12.24(0)	-	0	-	14.82(1)	-	-2.58(1)	-
Ru@T1T1(17,ns,p,ps)	none	12.30(5)	-	0.08(3)	-	14.82(1)	-	-2.51(6)	-
Ru@T1T3(11,s,nz,2vLi(int))	$T3T3 \rightarrow T56T43$	5.83(8)	-	0	-	11.58(8)	-	-5.75(0)	-
Ru@T1T3(11,s,nz,2vLi(cor))	$T1T3 \rightarrow T1T3$	7.23(5)	-	1.13(4)	-	11.58(8)	-	-4.35(2)	-
Ru@T1T3(15,s,nz,2vLi(int))	$T3T3 \rightarrow T56T3$	6.32(7)	-	-0.07(9)	-	11.58(8)	-	-5.26(0)	-
Ru@T1T1(13,s,nz,3vLi(int,cor,suf))	$T5T5 \rightarrow T36T4'3$	5.96(6)	-	-0.0002	-	14.82(1)	-	-8.85(5)	-
Ru@T1T1(17,s,nz,3vLi(int,2cor))	$T5T1 \rightarrow T36T4'3$	7.46(7)	-	0	-	14.82(1)	-	-7.97(4)	-
Ru@T2T4(9,ns,nz,ps)	none	2.37(3)	2.66(6)	-0.30(3)	-0.32(0)	5.65(2)	6.62(5)	-3.28(0)	-3.96(9)
Ru@T2T4(13,ns,nz,ps)	none	2.50(4)	2.17(7)	0.35(7)	0.37(3)	5.65(2)	6.62(5)	-3.14(8)	-4.44(8)
Ru@T2T3(10,ns,p,ps)	$T2T3 \rightarrow T23T3$	4.10(2)	4.23(9)	0	0	7.17(3)	7.93(3)	-3.07(5)	-3.69(4)
Ru@T2T3(14,ns,p,ps)	none	4.23(0)	3.70(5)	0	0	7.17(3)	7.93(3)	-2.94(3)	-4.22(7)
Ru@T2T2(11,ns,p,ps)	$T2T2 \rightarrow T2T4'$	1.93(2)	2.04(2)	0.58(7)	0	5.99(1)	6.75(1)	-4.05(9)	-4.70(9)
Ru@T2T2(15,ns,p,ps)	$T2T2 \rightarrow T2T4'$	2.23(0)	1.92(5)	1.37(6)	1.41(5)	5.99(1)	6.75(1)	-3.76(1)	-4.82(7)
Ru@T2T1(12,s,n,ps)	$T2T1 \rightarrow T23T65$	7.02(5)	6.84(2)	-0.19(0)	0	10.40(6)	11.17(0)	-3.38(1)	-4.32(9)
Ru@T2T1(16,s,n,ps)	$T2T1 \rightarrow T2T65$	7.08(8)	6.26(7)	0.07(8)	0	10.40(6)	11.17(0)	-3.31(8)	-4.90(3)
Ru@T2T3(10,ns,nz,vLi(cor))	$T2T3 \rightarrow T2T43$	2.42(3)	2.79(3)	0	0	7.17(3)	7.93(3)	-4.75(0)	-5.14(0)
Ru@T2T3(14,ns,nz,vLi(cor))	none	3.08(7)	2.84(7)	-0.10(6)	0	7.17(3)	7.93(3)	-4.08(5)	-3.35(2)
Ru@T2T2(11,ns,nz,vNH$_2$(cor))	$T2T2 \rightarrow T2T4'$	3.13(2)	3.43(3)	0.51(7)	0	5.99(1)	6.75(1)	-2.85(9)	-3.31(8)
Ru@T2T2(11,ns,nz,vNH$_2$(suf))	$T2T2 \rightarrow T2T4'$	2.65(8)	2.86(6)	-0.37(2)	0	5.99(1)	6.75(1)	-3.33(3)	-3.88(5)

V.4.2 Case of $LiNH_2$(001) reconstruction

After geometry optimization with GGA PBE functional, 10 among 25 interface models keep their initial structural arrangement, at the exception of course of local geometric relaxations, especially in the $LiNH_2$(001) materials and at the interface with Ru(0001). These systems, which do not undergo a significant reconstruction in the $LiNH_2$ materials, are mentioned as "none" in the corresponding column of Table V.5 and they correspond mostly to plain interfaces with no vacancy (except one case Ru@T2T3(14,ns,nz,vLi(cor))). Regarding interface energies, at the GGA PBE level, these non-reconstructed systems cover almost the whole range of stability from the most competitive systems (2.37 $J.m^{-2}$ for the Ru@T2T4(9,ns,nz,ps), as illustrated in Figure V.10 b) to the least stable model (12.30 $J.m^{-2}$ for the Ru@T1T1(17,ns,p,ps)). This family of non-reconstructed interfaces is composed of systems with T1 and T2 contacts, with a large preference for T2 contacts (more stable interfaces).

Among the 25 interfaces, 15 models have undergone a significant reconstruction in the $LiNH_2$(001) materials (see column 2 of Table V.5). 6 systems have undergone a systematic reconstruction in the terminal T2 plane (exposed to vacuum) where the NH_2 fragments have been rotated from a "NH_2 down" configuration toward a "NH_2 up" situation (2 systems being in T1 contact with Ru, and 4 being in T2 contact). Such a reconstruction has thus been noted T4' in the manuscript. This can be explained easily by the energetic gain encountered from T2 to T4 terminations and related surface energies, as reported previously on Table V.3. Such a reconstruction is also possible thanks to the free rotations of NH_2 fragments at the terminal plane of the interface models. For a sake of simplicity, the final notations of reconstructed interfaces are kept as identical to those of the initial configurations (see column 1 of Table V.5).

In the remaining 9 interface models presenting a significant reconstruction different from T2T4', 6 systems correspond to defective interfaces only with Li vacancies (both T1 and T2 contacts, with 5 and 1 interface models, respectively), while the 3 remaining ones are plain interfaces with a T2 contact. At the level of interface energies, the 5 defective interface models, with a T1 contact and showing a complex reconstruction, present a much more stable interface energy with respect to their corresponding plain interface model, discussed before. In other words, the generation of Li vacancies for interface models, with a T1 contact with Ru, leads to more stable systems (in the range 5.83-7.46 $J.m^{-2}$ by comparison with 9.14-12.30 $J.m^{-2}$ for non defective systems). Nonetheless such Li vacancies for defective interfaces with T1 contact do not provide competitive candidates with respect to the most stable system.

Regarding the reconstructions, 4 systems, among the corresponding 5 interfaces with a T1 contact, present a complex rearrangement along the $LiNH_2$ materials, in particular at the interface with Ru and at the surface (with vacuum above), with the possibility of merging two different planes composed of Li atoms and NH_2 fragments. Such complex rearrangements have been noted Tij with i and j referencing to P1, P2, P3 or P4 usual planes ($LiNH_2$ bulk). Moreover, two additional notations have been introduced to encounter for half-Li planes ("P5", with two Li atoms, intermediate between P1 and P3) and for half-NH_2 planes ("P6", with one NH_2 fragment instead of 2, such as P2 and P4). i and j follow the initial ordering of the $LiNH_2$planes along

the z axis, from Ru(0001) to the surface terminating $LiNH_2$(001).

In this latter family of 6 reconstructed interfaces based on defective systems, the last one Ru@T2T3(10,ns,nz,vLi(cor)) (see Figure V.10.c) is by far the most stable one with a low interface energy of 2.42 $J.m^{-2}$, making this system competitive with respect to the T2T4' family of reconstructed interfaces. Concerning now the family of 3 plain interfaces undergoing a significant reconstruction different from T2T4', they all present a T2 contact with Ru(0001) and complex rearrangements notably at the interface with Ru(0001) and at the surface of $LiNH_2$(001), leading to the formation of P5 and P6 merged planes. These non defective systems are however not much competitive because of large interface energies (in the range 4.10-7.08 $J.m^{-2}$).

V.4.3 Ru(0001)-$LiNH_2$(001) interface energies results

Concerning interface energies, the two systems in T1 contact with Ru(0001) (plain interfaces) are not competitive in stability with a large interface energy in the range 7.09-7.21 $J.m^{-2}$, whereas the family of 4 systems presenting a T2 contact and a T4' surface reconstruction (two plain and two defective interfaces containing NH_2 vacancies) constitutes the set of the most stable interfaces with values in the range 1.93-3.13 $J.m^{-2}$ (cf. Figure V.10 a and d). The most stable interface model predicted in this work Ru@T2T2(11,ns,p,ps) belongs to this family and exhibits a minimal interface energy of 1.93 $J.m^{-2}$ (cf. Figure V.10.a). When the thickness of $LiNH_2$ materials is extended by 4 planes with respect to the most stable system, we have obtained the interface model Ru@T2T2(15,ns,p,ps) (cf. Figure V.10.d) with the same surface reconstruction T2T4' and a very similar layer-by-layer optimized structure. The interface energy is destabilized (2.23 $J.m^{-2}$) by comparison with the most stable thinner model.

V.4.3.1 Effect of $LiNH_2$ thickness on interface energy

An interesting analysis concerns the discussion of the stability trends of the interface models as a function of the thickness of $LiNH_2$ materials, as depicted in Figure V.9.a at the GGA PBE level. The two families of colored points correspond to the two considered contacts with Ru(0001): T1 contact with red circles and T2 contact with black squares. Among the 13 interface models presenting a T2 contact with Ru(0001), the 8 most stable systems have been kept, thickness by thickness, from 9 to 16 planes. These 8 systems introduced in Table V.5 can be stoichiometric or not, neutral, polar or neutralized, pristine or defective. This family of T2 contact with Ru is the most competitive one regarding their stability.

When the $LiNH_2$ thickness increases from 9 to 11 layers, the interface energy becomes minimal with the most stable system at 11 layers (1.93 $J.m^{-2}$). From 13 to 15 layers, the thicker and equivalent systems describe a similar trend with a global loss of stability (larger interface energy in average). The two singularities at 12 and 16 layers correspond to the same interface model, ending with a surface plane of $LiNH_2$(001) composed of 3 Li atoms (i.e. least stable T1 termination). The interface energies are not competitive at all due to the energetic cost to generate T1 termination. From a more general standpoint, the increase of the $LiNH_2$ materials thickness tends to destabilize the interface energy.

Among the 12 interface models related to a T1 contact with Ru(0001), the 8 most stable systems have been also reported in Figure V.9.a, from 10 to 17 layers, by keeping the most stable system, thickness by thickness, similarly as T2 contact. The corresponding family of interfaces is globally much less stable than the family presenting a T2 contact with Ru. In addition, when the thickness of $LiNH_2$ materials increases, the interface energy is progressively destabilized in average.

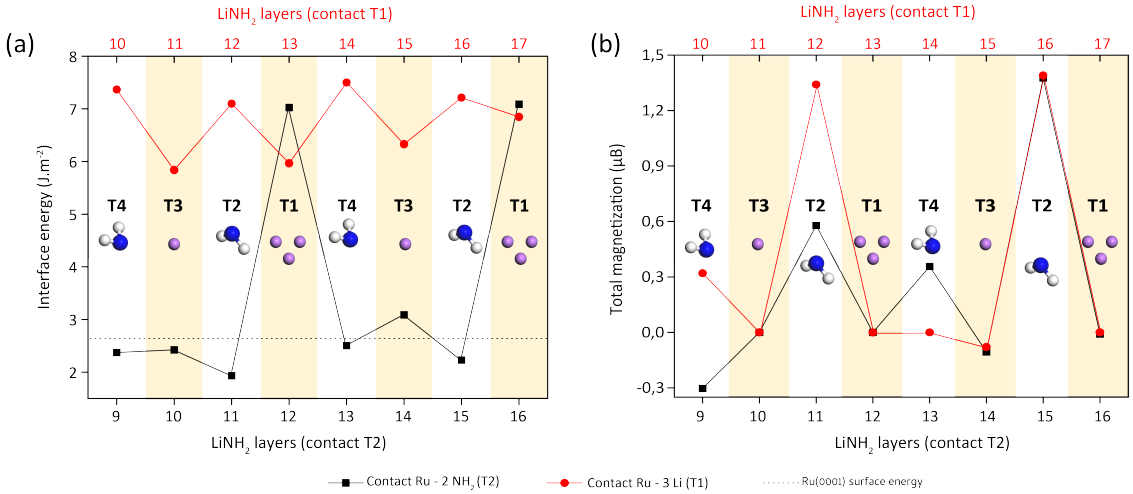

Figure V.9: (a) Interface energies ($J.m^{-2}$) of optimized Ru(0001)/$LiNH_2$(001) systems (GGA PBE) as a function of the thickness of $LiNH_2$(001) slab (see Table V.5 for details). The two considered contacts between materials is marked by different colors : black for a contact with an atomic Li plane P1 (related to T1 termination) and red for a contact with a NH_2 molecular plane P2 (related to T2 termination). See Figure V.8 for definitions of planes in $LiNH_2$. For a given thickness, only the interface energy of the most stable model is reported from Table V.5. The horizontal black line corresponds to the calculated value of the surface energy of the clean reference Ru(0001). (b) Total magnetization (μB) of optimized Ru(0001)/$LiNH_2$(001) interfaces (GGA PBE) as a function of the thickness of $LiNH_2$(001) slab.

As an intermediate conclusion, the contact between Ru(0001) and P2 plane of $LiNH_2$ materials composed of NH_2 fragments leads to more favorable interfaces. This result is by far counter-intuitive with respect to the DFT calculations comparing Li and NH_2 adsorption on Ru(0001). Moreover the thinner the extent of $LiNH_2$ (001) slab in the interface with Ru(0001), the more stable is the interface. The 4 most stable interface models belonging to the family of T2 contact with Ru(0001) exhibit an interface energy in the range 1.93-2.42 $J.m^{-2}$, which is lower than the calculated surface energy of clean Ru(0001) surface (2.59 $J.m^{-2}$ at GGA PBE level). This means that these interface models are more stable than the clean metallic surface, so the T2 contact with $LiNH_2$(001) is thermodynamically favorable. Hence this latter comparison justifies the relevance of our choices for the interface models.

At the level of magnetism, the spin polarization predicted for the most stable interface models, thickness by thickness, discussed before, have been reported in Figure V.9.b at the GGA PBE level, by keeping the correspondence of color labeling. As addressed in the Methodology section, all the interface models have been optimized with spin-polarized calculations. According to the total magnetization obtained as a function of

the contact between $LiNH_2$ and Ru, and as a function of the thickness of $LiNH_2$ materials in the interface model, no clear trend is observed. The evolution of spin properties is by far complex (with non magnetic, weakly and strongly magnetic systems) and justifies the exigence of considering magnetization throughout the study.

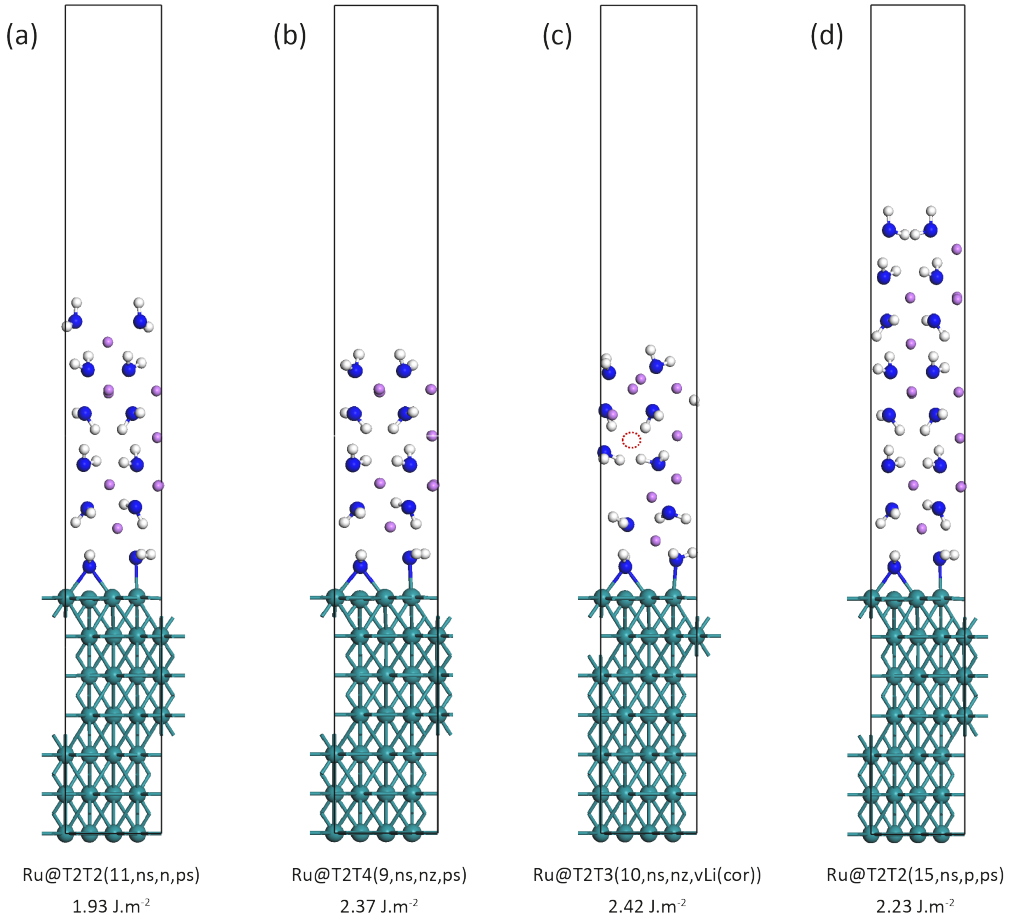

Figure V.10: Lateral views of optimized structures of Ru(0001)/$LiNH_2$(001) most stable interfaces (GGA PBE): (a) non-stoichiometric (ns), polar (p) and pristine (ps) Ru@T2T2(11,ns,p,ps) reconstructed interface (composed of 11 layers of $LiNH_2$ reconstructed in T2T4'); (b) non-stoichiometric, neutralized (nz) and pristine Ru@T2T4(9,ns,nz,ps) interface (composed of 9 layers of $LiNH_2$); (c) non-stoichiometric, neutralized and defective Ru@T2T3(10,ns,nz,vLi(cor)) reconstructed interface (with a single Li vacancy in the core, noted vLi(cor), of 10 layers of $LiNH_2$ reconstructed in T2T43); (d) non-stoichiometric, polar and pristine Ru@T2T2(15,ns,p,ps) reconstructed interface (composed of 15 layers of $LiNH_2$ reconstructed in T2T4'). Single vacancies are marked by red dotted line circles. Interface energies are expressed in $J.m^{-2}$. The colors and atom labels are those depicted in previous Figures V.8-V.7.

V.4.3.2 Sum of surface energies and adhesion energy analyses

In order to go further in the understanding of the absolute stability of the considered interface models, one can decompose the interface energies into the sum of surface energies to form the two separate materials slabs put in contact (positive and destabilizing contribution) and the adhesion energy corresponding to the

energetic gain (negative and stabilizing contribution) related to the chemical bonding between materials and the likely reconstruction at the terminations of $LiNH_2$(001) slab if it occurs. Such decomposition has then been derived as follows:

$$\Gamma_{LiNH_2(001)/Ru(0001)} = \sum \gamma_{Ru(0001)} + \sum \gamma_{LiNH_2(001)} + \gamma_{adh} \quad \text{(V.8)}$$

where γ_{adh} is the adhesion energy between both materials normalized by the surface area of the interface model. Those interface energies have been interpreted by evaluating the charge transfer and its variation from the bulk references, through the Bader charge analysis[433, 434, 435] at an accurate computational level regarding the charge density and the wavefunction grids.

According to the previous analysis, the most stable family of interfaces exhibits a T2 contact with Ru(0001) and corresponds to non-stoichiometric, polar or neutralized systems (neutralization either by contact with Ru or via the generation of vacancies), pristine or defective, if we keep the five most competitive systems having an interface energy in the range 1.93-2.50 J.m^{-2} at the GGA PBE level. None of these interfaces are stoichiometric and neutral with respect to $LiNH_2$(001) slab, such as Ru@T2T1(12,s,n,ps) or Ru@T2T1(16,s,n,ps). This is then counter-intuitive to favor complex interfaces as those belonging to the most stable family. The absolute stability of the most stable system Ru@T2T2(11,ns,p,ps) (1.93 J.m^{-2}) results from a significant energetic cost to form $LiNH_2$(001)-T2T2 and Ru(0001) slabs (5.99 J.m^{-2}) and the counter-balancing energetic gain due to adhesion (-4.05 J.m^{-2}), according to Table V.5.

By increasing the thickness of the $LiNH_2$(001) slab, we obtain a similar Ru@T2T2(15,ns,p,ps) system, which is however less stable than the thinner equivalent system, because of a weakening of the adhesion energy (-3.76 J.m^{-2}), the cost for generating the slabs being identical. In fact, $LiNH_2$(001) has a weaker propensity to accommodate the structural mismatch with the Ru(0001) surface for thicker slabs due to the larger cohesion energy in its crystal at GGA PBE. By decreasing the thickness of $LiNH_2$(001) from the most stable system Ru@T2T2(11,ns,p,ps), one generate a non stoichiometric neutralized interface model Ru@T2T4(9,ns,nz,ps), which combines two intrinsic qualities : the spontaneous loss of polarity due to the T2 contact with Ru(0001) and the minimal energetic cost to form $LiNH_2$(001)-T2T4 and Ru(0001) slabs (5.65 J.m^{-2}). However, as reported in Table V.5, the adhesion energy is less stabilizing (-3.28 J.m^{-2}), hence showing the benefit of the T2T4' reconstruction (estimated to -0.77 J.m^{-2}), in the case of the most stable system (with an adhesion energy of -4.05 J.m^{-2}).

For Ru@T2T4(9,ns,nz,ps), the increase of the thickness of $LiNH_2$ leads to similar conclusions (destabilizing of interface energy due to a weakening of adhesion energy). Finally, the generation of one Li vacancy results in a fifth competitive interface model Ru@T2T3(10,ns,nz,vLi(cor)) with an interface energy of 2.42 J.m^{-2}. This defective system has a better ability to minimize the structural mismatch with Ru(0001) (more exothermic adhesion energy of -4.75 J.m^{-2}) at the detriment of a much larger energetic cost to form $LiNH_2$(001)-T2T3 and Ru(0001) slabs (7.17 J.m^{-2}), due to the larger surface energy of T3 termination composed of one Li atom. In summary, Ru@T2T2(11,ns,p,ps) is the most stable interface model since it combines a minimal cost to

generate both slabs to put in contact with a significant energetic gain related to adhesion energy.

Regarding now the other less competitive systems presenting a T2 contact with Ru(0001), the interface energies are larger due either to the presence of NH_2 vacancies which diminishes the adhesion energy or to the presence of T1 or T3 terminations in the $LiNH_2$(001) slab leading to a much larger energetic cost to form it. The worst cases correspond to the stoichiometric and neutral systems Ru@T2T1(12,s,n,ps) and Ru@T2T1(16,s,n,ps) exhibiting the largest cost to form the slabs (10.40 $J.m^{-2}$). For the same reasons, all the interface models involving a T1 contact with Ru(0001) imply a much larger interface energy, because of a high energetic cost to generate the two slabs (in the range 10.06-14.82 $J.m^{-2}$). Such a cost is never counterbalanced by the adhesion energy and even the T1 contact with Ru(0001) through 3 Li atoms may be more favorable (with adhesion energies up to -8.85 $J.m^{-2}$).

The whole energetic analysis has been extended to the DFT calculations including dispersion (van der Waals forces) thanks to the PBE-dDsC functional (see the methodology section). Due to the weak competition of interface models involving a T1 contact with Ru(0001) at the GGA PBE level, only the 12 interface models presenting a T2 contact with Ru have been reoptimized with PBE-dDsC and the corresponding results are exposed in Table V.5 and in the appendix for optimized geometries. By the light of these complementary results, our conclusions drawn from GGA PBE calculations have been confirmed (at the exception of the effect of $LiNH_2$(001) thickness), thus showing the robustness of our theoretical approach (the interface energies being similar between functionals).

V.4.4 Bader charge analysis

The stability of the interfaces between both materials can be related to an electronic analysis based on Bader charge transfers, as reported in Figure V.11. For the separate Ru(0001) and $LiNH_2$ bulk systems, the Bader charge analyses (see Figure V.11.a) show that the two surface layers of clean Ru(0001) have gained electrons at the detriment of the two subsurface layers which are positively charged, while the $LiNH_2$ bulk (see Figure V.11.b-d) exhibits a distribution of charges in agreement with the electronegativity of atoms and fragments (Li atoms being positively charged, while NH_2 moities being negatively charged, and the charges being hold by N atoms).

For the most stable interface model Ru@T2T2(11,ns,p,ps), the contact between materials induces a charge transfer from the surface layer of Ru(0001) (see Figure V.11(a)), in contact with lithium amide, to the internal NH_2 planes of $LiNH_2$(001), as illustrated in Figure V.11.c. Hence the initially available negative charge at the surface of Ru(0001) is transfered to the core of $LiNH_2$(001). Moreover, all the Li and H atoms (positively charged) are spectator in such charge transfer due to the interfacing.The generation of a NH_2 single vacancy at the core of $LiNH_2$(001) interfaced with Ru(0001) leads to a significant destabilization of the interface (see for instance Ru@T2T2(11,ns,nz,vNH_2(cor))). The Bader charge transfer is less for this defective and neutralized system than the one previously discussed for the most stable interface model. Hence there is a correlation between the Bader charge transfer and the stability of the catalytic interface. At the opposite,

in the case of the most stable interface between materials with a T1 contact (Ru@T1T2(12,s,n,ps) which is by far less stable than the majority of interfaces with a T2 contact), we obtained a charge transfer from $LiNH_2$(001) to the interface with Ru(0001), which is characterized by an electronic depletion of the N atoms belonging to the terminal plane of $LiNH_2$(001) composed of a reconstructed T4' termination (NH_2(up)) and concomitant significant electronic gains at the interface between Ru(0001) and $LiNH_2$(001), especially at the surface layer of Ru(0001), at the adsorbed Li atomic plane and at the NH_2 plane closest to the interface. Finally the counter-intuitive and opposite charge transfer from $LiNH_2$(001) to Ru(0001) in the case of a T1 contact explains the high metastability of such interfaces.

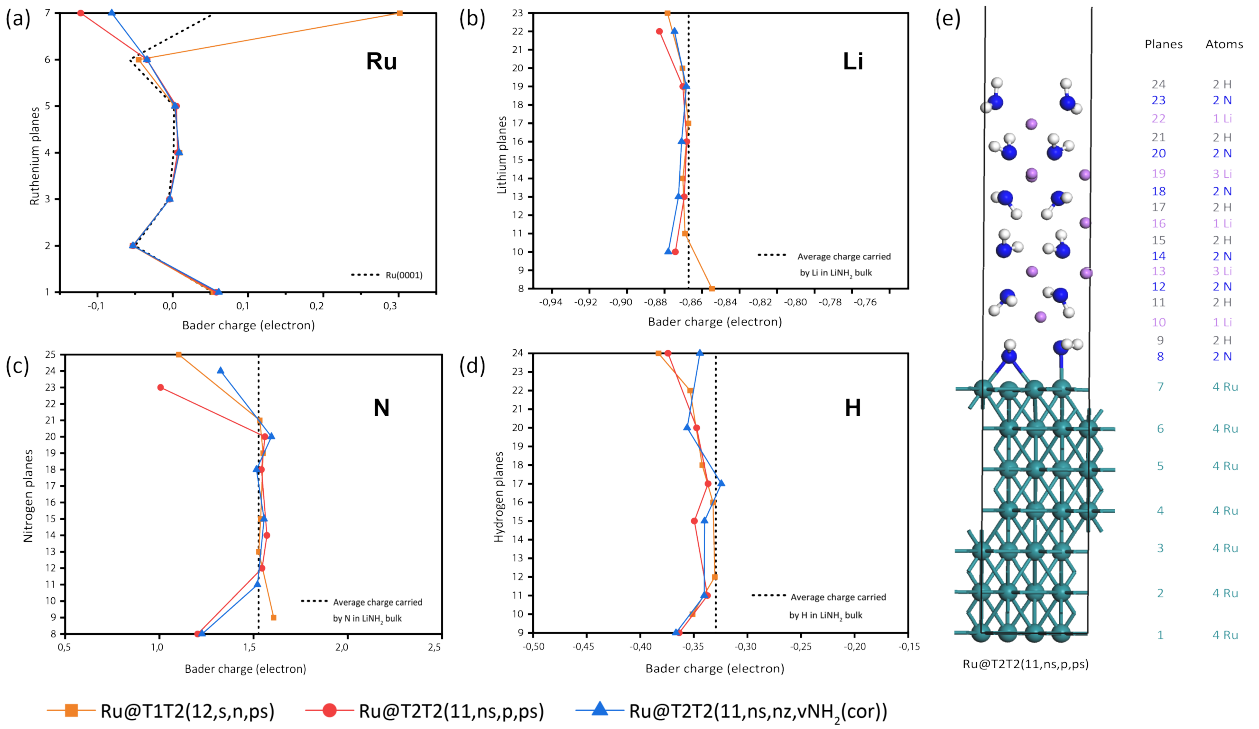

Figure V.11: Bader transfer charge transfer analysis of separate Ru(0001), $LiNH_2$ bulk systems (black dotted lines) and Ru@T2T2(11,ns,p,ps) (red full line), Ru@T2T2(11,ns,nz,vNH_2(cor)) (blue full line) and Ru@T1T2(12,s,n,ps) (orange full line) interfaces. The chosen pristine Ru@T2T2(11,ns,p,ps) and Ru@T1T2(12,s,n,ps) interfaces are the most stable ones through a T2 or a T1 contact with $LiNH_2$, respectively. The selected defective Ru@T2T2(11,ns,nz,vNH_2(cor)) interface presents the influence of a single NH_2 vacancy in the core of $LiNH_2$ materials on the Bader charge transfer. (a) layer by layer average Bader charge per Ru atom in the Ru(0001) seven-layer slab, in presence or in absence of the contact with $LiNH_2$; (b) layer by layer average Bader charge per Li atom in the Li atomic planes of $LiNH_2$, in presence or in absence of the contact with Ru(0001); (c) layer by layer average Bader charge per N atom in the NH_2 planes of $LiNH_2$, in presence or in absence of the contact with Ru(0001); (d) layer by layer average Bader charge per H atom in the NH_2 planes of $LiNH_2$, in presence or in absence of the contact with Ru(0001); (e) an example of the definitions of the planes is given in the structure illustrating the most stable interface Ru@T2T2(11,ns,p,ps). In our definition, the Bader charges are calculated by taking the valence of the isolated atoms as references. Ru atoms exhibit positive or negative Bader charges meaning that they can be either negatively or positively charges, respectively. N atoms of $LiNH_2$ present systematically positive Bader charges meaning they are negatively charged. At the opposite, Li and H atoms of $LiNH_2$ are always positively charged.

V.5 Conclusion

In this chapter, we have exposed DFT calculations of clean $LiNH_2$(001) surfaces, adsorption properties of atomic Li and NH_2 fragment on Ru(0001) as well as interface models for the Ru(0001)/$LiNH_2$(001) catalyst, with various exchange-correlation functionals and a systematic description of spin polarization. Although the standard GGA PBE functional provides a satisfactory level of predictions for separate Ru and $LiNH_2$ bulk materials, the consideration of van der Waals forces has also been explored in this chapter, showing a less predictive power concerning structure and energetics of bulk materials. Among the dispersion-corrected functionals, PBE-dDsC has been selected as the best compromise for describing weak van der Waals interactions without deviating too much with respect to the satisfactory GGA PBE level.

Regarding Ru(0001)/$LiNH_2$(001) interfaces, a large set of possibilities has been explored by varying the chemical contact between both materials, the thickness of the $LiNH_2$(001) slab, its stoichiometry and its polarity. Five interface models have shown a remarkable stability with an interface energy lower than the surface energy of the clean Ru(0001) surface. This means that the absolute stability of those five interfaces is intermediate between the high stability of $LiNH_2$(001) most stable termination (NH_2 terminal planes with hydrogen atoms pointing toward vacuum) and Ru(0001). Hence the contact between Ru and $LiNH_2$ materials induces a significant loss of stability for $LiNH_2$ moiety which can compensate this by structural reconstructions. These reconstructions can be all the more important than $LiNH_2$ is defective with the presence of vacancies. Our theoretical models show that the contact between Ru(0001) and a NH_2 terminal plane of $LiNH_2$(001) is much more favored than the one between Ru(0001) and a Li terminal plane of $LiNH_2$(001). The five most competitive interfaces are all non stoichiometric, polar or neutralized, pristine or defective with the presence of one single lithium vacancy. The stoichiometric interfaces are particularly high in energy. The most frequent reconstruction which has been registered in all the interface models corresponds to a rotation of the terminal NH_2 plane from a bulk configuration oriented toward $LiNH_2$(001) to a conformation where the hydrogen atoms of NH_2 fragments are pointing toward vacuum. The corresponding energy gain has been evaluated to -0.77 $J.m^{-2}$.

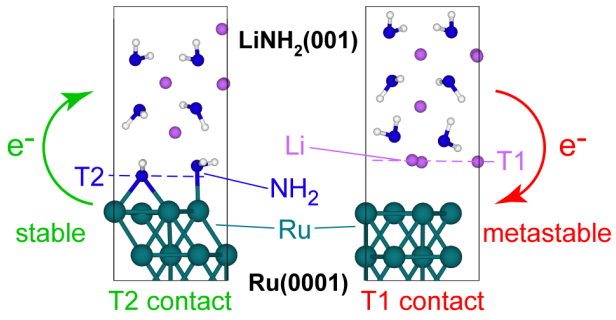

Figure V.12: Schematic representation of the electronic transfer between $LiNH_2$ and Ru depending on the nature of the contact plane.

This theoretical study opens interesting perspectives for developing relevant interface models in the con-

text of the decomposition of ammonia on $Ru/LiNH_2$ catalyst. Thanks to the particular interfacial structure between both materials, several assumptions could be postulated for elucidating the reaction mechanism. Since the most stable candidates for interfacing Ru and $LiNH_2$ materials are composed of a contact through NH_2 fragments, the role of lithium atoms present in the amide could be either indirect, i.e. at distance from the transition state of the rate determining step (through an electrostatic control), or direct by generating new lithiated surface species (through an orbitalar control).

Building on these results, the next step involves developing a model to investigate the reactivity of ammonia decomposition on $Ru/LiNH_2$ catalyst. Designing a catalytic model that accurately captures an active site representative of the reaction mechanism remains a significant challenge. Striking the right balance between interface stability and catalytic reactivity is crucial, as is addressing the potential steric hindrance at the solid-solid interface between Ru and $LiNH_2$. These considerations will be instrumental in refining and optimizing future catalytic models.

V.6 Appendix

- **Optimized structures of $LiNH_2$(001) terminations**

Table S1: Table summarizing the $LiNH_2$(001) systems.

System	Functional	Figure
$LiNH_2$(001) T1T2	GGA PBE, PBE-dDsC	V.S1
$LiNH_2$(001) T3T4	GGA PBE, PBE-dDsC	V.S2
$LiNH_2$(001) T1T1	GGA PBE, PBE-dDsC	V.S3
$LiNH_2$(001) T2T2	GGA PBE, PBE-dDsC	V.S4
$LiNH_2$(001) T3T3	GGA PBE, PBE-dDsC	V.S5
$LiNH_2$(001) T4T4	GGA PBE, PBE-dDsC	V.S6

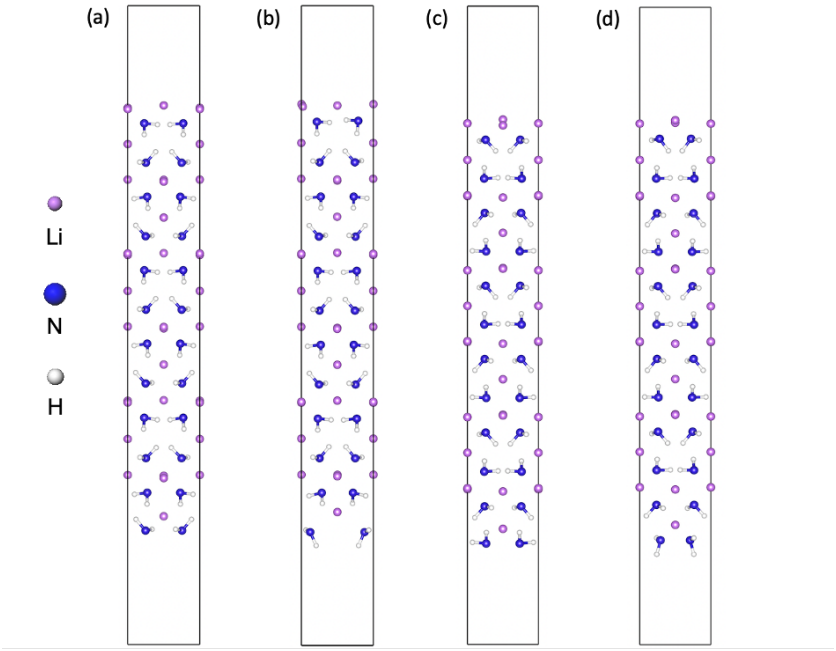

Figure S1: Lateral views of optimized structures of $LiNH_2$(001) T1T2 at the GGA PBE level (a) with geometric constraints for terminal planes (b) without constraint and presenting a surface reconstruction; at the PBE-dDsC level (c) with geometric constraints for terminal planes (d) without constraint and presenting a surface reconstruction. Labels and colors of atoms are depicted.

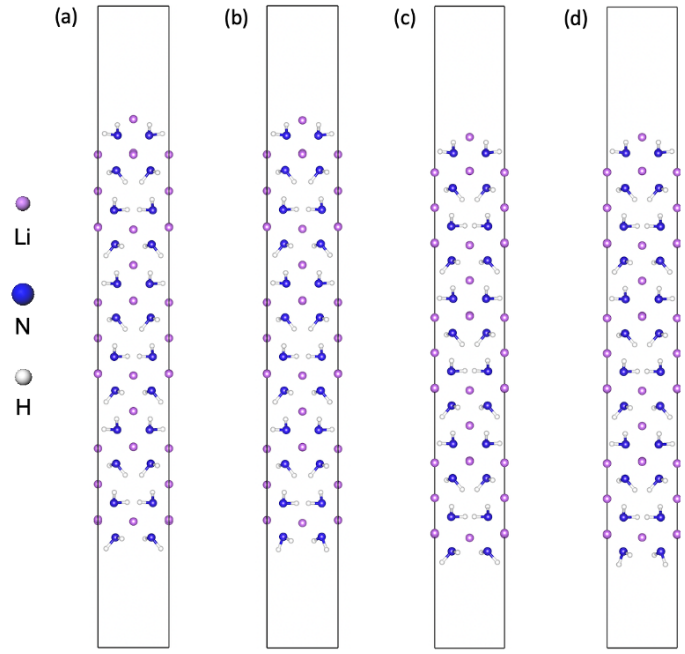

Figure S2: Lateral views of optimized structures of $LiNH_2$(001) T3T4 at the GGA PBE level (a) with geometric constraints for terminal planes (b) without constraint; at the PBE-dDsC level (c) with geometric constraints for terminal planes (d) without constraint and presenting a surface reconstruction. Labels and colors of atoms are depicted.

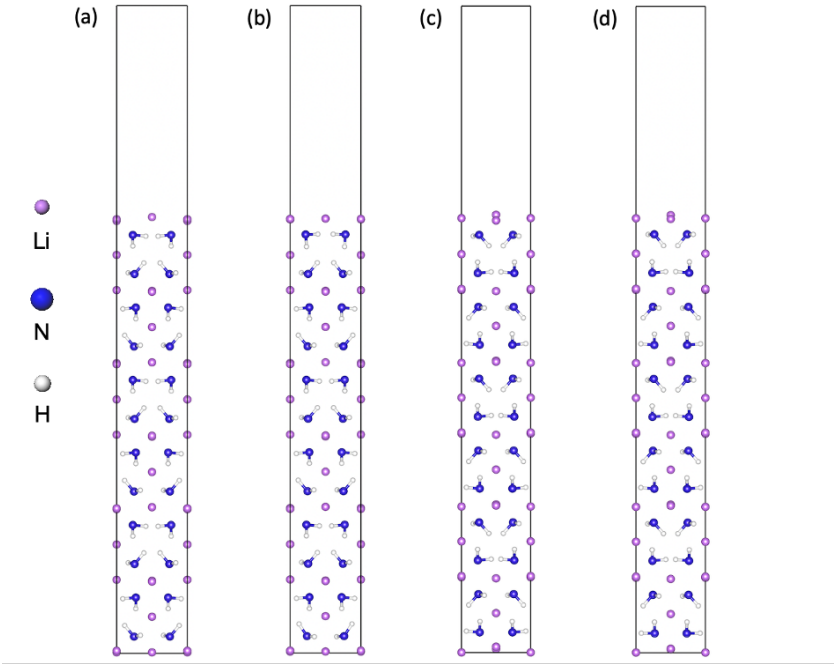

Figure S3: Lateral views of optimized structures of $LiNH_2$(001) T1T1 at the GGA PBE level (a) with geometric constraints for terminal planes (b) without constraint; at the PBE-dDsC level (c) with geometric constraints for terminal planes (d) without constraint. Labels and colors of atoms are depicted.

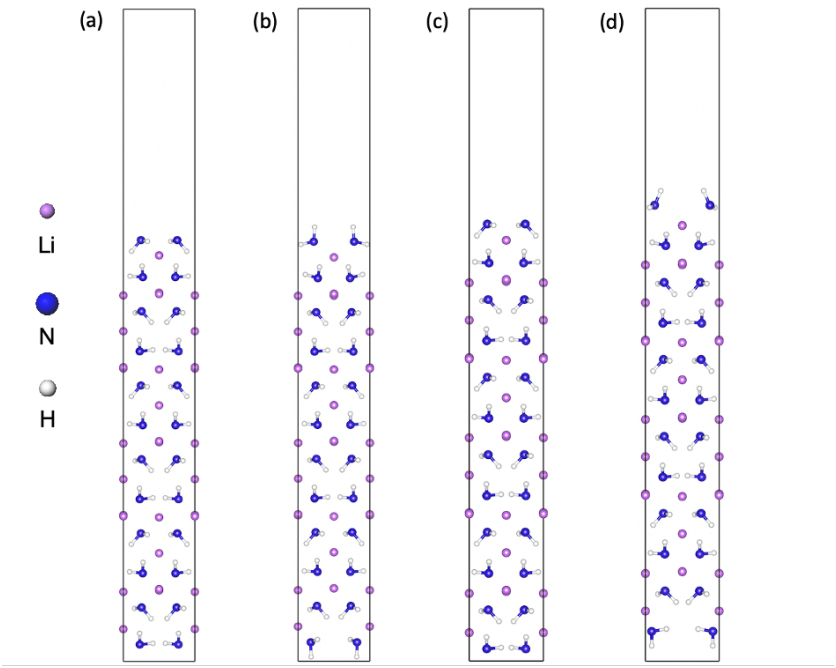

Figure S4: Lateral views of optimized structures of $LiNH_2$(001) T2T2 at the GGA PBE level (a) with geometric constraints for terminal planes (b) without constraint and presenting a surface reconstruction; at the PBE-dDsC level (c) with geometric constraints for terminal planes (d) without constraint and presenting a surface reconstruction. Labels and colors of atoms are depicted.

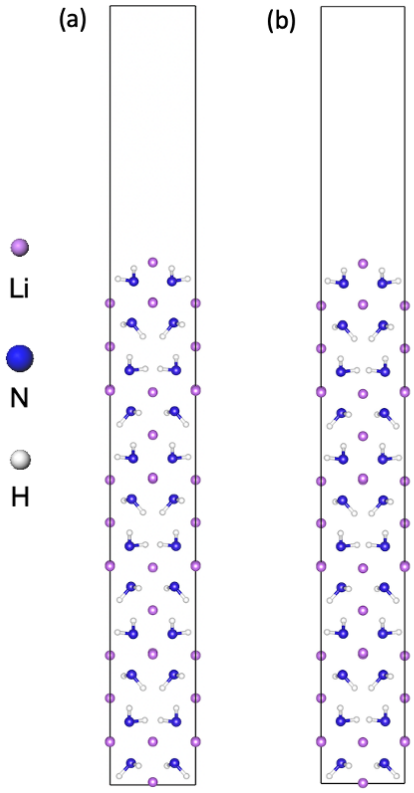

Figure S5: Lateral views of optimized structures of $LiNH_2$(001) T3T3 (a) at the GGA PBE level and (b) at the PBE-dDsC level. Labels and colors of atoms are depicted.

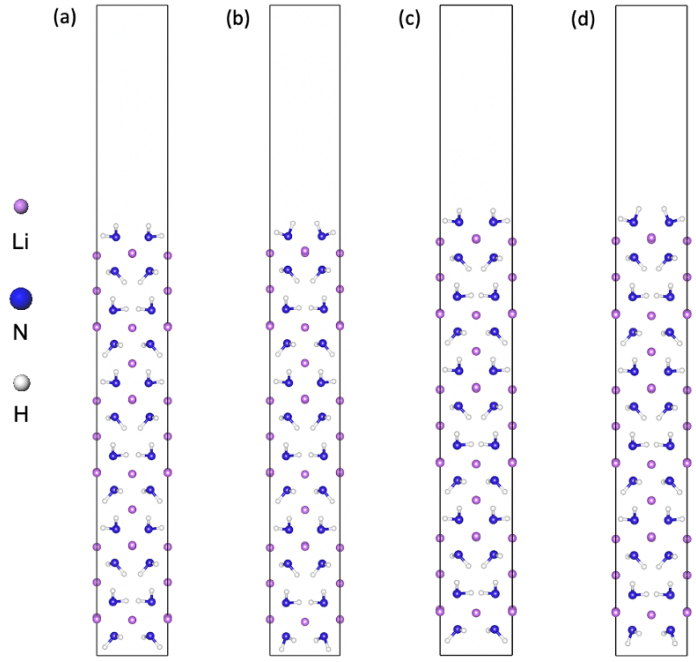

Figure S6: Lateral views of optimized structures of $LiNH_2$(001) T4T4 at the GGA PBE level (a) with geometric constraints for terminal planes (b) without constraint; at the PBE-dDsC level (c) with geometric constraints for terminal planes (d) without constraint. Labels and colors of atoms are depicted.

- **Optimized structures of Ru(0001)/$LiNH_2$(001) interfaces**

Table S2: Table summarizing the Ru(0001)/$LiNH_2$(001) interfaces systems.

System	$LiNH_2$ thickness	Functional	Figure
Ru@T1T4, Ru@T1T3, Ru@T1T2, Ru@T1T1	10-13 layers	GGA PBE	V.S7
Ru@T1T4, Ru@T1T3, Ru@T1T2, Ru@T1T1	14-17 layers	GGA PBE	V.S8
Defective Ru@T1T3	11 and 15 layers	GGA PBE	V.S9
Defective Ru@T1T1	13 and 17 layers	GGA PBE	V.S10
Ru@T2T4, Ru@T2T3, Ru@T2T2, Ru@T2T1	9-12 layers	GGA PBE	V.S11
Ru@T2T4, Ru@T2T3, Ru@T2T2, Ru@T2T1	13-16 layers	GGA PBE	V.S12
Defective Ru@T2T3	10 and 14 layers	GGA PBE	V.S13
Defective Ru@T2T2	11 layers	GGA PBE	V.S14
Ru@T2T4, Ru@T2T3, Ru@T2T2, Ru@T2T1	9-12 layers	PBE-dDsC	V.S15
Ru@T2T4, Ru@T2T3, Ru@T2T2, Ru@T2T1	13-16 layers	PBE-dDsC	V.S16
Defective Ru@T2T3	10 and14 layers	PBE-dDsC	V.S17
Defective Ru@T2T2	11 layers	PBE-dDsC	V.S18

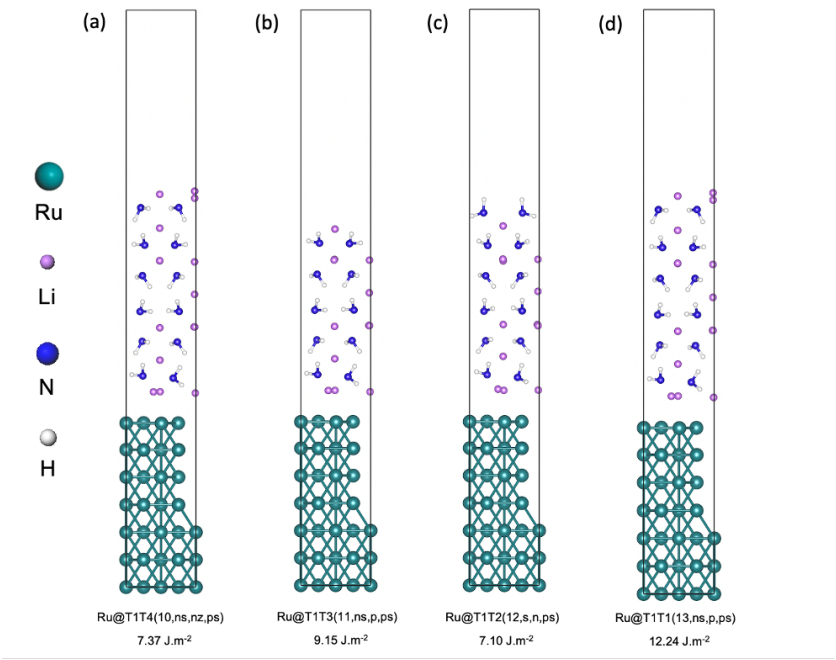

Figure S7: Lateral views of the four finest optimized structures of Ru(0001)/$LiNH_2$(001) at GGA PBE level, through a contact with Ru by a 3 Li plane (T1) (a) Ru@T1T4(10,ns,nz,ps), (b) Ru@T1T3(11,ns,p,ps), (c) Ru@T1T2(12,s,n,ps), (d) Ru@T1T1(13,ns,p,ps). Labels and colors of atoms are depicted.

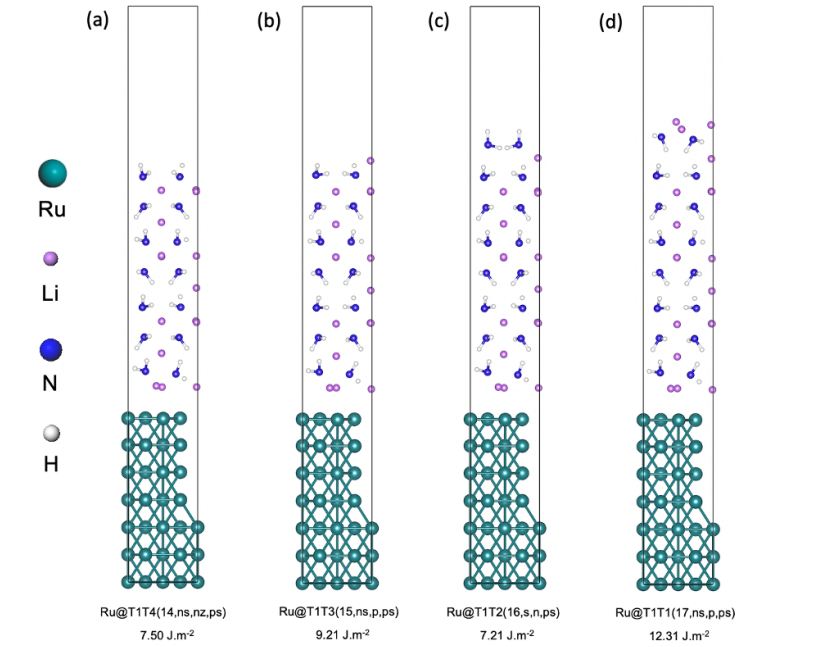

Figure S8: Lateral views of the four thickest optimized structures of Ru(0001)/$LiNH_2$(001) at GGA PBE level, through a contact with Ru by a 3 Li plane (T1) (a) Ru@T1T4(14,ns,nz,ps), (b) Ru@T1T3(15,ns,p,ps), (c) Ru@T1T2(16,s,n,ps), (d) Ru@T1T1(17,ns,p,ps). Labels and colors of atoms are depicted.

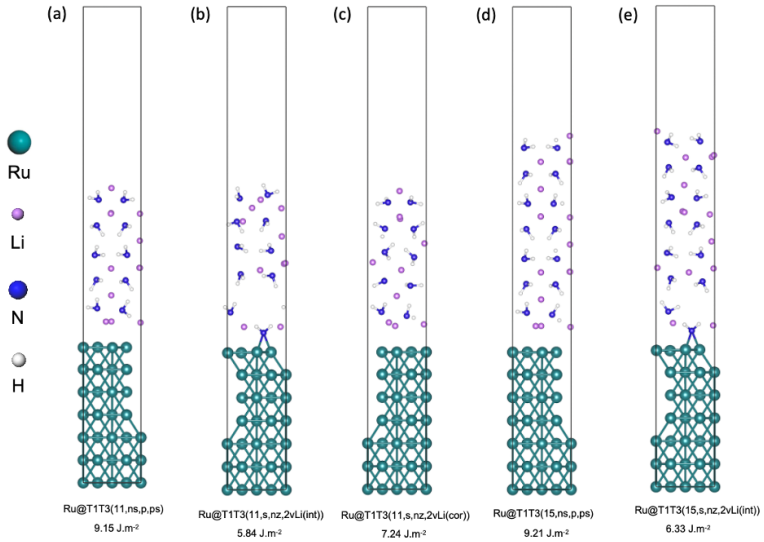

Figure S9: Lateral views of the optimized defective structures of Ru@T1T3 at GGA PBE level, through a contact with Ru by a 3 Li plane (T1) and with two Li vacancies (which may be initially in the core or at the interface of $LiNH_2$) (a) non defective Ru@T1T3(11,ns,p,ps) compared to (b) defective Ru@T1T3(11,s,nz,2vLi(int)) and (c) defective Ru@T1T3(11,s,nz,2vLi(cor)), (d) non defective Ru@T1T3(15,ns,p,ps) compared to (e) defective Ru@T1T3(15,s,nz,2vLi(cor)). Labels and colors of atoms are depicted.

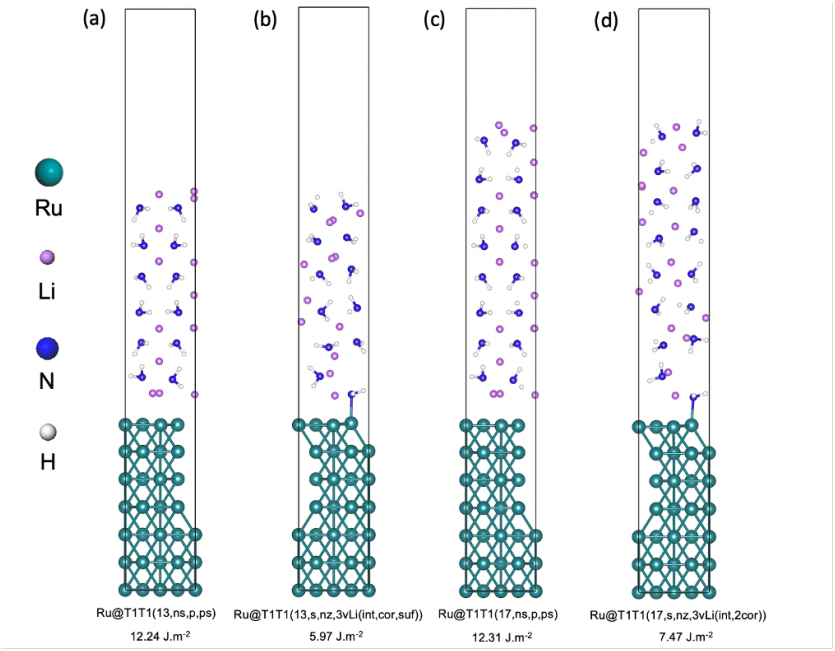

Figure S10: Lateral views of the optimized defective structures of Ru@T1T1 at GGA PBE level, through a contact with Ru by a 3 Li plane (T1) and with three Li vacancies (which are initially in the core, at the interface or at the surface of the $LiNH_2$) (a) non defective Ru@T1T1(13,ns,p,ps) compared to (b) defective Ru@T1T1(13,s,nz,3vLi(int,cor,suf)), (c) non defective Ru@T1T1(17,ns,p,ps) compared to (d) defective Ru@T1T1(17,s,nz,3vLi(int,2cor)). Labels and colors of atoms are depicted.

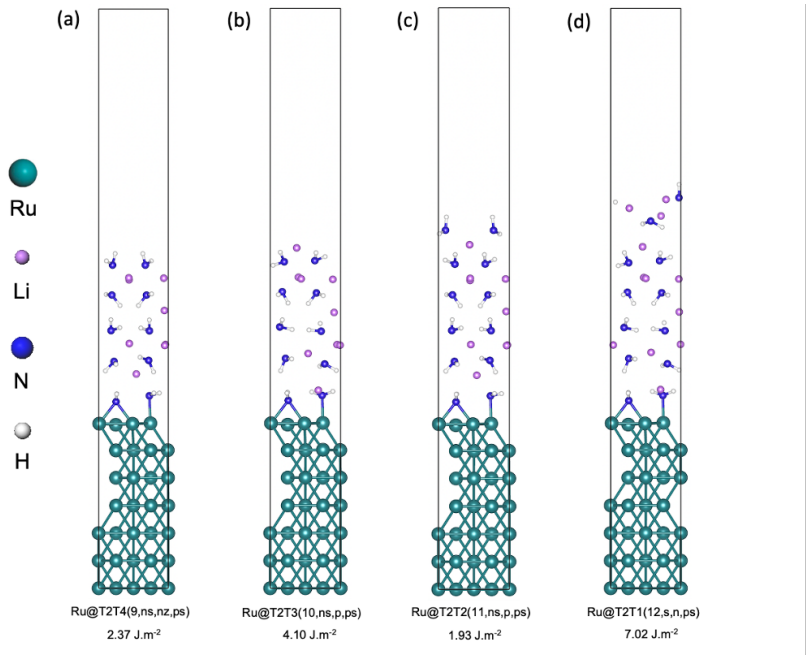

Figure S11: Lateral views of the four finest optimized structures of Ru(0001)/$LiNH_2$(001) at GGA PBE level, through a contact with Ru by a two NH_2 plane (T2) (a) Ru@T2T4(9,ns,nz,ps), (b) Ru@T2T3(10,ns,p,ps), (c) Ru@T2T2(11,ns,p,ps), (d) Ru@T2T1(12,s,n,ps). Labels and colors of atoms are depicted.

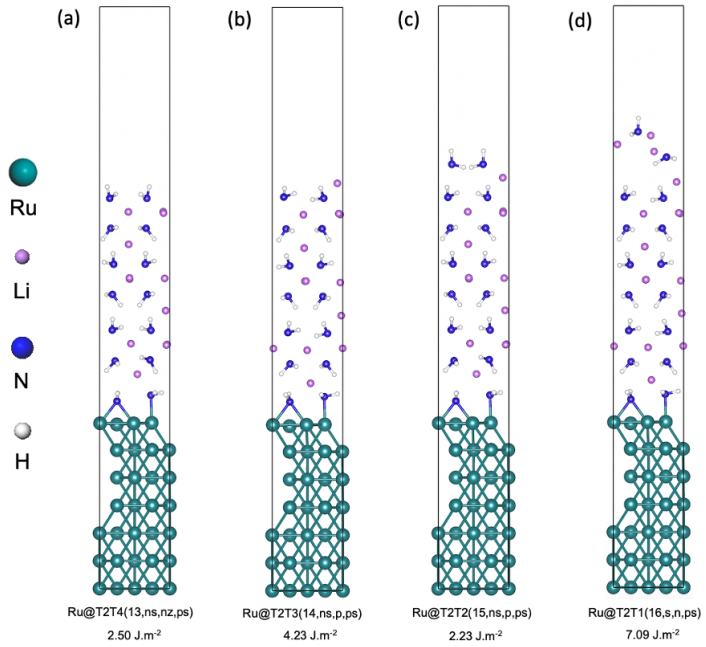

Figure S12: Lateral views of the four thickest optimized structures of Ru(0001)/$LiNH_2$(001) at the GGA PBE level, through a contact with Ru by a two NH_2 plane (T2) (a) Ru@T2T4(13,ns,nz,ps), (b) Ru@T2T3(14,ns,p,ps), (c) Ru@T2T2(15,ns,p,ps), (d) Ru@T2T1(16,s,n,ps). Labels and colors of atoms are depicted.

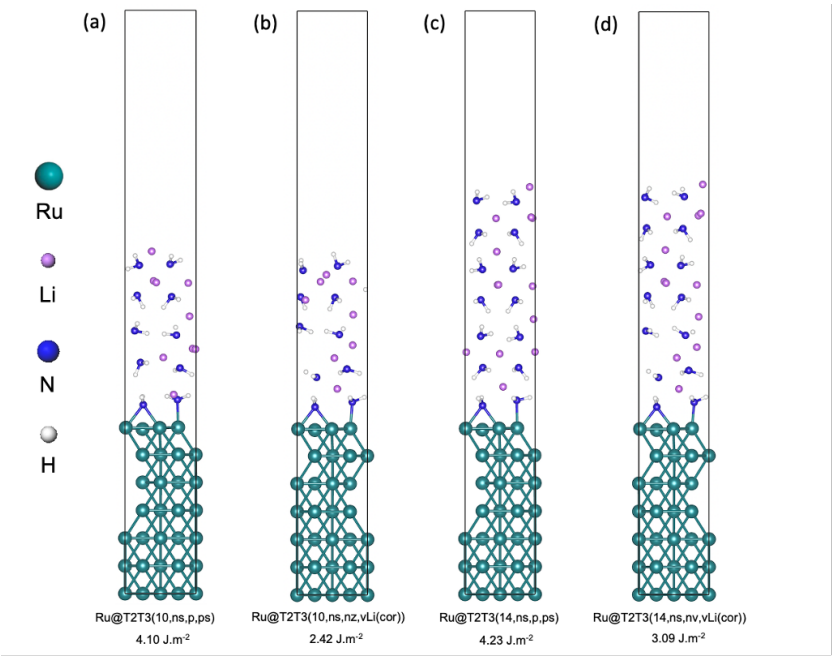

Figure S13: Lateral views of the optimized defective structures of Ru@T2T3 at the GGA PBE level, through a contact with Ru by a two NH_2 plane (T2) and with a Li vacancy in the core of $LiNH_2$ (a) non defective Ru@T2T3(10,ns,p,ps) compared to (b) defective Ru@T2T3(10,ns,nz,vLi(cor)), (c) non defective Ru@T2T3(14,ns,p,ps) compared to (d) defective Ru@T2T3(14,ns,nz,vLi(cor)). Labels and colors of atoms are depicted.

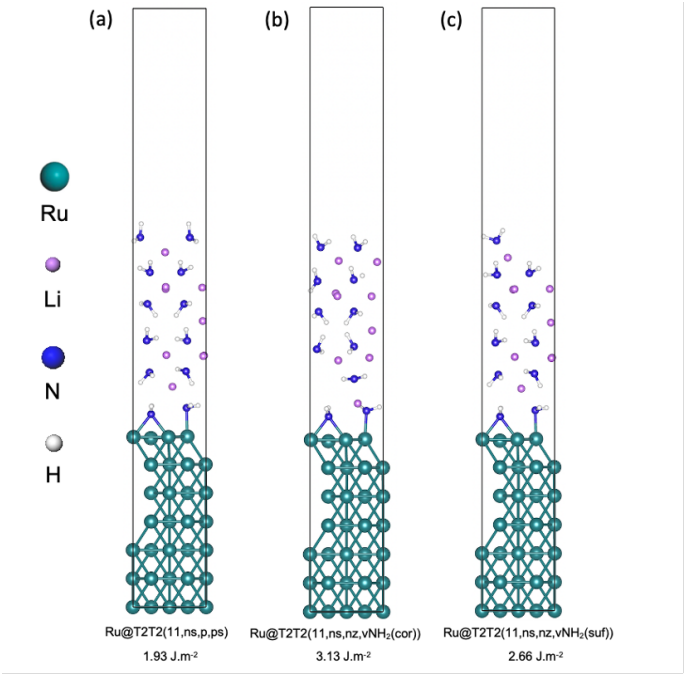

Figure S14: Lateral views of the optimized defective structures of Ru@T2T2 at the GGA PBE level, through a contact with Ru by a two NH_2 plane (T2) and with a Li vacancy in the core of $LiNH_2$ (a) non defective Ru@T2T2(11,ns,p,ps) compared to (b) defective Ru@T2T2(11,ns,nz,vNH2(cor)) and (c) defective Ru@T2T2(11,ns,nz,vNH2(suf)). Labels and colors of atoms are depicted.

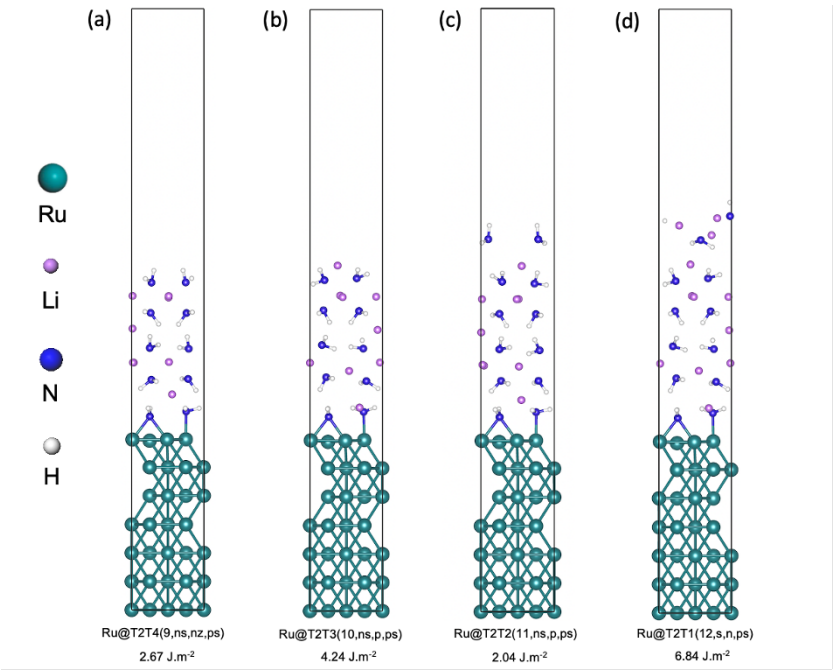

Figure S15: Lateral views of the four finest optimized structures of Ru(0001)/$LiNH_2$(001) at the PBE-dDsC level, through a contact with Ru by a two NH_2 plane (T2) (a) Ru@T2T4(9,ns,nz,ps), (b) Ru@T2T3(10,ns,p,ps), (c) Ru@T2T2(11,ns,p,ps), (d) Ru@T2T1(12,s,n,ps). Labels and colors of atoms are depicted.

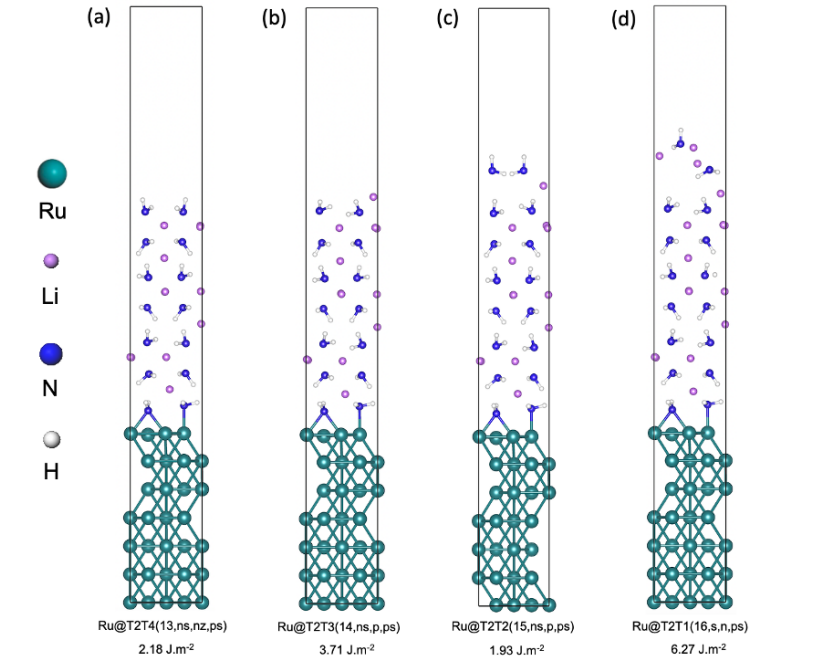

Figure S16: Lateral views of the four thickest optimized structures of Ru(0001)/$LiNH_2$(001) at the PBE-dDsC level, through a contact with Ru by a two NH_2 plane (T2) (a) Ru@T2T4(13,ns,nz,ps), (b) Ru@T2T3(14,ns,p,ps), (c) Ru@T2T2(15,ns,p,ps), (d) Ru@T2T1(16,s,n,ps). Labels and colors of atoms are depicted.

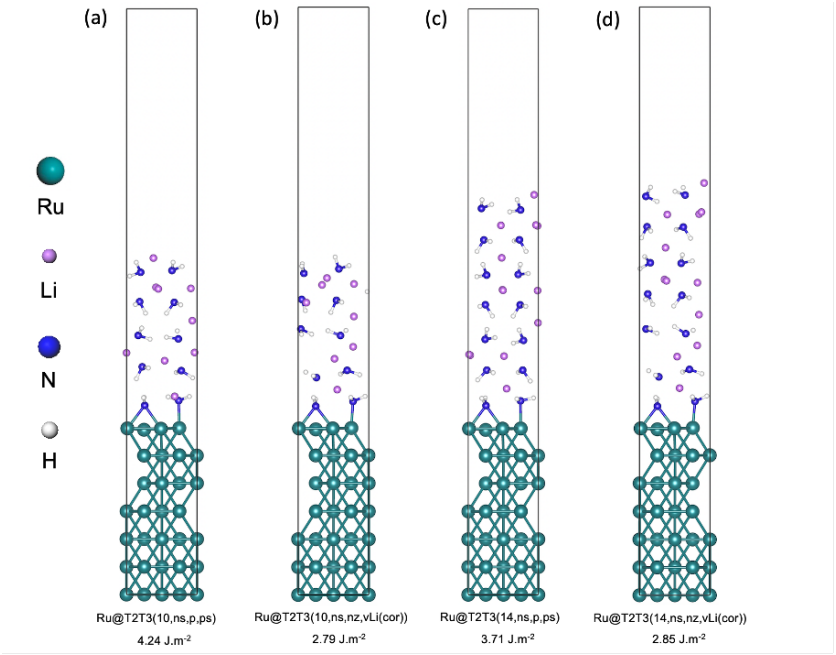

Figure S17: Lateral views of the optimized defective structures of Ru@T2T3 at the PBE-dDsC level, through a contact with Ru by a two NH_2 plane (T2) and with a Li vacancy in the core of $LiNH_2$ (a) non defective Ru@T2T3(10,ns,p,ps) compared to (b) defective Ru@T2T3(10,ns,nz,vLi(cor)), (c) non defective Ru@T2T3(14,ns,p,ps) compared to (d) defective Ru@T2T3(14,ns,nv,vLi(cor)). Labels and colors of atoms are depicted.

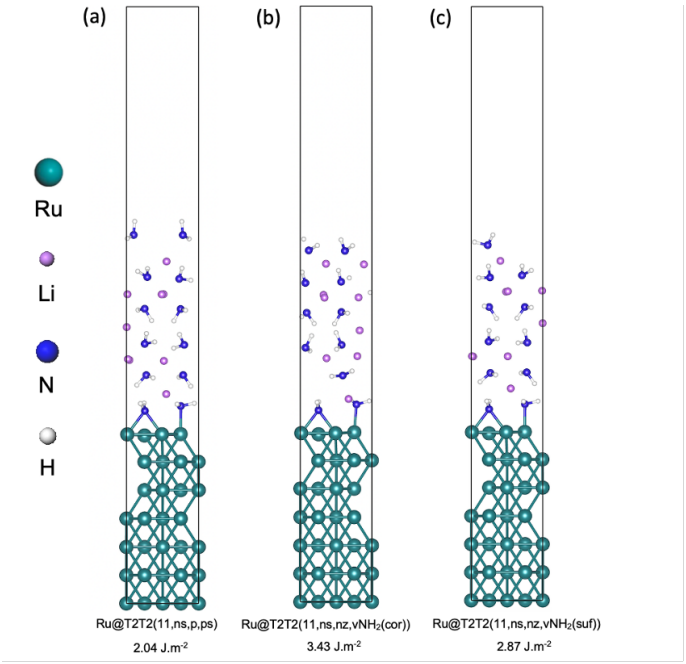

Figure S18: Lateral views of the optimized defective structures of Ru@T2T2 at the PBE-dDsC level, through a contact with Ru by a two NH_2 plane (T2) and with a Li vacancy in the core of $LiNH_2$ (a) non defective Ru@T2T2(11,ns,p,ps) compared to (b) defective Ru@T2T2(11,ns,nz,vNH2(cor)) and (c) defective Ru@T2T2(11,ns,nz,vNH2(suf)). Labels and colors of atoms are depicted.

Chapter VI

DFT models of ruthenium and lithium amide catalytic interfaces for ammonia decomposition

This chapter is dedicated to the design of a catalytic model aiming to describe the reaction mechanism of ammonia decomposition, on the basis of the stability results of the solid-solid interfaces between Ru(0001) and $LiNH_2$(001), exposed in Chapter V. Initially, a Ru(0001)/$LiNH_2$(001) hydrogenated and hollow catalytic model, was developed by expanding the most stable interface previously identified and introducing a defect in the $LiNH_2$ component. The goal was to facilitate the adsorption of NH_3 reactant, its decomposition, and the desorption of N_2, and H_2 products at the interface between the two materials where catalysis may occur. However, our initial hypothesis of a hollow interface aiming to promote the formation of N_2 from N atoms adsorbed on Ru(0001) interacting with nearby Li atoms was not successful.

In response, the catalytic model was redesigned with an emphasis on N_2 formation, aiming to enrich the interface with lithium through the dehydrogenation and subsequent desorption of H_2 from $LiNH_2$ material. Such dehydrogenation has been examined by thermodynamics of the complete dehydrogenation of two adsorbed NH_2 fragments from $LiNH_2$(001) assisted by Ru(0001).

Then, various DFT functionals predicting the bulk and surface properties of Li_3N and Li_2NH materials were considered and compared in order to develop, a new partially hydrogenated interface model with Ru(0001) offering a more favorable catalytic environment for N_2 formation.

Contents

VI.1 Hydrogenated and hollow interface model Ru(0001)/$LiNH_2$(001) . . . 187
VI.1.1 Plain and hydrogenated interface: Ab initio molecular dynamics simulations . . . 187
VI.1.2 Hollow and hydrogenated interface: static DFT model . . . 190
VI.1.3 Reactivity hypothesis: formation of N_2 via NLi_2 species adsorbed on Ru(0001) . . . 191
VI.1.4 Conclusion . . . 194
VI.2 Dehydrogenation of $LiNH_2$ at the Ru(0001) surface . . . 196
VI.2.1 Dehydrogenation Models and thermodynamic analysis . . . 196
VI.2.2 Hydrogen adsorption sites . . . 197
VI.2.3 Dihydrogen formation from $LiNH_2$ at the Ru(0001) surface . . . 199
VI.2.4 Conclusion . . . 204
VI.3 Partially hydrogenated interface model: Ru(0001)/Li_3N(001)/Li_2NH(001)/ $LiNH_2$(001)/Gas . . . 205
VI.3.1 Preliminary study of lithium nitride and lithium imide . . . 205
VI.3.1.1 Bulk materials . . . 205
VI.3.1.1.1 Li_2NH bulk . . . 205

VI.3.1.1.2 Li_3N bulk 208
VI.3.1.2 Non-stoichiometric Li_3N and Li_2NH bulk energetic model 210
VI.3.1.3 Clean surfaces 210
VI.3.1.3.1 Li_2NH surfaces 211
VI.3.1.3.2 Li_3N surfaces 213
VI.3.2 Partially hydrogenated interface model 216
VI.3.2.1 Adsorption of N on Ru(0001) 216
VI.3.2.2 Optimized plain interface 217
VI.3.2.3 Hollow interface and reactivity 218
VI.3.3 Conclusion 220
VI.4 Conclusion 221
VI.5 Appendix 222

VI.1 Hydrogenated and hollow interface model Ru(0001)/$LiNH_2$(001)

The decomposition of ammonia catalyzed by Ru(0001) surface is a well-documented reaction at the experimental level with, extensive research. A few theoretical studies are available in the literature at the DFT level where the reaction mechanism is addressed in details, although the first works were published three decades ago.[436] This being said, they have provided significant contributions and improved our understanding of catalytic processes on ruthenium surfaces.[432, 280, 437] Experimental and theoretical studies concluded that the rate determining step in ammonia decomposition on Ru(0001) is the recombinant desorption of two nitrogen atoms adsorbed on the metallic surface to form N_2, which is significantly influenced by the rate of nitrogen coverage on the Ru surface.[280, 438]

Our investigation into the reactivity of Ru(0001)/$LiNH_2$(001) builds upon the hypotheses proposed by Guo et al (see Figure VI.1). They suggested that Ru acts as a catalyst for the decomposition of $LiNH_2$ into Li_2NH, H_2, and N_2. This hypothesis gains partial support from thermogravimetric (TG) measurements, which demonstrate a notably quicker weight loss in the Ru-containing sample compared to the pure $LiNH_2$ sample. Furthermore, the presence of Li_2NH was confirmed by X-ray diffraction (XRD) analyses conducted during their experiments.[15]

As Ru/$LiNH_2$ co-catalysis demonstrates a positive effect compared to Ru alone in the decomposition of ammonia, it is likely that the recombinant desorption of N_2 will be facilitated in this environment. Our objective is therefore to identify catalytic models to be able to carry out this recombinant desorption of N_2 from $LiNH_2$ in this environment, as well as to identify the structures of the transition states of N_2 formation at the interface between the two solids.

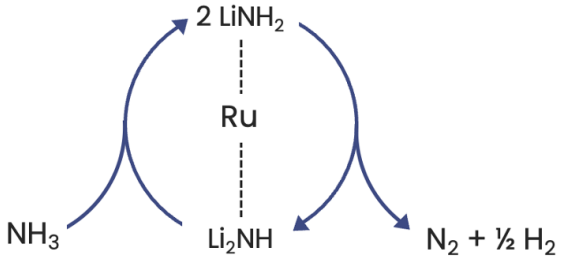

Figure VI.1: Assumed catalytic cycle for ammonia decomposition on for Ru/$LiNH_2$ (adapted from[15]).

VI.1.1 Plain and hydrogenated interface: Ab initio molecular dynamics simulations

The synthesis and decomposition of ammonia proceed under specific pressure and temperature conditions. Static DFT calculations performed at idealistic temperature and pressure (0 K and 0 atm), cannot capture these conditions when modeling heterogeneous catalytic interfaces. However, molecular dynamics (MD)

allow the simulation of atomic movements along time within specific temperature and pressure environments.[439] By solving Newton's second law of motion ($F = -\nabla V$, where V is the potential energy function), classical MD tracks the trajectories of atoms, using interatomic potentials or molecular mechanical force fields to calculate forces and potential energies.[439] Unfortunately, one cannot find a suitable classical force field predicting accurately the electronic properties of complex solid-solid interfaces such as $LiNH_2$/Ru.

Ab initio molecular dynamics (AIMD) integrates quantum mechanical calculations with classical MD principles to explore the thermodynamic and kinetic properties of materials and catalytic reactions. AIMD provides a detailed representation but is computationally very expensive, as it involves solving the electronic structure of the chemical systems at every MD timestep. The computational cost unfortunately imposes to restrict the system size, its electronic complexity and the length of the trajectories or the total integration time (usually reaching picoseconds as the result of thousands of structures computed at the time step being of the typical order of one femtosecond).

In catalysis, AIMD serves as a powerful tool for elucidating complex mechanisms, such as the formation and breaking (or cleavage) of chemical bonds during catalytic reactions. AIMD is particularly useful for identifying reaction intermediates and reaction pathways that are challenging to predict, especially in the absence of experimental data. This is particularly relevant in cases where there is neither a direct characterization of the catalytic interface, nor any known intermediate species. Therefore, we have utilized AIMD to study the time evolution of the most stable Ru(0001)/$LiNH_2$(001) interface (Ru@T2T2(11,ns,p,ps)), as exposed in Chapter V, in order to uncover mechanistic insights into the formation of N_2 and H_2 at the interface between the two materials at relevant operating conditions.

However, the high computational cost associated with AIMD simulations and the existing magneto-structural relationship, prevent us from carrying out spin-polarized MD calculations. In fact, exploring the same magnetic state of the chemical system all along the MD trajectory when the movement of the nuclei is significant is out-of-reach with standard integration time step (1 fs). Nevertheless, at the GGA PBE level, our Ru@T2T2(11,ns,p,ps) interface exhibited a relatively weak global magnetic moment of 0.58(7) μB (see Figure VI.2.a), thus justifying further our attempt of AIMD simulations at the restricted level. In this framework, an AIMD simulation was conducted to explore dynamic behaviors under high temperature. These simulations were carried out in the canonical (NVT) ensemble at an initial temperature of 650 K, relevant for experiments. We integrated the equations of motion by using a time step of 2 fs, over a total of 1000 ionic steps, allowing the system to evolve for up to 2 ps. Temperature control was managed by a velocity rescaling thermostat[440] ensuring temperature stability throughout the simulation period.

The AIMD simulations carried out at the restricted GGA PBE level, have shown an unsatisfactory result for our Ru(0001)/LiNH2(001) interface model. During the trajectory, the lithium amide layer divided into two distinct fragments: one fragment composed of two layers remaining adsorbed on the Ru(0001) surface and a second fragment containing the rest of the $LiNH_2$ materials (see Figure VI.2.b). Such dissociation inside the $LiNH_2$ part of the interface occurred because the GGA PBE functional does not adequately account for

the weak van der Waals (VDW) interactions, which turn out to be essential for maintaining the structural integrity of the $LiNH_2$ material at finite temperature. Such phenomenon had not been observed in previous AIMD simulations at the standard GGA level for lithium amide bulk materials thanks to the constraints due to periodicity of the crystal and to the absence of vacuum space.[441] The GGA PBE functional was chosen for AIMD simulations in our works because it allows the most relevant predictions of Ru and $LiNH_2$ bulk properties, simultaneously. Concerning energetics, the total electronic energy constantly increases along the trajectory with a loss of around 5 eV (see Figure VI.S1). Since the DFT calculations at the PBE-dDsC level had shown a contribution of -11 eV of van der Waals energy to the total electronic energy, one can expect by extending the AIMD simulations that the interface will continue to lose stability in parallel to the dislocation process in the $LiNH_2$ materials.

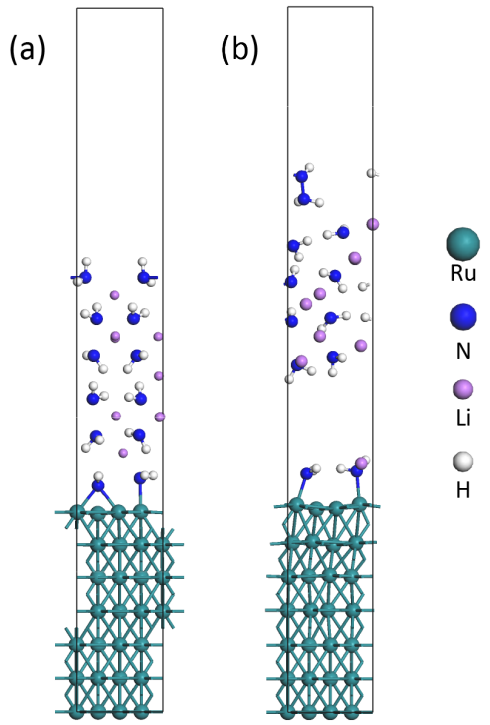

Figure VI.2: Lateral views of (a) optimized structures (static model) of Ru(0001)/$LiNH_2$(001) most stable interface Ru@T2T2(11,ns,p,ps) (GGA PBE), (b) structure extracted from the trajectory after 2 ps of AIMD simulations performed at the GGA PBE level for the same Ru@T2T2(11,ns,p,ps) interface model. Labels and colors of atoms are depicted.

Given the challenges associated with AIMD simulations (computational cost, required weak van der Waals interactions and spin polarization), this approach for investigating the mechanistic aspects of the Ru/$LiNH_2$ interface has been abbreviated. Consequently, the identification of reaction intermediates has to be ”guessed” and built (Heuristic approach using the chemical intuition). To proceed so, we will follow an assumption and check it by performing static DFT calculations.

VI.1.2 Hollow and hydrogenated interface: static DFT model

The initial step in our study of reactivity involves conceptualizing a model that facilitates interaction between the surrounding ammonia and the catalytic interface, while also allowing the products, H_2 and N_2, to desorb quite easily. The developed new model results from the most stable Ru(0001)/$LiNH_2$(001) interface we have identified, referred to as Ru@T2T2(11,ns,p,ps) (see Figure VI.3). A key feature of this model, tailored for reactivity studies, is its ability to grant direct access to the area identified as catalytically active: the contact plane between the two solid materials. This strategic configuration is designed to mimic the dynamic environment of a working catalyst, which naturally contains defects in its structure. Lithium amide was chosen for the defect creation due to its greater tolerance for deformation compared to the more rigid ruthenium. In addition, the components of $LiNH_2$ are held together by weaker electrostatic and dispersion interactions, unlike the strongly bonded metallic atoms in ruthenium. Hence defects in the $LiNH_2$ materials are expected to be less energetic.

In this model, lithium amide has been stoichiometrically cut, meaning an equal number of Li and NH_2 fragments were removed. This approach prevents from the generation of a polar interface that would have resulted from the formation of a non-stoichiometric defect. To allow the formation of such a defect, we have now opted to represent the Ru(0001)/$LiNH_2$(001) interface by using an extended $(8 \times \sqrt{3})$ supercell, which includes 16 Ru atoms per layer. The vacuum space that separates two equivalent slabs along the z-axis is of 15 Å in our slab model. Similarly, the three bottom-most atomic layers are fixed in the ideal geometry of the optimal Ru HCP bulk, which varies according to the choice of the DFT functional.

After geometry optimization, at the spin polarized GGA PBE level, the interface energy of the hollow interface model is 0.78(4) J.m^{-2}, with a total magnetization of 1.73(6) µB . The interface energy between Ru(0001) and $LiNH_2$(001) slabs in this model, has been calculated by considering Ru and $LiNH_2$ bulks as references, using the interface energy equation for Ru(0001)/$LiNH_2$(001) defined in Chapter V (see Equation V.X) This value is significantly lower than 2.37(3) J.m^{-2} obtained for the defect-free or plain interface model. The optimal structure exposed in Figure VI.3.b shows several differences by comparison with the starting geometry. First the adsorbed NH_2 fragments at the surface of Ru(0001) can diffuse from top to hollow positions, especially in the region of the hollow space. Second, the Li planes can adapt their configurations by translational movements of Li atoms in particular at the vicinity of the cut $LiNH_2$ surfaces (see for example the vertical movement of one Li atom in Figure VI.3.b). Third, the orientation of the NH_2 fragments in the corresponding planes can also change with largest rotational movements at the $LiNH_2$ surfaces of the hollow interface model. Note that one N_2H_4 species is formed at the topmost and terminal NH_2 layer of the interface. The decrease of interface energy (meaning a gain of stability) can not only be attributed to the formation of such a N_2H_4 from two NH_2 fragments located at the terminal plane of $LiNH_2$, because it was already formed before the defect creation. Such a global energy gain results from the reorganization of the NH_2 fragments exposed to vacuum, and to the relocation of one of the lithium atoms near the contact plane to the upper lithium plane. Such changes at the hollow interface model evoke the generation of a reconstructed hollow $LiNH_2$ material at the contact of Ru(0001).

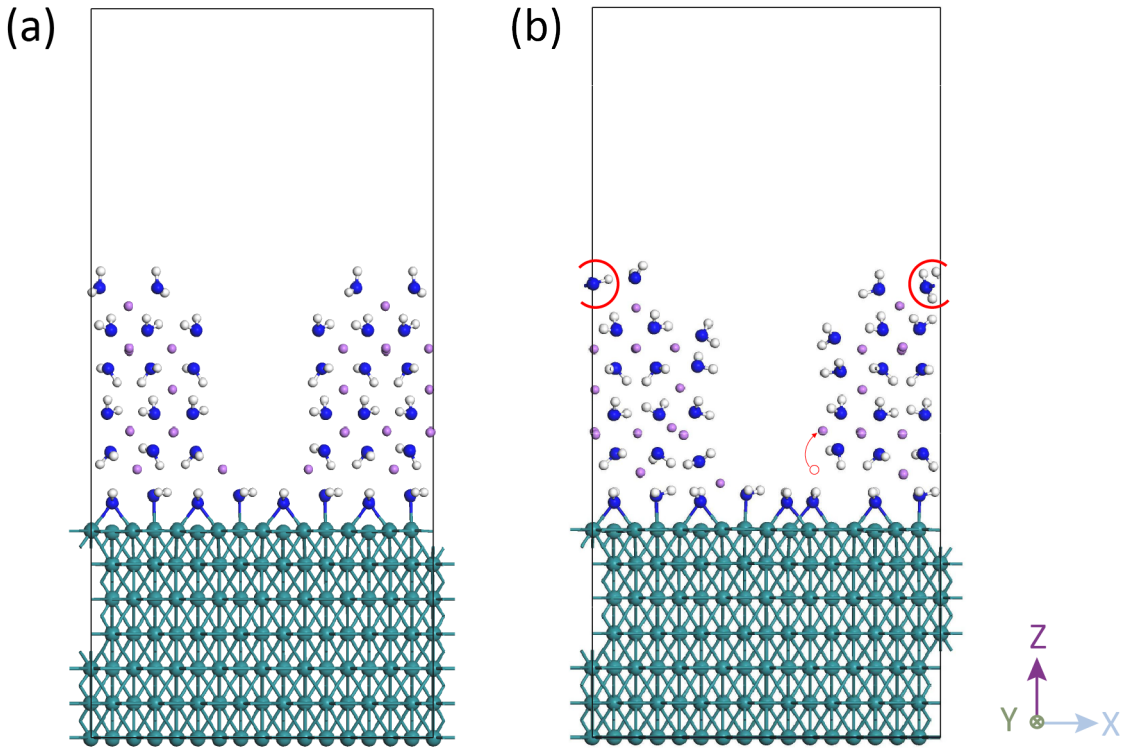

Figure VI.3: Lateral views of the hollow and hydrogenated interface model of Ru(0001)/$LiNH_2$(001) using a large ($8 \times \sqrt{3}$) supercell: (a) before geometry optimization; (b) optimized at the GGA PBE level. The N_2H_4 species formed is circled in red, while a red arrow shows a specific movement of one Li atom initially located close to the interface and which is translated vertically toward a richer Li-layer of the cut $LiNH_2$ material. The colors and atom labels are those depicted in Figure VI.2.

In summary, a lack of lithium atoms is seen around the interfacial hollow region between the two materials, which stems from the nature of the created interface. The chosen interface model, Ru@T2T2(11,ns,p,ps), features a second layer, following the nitrogen contact layer with the metal, that is intrinsically poor in lithium. Particularly, this plane, which is naturally not rich in lithium, becomes even more depleted after geometry optimization due to the relocation of a Li atom towards the upper lithium planes. This will certainly not help to evaluate the potential impact of Li atomic layers on the catalytic transformation of NH_3 at the interface hollow region and it already questions the relevance of generating such a defective interface.

VI.1.3 Reactivity hypothesis: formation of N_2 via NLi_2 species adsorbed on Ru(0001)

The theoretical investigation of the reaction mechanism of ammonia decomposition begins by proposing potential structures for the transition states (TS) involved in the elementary step of recombining two nitrogen atoms into an N_2 molecule. In scenarios where the catalyst is solely Ru, the two nitrogen atoms are firmly adsorbed on the metal surface, each forming three bonds with three separate Ru atoms (named threefold

hollow sites). Consequently, the formation of N_2 involves the breaking of a maximum of six Ru-N bonds and the formation of a triple N-N bonds. Our hypothesis for the Ru/$LiNH_2$ co-catalysis scenario implies that the presence of Li atoms during this elementary step impacts the strength of the Ru-N bonds, potentially weakening them to facilitate the Ru-N bond dissociation. We assumed that the adsorbed species consists of two N atoms interacting directly with two Li atoms. This arrangement aligns with the stoichiometry of lithium imide, Li_2NH, which is typically observed post-reaction.

However, as pointed out earlier, the lack of Li atoms in our catalytic model after geometry optimization does not fit with this mechanistic hypothesis. So, to verify the mechanistic hypothesis involving 'NLi_2' adsorbed species, it's essential to adjust the Li atom distribution, as their current lack in our constructed model at the interface contradicts the expected formation conditions for these species. Therefore, our approach is to increase lithium concentration at the contact plane using Li atoms from the surrounding $LiNH_2$ structure. The initial phase in creating a favorable environment for this hypothesized activated complex involves the decrease of the surface coverage on the Ru(0001) surface by desorbing NH_3 molecules. This strategy aligns with the properties of $LiNH_2$, which, as discussed in Chapter III and supported by extensive literature, decomposes at around 380°C to yield Li_2NH and ammonia. This preparatory step is crucial for validating the stability and potential role of "NLi_2" in facilitating the catalytic process.

To establish an appropriate environment for the catalytic reaction, we proposed a step-by-step mechanism beginning with the migration of an H atom from an NH_2 fragment, in the upper NH_2 plane from the NH_2 contact plane, up to an adsorbed NH_2 forming an adsorbed NH_3 on the metallic surface. This migration triggers the desorption of this newly formed NH_3 molecule, as illustrated in Figure VI.4.a. This process is symmetrically repeated for the opposite NH_2, resulting in the formation and desorption of a second NH_3 molecule (shown in Figures VI.4.b and VI.4.c). At this point, the system contains two 'Li_2NH' species integrated within the $LiNH_2$ matrix. The dehydrogenation process extends beyond this phase, culminating in the formation of an 'NLi_2' fragment within the $LiNH_2$ part of the model and a third NH_2 molecule adsorbed on the Ru(0001), as depicted in Figure VI.4.c. This third molecule is then desorbed, and followed by the formation of a second 'NLi_2' species within the $LiNH_2$ (see Figure VI.4.d). Simultaneously, the initially formed 'NLi_2' is adsorbed on top of a Ru atom, exploiting the space made available by the desorption of multiple NH_3 molecules (see Figure VI.4.d). This is followed by the formation of a second species 'NLi_2' fragment, then its adsorption onto the metal surface. Concurrently, the final ammonia molecule produced is sent to occupy the space created by this recent adsorption. This sequence of events is depicted in Figures VI.4.e and VI.4.f.

Among all these proposed guessed structures, only the final one, represented in Figure VI.4.f, has been considered for geometry optimization using GGA PBE, with and without spin-polarization. This approach is crucial because if this structure cannot stabilize under these conditions, it invalidates our initial assumption After only a few electronic minimizations and related optimization steps, the two 'NLi2' species rapidly dissociate on the surface leading to threefold hollow coadsorbed N atoms on Ru(0001) surrounded by above-lying Li atoms , and thus invalidating our catalytic model (see Figure VI.5.a). This outcome confirms that further

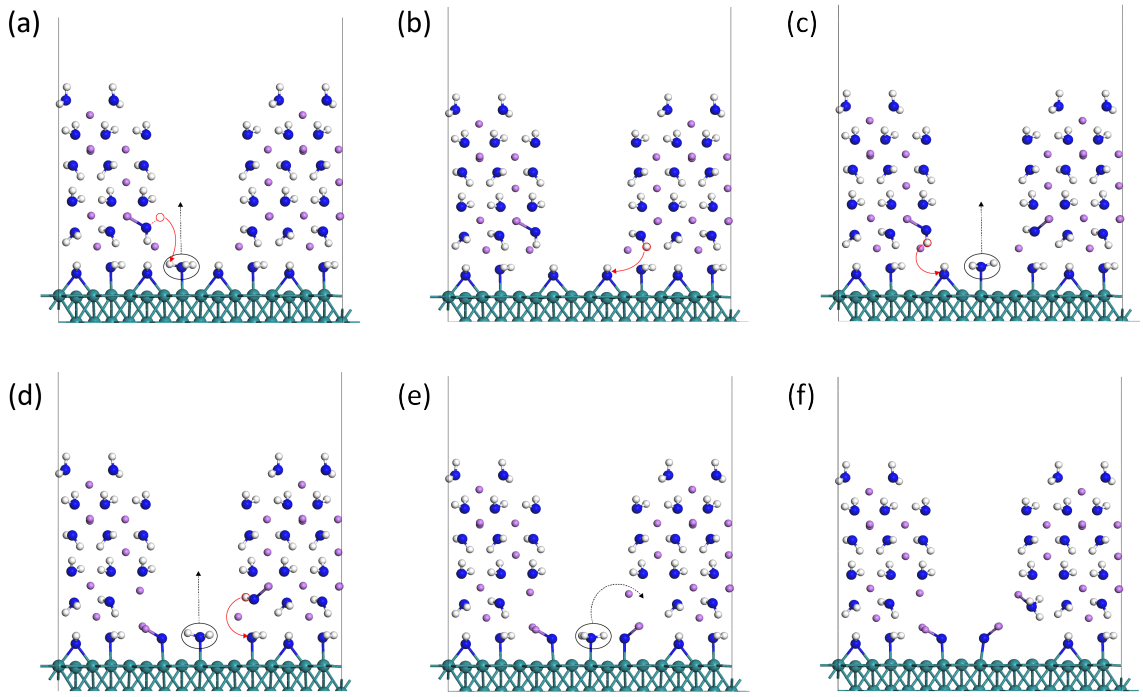

Figure VI.4: Lateral and zoomed views of the hollow and hydrogenated Ru(0001)/$LiNH_2$(001) interface in the $(8 \times \sqrt{3})$ supercell and defective catalytic model for the formation of NLi_2 species at the solid-solid interface: (a) formation of a Li_2NH species in the $LiNH_2$ material and ammonia formation and desorption; (b) formation of a second Li_2NH species in the $LiNH_2$ material and ammonia diffusion to a top site; (c) formation of third ammonia molecule and desorption of the second one with the formation of one NLi_2 in the modify $LiNH_2$ material; (d) formation of fourth ammonia molecule and desorption of the third one, with the formation of a second NLi_2 in the modify $LiNH_2$ material, as well as the adsorption of the first NLi_2 species on the metallic surface; (e) adsorption of the second NLi_2 formed species on Ru(0001) with the desorption of fourth ammonia formed into the modified $LiNH_2$ material; and (f) two NLi_2 adsorbed species on Ru(0001) at vicinity. Black circles and lines indicate the desorption of formed ammonia molecules. Red arrows indicate the movements of hydrogen atoms. The colors and atom labels are those depicted in Figure VI.2.

optimization of all the developed structures would be pointless. However, it's noteworthy that the ammonia molecule desorbed from the Ru surface to the lithiated material remained in position. This observation provides insights into the regeneration of the catalyst and a potential step in the decomposition of ammonia, the potential absorption of ammonia molecules to fill vacancies within the lithiated material (see Figure VI.5.a).

However, the failure to stabilize a TS involving N atoms interacting with two Li atoms does not totally invalidate our working hypothesis. The issue may lie with the chosen model. Attempting to stabilize such an activated complex in an environment naturally richer in lithium may provide insights in the impact of lithium in this elementary step.

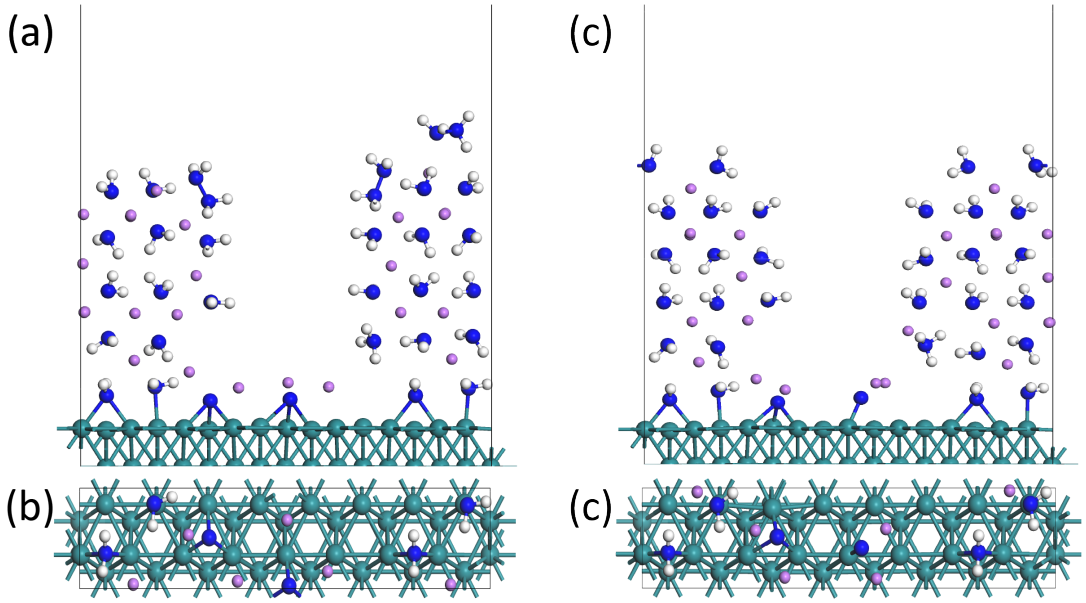

Figure VI.5: (a) Lateral and (b) top views of Ru(0001)/$LiNH_2$(001) ($8 \times \sqrt{3}$) catalytic model including two NLi_2 species at solid-solid interface, who have dissociated, at the GGA PBE level without spin polarization; (a) Lateral and (b) top views of Ru(0001)/$LiNH_2$(001) ($8 \times \sqrt{3}$) catalytic model modified to include two NLi_2 species at solid-solid interface, who have dissociated, at the spin polarized GGA PBE level. The colors and atom labels are those depicted in Figure VI.2.

VI.1.4 Conclusion

To conclude on this first part of our reactivity study, we attempted an AIMD simulation at 650 K to explore the interaction between the two materials under more realistic conditions. The simulation was not conclusive at two levels: the van der Waals interactions cannot be neglected and spin polarization make those simulations really expensive (if feasible). Consequently, our investigation is now solely based on constructing a model akin to the different possible TS structures. This involves deducing the catalyst's configuration from the possible $Li_xN_yH_z$ phases and various TS structures, guided by both experimental and theoretical insights of the decomposition of ammonia catalyzed by Ru, as well as the catalytic performances and characterization results of Ru/$LiNH_2$ catalyst.

The initial catalytic model we designed is based on the most stable Ru@T2T2(11,ns,p,ps) interface identified earlier. It utilizes a ($8 \times \sqrt{3}$) supercell, expanded to facilitate the introduction of a central defect. This defect was meticulously designed by stoichiometrically removing equal numbers of Li and NH_2 from the $LiNH_2$ section, enabling direct access to the catalytically supposed relevant contact plane between the two materials. The interface energy of this model is notably lower than that of its intact counterpart, primarily due to surface reconstruction, including the pivoting of NH_2 fragments. This model demonstrates that introducing defects into the $LiNH_2$ component is not only feasible but also stabilizes the entire model, a finding that could be crucial with regard to reactivity.

To explore the beneficial impact of $LiNH_2$ on catalytic activity, we hypothesized that the presence of lithium could alter the TS geometry of N_2 recombination. Accordingly, we adapted the defective catalytic model to incorporate two 'NLi_2' species adsorbed on the Ru(0001) surface. This configuration was facilitated by the formation and subsequent desorption of an NH_3 molecule from the contact plane of $LiNH_2$. Despite these adjustments, the 'NLi_2' species proved to be unstable and ultimately dissociated, suggesting that further refinements are needed to stabilize this interaction in the catalytic model.

Based on the initial results, we refined our mechanistic hypotheses to focus on stabilizing N atoms in interaction with Li atoms at the contact plane. The challenge in stabilizing these potential adsorbed species likely stems from an insufficient presence of Li atoms at the contact plane. Additionally, the formation and desorption of ammonia molecules do not align well with our hypothesis, which requires a contact plane rich in both Li and N. Consequently, we now hypothesize that upon contact with the metal, $LiNH_2$ will not just dehydrogenate to Li_2NH but will continue to decompose completely, forming Li_3N, lithium nitride. This adjustment aims to better accommodate the catalytic requirements and explore new pathways of the reactivity at the interface.

Indeed, Li_3N appears to be a more suitable environment for our reaction hypotheses. First, we need to explore the feasibility of forming Li_3N from $LiNH_2$ at the interface with Ru. In a second time, the feasibility for N_2 formation from Li_3N while in contact with Ru is evaluate. Additionally, we must evaluate the possibility of regenerating the lithiated material through the absorption or adsorption of ammonia. This step-by-step verification process aims to enhance our understanding of the Ru/$LiNH_2$ catalytic system, or to guide us toward exploring other avenues for its comprehension.

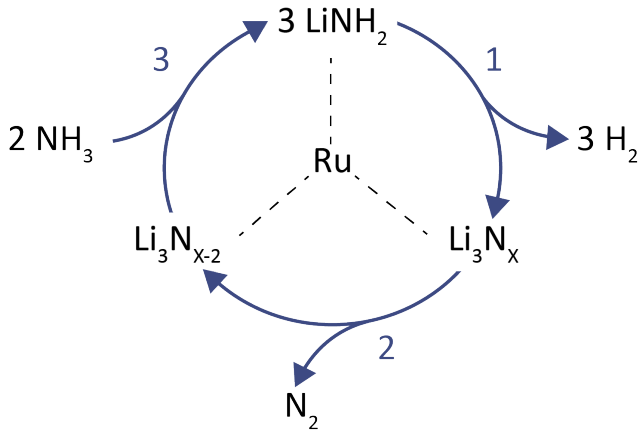

Figure VI.6: Proposed Catalytic Mechanism for Ammonia Decomposition by Ru/$LiNH_2$.

VI.2 Dehydrogenation of $LiNH_2$ at the Ru(0001) surface

VI.2.1 Dehydrogenation Models and thermodynamic analysis

The model employed to investigate the initial step in our proposed catalytic mechanisms—the dehydrogenation of $LiNH_2$ in contact with Ru—differs from the Ru(0001)/$LiNH_2$(001) model used for studying the stability of the interface, as detailed in Chapter V (see Figure VI.7.a), and from the previously studied defective catalytic model. The new supercell, sized at $(4 \times 2\sqrt{3})$, expands in both the x and y dimensions compared to the plain interface model, which was a $(2 \times \sqrt{3})$. Although it is narrower in x than the defective model $(8 \times \sqrt{3})$, it compensates by being larger in y. This configuration maintains the same count of Ru atoms—16 per plane—as the defective model but allows for a different exploration of the contact surface. The goal of this model is to provide ample space to investigate the adoption of new adsorbed species not yet examined in this environment, facilitating a thorough analysis of potential catalytic sites.

This model measures 35 Å in the z-direction, incorporating a vacuum space of approximately 14 Å. To ensure a converged surface energy, it maintains seven metallic layers; the three bottommost planes are fixed in the ideal relaxed geometry of the Ru HCP bulk, while the top four layers are fully relaxed. The $LiNH_2$ slab in this model is thinner, consisting of five layers: two layers of Li atoms and three layers of NH_2 fragments. The interaction between the two materials is done by eight NH_2 fragments—four positioned in bridge sites and four in top sites, as illustrated in Figure VI.7.c. This arrangement is predicated on the stability results of the Ru/$LiNH_2$ interface, where the obtained optimal terminal contact planes found was composed of NH_2 fragments.

However, the $LiNH_2$ component is intentionally reduced for two main reasons. Firstly, the diminished thickness helps offset the increased computational cost due to the model's expansion in x and y dimension. Secondly, it aims to simulate a potential solid-solid contact that might emerge following defect formation. In fact, the $LiNH_2$ thickness in previous catalytic models was even thinner, consisting of only one NH_2 plane and one Li plane at the interface with Ru and the vacuum space. This setup positions this model between the highly reduced defective interface and the complete interface of the stability study model, providing a balance that captures potential real-world catalytic interactions while managing computational resources effectively.

At the unrestricted GGA PBE level, the interface energy of this model is 2.15(9) $J.m^{-2}$ (calculated by considering Ru and $LiNH_2$ bulks as reference, in the same way than Ru/$LiNH_2$ interface in chapter V and in section V.4.3), with a magnetic moment of 0.51(8) μ_B. This is slightly higher than the 1.93 $J.m^{-2}$ interface energy of the most stable Ru(0001)/$LiNH_2$(001) interface identified in section V.4.3. This increase in interface energy is understandable, given that the $LiNH_2$ terminal plane (T4) in the new model is not the reconstructed termination (T4') found in the previous configuration (see section V.4.3). The final geometry closely resembles the initial one, with only minor rotations observed for some H atoms and some relaxation of Li atoms. Notably, there are no changes in the nature of the various planes of $LiNH_2$. These subtle adjustments are

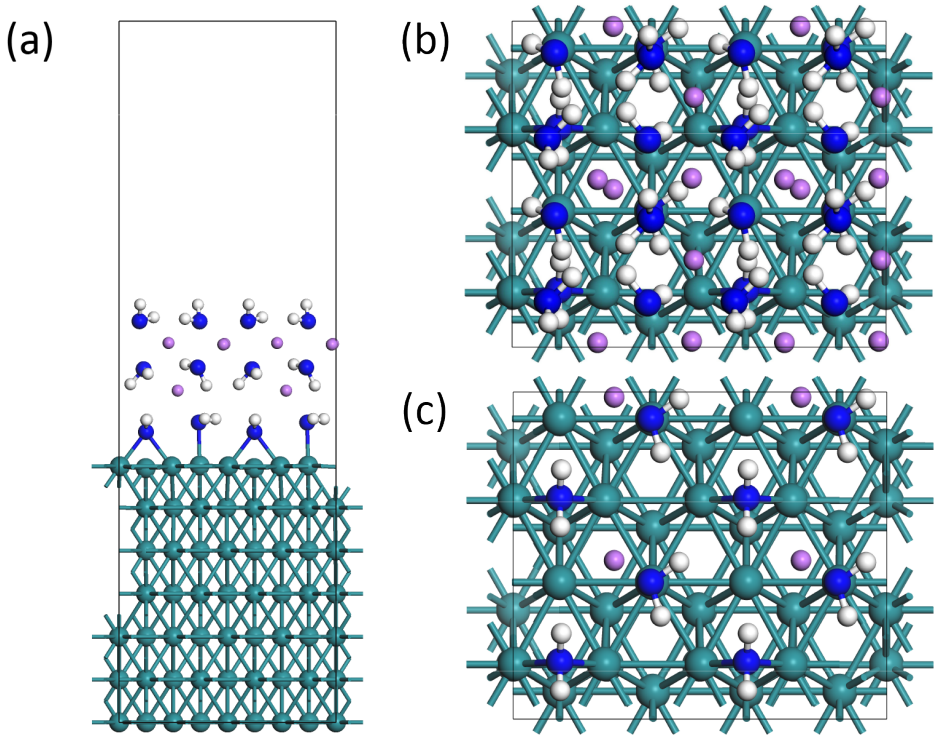

Figure VI.7: (a) Lateral views and (b) top view of initial structures of Ru(0001)/$LiNH_2$(001) dehydrogenation model, (c) top view without the last three planes of $LiNH_2$ to allow better visualization of the NH_2 contact plane with Ru(0001). The colors and atom labels are those depicted in Figure VI.2.

detailed in Figure VI.S2 in the Appendices.

As for the PBE-dDsC functional, the calculation with spin polarization is still in progress with, for the moment, an interface energy of 3.22(5) $J.m^{-2}$, and with almost no magnetic moment (-0.00(6) μ_B). Unfortunately, the calculation is not advanced enough to draw a conclusion on the difference in interface energy between the two functionals. It is anticipated that the interface energy using PBE-dDsC will continue to decrease, potentially aligning closer to the values obtained with GGA PBE, similar to the observations made for the complete Ru/$LiNH_2$ interfaces discussed in section V.4.1 of the previous chapter.

VI.2.2 Hydrogen adsorption sites

Based on the newly developed model, we aim to explore the dehydrogenation of the NH_2 fragments from $LiNH_2$ adsorbed on the metal surface. Previous studies have examined the adsorption of H atoms, indicating a preference for hollow free sites,[432, 442, 282] followed by hollow hcp,[442, 282] bridge,[442, 282] and top sites.[442] However, these studies were limited to the adsorption of hydrogen on Ru(0001) alone. The presence of $LiNH_2$ could potentially influence the preferred sites for hydrogen adsorption. Therefore, it is essential to investigate the various possible adsorption sites under the influence of $LiNH_2$ to understand any alterations in the adsorption properties.

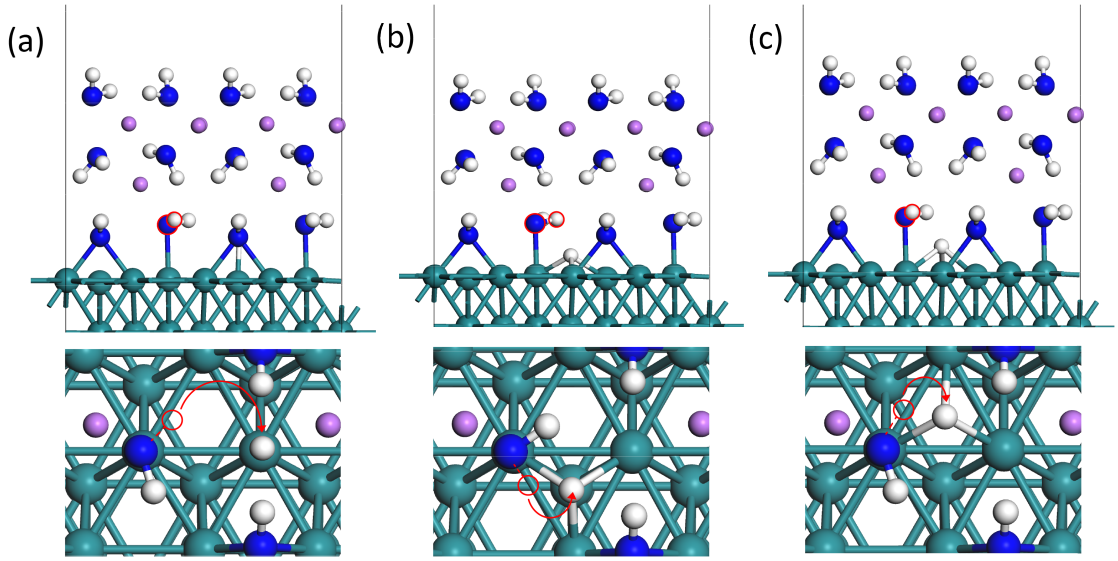

Figure VI.8: Lateral views and top view of initial structures of Ru(0001)/$LiNH_2$(001) dehydrogenation model, (a) with an H removed from NH_2 and placed on top of a Ru surface atom, (b) with an H removed from NH_2 and placed on near hollow hcp site, and (c) with an H removed from NH_2 and placed on near hollow hcp site. The red circle symbolizes the initial position of the substituted hydrogen atom, and the red arrow indicates the position of a new adsorption site. The colors and atom labels are those depicted in Figure VI.2.

The NH_2 fragment selected for dehydrogenation is positioned on top of a Ru atom. During the dehydrogenation process, a hydrogen atom is removed and subsequently placed in three potential adsorption sites for investigation: top (see Figure VI.8.a), hollow hcp (see Figure VI.8.b), and hollow free (see Figure VI.8.c). The bridge site was excluded from my consideration due to the density of N on the Ru surface. Placing the removed hydrogen in an adjacent bridge site would require to share the Ru surface charge density with adjacent NH and an NH_2 adsorbates. Such competition can be expected to be really unfavorable so it was not considered in this study.

Table VI.1: Model name, interface energy ($J.m^{-2}$), total magnetization (μ_B), Ru-N and Ru-H bonds length (Å), and reference of the model geometry figure for both GGA PBE and PBE-dDsC functionals. The values in italics for the PBE-dDsC functional correspond to the current values, which are still being optimized.

Ru(0001)/$LiNH_2$(001) dehydrogenation model	Initial H adsorption site	Final H adsorption site	Interface energy		Magnetization		Ru-N bond length	Ru-H bond length	Model figure
			GGA PBE	PBE-dDsC	GGA PBE	PBE-dDsC	GGA PBE	GGA PBE	
Initial configuration: 8 NH_2 adsorbed	-	-	2.15(9)	*3.22(5)*	0.51(8)	*-0.00(6)*	-	-	see Figure VI.7
H adsorption model: 7 NH_2, 1NH, and 1H adsorbed	Top	Hollow free	2.04(2)	*3.39(0)*	-0.74(4)	*0.87(5)*	2.01, 2.03, and 1.98	2.00, 1.78, and 1.97	see Figures VI.8.a and Figure VI.9.a
	Hollow hcp	Hollow free	1.94(1)	*2.98(9)*	0	*0*	2.08, 2.08 and 1.98	1.84, 1.89 and 1.90	see Figures VI.8.b and Figure VI.9.b
	Hollow free	Hollow free	2.23(4)	*3.27(3)*	0.48(4)	*0.48(6)*	2.07 and 2.06	1.96, 1.80, and 1.90	see Figures VI.8.c and Figure VI.9.c

After spin-polarized GGA PBE optimization, the initial top-site adsorption of the H atom shifted to a hollow free site, as depicted in Figure VI.9.a. Conversely, the H atom initially in the hollow hcp site did not maintain

its position, moving instead to the bridge site (see VI.9.b). As for the original hollow free site, its configuration was preserved (see Figure VI.9.c). The interface energy for the non-altered dehydrogenation model is higher (2.15(9) $J.m^{-2}$) compared to those where H was removed from an adsorbed NH_2 and subsequently adsorbed on the Ru(0001) surface. This means that the dehydrogenation process is globally exothermic. Notably, the model with H initially in the hollow hcp site, which relocated to the opposite hollow free site, displayed a reduced interface energy of 1.94(1) $J.m^{-2}$, significantly lower. This is closely followed by the model where H started at the top and ended in the hollow free position, with an interface energy of 2.04(2) $J.m^{-2}$. Despite the similar final adsorption sites, this interface energy is substantially lower than that of the model where H was originally positioned at the hollow free site. This discrepancy is attributed mainly to subtle alterations in the interactions among Ru atoms and the H atom (refer to Table VI.1 and Figures VI.9.a and VI.9.c), but predominantly results from the lack of reconstruction in the NH configuration, which remains adsorbed on the metal surface. In the most stable configuration, the NH shifts from its bridge position to the adjacent hollow hcp site, positioning its H atom directly atop its N atom. However, in the initial model with H in the hollow hcp, the NH stayed in the bridge site, and its H atom was not aligned above the N atom. This result highlights that a DFT calculation might conclude with a geometry that appears to be the most stable, but that a more stable configuration might exist nearby.

In the PBE-dDsC equivalent, similar reconstructions of the initial adsorption sites for H and NH are observed. Regarding energetics, at the moment, hydrogen adsorption on the surface appears slightly endothermic for most sites, see Table VI.1. However, as the calculations are still in progress, it is unclear whether this endothermicity is fully attributable to genuine energy differences or to the varying completion stages of the calculation, especially given the slow reconstruction of H and NH adsorption sites compare to the initial configurations. Nevertheless, based on the ongoing structural rearrangements, the hollow free site currently appears to be the most stable with PBE-dDsC functional, , in agreement with GGA PBE results.

VI.2.3 Dihydrogen formation from $LiNH_2$ at the Ru(0001) surface

Building on the insights gained from the adsorption properties of a hydrogen atom on Ru(0001) from an adsorbed NH_2 fragment of $LiNH_2$, various models were developed to explore the formation of H_2. Firstly, this exploration is based on the newly obtained NH fragment that had just been optimized through NH_2 dehydrogenation. For this purpose, a second NH_2 fragment adsorbed on Ru(0001) was dehydrogenated by removing one H atom, resulting in two NH fragments adsorbed on the metal, each paired with a recently removed hydrogen atom. Then, the two H atoms are removed from the model, mimicking the desorption of H_2.

In a second step, based on the model depleted of these two H atoms from the H_2 desorption, the investigation extends to the complete dehydrogenation of the two NH fragments. The aim is to ascertain if full dehydrogenation—to the extent of nitrogen adsorption on Ru(0001)—is feasible. Not only, this step is critical to confirm whether the formation of Li_3N from $LiNH_2$ at the interface with Ru can occur, but it is also crucial. This step is crucial for validating the initial phase of our proposed catalytic mechanism for ammonia

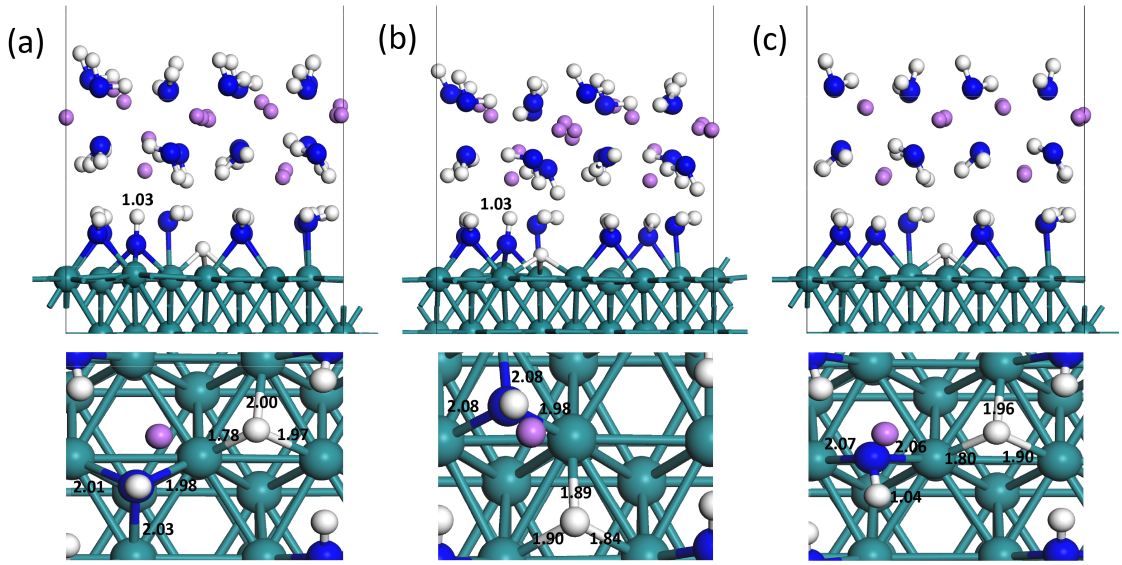

Figure VI.9: Lateral views and top view of optimized structures of Ru(0001)/$LiNH_2$(001) dehydrogenation model, (a) H initial top-site adsorption model, where H shifted to a hollow free site, (b) H initial hollow hcp-site adsorption model, where H shifted to a hollow free site, and (c) H initial hollow free-site adsorption model, where H did not shift position. The distances between Ru and N, as well as that between N and H are expressed in Å. The colors and atom labels are those depicted in Figure VI.2.

decomposition facilitated by Ru/$LiNH_2$ catalyst.

- **Formation of H_2 from two NH_2 adsorbed on Ru(0001): ability to form Li_2NH**

In the previous section, we confirmed the feasibility to form locally Li_2NH from $LiNH_2$ on the Ru(0001) surface. The dissociation of NH_2(ads) into NH(ads) and H(ads) has been established as an exothermic elementary step at standard GGA PBE level of calculation. Following this, one hydrogen atom is removed from another NH_2(ads) fragment adsorbed on the metal. The resulting two NH(ads) fragments are positioned as follows: the previously optimized fragment in the hollow hcp site and the newly created one in the hollow free site (see Figure VI.10.a and VI.10.c). This arrangement not only verifies the stability of having two NH(ads) fragments and two H(ads) on Ru(0001) in an $LiNH_2$ environment, but ir also evaluates the viability of the hollow free site for NH(ads) adsorption.

For the adsorption sites of the two hydrogen atoms in our study, the first model positions both H(ads) atoms in the hollow free site (see Figure VI.10.a), while the second model places one H(ads) in the hollow hcp site and the other in a hollow free site (see Figure VI.10.c). These choices for adsorption sites deviate from the most stable configurations identified in the previous section (with the initial H(ads) site hollow hcp moving to the bridge site). This variation stems from the fact that when these models were designed, the initial single H(ads) atom and NH(ads) fragment adsorption calculations had not yet been fully finalized. As a result, the models being discussed are based on the most stable geometries currently available from ongoing optimizations at the time, which guided the selection of these particular adsorption sites.

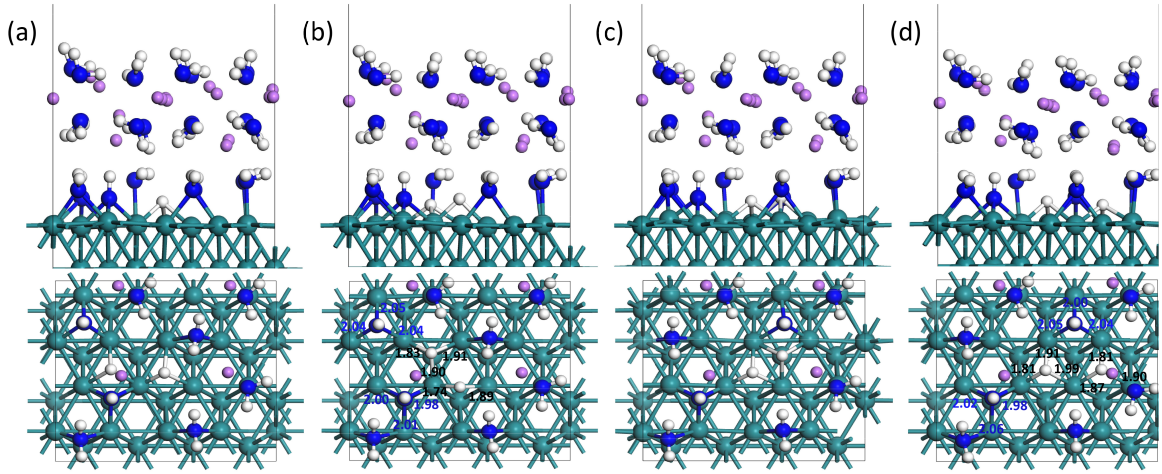

Figure VI.10: Lateral and top views of the optimized structures for the Ru(0001)/$LiNH_2$(001) dehydrogenation model: (a) initial configuration with two H atoms in hollow free co-adsorption sites, (b) after geometry optimization, where the H atoms shift to hollow hcp and bridge co-adsorption sites, (c) initial configuration with two H atoms in hollow free and hcp co-adsorption sites, and (d) after geometry optimization, where both H atoms shift to hollow free co-adsorption sites. The colors and atom labels correspond to those shown in Figure VI.2.

After spin polarized GGA PBE optimization, the geometries of the adsorption sites underwent significant changes, differing substantially from those observed during the adsorption of a single H atom on the metal surface. In the first model, where both H(ads) were initially in hollow-free sites, one H(ads) shifted to the adjacent hollow hcp site. This shift likely caused the displacement of the second H(ads) due to spatial constraints from multiple species on Ru(0001) (illustrated in Figure VI.10.b). In contrast, in the second model—initially featuring H(ads) in both hollow-free and hcp sites—the adsorption sites exhibited another type of relaxation. The H(ads) initially in the hollow-free site maintained its adsorption site post-optimization, demonstrating stability in this configuration also. Conversely, the H(ads) initially in the hollow hcp site relocated to an adjacent hollow-free site (see Figure VI.10.d). Similar diffusional movements are observed with the PBE-dDsC functional, as shown in Figure VI.S3 in the appendix. These two models illustrate that preference for H adsorption site can shift depending on the proximity of other NH_2, NH and H coadsorbed fragments.

Comparing the interface energies of the two models reveals that one configuration is more stable than the other, likely due to the effect of hydrogen adsorption sites on the metal surface. The less stable interface, with an interface energy of 4.95(2) $J.m^{-2}$, positions nitrogen atoms at the preferential adsorption site (both in hollow free positions), while the two hydrogens occupy hollow hcp and bridge sites. In contrast, the more stable interface, with an interface energy of 3.49(2) $J.m^{-2}$, places both hydrogens in hollow free sites. This outcome aligns with studies indicating hollow free as the preferred adsorption site.[432, 442, 282]

As previously mentioned, the interface energy between Ru(0001) and $LiNH_2$(001) slabs was calculated us-

ing Ru and $LiNH_2$ bulk energies as references. However, to enable a consistent comparison post-H_2 desorption, the expression for $\Gamma_{LiNH_2(001)@Ru(0001)}$ has been modified to account for the release of a hydrogen gas molecule, ensuring energy consistency across different models. The adjusted interface energy expression is as follows:

$$\Gamma_{LiNH_2(001)@Ru(0001)} = \frac{(E_{LiNH_2(001)@Ru(0001)} + N_{H_{2(gas)}} \times E_{H_{2(gas)}}) - (E_{LiNH_{2(\sigma)}} + E_{Ru})}{\mathcal{A}_{LiNH_2@Ru}} \quad \text{(VI.1)}$$

where $E_{LiNH_2(001)@Ru(0001)}$ is the total electronic energy of the interface model between Ru(0001) and $LiNH_2$(001) slabs, $E_{H_2\,(gas)}$ represents the total electronic energy of gas-phase H_2, $E_{LiNH_2\,(\sigma)}$ the total electronic energy of the non-stoichiometric $LiNH_2$ bulk, and E_{Ru} the total electronic energy of the Ru bulk. $N_{H_2\,(gas)}$ is the number of desorbed H_2 molecules, and $\mathcal{A}_{(LiNH_2@Ru)}$ denotes the surface area of the interface model.

Table VI.2: Model name, interface energy (J.m^{-2}), total magnetization (μ_B), Ru-N and Ru-H bonds length (Å), and reference of the model figure for both GGA PBE and PBE-dDsC functionals. The values in italics correspond to the current values, which are still being optimized.

Dehydrogenation model	Initial H adsorption site	Final H adsorption site	Interface energy		Magnetization		Ru-N bond length	Ru-H bond length	Model figure
			GGA PBE	PBE-dDsC	GGA PBE	PBE-dDsC	GGA PBE	GGA PBE	
2 NH and 2 H co-adsorbed	2 Hollow free	Hollow hcp Bridge	4.95(2)	*3.09(8)*	-0.68(0)	*0.00(5)*	2.04, 2.05 and 2.04 2.00, 2.01 and 1.98	1.83, 1.91 and 1.90 1.74 and 1.89	Figure VI.10.a and VI.10.b
	Hollow hcp Hollow free	2 Hollow free	3.49(2)	*3.10(3)*	-0.74(4)	-0.02(3)	2.02, 1.98 and 2.06 2.00, 2.05 and 2.05	1.91, 1.81 and 1.99 1.81, 1.87 and 1.90	Figure VI.10.c and VI.10.d
2 NH co-adsorbed and H_2 desorbed	-	-	4.95(2)	*4.73(2)*	-0.40(4)	*4.73(2)*	2.04, 2.05 and 2.04 2.00, 2.01 and 1.98	-	Figure VI.10.a and VI.10.b
2 N and 2 H co-adsorbed	2 Hollow free	2 Hollow free	*8.01(8)*	*6.37(3)*	*0.57(4)*	*0.43(7)*	1.90, 1.90 and 1.98 1.92, 1.99 and 2.00	1.85, 1.90 and 1.94 1.82, 1.85 and 1.93	Figure VI.11.a and VI.11.b
	Hollow hcp Hollow free	2 Hollow free	*9.46(9)*	*7.90(3)*	*-0.57(8)*	*-0.00(8)*	1.90, 1.90 and 1.98 1.91, 1.99 and 2.00	1.85, 1.90 and 1.94 1.82, 1.85 and 1.93	Figure VI.11.c and VI.11.d
2 N co-adsorbed and H_2 desorbed	-	-	*11.00(8)*	*9.52(2)*	*0.53(5)*	*-0.53(5)*	1.90, 1.91 and 1.99 1.94, 1.96 and 1.96	-	Figure VI.10.a and VI.10.b

The differences in interface energies among models after H_2 desorption are reasonable. Specifically, between the models with 2 adsorbed H atoms (2 H(ads)) and its counterpart simulating desorption—where two H atoms are removed—the energy difference is only 1.46(0) J.m^{-2} (or 0.67(0) eV) in GGA PBE, as shown in Table VI.2, indicating a weakly endothermic process. This energy change supports the feasibility of H_2 formation directly from $LiNH_2$, suggesting that the local formation of Li_2NH on the Ru(0001) surface could occur under comparable conditions. Even in the preliminary results from PBE-DsC, the difference is similar, at 1.63(4) J.m^{-2} (or 0.70(0) eV), as depicted in Table VI.2.

- **Formation of H_2 from two NH adsorbed on Ru(0001): ability to form Li_3N**

This initial verification however is not sufficient to conclude regarding the formation of Li_3N on the Ru(0001) surface from $LiNH_2$. Building upon the model from which two H atoms and their corresponding NH(ads) were removed, the dehydrogenation process was further explored. The two NH fragments that were previously optimized were further dehydrogenated, resulting in two N atoms remaining adsorbed on the Ru(0001) in the optimized hollow hcp and free sites. Regarding the placement of H atoms, the study continued to explore two configurations were considered: one where both H atoms are in hollow free sites (see Figure

VI.11.a), and another where one H atom is in a hollow hcp site and the other in a hollow free site (see Figure VI.11.c).

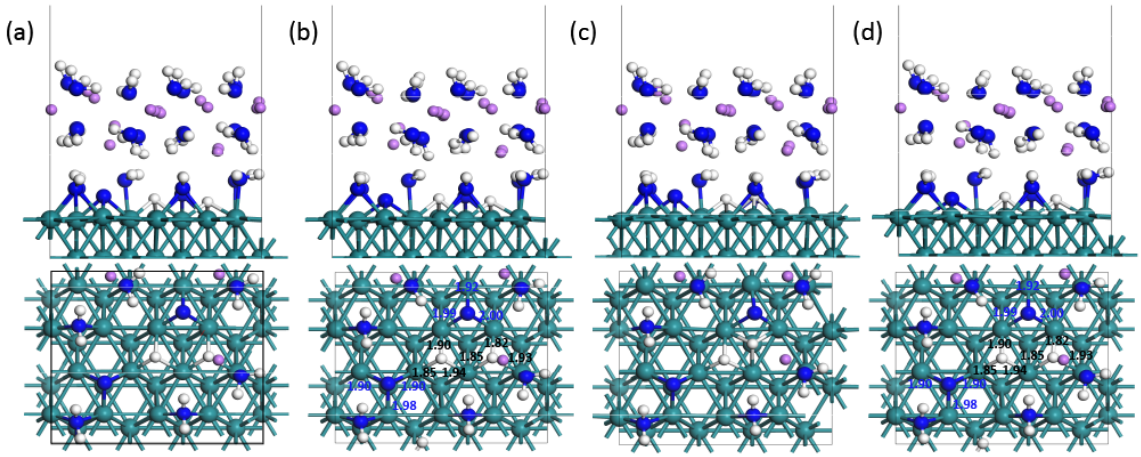

Figure VI.11: Lateral and top views of the optimized structures for the Ru(0001)/$LiNH_2$(001) dehydrogenation model: (a) initial configuration with two H atoms in hollow free co-adsorption sites, (b) after geometry optimization, with no change in the co-adsorption sites, (c) initial configuration with two H atoms in hollow free and hcp co-adsorption sites, and (d) after geometry optimization, where the H atom initially in the hollow hcp site shifts to a hollow free site. The colors and atom labels correspond to those shown in Figure VI.2.

The optimization of the geometries for the two adsorption models is still in progress for both the GGA PBE and PBE-dDsC functionals. Nevertheless, the adsorption sites for N(ads) and H(ads) remain consistent between the two functionals and align with previous findings, as shown in Figure VI.11, with hollow hcp site for N(ads) atoms and hollow free sites for H(ads) atoms. The current differences in interface energy between the two adsorption models, despite their geometric similarity, are attributed to their incomplete optimization. It is anticipated that, once these calculations are finalized, the interface energies will converge between the two models, regardless of whether the GGA PBE or PBE-dDsC functional is used.

Regarding the energetic comparison between the initial state, where two NH fragments are adsorbed on the Ru(0001) surface after the release of a molecule of H_2(gas), and the state of adsorption of two N(ads) and two atomic H(ads), the difference between the models may seem high. There is in fact approximately 3 $J.m^{-2}$ difference between the initial state and the most stable state identified to date (see Table VI.2. This, however, only represents a difference of 0.46 eV for the GGA PBE functional, and 0.74 eV for the PBE-dDsC. In addition this energy difference will continue to decrease as the geometric optimization calculations progress for both functionals.

Regarding the desorption of an additional H_2(gas) molecule, the change in adsorption energy is of a similar magnitude to that observed in the initial state and in the co-adsorption of two hydrogen atoms (around 3 $J.m^{-2}$), with values of 0.57 eV for the GGA PBE functional and 0.65 eV for the PBE-dDsC functional. However, it is still premature to conclude on the final trend of this energy difference, whether it will increase or

decrease, as all considered models are still currently optimized. Nonetheless, the barrier for the complete dehydrogenation of a previously dehydrogenated NH fragment of lithium amide in contact with ruthenium appears reasonable. In the current analysis of my results, it is therefore highly likely that the lithium material part in direct contact with ruthenium will undergo full dehydrogenation.

VI.2.4 Conclusion

At the GGA PBE level, the desorption of a hydrogen atom from an NH_2 fragment is exothermic (1.39 eV of energy gain), resulting in an NH fragment adsorbed at the hollow hcp site and the hydrogen atom at the hollow free site. The dehydrogenation of a second NH_2 fragment is slightly endothermic (0.64 eV of energy loss), likely due to the steric hindrance on the ruthenium surface. Here, the NH fragment remains in the hollow hcp site, while the second hydrogen atom adsorbs in the hollow free site. The formation of H_2(gas) from these two adsorbed hydrogens is also weakly endothermic (0.67 eV of energy loss). The overall energy difference between the initial state, with 8 NH_2 fragments adsorbed on the metal, and the final state, with 6 NH_2 fragments and two NH fragments, is slightly exothermic (0.08 eV of energy gain), as depicted in Figure VI.12.

The complete dehydrogenation of the two NH fragments adsorbed on the ruthenium surface is endothermic (0.46 eV of energy loss). Both nitrogen atoms remain adsorbed at the hollow hcp sites, while the two hydrogen atoms occupy the hollow free sites. Following H_2 formation and desorption, the process is also endothermic (0.57 eV of energy loss). Thus, the formation of two nitrogen atoms adsorbed on the ruthenium surface, from NH fragment, is endothermic (1.03 eV of energy loss), as illustrated Figure VI.12.

In the literature, recombinant desorption of H_2 is reported as endothermic. Logadottir *et al.* identified an energy loss of 3.2 eV between models with 6 H(ads) and desorbed 3 H_2, corresponding to approximately 1 eV loss per H_2 molecule,[280] a value consistent with our results. Similarly, Mhadeshwar *et al.* reported an activation energy of 0.85 ± 0.30 θ_H eV.[284] The formation and desorption of H_2 are highly dependent on the surface coverage rate. In our case, due to the nature of $LiNH_2$, the Ru(0001) surface exhibits high atomic coverage. Nonetheless, the formation of two nitrogen atoms adsorbed on the ruthenium surface remains feasible.

In summary, the study of the successive dehydrogenation of NH_2 fragments in lithium amide indicates that its conversion into lithium nitride is feasible through contact with the ruthenium metal surface, particularly under ammonia decomposition conditions.

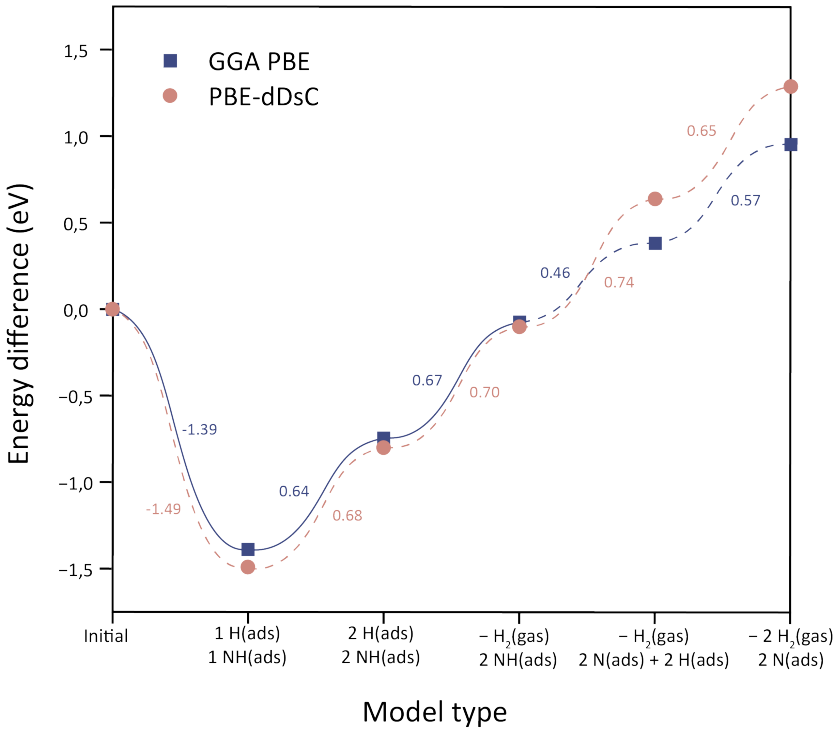

Figure VI.12: Energy profile of the complete desorption of two NH_2 fragments from $LiNH_2$, adsorbed on the Ru(0001) surface, at the GGA PBE and PBE-dDsC level. The dotted lines indicate that the current energy differences between models are still in progress due to ongoing geometry optimizations.

VI.3 Partially hydrogenated interface model: Ru(0001)/Li_3N(001)/Li_2NH(001)/ $LiNH_2$(001)/Gas

VI.3.1 Preliminary study of lithium nitride and lithium imide

VI.3.1.1 Bulk materials

VI.3.1.1.1 Li_2NH bulk

Lithium imide (Li_2NH) can be synthesized by the decomposition of $LiNH_2$ at high temperatures under vacuum or through the reaction of ammonia gas with lithium hydride (LiH). The crystal structure of Li_2NH has inspired numerous studies, particularly due to its potential role as a hydrogen storage material.[443]

The first Li_2NH proposed structure was an antifluorite structure, isomorphous with Li_2O, although it lacked information on the position of hydrogen atoms.[444] Subsequently, two cubic structures were suggested. First, Ohoyama *et al.* proposed a face-centered cubic (fcc) structure within space group $F\bar{4}3m$, with hydrogen atoms randomly occupying four of the tetrahedral 16e sites surrounding the nitrogen atom.[445] Later, Noritake *et al.* also suggested an fcc structure but in space group $Fm\bar{3}m$, similarly with hydrogen atoms distributed randomly across four of the 48h sites surrounding the nitrogen atom.[446]

Several studies converge on the antifluorite structure ($Fm\bar{3}m$) as the most stable high-temperature phase of Li_2NH.[447, 337, 448] However, the low-temperature structure remains debated.[447, 449, 450] Initially, a cubic phase ($Fd\bar{3}m$) was proposed, but this model displayed unrealistically short Li-Li distances, leading to inconsistencies during DFT geometry optimizations. Alternative lower-energy structures with $Pnma$ and $Pbca$ space groups have been suggested, but they fail to fully align with diffraction data or vibrational spectra. The difficulty in determining the precise crystal structure of Li_2NH arises from its synthesis methods, which heavily influence its crystal structure and phase transitions.[451]

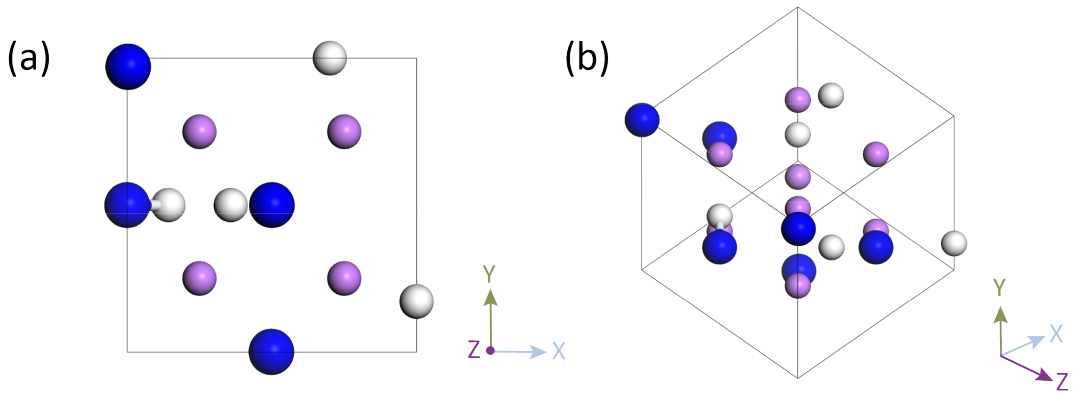

Figure VI.13: Bulk structure of Li_2NH $Fm\bar{3}m$ (a) along the [100] direction and (b) perspective projection. Labels and colors of atoms are depicted in Figure VI.2.

In our study, we used the revised Li_2NH bulk structure as reported by Ohoyama *et al.*, specifically the $Fm\bar{3}m$ cubic phase,[445] as shown in Figure VI.13. This structure corresponds to the high-temperature phase of Li_2NH, which aligns with our experimental conditions where Li_2NH is formed by heating $LiNH_2$. The cubic symmetry of this structure also limits the structural mismatch with our optimized Ru(0001) surface cell, despite a remaining mismatch of 6.7%.

Accurately modeling the crystal structure of Li_2NH using DFT has proven to be challenging due to incomplete knowledge of the hydrogen atom positions. The random distribution of hydrogens hinders successful geometry optimization, where it leads to the loss of the original symmetry group, complicating precise computational simulations.

This phenomenon was previously observed by Miceli *et al.*, where the Li_2NH structure, initially belonging to the $Ima2$ space group, transformed into $Imma$ due to the migration of interstitial Li atoms to octahedral sites.[337, 441] To counter this structural reconstruction, they introduced Li vacancies at the centers of tetrahedral clusters, distributing them uniformly across the cell. This not only neutralized the system by balancing the charge but, more importantly, prevented the migration of Li atoms, thus preserving the original symmetry of the structure.[441]

In our case, the cubic structure of the cell can be maintained without introducing any vacancy by adjusting

the position of the Li atom. This is achieved by optimizing simultaneously the stress tensor on the supercell (relaxing the volume while keeping the cell shape constant) and the atomic positions inside the supercell. The VASP corresponding tag is called ISIF, and the value 8 only available in VASP version 6.4, enables the relaxation of all parameters except the cell shape. This allows us to retain the symmetry of the Li_2NH bulk, as described in the literature.

For the DFT predictions of Li_2NH bulk material (see Figure VI.13), we rely on the experimental lattice parameters to assess the quality of the modeling. The standard GGA PBE functional provides an accurate description of Li_2NH, with an error of only 1.1% for the lattice parameter a, compared to experimental values. Similarly, the dispersion-corrected functional, PBE-dDsC, also shows a -1.1% error for a. Therefore, both functionals offer a reliable description of Li_2NH. All calculated and experimental lattice parameters of Li_2NH bulk can be found in Table VI.3.

As for the comparison with theoretical studies of Li_2NH, Song *et al.* examined the $Fm\bar{3}m$ structure by using the standard GGA PBE. Their geometry optimization yielded a lattice parameter of 5.2968 Å, reflecting a 4.1% deviation from the experimental value.[329] This error is significantly larger than ours and may stem from their 5 $\times$5 $\times$5 k-points grid, whereas we employed a more dense 23 $\times$23 $\times$23 grid, which likely enhances the accuracy of our calculations. Another, geometry optimization done in another study gave for a 5.045 Å, so with a reduce error of -0.63% compared with measurement.[334]

To our knowledge, experimental values for the bulk modulus, the cohesive energy and the formation energy are not available in the literature for Li_2NH. Theoretical studies have calculated bulk moduli ranging from 42 to 97 GPa using GGA PBE, with the variation attributed to different calculation conditions.[329, 334] Our calculated values of 72 GPa for GGA PBE and 73 GPa for PBE-dDsC fall within this range, as depicted in Table VI.3. Additionally, our value of 3.6 for B'_0 is consistent with the previously computed value of 3.714.[334]

Regarding the cohesive energy, the theoretical study by Song *et al.* reported a value of -2.996 eV/atom,[329] which is in the same range as our calculated values of -2.21(7) eV/atom (GGA PBE) and -2.22(1) eV/atom (PBE-dDsC). The cohesive energies are presented in Table VI.3 and defined as follows:

$$E_{coh,\,Li_2NH} = \frac{E_{Li_2NH} - (N_{Li} \cdot E_{Li} + N_N \cdot E_N + N_H \cdot E_H)}{N_{atoms,\,Li_2NH}} \tag{VI.2}$$

where E_{Li_2NH}, E_{Li}, E_{N}, and E_{H} represent the total electronic energies of stoichiometric bulk Li_2NH, isolated gas-phase Li, N, and H atoms, respectively; where N_{Li}, N_N,and N_H are the total numbers of Li , N and H atoms in the Li_2NH stoichiometric bulk, respectively; and where $N_{atoms,\,Li_2NH}$ is the total number of atoms in the Li_2NH stoichiometric bulk.

The calculated formation energy of Li_2NH bulk has been calculated at the GGA PBE level is -2.05(6) eV, and at -1.97(8) eV with dispersion corrected functional (see Table VI.3). The definition of the formation energy is defined as follows as follows:

$$E_{form,\,Li_2NH} = \frac{E_{Li_2NH}}{N_{unit,\,Li_2NH}} - \left(\frac{N_{Li}}{2} \cdot E_{Li,\,bulk} + \frac{N_N}{2} \cdot E_{N_2,\,gas}\right) \quad \text{(VI.3)}$$

where E_{Li_2NH}, $E_{Li,\,bulk}$, and E_{N_2} represent the total electronic energies of the stoichiometric bulk Li_2NH, of Li BCC bulk and gas phase N_2 isolated molecules, respectively; and where N_{Li}, N_N, and $N_unit,\ Li_2NH$ represent the total numbers of Li atoms, N atoms and Li_2NH units in the Li_2NH stoichiometric bulk, respectively.

Table VI.3: Ground-state structural and energetic properties of optimized Li_2NH and Li_3N bulks predicted by DFT calculations with pure GGA PBE, and dispersion-corrected PBE-dDsC. Those optimized bulks are non-magnetic. Lattice parameters (a, c, Å), cohesion energy (E_{coh}, eV/at.), formation energy (E_{form}, eV), bulk modulus (B_0, GPa) and its derivative (B_0, dimensionless). Experimental crystallographic and energetic data are also reported.

System	Li_2NH			Li_3N		
Functional	GGA PBE	PBE-dDsC	Exp.	GGA PBE	PBE-dDsC	Exp.
a (Å)	5.13(1)	5.03(6)	5.07(7)	4.88(8)	4.84(3)	4.5 [452]
E_{coh} (eV/at.)	-2.21(7)	-2.22(1)		-2.74(7)	-2.81(8)	
E_{form} (eV)	-2.05(6)	-1.97(8)		-0.94(7)	-1.14(5)	
B_0 (GPa)	72	73		70	72	78($\pm$13) [452]; 82.8 [453]
B'_0	3.6	3.6		4.1	4.2	4.2($\pm$0.2) [452]; 3.84 [453]

VI.3.1.1.2 Li_3N bulk

Lithium nitride (Li_3N) is synthesized through the direct reaction of metallic lithium with nitrogen gas.[454] At ambient temperature and pressure, its crystal structure is known as α-Li_3N ($P6/mmm$).[455] Around 0.5 GPa, α-Li_3N undergoes a phase transition to a secondary hexagonal structure, β-Li_3N ($P6_3/mmc$).[452, 456] Although β-Li_3N is metastable at ambient pressure and typically coexists with the α-phase, it remains stable under pressures up to 35 GPa.[452] Additionally, β-Li_3N can form from α-Li_3N through ball milling.[455] Above 35 GPa, Li_3N undergoes another phase transition, forming the γ-Li_3N phase ($Fm3m$), which adopts a cubic structure and remains stable at pressures up to at least 200 GPa.[452] The crystallographic data of Li_3N are specified in Figure VI.14 and Table VI.3.

For our DFT modeling, we chose the γ-Li_3N crystalline structure. Although this is the high-pressure phase of Li_3N, it presents the smallest structural mismatch with our optimized Ru(0001) cell. Nevertheless, the mismatch between the two lattice parameters remains significant at -17.1%.

The DFT predictions for the lattice parameters of γ-Li_3N are not as reliable as those for $LiNH_2$ and Li_2NH, as depicted in Table VI.3. Indeed, systematic errors in lattice constants are higher, with deviations of -8.6% in the GGA PBE and -7.6% in the PBE-dDsC calculations. However, this lattice expansion helps to slightly reduce the mismatch between Li_3N and Ru(0001). In GGA PBE, the mismatch decreases to -9.9%, while in PBE-dDsC, it is reduced more modestly to -10.8%.

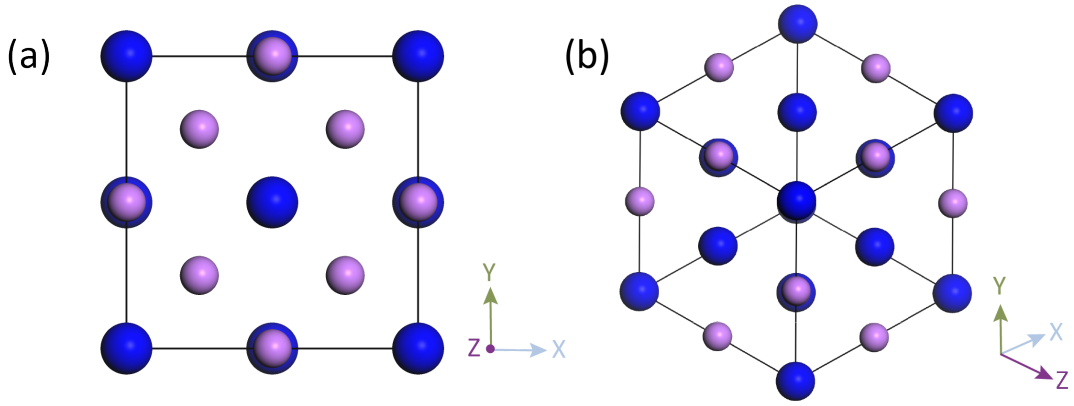

Figure VI.14: Bulk structure of γ-Li_3N $Fm3m$ (a) along the [100] direction and (b) perspective projection. Labels and colors of atoms are depicted in Figure VI.2.

The bulk modulus of γ-Li_3N was calculated at the standard GGA PBE level at 70 GPa with a B_0' of 4.1, and for the dispersion-corrected PBE-dDsC functional, the bulk modulus value is very close at 72 GPa and with a B_0' of 4.2. These two values are in good agreement with the experimental bulk modulus values of γ-Li_3N, measured between 78 $\pm$ 13 and 82.8 GPa.[452, 453] Similarly, for B_0', the measured values range between 3.84 and 4.2 $\pm$ 0.2.[452, 453]

Concerning the cohesive energy and formation energy of γ-Li_3N, a direct comparison with experimental measurements is not feasible due to the absence of relevant data. However, the cohesive energy is comparable to those of $LiNH_2$ and Li_2NH, with values of -2.74(7) eV.at^{-1} (GGA PBE) and -2.81(8) eV.at^{-1} (PBE-dDsC). As with these other compounds, the cohesive energy increases when dispersion corrections are included. The cohesive energy values, listed in Table VI.3, have been calculated as follows:

$$E_{coh,\ Li_3N} = \frac{E_{Li_3NH} - (N_{Li} \cdot E_{Li} + N_N \cdot E_N)}{N_{atoms,\ Li_3N}} \tag{VI.4}$$

where E_{Li_3N}, E_{Li}, and E_{N} represent the total electronic energies of stoichiometric bulk Li_3N, isolated gas-phase Li and N atoms, respectively; where N_{Li} and N_N are the total numbers of Li and N in the Li_3N stoichiometric bulk, respectively; and where $N_{atoms,\ Li_3N}$ is the total number of atoms in the Li_3N stoichiometric bulk.

The formation energy of γ-Li_3N bulk has been calculated at the GGA PBE level to be -0.94(7) eV, and at -1.14(5) eV with dispersion adjusted functional (see Table VI.3). The definition of the formation energy is defined as follows as follows:

$$E_{form,\ Li_3N} = \frac{E_{Li_3N}}{N_{unit,\ Li_3N}} - \left(\frac{N_{Li}}{2} \cdot E_{Li,\ bulk} + \frac{N_N}{2} \cdot E_{N_2,\ gas} \right) \tag{VI.5}$$

where E_{Li_3N}, $E_{Li,\,bulk}$, and E_{N_2} represent the total electronic energies of the stoichiometric bulk Li_3N, of Li BCC bulk and gas phase N_2 isolated molecules, respectively; and where N_{Li}, N_N, and $N_unit,\ Li_3N$ represent the total numbers of Li atoms, N atoms and Li_3N units in the Li_3N stoichiometric bulk, respectively.

VI.3.1.2 Non-stoichiometric Li_3N and Li_2NH bulk energetic model

In a similar manner to lithium amide, studying the interface and surface properties of Li_3N and Li_2NH necessitates the development of their respective bulk additive models. For both Li_2NH and Li_3N, the bulk additive models were designed using an Energy Decomposition Analysis (EDA). In the case of Li_2NH, its stoichiometric bulk was modeled by considering the two-body interaction terms: the interactions between lithium atoms E_{Li-Li}, between the NH fragments E_{NH-NH}, and between the lithium and NH fragments $\tilde{E}_{Li-NH}$. The equation for the bulk additive model of Li_2NH is expressed as follows:

$$E_{Li_2NH} = N_{Li} \cdot (E_{Li-Li} + E_{Li}) + N_{NH} \cdot (E_{NH-NH} + E_{NH}) + N_{Li-NH} \cdot \tilde{E}_{Li-NH} \qquad \text{(VI.6)}$$

where N_{Li}, N_{NH}, and N_{Li-NH} represent the number of lithium atoms, NH fragments, and Li-NH chemical bonds, respectively. E_{Li} and E_{NH} refer to the total electronic energies of the lithium atom and the NH fragments, respectively. All two-body interaction energy terms for Li_2NH can be found in Table VI.4.

Regarding Li_3N, the interactions between lithium atoms E_{Li-Li} in the bulk were also considered to develop its bulk additive model. Similarly, the interactions between the nitrogen atoms E_{N-N}, and between the lithium and N atoms $\tilde{E}_{Li-N}$ were included. The equation for the bulk additive model of Li_3N is expressed as follows:

$$E_{Li_3N} = N_{Li} \cdot (E_{Li-Li} + E_{Li}) + N_N \cdot (E_{N-N} + E_N) + N_{Li-N} \cdot \tilde{E}_{Li-N} \qquad \text{(VI.7)}$$

where N_{Li}, N_N, and N_{Li-N} represent the number of lithium atoms, nitrogen atoms, and Li-N chemical bonds, respectively. E_{Li} and E_N refer to the total electronic energies of the lithium atom and the nitrogen atoms, respectively. All two-body interaction energy terms for Li_3N can be found in Table VI.4.

VI.3.1.3 Clean surfaces

To interface four different crystal structures, the study of clean surfaces focuses on minimizing structural mismatch. In the previous interface model between Ru HCP and $LiNH_2$ BCT, the (001) surface of $LiNH_2$ was selected to match the thermodynamically favorable surface of the metal (0001). Similar considerations are applied to the study of Li_3N and Li_2NH surfaces.

Table VI.4: Additive model of Li_2NH bulk: two-body interaction energy terms (Li–Li, NH–NH), non-additivity of the model (Li–NH) and Li_3N bulk: two-body interaction energy terms (Li–Li, N–N), non-additivity of the model (Li-N) at the GGA PBE and PBE-dDsC levels in eV.

Functional	Li_2NH two-body interactions			Li_3N two-body interactions		
	Li–Li	NH–NH	Li–NH	Li–Li	N–N	Li–N
GGA PBE	-1.32(1)	0.03(7)	-2.95(8)	-0.42(1)	0.06(0)	-3.25(1)
PBE-dDsC	-1.41(9)	-0.06(5)	-3.13(1)	-0.42(8)	-0.01(1)	-3.33(6)

VI.3.1.3.1 Li_2NH surfaces

For the Li_2NH surfaces, we studied the (100) and (111) terminations. The structural mismatch between these planes and the $(2 \times \sqrt{3})$ supercell relative to Ru(0001) is summarized in Table VI.5. Among the surfaces analyzed, Li_2NH(100) exhibits the smallest mismatch with the $(2 \times \sqrt{3})$ cell. For Li_2NH(111), the mismatch along a can be minimized by interfacing a Ru $(17 \times \sqrt{3})$ supercell with a Li_2NH surface projected onto a $\left(3 \times \frac{\sqrt{3}}{2}\right)$ cell.

Table VI.5: The calculated lattice mismatch between Ru(0001) and Li_2NH(100) or Li_2NH(111), expressed as a percentage error, considering both the revised and unrevised a or c lattice parameters. Results are provided for calculations at the GGA PBE and PBE-dDsC levels.

	Error on a		Error on c		Revised error on a	
	GGA PBE	PBE-dDsC	GGA PBE	PBE-dDsC	GGA PBE	PBE-dDsC
Li_2NH(100)	-7.0	-7.8	7.4	6.6	-	-
Li_2NH(111)	24.4 [a]	23.8 [a]	10.7 [a]	9.9 [a]	11.8 [b]	11.1 [b]

[a] Mismatch calculated by projection onto a $\left(1 \times \frac{\sqrt{3}}{2}\right)$ cell; [b] Revised error on a considering a $(17 \times \sqrt{3})$ supercell for Ru interfaced with a $\left(3 \times \frac{\sqrt{3}}{2}\right)$ cell.

All lithium imide surface energies ($\gamma_{Li_2NH(hkl)}$) were calculated by predicting the total electronic energies of either the stoichiometric or non-stoichiometric Li_2NH bulks energy $E_{Li_2NH\ (\sigma)}$, depending on the model's stoichiometry, along with the corresponding model surface area $\mathcal{A}_{Li_2NH(hkl)}$. The equation allowing to calculate surface energies equation used is expressed as follows:

$$\gamma_{Li_2NH(hkl)} = \frac{E_{Li_2NH(hkl)} - E_{Li_2NH\ (\sigma)}}{\mathcal{A}_{Li_2NH(hkl)}} \tag{VI.8}$$

For Li_2NH(100), three possible terminations were studied: the stoichiometric one, featuring a termination composed of NH fragments and the other one composed of lithium atoms (see Figure VI.S4.a), as well as two non-stoichiometric terminations, with termination composed exclusively of NH fragments or of lithium atoms on both ends (see Figures VI.S5.a and VI.S6.a, respectively). The thickness of these three models varies from 15 to 17 atomic layers, see Table VI.6 for details.

After geometry optimization with both functionals, some reconstruction of the NH-based termination can occur, but these reconstructions are not systematic. In the stoichiometric structure, no reconstruction altering the nature of the terminations is observed; the only changes occur at the N-H bond level, with the hydrogen atoms orienting towards the vacuum slab after relaxation (see Figure VI.S4.b). In the case of the non-stoichiometric structure terminated with NH fragments, the reconstructions proved to be more significant. An initially pure NH-fragment terminated surface became mixed with lithium atoms from the plane below the termination, and at the opposite termination, the two NH fragments moved closer together and bonded, forming an N_2H_2 specie (see Figure VI.S5.b). Therefore to force the NH terminal planes of the non-stoichiometric structure to stay at their bulk configurations and orientations (or in order to hinder surface reconstructions), the nitrogen atoms in the terminal planes, as well as the lithium atoms in the plane adjacent to these terminals, were were kept fixed during the geometry optimizations. Finally, for the non-stoichiometric lithium-terminated surface, no significant reconstructions was observed, aside from minor atomic relaxations in the terminal planes (see Figure VI.S6.b).

Regarding the stability of these three surfaces, the NH-terminated surface is the most stable one, with a surface energy of 0.19(3) $J.m^{-2}$ at the GGA PBE level and -0.15(5) $J.m^{-2}$ at the PBE-dDsC level. The negative value obtained with the dispersion-corrected functional is unusual, as surface energy calculations, referenced to the lithium imide bulk, are expected to yield positive values. This particular case corresponds to a strongly magnetic and polar surface for which several planes had to be kept frozen to avoid surface reconstruction. Hence the computed surface energies contain an additional energy strain/stress which could be stabilizing or destabilizing depending on its impact on the surface charge.

The three structures considered exhibit magnetic moments ranging from 1.96(5) to 3.99(7) μ_B at the GGA PBE level. The spin density is localized on nitrogen atoms. At the PBE-dDsC level, the two structures with lithium-containing terminations show no dipole moment, whereas the structure terminated by frozen NH fragments exhibits a magnetic moment of 3.99(4) μ_B, likely due to the suppression of surface reconstruction as evoked previously.

For the $Li_2NH(111)$ surface, the same three types of terminations were studied: the stoichiometric termination, featuring a termination composed of NH fragments and the other one composed of lithium atoms (see Figure VI.S7.a), as well as two non-stoichiometric terminations, with termination composed exclusively of NH fragments or of lithium atoms on both ends (see Figures VI.S8.a and VI.S9.a, respectively).

After relaxation, the planes composed of NH fragments became mixed with lithium atoms from the plane below the terminal one (see Figure VI.S7.b for the stoichiometric model and Figure VI.S8.b for the non-stoichiometric model). This reconstruction recalls the one previously seen for the equivalent (100) surface. To hinder such a phenomenon, the nitrogen atoms in the terminal planes and the lithium atoms in the adjacent planes were fixed. For terminations composed solely of lithium, only a minor atomic relaxation of the terminal plane was observed, similar to what occurs on the (100) surface, as shown in Figures VI.S7.b and VI.S9.b.

A similar energy trend is observed for the surface energies across the three models of the (111) and (100) surfaces. Notably, the surface energy of the model with NH terminations is negative for both functionals considered (see Table VI.6), which can again be attributed to the presence of a stabilizing strain/stress term in our models. Regarding magnetism, the lithium-terminated surfaces exhibit no magnetic moment, whereas the other two models display magnetic moments ranging from 7.03(5) to 7.99(9) μ_B (GGA PBE) and from 3.90(4) to 7.79(4) μ_B (PBE dDsC). The stronger magnetic properties of these models are likely a consequence of the constraints applied to the lithium and nitrogen atoms during the calculations.

Table VI.6: Surface energies (J.m^{-2}) and magnetization (μ_B) of optimized Li_3N(100), Li_3N(111), Li_3N(110), Li_2NH(100), Li_2NH(111) and Li_2NH(110) clean slabs according to pure GGA PBE and dispersion corrected PBE-dDsC functionals. The values in italics correspond to the current values, which are still being optimized. All models with identical terminations (e.g., N–N) are non-stoichiometric, while those with different terminations (e.g., Li–NH) are stoichiometric.

System	Atomic layers	Terminations	Surface energy		Magnetization	
			GGA PBE	PBE-dDsC	GGA PBE	PBE-dDsC
	16	Li - NH	*2.24(2)*	*2.27(7)*	*3.52(5)*	*-0.05(2)*
Li_2NH(100)	17	NH - NH	0.19(3)	*-0.15(5)*	3.99(7)	*3.99(4)*
	15	Li - Li	*4.85(6)*	*4.40(8)*	*1.96(5)*	*0*
	10	Li - NH	*2.54(9)*	*2.67(5)*	*7.03(5)*	*3.90(4)*
Li_2NH(111)	8	NH - NH	*-0.14(9)*	*-0.41(4)*	*7.99(9)*	*7.79(4)*
	8	Li - Li	*4.83(7)*	*5.00(1)*	*0*	*0*
	16	Li - NLi	2.32(0)	1.10(5)	3.69(9)	2.09(4)
Li_3N(100)	13	NLi - NLi	0.52(5)	0.13(1)	3.99(8)	3.99(9)
	15	Li - Li	4.21(5)	3.80(0)	3.94(7)	3.94(3)
	16	N - Li	2.89(1)	2.48(5)	8.32(4)	8.13(5)
Li_3N(111)	13	N - N	-0.16(5)	-0.12(6)	12.00(0)	12.00(0)
	15	Li - Li	5.66(9)	5.68(2)	0	0
Li_3N(110)	12	N - Li	0.84(0)	0.39(6)	0	0

In conclusion, the most stable terminations identified are those composed of NH fragments for the Li_2NH(100) and Li_2NH(111) surfaces. However, energy considerations alone are insufficient to distinguish between these two surface planes; the structural mismatch with the Ru(0001) must also be taken into account. The structural mismatch for Li_2NH(100) is lower than that of Li_2NH(111). Even with a larger supercell size for Li_2NH(111), the mismatch does not improve. For this reason, in future models, the Li_2NH(100) surface will be considered, preferably terminated by NH planes.

VI.3.1.3.2 Li_3N surfaces

For the Li_3N surfaces, we examined the (100), (111), and (110) planes. The structural mismatch between these planes and the ruthenium surface, compared to Ru(0001) ($2 \times \sqrt{3}$), is detailed in Table VI.7. Among these, the Li_3N(100) surface exhibits the smallest mismatch with the ($2 \times \sqrt{3}$) supercell. The mismatch along

a for Li_3N(111) can be minimized by interfacing a Ru ($17 \times \sqrt{3}$) supercell with a Li_3N(111) surface projected onto a $\left(3 \times \frac{\sqrt{3}}{2}\right)$ supercell of Ru. Similarly, the mismatch along c for Li_3N(110) can be reduced by interfacing a Ru ($6 \times \sqrt{3}$) supercell with a Li_3N (1×2) cell.

Table VI.7: The calculated lattice mismatch between Ru(0001) and Li_3N(100), Li_3N(111), or Li_3N(110), expressed as a percentage error, considering both the revised and unrevised a or c lattice parameters. Results are provided for calculations at the GGA PBE and PBE-dDsC levels.

	Error on a		Error on c		Revised error on a		Revised error on c	
	GGA PBE	PBE-dDsC	GGA PBE	PBE-dDsC	GGA PBE	PBE-dDsC	GGA PBE	PBE-dDsC
Li_3N(100)	-11.1	-12.1	3.7	2.9	-	-	-	-
Li_3N(111)	21.4 [a]	20.7 [a]	9.3 [a]	8.5 [a]	8.4 [b]	7.5 [b]	-	-
Li_3N(110)	-7.8	-8.6	32.0	31.3	-	-	-2.0 [c]	-3.0 [c]

[a] Mismatch calculated by projection onto a $\left(1 \times \frac{\sqrt{3}}{2}\right)$ cell; [b] Revised error on a considering a $(17 \times \sqrt{3})$ supercell for Ru interfaced with a $\left(3 \times \frac{\sqrt{3}}{2}\right)$ cell; [c] Revised error on c for Li_3N(110) considering a $(6 \times \sqrt{3})$ supercell for Ru interfaced with a (1×2) cell.

All lithium nitride surface energies ($\gamma_{Li_3N(hkl)}$) were calculated by predicting the total electronic energies of either the stoichiometric or non-stoichiometric Li_3N(100) bulks energy $E_{Li_3N\ (\sigma)}$, depending on the model's stoichiometry, along with the corresponding model surface area $\mathcal{A}_{Li_3N(hkl)}$. The equation allowing to calculate surface energies equation used is expressed as follows:

$$\gamma_{Li_3N(hkl)} = \frac{E_{Li_3N(hkl)} - E_{Li_3N\ (\sigma)}}{\mathcal{A}_{Li_3N(hkl)}} \tag{VI.9}$$

For Li_3N(100), all three possible structures were studied: the stoichiometric one, featuring a termination composed of both nitrogen and lithium atoms and the other one composed of solely lithium atoms (see Figure VI.S10.a), as well as two non-stoichiometric terminations, with termination composed exclusively of lithium atoms or a combination of nitrogen and lithium atoms on both ends (see Figures VI.S11.a and VI.S12.a, respectively). The thickness of these three models varies from 13 to 16 atomic layers, see Table VI.6 for details.

After geometry optimization with both functionals, the mixed lithium and nitrogen plane (NLi) underwent reconstruction, with the two lithium atoms in the terminal plane shifting above the initial terminal plane (see Figures VI.S10.b and VI.S11.b). This resulted in the division of the initial terminal plane into two distinct atomic layers. To force this termination to stay in the bulk configuration (no surface reconstruction) nitrogen and lithium atoms in the NLi mixed planes were kept fixed. The values reported in Table VI.6 correspond to these constrained structures.

For the lithium-only terminations, no significant reconstructions was observed after geometry optimization, except in the stoichiometric model, where the terminal atoms relaxed along the z-axis at the PBE-dDsC (see Figure VI.S10.d). However, this relaxation did not alter the nature of the terminations, so no atoms was

constrained in these terminal planes.

In terms of surface energies for these different terminations, the most stable configuration is obtained when both terminations are composed of NLi in the slab (0.52(5) J.m^{-2}). This result is the similar than (001) surface of $LiNH_2$ and (100) surface of Li_2NH, as lithium terminations were also unfavorable. All the structures considered have similar magnetic moments, ranging from 3.69(9) to 3.99(8) μ_B. The spin density is localized on nitrogen atoms.

For Li_3N(111), three structural configurations were examined: the stoichiometric model with a termination of nitrogen atoms on one end and lithium atoms on the other one (see Figure VI.S13.a), as well as two non-stoichiometric terminations, one with lithium atoms on both ends and another with nitrogen atoms on both ends (see Figures VI.S15.a and VI.S14.a, respectively). The thickness of these models ranges from 13 to 16 atomic layers, similar to that of Li_3N(100); see Table VI.6 for details.

The nitrogen-based termination exhibits a stronger reconstruction compared to the mixed NLi plane of the (100) surface (see Figures VI.S13.b and VI.S14.b), with Li atoms migrating from the lower plane to the terminal plane. To maintain purely elemental terminations, the two N-2 planes from the terminal plane, composed solely of Li atoms, were kept frozen. For Li-only terminations, the terminal atoms relaxed along the z-axis (see Figures VI.S13.c and VI.S15.b), similar as the (100) planes.

The order of magnitude of the interface energies is comparable to those found for the various terminations of the (100) surface plane. However, the interface energies calculated for nitrogen-based terminations are negative (-0.16(5) J.m^{-2} at the GGA PBE level and -0.12(6) J.m^{-2} at the PBE-dDsC level). This does not imply that this termination is inherently stabilizing but rather suggests the presence of a stabilizing strain/stress term in our models, as suggested before for Li_2NH. The trend in magnetic moment differs significantly from that of the (100) plane surface terminations. The geometrically constrained surfaces exhibit strong magnetism, with values of 8.32(4) μ_B and 8.13(5) μ_B for the stoichiometric model at the GGA PBE and PBE-dDsC levels, respectively, and 12.00(0) μ_B for the nitrogen-based termination with both functionals. The spin density is localized on nitrogen atoms. In contrast, the lithium-based terminations, which are unconstrained, exhibit no magnetic moment.

Finally, for Li_3N(110), the only possible surface is a stoichiometric one with NLi terminations, as shown in Figure VI.S16.a. Due to strong reconstructions throughout the lithium nitride layer, the six central planes were kept frozen (see Figure VI.S16.b for the reconstructed model and Figures VI.S16.c and VI.S16.d for the frozen model at the GGA PBE and PBE-dDsC levels). The interface energy at the GGA PBE level is 0.84(0) J.m^{-2}, and 0.39(6) J.m^{-2} with dispersion, with no dipole moment in either case. This trend is consistent with that observed for the (100) and (111) surface planes, with an intermediate interface energy between the most stable nitrogen-based termination and the least stable lithium-based termination.

As a result, the most stable terminations identified are nitrogen-based for the Li_3N(100) and Li_3N(111) sur-

faces. However, to distinguish between these two surface planes, energy considerations alone are insufficient; the structural mismatch with the Ru(0001) layer in the future interface must also be considered. Although the mismatch for Li_3N(100) is not ideal, it represents the best compromise, as the required supercell size for the interface is minimal compared to the $(17 \times \sqrt{3})$ supercell needed to interface Ru(0001) with Li_3N(111).

VI.3.2 Partially hydrogenated interface model

VI.3.2.1 Adsorption of N on Ru(0001)

The hypothesis of a partially dehydrogenated interface suggests the formation of an interface not only between different lithium phases but also with the metal. In this case, we assume that the material undergoes a progressive dehydrogenation from $LiNH_2$ to Li_3N, with a complete dehydrogenation occurring at the contact with the ruthenium. Therefore, it is necessary to establish a connection between the Ru(0001) surface and the Li_3N(100) surface.

As observed in the study of the Ru(0001)/$LiNH_2$(001) interface, a contact plane composed of lithium atoms is energetically unfavorable. Thus, we opt for a nitrogen contact plane. The key question then concerns the adsorption site of the nitrogen atoms in Li_3N. We evaluated four possible sites—bridge, top, hollow hcp, and hollow fcc—for our Ru(0001) surface model and calculation conditions with a surface coverage of 1/4 ML.

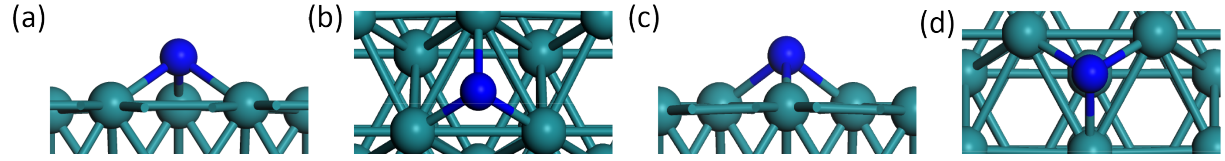

Figure VI.15: Optimized adsorption structures of a nitrogen atom on Ru(0001): (a) lateral and (b) top view of hollow free adsorption site, and (b); (c) lateral and (d) top view of hollow hcp adsorption site. Labels ans colors of atoms are depicted in Figure VI.2.

The comparison of different adsorption sites was made by evaluating their respective adsorption energies, calculated using the formula presented in Section V.3 of the previous chapter. Nitrogen preferentially adsorbs on Ru(0001) on hollow hcp site (see Figure VI.15), with an adsorption energy of -6.24(3) eV. This finding aligns with previous theoretical studies and experiments . However, a slight discrepancy exists between our result and that calculated by Herron et al., who reported an adsorption energy of -5.46 eV using the GGA-PW91 functional for a surface coverage of 1/4 ML.[282] Their value closely matches the experimental result of -5.65 eV obtained via thermal desorption spectroscopy (TDS),[457] while our calculation shows a 9.5% deviation from the experimental data.

For the hollow free site (see Figure VI.15), we calculated an adsorption energy of -5.48(5) eV, which also

exhibits a discrepancy when compared to Herron et al.'s value of -4.92 eV. While this site is less energetically favorable than the hcp site, it remains the second most stable option. Given the structure of Li_3N, both adsorption sites—hollow hcp and free—are relevant, with equal utilization of these sites in the interface model. For both adsorption sites, the Ru–N bond lengths were calculated to be 1.94 Å, which is in close agreement with the experimental value of 1.93 Å, measured using low-energy electron diffraction (LEED).[458]

VI.3.2.2 Optimized plain interface

In the partially dehydrogenated model of the lithiated material, designed to simulate the dehydrogenation induced by contact with the metal on $LiNH_2$, we used the same supercell size as in the study of the ruthenium-lithium amide interface. This corresponds to a $(2 \times \sqrt{3})$ supercell with a height of 50 Å and a 15 Å vacuum space separating two equivalent slabs along the z-axis. As in the previous models, it includes 7 layers of ruthenium atoms, with the three bottom layers fixed in their optimal HCP bulk geometry.

For the lithium-containing part of our model, the contact plane with the metal surface is formed by a nitrogen plane of Li_3N(001), followed by six layers of lithium nitride (including the contact plane) before transitioning to lithium imide. The Li_2NH(001) part contains 4 layers before transitioning to the lithium amide phase, which contains 7 layers. The transitions between the amide, imide, and nitride phases are mediated by lithium planes (see Figure VI.16.a).

The interface energy between Ru(0001) and lithium amide, imide, and nitride slabs was calculated using the bulk energies of Ru, $LiNH_2$, Li_3N, and Li_2NH as references. The expression for the interface energy is given by:

$$\Gamma_{LiNH_2(001)@Li_2NH(001)@Li_3N(001)@Ru(0001)} = \frac{E_{LiNH_2(001)@Li_2NH(001)@Li_3N(001)@Ru(0001)} - (E_{LiNH_{2(s)}} + E_{Li_2NH_{(s)}} + E_{Li_3N_{(ns)}} + E_{Ru})}{\mathcal{A}_{LiNH_2@Li_2NH@Li_3N@Ru}} \quad \text{(VI.10)}$$

where $E_{LiNH_2(001)@Li_2NH(001)@Li_3N(001)@Ru(0001)}$ is the total electronic energy of the plain interface model containning Ru(0001), $LiNH_2$(001), Li_2NH(001), and Li_3N(001) slabs; $E_{LiNH_{2\,(s)}}$ is the total electronic energy of the stoichiometric $LiNH_2$ bulk; $E_{Li_2NH_{(s)}}$ is the total electronic energy of the stoichiometric Li_2NH bulk; $E_{Li_3N_{(ns)}}$ represents the total electronic energy of the non-stoichiometric Li_3N bulk; and E_{Ru} is the total electronic energy of the Ru bulk. $\mathcal{A}_{LiNH_2@Li_2NH@Li_3N@Ru}$ denotes the surface area of the interface model.

The geometric optimization of the partially hydrogenated model is ongoing for both functionals. Currently, the interface energy is 0.24(8) J.m^{-2} at the GGA PBE level and 0.21(4) J.m^{-2} at the PBE-dDsC level. The magnetic moments are also comparable, with values of 0.84(9) μ_B for GGA PBE and 0.84(7) μ_B for PBE-dDsC. The spin density is localized on some nitrogen atoms.

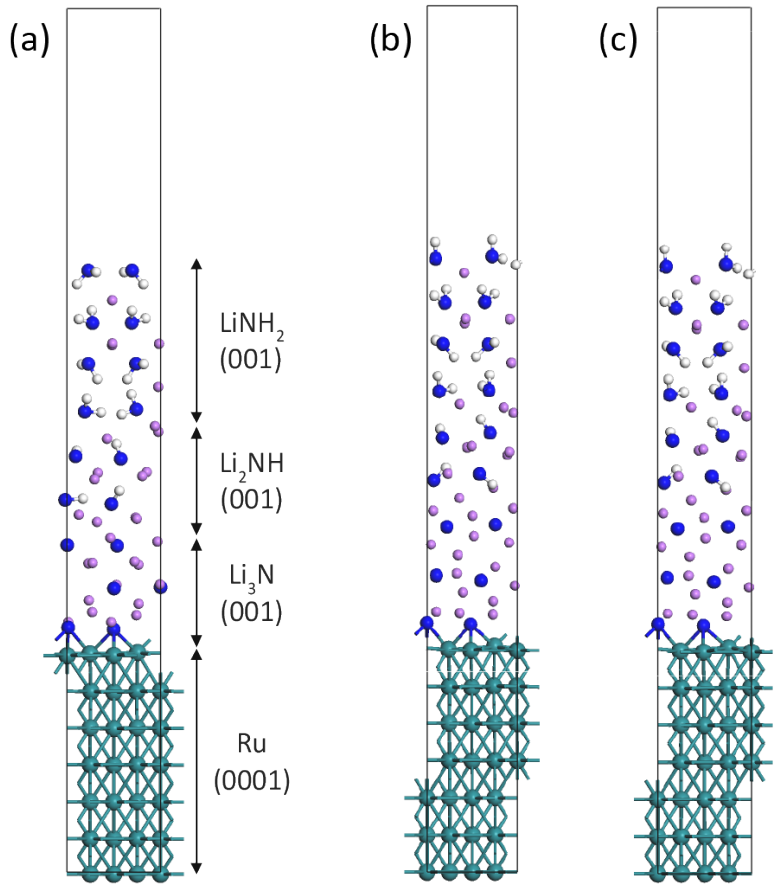

Figure VI.16: (a) Ru(0001)/Li_3N(001)/Li_2NH(001)/$LiNH_2$(100) partially hydrogenated model , on-going geometry optimization (b) at the GGA PBE level and (c) at the PBE-dDsC level. Labels and colors of atoms are depicted in Figure VI.2.

The interface energy found here is significantly lower than that of the fully hydrogenated Ru(0001)/$LiNH_2$(001) model reported in the previous chapter, which was 1.93(2) J.m^{-2} at the GGA PBE level and 2.04(2) J.m^{-2} at the PBE-dDsC level. This increased stability can be attributed to the presence of lithium nitride and imide, as the lithium amide layer reconstruction remains consistent between the fully and partially hydrogenated models.

VI.3.2.3 Hollow interface and reactivity

Although our partially dehydrogenated model remains in a state of ongoing optimization, the next phase was initiated once the geometry was sufficiently refined. Following the approach in Section VI.1.2 of this chapter, a defect was introduced to facilitate the desorption of ammonia decomposition products (N_2 and H_2) and the adsorption of NH_3 on the metal surface (see Figure VI.17.a). To allow for this defect, the model size was expanded by a factor of four in the x direction and two in the y direction, resulting in a $(8 \times 2\sqrt{3})$ supercell for the new hollow-interface model. Otherwise, the model remains identical to the previous partially dehydrogenated version in terms of z-dimension and chemical composition, excluding defects. As for the defect, it was created through stoichiometric removal: an equal number of Li and NH_2 fragments were removed from the amide layer, two Li atoms per NH fragment from the imide layer, and three Li atoms for

each N atom from the nitride layer.

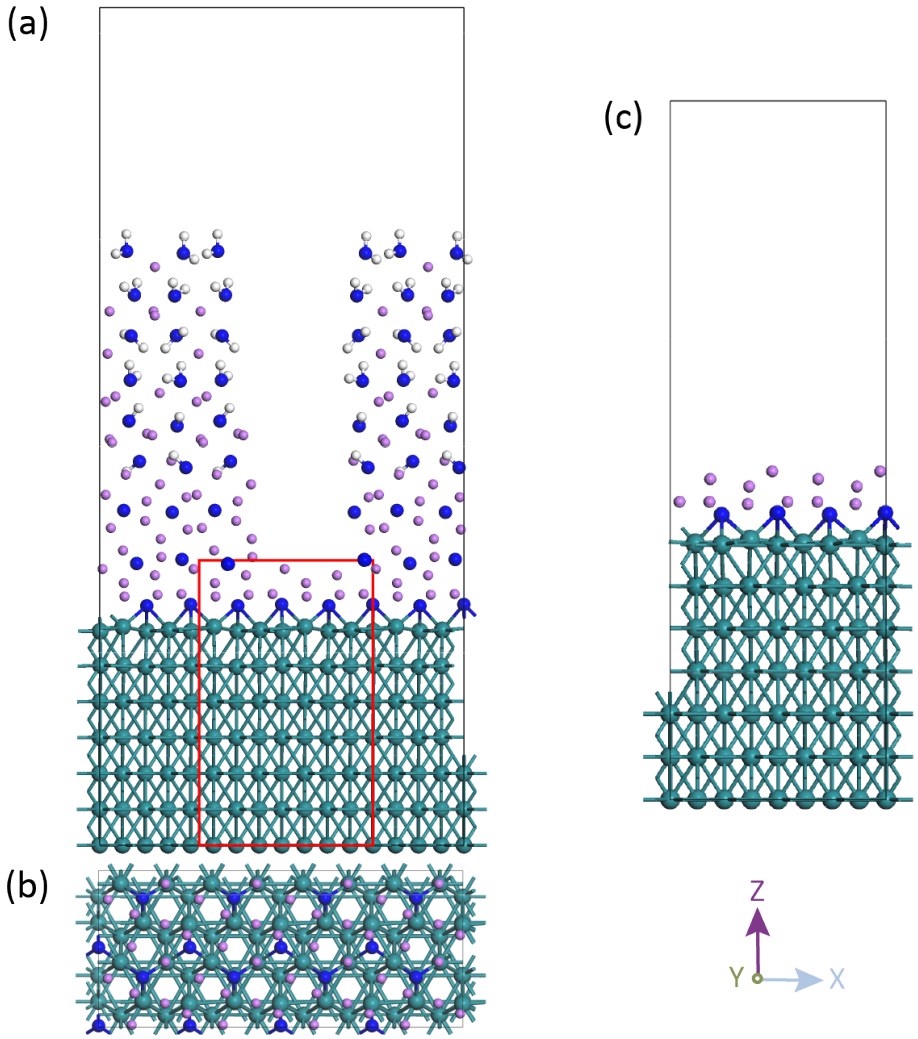

Figure VI.17: (a) Ru(0001)/Li_3N(001)/Li_2NH(001)/$LiNH_2$(100) partially hydrogenated model and hollow interface, (b) top view of the three lithium nitride planes close to the Ru(0001), and (c) Ru(0001)/Li_3N(001) simplified model extracted from the partially hydrogenated model and hollow interface. Labels and colors of atoms are depicted in Figure VI.2.

Although the geometric optimization of the partially hydrogenated model, Ru(0001)/Li_3N(001)/Li_2NH(001)/ $LiNH_2$(100), proceeded without difficulty, the same cannot be said for its truncated equivalent. The optimization of this reactivity model was challenging for several reasons. Firstly, it contains significantly more atoms than previous models, increasing the computational cost. Secondly, it exhibits magnetic properties (12.42(1) μ_B), adding complexity to the optimization process. Lastly, creating a non-polar cut in the dehydrogenated part of the lithiated material was particularly delicate due to the presence of three distinct types of lithium-containing materials, requiring multiple attempts to achieve. Despite ensuring stoichiometry in the cut, the amide, imide, and nitride part are not all strictly stoichiometric, resulting in a system that, despite

best efforts, remains polar.

In an effort to advance the study of ammonia decomposition, with the developed catalytic model, a simplified one was extracted from the defective partially hydrogenated model. The reactive portion of our model, which is directly in contact with Ru(0001) and the gaseous medium, consists of a thin Li_3N layer (only three planes) in contact with Ru(0001), as shown in Figure VI.17.c. This section was isolated for the reactivity study to streamline analysis.

The advantage of this simplified model lies in its reduced size, which facilitates faster the exploration of reactivity. However, the ultimate goal is to optimize the relevant TS structures identified with this simplified model into the partially dehydrogenated and defective model.

VI.3.3 Conclusion

In this final section, we explored the DFT modeling of Li_2NH ($Fm\bar{3}m$) and γ-Li_3N using the standard GGA PBE and the dispersion-corrected PBE-dDsC functionals. While both functionals provide a reliable description of Li_2NH, the same level of accuracy was not achieved for Li_3N. The study of the clean surfaces of Li_2NH and Li_3N ultimately led to the selection of (100) planes for the creation of interfaces with Ru(0001) and $LiNH_2$(001).

The partially hydrogenated and plain Ru(0001)/Li_3N(001)/Li_2NH(001)/$LiNH_2$(001) interface was constructed based on the stability results of the Ru(0001)/Li_2NH(001) interface and the clean surfaces of Li_3N(001) and Li_2NH(001). The interface energy obtained for this system is significantly lower than that of Ru(0001)/$LiNH_2$(001), the fully hydrogenated interface.

Thanks to the partially hydrogenated model, and the expansion of the supercell in the x and y directions, a reactivity model was developed by introducing a defect into the lithium material, leading to a hollow interface. However, optimizing this model was challenging due to its large size, inherent polarity, and significant magnetism.

To go beyond the challenges associated with this defective partially hydrogenated model and hollow interface, a simplified version was proposed. It was built by considering an extracted portion of the complete hollow interface, consisting of thin layers of Li_3N adsorbed on Ru(0001) and in direct contact this the gaseous medium. This new simplified model was thus proposed for studying the desorption of recombinant N_2.

VI.4 Conclusion

To conclude this chapter, an initial reactivity study was attempted, via an AIMD simulation at 650 K to investigate the interactions between the materials under realistic conditions. However, this approach was not conclusive due to the significant role of van der Waals interactions and the high computational cost of spin-polarized calculations. Consequently, our efforts were shifted to constructing static models. The first catalytic model was based on the stable Ru@T2T2(11,ns,p,ps) fully hydrogenated and hollow interface and employed a $(8 \times \sqrt{3})$ supercell with a central defect formed by removing equal amounts of Li and NH_2, exposing a catalytically relevant contact plane. This defect stabilized the model, indicating that defect introduction could enhance reactivity. To assess the influence of lithium on the TS geometry of N_2 recombination, two 'NLi_2' species were introduced on Ru(0001) after NH_3 desorption. However, these proved unstable, prompting a refined hypothesis focusing on stabilizing N atoms with Li at the contact plane. The difficulty in stabilization was linked to insufficient Li at the contact plane.

In the next step, we explore the possibility of dehydrogenating $LiNH_2$ leading progressively to Li_3N upon contact with Ru(0001), potentially providing a more favorable environment for N_2 formation. To assess the feasibility of Li_3N formation, the successive dehydrogenation of two NH_2 fragments adsorbed on Ru(0001) was investigated. At the GGA PBE level, removing a hydrogen atom from an NH_2 fragment is exothermic (-1.39 eV), resulting into a NH fragment and an adsorbed hydrogen atom, with both occupying threefold hcp and free sites, respectively. The dehydrogenation of a second NH_2 fragment is weakly endothermic (0.64 eV), likely due to steric effects on the surface. Subsequent H_2 formation from the two adsorbed hydrogens is also endothermic (0.67 eV). Overall, the transformation from two NH_2 fragments to two NH fragments, with the release of H_2 gas, is slightly exothermic (-0.08 eV). Complete dehydrogenation of the two NH fragments to nitrogen atoms on Ru(0001) surface is endothermic (0.46 eV), as well as H_2 desorption (0.57 eV), leading to an overall endothermic formation of two adsorbed nitrogen atoms (1.03 eV). These findings of moderate global endothermicity suggest that NH_2 fragments in lithium amide can undergo dehydrogenation to form lithium nitride on ruthenium, especially under ammonia decomposition conditions (high temperature).

Finally, in this chapter, we explore DFT modeling of Li_2NH and Li_3N bulks and surfaces by using GGA PBE and PBE-dDsC functionals. While both functionals accurately predict Li_2NH bulk properties, for Li_3N the same level of accuracy was not achieved. Studies of clean surfaces led to the selection of (100) planes generating the interface creation with Ru(0001) and $LiNH_2$(001).
A partially hydrogenated Ru(0001)/Li_3N(001)/Li_2NH(001)/$LiNH_2$(001) plain interface showed improved stability compared to the fully hydrogenated counterpart. A reactivity model with a defect was also explored but faced optimization challenges due to size, polarity, and magnetism. To address this, a simplified model with thin Li_3N layers on Ru(0001) was proposed to study N_2 desorption.

VI.5 Appendix

- **Ab initio molecular dynamics simulations**

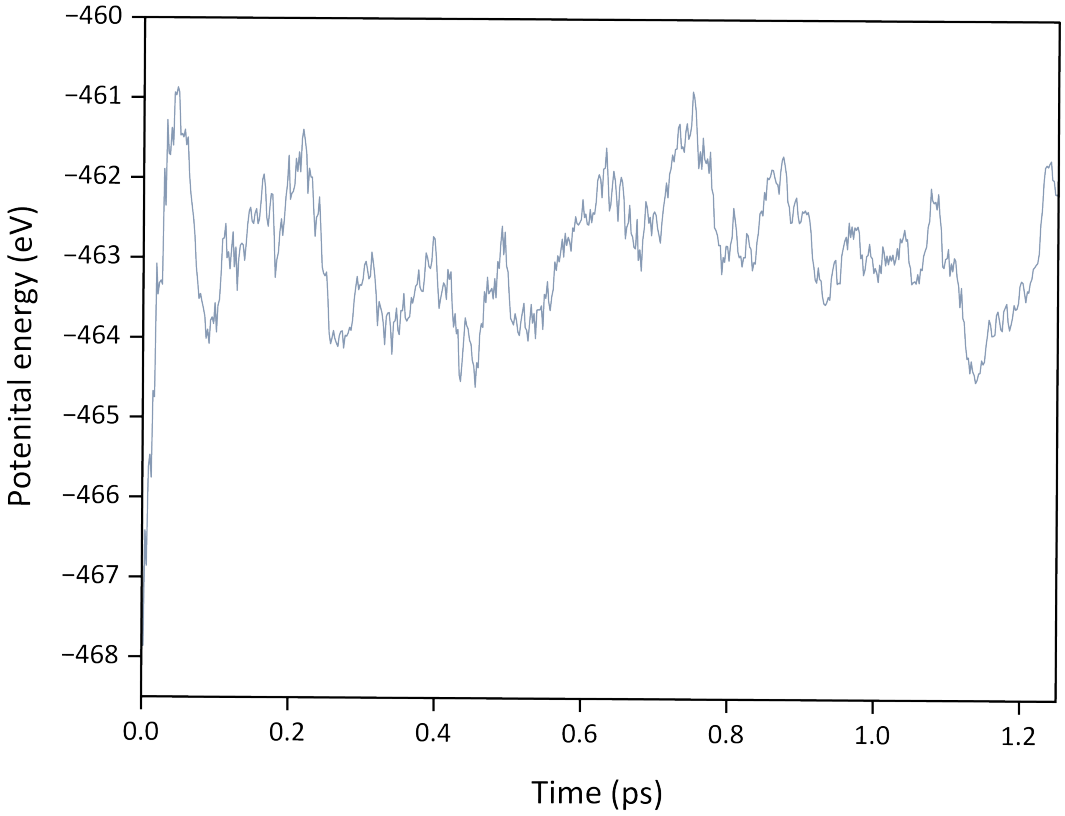

Figure VI.S1: Ab initio molecular dynamics (AIMD) trajectories at 650K of the most stable Ru(0001)/$LiNH_2$(001) interface (Ru@T2T2(11,ns,p,ps)).

- **Dehydrogenation Models of $LiNH_2$ at the Ru(0001) surface**

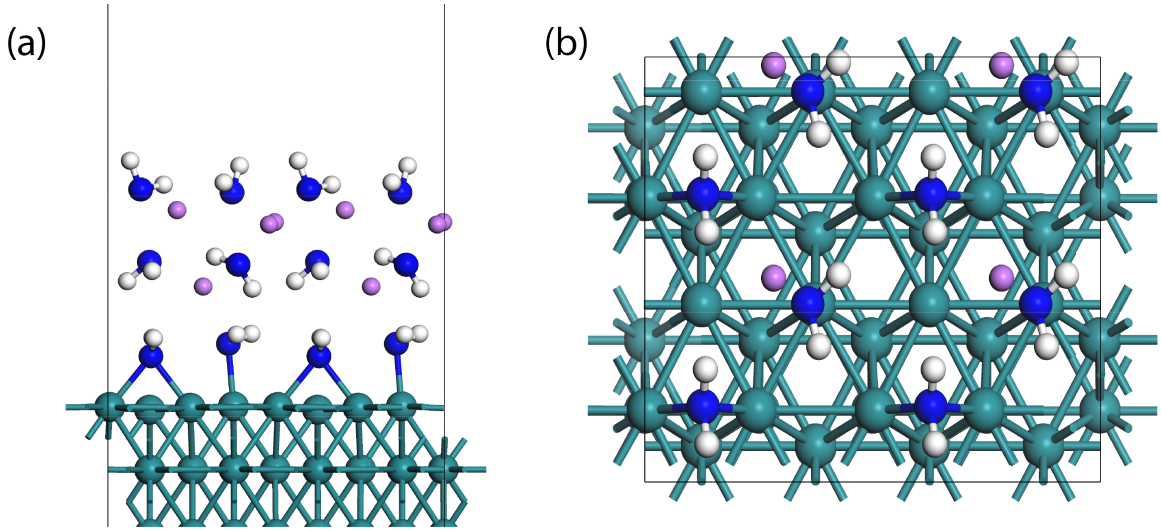

Figure VI.S2: (a) Lateral views of Ru(0001)/$LiNH_2$(001) optimized geometry dehydrogenation model at the GGA PBE level, (b) top view without the last three planes of $LiNH_2$ to allow better visualization of the NH_2 contact plane with Ru(0001).

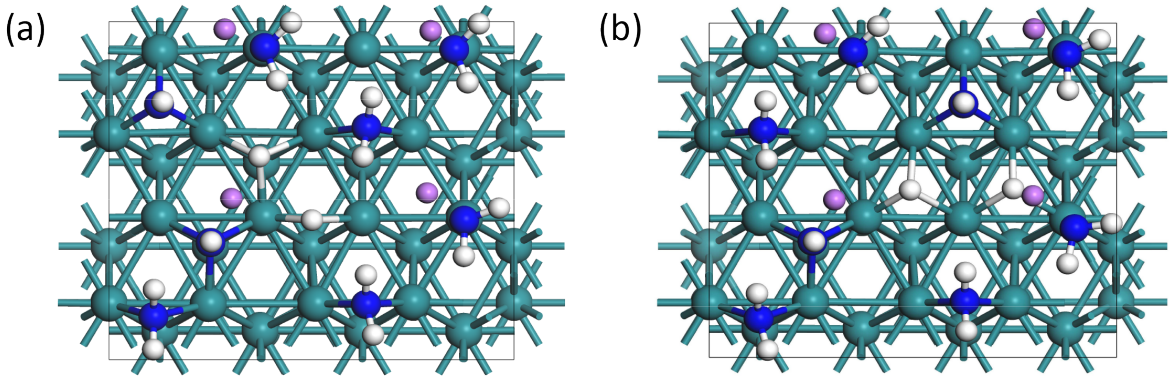

Figure VI.S3: Top view of ongoing Ru(0001)/$LiNH_2$(001) dehydrogenation model at the PBE-dDsC level, shown without the last three planes of $LiNH_2$ to enhance visualization of the NH_2 contact plane with Ru(0001). In (a) two hydrogen atoms initially adsorbed at hollow free sites hat switched to hollow hcp and bridge site; and in (b) two hydrogen atoms initially adsorbed in hollow free and hollow hcp adsorptions site for hydrogen that switched to two hollow free sites. The colors and atom labels are those depicted in Figure VI.2.

- **Optimized structures of Li_2NH and Li_3N surfaces**

Table VI.S1: Table summarizing the Li_2NH and Li_3N surfaces structure.

System	Terminations	Functional	Figure
$Li_2NH(100)$	Li - NH	GGA PBE, PBE-dDsC	VI.S4
$Li_2NH(100)$	NH - NH	GGA PBE, PBE-dDsC	VI.S5
$Li_2NH(100)$	Li - Li	GGA PBE, PBE-dDsC	VI.S6
$Li_2NH(111)$	Li - NH	GGA PBE, PBE-dDsC	VI.S7
$Li_2NH(111)$	NH - NH	GGA PBE, PBE-dDsC	VI.S8
$Li_2NH(111)$	Li - Li	GGA PBE, PBE-dDsC	VI.S9
$Li_3N(100)$	NLi - Li	GGA PBE, PBE-dDsC	VI.S10
$Li_3N(100)$	NLi - NLi	GGA PBE, PBE-dDsC	VI.S11
$Li_3N(100)$	Li - Li	GGA PBE, PBE-dDsC	VI.S12
$Li_3N(111)$	Li - N	GGA PBE, PBE-dDsC	VI.S13
$Li_3N(111)$	N - N	GGA PBE, PBE-dDsC	VI.S14
$Li_3N(111)$	Li - Li	GGA PBE, PBE-dDsC	VI.S15
$Li_3N(110)$	NLi - NLi	GGA PBE, PBE-dDsC	VI.S16

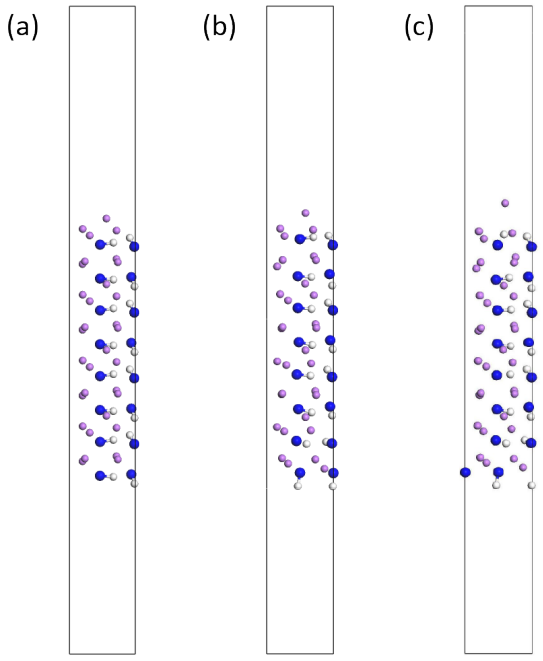

Figure VI.S4: Lateral views of the stoichiometric $Li_2NH(100)$ surface at the GGA PBE level, with one termination composed of both NH fragments and Li atoms and another termination consisting solely of Li atoms; (a) initial structure; (b) after geometry optimization; and (c) after geometry optimization at the PBE-dDsC level. The colors and atom labels correspond to those shown in Figure VI.2.

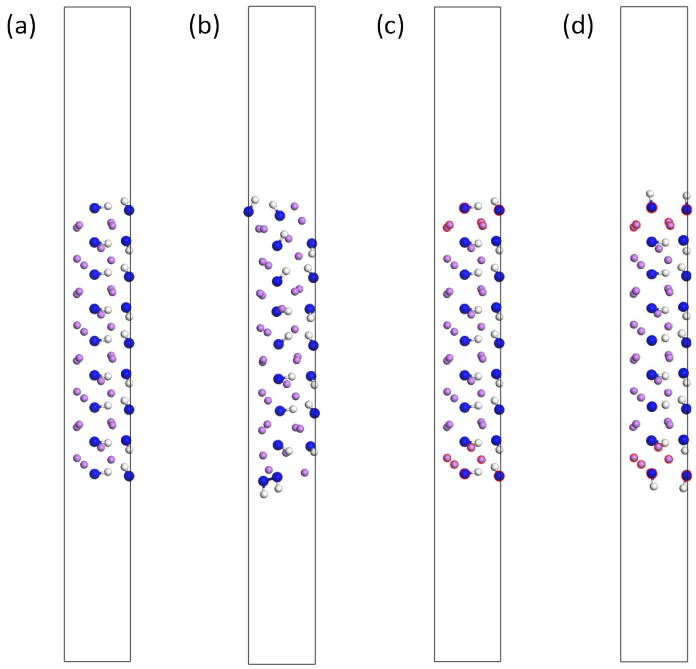

Figure VI.S5: Lateral views of the non-stoichiometric $Li_2NH(100)$ surface at the GGA PBE level, with two terminations composed of two NH fragments; (a) initial structure; (b) after geometry optimization with reconstruction; (c) structure with geometric constraints applied to the N and Li atoms; and (d) structure with geometric constraints applied to the N and Li atoms at the PBE-dDsC level. Atoms that are frozen are circled in red. The colors and atom labels correspond to those shown in Figure VI.2.

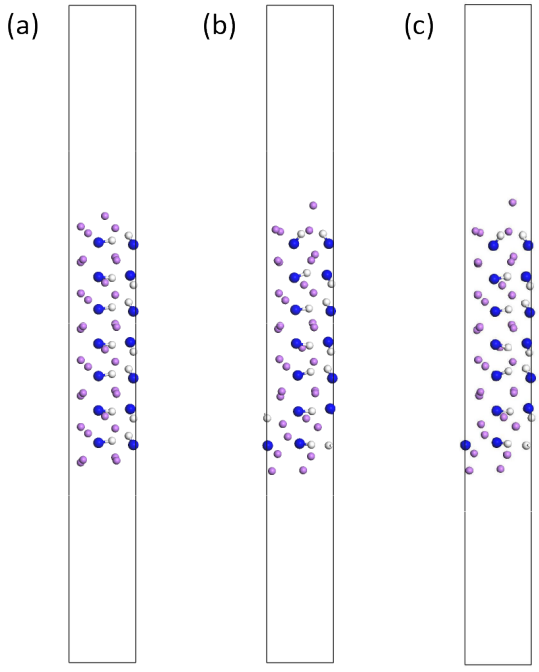

Figure VI.S6: Lateral views of the non-stoichiometric $Li_2NH(100)$ surface at the GGA PBE level, with two terminations composed of Li atoms; (a) initial structure; (b) after geometry optimization; and (c) after geometry optimization at the PBE-dDsC level. The colors and atom labels correspond to those shown in Figure VI.2.

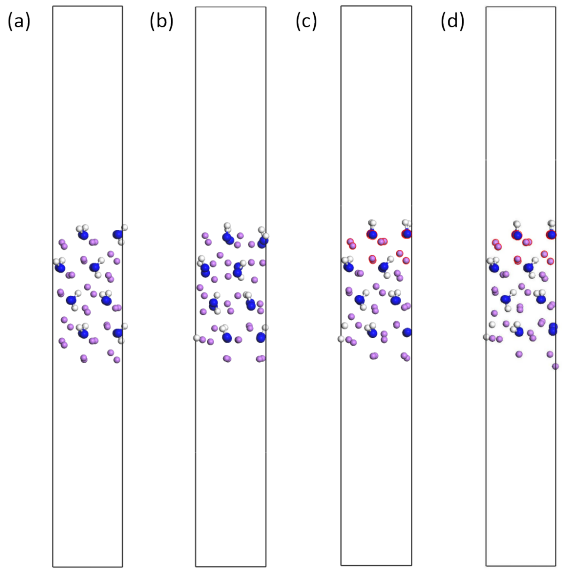

Figure VI.S7: Lateral views of the stoichiometric $Li_2NH(111)$ surface at the GGA PBE level, with one termination composed of both NH fragments and another termination consisting solely of Li atoms; (a) initial structure; (b) after geometry optimization with reconstruction on the NH termination; (c) structure with geometric constraints applied to the two Li planes near the NH termination; and (d) structure with geometric constraints applied to the two Li planes near the NH termination; at the PBE-dDsC level. Atoms that are frozen are circled in red. The colors and atom labels correspond to those shown in Figure VI.2.

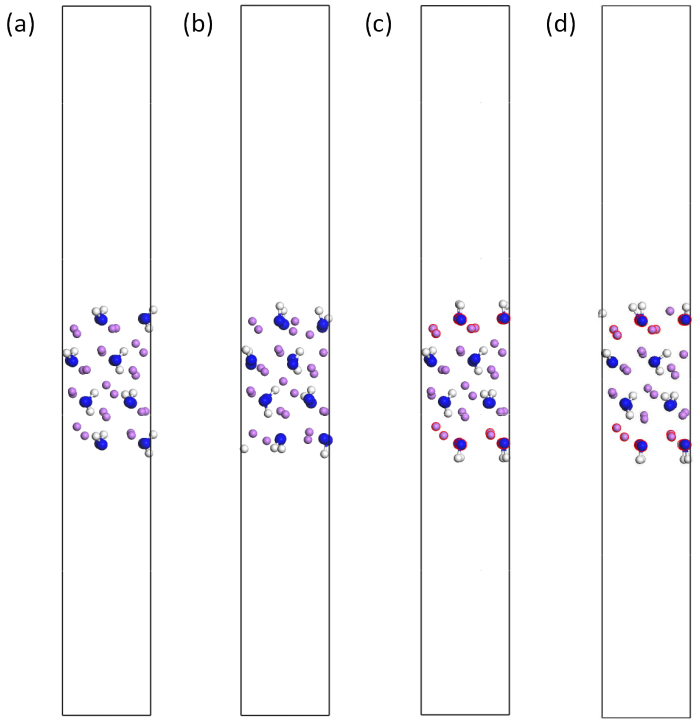

Figure VI.S8: Lateral views of the non-stoichiometric $Li_2NH(111)$ surface at the GGA PBE level, with two terminations composed of two NH fragments; (a) initial structure; (b) after geometry optimization with reconstruction; (c) structure with geometric constraints applied to the N and Li atoms; and (d) structure with geometric constraints applied to the N and Li atoms at the PBE-dDsC level. Atoms that are frozen are circled in red. The colors and atom labels correspond to those shown in Figure VI.2.

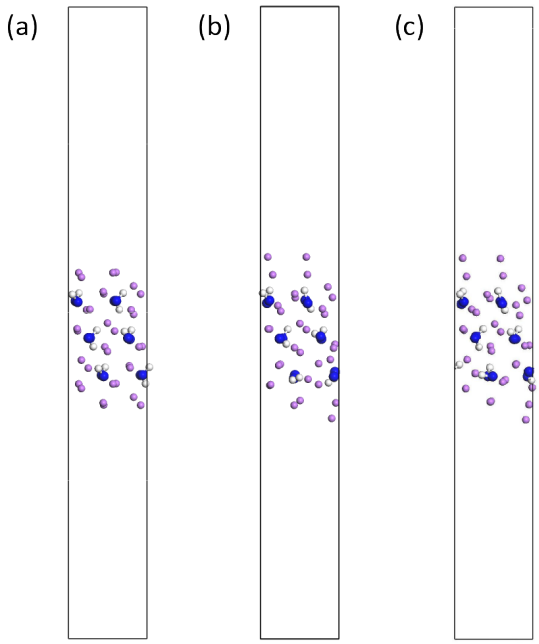

Figure VI.S9: Lateral views of the non-stoichiometric $Li_2NH(111)$ surface at the GGA PBE level, with two terminations composed of Li atoms; (a) initial structure; (b) after geometry optimization; and (c) after geometry optimization at the PBE-dDsC level. The colors and atom labels correspond to those shown in Figure VI.2.

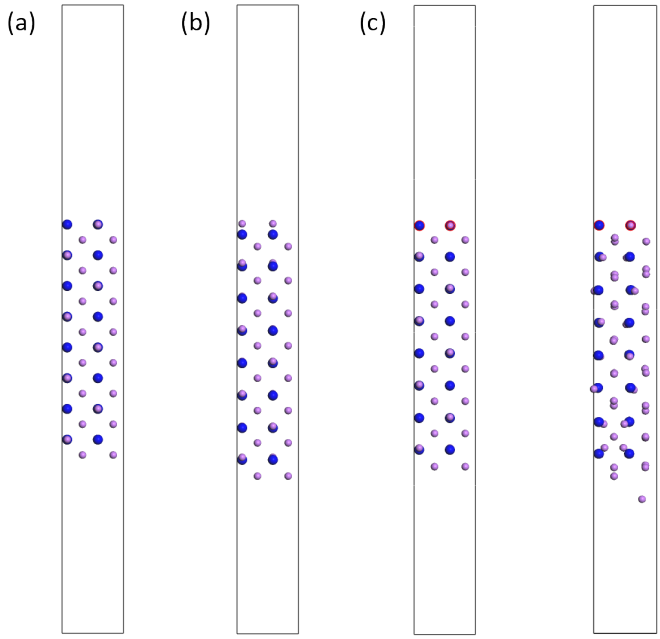

Figure VI.S10: Lateral views of the stoichiometric $Li_3N(100)$ surface at the GGA PBE level, with one termination composed of both N and Li atoms and another termination consisting solely of Li atoms; (a) initial structure; (b) after geometry optimization with reconstruction on the N-Li termination; (c) structure with geometric constraints applied to the N-Li terminal plane; and (d) structure with geometric constraints applied to the Li planes close to the N termination at the PBE-dDsC level. Atoms that are frozen are circled in red. The colors and atom labels correspond to those shown in Figure VI.2.

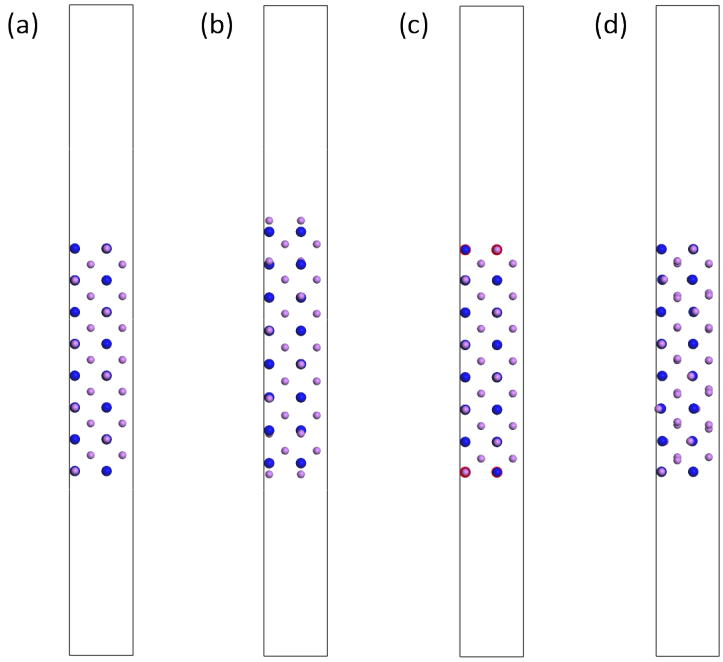

Figure VI.S11: Lateral views of the non-stoichiometric $Li_3N(100)$ surface at the GGA PBE level, with two terminations composed of both N and Li atoms; (a) initial structure; (b) after geometry optimization with reconstruction on the N-Li terminations; (c) structure with geometric constraints applied to the N-Li terminal planes; (d) structure with geometric constraints applied to the Li planes close to the N termination at the PBE-dDsC level. Atoms that are frozen are circled in red. The colors and atom labels correspond to those shown in Figure VI.2.

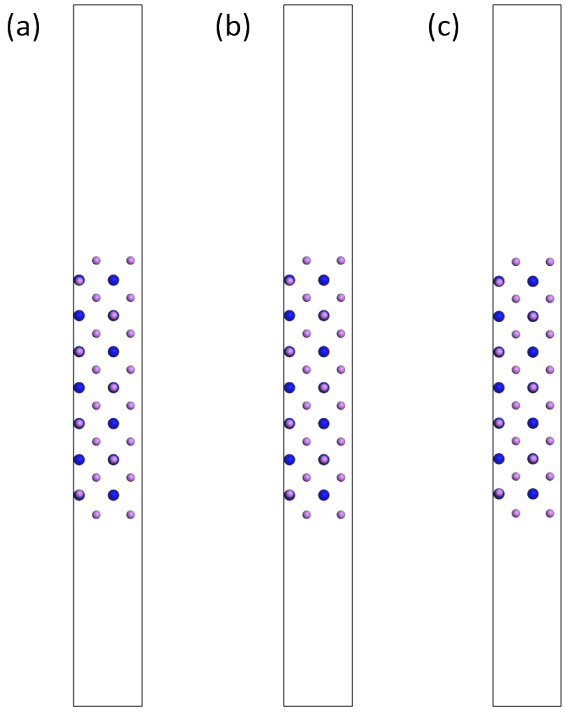

Figure VI.S12: Lateral views of the non-stoichiometric $Li_3N(100)$ surface at the GGA PBE level, with two terminations composed solely of Li atoms; (a) initial structure; (b) after geometry optimization; and (c) after geometry optimization at the PBE-dDsC level. The colors and atom labels correspond to those shown in Figure VI.2.

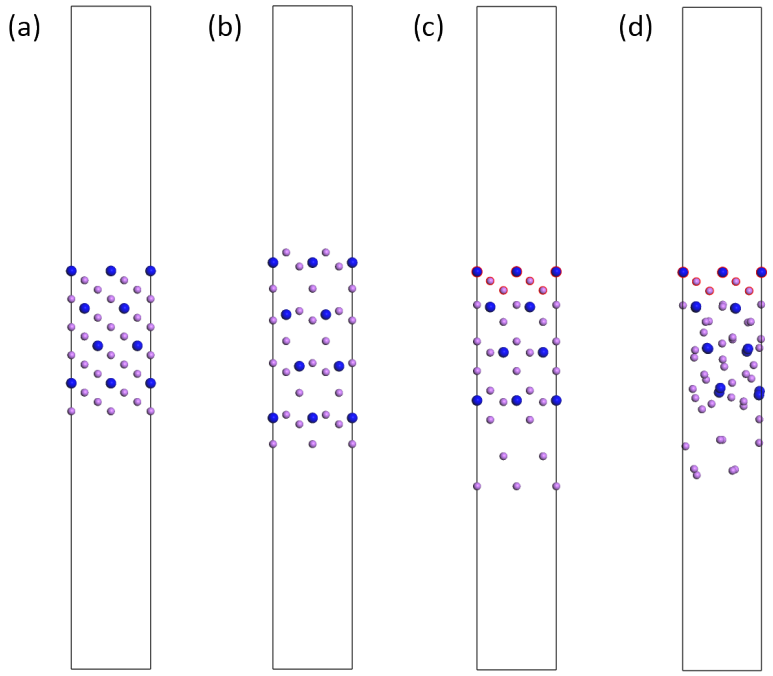

Figure VI.S13: Lateral views of the stoichiometric $Li_3N(111)$ surface at the GGA PBE level, with one termination composed of N atoms and another termination composed of Li atoms; (a) initial structure; (b) after geometry optimization with reconstruction on the N-Li termination; and (c) structure with geometric constraints applied to the N-Li terminal plane. Atoms that are frozen are circled in red. The colors and atom labels correspond to those shown in Figure VI.2.

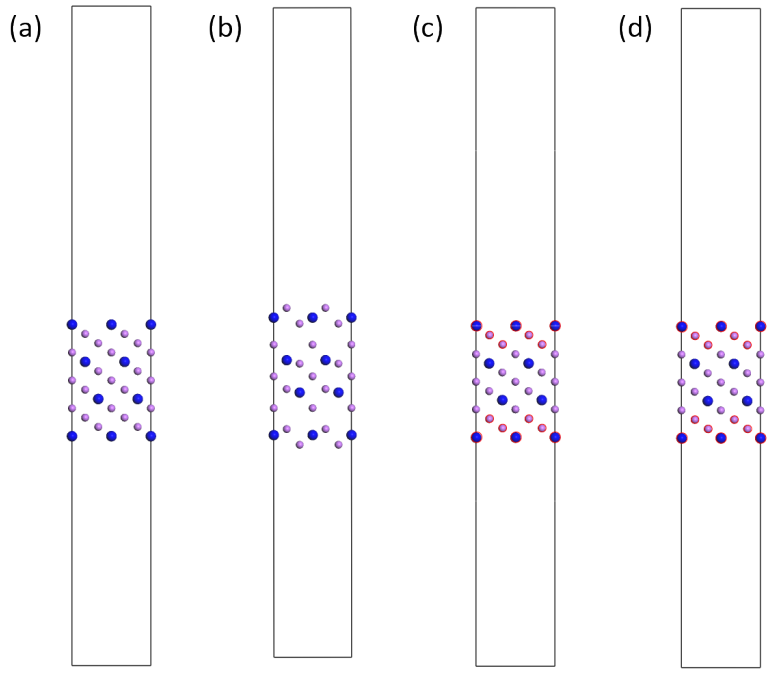

Figure VI.S14: Lateral views of the non-stoichiometric $Li_3N(111)$ surface at the GGA PBE level, with two terminations composed solely of N atoms; (a) initial structure; (b) after geometry optimization with reconstruction; (c) structure with geometric constraints applied to the Li planes close to the N termination; and (d) structure with geometric constraints applied to the Li planes close to the N termination at the PBE-dDsC level. Atoms that are frozen are circled in red. The colors and atom labels correspond to those shown in Figure VI.2.

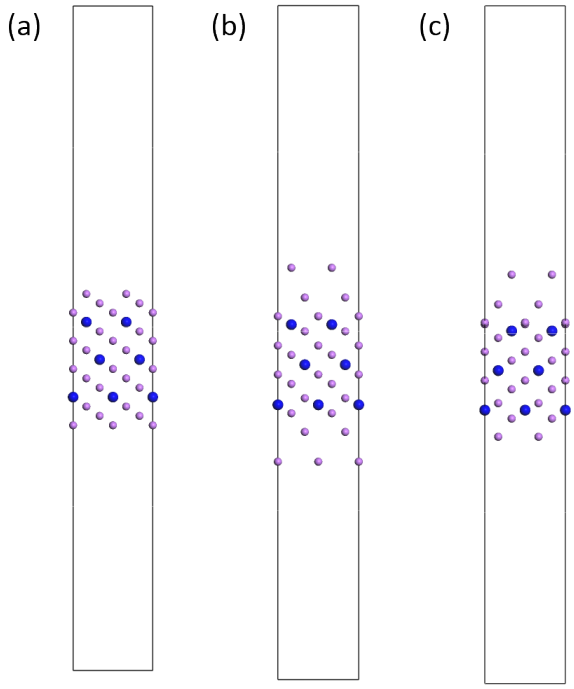

Figure VI.S15: Lateral views of the non-stoichiometric $Li_3N(111)$ surface at the GGA PBE level, with two terminations composed solely of Li atoms; (a) initial structure; (b) after geometry optimization; and (c) after geometry optimization at the PBE-dDsC level. The colors and atom labels correspond to those shown in Figure VI.2.

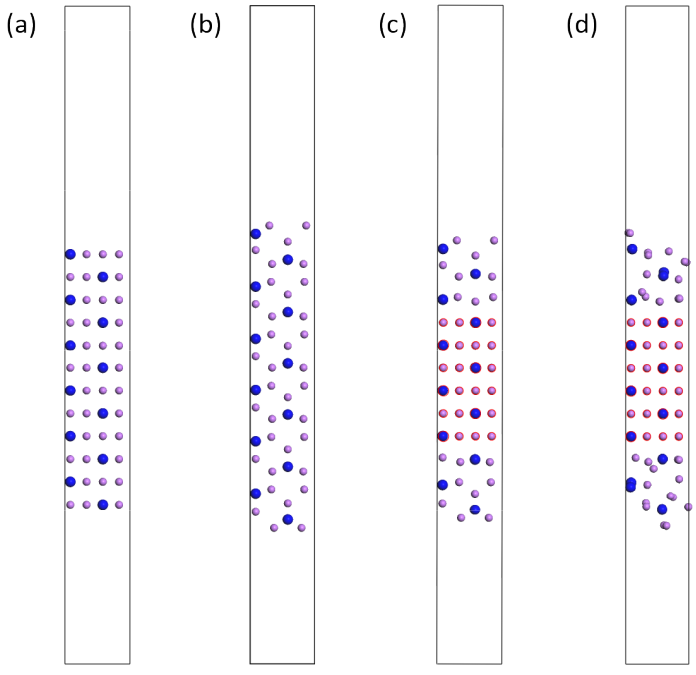

Figure VI.S16: Lateral views of the stoichiometric $Li_3N(110)$ surface at the GGA PBE level, with two terminations composed N and Li atoms; (a) initial structure; (b) after geometry optimization with reconstruction; (c) structure with geometric constraints applied to the six central planes; and (d) structure with geometric constraints applied to the Li planes close to the N termination at the PBE-dDsC level. Atoms that are frozen are circled in red. The colors and atom labels correspond to those shown in Figure VI.2.

Chapter VII

Catalytic DFT models of ruthenium and lithium nitride dehydrogenated catalytic interface

After having examined the solid-solid interface between ruthenium and lithium amides, this chapter focuses on the reactivity study of the dehydrogenated Ru(0001)/Li_3N(001) interface; a simplified catalyst model used for investigating ammonia decomposition. The theoretical study mainly deals with the associative desorption of N_2 from Li_3N (surface recombination of two coadsorbed nitrogen atoms), promoted by the ruthenium surface. The investigation of the possible reaction pathways and related transition states first requires the exploration of the coadsorption structures for atomic nitrogen. The most stable initial systems were compared to an equivalent catalytic model without lithium, to assess the influence of lithium on this elementary act. Activation barriers of the recombination of two adjacent and coadsorbed nitrogen atoms could be compared between catalyst models and interpreted thanks to a Bader charge analysis. Additionally, the regeneration of the catalyst following the formation and desorption of N_2 was examined by introducing two ammonia molecules, on the basis of a thermodynamic approach of the corresponding elementary steps.

Contents

VII.1 Simplified catalyst model for reactivity study: dehydrogenated Ru(0001)/ Li_3N(001) interface 232
VII.1.1 Optimized structure of Ru(0001)/Li_3N(001) interface 232
VII.1.2 Equivalent delithiated ruthenium surface model: Ru(0001)/8N 234
VII.2 Transition states search and kinetic study 235
VII.2.1 Atomic nitrogen coadsorption structures 236
VII.2.2 Comparison: effect of lithium 238
VII.2.3 Bader charge analysis 246
VII.2.4 Conclusion 248
VII.3 Catalyst regeneration and ammonia decomposition from thermodynamics 249
VII.3.1 Successive ammonia adsorption and dissociation steps 249
VII.3.2 Comparison: effect of lithium 252
VII.3.3 Conclusion 254
VII.4 Overall comparison of all studied reactivity models 256
VII.5 Conclusion 260
VII.6 Appendix 262

VII.1 Simplified catalyst model for reactivity study: dehydrogenated Ru(0001)/Li_3N(001) interface

VII.1.1 Optimized structure of Ru(0001)/Li_3N(001) interface

As discussed in the previous chapter, optimizing the Ru(0001)/Li_3N(001)/Li_2NH(001)/$LiNH_2$(100) reactivity model proved to be highly challenging. To advance the theoretical investigation of ammonia decomposition at the developed catalytic interface, the reactivity study began with a simplified surface model focused on the interfacial region between Ru(0001) and the fully dehydrogenated component of the lithiated material. The working principle used at this stage is linked to the definition of an active site which does not spread over a large area of the catalyst and for which the influence of the chemical environment at distance can be neglected in a first approximation. This resulted in a thin layer of Li_3N (only three planes) interfacing with Ru(0001), as depicted in Figure VII.1.a and VII.1.b.

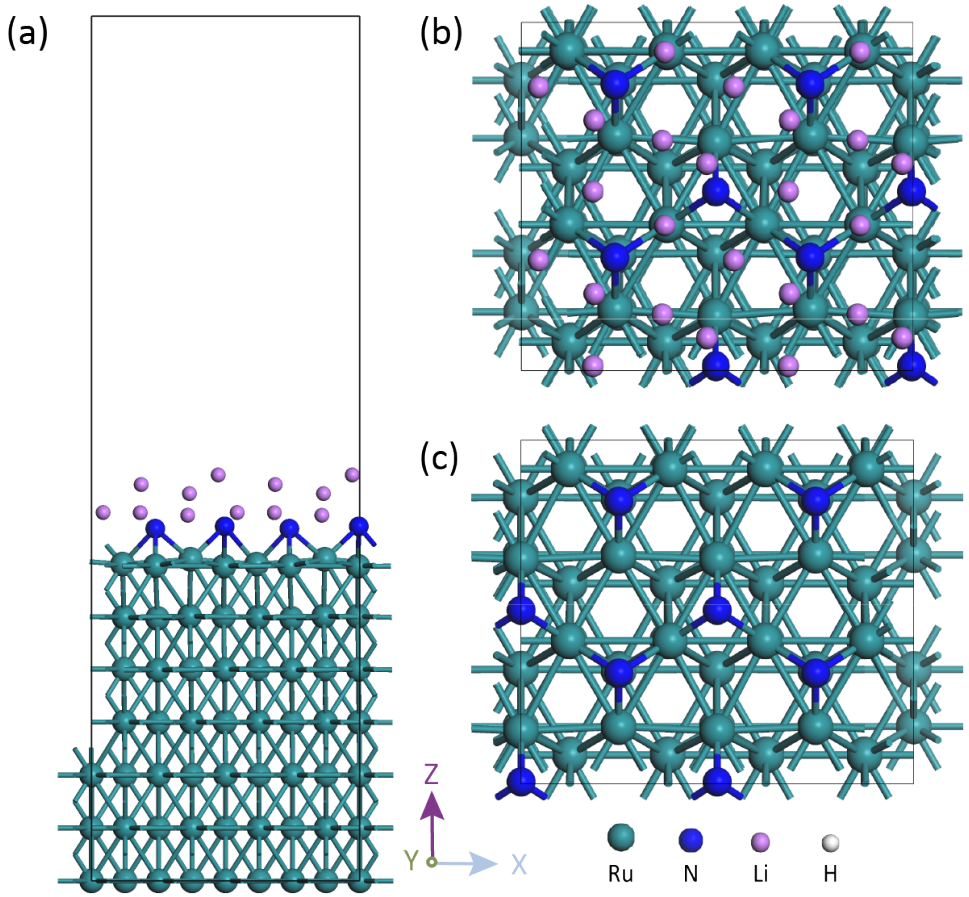

Figure VII.1: (a) Ru(0001)/Li_3N(001) simplified model extracted from the model partially hydrogenated model, (b) top view of the extracted Ru(0001)/Li_3N(001) model extracted, and (c) top view of Ru(0001)/8N delithiated model for comparison. Labels and colors of atoms are depicted.

The advantage of this simplified model lies in its reduced size (less valence electrons) and supercell, which

fasten the exploration of chemical reactivity. Then, if possible, the ultimate goal is to optimize the transition state structures with this simplified model and transfer them in the comprehensive dehydrogenated model in order to evaluate the change of activation barrier due to a more complex lithium amide/imide environment. However, due to time constraints, this verification could not be completed within the scope of this thesis and is therefore not included in this manuscript.

Regarding the choice of the supercell sizes which have been used in the previous DFT studies of ammonia synthesis and decomposition, the (2×2)[280, 284, 282] supercell is commonly employed (i.e. a larger surface coverage), but larger supercells like p(4×4)[432, 285] (meaning a lower coverage) and c(4×4)[459] have also been considered sometimes. As for the thickness of the Ru(0001) slab, it varied widely in the different studies, with anything from two to five layers being employed. In the simplified Ru(0001)/Li_3N(001) model, the supercell is $(4 \times 2\sqrt{3})$, with 16 Ru atoms per layer, with a vacuum space considered in this model of approximatively 17 Å, and with 7 atomic layers of Ru for which the three bottommost atomic planes have been kept frozen to the ideal relaxed geometry of the Ru HCP bulk while the four uppermost ones being completely relaxed. Our model is therefore among the largest ones in this context. This allows the possibility to explore various coadsorption configurations for nitrogen atoms, depending on the chosen coverage.

As depicted in Figure VII.1.b, the interface layer of Li_3N(001) in contact with Ru(0001) is composed of an overlayer of coadsorbed atomic nitrogen with a regular $(4 \times 2\sqrt{3})$-8N(coads) motif leading to a surface coverage of 0.5 ML. Among the eight coadsorbed N atoms, half of them occupy the threefold hollow hcp sites whereas the others are positioned in threefold hollow free sites. Although adsorption at the hollow hcp site is slightly more favorable as demonstrated in Chapter V at a coverage of 0.25 ML, this specific overlayer is imposed by the epitaxic positions of the N atoms related to the nitrogen terminated surface of Li_3N(001). Because of such matching constraint between Li_3N and Ru, the interface stability will pay some penalty each time atomic nitrogen is adsorbed at the hollow free site which is less stable compared to the hollow hcp site of 0.75(8) eV and 0.73(0) eV at the GGA PBE and PBE-dDsC levels, respectively (see section VI.3.2.1).

After the geometry optimization at the GGA PBE level with and without spin polarization, the terminal plane of Li_3N (in the direction of vacuum) becomes detached from the rest of the material, along the z-axis with a vertical average shift of 2.2 Å, thus reducing the vacuum space to approximatively 15 Å. Initially, the two planes containing lithium were not as distinguishable, and 12 Li atoms were belonging to the terminal planes. However, after geometry optimization and the subsequent z-axis shift, only 8 Li atoms are remaining on the terminal plane of Li_3N (as shown Figure Figure VII.S1 in appendix). Such a vertical shift of a fraction of the Li atoms is not due to the loss of weak van der Waals interactions at the GGA PBE level. In fact, a significant part of the interaction between Li and N atoms in Li_3N materials are due to electrostatic interactions which are well described at the standard GGA level. After geometry optimization, the magnetic moment (spin polarization) was found to be zero. Therefore, for the remainder of this study, calculations will be performed without considering spin polarization. After optimizations, the magnetism will be verified by using a spin-polarized GGA-PBE calculation.

In order to evaluate the importance of van der Waals interactions, the same model has been optimized at the PBE-dDsC level without spin polarization and the corresponding optimal geometry has been reported in the appendix Figure VII.S1.c. After geometry optimization, similar z-axis shift, with a vertical average shift of 1.8 Å, of 8 Li atoms are observed and formed the new terminal plane of Li_3N.

At the restricted GGA-PBE level, N atoms are coadsorbed on the Ru(0001) surface with bond distances ranging from 2.03 to 2.12 Å for N(ads) in hollow hcp sites and from 2.07 to 2.14 Å for N(ads) in hollow fcc sites, with average distances along z axis from the terminal plane of Ru(0001) of 1.39 Å and 1.49 Å, respectively. Similarly, at the PBE-dDsC level, N atoms are coadsorbed on the Ru(0001) surface with bond distances ranging from 2.03 to 2.11 Å for N(ads) in hollow hcp sites and from 2.07 to 2.14 Å for N(ads) in hollow fcc sites, with the same average distances from the terminal plane of Ru(0001) of 1.39 Å and 1.49 Å, respectively. The interface energy of the model at the GGA PBE level is 3.97(3) J.m^{-2}, and 5.63(1) J.m^{-2} at the PBE-dDsC level, and has been evaluated according to the following formula:

$$\Gamma_{Ru(0001)/Li_3N(001)} = \frac{E_{Ru(0001)/Li_3N(001)} - (E_{Li_3N_{(s)}} + E_{Ru})}{\mathcal{A}_{Li_3N@Ru}} \quad \text{(VII.1)}$$

where $E_{\text{Ru(0001)/Li}_3\text{N(001)}}$ is the total electronic energy of the interface model between Ru(0001) and Li_3N(001) slabs, $E_{\text{Li}_3}N_{\text{(s)}}$ the total electronic energy of the stoichiometric Li_3N bulk, E_{Ru} the total electronic energy of the Ru bulk, and $\mathcal{A}_{\text{Ru(0001)/Li}_3\text{N(001)}}$ denotes the surface area of the interface model.

This interface energy is greater than those previously calculated for Ru(0001)/$LiNH_2$(001) interfaces and also exceeds that of the partially hydrogenated $[Li_xNH_{3-x}(001)]_{x=1-3}$/Ru(0001) interface. This trend can be attributed to the substantial energy cost associated with cleaving the Li_3N material along the (001) plane to create a very thin slab, as employed in our interface model. Such a cost cannot be totally compensated by the stabilizing adhesion energy between Ru(0001) and the adsorption of the 8 nitrogen atoms.

VII.1.2 Equivalent delithiated ruthenium surface model: Ru(0001)/8N

To better understand the impact of lithium on reactivity, a comparative model identical to the one developed, but devoid of lithium, was also created. This Ru(0001)/8N contains the exact same number of Ru and N atoms, positioned in the same adsorption sites on Ru(0001) as its lithium-containing counterpart (see Figure VII.1.c and Figure VII.S2.a in appendix). The supercell considered is also equivalent to the Ru(0001)/Li_3N(001) model, however this new delithiated model is thinner by around 3 Å (absence of Li), its vacuum space is therefore higher (around 21 Å). The interface energy of the Ru(0001)/8N models was calculated relatively to the N_2 molecule and the Ru bulk, as follows:

$$\Gamma_{Ru(0001)/8N} = \frac{\left(E_{Ru(0001)/8N}\right) - \left(E_{N_{2,gas}} + E_{Ru}\right)}{\mathcal{A}_{Ru/8N}} \quad \text{(VII.2)}$$

where $E_{\text{Ru(0001)/8N}}$ is the total electronic energy of the interface model between Ru(0001) and the N(ads), E_{Ru} the total electronic energy of the Ru bulk, E_{N_2} the total electronic energy of the $N_{2\,\text{(gas)}}$, and $\mathcal{A}_{\text{Ru/8N}}$

denotes the surface area of the interface model.

After geometric optimization, the interface energy of this model is 4.75(3) $J.m^{-2}$ at the GGA PBE level and 6.31(4) $J.m^{-2}$ at the PBE-dDsC level, without any magnetic moment. On Ru(0001) surface, the N are absorbed in hollow hcp site with distances ranging from 1.85 to 1.94 Å , and between 1.90 to 1.97 Å for the N* in hollow free site (see Figure VII.S2.b in appendix), comparable to the measured experimental value, 2.00 ± 0.05.[460] One can note also the fact that the interface energies of the delithiated models are higher (thus less stable) than those of the Li_3N(001)Ru(0001) model.

VII.2 Transition states search and kinetic study

Understanding a reaction mechanism requires the identification of the relevant intermediates involved in the elementary steps and transition state (TS) structures, as well as the estimation of their stabilities based on total electronic energies. To identify the likely TS for the recombinant desorption of N_2, a Heuristic approach based on chemical intuition was employed to generate the initial geometries. Various TS geometries have been built taking inspiration from existing theoretical results of previously published DFT studies about ammonia decomposition on the Ru(0001) surface. These initial geometries were then optimized in accurate computational conditions by following a systematic strategy.

The selected strategy is a five-step method aiming to determine the TS is the following one. First, the initial step involves the optimization of a constrained-geometry starting structure, where the positions of the two nitrogen atoms coadsorbed close to each other at a distance corresponding to previous studies are kept ”frozen”. Different starting configurations have been considered at this stage. Then among the most stable situations, one of these partially optimized structures is selected and its saddle-point nature is verified by a restricted vibrational analysis including only the degrees of freedom of the two nitrogen atoms. In case an imaginary frequency is found and corresponds to the movement of the considered elementary step (nitrogen atom recombination), the improved dimer method[408] can then be used in a third step on the basis of the previously optimized constrained structure and the normal mode related to the imaginary frequency, to refine the geometry of this guessed TS structure by relaxing the positions of the two coadsorbed nitrogen atoms which were kept frozen at the previous step. The tight convergence criteria chosen for the dimer method is 10^{-6} eV for the total electronic energy and ±0.01 $eV.Å^{-1}$ for the residual forces. However, the completion of the optimization process rarely meets such criteria because of the intrinsic limits of this method. One way to further optimize and refine the TS structure and meet the tight convergence criteria is the use of the quasi-Newton (QN) algorithm in VASP which minimizes the residual forces hold by the nuclei without considering the variations of the total electronic energy in the region on the potential energy surface surrounding the saddle-point. Once the geometry optimization is completed for the TS structure with QN in a fourth step, a further and complete vibrational analysis including all the degrees of freedom of the nitrogen atoms and relaxed surface Ru layers is performed in a fifth and last step to finally confirm the nature of the stationary point by demonstrating the existence of only one purely imaginary frequency

meaning the finding of a first-order saddle point corresponding to a TS.

From the TS having the lowest total electronic energy the activation energy of the elementary act can be determined by comparison with that of the presumed initial state. The previously evaluated imaginary frequency and related normal mode locally describes the nature of the geometric movement associated with the minimal energy pathway linking both the initial state (IS) and final state (FS) of the elementary step. This being said, this local movement is not a mathematical proof demonstrating that those assumed initial and final states are effectively connected with the TS along a minimal energy pathway. Such a verification can be achieved thanks to the intrinsic reaction coordinate (IRC)[461, 462] approach which uses the normal mode of the imaginary frequency as a starting direction and the geometry of the TS as the starting structure, for running two independent calculations. Those two DFT calculations progressively follow the minimal energy pathways leading to the closest linked local minima on the basis of a damped velocity Verlet algorithm, as proposed by Hratchian and Schlegel.[463] These local minima correspond to the true initial and final states of the elementary steps, so that one can check whether they coincide with the presumed ones. The IRC method is a powerful technique which undeniably allows the demonstration of the existence of a minimal energy pathway linking initial, transition and final states, at the opposite of the Nudged-Elastic Band method, often used in chemical reactivity at surfaces, which only gives an idea of the potential energy surface linking these states.

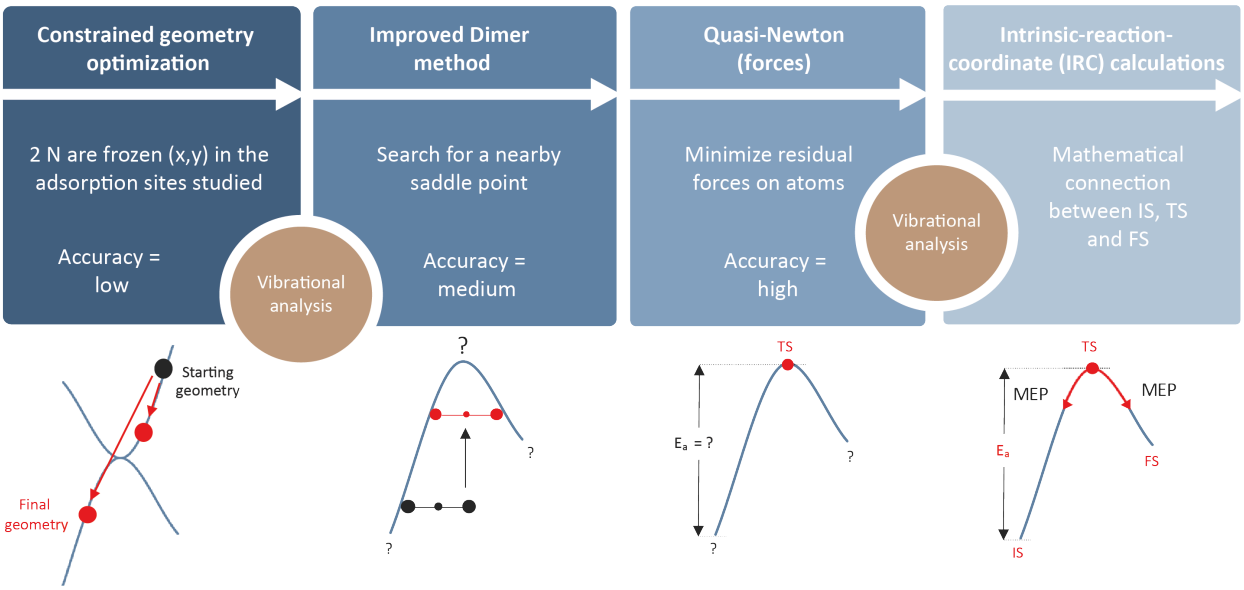

Figure VII.2: Principle of the Heuristic method for transition state search, the acronym MEP in the figure stands for minimal energy pathway.

VII.2.1 Atomic nitrogen coadsorption structures

The most abundant reaction intermediate (MARI) can significantly influence the surface species coverages involved in the RDS, as well as the apparent reaction orders of reactants. For Ru catalysts, N adsorbed N(ads)

is commonly considered as the MARI. However, Dahl et al. demonstrated that the identity of the MARI on Ru shifts depending on the concentration of inlet NH_3. At a low NH_3 content of 0.02%, the hydrogen adsorbed acts as the MARI, while at a higher NH_3 concentration of 0.2%, N(ads) becomes the MARI.[464]

Another critical aspect to consider is the rate of N(ads)-coverage on Ru. Experimentally, stable N(ads)-coverage were observed at θ_N = 0.25 and θ_N = 0.33,[458] although some measurements reached as high as θ_N = 0.38[465] and θ_N = 0.44.[466] Using an N atom beam generated by microwave discharge, Diekhöner et al. achieved N(ads)-coverages close to 1. However, these higher coverage structures were proposed to be metastable.[467] According to DFT simulations, Jacobi suggested that, N(ads)-coverages greater than 0.7 are likely to be unstable.[468] Despite this, theoretical studies of ammonia decomposition have explored a wide range of N(ads)-coverages, including 0.25,[284, 459] 0.5,[284, 459] 0.75,[284, 459] and 1.0.[284, 438]

There is no consensus on how N(ads)-coverage affects the activation energy for desorption. According to Jacobi,[468] Hammer,[459] Logadottir,[280] and Mhadeshwar,[284] DFT calculations reveal strong N–N interactions, suggesting that both the activation energy and the heat of reaction for associative desorption of N_2 are coverage-dependent. This assertion is supported by N_2-TPD results with initial N(ads)-coverages variation, where desorption peaks shift to lower temperatures as coverage increases, indicating potential repulsion between nitrogen atoms adsorbed on Ru.[469, 470] However, Tsai et al. concluded that desorption activation energy is largely independent of N(ads)-coverage.[438] This discrepancy between studies could be attributed to variations in experimental conditions and used catalysts.

In our study of the recombination of nitrogen atoms leading to N_2 desorption, the N(ads)-coverage for our systems is set at θ_N = 0.5, which is below the critical limit of 0.7. This specific N(ads)-coverage is imposed by the surface structure of Li_3N(001) which has been interfaced with Ru(0001). As a matter of fact, the terminal plane employed for interfacing Li_3N(001) with Ru(0001) contains six N atoms in direct contact with the twelve surface Ru atoms present in the supercell ($4 \times 2\sqrt{3}$).

For ammonia synthesis on Ru(0001), the dissociative adsorption of N_2 has been investigated in DFT. It has been shown that the N_2 molecule initially adsorbs vertically on onefold top of a single Ru atom. It then rotates until being horizon- tally adsorbed on the metallic surface, entering a metastable state. As the reaction progresses, the energy increases up to the TS, where the N-N distance in the molecule becomes significantly elongated. At the saddle-point, one nitrogen atom approaches its final position near a threefold hollow site, while the other remains twofold coordinated to Ru in a bridge position. The elementary step of dissociation ends with a final state structure where both nitrogen atoms adsorbed in adjacent threefold hollow hcp sites on Ru(0001).[436] For ammonia decomposition, recombinant N_2 desorption follows the exact reverse elementary mechanism with respect to that of dissociation, this means that the TS geometry is composed of coadsorbed N(ads) in threefold hollow site and twofold bridge position on Ru(0001).[29, 432]

However, in the case of the associative desorption of N_2 at the Li_3N(001)/Ru(0001) interface, the presence of lithium atoms can significantly influence both coadsorption structures of nitrogen atoms, transition state

structures and the adsorption geometry of the molecular adsorbed state of N_2. As a matter of fact, although the adlayer of nitrogen atoms is quite regular on the Ru(0001) surface, the physisorbed upper layers of lithium atoms make all the adsorption sites of nitrogen atoms quite inequivalent in the considered supercell. This means that several configurations of coadsorption states between two adjacent nitrogen atoms have to be examined, in order to ensure that the lowest transition state is found for the recombination of nitrogen atoms. This is illustrated in Figure VII.3 where five different possibilities have been built to search for transition state structures:

- **TS(Li)-1**: Two N(ads) in twofold bridge sites both being adjacent to a threefold hollow HCP site (see Figure VII.3.a),
- **TS(Li)-2**: One N(ads) on a twofold bridge site and one N(ads) on a threefold hollow free site (see Figure VII.3.d),
- **TS(Li)-3**: One N(ads) on a twofold bridge site and one N(ads) on a threefold hollow hcp site (see Figure VII.3.e).
- **TS(Li)-4**: One N(ads) on a twofold bridge site and one N(ads) on a near-top site both being adjacent to a threefold hollow HCP site (see Figure VII.3.b),
- **TS(Li)-5**: Both N(ads) on near-top sites along a twofold bridge position separating two threefold hollow FREE and HCP sites (see Figure VII.3.c),

To mimick the previously published TS structure for N_2 dissociation or recombination at the gas/metal interface of Ru(0001), the two nitrogen atoms are initially positioned at a N-N distance of approximately 1.7 Å. For some N atom coadsorption structures, the displacements of some N(ads) atoms from their epitaxial positions at the interface Li_3N(001)/Ru(0001) to their new positions at the guessed TS structures have required the lateral movements of several lithium atoms, which were hindering the elementary step of recombination at the Ru(0001) surface. Such geometric adjustments were made by maintaining N(ads)-Li distances to values compatible with the optimized Ru(0001)/Li_3N(001) interface. To enable a direct comparison with the gas/metal interface or with the delithiated Ru(001) surface and determine the impact of lithium in this elementary act, the same co-adsorption structures (TS(øLi)-X) have been considered in the case of the delithiated Ru(0001)/8N(ads) surface model (see Figure VII.S3 in appendix).

VII.2.2 Comparison: effect of lithium

The geometric optimization of the transition states systematically followed the Heuristic optimization method described earlier. No changes occurred in the initial step regarding the adsorption sites of the nitrogen atoms studied for N_2 formation, as these positions were frozen. However, notable adjustments were observed for the Ru/Li_3N catalytic models, where translational movements of the lithium atoms surrounding the two N coadsorbed occurred to align their positions with those of the N(ads) adsorption sites.

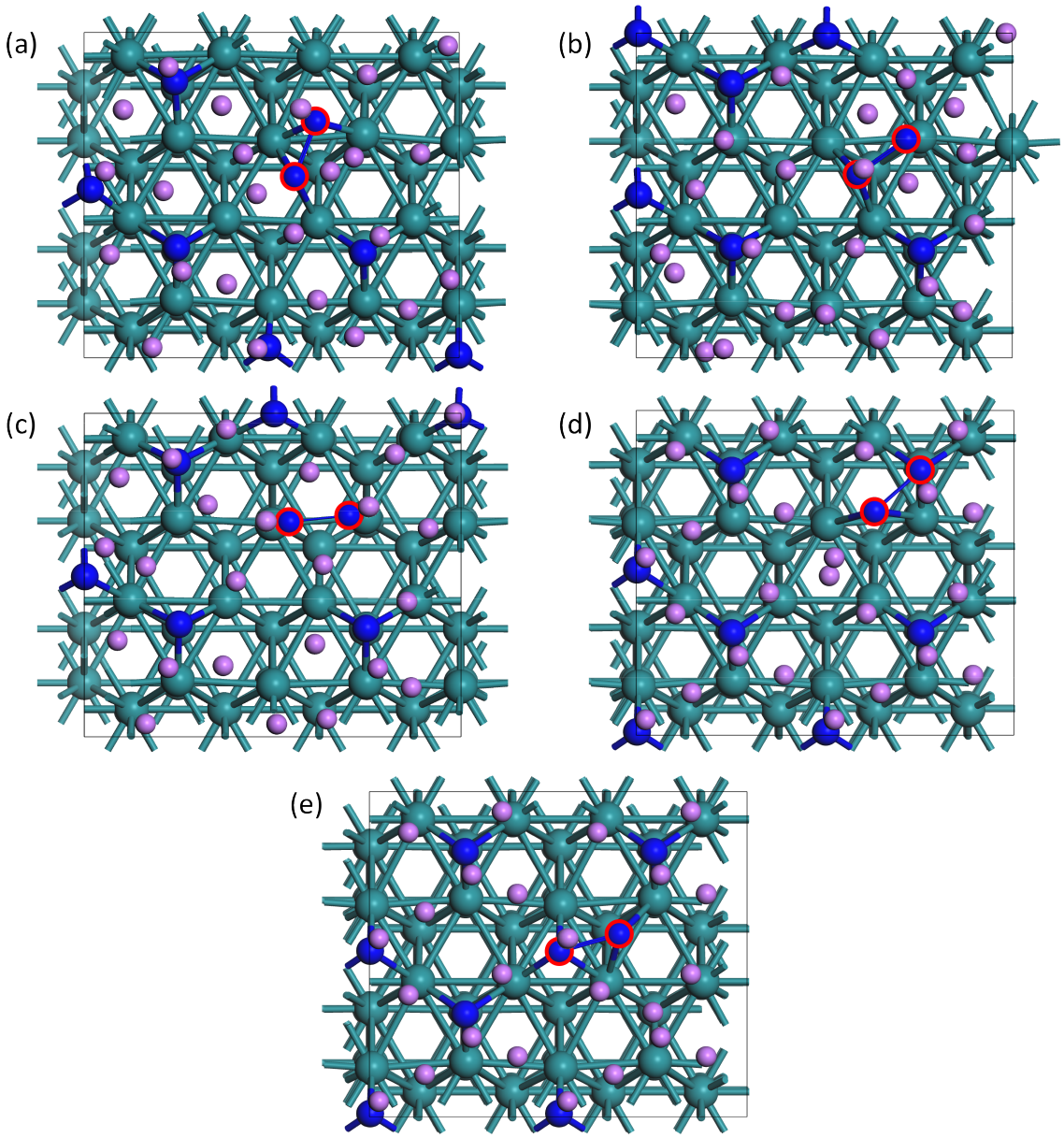

Figure VII.3: N(ads) coadsorption structures in the guessed transition states related to the recombination of two adjacent nitrogen atoms leading to the formation of N_2 and its subsequent desorption from the Ru(0001)/Li_3N(001) interface model, (a) both N(ads) in bridge sites, (b) one N (ads)on bridge site and one N(ads) on top site, (c) both N(ads) in top sites, (d) one N(ads) on bridge site and one N(ads) on hollow hcp site, and (e) one N(ads) on bridge site and one N(ads) on hollow free site. The N(ads) atoms involved in the guessed transition state structures are circled in red. The colors and atom labels are those depicted in previous Figure VII.1.

While only the Li atoms underwent reconstruction during the first step of TS optimization, significant geometric changes were observed during the second step—using the improved dimer method. In particular, some N(ads) coadsorbed systems for the Ru/Li_3N catalytic models exhibited substantial rearrangements. Adjustments in N(ads) sites were also noted. For instance, in two systems initially featuring N(ads) in hollow hcp (TS(Li)-3) and hollow free sites (TS(Li)-2) (as illustrated in Figure VII.3.d and VII.3.e), the N(ads) atoms

migrated from their original hollow positions to nearby bridge sites. This relocation was directed towards the other N(ads), which had already been pre-positioned at bridge sites during the initial model construction (see Figure VII.6.b for the reconstructed structure of the initial N(ads) hollow hcp TS(Li)-3 and Figure VII.S4.d for the reconstructed structure of the initial N(ads) hollow free TS(Li)-2).

Unexpectedly, the transition states of the delithiated Ru/8N models also underwent significant structural reconstructions during the second step of TS optimization. While applying the improved dimer method, the initial geometries of N coadsorbed at hollow and bridge sites (TS(øLi)-2 and TS(øLi)-3)—commonly reported in the literature as the actual geometry for this elementary act on Ru(0001)[436]—were not preserved. Unlike the Ru/Li_3N systems, these adjustments involved the migration of N(ads) from a bridge site to an adjacent hollow site.

Specifically, in the first case (TS(øLi)-3), where the two N(ads) were initially positioned at hollow hcp and bridge sites (refer to Figure VII.S3.d in the appendix), the N(ads) at the bridge site relocated to the adjacent hollow free site (see Figure VII.7.b). Similarly, in the second case (TS(øLi)-2), where the two N(ads) were initially located at hollow free and bridge sites (refer to Figure VII.S3.e), the N(ads) at the bridge site migrated to the adjacent hollow hcp site (as depicted in Figure VII.S5.d in the appendix). These deviations from literature-reported geometries may be attributed to differences in our N-coverage rate or the size of our supercell.

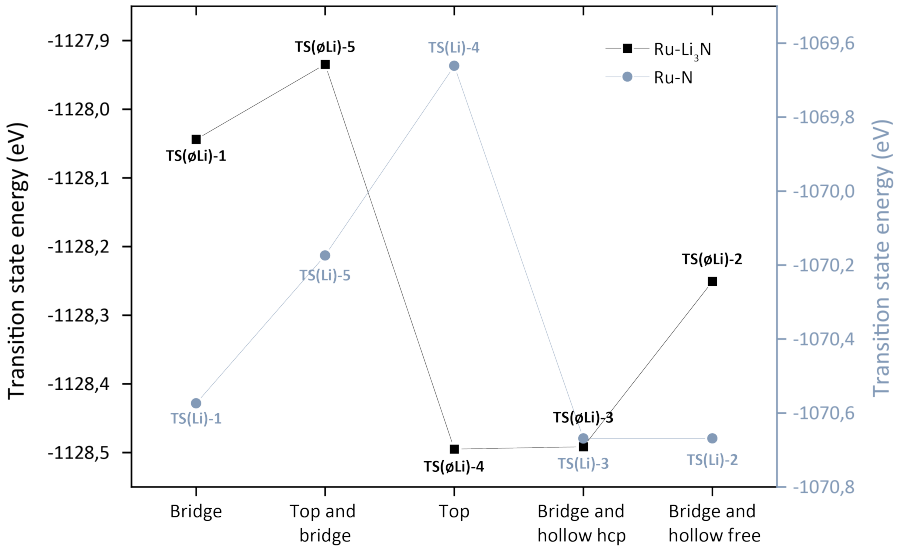

Figure VII.4: Interface energy (J.m^{-2}) comparison of the different transition states geometries at the GGA PBE level, depending on the N co-adsorption sites, as well as the presence of lithium (blue curve, round) or not (black curve, square).

After optimizing the geometries of the various transition states (TS) considered with the Heuristic method, we can now compare the stability of the different N(ads) co-adsorption sites within the Ru/Li_3N catalytic models and subsequently between the Ru/Li_3N and Ru/8N models. At the GGA-PBE level, the most stable

Table VII.1: Transition state (TS) structures and numbers, along with the initial and final N co-adsorption sites, are reported for both reactivity model types (Ru(0001)/Li_3N(001) and Ru(0001)/8N). The interface energy ($J.m^{-2}$) are presented after Constrained Geometry Optimization, Improved Dimer at the GGA-PBE level, and Quasi-Newton optimization at the GGA-PBE and PBE-dDsC levels. Interface energy values in *italics* for the PBE-dDsC functionality are based on ongoing geometric optimization.

Reactivity Model Type	TS model number	Initial N Co-adsorption Site	Final N Co-adsorption Site	Constrained Geometry Optimization	Improved Dimer Method	Quasi-Newton GGA PBE	Quasi-Newton PBE-dDsC
Ru(0001)/Li_3N(001)	TS(Li)-1	2 N in bridge site	2 N in bridge site	4.40(4)	4.39(1)	4.39(1)	–
	TS(Li)-2	1 N in bridge site and 1 N in hollow free site	2 N in bridge site	4.43(7)	4.36(9)	4.36(9)	*5.99(1)*
	TS(Li)-3	1 N in bridge site and 1 N in hollow hcp site	2 N in bridge site	4.39(6)	4.33(1)	4.33(1)	*5.99(1)*
	TS(Li)-4	1 N in bridge site and 1 N in top site	1 N in bridge site and 1 N in top site	4.36(0)	4.41(8)	4.41(8)	*5.99(2)*
	TS(Li)-5	2 N in top site	2 N in top site	4.32(8)	4.33(0)	4.33(0)	*5.79(4)*
Ru(0001)/8N	TS(øLi)-1	2 N in bridge site	2 N in bridge site	5.06(4)	5.60(0)	5.06(0)	*6.41(1)*
	TS(øLi)-2	1 N in bridge site and 1 N in hollow free site	1 N in hollow hcp site and 1 N in hollow free site	5.10(4)	5.07(3)	5.07(3)	*6.52(8)*
	TS(øLi)-3	1 N in bridge site and 1 N in hollow hcp site	1 N in hollow hcp site and 1 N in hollow free site	5.05(8)	5.04(5)	5.07(1)	*6.38(1)*
	TS(øLi)-4	1 N in bridge site and 1 N in top site	1 N in bridge site and 1 N in top site	5.12(4)	5.11(9)	5.12(3)	*6.66(6)*
	TS(øLi)-5	2 N in top site	2 N in top site	5.19(8)	5.20(3)	5.20(3)	*6.31(9)*

transition states identified involve both nitrogen atoms co-adsorbed at bridge sites (TS(Li)-1, TS(Li)-2 and TS(Li)-3). However, there is an energetic gap between the initial bridge co-adsorbtion site configurations (TS(Li)-1) and final systems where hollow N(ads) sites—whether free (TS(Li)-2) or hcp (TS(Li)-3)—have transitioned to bridge sites (see Figure VII.4 and Table VII.1 for details on interface energies).

In most of the competitive models for the lithiated interface model, the final configurations feature two N atoms co-adsorbed at bridge sites. Although the Ru atoms involved in the adsorption differ between the three models—potentially influencing the interface energy—the key distinction lies in the relaxation of the lithium atoms. For reference, see the appendices: Figure VII.S4.a illustrates the optimized geometry where both N(ads) were initially in bridge sites (TS(Li)-1), Figure VII.S4.d illustrates the optimized geometry where one N(ads) was initially in bridge site and the other in a hollow free site (TS(Li)-2), and Figure VII.6.b depicts the equivalent initial hollow hcp configuration (TS(Li)-3).

These observations highlight two key factors: the influence of lithium relaxation on the interface energy in Ru/Li_3N models and the significant effect of initial geometry on the final optimized structure. Notably, while double adsorption at bridge sites is identified as one of the most favorable configuration, the model initially featuring this geometry is not the most stable after optimization.

Finally, another model stands out in terms of interface energy: the top-site coadsorption (TS(Li)-5). At the end of the TS optimization, the energy difference between the top-site and bridge-site coadsorption is only 0.039 eV, with the latter being more stable. This comparison is based on the most stable model identified, where one of the N(ads) was initially positioned in a hollow hcp site. Starting from the TS identified as the

most stable for the Ru/Li_3N models, namely:

- **TS(Li)-3**: Two N(ads) in twofold bridge sites, initially in bridge and hollow hcp site
- **TS(Li)-5**: Both N(ads) in top site

For the Ru/8N models, the geometries of the coadsorption sites were maintained for configurations where both N(ads) occupied bridge sites, for the one N(ads) was in a bridge site and the other in a top site, and for both N(ads) were in top sites. As mentioned previously, the geometric optimization of the configuration with one N(ads) in a threefold-coordinated site coupled with the other in a bridge site did not preserve this arrangement. Instead, both N(ads) in bridge sites shifted to either hollow free or hollow hcp sites, opposite to that occupied by the other N(ads). This resulted in two closely related models where the N(ads) are coadsorbed at hollow free and hcp sites. For reference, see Figure VII.7.b for the initial hollow hcp-bridge coadsorption configuration, and Figure VII.S5.d for the equivalent initial hollow free-bridge coadsorption configuration.

The two TS geometries with at least one N(ads) in a top site are not energetically competitive. However, for the TS with two N(ads) in bridge sites—whose final geometry is shown in the appendices in Figure VII.S5.a—the interface energy is comparable to the TS with threefold-coordinated N(ads), with a difference of only 0.01 eV (see Figure VII.4 and Table VII.1 for details). Notably, the TS with two N(ads) in bridge sites is the most stable configuration. Given these results, two models were selected for further study:

- **TS(øLi)-3**: Two N(ads) in hollow sites—one hcp and the other free—initially positioned in hollow and bridge sites
- **TS(øLi)-1**: Two N(ads) in bridge sites

Regarding the optimization results of these TS geometries using the PBE-dDsC functional, the relative stability order was verified by adapting the geometries obtained from this Heuristic study (following the Quasi-Newton optimization) to the supercell parameters corresponding to the PBE-dDsC functional. This adaptation was based on the bulk HCP parameters of Ru previously determined for this functional. Unfortunately, as the calculations are still ongoing and not yet complete, it is not currently possible to compare the interface energies of the TS geometries either among themselves or with the results obtained using the GGA-PBE functional.

To this day, only two TSs, amongst the most competitive ones, have been studied in detail in order to establish the apparent activation energy. For the Ru(0001)/Li_3N(001) model, the investigated TS corresponds to two N(ads) atoms in twofold bridge sites, initially located in bridge and hollow hcp sites (TS(Li)-3). For the Ru(0001)/N model, the studied TS involves two N(ads) atoms in hollow sites—one in an hcp site and the other in a free site—initially positioned in hollow and bridge sites (TS(øLi)-3). While the study of the two other additional TSs has been initiated, their progress remains insufficient for discussion in this manuscript.

- **IRC calculations**

IRC calculations were first initiated for one TS geometry per type of catalyst model, as mentioned above. For the lithium-containing model, the TS involves two N(ads) atoms in hollow sites—one in an hcp site and the other in a free site (TS(Li)-3). For the lithium-free model, the TS also features two N(ads) atoms in hollow sites—one in an hcp site and the other in a free site—but initially positioned in hollow and bridge sites (TS(øLi)-3). IRC calculations aimed to trace the reaction pathway back to the IS and FS of the elementary step of N_2 recombination, thereby enabling the determination of the activation energy. This approach was employed to compare the activation energies for this elementary step in the presence and absence of lithium.

For the catalytic model containing lithium, IRC calculations were also useful to determine the IS structure for the N_2 recombination step. While the adsorption of both N(ads) atoms in hollow sites on the Ru(0001) surface was expected, the positioning of the lithium atoms proved less predictable. The positioning of Li significantly impacts the total energy of the system, underscoring the value of the IRC method in evaluating reaction dynamics. However, this method is not systematically successful, since it depends on the used accuracy to search the minimal energy pathway (difficult to handle from one system to another one). If not sufficiently accurate, the IRC approach can lead the system towards a shoulder on the potential energy surface with a local plateau (such as an inflection point where the second derivative of the total electronic energy with respect to the coordinate is zero and where the potential presents a change of curvature). These structures are often related to highest energy points of diffusion for atoms. The IRC approach can also fail in finding the minimal energy pathway and lead the system towards another saddle-point (lower in energy), such as a diffusion transition state of adsorbed atoms. As for the Ru/8N model, it was not possible to directly connect the IS to the TS using IRC calculations, after several attempts. The IRC approach seems to find either a saddle-point of diffusion or a shoulder on the potential energy surface.

To address this limitation, the Ru/8N TS model was constructed using insights from previous theoretical studies on the synthesis[459, 436] and decomposition[29, 432] of ammonia. These studies provided valuable information regarding the IS of this elementary step. In both cases, with or without lithium, the two N(ads) atoms in the IS are adsorbed at hollow hcp sites, which are known to be the most stable adsorption sites (as depicted in Figure VII.6.a for Li rich model and Figure VII.7.a for delithiated model).

The most notable finding from this study is the significant variation in activation energies influenced by the presence of lithium. For the Ru/8N model, the activation energy was determined to be 2.28 eV, as shown in Figure VII.5.b, aligning well with previously reported values: 2.93 eV[29], 2.21 eV[284], and approximately 2 eV[436]. This consistency validates the optimized IS structure for the Ru/8N model.

In contrast, the activation energy for N_2 recombination with the Ru/Li_3N catalytic model is notably lower, at 1.56 eV as obtained from the IRC calculation (see Figure VII.5.a), and 1.84 eV following Quasi-Newton optimization of the IS geometry derived from the IRC. This represents a reduction of 0.44 eV compared to the lithium-free model, highlighting the significant role of lithium in facilitating this elementary step.

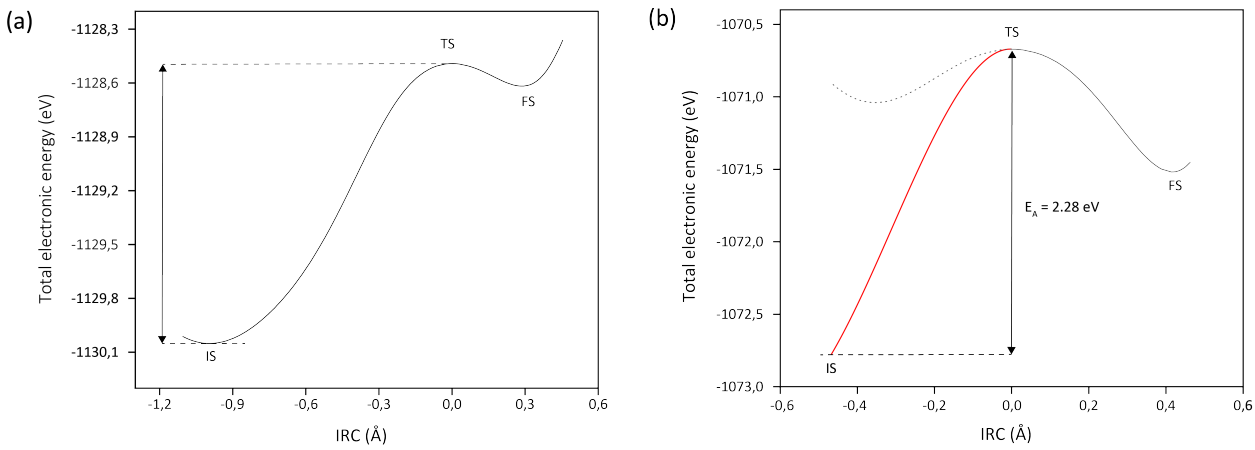

Figure VII.5: Potential energy profile along intrinsic reaction coordinate for N_2 recombination, at the GGA PBE level, for (a) Ru(0001)/Li_3N(001) catalytic model, and (b) Ru(0001)/8N catalytic model; the solid black curve represents the potential energy profile traced by the IRC calculation, while black dotted curve indicates an incorrect pathway obtained by IRC calculation. The red curve illustrates the energy comparison between the transition state and the IS geometry developed and optimized for Ru(0001)/8N model.

Additionally, the imaginary frequencies associated with the N–N bond in these TS geometries show marked differences: with lithium, the frequency is 473 cm^{-1}, whereas without lithium, it increases significantly to 693 cm^{-1}. These frequencies correlate with the activation energies; a higher frequency indicates a narrow curvature of the potential energy surface and an expected higher TS, while a lower frequency, as observed in the lithium-containing model, corresponds to a more open curvature of the potential energy surface and consequently a lower energy barrier. This evidence highlights the critical role of lithium in facilitating this elementary step during ammonia decomposition.

However, the differences between the two models extend beyond activation energy to include variations in the geometries in the different steps. In the IS, the N-Ru bond lengths of N adsorbed in hollow hcp sites differ depending on whether lithium is present. For Ru/8N model, the N-Ru bond lengths of one N(ads) is very close to the one obtained after geometry optimization of one N(ads) atom in hollow hcp on Ru(0001), 1.91 Å for IS (as depicted in Figure VII.7.a) against 1.93 Å (see section VI.3.2.1). As for the second adsorbed N, its adsorption is not as perfectly symmetrical as its Ru-N bonds vary from 1.87 to 1.97 Å, they however remain very close to the length of the Ru-N bond in the reference hollow site. While for the models with lithium, the two N(ads) are slightly more detached from the surface of the Ru(0001): one N is bound to the metal with a bond of length of 2.05 and 2.09 Å, and the second with a bond of length of 1.97 and 2.19 Å (see Figure VII.6.a), again with a slightly less symmetrical adsorption than in the model of adsorption of a N on Ru(0001).

Likewise, as the geometry of the transition state is different, the bonding of N(ads) to Ru(0001) varies with and without lithium. In the Ru/Li_3N model, the N(ads) atoms are twofold coordinated to the metal, indicating a slightly larger distance from the metal surface compared to the catalytic model without lithium, where two N(ads) atoms are threefold coordinated to Ru. In fact, the N–N bond lengths remain comparable across both scenarios, measuring 1.73 Å with lithium and 1.71 Å without (as depicted in Figure VII.7.b and

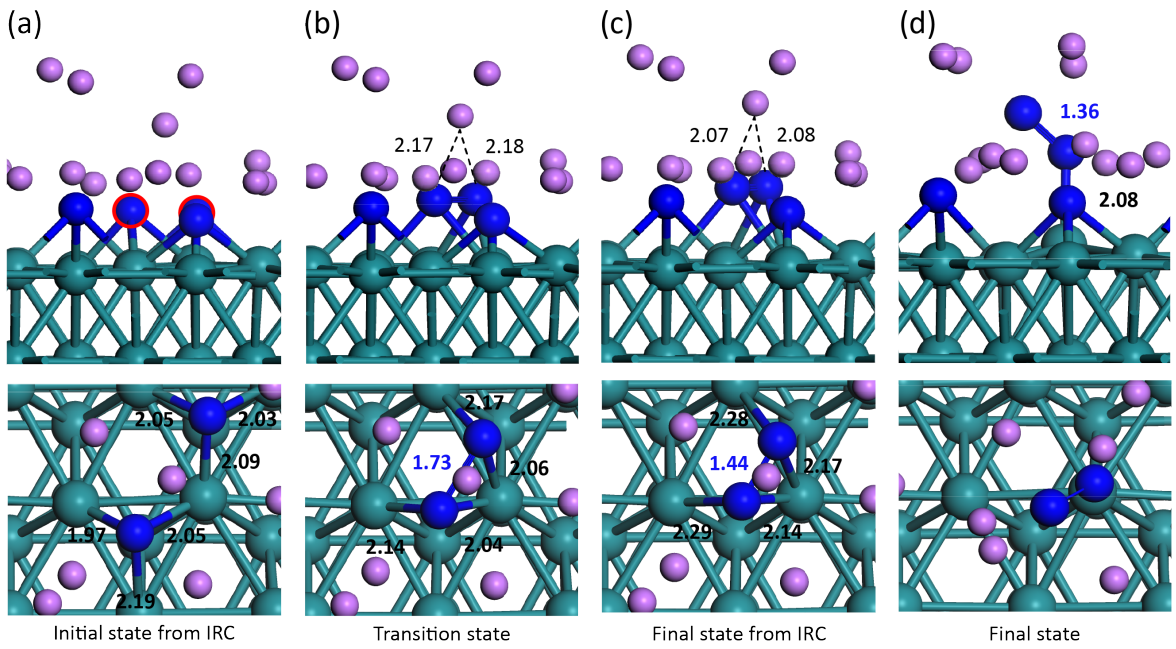

Figure VII.6: Ru(0001)-Li_3N(001) DFT structures (GGA PBE) for the different steps of recombinant N_2 desorption are illustrated as follows: (a) initial state obtained from IRC calculations, (b) transition state, (c) metastable N_2 adsorption on Ru(0001) as derived from IRC calculations, and (d) final state with N_2 adsorbed on top of a Ru atom. The black and bold values correspond to the Ru-N distance, those in bold blue correspond to the N-N distance, and the standard black values denote the Li-N distances. All atomic bounds are expressed in Å. The colors and atom labels are those depicted in previous Figure VII.1.

Figure VII.6.b, respectively). A key observation of TS for the Ru/Li_3N model is the positioning of a lithium atom directly above and bound to the two N(ads) atoms that are converging to form N_2. This lithium atom is centrally located along the N-N bond axis and accompanies the movement of the two N(ads) atoms from the initial state to the N-N bond formation at the TS, and follows the pathway down to the FS (see Figure VII.6 a and b).

Regarding, the FS derived from IRC calculations corresponds to the metastable horizontally adsorbed N_2 for both models, already well-documented in previous studies.[436] The presence of lithium still affects the adsorption behavior; the molecule is adsorbed at a greater distance from the metal, and the N-N bond length increases to 1.44 Å, compared to 1.25 Å without lithium. The metastable adsorption geometry remains similar in both scenarios.

While in the actual FS with N_2 adsorbed in top of one Ru, for the Ru/Li_3N model, the crystal field of the lithium planes above N_2 constrains the molecule to bend. However, again, the Ru-N bond is more elongated, as is the N-N bond in the Ru/Li_3N model.

Nevertheless, the geometry for the final adsorption step, right before the desorption of N_2 gas shows significant differences. Without lithium and as expected, N_2 adopts a perpendicular orientation relative to the

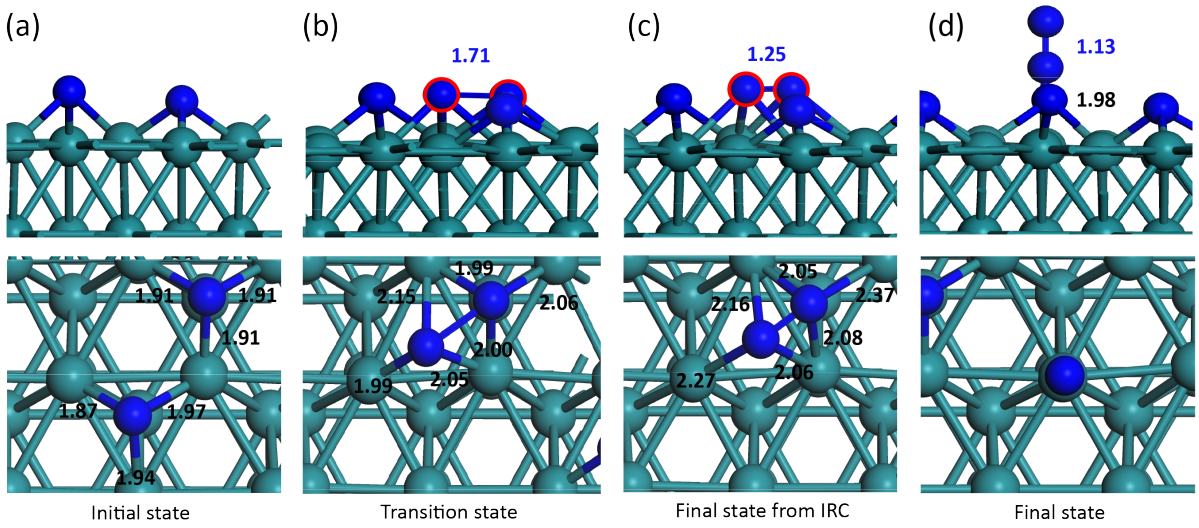

Figure VII.7: Ru(0001)/8N DFT structures (GGA PBE) for the different steps of recombinant N_2 desorption are illustrated as follows: (a) initial state obtained from geometry optimization, (b) transition state, (c) metastable N_2 adsorption on Ru(0001) as derived from IRC calculations, and (d) final state with N_2 adsorbed on top of a Ru atom. The black and bold values correspond to the Ru-N distance, those in bold blue correspond to the N-N distance, and the standard black values denote the Li-N distances. All atomic bounds are expressed in Å. The colors and atom labels are those depicted in previous Figure VII.1.

metal surface. The top adsorption on a Ru atom exhibits a Ru–N bond of 1.98 Å (see Figure VII.7.d), aligning with DFT-derived (2.00 Å)[436] and experimentally measured (2.00 $\pm$ 0.05)[460] bound lengths. At this step, the N–N bond length is 1.13 Å, consistent with prior DFT modeling (1.13 Å)[436] and experimental data (1.10 $\pm$ 0.04).[460] For the Ru/Li_3N model, due to a longer Ru–N bound, as well as from the crystalline field effect of lithium layers above N_2 force the molecule to bend, resulting in elongated N–N bonds compared to the model without lithium (see Figure VII.6.d).

From an energetic perspective, the energy barrier between the TS and FS is -2.27 eV for the lithium-free model, compared to -1.03 eV for the lithium-containing model. This difference arises from the trapped adsorption of N_2 on Ru(0001) in the presence of lithium planes, resulting in a less stable geometry compared to the lithium-free case.

VII.2.3 Bader charge analysis

To further explore the reactivity and understand lithium's influence on the recombinant desorption of N_2, we conducted an electronic analysis using Bader charge on the IS, TS, and FS structures of both Ru(0001)/Li_3N(001) and Ru(0001)/8N models. Additionally, we compared these findings with charge analyses performed on the Ru(0001) surface and the bulk of Li_3N to draw comprehensive insights into the electronic interactions.

The average Bader charge carried by the negatively charged N atoms in the bulk of Li_3N is 2.42 e^- gain of electrons or accumulation), in contrast to an average of -0.81 e^- for the positively charged Li atoms (loss

of electrons or depletion). As for the Ru surface, the charge varies mainly on the contact terminal plane between all different models, when the surface is bare, the average Bader charge carried by the atoms is -0.12 e^- (depletion).

For the Ru/8N models, the contact plane of Ru(0001) is depleted of electrons going from -0.12 e^- to -0.34 e^- for the IS, -0.32 e^- for the TS, and -0.27 e^- for the FS (see Table VII.4). This phenomenon is understandable because the metal engages its electrons to form bonds with the adsorbed N. Consequently, in the FS, the metal regains some electron density as it bonds with only seven nitrogen atoms thanks to the newly formed N_2 molecule, compared to eight in earlier states. For the Ru/Li_3N model, the trend is reversed. indeed, the average charge of the contact plane of the metal is -0.08 e^- for the IS, -0.04 e^- for the TS, and 0.05 e^- for the FS. Which means that when lithium is present in the catalyst, Ru(0001) is richer in electrons, even richer than the bare surface (see Table VII.4).

However, the N of the lithium-rich model are not negatively affected by the electron enrichment of the metallic slab. On the contrary, the N(ads) of the Ru/Li_3N model benefit from the presence of Li atoms and are twice as rich in electrons as in the Ru/8N model. In addition to this, the two N atoms forming the N_2 molecule in the FS are also much richer in electrons with on average between the different states: 1.55 and 1.64 e^-, compared to only 0.50 and 0.38 e^- for the N_2 molecule in Ru/8N model.

Table VII.2: Average charge carried by the nitrogen atoms and ruthenium atoms obtained by Bader charge analysis for the two reactivity models Ru(0001)/Li_3N(001) and Ru(0001)/8N for the three different steps of recombinant N_2 desorption : initial state (IS), transition state (TS) and final state (FS).

		N adsorbed on Ru(0001)									Ru(0001)	
		Hollow hcp			Hollow free			TS		Ref. bulk Li_3N	Contact plane	Ref.
	IS	0.75	0.75	0.73	0.72	0.68	0.70	0.70	0.72	-	-0.34	
Ru(0001)/8N	TS	0.77	0.75	0.76	0.71	0.68	0.72	0.53	0.55	-	-0.32	-0.12
	FS	0.77	0.77	0.78	0.75	0.72	0.73	0.28	-0.13	-	-0.27	
	IS	1.46	1.53	1.41	1.60	1.46	1.49	1.48	1.47		-0.08	
Ru(0001)/Li_3N(001)	TS	1.46	1.52	1.42	1.59	1.48	1.50	1.27	1.26	2.41	-0.04	-0.12
	FS	1.52	1.48	1.47	1.58	1.52	1.54	1.86	1.42		0.05	

Table VII.3: Average charge carried by the lithium atoms obtained by Bader charge analysis for Ru(0001)/Li_3N(001) reactivity models, for the three different steps of recombinant N_2 desorption : initial state (IS), transition state (TS) and final state (FS).

	Li from the first plane	Li from the second plane	Li in interaction in with N(ads) TS	Ref. bulk Li_3N
IS	-0.56	-0.12	-0.80	
TS	-0.70	0.16	-0.80	-0.81
FS	-0.52	-0.57	-0.81	

In the Ru(0001)/Li_3N(001) models, the Bader charge of lithium atoms varies significantly across the three models of the reactivity states. However, this variation is not consistent for all Li atoms; some maintain a charge similar to that found in the bulk of Li_3N, and those regardless of the state model. Furthermore, those Li atoms that do experience a change in charge do not exhibit a continuous variation across the different states. For instance, among the Li atoms from the detached plane, three exhibit an excess of electrons in the

IS, four in the transition state TS, and in the FS, the lithium charges are nearly equivalent to those in the bulk of Li_3N, with one exception (see Table VII.3). This variability in the Bader charge during the final state might be influenced by the presence of the N_2 molecule between the two lithium planes. However, the lithium atoms that become positively charged in the FS are distanced from this molecule. Additionally, while the electron enrichment of Li atoms in the initial and transition states could be attributed to the proximity of adsorbed N atoms, this effect is not uniform across all lithium atoms in this plane, and does not align with a specific geometric arrangement. Especially since the Li atoms close to the Ru(0001) surface and therefore the adsorbed N atoms, are sometimes also negatively charged (see Table VII.3). On the other hand, the Bader charge of the lithium atom that accompanies the formation of N_2 on the metal surface remains constant across all three states with a value close to Li_3N bulk. This consistency is likely due to its continuous interaction with the two N atoms.

More interestingly, the change of Bader charge (depletion) for the two nitrogen atoms involved in the TS structure, with respect to the IS, is larger for the lithiated system (0.21 e-) than for the delithiated system (0.17 e^-). This means that the presence of Li atoms assisting the elementary step of N2 recombination helps diminish the negative charge hold by the N atoms, thus weakening the bond strength with surface Ru atoms (which become less depleted) and promoting the movement of these atoms to form the N-N bond (decrease of the activation barrier).

VII.2.4 Conclusion

This study investigated the TS geometries and reaction energetics for N_2 recombination and catalyst regeneration via ammonia decomposition at the Ru(0001)/Li_3N(001) and Ru(0001)/N interfaces. TS optimizations revealed significant structural reconstructions, particularly for the lithium-containing models, where Li atoms exhibited translational adjustments to align with N adsorption sites. Additionally, N(ads) migration from hollow to bridge sites was observed, underscoring the influence of initial geometry and lithium on the system's stability.

The comparison of effective activation energies demonstrated that lithium significantly reduces the energy barrier for N_2 recombination, lowering it to 1.84 eV compared to 2.28 eV for the lithium-free model. This reduction is attributed to lithium's promoting role in modifying the reaction dynamics and catalytic properties, as reflected in the lower imaginary frequency of the N-N bond and lithium's interaction along the bond axis.

Bader charge analysis revealed that lithium enriches the Ru surface with electrons, while the N atoms in the Ru/Li_3N model exhibit a considerably higher electron density than those in the Ru/8N model. The variability in lithium atom charges across reaction states highlights complex electronic interactions influenced by the proximity to N atoms and the evolving N_2 molecule. The lithium atom at the TS in interaction with the reacting N atoms helps decrease the negative charge of the two latter atoms and consequently their adsorption strength with Ru surface, thus leading to a significant decrease of the activation barrier. The catalytic and

promoting role of lithium is thus direct and mediated through electronic interactions and charge transfers.

Overall, the presence of lithium enhances N_2 formation by stabilizing the transition state and enriching the electronic environment, albeit introducing geometric constraints that impact adsorption stability and final N_2 desorption.

Despite these findings, the exact nature of lithium's involvement—whether dominated by electrostatic forces, iono-covalent interactions, or other mechanisms—remains unresolved. Future studies employing the Electron Localization Function (ELF) are anticipated to elucidate the chemical bonding dynamics at different stages of the reaction. Additionally, further vibrational and IRC analyses of the other identified TS geometries, for both lithium-containing and lithium-free models, are necessary to provide deeper insights into the reaction mechanisms.

VII.3 Catalyst regeneration and ammonia decomposition from thermodynamics

VII.3.1 Successive ammonia adsorption and dissociation steps

Following the study of recombinant N_2 desorption, the investigation progressed by examining the catalyst regeneration through successive steps of adsorption and dissociation of two ammonia molecules.

DFT calculations[280, 432, 285] and STM analysis[285] revealed that ammonia preferentially adsorbs onto the top sites of the Ru(0001) surface. In this configuration, the N–H bonds are oriented toward the Ru atoms underneath, while the H atoms point upward, opposite from the metallic surface.[285] The mechanism of ammonia dissociation on Ru(0001) occurs through successive N–H bond cleavages, producing NH_x fragments (x = 0-2) adsorbed on the Ru surface.[285] The apparent height of these NH_x species, as observed via STM, decreases with the number of hydrogen atoms.[285]

The presence of coadsorbates, such as hydrogen atoms, significantly influences the dissociation process of NH_3 on Ru(0001).[284, 285] NH_3 interacts attractively with H atoms located at nearby fcc sites, forming stable NH_3-nH complexes. Additionally, these hydrogen atoms can modify both the activation energy and the desorption kinetics of NH_x species, highlighting the complex interplay between coadsorbates and ammonia dissociation on the Ru surface.[284, 285]

- **First ammonia adsorption**

To investigate the adsorption of NH_3 for regenerating the lithium nitride phase on the Ru(0001) surface, at the GGA PBE level, the final geometry from the previous study—where an N_2 molecule was adsorbed on top of a Ru atom—was used as the starting point. The adsorbed N_2 molecule was removed to simulate its

desorption, and the system was subsequently re-optimized (see Figure VII.S6 in the appendix). Following this optimization, an ammonia molecule was adsorbed on top of a Ru atom, specifically the Ru atom corresponding to the common atom in the two hollow hcp coadsorption sites, in the IS geometry previously identified.

In the same way as previously, to assess the influence of lithium on NH_3 adsorption, the same procedure was applied to a model without any lithium atoms, enabling a direct comparison of the adsorption behavior in the presence and absence of lithium.

However, this initial step encountered challenges. Specifically, during the construction of the new models, NH_3 was adsorbed at a distance of approximately 2.2 Å from the Ru atom, to align with previous theoretical results indicating an adsorption distance of 2.228 Å at the top site of Ru.[432] In the presence of lithium atoms, however, the NH_3 molecule rises to the level of the first Li plane (see Figure VII.8.a). Since the model was pre-optimized without the presence of NH_3, the Li atoms had sufficient space to relax and occupy this region (see Figure VII.S6 in the appendix). Successfully positioning NH_3 correctly on the Ru(0001) surface—without disrupting the hydrogen or lithium atoms—has not yet been achieved. Consequently, in models containing lithium, NH_3 often tends to desorb.

Regarding the adsorption of ammonia on Ru(0001), the top adsorption site remained stable throughout the geometric optimization for the model without lithium. The Ru–N bond length is consistent with previously reported values in the literature, measuring approximately 2.21 Å, as shown in Figure VII.8.c. Similarly, the N–H bond lengths are comparable, ranging from 1.02 to 1.03 Å, which aligns with the reported value of 1.016 Å in the literature.[432]

- **Dissociation of ammonia into NH and desorption of H_2**

In parallel with the NH_3 adsorption study, a model with an N–H fragment adsorbed at a hollow hcp site was investigated for both types of models to simulate the successive dissociation of NH_3 into NH and the subsequent desorption of H_2. Unlike the NH_3 adsorption case, this configuration optimized smoothly without any complications.

The N–H adsorption at the hollow hcp site is comparable between the two models, with only slight differences in bond lengths. In the presence of lithium, the Ru–N bonds range from 2.07 to 2.09 Å, whereas without lithium, they vary more significantly, from 2.01 to 2.27 Å. Similarly, the N–H bond is slightly shorter with lithium, measuring 1.07 Å, compared to 1.02 Å without lithium (see Figures VII.8.b and VII.8.d). The difference between the adsorption of N–H and N at the hollow hcp site on Ru(0001) is minimal in the presence of lithium, with Ru–N bond lengths ranging between 2.05 and 2.09 Å for the exact same site. In contrast, without lithium, the Ru–N bonds for N adsorption are significantly shorter, measured at 1.91 Å at the same site.

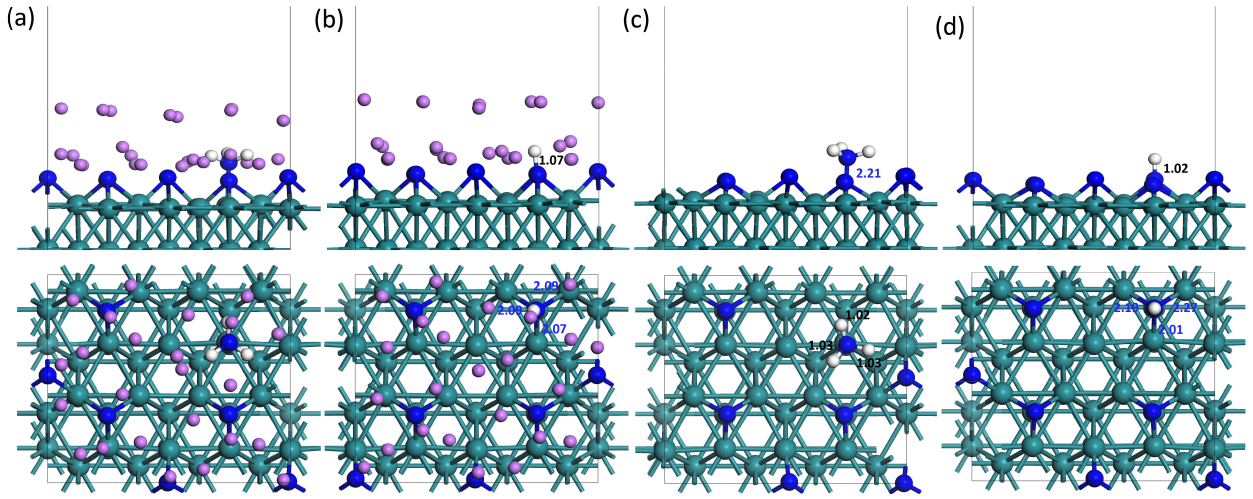

Figure VII.8: Ru(0001)/Li_3N(001) catalytic model following N_2 desorption at GGA PBE level: (a) ongoing calculation of NH_3 adsorption on top of a Ru atom, and (b) optimized geometry of NH adsorption at a hollow hcp site after NH_3 adsorption, successive dehydrogenation, and H_2 desorption; Ru(0001)/N catalytic model following N_2 desorption at GGA PBE level: (c) optimized geometry of NH_3 adsorption on top of a Ru atom, and (d) optimized geometry of NH adsorption at a hollow hcp site after NH_3 adsorption, successive dehydrogenation, and H_2 desorption. The colors and atom labels are those depicted in previous Figure VII.1.

- **Second ammonia adsorption**

Following the adsorption of the first ammonia molecule and the formation of an NH species adsorbed on Ru(0001), a second ammonia molecule is adsorbed onto the surface. The selected Ru atom for the second adsorption of NH_3 is equidistant from the four hollow hcp sites where nitrogen atoms are already adsorbed, and NH_3 is still positioned at the top of this atom. Like the first adsorption, stabilizing NH_3 in the presence of lithium remains challenging due to steric hindrance, with a pronounced tendency for NH_3 desorption. This model, like the initial NH_3 adsorption case, is still in the early stages of optimization, and thus the N–H bond lengths and the Ru–N bond length will not be analyzed at this time.

In contrast, the geometry optimization for the lithium-free model progressed smoothly, with the N–H bond lengths remaining consistent with those observed during the first adsorption. However, the Ru–N bond is slightly shorter, measuring 2.12 Å compared to 2.21 Å in the previous case (see Figure VII.9.c). The only difference between the two NH_3 adsorption scenarios is the number of nitrogen atoms adsorbed on the Ru(0001) surface. This suggests that the number of adsorbed nitrogen atoms may influence the Ru–N bond length during NH_3 adsorption.

- **Second dissociation of ammonia into NH and desorption of two H_2 molecules**

Then, the newly adsorbed ammonia molecule is positioned in an adjacent hollow free site, where two of its hydrogen atoms are removed to simulate the dissociation of NH_3 into NH and the subsequent formation and desorption of H_2. After optimizing this new structure for both models, the NH adsorption geometry in the hollow free site closely resembles that of NH(ads) in the adjacent hollow hcp site. The Ru–N bond

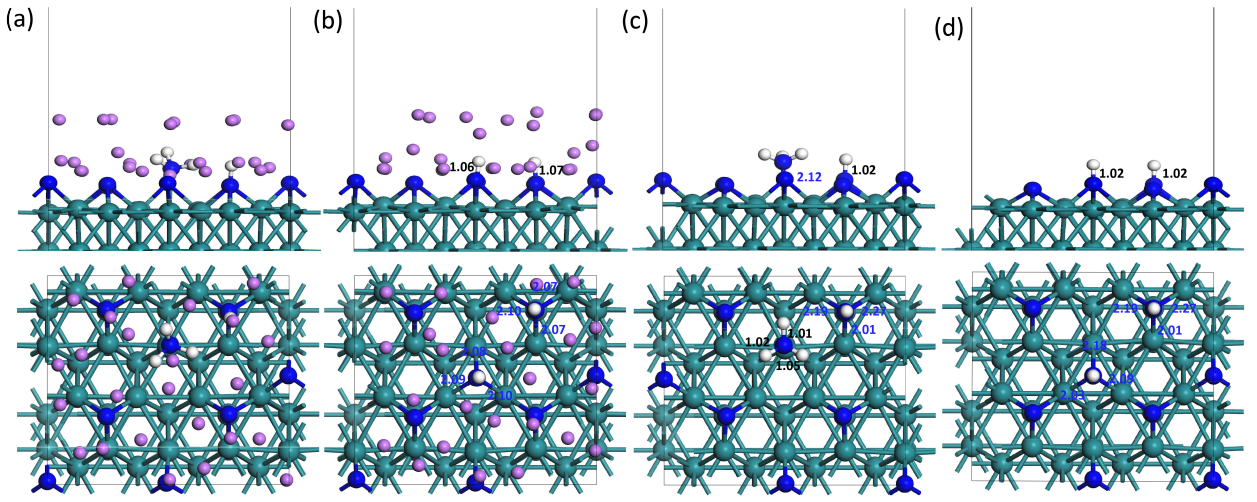

Figure VII.9: Ru(0001)/Li_3N(001) catalytic model following NH_3 adsorption and H_2 formation at GGA PBE level: (a) ongoing calculation of the second NH_3 adsorption on top of a Ru atom, and (b) optimized geometry of the second NH adsorption at a hollow hcp site after the second NH_3 adsorption, successive dehydrogenation, and H_2 desorption; Ru(0001)/N catalytic model following NH_3 adsorption and H_2 formation at GGA PBE level: (c) optimized geometry of the second NH_3 adsorption on top of a Ru atom, and (b) optimized geometry of the second NH adsorption at a hollow hcp site after the second NH_3 adsorption, successive dehydrogenation, and H_2 desorption. The colors and atom labels are those depicted in previous Figure VII.1.

lengths range from 2.08 to 2.10 Å in the presence of lithium, compared to 2.03 to 2.18 Å without lithium. Similarly, the N–H bond lengths are consistent, measuring 1.06 Å with lithium and 1.02 Å without lithium (see Figure VII.9.b and VII.9.d, respectively).

Finally, to obtain the initial geometry used at the start of the N_2 formation study from Li_3N assisted by Ru(0001), as illustrated in Figure VII.1, the two hydrogen atoms of the NH fragments were removed. The resulting structure was then optimized to fully regenerate the catalyst and enable the complete decomposition of ammonia.

VII.3.2 Comparison: effect of lithium

Regarding the comparison of NH_3 adsorption and dissociation introduced in the previous section, especially with regard to the evaluation of lithium's impact, a definitive conclusion cannot yet be drawn due to ongoing calculations. Nevertheless, a preliminary estimation of this effect is provided.

The interface energy of the lithium-containing models was calculated using the bulk phases of Ru and Li_3N, as in the previous analysis. To enable a meaningful comparison between these models and those discussed in Section VII.2, the energies of N_2, H_2, and NH_3 molecules were either added or subtracted, depending on the stoichiometry of the individual models. The resulting interface energy equations are as follows:

$$\Gamma_{Ru(0001)/Li_3N(001)} = \frac{\left(E_{Ru(0001)/Li_3N(001)} + E_{N_{2,gas}} + x \times E_{H_{2,gas}}\right) - \left(E_{Li_3N_{(s)}} + E_{Ru} + y \times E_{NH_{3,gas}}\right)}{\mathcal{A}_{Ru/Li_3N}} \quad \text{(VII.3)}$$

where $E_{\text{Ru(0001)/Li}_3\text{N(001)}}$ is the total electronic energy of the interface model between Ru(0001) and $Li_3N(001)$ slabs, $E_{\text{Li}_3\text{N}_{(s)}}$ the total electronic energy of the stoichiometric Li_3N bulk, E_{Ru} the total electronic energy of the Ru bulk, E_{N_2} the total electronic energy of the $N_{2\,(gas)}$, E_{H_2} the total electronic energy of the $H_{2\,(gas)}$, E_{NH_3} the total electronic energy of the $NH_{3\,(gas)}$, and $\mathcal{A}_{\text{Li}_3\text{N@Ru}}$ denotes the surface area of the interface model.

The same approach is applied to the calculation of the lithium-free models, with the only difference being that the interface energy is calculated relative to the N_2 molecule instead of Li_3N bulk, similar as the previous lithium-free models. The results of these interface energy equations are as follows:

$$\Gamma_{Ru(0001)/N} = \frac{\left(E_{Ru(0001)/N} + E_{N_{2,gas}} + x \times E_{H_{2,gas}}\right) - \left(yE_{N_{2,gas}} + E_{Ru} + z \times E_{NH_{3,gas}}\right)}{\mathcal{A}_{Ru/N}} \quad \text{(VII.4)}$$

where $E_{\text{Ru(0001)/N}}$ is the total electronic energy of the interface model between Ru(0001) and the N(ads), E_{Ru} the total electronic energy of the Ru bulk, E_{N_2} the total electronic energy of the $N_{2\,(gas)}$, E_{H_2} the total electronic energy of the $H_{2\,(gas)}$, E_{NH_3} the total electronic energy of the $NH_{3\,(gas)}$, and $\mathcal{A}_{\text{N@Ru}}$ denotes the surface area of the interface model.

Table VII.4: Interface name, corresponding number of N(ads) and H_2 molecules desorbed, and interface energy ($J.m^{-2}$) for all DFT models of catalyst regeneration for Ru(0001)/Li_3N(001) and Ru(0001)/N systems at the GGA-PBE level. Interface energy values in *italics* are based on ongoing geometric optimization.

Interface name	Number of N(ads)	Number of H_2 desorbed	Interface energy	
			Ru(0001)/Li_3N(001)	Ru(0001)/N
After N_2 desorption	6	-	4.30(6)	4.77(0)
First NH_3 adsorption	7	-	*4.78(9)*	4.59(6)
First NH formation	7	1	4.41(4)	4.76(2)
Second NH_3 adsorption	8	1	*4.98(8)*	4.59(2)
Second NH formation	8	2	4.51(8)	4.79(7)
Regenerated catalyst	8	3	*4.40(4)*	5.05(1)

The energy difference associated with NH_3 adsorption on the Ru(0001), for the model without Li, is slightly endothermic, with a value of -0.18 eV. This result differs from previously reported values in the literature, where the adsorption is more strongly endothermic, ranging between -0.86[280] and -1.00 eV.[282] This discrepancy could be attributed to differences in calculation conditions, such as the choice of functional or supercell

size, as well as the surface coverage rate, with one of the referenced studies employing a coverage rate of 1/4.[282] For the model with lithium, the adsorption model of NH_3 on Ru(0001) is still in progress for the geometry optimization. At the current stage, the energy difference is exothermic, with a value of 0.48 eV. Since it is possible that this value may decrease as the optimization progresses, it remains uncertain whether the exothermic nature of the adsorption will be maintained, given the current progress of the calculation.

For the formation of an NH species adsorbed on Ru(0001) and the desorption of an H_2 molecule (gas), comparing the energy difference between the two models with values reported in the literature is challenging. In previous studies, NH_3 is typically fully dehydrogenated, with the resulting hydrogen atoms adsorbed on the side on Ru(0001).[280, 282] Additionally, in some cases, a second NH_3 molecule is completely dehydrogenated before the first H_2 molecule is formed.[280] This approach can be attributed to the lower surface coverage rates in those studies, as fully dehydrogenating two NH_3 molecules in our models would not be favorable due to steric hindrance.

In our case, the energy difference between the NH_3(ads) model and the NH(ads) model is 0.17 eV for the lithium-free case and -0.38 eV when lithium is present. However, the energy difference for the lithium-containing model is provided for reference only, as the NH_3(ads) model is currently being optimized optimization. It is likely that the exothermic nature of this process will decrease as the calculations progress.

The second NH_3 adsorption for the lithium-free model is of the same order of magnitude as the first one (see Figure VII.10). This aligns with observations in the literature, although the reported energy difference is still more endothermic, at -0.83 eV.[280] The subsequent steps—NH_3 adsorption, NH formation and H_2 desorption—is of the same order of magnitude to the first sequence for both the lithium-containing and lithium-free models. However, as before, the energy differences for the lithium-containing case may still change, given that the geometry optimization of the second NH_3 adsorption model is still in progress.

Finally, for the formation of the third and final H_2 molecule, the energy difference between the NH(ads) coadsorption models and the N(ads) coadsorption models is 0.32 eV, indicating a slightly endothermic process for the lithium-free model, compared to -0.12 eV for the lithium-containing model at the current stage of calculations.

VII.3.3 Conclusion

This study provides insights into the adsorption and dissociation of NH_3 on Ru(0001) for both Ru(0001)/Li_3N(001) and Ru(0001)/N models, with the aim of evaluating the influence of lithium. The first NH_3 adsorption on Ru(0001) for the lithium-free model aligns well with literature reports, while the lithium-containing model faces challenges in stabilizing NH_3, often leading to desorption due to steric hindrance caused by lithium. This highlights the complexities of developing accurate models when the literature provides limited precedents for certain systems. Considerable effort and time may be required to establish correct initial geometries for such models.

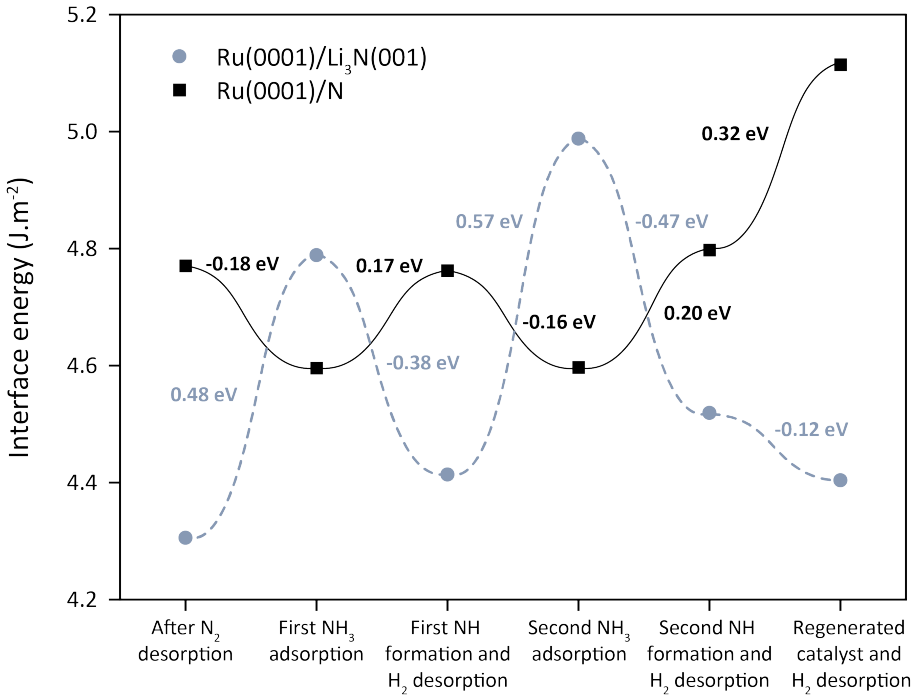

Figure VII.10: Energy profile for catalyst regeneration after N_2 desorption through successive ammonia adsorption and dehydrogenation for Ru(0001)/Li_3N(001) (blue curve, circles) and Ru(0001)/N (black curve, squares) systems at the GGA-PBE level. The dotted lines indicate that the current energy differences between models are still in progress due to ongoing geometry optimizations.

Thus far, successive steps, NH formation and H_2 desorption, are comparable in terms of endothermicity and exothermicity across the different steps for both types of models, with small variations in energy differences. For the lithium-free model, NH_3 adsorption is slightly exothermic (-0.18 eV), while the presence of lithium introduces a preliminary endothermic trend (0.48 eV). The second NH_3 adsorption and dissociation follow similar patterns to the first, with consistent bond lengths and energy differences. The steric hindrance imposed by multiple adsorbed nitrogen atoms appears to modulate the Ru–N bond length during adsorption.

Finally, the formation of the third H_2 molecule is slightly endothermic for the lithium-free model (0.32 eV) and weakly exothermic for the lithium-containing model (-0.12 eV). While the optimization of lithium-containing models are still ongoing, preliminary findings suggest that lithium may alters adsorption behavior, reaction pathways, and energy profiles. Notably, the Ru(0001)/Li_3N(001) catalyst shows potential for the regeneration after N_2 desorption through the adsorption and successive dissociation of two NH_3 molecules.

However, verifying catalyst regeneration requires a detailed analysis of the apparent activation energy barriers for the various elementary steps of the reaction mechanism, which remains out of reach in a reasonable human time. Additionally, the formation of H_2 has not been extensively studied in this work and remains an area for further investigation. The role of coadsorbates, such as hydrogen atoms, which are known to significantly influence NH_3 dissociation on Ru(0001),[285] will also need to be explored. Finally, reproducing

this study with the PBE-dDsC functional is essential for more comprehensive insights into the system.

VII.4 Overall comparison of all studied reactivity models

To conclude this thesis, the main models developed for studying ammonia decomposition catalyzed by Ru–$LiNH_2$-based catalysts were compared. Since these models differ in their chemical composition, it was necessary to establish equivalence in terms of composition to calculate comparable interface energies. By systematically adding or removing N_2, H_2, and NH_3 molecules, as well as bulk reference phases, the various models were made energetically comparable.

For this final comparison, one model from the study of the stability of the solid-solid contact between Ru(0001) and $LiNH_2$(001) was selected, the most stable interface obtain (Ru@T2T2(11,ns,p,ps)). Regarding the study of $LiNH_2$ dehydrogenation, six models were retained, based on their relative stability:

- The initial configuration.
- The most stable model of the dehydrogenation of an NH_2(ads) fragment (into coadsorbed NH and H) belonging to $LiNH_2$, on the surface of Ru(0001).
- The most stable model of the dehydrogenation of a second NH_2(ads) fragment (into coadsorbed NH and H) belonging to $LiNH_2$, on the surface of Ru(0001).
- The model with the two coadsorbed H removed, simulating the desorption of H_2.
- The most stable model for the double dehydrogenation of the two NH(ads) fragments (into coadsorbed N and H) belonging to $LiNH_{x-2}$, on the surface of Ru(0001).
- The model with the two coadsorbed H removed, simulating the second desorption of H_2.

For the study of recombinant N_2 desorption at the Ru(0001)/$LiNH_2$(001) interface, five models were selected based on their relative stability:

- The initial configuration.
- The precursor model representing N diffusion, from hollow free to hollow hcp, on the Ru(0001) surface.
- The TS model, discussed in detail in this chapter, where both N atoms are coadsorbed near bridge sites (initially adsorbed in bridge and hollow hcp sites).
- The adsorption model with N_2 formed on top of a Ru atom.
- The model where the adsorbed N_2 molecule is removed to simulate its desorption.

For the successive ammonia adsorption to regenerate the catalyst after N_2 desorption, five models were selected based on their relative stability:

- The model with one ammonia molecule adsorbed on top of a Ru atom (geometry optimization still in progress).
- The model simulating the double dehydrogenation of ammonia, along with H_2 formation and desorption, containing one NH(ads) on Ru(0001).
- The model with a second ammonia molecule adsorbed on top of a Ru atom (geometry optimization still in progress).
- The model simulating the double dehydrogenation of the second ammonia molecule, along with H_2 formation and desorption, containing two NH(ads) on Ru(0001).
- The model simulating the final dehydrogenation of the two NH(ads) fragments, the third H_2 formation and its desorption, leaving only two N(ads) on Ru(0001): the regenerated catalyst.

Finally, for the study of recombinant N_2 desorption and the successive ammonia adsorption required to regenerate the catalyst after N_2 desorption, equivalent models without lithium were also included to assess the effect of lithium on reactivity. For both studies, models analogous to those described for the lithium-containing system were selected for comparison.

Details of the equations used to adjust the interface energies for enabling energetic comparisons between all these models are provided in Table VII.S1 for models which contains Li and Table VII.S2 for models that does not contain Li, while the corresponding adjusted interface energy values are presented in Table VII.5.

By calculating these new comparative interface energies, it becomes evident that, in addition to offering a lower activation energy for N_2 recombination, the interface energy of the Ru(0001)/Li_3N(001) models is lower than that of Ru(0001)/xN (see Table VII.5 and VII.11). This indicates that models containing Li are thermodynamically more favorable than the delithiated models.

Table VII.5: DFT-developed models selected for the final comparison along with their location in the manuscript, the objective of their DFT study, their interface number and name for this comparison, a brief description, their interface energy ($J.m^{-2}$) as calculated in their respective studies with GGA PBE and PBE-dDsC functionals, and the adapted interface energy ($J.m^{-2}$) refined for the purpose of this comparison at GGA PBE level. A description of the species adsorbed on the Ru(0001) surface is provided in brackets of the interface name.

Location in the manuscript	Objective of the DFT study	Model number	Name of the model	Description	Interface energy		Adapted interface energy
				GGA PBE	PBE-dDsC	GGA PBE	
Chapter V (V.4.)	Solid-solid interface of Ru-$LiNH_2$	1	Ru@T2T2(11,ns,p,ps)		1.93(2)	2.04(2)	506.02(8)
Chapter VI (VI.2.)	Dehydrogenation of $LiNH_2$ at the Ru(0001) surface	2	Ru(0001)/$LiNH_2$(001) [8 NH_2(ads)]	Initial configuration	2.15(9)	3.22(5)	20.74(2)
		3	Ru(0001)/$LiNH_2$(001) [7 NH_2(ads) + 1 NH(ads) + 1 H(ads)]	Dehydrogenation of NH_2	1.94(1)	2.89(9)	20.52(4)
		4	Ru(0001)/$LiNH_2$(001) [6 NH_2(ads) + 2 NH(ads) + 2 H(ads)]	2nd dehydrogenation of NH_2	3.49(2)	*3.10(3)*	20.62(5)
		5	Ru(0001)/$LiNH_x$(001) [6 NH_2(ads) + 2 NH(ads)]	Desoprtion of H_2	4.95(2)	*4.73(2)*	20.73(2)
		6	Ru(0001)/$LiNH_x$(001) [6 NH_2(ads) + 2 N(ads) + 2 H(ads)]	Dehydrogenation of 2 NH	*8.01(8)*	*6.37(3)*	*20.80(3)*
		7	Ru(0001)/$LiNH_x$(001) [6 NH_2(ads) + 2 N(ads)]	2nd desoprtion of H_2	*11.00(8)*	*9.52(2)*	*20.89(5)*
Chapter VII (VII.2.)	Study of recombinant N_2 desorption	8	Ru(0001)/Li_3N(001) [8 N(ads)]	Initial configuration	3.97(3)	5.63(1)	10.10(7)
		9	Ru(0001)/Li_3N(001) [6 N(ads) + 2 N(ads)]	Diffusion of N on Ru(0001)	3.96(8)	–	10.17(7)
		10	Ru(0001)/Li_3N(001) [6 N(ads) + TS]	Transition state	4.33(0)	5.79(4)	10.46(5)
		11	Ru(0001)/Li_3N(001) [6 N(ads) + N_2(ads)]	N_2 adsorbed on Ru(0001)	4.16(9)	–	10.30(2)
		12	Ru(0001)/Li_3N_x(001) [6 N(ads)]	N_2 desorbed	4.30(6)	–	10.43(9)
Chapter VII (VII.3.)	NH_3 adsorption for catalyst regeneration	13	Ru(0001)/Li_3N_x(001) [6 N(ads) + NH_3(ads)]	Adsorption of NH_3	*4.78(9)*	–	*10.73(9)*
		14	Ru(0001)/Li_3N_x(001) [6 N(ads) + NH(ads)]	NH_3 dehydrogenation and H_2 desorption	4.41(4)	–	10.41(1)
		15	Ru(0001)/Li_3N_x(001)[6 N(ads) + NH(ads) + NH_3(ads)]	2nd adsorption of NH_3	*4.98(8)*	–	*10.84(9)*
		16	Ru(0001)/Li_3N_x(001)[6 N(ads) + 2 NH(ads)]	2nd NH_3 dehydrogenation and H_2 desorption	4.51(8)	–	10.84(9)
		17	Ru(0001)/Li_3N_x(001)[6 N(ads) + 2 N(coads)]	3rd H_2 desorption	*4.40(4)*	–	*10.26(6)*
Chapter VII (VII.2.)	Study of recombinant N_2 desorption	18	Ru(0001)/8N [8 N(ads)]	Initial configuration	4.77(8)	6.31(4)	11.16(8)
		19	Ru(0001)/8N [6 N(ads) + 2 N coads]	Diffusion of N on Ru(0001)	4.71(5)	6.27(6)	11.10(4)
		20	Ru(0001)/8N [6 N(ads) + TS]	Transition state	5.07(1)	*6.38(1)*	11.46(1)
		21	Ru(0001)/xN [6 N(ads) + N_2(ads)]	N_2 adsorbed on Ru(0001)	4.71(5)	–	11.10(5)
		22	Ru(0001)/xN [6 N(ads)]	N_2 desorbed	4.77(0)	–	11.16(0)
Chapter VII (VII.3.)	NH_3 adsorption for catalyst regeneration	23	Ru(0001)/xN [6 Nads + NH_3(ads)]	Adsorption of NH_3	4.59(6)	–	10.84(9)
		24	Ru(0001)/xN [6 N(ads) + NH(ads)]	NH_3 dehydrogenation and H_2 desorption	4.76(2)	–	11.01(6)
		25	Ru(0001)/xN [6 N(ads) + NH(ads) + NH_3(ads)]	2nd adsorption of NH_3	4.59(2)	–	10.71(4)
		26	Ru(0001)/xN [6 N(ads) + 2 NH(ads)]	2nd NH_3 dehydrogenation and H_2 desorption	4.79(7)	–	10.91(5)
		27	Ru(0001)/xN [6 N(ads) + 2 N(ads)]	3rd H_2 desorption	*5.05(1)*	–	*11.23(2)*

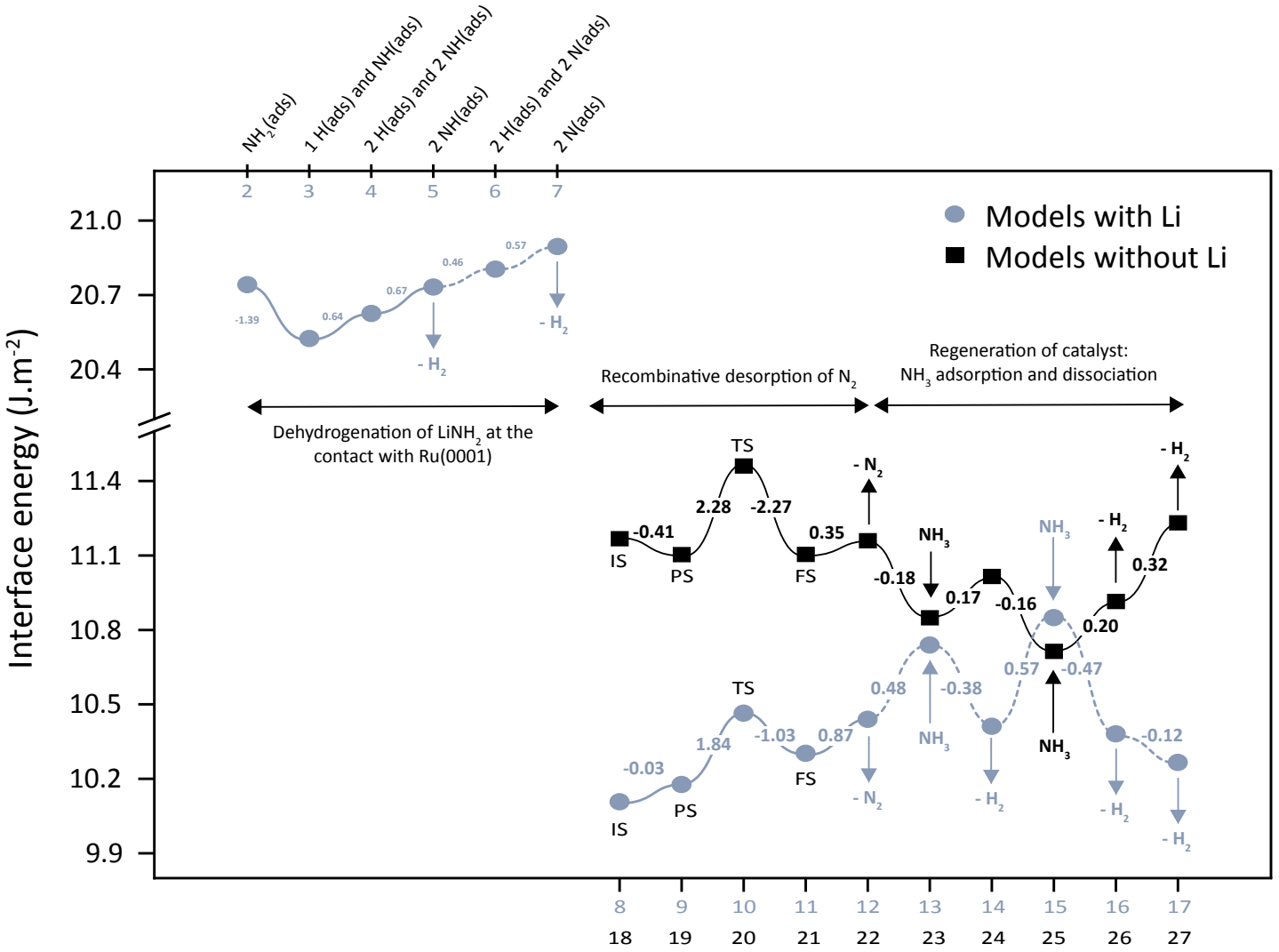

Figure VII.11: Energy profile of the dehydrogenation of $LiNH_2$ at the Ru(0001) interface, the recombinant desorption of N_2, and the regeneration of the catalyst through successive ammonia decomposition and dehydrogenation. Results are shown for the Li-based catalytic model (blue curve, circles) and the Li-free model (black curve, squares). The interface energies of all these DFT models were calculated using the adapted interface energy. Energy differences between models are expressed in eV along the curves. The dotted curves indicate that at least one calculation is still in progress, and the energy differences may be subject to revision. The number assigned to each model is indicated on the x-axis.

VII.5 Conclusion

In this chapter, TS geometries were investigated using a heuristic approach to analyze N_2 recombination, followed by the study of catalyst regeneration through successive ammonia adsorption and dehydrogenation at the Ru(0001)/Li_3N(001) and Ru(0001)/N interfaces.

Regarding N_2 recombination, TS optimizations showed significant structural reconstructions, particularly for lithium-containing models, where Li atoms underwent translational movements to align with N adsorption sites. Additionally, the migration of N(ads) atoms from hollow to bridge sites highlighted the importance of initial geometries and the stabilizing influence of lithium on the system.

The comparison of effective activation energies demonstrated a substantial decrease in the energy barrier for N_2 recombination in the presence of lithium, with values decreasing from 2.28 eV for the lithium-free model to 1.84 eV for the lithium-containing model. This reduction was attributed to lithium's impact on reaction dynamics, as evidenced by the lower imaginary frequency of the N–N bond and its interaction along the bond axis. Bader charge analysis further revealed that lithium enriches the Ru surface with electrons, while the N atoms in the Ru/Li_3N model exhibit higher electron densities compared to those in the Ru/8N model. These results underscore lithium's dual role in enhancing electronic interactions and stabilizing the TS, while also introducing geometric constraints that affect adsorption stability and N_2 desorption in FS.

The investigation into NH_3 adsorption and dissociation provided additional insights into the regeneration of the catalyst. For the lithium-free model, NH_3 adsorption was slightly exothermic (-0.18 eV) and aligned with previous literature results. In contrast, the lithium-containing model exhibited initial challenges in stabilizing NH_3, often leading to desorption due to steric hindrance from Li atoms. Successive NH formation and H_2 desorption steps showed comparable trends in terms of energy variations for both models, though steric effects modulated the Ru–N bond lengths in lithium-containing systems. Notably, the formation of the third H_2 molecule displayed opposite trends: slightly endothermic for the lithium-free model (0.32 eV) and weakly exothermic for the lithium-containing model (-0.12 eV). These preliminary findings suggest that lithium influences adsorption behavior, reaction pathways, and energy profiles, with the Ru(0001)/Li_3N(001) catalyst showing potential for regeneration through successive ammonia decomposition steps.

While this study provides interesting insights, several aspects warrant further investigation to comprehensively understand the role of lithium in catalytic processes:

- **Topological Analyses:** The exact nature of lithium's involvement—whether through electrostatic, iono-covalent, or other interactions—remains to be elucidated. Future studies employing the Electron Localization Function (ELF) will provide a deeper understanding of the bonding mechanisms at different stages of the reaction.
- **Vibrational and IRC Studies:** Additional vibrational analyses and IRC calculations for the other identified TS geometries, particularly for lithium-containing models, are essential to clarify the reaction

pathways and establish accurate apparent activation energy barriers.

- **H_2 Formation Pathways:** A detailed investigation into H_2 formation mechanisms, including the role of coadsorbates like hydrogen atoms, is necessary. Coadsorbates are known to significantly influence NH_3 dissociation on Ru(0001) and may provide further insight into reaction energetics.
- **Dispersion-corrected Functionals:** Reproducing these studies with PBE-dDsC functional is crucial to confim interface energies, structural predictions, and electronic properties.

By addressing these areas, future work will refine our understanding of lithium's role in N_2 recombination and ammonia decomposition, advancing the development of efficient and regenerable Ru-based catalytic systems.

VII.6 Appendix

- **Initial geometries for Ru(0001)/Li_3N(001) and Ru(0001)/8N catalytic model**

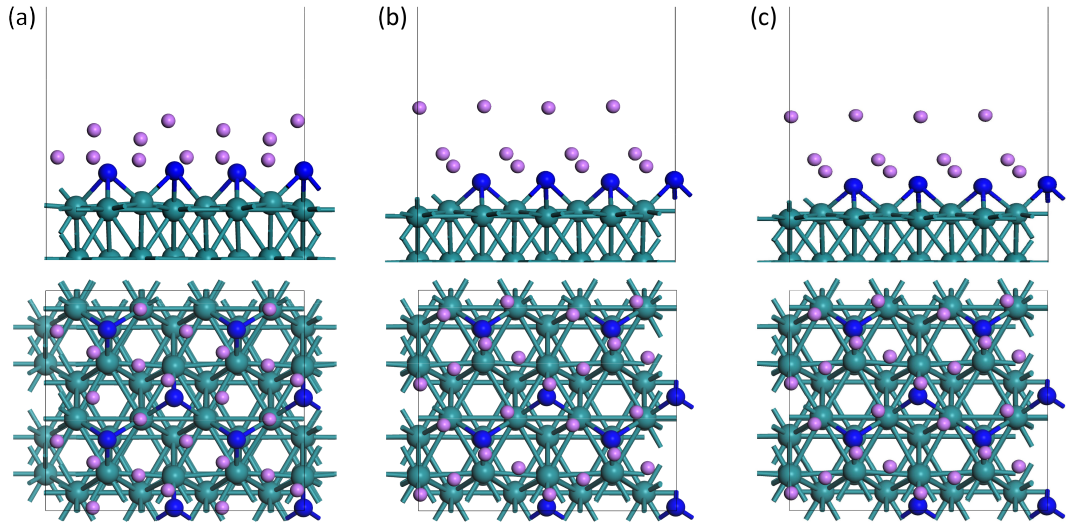

Figure VII.S1: Top and lateral views of Ru(0001)/Li_3N(001) catalytic model (a) initial geometry from optimized Ru(0001) surface and Li_3N bulk at the GGA PBE level; (b) geometry after optimization at GGA PBE level; and (c) geometry after optimization at PBE-dDsC level. The colors and atom labels are those depicted in previous Figure VII.1.

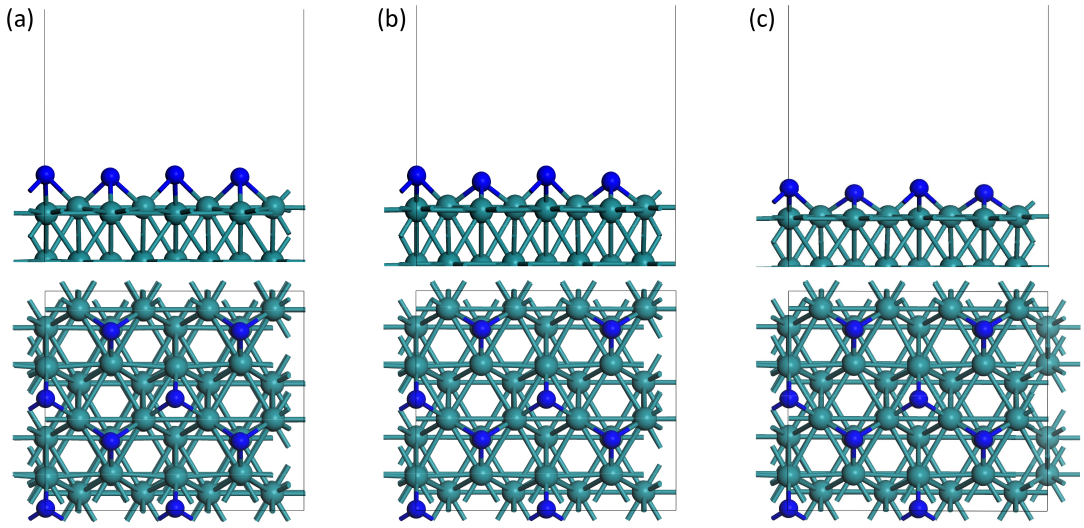

Figure VII.S2: Top and lateral views of Ru(0001)/8N catalytic model (a) initial geometry, (b) geometry after optimization at GGA PBE level; and (c) geometry after optimization at PBE-dDsC level. The colors and atom labels are those depicted in previous Figure VII.1.

- **Initial TS geometries for Ru(0001)/8N catalytic model**

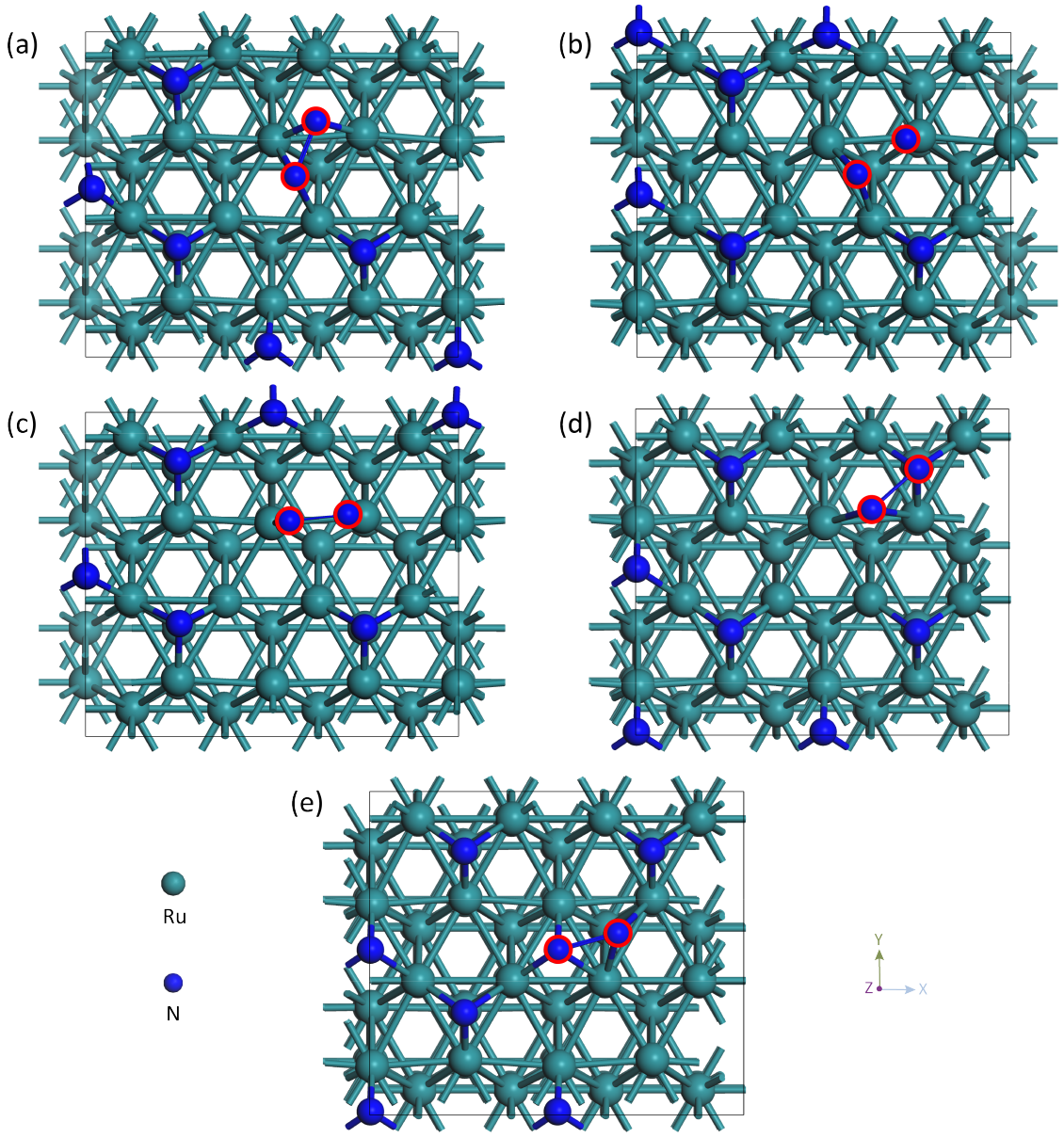

Figure VII.S3: N(ads) coadsorption structures related to the guessed transition states for recombination of two adjacent nitrogen atoms leading to the formation of N_2 and its subsequent desorption from the Ru(0001)/8N(ads) surface model, (a) both N(ads) in bridge sites, (b) one N(ads) on bridge site and one N(ads) on top site, (c) both N(ads) in top sites, (d) one N(ads) on bridge site and one N(ads) on hollow hcp site, and (e) one N(ads) on bridge site and one N(ads) on hollow free site. The N(ads) involved in the guessed transition state structures are circled in red. Labels and colors of atoms are depicted.

- **Final TS geometries for Ru(0001)/Li_3N(001) and Ru(0001)/8N catalytic model**

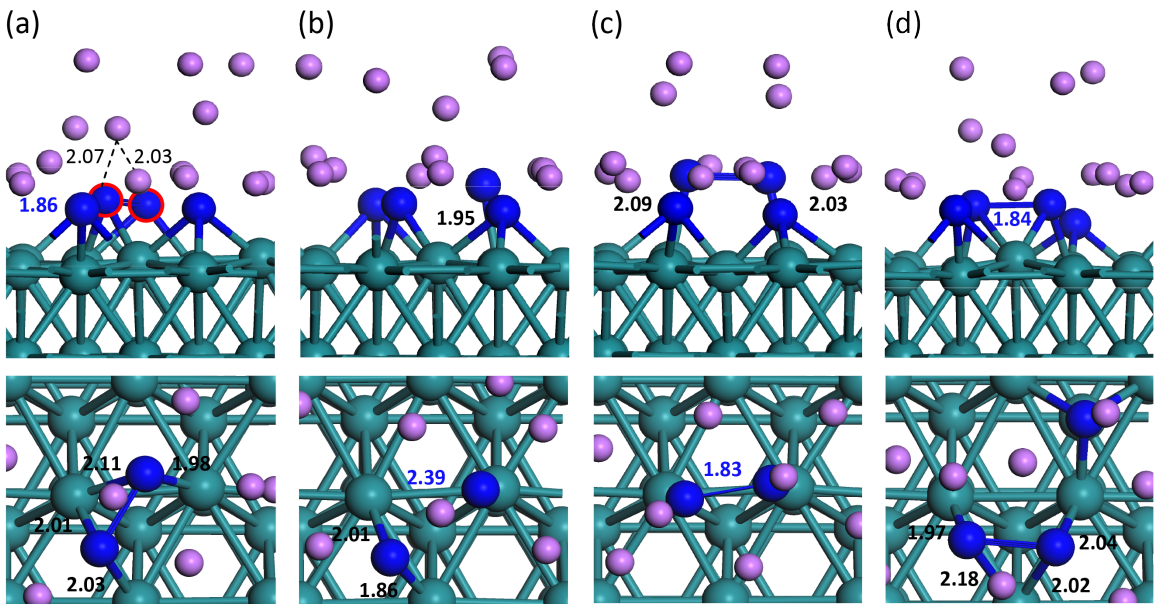

Figure VII.S4: Top and lateral views of optimized Ru(0001)/Li_3N(001) transition state at the GGA PBE level, with as initial N co-adsorption site: (a) both N in bridge site, (b) one N on bridge site and one N on top site, (c) both N in top site, and (d) one N on bridge site and one N on hollow free site. The N involved in the transition state are circled in red. The colors and atom labels are those depicted in previous Figure VII.1.

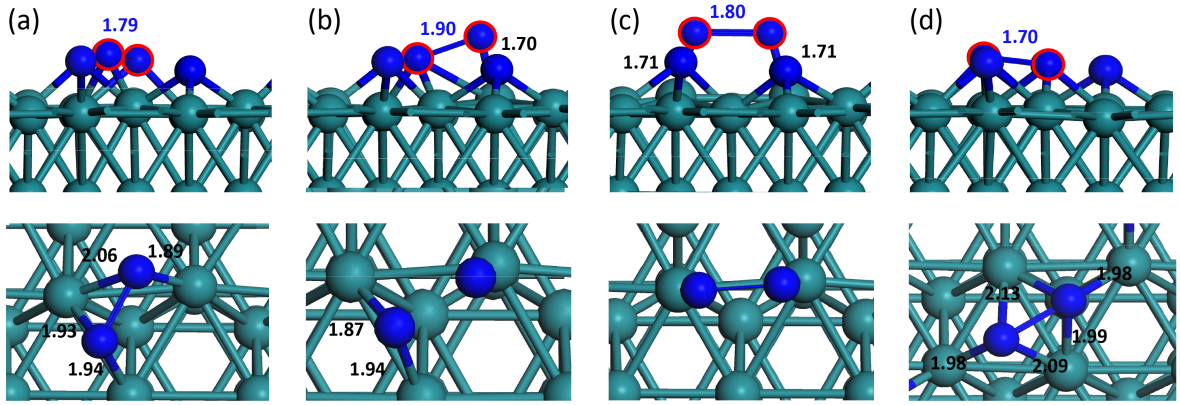

Figure VII.S5: Top and lateral views of optimized Ru(0001)/8N transition state at the GGA PBE level, with as initial N co-adsorption site: (a) both N in bridge site, (b) one N on bridge site and one N on top site, (c) both N in top site, and (d) one N on bridge site and one N on hollow free site. The N involved in the transition state are circled in red. The colors and atom labels are those depicted in previous Figure VII.1.

- **Ru(0001)/Li_3N(001) and Ru(0001)/8N catalytic model following N_2 desorption**

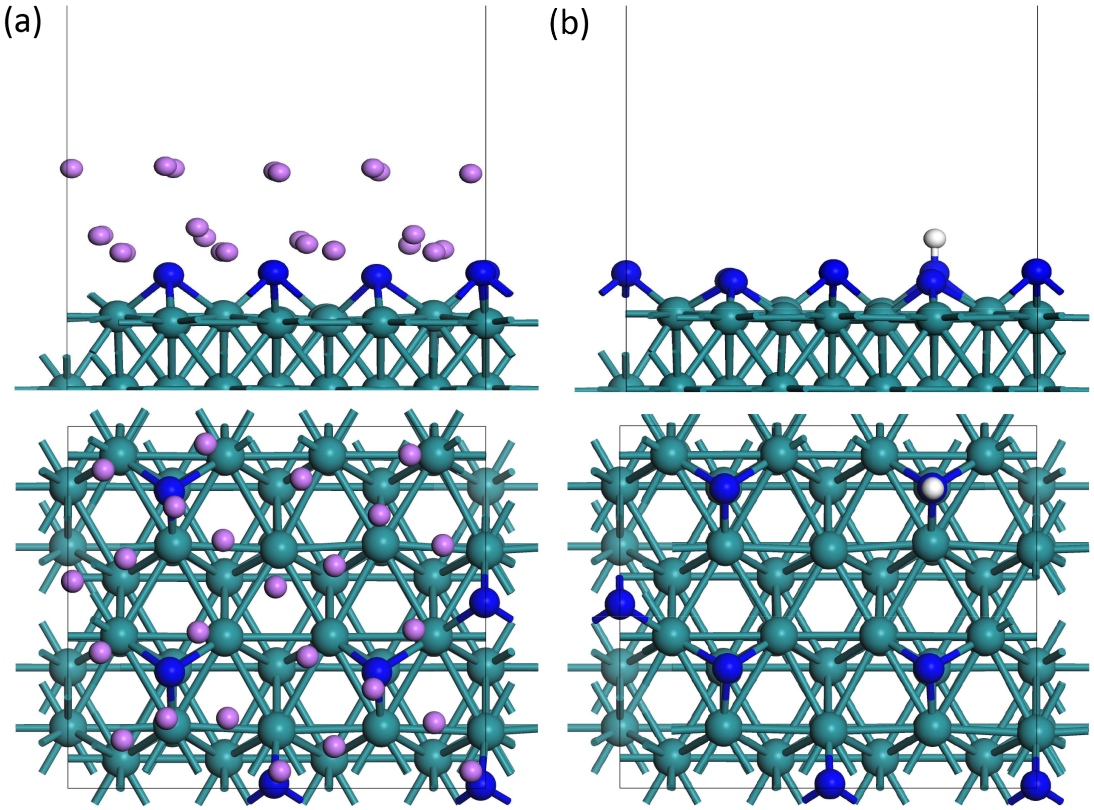

Figure VII.S6: (a) Top and lateral views of the optimized Ru(0001)/Li_3N(001) model following N_2 desorption at the GGA-PBE level, and (b) top and lateral views of the optimized Ru(0001)/N model following N_2 desorption at the GGA-PBE level. The colors and atom labels are those depicted in previous Figure VII.1.

Table VII.S1: Name of the model and adapted interface energy equation for comparison between Ru(0001)/$LiNH_2$(001) and Ru(0001)/Li_3N(001) models. A description of the species adsorbed on the Ru(0001) surface is provided in brackets. The terms used in the adapted interface energy equations are defined as follows: $E_{\text{Ru@T2T2(11,ns,p,ps)}}$ and $\mathcal{A}_{\text{Ru@T2T2(11,ns,p,ps)}}$ represent the total electronic energy and surface area of the Ru@T2T2(11,ns,p,ps) interface. Similarly, $E_{\text{Ru(0001)/LiNH}_2\text{(001)}}$ and $\mathcal{A}_{\text{Ru/LiNH}_2}$ refer to the total electronic energy and surface area of the Ru(0001)/$LiNH_2$(001) interface, while $E_{\text{Ru(0001)/Li}_3\text{N(001)}}$ and $\mathcal{A}_{\text{Ru/Li}_3\text{N}}$ correspond to the total electronic energy and surface area of the Ru(0001)/Li_3N(001) interface. Additional terms include $E_{\text{LiNH}_{2\,(ns)}}$, representing the total electronic energy of the non-stoichiometric $LiNH_2$ bulk; $E_{\text{LiNH}_{2\,(s)}}$, the total electronic energy of the stoichiometric $LiNH_2$ bulk; E_{Ru}, the total electronic energy of the Ru bulk; and $E_{\text{NH}_{3,\,\text{gas}}}$, $E_{\text{H}_{2,\,\text{gas}}}$, and $E_{\text{N}_{2,\,\text{gas}}}$, which denote the total electronic energies of $NH_{3\,(gas)}$, $H_{2\,(gas)}$, and $N_{2\,(gas)}$, respectively.

Name of the model	Adapted interface energy equation
Ru@T2T2(11,ns,p,ps)	$\frac{\left(4\times E_{Ru@T2T2(11,ns,p,ps)} + E_{LiNH_{2(ns)}} + 4\times E_{H_{2,gas}}\right) - \left(E_{Ru} + 24\times E_{LiNH_{2(s)}} + 8\times E_{NH_{3,gas}}\right)}{4\times \mathcal{A}_{Ru@T2T2(11,ns,p,ps)}}$
Ru(0001)/$LiNH_2$(001) [8 NH_2(ads)] Ru(0001)/$LiNH_2$(001) [7 NH_2(ads) + 1 NH(ads) + 1 H(ads)] Ru(0001)/$LiNH_2$(001) [6 NH_2(ads) + 2 NH(ads) + 2 H(ads)]	$\frac{\left(E_{Ru(0001)/LiNH_2(001)} + E_{LiNH_{2(ns)}} + 2\times E_{NH_{3,gas}} + 3\times E_{H_{2,gas}}\right) - \left(E_{Ru} + E_{LiNH_{2(ns)}}\right)}{\mathcal{A}_{Ru/LiNH_2}}$
Ru(0001)/$LiNH_x$(001) [6 NH_2(ads) + 2 NH(ads)] Ru(0001)/$LiNH_x$(001) [6 NH_2(ads) + 2 N(ads) + 2 H(ads)]	$\frac{\left(E_{Ru(0001)/LiNH_2(001)} + E_{LiNH_{2(ns)}} + 2\times E_{NH_{3,gas}} + 4\times E_{H_{2,gas}}\right) - \left(E_{Ru} + E_{LiNH_{2(ns)}}\right)}{\mathcal{A}_{Ru/LiNH_2}}$
Ru(0001)/$LiNH_x$(001) [6 NH_2(ads) + 2 N(ads)]	$\frac{\left(E_{Ru(0001)/LiNH_2(001)} + E_{LiNH_{2(ns)}} + 2\times E_{NH_{3,gas}} + 5\times E_{H_{2,gas}}\right) - \left(E_{Ru} + E_{LiNH_{2(ns)}}\right)}{\mathcal{A}_{Ru/LiNH_2}}$
Ru(0001)/Li_3N(001) [8 N(ads)] Ru(0001)/Li_3N(001) [6 N(ads) + 2 N(ads)] Ru(0001)/Li_3N(001) [6 N(ads) + TS] Ru(0001)/Li_3N(001) [6 N(ads) + N_2(ads)]	$\frac{\left(E_{Ru(0001)/Li_3N(001)} + 24\times E_{NH_{3,gas}}\right) - \left(E_{Ru} + 3\times E_{LiNH_{2(s)}} + 8\times E_{NH_{3,gas}}\right)}{\mathcal{A}_{Ru/Li_3N}}$
Ru(0001)/Li_3N_x(001) [6 N(ads)]	$\frac{\left(E_{Ru(0001)/Li_3N(001)} + 24\times E_{NH_{3,gas}} + E_{N_{2,gas}}\right) - \left(E_{Ru} + 3\times E_{LiNH_{2(s)}} + 8\times E_{NH_{3,gas}}\right)}{\mathcal{A}_{Ru/Li_3N}}$
Ru(0001)/Li_3N_x(001) [6 N(ads) + NH_3(ads)]	$\frac{\left(E_{Ru(0001)/Li_3N(001)} + 23\times E_{NH_{3,gas}} + E_{N_{2,gas}}\right) - \left(E_{Ru} + 3\times E_{LiNH_{2(s)}} + 8\times E_{NH_{3,gas}}\right)}{\mathcal{A}_{Ru/Li_3N}}$
Ru(0001)/Li_3N_x(001) [6 N(ads) + NH(ads) + NH_3(ads)]	$\frac{\left(E_{Ru(0001)/Li_3N(001)} + 22\times E_{NH_{3,gas}} + E_{N_{2,gas}} + E_{H_{2,gas}}\right) - \left(E_{Ru} + 3\times E_{LiNH_{2(s)}} + 8\times E_{NH_{3,gas}}\right)}{\mathcal{A}_{Ru/Li_3N}}$
Ru(0001)/Li_3N_x(001) [6 N(ads) + NH(ads)]	$\frac{\left(E_{Ru(0001)/Li_3N(001)} + 23\times E_{NH_{3,gas}} + E_{N_{2,gas}} + E_{H_{2,gas}}\right) - \left(E_{Ru} + 3\times E_{LiNH_{2(s)}} + 8\times E_{NH_{3,gas}}\right)}{\mathcal{A}_{Ru/Li_3N}}$
Ru(0001)/Li_3N_x(001) [6 N(ads) + 2 NH(ads)]	$\frac{\left(E_{Ru(0001)/Li_3N(001)} + 23\times E_{NH_{3,gas}} + E_{N_{2,gas}} + 2\times E_{H_{2,gas}}\right) - \left(E_{Ru} + 3\times E_{LiNH_{2(s)}} + 8\times E_{NH_{3,gas}}\right)}{\mathcal{A}_{Ru/Li_3N}}$
Ru(0001)/Li_3N(001) [6 N(ads) + 2 N(ads)]	$\frac{\left(E_{Ru(0001)/Li_3N(001)} + 23\times E_{NH_{3,gas}} + E_{N_{2,gas}} + 3\times E_{H_{2,gas}}\right) - \left(E_{Ru} + 3\times E_{LiNH_{2(s)}} + 8\times E_{NH_{3,gas}}\right)}{\mathcal{A}_{Ru/Li_3N}}$

Table VII.S2: Name of the model and adapted interface energy equation for comparison between Ru(0001)/N and Ru(0001)/$LiNH_2$(001) and Ru(0001)/Li_3N(001) models. A description of the species adsorbed on the Ru(0001) surface is provided in brackets. The terms used in the adapted interface energy equations are defined as follows: $E_{\text{Ru(0001)/N}}$ and $\mathcal{A}_{\text{Ru/N}}$ represent the total electronic energy and surface area of the Ru(0001)/xN interface. Additional terms include $E_{\text{LiNH}_{2\,(s)}}$, the total electronic energy of the stoichiometric $LiNH_2$ bulk; $E_{\text{Li}_3\text{N}_{(s)}}$, the total electronic energy of the stoichiometric Li_3N bulk; E_{Ru}, the total electronic energy of the Ru bulk; and $E_{\text{NH}_3,\,\text{gas}}$, $E_{\text{H}_2,\,\text{gas}}$, and $E_{\text{N}_2,\,\text{gas}}$, which denote the total electronic energies of NH_3 (gas), H_2 (gas), and N_2 (gas), respectively.

Name of the model	Adapted interface energy equation
Ru(0001)/8N [8 N(ads)] Ru(0001)/8N [6 N(ads) + 2 N(ads)] Ru(0001)/8N [6 N(ads) + TS] Ru(0001)/8N [6 N(ads) + N_2(ads)]	$\frac{\left(E_{Ru(0001)/N} + 3\times E_{Li_3N_{(s)}} + 16\times E_{NH_{3,gas}} + 12\times E_{H_{2,gas}}\right) - \left(E_{Ru} + 3\times E_{LiNH_{2(s)}} + 8\times E_{NH_{3,gas}}\right)}{\mathcal{A}_{Ru/N}}$
Ru(0001)/xN [6 N(ads)]	$\frac{\left(E_{Ru(0001)/N} + 3\times E_{Li_3N_{(s)}} + 16\times E_{NH_{3,gas}} + 12\times E_{H_{2,gas}} + E_{N_{2,gas}}\right) - \left(E_{Ru} + 3\times E_{LiNH_{2(s)}} + 8\times E_{NH_{3,gas}}\right)}{\mathcal{A}_{Ru/N}}$
Ru(0001)/xN [6 N(ads) + NH_3(ads)]	$\frac{\left(E_{Ru(0001)/N} + 3\times E_{Li_3N_{(s)}} + 15\times E_{NH_{3,gas}} + 12\times E_{H_{2,gas}}\right) - \left(E_{Ru} + 3\times E_{LiNH_{2(s)}} + 8\times E_{NH_{3,gas}}\right)}{\mathcal{A}_{Ru/N}}$
Ru(0001)/xN [6 N(ads) + NH(ads)]	$\frac{\left(E_{Ru(0001)/N} + 3\times E_{Li_3N_{(s)}} + 15\times E_{NH_{3,gas}} + 13\times E_{H_{2,gas}}\right) - \left(E_{Ru} + 3\times E_{LiNH_{2(s)}} + 8\times E_{NH_{3,gas}}\right)}{\mathcal{A}_{Ru/N}}$
Ru(0001)/xN [6 N(ads) + NH(ads) + NH_3(ads)]	$\frac{\left(E_{Ru(0001)/N} + 3\times E_{Li_3N_{(s)}} + 14\times E_{NH_{3,gas}} + 13\times E_{H_{2,gas}}\right) - \left(E_{Ru} + 3\times E_{LiNH_{2(s)}} + 8\times E_{NH_{3,gas}}\right)}{\mathcal{A}_{Ru/N}}$
Ru(0001)/xN [6 N(ads) + 2 NH(ads)]	$\frac{\left(E_{Ru(0001)/N} + 3\times E_{Li_3N_{(s)}} + 14\times E_{NH_{3,gas}} + 14\times E_{H_{2,gas}}\right) - \left(E_{Ru} + 3\times E_{LiNH_{2(s)}} + 8\times E_{NH_{3,gas}}\right)}{\mathcal{A}_{Ru/N}}$
Ru(0001)/8N [6 N(ads) + 2 N(ads)]	$\frac{\left(E_{Ru(0001)/N} + 3\times E_{Li_3N_{(s)}} + 14\times E_{NH_{3,gas}} + 15\times E_{H_{2,gas}}\right) - \left(E_{Ru} + 3\times E_{LiNH_{2(s)}} + 8\times E_{NH_{3,gas}}\right)}{\mathcal{A}_{Ru/N}}$

Conclusion and perspectives

In this thesis, we explored the potential of ammonia as a hydrogen carrier. While ammonia offers numerous advantages for this application, certain challenges remain, particularly the harsh conditions required for its synthesis and decomposition. Although the synthesis of ammonia has been extensively studied, its decomposition—critical for hydrogen extraction—has received comparatively much less attention. Among the limits related to this process, reducing the decomposition temperature would significantly improve ammonia's viability as a practical hydrogen storage medium.

From this perspective, the development of cost-efficient catalysts at low temperatures becomes essential. In the literature, research efforts are directed towards identifying cost-effective alternatives exhibiting at least a comparable performance to those of ruthenium-based catalysts. Lithium amide, when combined with transition metals, has demonstrated high catalytic activity for ammonia decomposition. However, this type of catalyst is uncommon in heterogeneous catalysis, and its catalytic phase, active site and reaction mechanisms remain unclear, in the context of ammonia decomposition. In order to tackle this challenging question and progress on this research domain, this thesis adopted a combined experimental and theoretical approach, focusing on the study of ammonia decomposition promoted by Ru-$LiNH_2$-based catalysts.

Experimentally, Ru-$LiNH_2$-based catalysts were synthesized, characterized, and evaluated for ammonia decomposition at atmospheric pressure. Theoretically, DFT studies modeled the Ru/$LiNH_2$ interface to investigate the active site and reaction mechanisms, including the catalytic formation of N_2 and H_2, as well as the catalyst regeneration.

First, a custom stainless steel catalytic reactor was developed to test $LiNH_2$-based catalysts. While this system confirmed catalytic activity, it also highlighted challenges such as interactions with support materials and design limitations. The study demonstrated the catalytic activity of Ru-$LiNH_2$, with activation energies ranging from 84.3 ± 5.5 to 125.5 ± 6.8 kJ.mol^{-1}, with the synthesis pathway as a potential explanation for this difference in activity. Preliminary investigations into Ru-$LiNH_2$/MgO catalysts revealed comparable performance to commercial Ru/Al_2O_3, despite using only half the amount of ruthenium, with a reduced apparent activation energy of 74.6 ± 6.6 kJ.mol^{-1}. Li_3N also showed promising properties as a precursor but required stabilization at 400–450°C under ammonia exposure. Although these catalysts were characterized by various experimental techniques, including DRX diffraction, vibrational spectroscopies (IR and Raman) and ATG, the nature of the active site explaining the better performance of the Ru-$LiNH_2$ system and the origin of the decrease of the activation barrier could not be explained only from measurements. A theoretical approach based on atomistic and ab initio models was necessary to investigate the chemical nature of the catalytic interface between Ru and $LiNH_2$ materials and to elucidate the role of lithium in reaction kinetics of ammo-

nia decomposition.

To address these scientific questions, theoretical models of the Ru-$LiNH_2$ catalytic interface were developed, for the first time at the international level, on the basis of DFT calculations. Five stable interface models for Ru(0001)/$LiNH_2$(001), thermodynamically more stable than the clean Ru(0001) surface, were identified thanks to spin-polarized DFT calculations, using standard GGA and dispersion-corrected functionals. These models provided insights into interfacial structures and guided the selection of a catalytic model relevant for investigating the reactivity. Since the fully hydrogenated interface model between Ru and $LiNH_2$ materials did not allow the stabilization of an active site suitable to describe the rate determining step of the ammonia decomposition, namely the recombinant desorption of N_2, new partially hydrogenated and dehydrogenated interface models were developed to explore other types of active sites at the surface of Ru and involving lithium atoms. Among them, the dehydrogenated catalytic interface composed of Ru(0001)/Li_3N(001) appeared as a stable system, able to examine the rate-determining step of the reaction mechanism, in presence of lithium. To probe precisely the role of lithium in kinetics, a comparative delithiated interface model Ru(0001)/8N was also developed.

A comparison of effective activation energies related to the associative desorption of N_2 showed a significant reduction in the barrier for lithium-containing models (1.84 eV) compared to lithium-free models (2.28 eV). This theoretical result thus supports our experimental measurements. The decrease was attributed to lithium's impact on reaction kinetics, through a direct assistance of the elementary step at the transition state, as indicated by a lower imaginary frequency. Bader charge analysis further highlighted lithium's role in enriching the Ru surface with electrons, increasing the electron density of adsorbed N atoms, enhancing electronic interactions, and stabilizing the transition state. The theoretical modeling has then proposed an explanation of the enhancement of the catalytic performance for the Ru-$LiNH_2$ catalyst, at the atomic scale.

In conclusion, this thesis highlights the potential of this type of catalyst for ammonia decomposition and provides valuable insights into lithium's role in influencing adsorption behavior, reaction mechanisms, and energy profiles. A first element for a deeper understanding of the reactivity of this type of catalyst.

In future work, several key aspects require further investigation regarding lithium's role in catalytic processes. Topological analyses are essential to determine whether lithium's interactions are electrostatic, iono-covalent, or otherwise. Additionally, a detailed exploration of H_2 formation mechanisms, including the impact of coadsorbates, could provide deeper insights into the energetics of ammonia dissociation.

Achieving a precise characterization of the $Li_xN_yH_z$-Ru interface is equally critical, particularly by elucidating the composition of the lithium phase at the interface and its evolution as a function of temperature. While this work was initiated through DFT modeling in this thesis, only a simplified model was proposed for the reactivity study. The actual interface between these materials is likely far more complex. Studying the various lithium phases via DFT remains challenging. Our choice to begin with a Ru(0001)/Li_3N(001) model was influenced by these difficulties, as this model is computationally more manageable, notably due to its lack of

a magnetic moment. This allowed us to progress on the potential geometries of key reaction stages within a reasonable timeframe for this thesis. A clearer understanding of the composition of the lithium material would enable further exploration of reactivity in DFT with a more efficient computational approach.

Finally, it is essential to adapt the developed catalytic reactor to accurately measure the catalytic activity of $LiNH_2$, Ru-$LiNH_2$/MgO, and Li_3N, ensuring the absence of undesirable species such as SiC and SiO_2, which could induce parasitic reactions. Similarly, accurate quantification of Ru is crucial to assess the true impact of $LiNH_2$ on the catalyst's reactivity.

To deepen the understanding of these catalysts, evaluating the catalytic performance of both $LiNH_2$ and Li_3N under varying thermal pretreatments would be highly beneficial. This is especially relevant for Li_3N, as its activity may only be accurately assessed in the absence of other Li_xNH_y phases. If the reactivity of Li_3N is primarily linked to its initial nitride phase, further investigation into the incorporation of transition metals and their impact on Li_3N's reactivity will be essential. However, the synthesis method used for $LiNH_2$ cannot be directly transferred, as Li_2N reacts with anhydrous ammonia to form lithium amide, altering its original composition.

Looking ahead, scaling up this type of catalyst, whether derived from $LiNH_2$ or another lithium phase, for ammonia decomposition requires careful selection of the transition metal to be paired, as ruthenium is not a viable option. While Mn-$LiNH_2$ has shown promising performance in the literature, the potential benefits of incorporating additional transition metals, as demonstrated in bimetallic catalysts, remain an area for further exploration. The development of a viable catalyst for ammonia decomposition will depend on achieving both high performance and economic feasibility. Furthermore, catalytic reactor designs must be tailored to address the unique characteristics of these systems, including phase transitions and the requirement for inert operating conditions.

References

[1] United Nations Framework Convention on Climate Change (UNFCCC). The World Needs a Swift Transition to Sustainable Energy. https://unfccc.int/news/the-world-needs-a-swift-transition-to-sustainable-energy. Accessed: 2024-04-19. 2021.

[2] Vishal Dagar et al. "Economic policy uncertainty: Global energy security with diversification". In: Economic Analysis and Policy 82 (2024), pp. 248–263. ISSN: 0313-5926. DOI: 10.1016/j.eap.2024.03.008.

[3] Kasper T. Møller et al. "Complex Metal Hydrides for Hydrogen, Thermal and Electrochemical Energy Storage". In: Energies 10.10 (2017), p. 1645. DOI: 10.3390/en10101645.

[4] Magdalena Momirlan and T.N. Veziroglu. "The properties of hydrogen as fuel tomorrow in sustainable energy system for a cleaner planet". In: International Journal of Hydrogen Energy 30.7 (2005), pp. 795–802. ISSN: 0360-3199. DOI: 10.1016/j.ijhydene.2004.10.011.

[5] Ujwal Kishor Zore et al. "A review on recent advances in hydrogen energy, fuel cell, biofuel and fuel refining via ultrasound process intensification". In: Ultrasonics Sonochemistry 73 (2021), p. 105536. ISSN: 1350-4177. DOI: 10.1016/j.ultsonch.2021.105536.

[6] Andreas Züttel. "Hydrogen storage methods". In: Naturwissenschaften 91.4 (2004), pp. 157–172. ISSN: 1432-1904. DOI: 10.1007/s00114-004-0516-x.

[7] Niraj Kumar, Seul-Yi Lee, and Soo-Jin Park. "Advancements in hydrogen storage technologies: A comprehensive review of materials, methods, and economic policy". In: Nano Today 56 (2024), p. 102302. ISSN: 1748-0132. DOI: 10.1016/j.nantod.2024.102302.

[8] Xiangyong Huang et al. "Recent Progress on Hydrogen Production from Ammonia Decomposition: Technical Roadmap and Catalytic Mechanism". In: Molecules 28.13 (2023), p. 5245. DOI: 10.3390/molecules28135245.

[9] Asbjørn Klerke et al. "Ammonia for hydrogen storage: challenges and opportunities". In: Journal of Materials Chemistry 18.20 (2008), pp. 2304–2310. DOI: 10.1039/B720020J.

[10] J.C. Ganley et al. "A priori catalytic activity correlations: The difficult case of hydrogen production from ammonia". In: Catalysis Letters 96.3 (2004), pp. 117–122. DOI: 10.1023/B:CATL.0000030108.50691.d4.

[11] T. E. Bell and L. Torrente-Murciano. "H2 Production via Ammonia Decomposition Using Non-Noble Metal Catalysts: A Review". In: Topics in Catalysis 59.15 (2016), pp. 1438–1457. ISSN: 1572-9028. DOI: 10.1007/s11244-016-0653-4.

[12] Joshua W. Makepeace et al. "Ammonia decomposition catalysis using non-stoichiometric lithium imide". In: Chemical Science 6.7 (2015), pp. 3805–3815. ISSN: 2041-6539. DOI: 10.1039/C5SC00205B.

[13] Thomas J. Wood, Joshua W. Makepeace, and William I. F. David. "Isotopic studies of the ammonia decomposition reaction using lithium imide catalyst". In: Physical Chemistry Chemical Physics 19.6 (2017), pp. 4719–4724. ISSN: 1463-9084. DOI: 10.1039/C6CP07734J.

[14] Wenbo Gao, Jianping Guo, and Ping Chen. "Hydrides, Amides and Imides Mediated Ammonia Synthesis and Decomposition". In: Chinese Journal of Chemistry 37.5 (2019), pp. 442–451. ISSN: 1614-7065. DOI: 10.1002/cjoc.201800586.

[15] Jianping Guo et al. “Electronic Promoter or Reacting Species? The Role of LiNH2 on Ru in Catalyzing NH3 Decomposition”. In: Chem. Commun. 51.82 (2015), pp. 15161–15164. DOI: 10.1039/C5CC04645A.

[16] Jianping Guo et al. “Lithium Imide Synergy with 3d Transition-Metal Nitrides Leading to Unprecedented Catalytic Activities for Ammonia Decomposition”. In: Angewandte Chemie International Edition 54.10 (2015), pp. 2950–2954. DOI: 10.1002/anie.201410773.

[17] Caitlin Brooker-Davis, Joshua Makepeace, and Thomas Wood. “Enhancement of the Catalytic Activity of Lithium Amide towards Ammonia Decomposition by Addition of Transition Metals”. In: Journal of Ammonia Energy (2023). DOI: 10.18573/jae.11.

[18] A. A. Solomon, Nelson Bunyui Manjong, and Christian Breyer. “The necessity to standardise primary energy quality in achieving a meaningful quantification of related indicators”. In: Smart Energy 12 (2023), p. 100115. ISSN: 2666-9552. DOI: 10.1016/j.segy.2023.100115.

[19] Fabio Orecchini. “The era of energy vectors”. In: International Journal of Hydrogen Energy 31.14 (2006), pp. 1951–1954. ISSN: 0360-3199. DOI: 10.1016/j.ijhydene.2006.01.015.

[20] Planète Énergies. What Is an Energy Mix? https://www.planete-energies.com/en/media/article/what-energy-mix. Accessed: 2024-04-19. 2024.

[21] Muhammad Iftikhar ul Husnain et al. “Do geopolitical risk and energy consumption contribute to environmental degradation? Evidence from E7 countries”. In: Environmental Science and Pollution Research 29.27 (2022), pp. 41640–41652. ISSN: 1614-7499. DOI: 10.1007/s11356-021-17606-z.

[22] Hisham Khatib. “IEA World Energy Outlook 2011—A comment”. In: Energy Policy. Special Section: Frontiers of Sustainability 48 (2012), pp. 737–743. ISSN: 0301-4215. DOI: 10.1016/j.enpol.2012.06.007.

[23] Fabio Orecchini and Adriano Santiangeli. “Beyond smart grids – The need of intelligent energy networks for a higher global efficiency through energy vectors integration”. In: International Journal of Hydrogen Energy. Hysydays 36.13 (2011), pp. 8126–8133. ISSN: 0360-3199. DOI: 10.1016/j.ijhydene.2011.01.160.

[24] Viktor M. Kiss, Zsolt Hetesi, and Tibor Kiss. “The effect of time resolution on energy system simulation in case of intermittent energies”. In: Renewable and Sustainable Energy Reviews 191 (2024), p. 114099. ISSN: 1364-0321. DOI: 10.1016/j.rser.2023.114099.

[25] Florian D’Ambra and Gérard Gébel. “Literature review: state-of-the-art hydrogen storage technologies and Liquid Organic Hydrogen Carrier (LOHC) development”. In: Science and Technology for Energy Transition 78 (2023), p. 32. ISSN: 2804-7699. DOI: 10.2516/stet/2023029.

[26] P. Taylor et al. Pathways for Energy Storage in the UK. Tech. rep. Consulté le 27 novembre 2024. The Open University, 2012. URL: https://oro.open.ac.uk/40087/2/Pathways_for_Energy_Storage_in_the_UK.pdf.

[27] Ulrich Eberle and Rittmar von Helmolt. “Sustainable transportation based on electric vehicle concepts: a brief overview”. In: Energy & Environmental Science 3.6 (2010), pp. 689–699. ISSN: 1754-5706. DOI: 10.1039/C001674H.

[28] Michael Felderhoff et al. “Hydrogen storage: the remaining scientific and technological challenges”. In: Physical Chemistry Chemical Physics 9.21 (2007), pp. 2643–2653. ISSN: 1463-9084. DOI: 10.1039/B701563C.

[29] Yi Zhang et al. “Mechanistic investigation of ammonia adsorption and reforming over Ni, Ru loaded catalysts toward green H_2 production of marine engines: DFT calculation and experimental evaluation”. In: Journal of Alloys and Compounds 1001 (2024), p. 175124. ISSN: 0925-8388. DOI: https://doi.org/10.1016/j.jallcom.2024.175124.

[30] Jongho Kim et al. “Advances in catalytic hydrogen combustion research: Catalysts, mechanism, kinetics, and reactor designs”. In: International Journal of Hydrogen Energy 46.80 (2021), pp. 40073–40104. ISSN: 0360-3199. DOI: 10.1016/j.ijhydene.2021.09.236.

[31] Saman Rashidi et al. “Progress and challenges on the thermal management of electrochemical energy conversion and storage technologies: Fuel cells, electrolysers, and supercapacitors”. In: Progress in Energy and Combustion Science 88 (2022), p. 100966. ISSN: 0360-1285. DOI: 10.1016/j.pecs.2021.100966.

[32] Pradyot Patnaik. Handbook of Inorganic Chemicals. McGraw-Hill, 2003. ISBN: 978-0-07-049439-8.

[33] Jin Zhong Zhang et al. Hydrogen Generation, Storage and Utilization. John Wiley & Sons, 2014. ISBN: 978-1-118-14063-5.

[34] Alberto Boretti. “Hydrogen internal combustion engines to 2030”. In: International Journal of Hydrogen Energy 45.43 (2020), pp. 23692–23703. ISSN: 0360-3199. DOI: 10.1016/j.ijhydene.2020.06.022.

[35] Antonio Escamilla, David Sánchez, and Lourdes García-Rodríguez. “Assessment of power-to-power renewable energy storage based on the smart integration of hydrogen and micro gas turbine technologies”. In: International Journal of Hydrogen Energy 47.40 (2022), pp. 17505–17525. ISSN: 0360-3199. DOI: 10.1016/j.ijhydene.2022.03.238.

[36] Andreas Züttel et al. “Properties of Hydrogen”. In: Hydrogen as a Future Energy Carrier. John Wiley & Sons, Ltd, 2008, pp. 71–147. ISBN: 978-3-527-62289-4. DOI: 10.1002/9783527622894.ch4.

[37] Raffaella Aversa et al. The Basic Elements of Life’s. Rochester, NY, 2016. URL: https://papers.ssrn.com/abstract=3074489.

[38] Seyed Ehsan Hosseini and Mazlan Abdul Wahid. “Hydrogen production from renewable and sustainable energy resources: Promising green energy carrier for clean development”. In: Renewable and Sustainable Energy Reviews 57 (2016), pp. 850–866. ISSN: 1364-0321. DOI: 10.1016/j.rser.2015.12.112.

[39] Hydrogen from renewable power: Technology outlook for the energy transition. 2018. URL: https://www.irena.org/publications/2018/Sep/Hydrogen-from-renewable-power (visited on 04/17/2024).

[40] A. Ajanovic, M. Sayer, and R. Haas. “The economics and the environmental benignity of different colors of hydrogen”. In: International Journal of Hydrogen Energy 47.57 (2022), pp. 24136–24154. ISSN: 0360-3199. DOI: 10.1016/j.ijhydene.2022.02.094.

[41] alex. Hydrogen: Clearing Up the Colours. 2020. URL: https://www.enapter.com/blog/hydrogen-clearing-up-the-colours/.

[42] Marcus Newborough and Graham Cooley. “Developments in the global hydrogen market: The spectrum of hydrogen colours”. In: Fuel Cells Bulletin 2020.11 (2020), pp. 16–22. ISSN: 1464-2859. DOI: 10.1016/S1464-2859(20)30546-0. (Visited on 2024).

[43] Ashraf M. Amin, Eric Croiset, and William Epling. “Review of methane catalytic cracking for hydrogen production”. In: International Journal of Hydrogen Energy 36.4 (2011), pp. 2904–2935. ISSN: 0360-3199. DOI: 10.1016/j.ijhydene.2010.11.035.

[44] Rami S. El-Emam, Hasan Ozcan, and Calin Zamfirescu. “Updates on promising thermochemical cycles for clean hydrogen production using nuclear energy”. In: Journal of Cleaner Production 262 (2020), p. 121424. ISSN: 0959-6526. DOI: 10.1016/j.jclepro.2020.121424.

[45] S. Z. Zhiznin, V. M. Timokhov, and A. L. Gusev. “Economic aspects of nuclear and hydrogen energy in the world and Russia”. In: International Journal of Hydrogen Energy 45.56 (2020), pp. 31353–31366. ISSN: 0360-3199. DOI: 10.1016/j.ijhydene.2020.08.260.

[46] Fan Zhang et al. “The survey of key technologies in hydrogen energy storage”. In: International Journal of Hydrogen Energy 41.33 (2016), pp. 14535–14552. ISSN: 0360-3199. DOI: 10.1016/j.ijhydene.2016.05.293.

[47] Tatiane da Silva Veras et al. “Hydrogen: Trends, production and characterization of the main process worldwide”. In: International Journal of Hydrogen Energy 42.4 (2017), pp. 2018–2033. ISSN: 0360-3199. DOI: 10.1016/j.ijhydene.2016.08.219.

[48] Wolfgang Lubitz and William Tumas. “Hydrogen:□ An Overview”. In: Chemical Reviews 107.10 (2007), pp. 3900–3903. ISSN: 0009-2665. DOI: 10.1021/cr050200z.

[49] Bing-Shun Huang, Feng-Yim Chang, and Ming-Yen Wey. “Photocatalytic properties of redox-treated Pt/TiO_2 photocatalysts for H_2 production from an aqueous methanol solution”. In: International Journal of Hydrogen Energy 35.15 (2010), pp. 7699–7705. ISSN: 0360-3199. DOI: 10.1016/j.ijhydene.2010.05.103.

[50] S. Z. Baykara. “Hydrogen production by direct solar thermal decomposition of water, possibilities for improvement of process efficiency”. In: International Journal of Hydrogen Energy 29.14 (2004), pp. 1451–1458. ISSN: 0360-3199. DOI: 10.1016/j.ijhydene.2004.02.014.

[51] Zainul Abdin et al. “Hydrogen as an energy vector”. In: Renewable and Sustainable Energy Reviews 120 (2020), p. 109620. ISSN: 1364-0321. DOI: 10.1016/j.rser.2019.109620.

[52] J. D. Holladay et al. “An overview of hydrogen production technologies”. In: Catalysis Today 139.4 (2009), pp. 244–260. ISSN: 0920-5861. DOI: 10.1016/j.cattod.2008.08.039.

[53] Sung Hoon Hong et al. “High-activity electrodeposited NiW catalysts for hydrogen evolution in alkaline water electrolysis”. In: Applied Surface Science 349 (2015), pp. 629–635. ISSN: 0169-4332. DOI: 10.1016/j.apsusc.2015.05.040.

[54] Diego Feroldi and Marta Basualdo. “Description of PEM Fuel Cells System”. In: PEM Fuel Cells with Bio-Ethanol Processor Systems. Springer, 2012, pp. 49–72. ISBN: 978-1-84996-184-4. DOI: 10.1007/978-1-84996-184-4_2.

[55] Frano Barbir. “PEM electrolysis for production of hydrogen from renewable energy sources”. In: Solar Energy. Solar Hydrogen 78.5 (2005), pp. 661–669. ISSN: 0038-092X. DOI: 10.1016/j.solener.2004.09.003.

[56] Meng Ni et al. “An overview of hydrogen production from biomass”. In: Fuel Processing Technology 87.5 (2006), pp. 461–472. ISSN: 0378-3820. DOI: 10.1016/j.fuproc.2005.11.003.

[57] Tamer Y. A. Fahmy et al. “Biomass pyrolysis: past, present, and future”. In: Environment, Development and Sustainability 22.1 (2020), pp. 17–32. ISSN: 1573-2975. DOI: 10.1007/s10668-018-0200-5.

[58] A. Demirbas. “Hydrogen Production from Carbonaceous Solid Wastes by Steam Reforming”. In: Energy Sources, Part A: Recovery, Utilization, and Environmental Effects 30.10 (2008), pp. 924–931. ISSN: 1556-7036. DOI: 10.1080/10826070601082658.

[59] David B Levin, Lawrence Pitt, and Murray Love. “Biohydrogen production: prospects and limitations to practical application”. In: International Journal of Hydrogen Energy 29.2 (2004), pp. 173–185. ISSN: 0360-3199. DOI: 10.1016/S0360-3199(03)00094-6.

[60] Kaniz Farhana, Abu Shadate Faisal Mahamude, and Kumaran Kadirgama. “Comparing hydrogen fuel cost of production from various sources - a competitive analysis”. In: Energy Conversion and Management 302 (2024), p. 118088. ISSN: 0196-8904. DOI: 10.1016/j.enconman.2024.118088.

[61] International Energy Agency. Technology Roadmap - Hydrogen and Fuel Cells – Analysis. 2015. URL: https://www.iea.org/reports/technology-roadmap-hydrogen-and-fuel-cells.

[62] Jeffrey R. Bartels, Michael B. Pate, and Norman K. Olson. “An economic survey of hydrogen production from conventional and alternative energy sources”. In: International Journal of Hydrogen Energy 35.16 (2010), pp. 8371–8384. ISSN: 0360-3199. DOI: 10.1016/j.ijhydene.2010.04.035.

[63] International Energy Agency. Towards Hydrogen Definitions Based on their Emissions Intensity. OECD Publishing, 2023. DOI: 10.1787/44618fd1-en.

[64] Otto Machhammer, Andreas Bode, and Wolfgang Hormuth. “Financial and Ecological Evaluation of Hydrogen Production Processes on Large Scale”. In: Chemical Engineering & Technology 39.6 (2016), pp. 1185–1193. ISSN: 1521-4125. DOI: 10.1002/ceat.201600023.

[65] Karina Anaya, Abayomi Olufemi Oni, and Amit Kumar. “Investigating the techno-economic and environmental performance of chemical looping technology for hydrogen production”. In: Sustainable Energy Technologies and Assessments 56 (2023), p. 103008. ISSN: 2213-1388. DOI: 10.1016/j.seta.2022.103008.

[66] A. O. Oni et al. “Comparative assessment of blue hydrogen from steam methane reforming, autothermal reforming, and natural gas decomposition technologies for natural gas-producing regions”. In: Energy Conversion and Management 254 (2022), p. 115245. ISSN: 0196-8904. DOI: 10.1016/j.enconman.2022.115245.

[67] Jiaquan Li et al. “The carbon footprint and cost of coal-based hydrogen production with and without carbon capture and storage technology in China”. In: Journal of Cleaner Production 362 (2022), p. 132514. ISSN: 0959-6526. DOI: 10.1016/j.jclepro.2022.132514.

[68] Hydrogen - FutureCoal. 2023. URL: https://www.futurecoal.org/sustainable-coal/hydrogen/.

[69] Rami S. El-Emam and Hasan Özcan. “Comprehensive review on the techno-economics of sustainable large-scale clean hydrogen production”. In: Journal of Cleaner Production 220 (2019), pp. 593–609. ISSN: 0959-6526. DOI: 10.1016/j.jclepro.2019.01.309.

[70] Changming Gong et al. “Evaluation on combustion and lean-burn limit of a medium compression ratio hydrogen/methanol dual-injection spark-ignition engine under methanol late-injection”. In: Applied Energy 277 (2020), p. 115622. ISSN: 0306-2619. DOI: 10.1016/j.apenergy.2020.115622.

[71] Caneon Kurien and Mayank Mittal. “Review on the production and utilization of green ammonia as an alternate fuel in dual-fuel compression ignition engines”. In: Energy Conversion and Management 251 (2022), p. 114990. ISSN: 0196-8904. DOI: 10.1016/j.enconman.2021.114990.

[72] Hamed Chehrmonavari et al. “Hybridizing solid oxide fuel cells with internal combustion engines for power and propulsion systems: A review”. In: Renewable and Sustainable Energy Reviews 171 (2023), p. 112982. ISSN: 1364-0321. DOI: 10.1016/j.rser.2022.112982.

[73] Dong Hyup Jeon. “Computational fluid dynamics simulation of anode-supported solid oxide fuel cells with implementing complete overpotential model”. In: Energy 188 (2019), p. 116050. ISSN: 0360-5442. DOI: 10.1016/j.energy.2019.116050.

[74] Bahram Ghorbani et al. “An innovative hybrid structure of solar PV-driven air separation unit, molten carbonate fuel cell, and absorption–compression refrigeration system (Process development and exergy analysis)”. In: Energy Reports 7 (2021), pp. 8960–8972. ISSN: 2352-4847. DOI: 10.1016/j.egyr.2021.10.108.

[75] Yuncheng Lan et al. “Waste heat recovery from exhausted gas of a proton exchange membrane fuel cell to produce hydrogen using thermoelectric generator”. In: Applied Energy 334 (2023), p. 120687. ISSN: 0306-2619. DOI: 10.1016/j.apenergy.2023.120687.

[76] Rimika Kapoor et al. “Advances in biogas valorization and utilization systems: A comprehensive review”. In: Journal of Cleaner Production 273 (2020), p. 123052. ISSN: 0959-6526. DOI: 10.1016/j.jclepro.2020.123052.

[77] K. Andreas Friedrich et al. “Applications”. In: Hydrogen as a Future Energy Carrier. John Wiley & Sons, Ltd, 2008, pp. 335–414. ISBN: 978-3-527-62289-4. DOI: 10.1002/9783527622894.ch8.

[78] Mohammad Ali Abdelkareem et al. “On the technical challenges affecting the performance of direct internal reforming biogas solid oxide fuel cells”. In: Renewable and Sustainable Energy Reviews 101 (2019), pp. 361–375. ISSN: 1364-0321. DOI: 10.1016/j.rser.2018.10.025.

[79] M. Z. Jacobson, W. G. Colella, and D. M. Golden. “Cleaning the Air and Improving Health with Hydrogen Fuel-Cell Vehicles”. In: Science 308.5730 (2005), pp. 1901–1905. DOI: 10.1126/science.1109157.

[80] Manfred Klell. “Storage of Hydrogen in the Pure Form”. In: Handbook of Hydrogen Storage. John Wiley & Sons, Ltd, 2010, pp. 1–37. ISBN: 978-3-527-62980-0. DOI: 10.1002/9783527629800.ch1.

[81] Ying Su et al. “Review of the Hydrogen Permeability of the Liner Material of Type IV On-Board Hydrogen Storage Tank”. In: World Electric Vehicle Journal 12.3 (2021), p. 130. ISSN: 2032-6653. DOI: 10.3390/wevj12030130.

[82] Enyinnaya Ohaeri, Ubong Eduok, and Jerzy Szpunar. “Hydrogen related degradation in pipeline steel: A review”. In: International Journal of Hydrogen Energy 43.31 (2018), pp. 14584–14617. ISSN: 0360-3199. DOI: 10.1016/j.ijhydene.2018.06.064.

[83] Elena Galitskaya and Oleg Zhdaneev. “Development of electrolysis technologies for hydrogen production: A case study of green steel manufacturing in the Russian Federation”. In: Environmental Technology & Innovation 27 (2022), p. 102517. ISSN: 2352-1864. DOI: 10.1016/j.eti.2022.102517.

[84] Abdullah Emre Yüzbaşıoğlu, Cemre Avşar, and Ahmet Ozan Gezerman. “The current situation in the use of ammonia as a sustainable energy source and its industrial potential”. In: Current Research in Green and Sustainable Chemistry 5 (2022), p. 100307. ISSN: 2666-0865. DOI: 10.1016/j.crgsc.2022.100307.

[85] Stefano Sollai et al. “Renewable methanol production from green hydrogen and captured CO2: A techno-economic assessment”. In: Journal of CO2 Utilization 68 (2023), p. 102345. ISSN: 2212-9820. DOI: 10.1016/j.jcou.2022.102345.

[86] Susan van Dyk et al. “Production of lower carbon-intensity fuels by co-processing biogenic feedstocks: Potential and challenges for refineries”. In: Fuel 324 (2022), p. 124636. ISSN: 0016-2361. DOI: 10.1016/j.fuel.2022.124636.

[87] Xue Wan et al. “Conversion of agricultural and forestry biomass into bioethanol, water-soluble polysaccharides, and lignin nanoparticles by an integrated phosphoric acid plus hydrogen peroxide process”. In: Industrial Crops and Products 191 (2023), p. 115969. ISSN: 0926-6690. DOI: 10.1016/j.indcrop.2022.115969.

[88] Ahmed M. Elgarahy et al. “Hydrogen production from wastewater, storage, economy, governance and applications: a review”. In: Environmental Chemistry Letters 20.6 (2022), pp. 3453–3504. ISSN: 1610-3661. DOI: 10.1007/s10311-022-01480-3.

[89] Susan van Dyk et al. “Potential synergies of drop-in biofuel production with further co-processing at oil refineries”. In: Biofuels, Bioproducts and Biorefining 13.3 (2019), pp. 760–775. ISSN: 1932-1031. DOI: 10.1002/bbb.1974.

[90] Elham Abohamzeh et al. “Review of hydrogen safety during storage, transmission, and applications processes”. In: Journal of Loss Prevention in the Process Industries 72 (2021), p. 104569. ISSN: 0950-4230. DOI: 10.1016/j.jlp.2021.104569.

[91] Bernard Chukwudi Tashie-Lewis and Somtochukwu Godfrey Nnabuife. “Hydrogen Production, Distribution, Storage and Power Conversion in a Hydrogen Economy - A Technology Review”. In: Chemical Engineering Journal Advances 8 (2021), p. 100172. ISSN: 2666-8211. DOI: 10.1016/j.ceja.2021.100172.

[92] J. O. Abe et al. “Hydrogen energy, economy and storage: Review and recommendation”. In: International Journal of Hydrogen Energy 44.29 (2019), pp. 15072–15086. ISSN: 0360-3199. DOI: 10.1016/j.ijhydene.2019.04.068.

[93] G. Principi et al. “The problem of solid state hydrogen storage”. In: Energy 34.12 (2009), pp. 2087–2091. ISSN: 0360-5442. DOI: 10.1016/j.energy.2008.08.027.

[94] Ulrich Eberle, Michael Felderhoff, and Ferdi Schüth. “Chemical and Physical Solutions for Hydrogen Storage”. In: Angewandte Chemie International Edition 48.36 (2009), pp. 6608–6630. ISSN: 1521-3773. DOI: 10.1002/anie.200806293.

[95] Voiture hydrogène - Liste des modèles commercialisés et à venir. URL: https://www.h2-mobile.fr/vehicules/voiture-hydrogene/ (visited on 04/24/2024).

[96] Akira Yamashita et al. Development of High-Pressure Hydrogen Storage System for the Toyota “Mirai”. 2015-01-1169. Warrendale, PA: SAE International, 2015. DOI: 10.4271/2015-01-1169.

[97] Hydrogène | Encyclopédie des gaz Air Liquide. URL: https://encyclopedia.airliquide.com/fr/hydrogene#the-molecule (visited on 04/24/2024).

[98] Rittmar von Helmolt and Ulrich Eberle. “Fuel cell vehicles: Status 2007”. In: Journal of Power Sources. IBA – HBC 2006 165.2 (2007), pp. 833–843. ISSN: 0378-7753. DOI: 10.1016/j.jpowsour.2006.12.073.

[99] Hans J. Pasman and William J. Rogers. “Risk assessment by means of Bayesian networks: A comparative study of compressed and liquefied H2 transportation and tank station risks”. In: International Journal of Hydrogen Energy. HySafe 1 37.22 (2012), pp. 17415–17425. ISSN: 0360-3199. DOI: 10.1016/j.ijhydene.2012.04.051.

[100] Steffen Maus et al. “Filling procedure for vehicles with compressed hydrogen tanks”. In: International Journal of Hydrogen Energy 33.17 (2008), pp. 4612–4621. ISSN: 0360-3199. DOI: 10.1016/j.ijhydene.2008.06.052.

[101] Otto Pesonen and Tuomas Alakunnas. Energy Storage : A Missing Piece of the Puzzle for the Self-Sufficient Living. 2017. URL: http://www.theseus.fi/handle/10024/136086.

[102] Neda Hassannayebi et al. “Underground hydrogen storage: application of geochemical modelling in a case study in the Molasse Basin, Upper Austria”. In: Environmental Earth Sciences 78.5 (2019), p. 177. ISSN: 1866-6299. DOI: 10.1007/s12665-019-8184-5.

[103] Tianji Peng et al. “Choice of hydrogen energy storage in salt caverns and horizontal cavern construction technology”. In: Journal of Energy Storage 60 (2023), p. 106489. ISSN: 2352-152X. DOI: 10.1016/j.est.2022.106489.

[104] Commissariat général au développement. Bilan énergétique de la France. Chiffres clés de l’énergie - Édition 2021. URL: https://www.statistiques.developpement-durable.gouv.fr/edition-numerique/chiffres-cles-energie-2021/6-bilan-energetique-de-la-france.php.

[105] Nikolaos Diamantakis et al. “A review of analogue case studies relevant to large-scale underground hydrogen storage”. In: Energy Reports 11 (2024), pp. 2374–2400. ISSN: 2352-4847. DOI: 10.1016/j.egyr.2024.02.002.

[106] Can You Store CO_2 in a Salt Cavern? Lonquist & Co. LLC. 2023. URL: https://www.lonquist.com/salt-cavern-resources/2023/can-you-store-co2-in-salt-cavern.

[107] Muhammad R. Usman. “Hydrogen storage methods: Review and current status”. In: Renewable and Sustainable Energy Reviews 167 (2022), p. 112743. ISSN: 1364-0321. DOI: 10.1016/j.rser.2022.112743.

[108] Michael Hirscher et al. “Materials for hydrogen-based energy storage – past, recent progress and future outlook”. In: Journal of Alloys and Compounds 827 (2020), p. 153548. ISSN: 0925-8388. DOI: 10.1016/j.jallcom.2019.153548.

[109] Weiqiang Xu, Qianqian Li, and Minjie Huang. “Design and analysis of liquid hydrogen storage tank for high-altitude long-endurance remotely-operated aircraft”. In: International Journal of Hydrogen Energy 40.46 (2015), pp. 16578–16586. ISSN: 0360-3199. DOI: 10.1016/j.ijhydene.2015.09.028.

[110] Majid Aasadnia and Mehdi Mehrpooya. “Large-scale liquid hydrogen production methods and approaches: A review”. In: Applied Energy 212 (2018), pp. 57–83. ISSN: 0306-2619. DOI: 10.1016/j.apenergy.2017.12.033.

[111] Talal Yusaf et al. “Sustainable hydrogen energy in aviation – A narrative review”. In: International Journal of Hydrogen Energy 52 (2024), pp. 1026–1045. ISSN: 0360-3199. DOI: 10.1016/j.ijhydene.2023.02.086.

[112] G. D. Brewer. “The prospects for liquid hydrogen fueled aircraft”. In: International Journal of Hydrogen Energy 7.1 (1982), pp. 21–41. ISSN: 0360-3199. DOI: 10.1016/0360-3199(82)90205-1.

[113] Airbus reveals hydrogen-powered zero-emission engine | Airbus. 2022. URL: https://www.airbus.com/en/newsroom/press-releases/2022-11-airbus-reveals-hydrogen-powered-zero-emission-engine.

[114] David I. Barton, Cesare A. Hall, and Matthew K. Oldfield. “Design of a Hydrogen Aircraft for Zero Persistent Contrails”. In: Aerospace 10.8 (2023), p. 688. ISSN: 2226-4310. DOI: 10.3390/aerospace10080688.

[115] “Hydrogen production and storage: R & D priorities and gaps”. In: (2006). URL: https://www.osti.gov/etdeweb/biblio/20712341.

[116] Abdalla M. Abdalla et al. “Hydrogen production, storage, transportation and key challenges with applications: A review”. In: Energy Conversion and Management 165 (2018), pp. 602–627. ISSN: 0196-8904. DOI: 10.1016/j.enconman.2018.03.088.

[117] H. Barthelemy, M. Weber, and F. Barbier. “Hydrogen storage: Recent improvements and industrial perspectives”. In: International Journal of Hydrogen Energy. Special issue on The 6th International Conference on Hydrogen Safety (ICHS 2015), 19-21 October 2015, Yokohama, Japan 42.11 (2017), pp. 7254–7262. ISSN: 0360-3199. DOI: 10.1016/j.ijhydene.2016.03.178.

[118] R. K. Ahluwalia et al. “Supercritical cryo-compressed hydrogen storage for fuel cell electric buses”. In: International Journal of Hydrogen Energy 43.22 (2018), pp. 10215–10231. ISSN: 0360-3199. DOI: 10.1016/j.ijhydene.2018.04.113.

[119] B. P. Tarasov, M. V. Lototskii, and V. A. Yartys’. “Problem of hydrogen storage and prospective uses of hydrides for hydrogen accumulation”. In: Russian Journal of General Chemistry 77.4 (2007), pp. 694–711. DOI: 10.1134/S1070363207040329.

[120] Ramin Moradi and Katrina M. Groth. “Hydrogen storage and delivery: Review of the state of the art technologies and risk and reliability analysis”. In: International Journal of Hydrogen Energy 44.23 (2019), pp. 12254–12269. ISSN: 0360-3199. DOI: 10.1016/j.ijhydene.2019.03.041.

[121] Storage: a major hurdle for the hydrogen industry. Polytechnique Insights. URL: https://www.polytechnique-insights.com/en/braincamps/energy/sustainable-hydrogen-still-a-long-way-to-go/storage-a-major-hurdle-for-the-hydrogen-industry/ (visited on 05/01/2024).

[122] Liang Wu et al. “Hierarchically structured porous materials: synthesis strategies and applications in energy storage”. In: National Science Review 7.11 (2020), pp. 1667–1701. DOI: 10.1093/nsr/nwaa183.

[123] Chang Liu et al. “Hydrogen storage in carbon nanotubes revisited”. In: Carbon 48.2 (2010), pp. 452–455. ISSN: 0008-6223. DOI: 10.1016/j.carbon.2009.09.060.

[124] Li Zhou, Yaping Zhou, and Yan Sun. “Enhanced storage of hydrogen at the temperature of liquid nitrogen”. In: International Journal of Hydrogen Energy 29.3 (2004), pp. 319–322. ISSN: 0360-3199. DOI: 10.1016/S0360-3199(03)00155-1.

[125] W. Zhao et al. “Impact of synthesis conditions of KOH activated carbons on their hydrogen storage capacities”. In: International Journal of Hydrogen Energy 37.19 (2012), pp. 14278–14284. ISSN: 0360-3199. DOI: 10.1016/j.ijhydene.2012.06.110.

[126] P. Chen et al. “High H2 Uptake by Alkali-Doped Carbon Nanotubes Under Ambient Pressure and Moderate Temperatures”. In: Science 285.5424 (1999), pp. 91–93. DOI: 10.1126/science.285.5424.91.

[127] Gary G Tibbetts, Gregory P Meisner, and Charles H Olk. “Hydrogen storage capacity of carbon nanotubes, filaments, and vapor-grown fibers”. In: Carbon 39.15 (2001), pp. 2291–2301. ISSN: 0008-6223. DOI: 10.1016/S0008-6223(01)00051-3.

[128] C. Liu et al. “Hydrogen Storage in Single-Walled Carbon Nanotubes at Room Temperature”. In: Science 286.5442 (1999), pp. 1127–1129. DOI: 10.1126/science.286.5442.1127.

[129] Barbara Panella and Michael Hirscher. “Physisorption in Porous Materials”. In: Handbook of Hydrogen Storage. John Wiley & Sons, Ltd, 2010, pp. 39–62. ISBN: 978-3-527-62980-0. DOI: 10.1002/9783527629800.ch2.

[130] Dan Fraenkel and Joseph Shabtai. “Encapsulation of hydrogen in molecular sieve zeolites”. In: Journal of the American Chemical Society 99.21 (1977), pp. 7074–7076. ISSN: 0002-7863. DOI: 10.1021/ja00463a058.

[131] J. Weitkamp, M. Fritz, and S. Ernst. “Zeolites as media for hydrogen storage”. In: International Journal of Hydrogen Energy 20.12 (1995), pp. 967–970. ISSN: 0360-3199. DOI: 10.1016/0360-3199(95)00058-L.

[132] H. W. Langmi et al. “Hydrogen storage in ion-exchanged zeolites”. In: Journal of Alloys and Compounds 404-406 (2005), pp. 637–642. ISSN: 0925-8388. DOI: 10.1016/j.jallcom.2004.12.193.

[133] Jenny G. Vitillo et al. “Theoretical maximal storage of hydrogen in zeolitic frameworks”. In: Physical Chemistry Chemical Physics 7.23 (2005), pp. 3948–3954. ISSN: 1463-9084. DOI: 10.1039/B510989B.

[134] D. Ramimoghadam, E. MacA Gray, and C. J. Webb. “Review of polymers of intrinsic microporosity for hydrogen storage applications”. In: International Journal of Hydrogen Energy 41.38 (2016), pp. 16944–16965. ISSN: 0360-3199. DOI: 10.1016/j.ijhydene.2016.07.134.

[135] Neil B. McKeown et al. “Towards Polymer-Based Hydrogen Storage Materials: Engineering Ultramicroporous Cavities within Polymers of Intrinsic Microporosity”. In: Angewandte Chemie International Edition 45.11 (2006), pp. 1804–1807. DOI: 10.1002/anie.200504241.

[136] Mi Tian et al. “Nanoporous polymer-based composites for enhanced hydrogen storage”. In: Adsorption 25.4 (2019), pp. 889–901. ISSN: 1572-8757. DOI: 10.1007/s10450-019-00065-x.

[137] David J. Collins and Hong-Cai Zhou. “Hydrogen storage in metal–organic frameworks”. In: Journal of Materials Chemistry 17.30 (2007), pp. 3154–3160. ISSN: 1364-5501. DOI: 10.1039/B702858J.

[138] Hong-Cai Zhou, Jeffrey R. Long, and Omar M. Yaghi. “Introduction to Metal–Organic Frameworks”. In: Chemical Reviews 112.2 (2012), pp. 673–674. ISSN: 0009-2665. DOI: 10.1021/cr300014x.

[139] Ronny Grünker et al. “A new metal–organic framework with ultra-high surface area”. In: Chemical Communications 50.26 (2014), pp. 3450–3452. ISSN: 1364-548X. DOI: 10.1039/C4CC00113C.

[140] Zhijie Chen et al. “Balancing volumetric and gravimetric uptake in highly porous materials for clean energy”. In: Science 368.6488 (2020), pp. 297–303. DOI: 10.1126/science.aaz8881.

[141] Henrietta W. Langmi et al. “Hydrogen Storage in Metal-Organic Frameworks: A Review”. In: Electrochimica Acta 128 (2014), pp. 368–392. ISSN: 0013-4686. DOI: 10.1016/j.electacta.2013.10.190.

[142] E. Dendy Sloan. “Fundamental principles and applications of natural gas hydrates”. In: Nature 426.6964 (2003), pp. 353–359. ISSN: 1476-4687. DOI: 10.1038/nature02135.

[143] Wendy L. Mao and Ho-kwang Mao. “Hydrogen storage in molecular compounds”. In: Proceedings of the National Academy of Sciences 101.3 (2004), pp. 708–710. DOI: 10.1073/pnas.0307449100.

[144] Viktor V. Struzhkin et al. “Hydrogen storage in molecular clathrates”. In: Chemical Reviews 107.10 (2007), pp. 4133–4151. ISSN: 0009-2665. DOI: 10.1021/cr050183d.

[145] Huen Lee et al. “Tuning clathrate hydrates for hydrogen storage”. In: Nature 434.7034 (2005), pp. 743–746. DOI: 10.1038/nature03457.

[146] Kasper T. Møller et al. “Hydrogen - A sustainable energy carrier”. In: Progress in Natural Science: Materials International 27.1 (2017), pp. 34–40. ISSN: 1002-0071. DOI: 10.1016/j.pnsc.2016.12.014.

[147] Jason Graetz. “New approaches to hydrogen storage”. In: Chemical Society Reviews 38.1 (2008), pp. 73–82. ISSN: 1460-4744. DOI: 10.1039/B718842K.

[148] Z Dehouche et al. “Influence of cycling on the thermodynamic and structure properties of nanocrystalline magnesium based hydride”. In: Journal of Alloys and Compounds 305.1 (2000), pp. 264–271. ISSN: 0925-8388. DOI: 10.1016/S0925-8388(00)00718-0.

[149] Jianwei Ren et al. “Current research trends and perspectives on materials-based hydrogen storage solutions: A critical review”. In: International Journal of Hydrogen Energy 42.1 (2017), pp. 289–311. ISSN: 0360-3199. DOI: 10.1016/j.ijhydene.2016.11.195.

[150] Joseph Bloch and Moshe H Mintz. “Kinetics and mechanisms of metal hydrides formation—a review”. In: Journal of Alloys and Compounds 253-254 (1997), pp. 529–541. ISSN: 0925-8388. DOI: 10.1016/S0925-8388(96)03070-8.

[151] A. Züttel et al. “$LiBH_2$ a new hydrogen storage material”. In: Journal of Power Sources 118.1 (2003), pp. 1–7. ISSN: 0378-7753. DOI: 10.1016/S0378-7753(03)00054-5.

[152] A Zaluska, L Zaluski, and J. O Ström–Olsen. “Nanocrystalline magnesium for hydrogen storage”. In: Journal of Alloys and Compounds 288.1 (1999), pp. 217–225. ISSN: 0925-8388. DOI: 10.1016/S0925-8388(99)00073-0.

[153] I. P. Jain, Chhagan Lal, and Ankur Jain. “Hydrogen storage in Mg: A most promising material”. In: International Journal of Hydrogen Energy 35.10 (2010), pp. 5133–5144. ISSN: 0360-3199. DOI: 10.1016/j.ijhydene.2009.08.088.

[154] Louis Schlapbach and Andreas Züttel. “Hydrogen-storage materials for mobile applications”. In: Nature 414.6861 (2001), pp. 353–358. ISSN: 1476-4687. DOI: 10.1038/35104634.

[155] Maximilian Fichtner. “Properties of nanoscale metal hydrides”. In: Nanotechnology 20.20 (2009), p. 204009. ISSN: 0957-4484. DOI: 10.1088/0957-4484/20/20/204009.

[156] G. Liang et al. “Catalytic effect of transition metals on hydrogen sorption in nanocrystalline ball milled MgH2–Tm (Tm=Ti, V, Mn, Fe and Ni) systems”. In: Journal of Alloys and Compounds 292.1 (1999), pp. 247–252. DOI: 10.1016/S0925-8388(99)00442-9.

[157] Ying Wang and Yijing Wang. “Recent advances in additive-enhanced magnesium hydride for hydrogen storage”. In: Progress in Natural Science: Materials International 27.1 (2017), pp. 41–49. ISSN: 1002-0071. DOI: 10.1016/j.pnsc.2016.12.016.

[158] Zhirong Zhao-Karger et al. “Altered thermodynamic and kinetic properties of MgH2 infiltrated in microporous scaffold”. In: Chemical Communications 46.44 (2010), pp. 8353–8355. DOI: 10.1039/C0CC03072D.

[159] Jingzhu Li et al. “Kinetics of isothermal hydrogenation of magnesium with TiH2 additive”. In: International Journal of Hydrogen Energy 39.14 (2014), pp. 7373–7381. ISSN: 0360-3199. DOI: 10.1016/j.ijhydene.2014.02.159.

[160] Erika Michela Dematteis et al. “Hydrogen storage in complex hydrides: past activities and new trends”. In: Progress in Energy 4.3 (2022), p. 032009. DOI: 10.1088/2516-1083/ac7499.

[161] Hiroyuki Saitoh et al. “Hydrogen storage by earth-abundant metals, synthesis and characterization of Al3FeH3.9”. In: Materials & Design 208 (2021), p. 109953. DOI: 10.1016/j.matdes.2021.109953.

[162] N. A. A. Rusman and M. Dahari. “A review on the current progress of metal hydrides material for solid-state hydrogen storage applications”. In: International Journal of Hydrogen Energy 41.28 (2016), pp. 12108–12126. ISSN: 0360-3199. DOI: 10.1016/j.ijhydene.2016.05.244.

[163] Boris P. Tarasov et al. “Metal hydride hydrogen storage and compression systems for energy storage technologies”. In: International Journal of Hydrogen Energy 46.25 (2021), pp. 13647–13657. DOI: 10.1016/j.ijhydene.2020.07.085.

[164] C. Milanese et al. “Complex hydrides for energy storage”. In: International Journal of Hydrogen Energy 44.15 (2019), pp. 7860–7874. ISSN: 0360-3199. DOI: 10.1016/j.ijhydene.2018.11.208.

[165] Li Zhou. “Progress and problems in hydrogen storage methods”. In: Renewable and Sustainable Energy Reviews 9.4 (2005), pp. 395–408. DOI: 10.1016/j.rser.2004.05.005.

[166] Borislav Bogdanović, Michael Felderhoff, and Guido Streukens. “Hydrogen storage in complex metal hydrides”. In: Journal of the Serbian Chemical Society 74.2 (2009), pp. 183–196.

[167] E. C. Ashby and P. Kobetz. “The Direct Synthesis of Na3AlH6”. In: Inorganic Chemistry 5.9 (1966), pp. 1615–1617. DOI: 10.1021/ic50043a034.

[168] Prabhukhot Prachi R, Wagh Mahesh M, and Gangal Aneesh C. “A Review on Solid State Hydrogen Storage Material”. In: Advances in Energy and Power 4.2 (2016), pp. 11–22. DOI: 10.13189/aep.2016.040202.

[169] Billur Sakintuna, Farida Lamari-Darkrim, and Michael Hirscher. “Metal hydride materials for solid hydrogen storage: A review”. In: International Journal of Hydrogen Energy 32.9 (2007), pp. 1121–1140. ISSN: 0360-3199. DOI: 10.1016/j.ijhydene.2006.11.022.

[170] Huai-Jun Lin et al. “Understanding the Decomposition Mechanisms of LiNH2, Mg(NH2)2, and NaNH2: A Joint Experimental and Theoretical Study”. In: The Journal of Physical Chemistry C 123.30 (2019), pp. 18180–18186. DOI: 10.1021/acs.jpcc.9b03524.

[171] Ping Chen et al. “Metal–N–H systems for the hydrogen storage”. In: Scripta Materialia 56.10 (2007), pp. 817–822. DOI: 10.1016/j.scriptamat.2007.01.001.

[172] N. A. Ali, N. A. Sazelee, and M. Ismail. “An overview of reactive hydride composite (RHC) for solid-state hydrogen storage materials”. In: International Journal of Hydrogen Energy 46.62 (2021), pp. 31674–31698. DOI: 10.1016/j.ijhydene.2021.07.058.

[173] Shin-ichi Orimo et al. “Complex Hydrides for Hydrogen Storage”. In: Chemical Reviews 107.10 (2007), pp. 4111–4132. DOI: 10.1021/cr0501846.

[174] William I. F. David et al. “A Mechanism for Non-stoichiometry in the Lithium Amide/Lithium Imide Hydrogen Storage Reaction”. In: Journal of the American Chemical Society 129.6 (2007), pp. 1594–1601. ISSN: 0002-7863. DOI: 10.1021/ja066016s.

[175] Ping Chen et al. “Interaction between Lithium Amide and Lithium Hydride”. In: The Journal of Physical Chemistry B 107.39 (2003), pp. 10967–10970. DOI: 10.1021/jp034149j.

[176] Yun Hang Hu and Eli Ruckenstein. “Ultrafast Reaction between LiH and NH3 during H2 Storage in Li3N”. In: The Journal of Physical Chemistry A 107.46 (2003), pp. 9737–9739. DOI: 10.1021/jp036257b.

[177] Takayuki Ichikawa et al. “Lithium nitride for reversible hydrogen storage”. In: Journal of Alloys and Compounds 365.1 (2004), pp. 271–276. ISSN: 0925-8388. DOI: 10.1016/S0925-8388(03)00637-6.

[178] Shingo Ikeda, Nobuhiro Kuriyama, and Tetsu Kiyobayashi. “Simultaneous determination of ammonia emission and hydrogen capacity variation during the cyclic testing for LiNH2–LiH hydrogen storage system”. In: International Journal of Hydrogen Energy 33.21 (2008), pp. 6201–6204. DOI: 10.1016/j.ijhydene.2008.08.003.

[179] Zhang-Hui Lu and Qiang Xu. “Recent progress in boron- and nitrogen-based chemical hydrogen storage”. In: Functional Materials Letters 05.1 (2012), p. 1230001. ISSN: 1793-6047. DOI: 10.1142/S1793604712300010.

[180] Weifang Luo. “($LiNH_2$–MgH_2): a viable hydrogen storage system”. In: Journal of Alloys and Compounds 381.1 (2004), pp. 284–287. DOI: 10.1016/j.jallcom.2004.03.119.

[181] Zhitao Xiong et al. “Thermodynamic and kinetic investigations of the hydrogen storage in the Li–Mg–N–H system”. In: Journal of Alloys and Compounds 398.1 (2005), pp. 235–239. DOI: 10.1016/j.jallcom.2005.02.010.

[182] Charles W. Hamilton et al. “B–N compounds for chemical hydrogen storage”. In: Chemical Society Reviews 38.1 (2008), pp. 279–293. ISSN: 1460-4744. DOI: 10.1039/B800312M.

[183] Serdar Akbayrak and Saim Özkar. “Ammonia borane as hydrogen storage materials”. In: International Journal of Hydrogen Energy 43.40 (2018), pp. 18592–18606. ISSN: 0360-3199. DOI: 10.1016/j.ijhydene.2018.02.190.

[184] Miriam Rueda, Luis Miguel Sanz-Moral, and Ángel Martín. “Innovative methods to enhance the properties of solid hydrogen storage materials based on hydrides through nanoconfinement: A review”. In: The Journal of Supercritical Fluids 141 (2018), pp. 198–217. ISSN: 0896-8446. DOI: 10.1016/j.supflu.2018.02.010.

[185] F Baitalow et al. “Thermal decomposition of B–N–H compounds investigated by using combined thermoanalytical methods”. In: Thermochimica Acta 391.1 (2002), pp. 159–168. ISSN: 0040-6031. DOI: 10.1016/S0040-6031(02)00173-9.

[186] V. V Khvostov et al. “Surface modification of boron nitride in hydrogen plasma”. In: Applied Surface Science 157.3 (2000), pp. 178–184. ISSN: 0169-4332. DOI: 10.1016/S0169-4332(99)00569-3.

[187] I. A. Hassan et al. “Hydrogen storage technologies for stationary and mobile applications: Review, analysis and perspectives”. In: Renewable and Sustainable Energy Reviews 149 (2021), p. 111311. DOI: 10.1016/j.rser.2021.111311.

[188] Xiaowei Chen et al. “Nitrogen-containing carbon nanostructures: A promising carrier for catalysis of ammonia borane dehydrogenation”. In: Carbon 68 (2014), pp. 462–472. DOI: 10.1016/j.carbon.2013.11.022.

[189] Teng He, Qijun Pei, and Ping Chen. “Liquid organic hydrogen carriers”. In: Journal of Energy Chemistry 24.5 (2015), pp. 587–594. DOI: 10.1016/j.jechem.2015.08.007.

[190] Purna Chandra Rao and Minyoung Yoon. “Potential Liquid-Organic Hydrogen Carrier (LOHC) Systems: A Review on Recent Progress”. In: Energies 13.22 (2020), p. 6040. DOI: 10.3390/en13226040.

[191] Patrick Preuster, Christian Papp, and Peter Wasserscheid. “Liquid Organic Hydrogen Carriers (LOHCs): Toward a Hydrogen-free Hydrogen Economy”. In: Accounts of Chemical Research 50.1 (2017), pp. 74–85. DOI: 10.1021/acs.accounts.6b00474.

[192] Patrice Perreault et al. “Critical challenges towards the commercial rollouts of a LOHC-based H2 economy”. In: Current Opinion in Green and Sustainable Chemistry 41 (June 1, 2023), p. 100836. ISSN: 2452-2236. DOI: 10.1016/j.cogsc.2023.100836. URL: https://www.sciencedirect.com/science/article/pii/S2452223623000858 (visited on 05/07/2024).

[193] Muhammad R. Usman and David L. Cresswell. “Options for on-Board Use of Hydrogen Based on the Methylcyclohexane–Toluene–Hydrogen System”. In: International Journal of Green Energy 10.2 (2013), pp. 177–189. DOI: 10.1080/15435075.2011.647168.

[194] Sergey P. Verevkin et al. “Energetics of LOHC: Structure-Property Relationships from Network of Thermochemical Experiments and in Silico Methods”. In: Hydrogen 2.1 (2021), pp. 101–121. DOI: 10.3390/hydrogen2010006.

[195] Phillimon M. Modisha et al. “The Prospect of Hydrogen Storage Using Liquid Organic Hydrogen Carriers”. In: Energy & Fuels 33.4 (2019), pp. 2778–2796. DOI: 10.1021/acs.energyfuels.9b00296.

[196] Zainul Abdin et al. “Large-scale stationary hydrogen storage via liquid organic hydrogen carriers”. In: iScience 24.9 (2021), p. 102966. DOI: 10.1016/j.isci.2021.102966.

[197] Matthias Niermann et al. “Liquid Organic Hydrogen Carrier (LOHC) – Assessment based on chemical and economic properties”. In: International Journal of Hydrogen Energy 44.13 (2019), pp. 6631–6654. DOI: 10.1016/j.ijhydene.2019.01.199.

[198] Suhas G. Jadhav et al. “Catalytic carbon dioxide hydrogenation to methanol: A review of recent studies”. In: Chemical Engineering Research and Design 92.11 (Nov. 1, 2014), pp. 2557–2567. DOI: 10.1016/j.cherd.2014.03.005.

[199] Sandra Sá et al. “Catalysts for methanol steam reforming—A review”. In: Applied Catalysis B: Environmental 99.1 (2010), pp. 43–57. DOI: 10.1016/j.apcatb.2010.06.015.

[200] Michael C. Adams et al. “Stability of methanol, propanol, and SF6 as high-temperature tracers”. In: Proceedings of the World Geothermal Congress 2000. Kyushu - Tohoku, Japan, 2000. URL: https://www.geothermal-energy.org/pdf/IGAstandard/WGC/2000/R0010.PDF.

[201] C. Zhang et al. “Study of Catalysts for Hydrogen Production by the High Temperature Steam Reforming of Methanol”. In: Fuel Cells 6.6 (2006), pp. 466–471. DOI: 10.1002/fuce.200600010.

[202] Changsoo Kim et al. “Implementation of Formic Acid as a Liquid Organic Hydrogen Carrier (LOHC): Techno-Economic Analysis and Life Cycle Assessment of Formic Acid Produced via CO_2 Utilization”. In: Catalysts 12.10 (2022), p. 1113. DOI: 10.3390/catal12101113.

[203] Yuta Maenaka, Tomoyoshi Suenobu, and Shunichi Fukuzumi. “Catalytic interconversion between hydrogen and formic acid at ambient temperature and pressure”. In: Energy & Environmental Science 5.6 (2012), pp. 7360–7367. DOI: 10.1039/C2EE03315A.

[204] Hanen Abdelli et al. “H2 production from formic acid over highly stable and efficient Cu-Fe-O spinel based photocatalysts under flow, visible-light and at room temperature conditions”. In: Applied Materials Today 31 (2023), p. 101771. DOI: 10.1016/j.apmt.2023.101771.

[205] Elvira Spatolisano and Laura A. Pellegrini. “Haber-Bosch process intensification: A first step towards small-scale distributed ammonia production”. In: Chemical Engineering Research and Design 195 (2023), pp. 651–661.

[206] Ammoniac. Techniques de l’Ingénieur. URL: https://www.techniques-ingenieur.fr/base-documentaire/procedes-chimie-bio-agro-th2/fabrication-des-grands-produits-industriels-en-chimie-et-petrochimie-42319210/ammoniac-j6135/ (visited on 05/13/2024).

[207] Project Hafnium. NTU. URL: https://ebook.ntu.edu.sg/project-hafnium.html (visited on 05/29/2024).

[208] The Royal society. Ammonia: zero-carbon fertiliser, fuel and energy store. 2020. ISBN: 978-1-78252-448-9. URL: https://royalsociety.org/-/media/policy/projects/green-ammonia/green-ammonia-policy-briefing.pdf.

[209] O. Elishav et al. “Chapter 5 - Storage and Distribution of Ammonia”. In: Techno-Economic Challenges of Green Ammonia as an Energy Vector. Ed. by Agustin Valera-Medina and Rene Banares-Alcantara. Academic Press, 2021, pp. 85–103. DOI: 10.1016/B978-0-12-820560-0.00005-9.

[210] Global Hydrogen Trade to Meet the 1.5°C Climate Goal: Part II. 2022. URL: https://www.irena.org/publications/2022/Apr/Global-hydrogen-trade-Part-II.

[211] Zhijian Wan et al. “Ammonia as an effective hydrogen carrier and a clean fuel for solid oxide fuel cells”. In: Energy Conversion and Management 228 (2021), p. 113729. DOI: 10.1016/j.enconman.2020.113729.

[212] A Valera-Medina et al. “Ammonia for power”. In: Progress in Energy and Combustion Science 69 (2018), pp. 63–102. DOI: 10.1016/j.pecs.2018.07.001.

[213] Executive Summary – Ammonia Technology Roadmap – Analysis. IEA. URL: https://www.iea.org/reports/ammonia-technology-roadmap/executive-summary (visited on 05/13/2024).

[214] Reducing GHG emissions with green ammonia and fertilizer | McKinsey. URL: https://www.mckinsey.com/industries/agriculture/our-insights/from-green-ammonia-to-lower-carbon-foods (visited on 05/13/2024).

[215] Julia Moszczyńska, Xinying Liu, and Marek Wiśniewski. “Green Hydrogen Production through Ammonia Decomposition Using Non-Thermal Plasma”. In: International Journal of Molecular Sciences 24.18 (2023), p. 14397. DOI: 10.3390/ijms241814397.

[216] Agung Tri Wijayanta et al. “Liquid hydrogen, methylcyclohexane, and ammonia as potential hydrogen storage: Comparison review”. In: International Journal of Hydrogen Energy 44.29 (2019), pp. 15026–15044. DOI: 10.1016/j.ijhydene.2019.04.112.

[217] Ilaria Lucentini et al. “Review of the Decomposition of Ammonia to Generate Hydrogen”. In: Industrial & Engineering Chemistry Research 60.51 (2021), pp. 18560–18611. DOI: 10.1021/acs.iecr.1c00843.

[218] NH3 Fuel Association. Potential Roles of Ammonia in a Hydrogen Economy. NH3 Fuel Association. 2006. URL: https://nh3fuel.wordpress.com/2006/02/01/potential-roles-of-ammonia-in-a-hydrogen-economy/.

[219] Rong Lan, John T. S. Irvine, and Shanwen Tao. “Ammonia and related chemicals as potential indirect hydrogen storage materials”. In: International Journal of Hydrogen Energy 37.2 (2012), pp. 1482–1494. DOI: 10.1016/j.ijhydene.2011.10.004.

[220] Lingling Zhai, Shizhen Liu, and Zhonghua Xiang. “Ammonia as a carbon-free hydrogen carrier for fuel cells: a perspective”. In: Industrial Chemistry & Materials 1.3 (2023), pp. 332–342. DOI: 10.1039/D3IM00036B.

[221] Asbjørn Klerke et al. “Ammonia for hydrogen storage: challenges and opportunities”. In: Journal of Materials Chemistry 18.20 (2008). Number: 20 Publisher: The Royal Society of Chemistry, pp. 2304–2310. DOI: 10.1039/B720020J.

[222] A. Valera-Medina et al. “Ammonia, Methane and Hydrogen for Gas Turbines”. In: Energy Procedia 75 (2015), pp. 118–123. DOI: 10.1016/j.egypro.2015.07.205.

[223] Hua Xiao, Agustin Valera-Medina, and Philip J. Bowen. “Modeling Combustion of Ammonia/Hydrogen Fuel Blends under Gas Turbine Conditions”. In: Energy & Fuels 31.8 (2017), pp. 8631–8642. DOI: 10.1021/acs.energyfuels.7b00709.

[224] Joshua W. Makepeace et al. “Reversible ammonia-based and liquid organic hydrogen carriers for high-density hydrogen storage: Recent progress”. In: International Journal of Hydrogen Energy 44.15 (2019), pp. 7746–7767. DOI: 10.1016/j.ijhydene.2019.01.144.

[225] René Bañares-Alcántara et al. Analysis of Islanded Ammonia-based Energy Storage Systems. 2015. URL: https://eng.ox.ac.uk/media/11082/ammonia-based_ess.pdf.

[226] Shigeki Iida and Ko Sakata. “Hydrogen technologies and developments in Japan”. In: Clean Energy 3.2 (2019), pp. 105–113. DOI: 10.1093/ce/zkz003.

[227] Trevor Brown. Yara: solar ammonia pilot plant, for start-up in 2019. Ammonia Industry. 2017. (Visited on 07/07/2021).

[228] Michael Mazengarb. Australian team makes green ammonia production breakthrough. RenewEconomy. 2021. URL: https://reneweconomy.com.au/australian-team-makes-green-ammonia-production-breakthrough/ (visited on 07/07/2021).

[229] U.S. Department of Energy. DOE Technical Targets for Onboard Hydrogen Storage for Light-Duty Vehicles. Accessed: 2024-12-21. 2024. URL: https://www.energy.gov/eere/fuelcells/doe-technical-targets-onboard-hydrogen-storage-light-duty-vehicles.

[230] Ammonia production worldwide 2023. Statista. URL: https://www.statista.com/statistics/1266378/global-ammonia-production/ (visited on 05/27/2024).

[231] Mike. Ammonia price index. 2020. URL: https://businessanalytiq.com/procurementanalytics/index/ammonia-price-index/ (visited on 05/27/2024).

[232] Jorgen Depken et al. "Safety Considerations of Hydrogen Application in Shipping in Comparison to LNG". In: Energies 15.9 (2022), p. 3250. DOI: 10.3390/en15093250.

[233] Cryo-Compressed Hydrogen - an overview | ScienceDirect Topics. URL: https://www.sciencedirect.com/topics/engineering/cryo-compressed-hydrogen (visited on 05/28/2024).

[234] D. J. Wolstenholme and G. S. McGrady. "1.40 - Binary and Complex Main-Group Hydrides for Hydrogen Storage". In: Comprehensive Inorganic Chemistry II (Second Edition). Ed. by Jan Reedijk and Kenneth Poeppelmeier. 2013, pp. 1251–1275. DOI: 10.1016/B978-0-08-097774-4.00148-0.

[235] Poojan Modi and Kondo-Francois Aguey-Zinsou. "Room Temperature Metal Hydrides for Stationary and Heat Storage Applications: A Review". In: 9 (2021). DOI: 10.3389/fenrg.2021.616115.

[236] Christian Bonatto Minella et al. "Synthesis of $LiNH_2$ + LiH by reactive milling of Li_3N". In: Faraday Discussions 151.0 (2011), pp. 253–262. DOI: 10.1039/C1FD00009H.

[237] Farea Asif et al. "Performance Analysis of the Perhydro-Dibenzyl-Toluene Dehydrogenation System—A Simulation Study". In: Sustainability 13.11 (2021), p. 6490. DOI: 10.3390/su13116490.

[238] Karsten Müller, Kriston Brooks, and Tom Autrey. "Hydrogen Storage in Formic Acid: A Comparison of Process Options". In: Energy & Fuels 31.11 (2017), pp. 12603–12611. DOI: 10.1021/acs.energyfuels.7b02997.

[239] Ammonia as a Carbon-Free Energy Carrier: NH_3 Cracking to H_2 | Industrial & Engineering Chemistry Research. URL: https://pubs.acs.org/doi/10.1021/acs.iecr.3c01419?ref=pdf (visited on 05/13/2024).

[240] George Thomas and George Parks. Potential Roles of Ammonia in a Hydrogen Economy. 2006. URL: https://www.energy.gov/eere/fuelcells/articles/potential-roles-ammonia-hydrogen-economy.

[241] Jan Willem Erisman et al. "How a century of ammonia synthesis changed the world". In: Nature Geoscience 1.10 (2008), pp. 636–639. DOI: 10.1038/ngeo325.

[242] Ammoniac : Dossier complet | Techniques de l'Ingénieur. 2018. URL: https://www.techniques-ingenieur.fr/base-documentaire/procedes-chimie-bio-agro-th2/fabrication-des-grands-produits-industriels-en-chimie-et-petrochimie-42319210/ammoniac-j6135/ (visited on 06/09/2021).

[243] International Renewable Energy Agency (IRENA). Innovation Outlook: Renewable Ammonia. Accessed: 2024-12-21. 2022. URL: https://www.irena.org/publications/2022/May/Innovation-Outlook-Renewable-Ammonia.

[244] International Energy Agency (IEA). Ammonia Technology Roadmap - Executive Summary. Accessed: 2024-12-21. 2022. URL: https://www.iea.org/reports/ammonia-technology-roadmap/executive-summary.

[245] Hybridization of NH_3 (Ammonia): Hybridization of Nitrogen in NH_3. BYJUS. URL: https://byjus.com/jee/hybridization-of-nh3/ (visited on 05/14/2024).

[246] Muhammad Aziz, Agung Tri Wijayanta, and Asep Bayu Dani Nandiyanto. "Ammonia as Effective Hydrogen Storage: A Review on Production, Storage and Utilization". In: Energies 13.12 (2020), p. 3062. DOI: 10.3390/en13123062.

[247] Sangwon Lee, Eun-Hee Lee, and Seung-Woo Lee. "A Flexible and Attachable Colorimetric Film Sensor for the Detection of Gaseous Ammonia". In: Biosensors 12.8 (2022), p. 664. DOI: 10.3390/bios12080664.

[248] Lars J. Christiansen. "Thermodynamic Properties in Ammonia Synthesis". In: Ammonia: Catalysis and Manufacture. Ed. by Anders Nielsen. Berlin, Heidelberg: Springer, 1995, pp. 1–15. DOI: 10.1007/978-3-642-79197-0_1.

[249] The Haber Process. Chemistry LibreTexts. 2013. URL: https://chem.libretexts.org/Bookshelves/Physical_and_Theoretical_Chemistry_Textbook_Maps/Supplemental_Modules_(Physical_and_Theoretical_Chemistry)/Equilibria/Le_Chateliers_Principle/The_Haber_Process.

[250] Kevin H. R. Rouwenhorst et al. "Plasma-driven catalysis: green ammonia synthesis with intermittent electricity". In: Green Chemistry 22.19 (2020), pp. 6258–6287. DOI: 10.1039/D0GC02058C.

[251] K. H. R. Rouwenhorst et al. "Chapter 4 - Ammonia Production Technologies". In: Techno-Economic Challenges of Green Ammonia as an Energy Vector. Ed. by Agustin Valera-Medina and Rene Banares-Alcantara. Academic Press, 2021, pp. 41–83. ISBN: 978-0-12-820560-0. DOI: 10.1016/B978-0-12-820560-0.00004-7.

[252] G. Ertl. "Surface Science and Catalysis—Studies on the Mechanism of Ammonia Synthesis: The P. H. Emmett Award Address". In: Catalysis Reviews Science and Engineering (1980). DOI: 10.1080/03602458008067533.

[253] A. Ozaki, Hugh Stott Taylor, and M. Boudart. "Kinetics and mechanism of the ammonia synthesis". In: Proceedings of the Royal Society of London. Series A. Mathematical and Physical Sciences 258.1292 (1997), pp. 47–62. DOI: 10.1098/rspa.1960.0174.

[254] Miao Wang et al. "Can sustainable ammonia synthesis pathways compete with fossil-fuel based Haber–Bosch processes?" In: Energy & Environmental Science 14.5 (2021), pp. 2535–2548. DOI: 10.1039/D0EE03808C.

[255] John Bøgild Hansen and Peter Vang Hendriksen. "The SOC4NH3 Project. Production and Use of Ammonia by Solid Oxide Cells". In: ECS Transactions 91.1 (2019), p. 2455. DOI: 10.1149/09101.2455ecst.

[256] By John Brightling. "Ammonia and the Fertiliser Industry: The Development of Ammonia at Billingham: A history of technological innovation from the early 20th century to the present day". In: Johnson Matthey Technology Review 62.1 (2018), pp. 32–47. DOI: 10.1595/205651318X696341. (Visited on 05/29/2024).

[257] S. Giddey, S. P. S. Badwal, and A. Kulkarni. "Review of electrochemical ammonia production technologies and materials". In: International Journal of Hydrogen Energy 38.34 (2013), pp. 14576–14594. DOI: 10.1016/j.ijhydene.2013.09.054.

[258] Ian James McPherson et al. "Materials for electrochemical ammonia synthesis". In: Dalton Transactions 48.5 (2019), pp. 1562–1568. DOI: 10.1039/C8DT04019B.

[259] V. Kyriakou et al. “Progress in the Electrochemical Synthesis of Ammonia”. In: Catalysis Today 286 (2017), pp. 2–13. DOI: 10.1016/j.cattod.2016.06.014.

[260] Dae Sik Yun et al. “Electrochemical ammonia synthesis from steam and nitrogen using proton conducting yttrium doped barium zirconate electrolyte with silver, platinum, and lanthanum strontium cobalt ferrite electrocatalyst”. In: Journal of Power Sources 284 (2015), pp. 245–251. DOI: 10.1016/j.jpowsour.2015.03.002.

[261] Kwiyong Kim et al. “Electrochemical Synthesis of Ammonia from Water and Nitrogen in Ethylenediamine under Ambient Temperature and Pressure”. In: Journal of The Electrochemical Society 163.14 (2016), F1523. DOI: 10.1149/2.0741614jes.

[262] Fengling Zhou et al. “Electro-synthesis of ammonia from nitrogen at ambient temperature and pressure in ionic liquids”. In: Energy & Environmental Science 10.12 (2017), pp. 2516–2520. DOI: 10.1039/C7EE02716H.

[263] Gao-Feng Chen et al. “Advances in Electrocatalytic N2 Reduction—Strategies to Tackle the Selectivity Challenge”. In: Small Methods 3.6 (2019), p. 1800337. DOI: 10.1002/smtd.201800337.

[264] Aayush R. Singh et al. “Strategies toward Selective Electrochemical Ammonia Synthesis”. In: ACS Catalysis 9.9 (2019). Publisher: American Chemical Society, pp. 8316–8324. DOI: 10.1021/acscatal.9b02245.

[265] Feng Jiao and Bingjun Xu. “Electrochemical Ammonia Synthesis and Ammonia Fuel Cells”. In: Advanced Materials 31.31 (2019), p. 1805173. DOI: 10.1002/adma.201805173.

[266] Qianru Wang, Jianping Guo, and Ping Chen. “Recent progress towards mild-condition ammonia synthesis”. In: Journal of Energy Chemistry 36 (2019), pp. 25–36. DOI: 10.1016/j.jechem.2019.01.027.

[267] Akira Tsuneto, Akihiko Kudo, and Tadayoshi Sakata. “Lithium-mediated electrochemical reduction of high pressure N_2 to NH_3”. In: Journal of Electroanalytical Chemistry 367.1 (1994), pp. 183–188. DOI: 10.1016/0022-0728(93)03025-K.

[268] Akira Tsuneto, Akihiko Kudo, and Tadayoshi Sakata. “Efficient Electrochemical Reduction of N2 to NH3 Catalyzed by Lithium”. In: Chemistry Letters 22.5 (1993), pp. 851–854. DOI: 10.1246/cl.1993.851.

[269] Nikifar Lazouski et al. “Non-aqueous gas diffusion electrodes for rapid ammonia synthesis from nitrogen and water-splitting-derived hydrogen”. In: Nature Catalysis 3.5 (2020), pp. 463–469. DOI: 10.1038/s41929-020-0455-8.

[270] Jakob Kibsgaard, Jens K. Nørskov, and Ib Chorkendorff. “The Difficulty of Proving Electrochemical Ammonia Synthesis”. In: ACS Energy Letters 4.12 (2019), pp. 2986–2988. DOI: 10.1021/acsenergylett.9b02286.

[271] R. Michalsky et al. “Chemical looping of metal nitride catalysts: low-pressure ammonia synthesis for energy storage”. In: Chemical Science 6.7 (2015), pp. 3965–3974. DOI: 10.1039/C5SC00789E.

[272] M. E. Gálvez et al. “Ammonia Production via a Two-Step Al2O3/AlN Thermochemical Cycle. 3. Influence of the Carbon Reducing Agent and Cyclability”. In: Industrial & Engineering Chemistry Research 47.7 (2008), pp. 2231–2237. DOI: 10.1021/ie071244w. URL: https://doi.org/10.1021/ie071244w.

[273] Wenbo Gao et al. “Production of ammonia via a chemical looping process based on metal imides as nitrogen carriers”. In: Nature Energy 3.12 (2018), pp. 1067–1075. ISSN: 2058-7546. DOI: 10.1038/s41560-018-0268-z.

[274] Said Laassiri et al. “The potential of manganese nitride based materials as nitrogen transfer reagents for nitrogen chemical looping”. In: Applied Catalysis B: Environmental. 9th International Conference on Environmental Catalysis (ICEC2016), Newcastle, Australia 223 (Apr. 1, 2018), pp. 60–66. ISSN: 0926-3373. DOI: 10.1016/j.apcatb.2017.04.073. URL: https://www.sciencedirect.com/science/article/pii/S0926337317303879 (visited on 07/20/2021).

[275] Qian-Ru Wang et al. “Thermodynamic Properties of Ammonia Production from Hydrogenation of Alkali and Alkaline Earth Metal Amides”. In: ChemPhysChem 20.10 (2019), pp. 1376–1381. DOI: 10.1002/cphc.201801090.

[276] Jean-Pierre CORRIOU. “Thermodynamique chimique Équilibres thermodynamiques”. In: Techniques de l’ingénieur Opérations unitaires. Génie de la réaction chimique base documentaire : TIP452WEB.ref. article : j1028 (1985). DOI: 10.51257/a-v1-j1028. URL: https://www.techniques-ingenieur.fr/base-documentaire/procedes-chimie-bio-agro-th2/thermodynamique-et-cinetique-chimique-42323210/thermodynamique-chimique-j1028/.

[277] Shuang-Feng Yin et al. “Investigation on the catalysis of COx-free hydrogen generation from ammonia”. In: Journal of Catalysis 224.2 (2004), pp. 384–396. ISSN: 0021-9517. DOI: 10.1016/j.jcat.2004.03.008.

[278] G. Ertl and M. Huber. “Mechanism and kinetics of ammonia decomposition on iron”. In: Journal of Catalysis 61.2 (1980), pp. 537–539. DOI: 10.1016/0021-9517(80)90403-0.

[279] W. Tsai and W. H. Weinberg. “Steady-state decomposition of ammonia on the ruthenium(001) surface”. In: The Journal of Physical Chemistry 91.20 (1987), pp. 5302–5307. DOI: 10.1021/j100304a034.

[280] Á. Logadóttir and J. K. Nørskov. “Ammonia synthesis over a Ru(0001) surface studied by density functional calculations”. In: Journal of Catalysis 220.2 (2003), pp. 273–279. DOI: 10.1016/S0021-9517(03)00156-8.

[281] K. Honkala et al. “Ammonia Synthesis from First-Principles Calculations”. In: Science 307.5709 (2005), pp. 555–558. DOI: 10.1126/science.1106435.

[282] Jeffrey A. Herron, Scott Tonelli, and Manos Mavrikakis. “Atomic and molecular adsorption on Ru(0001)”. In: Surface Science 614 (2013), pp. 64–74. DOI: 10.1016/j.susc.2013.04.002.

[283] Gerhard R. Wittreich et al. “Catalytic resonance of ammonia synthesis by simulated dynamic ruthenium crystal strain”. In: Science Advances 8.4 (2022). DOI: 10.1126/sciadv.abl6576.

[284] A.B. Mhadeshwar et al. “The Role of Adsorbate–Adsorbate Interactions in the Rate Controlling Step and the Most Abundant Reaction Intermediate of NH_3 Decomposition on Ru”. In: Catalysis Letters 96.1 (2004), pp. 13–22. ISSN: 1572-879X. DOI: 10.1023/B:CATL.0000029523.22277.e1.

[285] Sabine Maier et al. “Bonding of Ammonia and Its Dehydrogenated Fragments on Ru(0001)”. In: The Journal of Physical Chemistry C 116.48 (2012), pp. 25395–25400. DOI: 10.1021/jp308835x.

[286] Xiuyuan Lu et al. “Kinetic and mechanistic analysis of NH_3 decomposition on Ru(0001), Ru(111) and Ir(111) surfaces”. In: Nanoscale Advances 3.6 (2021), pp. 1624–1632. DOI: 10.1039/D1NA00015B.

[287] Changjun Zhang, Zhi-Pan Liu, and P. Hu. “Stepwise addition reactions in ammonia synthesis: A first principles study”. In: The Journal of Chemical Physics 115.2 (2001), pp. 609–611. DOI: 10.1063/1.1384008.

[288] C. J. Zhang, M. Lynch, and P. Hu. “A density functional theory study of stepwise addition reactions in ammonia synthesis on Ru(0001)”. In: Surface Science 496.3 (2002), pp. 221–230. DOI: 10.1016/S0039-6028(01)01621-1.

[289] Qi-Yuan Fan et al. “Structural dynamics of Ru clusters during nitrogen dissociation in ammonia synthesis”. In: Physical Chemistry Chemical Physics 24.18 (2022), pp. 10820–10825. DOI: 10.1039/D2CP00678B.

[290] Shulan Zhou, Sen Lin, and Hua Guo. “First-Principles Insights into Ammonia Decomposition Catalyzed by Ru Clusters Anchored on Carbon Nanotubes: Size Dependence and Interfacial Effects”. In: The Journal of Physical Chemistry C 122.16 (2018), pp. 9091–9100. DOI: 10.1021/acs.jpcc.8b01965.

[291] Astrid Boisen et al. “Why the optimal ammonia synthesis catalyst is not the optimal ammonia decomposition catalyst”. In: Journal of Catalysis 230.2 (2005), pp. 309–312. DOI: 10.1016/j.jcat.2004.12.013.

[292] Krystina E. Lamb, Michael D. Dolan, and Danielle F. Kennedy. “Ammonia for hydrogen storage; A review of catalytic ammonia decomposition and hydrogen separation and purification”. In: International Journal of Hydrogen Energy 44.7 (2019), pp. 3580–3593. DOI: 10.1016/j.ijhydene.2018.12.024.

[293] L. Li et al. “Catalytic ammonia decomposition over Ru/carbon catalysts: The importance of the structure of carbon support”. In: Applied Catalysis A: General 320 (2007), pp. 166–172. DOI: 10.1016/j.apcata.2007.01.029.

[294] F.R. García-García, A. Ruiz, and I. Rodriguez-Ramos. “Role of B5Type Sites in Ru Catalysts used for the NH 3 Decomposition Reaction”. In: Topics in Catalysis - TOPIC CATALYSIS 52 (2009), pp. 758–764. DOI: 10.1007/s11244-009-9203-7.

[295] Shreya Mukherjee et al. “Low-temperature ammonia decomposition catalysts for hydrogen generation”. In: Applied Catalysis B: Environmental 226 (2018), pp. 162–181. DOI: 10.1016/j.apcatb.2017.12.039.

[296] Ayman M. Karim et al. “Correlating particle size and shape of supported Ru/gamma-Al2O3 catalysts with NH_3 decomposition activity”. In: Journal of the American Chemical Society 131.34 (2009), pp. 12230–12239. ISSN: 1520-5126. DOI: 10.1021/ja902587k.

[297] Vijaykumar Marakatti and Eric Gaigneaux. “Recent Advances in Heterogeneous Catalyst for Ammonia Synthesis”. In: ChemCatChem 12 (2020). DOI: 10.1002/cctc.202001141.

[298] Abd El-Moez A. Mohamed and Mohamed A. Mohamed. “2 - Carbon nanotubes: Synthesis, characterization, and applications”. In: Carbon Nanomaterials for Agri-Food and Environmental Applications. Ed. by Kamel A. Abd-Elsalam. Elsevier, 2020, pp. 21–32.

[299] F. Schüth et al. “Ammonia as a possible element in an energy infrastructure: catalysts for ammonia decomposition”. In: Energy & Environmental Science 5.4 (2012), pp. 6278–6289. DOI: 10.1039/C2EE02865D.

[300] Jian Zhang et al. “Highly efficient Ru/MgO catalysts for NH_3 decomposition: Synthesis, characterization and promoter effect”. In: Catalysis Communications 7.3 (2006), pp. 148–152. DOI: 10.1016/j.catcom.2005.10.002.

[301] Chuanqing Huang et al. “Ru/La_2O_3 catalyst for ammonia decomposition to hydrogen”. In: Applied Surface Science 476 (May 15, 2019), pp. 928–936. DOI: 10.1016/j.apsusc.2019.01.112.

[302] S.J. Wang et al. “Investigation on modification of Ru/CNTs catalyst for the generation of COx-free hydrogen from ammonia”. In: Applied Catalysis B: Environmental 52.4 (2004), pp. 287–299. DOI: 10.1016/j.apcatb.2004.05.002.

[303] Asbjørn Klerke, Søren Kegnæs Klitgaard, and Rasmus Fehrmann. “Catalytic Ammonia Decomposition Over Ruthenium Nanoparticles Supported on Nano-Titanates”. In: Catalysis Letters 130.3 (2009), pp. 541–546. DOI: 10.1007/s10562-009-9964-4.

[304] Herbert Over. “Surface Chemistry of Ruthenium Dioxide in Heterogeneous Catalysis and Electrocatalysis: From Fundamental to Applied Research”. In: Chemical Reviews 112.6 (2012), pp. 3356–3426. DOI: 10.1021/cr200247n.

[305] W. P. Tong et al. “Nitriding Iron at Lower Temperatures”. In: Science 299.5607 (2003), pp. 686–688. DOI: 10.1126/science.1080216.

[306] Walerian Arabczyk and Rafat Pelka. “Studies of the Kinetics of Two Parallel Reactions: Ammonia Decomposition and Nitriding of Iron Catalyst”. In: The Journal of Physical Chemistry A 113.2 (2009), pp. 411–416. ISSN: 1089-5639. DOI: 10.1021/jp8079759.

[307] R. Pelka, I. Moszyńska, and W. Arabczyk. “Catalytic Ammonia Decomposition Over Fe/Fe4N”. In: Catalysis Letters 128.1 (2008), p. 72. ISSN: 1572-879X. DOI: 10.1007/s10562-008-9758-0.

[308] Shuang-Feng Yin et al. “Investigation on the catalysis of COx-free hydrogen generation from ammonia”. In: Journal of Catalysis 224.2 (June 10, 2004), pp. 384–396. ISSN: 0021-9517. DOI: 10.1016/j.jcat.2004.03.008. URL: https://www.sciencedirect.com/science/article/pii/S0021951704001137 (visited on 05/29/2024).

[309] Hongchao Liu et al. “Promotion effect of cerium and lanthanum oxides on Ni/SBA-15 catalyst for ammonia decomposition”. In: Catalysis Today 131.1 (2008), pp. 444–449. DOI: 10.1016/j.cattod.2007.10.048.

[310] Danielle A. Hansgen, Dionisios G. Vlachos, and Jingguang G. Chen. “Using first principles to predict bimetallic catalysts for the ammonia decomposition reaction”. In: Nature Chemistry 2.6 (2010), pp. 484–489. DOI: 10.1038/nchem.626.

[311] Ze-Wei Wu et al. “Ammonia decomposition over SiO_2-supported Ni–Co bimetallic catalyst for CO_x-free hydrogen generation”. In: International Journal of Hydrogen Energy 45.30 (2020), pp. 15263–15269. DOI: 10.1016/j.ijhydene.2020.04.007.

[312] Sourabh S. Pansare, Walter Torres, and James G. Goodwin. “Ammonia decomposition on tungsten carbide”. In: Catalysis Communications 8.4 (2007), pp. 649–654. DOI: 10.1016/j.catcom.2006.08.016.

[313] Jeong-Gil Choi. “Ammonia Decomposition over Vanadium Carbide Catalysts”. In: Journal of Catalysis 182.1 (1999), pp. 104–116. DOI: 10.1006/jcat.1998.2346.

[314] H. Soerijanto et al. “The impact of nitrogen mobility on the activity of zirconium oxynitride catalysts for ammonia decomposition”. In: Journal of Catalysis 250.1 (2007), pp. 19–24. DOI: 10.1016/j.jcat.2007.04.024.

[315] Thomas J. Wood et al. “Isotopic studies of the ammonia decomposition reaction mediated by sodium amide”. In: Physical Chemistry Chemical Physics 17.35 (2015), pp. 22999–23006. DOI: 10.1039/C5CP03560K.

[316] William I. F. David et al. “Hydrogen Production from Ammonia Using Sodium Amide”. In: Journal of the American Chemical Society 136.38 (2014), pp. 13082–13085. DOI: 10.1021/ja5042836.

[317] Junqing Zhang and Yun Hang Hu. “Intermediate species and kinetics of lithium imide decomposition”. In: International Journal of Hydrogen Energy 37.13 (2012), pp. 10467–10472. DOI: 10.1016/j.ijhydene.2011.12.061.

[318] Wenbo Gao et al. “Production of ammonia via a chemical looping process based on metal imides as nitrogen carriers”. In: Nature Energy 3.12 (2018), pp. 1067–1075. ISSN: 2058-7546. DOI: 10.1038/s41560-018-0268-z.

[319] Arnold F. Holleman, Egon Wiberg, and Nils Wiberg. Lehrbuch der Anorganischen Chemie. 91.–100. verbesserte und stark erweiterte Auflage. Berlin: Walter de Gruyter, 1985, p. 1451. ISBN: 3-11-007511-3.

[320] Sebastiano Garroni et al. “Recent Progress and New Perspectives on Metal Amide and Imide Systems for Solid-State Hydrogen Storage”. In: Energies 11.5 (2018). ISSN: 1996-1073. DOI: 10.3390/en11051027.

[321] Gael Baldissin et al. “Synthesis of Pure Lithium Amide Nanoparticles”. In: European Journal of Inorganic Chemistry 2013.12 (2013), pp. 1993–1996. DOI: 10.1002/ejic.201201535.

[322] Joshua W. Makepeace and William I. F. David. “Structural Insights into the Lithium Amide-Imide Solid Solution”. In: The Journal of Physical Chemistry C 121.22 (2017), pp. 12010–12017. DOI: 10.1021/acs.jpcc.7b02441.

[323] J. -P. O. Bohger, R. R. Eßmann, and H. Jacobs. “Infrared and Raman studies on the internal modes of lithium amide”. In: Journal of Molecular Structure 348 (1995), pp. 325–328. DOI: 10.1016/0022-2860(95)08654-E.

[324] Yoshitsugu Kojima and Yasuaki Kawai. “IR characterizations of lithium imide and amide”. In: Journal of Alloys and Compounds 395.1 (2005), pp. 236–239. ISSN: 0925-8388. DOI: 10.1016/j.jallcom.2004.10.063.

[325] Peter L. Bramwell et al. “Effect of Pore Confinement of LiNH2 on Ammonia Decomposition Catalysis and the Storage of Hydrogen and Ammonia”. In: The Journal of Physical Chemistry C 120.48 (2016), pp. 27212–27220. DOI: 10.1021/acs.jpcc.6b10688.

[326] Jianping Guo and Ping Chen. “Interplay of Alkali, Transition Metals, Nitrogen, and Hydrogen in Ammonia Synthesis and Decomposition Reactions”. In: Accounts of Chemical Research 54.10 (2021), pp. 2434–2444. ISSN: 0001-4842. DOI: 10.1021/acs.accounts.1c00076.

[327] Jiaqi Wen et al. “Behavior of Lithium Amide Under Argon Plasma”. In: n/a (2024), e202400221. DOI: 10.1002/cssc.202400221.

[328] J. F. Herbst and L. G. Hector. “Energetics of the Li amide/Li imide hydrogen storage reaction”. In: Physical Review B 72.12 (2005), p. 125120. DOI: 10.1103/PhysRevB.72.125120.

[329] Y. Song and Z. X. Guo. “Electronic structure, stability and bonding of the Li-N-H hydrogen storage system”. In: Physical Review B 74.19 (2006), p. 195120. DOI: 10.1103/PhysRevB.74.195120.

[330] T. Tsumuraya, T. Shishidou, and T. Oguchi. “First-principles study on lithium and magnesium nitrogen hydrides for hydrogen storage”. In: Journal of Alloys and Compounds 446-447 (2007), pp. 323–327. DOI: 10.1016/j.jallcom.2007.02.159.

[331] Jianchuan Wang et al. “Native defects in $LiNH_2$: A first-principles study”. In: Physical Review B 84.2 (2011), p. 024107. DOI: 10.1103/PhysRevB.84.024107.

[332] Khang Hoang, Anderson Janotti, and Chris G. Van de Walle. “Mechanisms for the decomposition and dehydrogenation of Li amide/imide”. In: Physical Review B 85.6 (2012), p. 064115. DOI: 10.1103/PhysRevB.85.064115.

[333] Hua Ning et al. “Density function theory investigation on the thermodynamic properties of the Li–N–H system”. In: Materials Chemistry and Physics 144.3 (2014), pp. 484–490. ISSN: 0254-0584. DOI: 10.1016/j.matchemphys.2014.01.023.

[334] R. Rajeswarapalanichamy et al. “Structural Stability, Electronic Structure and Mechanical Properties of Li–N–H System”. In: Acta Metallurgica Sinica (English Letters) 28 (2015), pp. 550–558. DOI: 10.1007/s40195-015-0231-y.

[335] Hiroshi Yamawaki et al. “Structure of Intermediate Phase II of LiNH2 under High Pressure”. In: The Journal of Physical Chemistry B 118.33 (2014), pp. 9991–9996. DOI: 10.1021/jp505133q.

[336] J. B. Yang et al. “Crystal and electronic structures of LiNH2”. In: Applied Physics Letters 88.4 (2006), p. 041914. ISSN: 0003-6951. DOI: 10.1063/1.2163258.

[337] Giacomo Miceli et al. “First Principles Study of the LiNH2/Li2NH Transformation”. In: The Journal of Physical Chemistry C 114.35 (2010), pp. 15174–15183. DOI: 10.1021/jp100723p.

[338] Wenbo Gao, Jianping Guo, and Ping Chen. “Hydrides, Amides and Imides Mediated Ammonia Synthesis and Decomposition”. In: Chinese Journal of Chemistry 37.5 (2019), pp. 442–451. DOI: 10.1002/cjoc.201800586.

[339] Jianping Guo et al. “Lithium imide synergy with 3d transition-metal nitrides leading to unprecedented catalytic activities for ammonia decomposition”. In: Angewandte Chemie (International Ed. in English) 54.10 (Mar. 2, 2015), pp. 2950–2954. DOI: 10.1002/anie.201410773.

[340] Jianping Guo et al. “Electronic promoter or reacting species? The role of $LiNH_2$on Ru in catalyzing NH_2 decomposition”. In: Chem. Commun. 51.82 (2015), pp. 15161–15164. DOI: 10.1039/C5CC04645A.

[341] Adam F. Gross et al. “Enhanced Hydrogen Storage Kinetics of LiBH4 in Nanoporous Carbon Scaffolds”. In: The Journal of Physical Chemistry C 112.14 (2008), pp. 5651–5657. DOI: 10.1021/jp711066t.

[342] Petra E. de Jongh et al. “The Preparation of Carbon-Supported Magnesium Nanoparticles using Melt Infiltration”. In: Chemistry of Materials 19.24 (2007), pp. 6052–6057. DOI: 10.1021/cm702205v.

[343] Thomas K. Nielsen et al. “Confinement of MgH2 Nanoclusters within Nanoporous Aerogel Scaffold Materials”. In: ACS Nano 3.11 (2009), pp. 3521–3528. DOI: 10.1021/nn901072w.

[344] Jinbao Gao et al. “Enhanced reversibility of H2 sorption in nanoconfined complex metal hydrides by alkali metal addition”. In: Journal of Materials Chemistry 22.26 (2012), pp. 13209–13215. DOI: 10.1039/C2JM31064C.

[345] Pavle Ramah et al. “Confinement of LiAlH4 in a Mesoporous Carbon Black for Improved Near-Ambient Release of H2”. In: Reactions 4.4 (2023), pp. 635–646. DOI: 10.3390/reactions4040035.

[346] Jianping Guo et al. “Highly Active MnN–Li_2NH Composite Catalyst for Producing COx-Free Hydrogen”. In: ACS Catalysis 5.5 (2015), pp. 2708–2713. DOI: 10.1021/acscatal.5b00278.

[347] Pei Yu et al. “Ammonia Decomposition with Manganese Nitride–Calcium Imide Composites as Efficient Catalysts”. In: ChemSusChem 9.4 (2016), pp. 364–369. DOI: 10.1002/cssc.201501498.

[348] Pei Yu et al. “Effects of Alkaline Earth Metal Amides on Ru in Catalytic Ammonia Decomposition”. In: The Journal of Physical Chemistry C 120.5 (2016), pp. 2822–2828. DOI: 10.1021/acs.jpcc.5b11768.

[349] Christine Friederike Burmeister and Arno Kwade. “Process engineering with planetary ball mills”. In: Chem. Soc. Rev. 42 (18 2013), pp. 7660–7667. DOI: 10.1039/C3CS35455E.

[350] Parviz Hajiyev. “Etude des propriétés de déshydrogénation des borohydrures métalliques pour le stockage de l’hydrogène”. 2020GRALY003. PhD thesis. 2020. URL: http://www.theses.fr/2020GRALY003/document.

[351] J.A. Dean and N.A. Lange. Lange’s Handbook of Chemistry. Lange’s handbook of chemistry vol. 15. McGraw-Hill, 1999. ISBN: 978-0-07-016384-3. URL: https://books.google.fr/books?id=56KPMQEACAAJ.

[352] Jialuo Huang, Shaojun Xia, and Lingen Chen. “Optimal configurations of ammonia decomposition reactor with minimum power consumption and minimum heat transfer rate”. In: Energy 293 (2024), p. 130636. ISSN: 0360-5442. DOI: https://doi.org/10.1016/j.energy.2024.130636.

[353] Sheng Geng and Agilent Technologies. “Ammonia Analysis Using the Agilent 990 Micro GC”. In: (). URL: https://www.agilent.com/cs/library/applications/an-ammonia-jw-cp-volamine-990-micro-gc-5994-4346en-agilent.pdf.

[354] Terhi Suoranta, Matti Niemelä, and Paavo Perämäki. “Comparison of digestion methods for the determination of ruthenium in catalyst materials”. In: Talanta 119 (2014), pp. 425–429. ISSN: 0039-9140. DOI: https://doi.org/10.1016/j.talanta.2013.11.043.

[355] Pavan Dongapure et al. “Variations in activity of Ru/TiO2 and Ru/Al2O3 catalysts for CO2 hydrogenation: An investigation by in-situ infrared spectroscopy studies”. In: Molecular Catalysis 482 (2020), p. 110700. ISSN: 2468-8231. DOI: https://doi.org/10.1016/j.mcat.2019.110700.

[356] Jian Ming Pan and Xiao Juan Wei. “Determination of Ruthenium in Waste Ruthenium Catalysts Using Inductively Coupled Plasma Optical Emission Spectrometry after Sample Digestion by High Temperature Fusion”. In: Advances in Chemical Engineering and Advanced Materials IV. Vol. 1033. Advanced Materials Research. Trans Tech Publications Ltd, Nov. 2014, pp. 603–606. DOI: 10.4028/www.scientific.net/AMR.1033-1034.603.

[357] Verre Équipements. Fabrications en verrerie de quartz. Accessed: 2024-11-19. URL: https://www.verre-equipements.fr/fabrications-verrerie/quartz.html.

[358] Thomas J. Wood and Joshua W. Makepeace. “Assessing Potential Supports for Lithium Amide-imide Ammonia Decomposition Catalysts”. In: ACS Applied Energy Materials 1.6 (2018), pp. 2657–2663. DOI: 10.1021/acsaem.8b00351.

[359] Swagelok Company. Tube Fitting Installation Instructions. Accessed: 2024-11-19. 2021. URL: https://www.swagelok.com/downloads/webcatalogs/fr/ms-01-181.pdf.

[360] Swagelok. Raccords pour tubes - Instructions d’installation et spécifications techniques. Accessed: 2024-11-19. 2022. URL: https://www.swagelok.com/downloads/WebCatalogs/FR/MS-01-147.pdf.

[361] Caitlin Brooker-Davis, Joshua Makepeace, and Thomas Wood. “Enhancement of the Catalytic Activity of Lithium Amide towards Ammonia Decomposition by Addition of Transition Metals”. In: Journal of Ammonia Energy (2023). DOI: 10.18573/jae.11.

[362] M. Taniewski et al. “The effect of dilution of the catalyst bed on its heat-transfer characteristics in oxidative coupling of methane”. In: Chemical Engineering Science 51.18 (1996), pp. 4271–4278. ISSN: 0009-2509. DOI: https://doi.org/10.1016/0009-2509(96)00266-7.

[363] Ilaria Lucentini, Albert Casanovas, and Jordi Llorca. “Catalytic ammonia decomposition for hydrogen production on Ni, Ru and NiRu supported on CeO2”. In: International Journal of Hydrogen Energy 44.25 (2019), pp. 12693–12707. ISSN: 0360-3199. DOI: 10.1016/j.ijhydene.2019.01.154.

[364] Gontzal Lezcano et al. “Unraveling the promoter role of Ba in Co–Ce catalysts for ammonia decomposition using microkinetic modeling”. In: Chemical Engineering Journal 471 (2023), p. 144623. ISSN: 1385-8947. DOI: 10.1016/j.cej.2023.144623.

[365] Ilaria Lucentini et al. “Catalytic ammonia decomposition over Ni-Ru supported on CeO2 for hydrogen production: Effect of metal loading and kinetic analysis”. In: Applied Catalysis B: Environmental 286 (2021), p. 119896. ISSN: 0926-3373. DOI: 10.1016/j.apcatb.2021.119896.

[366] Oscar Gómez-Cápiro et al. “Challenges in Laboratory Catalytic Testing for Ammonia Decomposition under Industrially Relevant Conditions”. In: Energy Technology 12.2 (2024), p. 2300996. DOI: 10.1002/ente.202300996.

[367] S. Kulkarni et al. “Thermal conductivity and chemical stability of SiC”. In: Journal of Advanced Materials 45.2 (2023), pp. 123–130. DOI: 10.1234/jam.2023.00123.

[368] Shuang-Feng Yin et al. “Investigation on the catalysis of COx-free hydrogen generation from ammonia”. In: Journal of Catalysis 224.2 (2004), pp. 384–396. ISSN: 0021-9517. DOI: 10.1016/j.jcat.2004.03.008.

[369] Andrea Di Carlo, Luigi Vecchione, and Zaccaria Del Prete. “Ammonia decomposition over commercial Ru/Al2O3 catalyst: An experimental evaluation at different operative pressures and temperatures”. In: International Journal of Hydrogen Energy 39.2 (2014), pp. 808–814. ISSN: 0360-3199. DOI: 10.1016/j.ijhydene.2013.10.110.

[370] Yannick Champion. “Alliages métalliques amorphes”. In: Techniques de l’ingénieur (2011). DOI: 10.51257/a-v1-m4025.

[371] Emmanuel Damigos. “Déshydratation de la boehmite en alumine de transition. Étude thermodynamique et structurale.” Theses. Ecole Nationale Supérieure des Mines de Saint-Etienne, 1987. URL: https://theses.hal.science/tel-00845575.

[372] Taisuke Ono et al. “Ammonia Desorption Property and Structural Changes of LiAl(NH2)4 on Thermal Decomposition”. In: The Journal of Physical Chemistry C 115.20 (2011), pp. 10284–10291. DOI: 10.1021/jp111656v.

[373] Weitong Cai et al. “Destabilization of LiBH4 dehydrogenation through H+–H− interactions by cooperating with alkali metal hydroxides”. In: RSC Adv. 4 (6 2014), pp. 3082–3089. DOI: 10.1039/C3RA45847D.

[374] V. S. Gorelik et al. “Raman Scattering in LiOH and LiOD Polycrystals”. In: Inorganic Materials 55.3 (2019), pp. 271–276. DOI: 10.1134/S0020168519030087.

[375] Liudmyla Ivashchenko et al. “Advances in Material Science”. In: Materials Journal 10.2 (2020), pp. 123–130. DOI: 10.1000/j.jmb.2020.02.003.

[376] Caitlin Brooker-Davis, Joshua Makepeace, and Thomas Wood. “Enhancement of the Catalytic Activity of Lithium Amide towards Ammonia Decomposition by Addition of Transition Metals”. In: Journal of Ammonia Energy (2023). DOI: 10.18573/jae.11.

[377] Joshua W. Makepeace et al. “Compositional flexibility in Li–N–H materials: implications for ammonia catalysis and hydrogen storage”. In: Phys. Chem. Chem. Phys. 23 (28 2021), pp. 15091–15100. DOI: 10.1039/D1CP02440J.

[378] Priya Barik et al. “Tetravalent manganese-doped lithium meta-silicate red-emitting phosphors for LED applications: structural and luminescence properties”. In: Radiation Effects and Defects in Solids 179.9-10 (2024), pp. 1049–1073. DOI: 10.1080/10420150.2024.2332190.

[379] Xianji Qiao et al. “Synthesis and characterisation of the quaternary cyanamide Li2MgSn2(NCN)6”. In: Zeitschrift für anorganische und allgemeine Chemie 647.22 (2021), pp. 2162–2166. DOI: 10.1002/zaac.202100132.

[380] Olaf Reckeweg and Francis J. DiSalvo. “Calcium Carbodiimide Compounds Revisited – Syntheses, Single Crystal Structure Determination and Vibrational Spectra of Ca11N6[CN2]2, Ca4N2[CN2] and Ca[CN2]”. In: Zeitschrift für Naturforschung B 63.5 (2008), pp. 530–536. DOI: doi:10.1515/znb-2008-0509.

[381] Yinji Wan et al. “Enhanced carbon dioxide capture performance of natural mineral vermiculite-derived lithium silicate with Na doping”. In: Greenhouse Gases: Science and Technology 12.2 (2022), pp. 263–272. DOI: https://doi.org/10.1002/ghg.2142.

[382] Yoshitsugu Kojima, Yasuaki Kawai, and Nobuko Ohba. “Hydrogen storage of metal nitrides by a mechanochemical reaction”. In: Journal of Power Sources 159.1 (2006), pp. 81–87. DOI: https://doi.org/10.1016/j.jpowsour.2006.04.024.

[383] Nora Tapia-Ruiz, Alexander G. Gordon, and C. Mark et al. Jewell. “Low dimensional nanostructures of fast ion conducting lithium nitride”. In: Nature Communications 11 (2020), p. 4492. DOI: 10.1038/s41467-020-17951-6.

[384] A. D. Allen and C. V. Senoff. “Preparation and infrared spectra of some ammine complexes of ruthenium(II) and ruthenium(III)”. In: Canadian Journal of Chemistry 45.12 (1967), pp. 1337–1341. DOI: 10.1139/v67-220.

[385] J. Braun et al. “Surface phonon dispersion curves for a hexagonally close packed metal surface: Ru(0001)”. In: Surface Science 372.1 (1997), pp. 132–144. ISSN: 0039-6028. DOI: 10.1016/S0039-6028(96)01108-9.

[386] Rylan J. Terry et al. “Hydrothermal single crystal growth and second harmonic generation of Li2SiO3, Li2GeO3 and Li2Si2O5”. In: Journal of Crystal Growth 493 (2018), pp. 58–64. ISSN: 0022-0248. DOI: https://doi.org/10.1016/j.jcrysgro.2018.02.028.

[387] Feng Jiao and Bingjun Xu. “Electrochemical Ammonia Synthesis and Ammonia Fuel Cells”. In: Advanced Materials 31.31 (2019), p. 1805173. DOI: 10.1002/adma.201805173.

[388] H.R. Chandrasekhar et al. “Phonon spectra and lattice dynamics of lithium nitride”. In: Solid State Communications 22.11 (1977), pp. 681–684. ISSN: 0038-1098. DOI: 10.1016/0038-1098(77)90249-6.

[389] M. Born and R. Oppenheimer. “Zur Quantentheorie der Molekeln”. In: Annalen der Physik 389.20 (1927), pp. 457–484. DOI: 10.1002/andp.19273892002.

[390] D. R. Hartree. “The Wave Mechanics of an Atom with a Non-Coulomb Central Field. Part II. Some Results and Discussion”. In: Mathematical Proceedings of the Cambridge Philosophical Society 24.1 (1928), pp. 111–132. DOI: 10.1017/S0305004100011920.

[391] V. Fock. “Näherungsmethode zur Lösung des quantenmechanischen Mehrkörperproblems”. In: Zeitschrift für Physik 61.1 (Jan. 1, 1930), pp. 126–148. ISSN: 0044-3328. DOI: 10.1007/BF01340294.

[392] J. C. Slater. “The Self Consistent Field and the Structure of Atoms”. In: Phys. Rev. 32 (3 1928), pp. 339–348. DOI: 10.1103/PhysRev.32.339.

[393] L. H. Thomas. “The calculation of atomic fields”. In: Mathematical Proceedings of the Cambridge Philosophical Society 23.5 (1927), pp. 542–548. DOI: 10.1017/S0305004100011683.

[394] E. Fermi. “Un Metodo Statistico per la Determinazione di alcune Prioprietà dell’Atomo”. In: Rend. Accad. Naz. Lincei 32.6 (1927), pp. 602–607.

[395] P. A. M. Dirac. “Note on Exchange Phenomena in the Thomas Atom”. In: Mathematical Proceedings of the Cambridge Philosophical Society 26.3 (1930), pp. 376–385. DOI: 10.1017/S0305004100016108.

[396] W. Kohn and L. J. Sham. “Self-Consistent Equations Including Exchange and Correlation Effects”. In: Phys. Rev. 140 (4A 1965), A1133–A1138. DOI: 10.1103/PhysRev.140.A1133.

[397] John P. Perdew et al. “Atoms, molecules, solids, and surfaces: Applications of the generalized gradient approximation for exchange and correlation”. In: Phys. Rev. B 46 (11 1992), pp. 6671–6687. DOI: 10.1103/PhysRevB.46.6671.

[398] Chengteh Lee, Weitao Yang, and Robert G. Parr. “Development of the Colle-Salvetti correlation-energy formula into a functional of the electron density”. In: Phys. Rev. B 37 (2 1988), pp. 785–789. DOI: 10.1103/PhysRevB.37.785.

[399] John P. Perdew and Yue Wang. “Accurate and simple analytic representation of the electron-gas correlation energy”. In: Phys. Rev. B 45 (23 1992), pp. 13244–13249. DOI: 10.1103/PhysRevB.45.13244.

[400] John P. Perdew, Kieron Burke, and Matthias Ernzerhof. “Generalized Gradient Approximation Made Simple”. In: Phys. Rev. Lett. 77 (18 1996), pp. 3865–3868. DOI: 10.1103/PhysRevLett.77.3865.

[401] Stefan Grimme et al. “A consistent and accurate ab initio parametrization of density functional dispersion correction (DFT-D) for the 94 elements H-Pu”. In: The Journal of Chemical Physics 132.15 (2010), p. 154104. DOI: 10.1063/1.3382344.

[402] Stefan Grimme, Stephan Ehrlich, and Lars Goerigk. “Effect of the damping function in dispersion corrected density functional theory”. In: Journal of Computational Chemistry 32.7 (2011), pp. 1456–1465. DOI: https://doi.org/10.1002/jcc.21759.

[403] Stephan N. Steinmann and Clemence Corminboeuf. “A generalized-gradient approximation exchange hole model for dispersion coefficients”. In: The Journal of Chemical Physics 134.4 (2011), p. 044117. DOI: 10.1063/1.3545985.

[404] Stephan N. Steinmann and Clemence Corminboeuf. “Comprehensive Benchmarking of a Density-Dependent Dispersion Correction”. In: Journal of Chemical Theory and Computation 7.11 (2011), pp. 3567–3577. DOI: 10.1021/ct200602x.

[405] Felix Bloch. “Über die Quantenmechanik der Elektronen in Kristallgittern”. In: Zeitschrift für Physik 52.7 (July 1, 1929), pp. 555–600. ISSN: 0044-3328. DOI: 10.1007/BF01339455.

[406] Xavier Gonze and Fabio Finocchi. “Pseudopotentials Plane Waves–Projector Augmented Waves: A Primer”. In: Physica Scripta 2004.T109 (2004), p. 40. DOI: 10.1238/Physica.Topical.109a00040.

[407] P. E. Blöchl. “Projector augmented-wave method”. In: Phys. Rev. B 50 (24 1994), pp. 17953–17979. DOI: 10.1103/PhysRevB.50.17953.

[408] Graeme Henkelman and Hannes Jónsson. “A dimer method for finding saddle points on high dimensional potential surfaces using only first derivatives”. In: The Journal of Chemical Physics 111.15 (Oct. 1999), pp. 7010–7022. ISSN: 0021-9606. DOI: 10.1063/1.480097.

[409] Andreas Heyden, Alexis T. Bell, and Frerich J. Keil. “Efficient methods for finding transition states in chemical reactions: Comparison of improved dimer method and partitioned rational function optimization method”. In: The Journal of Chemical Physics 123.22 (Dec. 2005), p. 224101. ISSN: 0021-9606. DOI: 10.1063/1.2104507.

[410] Graeme Henkelman, Blas P. Uberuaga, and Hannes Jónsson. “A climbing image nudged elastic band method for finding saddle points and minimum energy paths”. In: The Journal of Chemical Physics 113.22 (Dec. 2000), pp. 9901–9904. ISSN: 0021-9606. DOI: 10.1063/1.1329672.

[411] Graeme Henkelman and Hannes Jónsson. “Improved tangent estimate in the nudged elastic band method for finding minimum energy paths and saddle points”. In: The Journal of Chemical Physics 113.22 (Dec. 2000), pp. 9978–9985. ISSN: 0021-9606. DOI: 10.1063/1.1323224.

[412] Kenichi Fukui. “The path of chemical reactions - the IRC approach”. In: Accounts of Chemical Research 14.12 (1981), pp. 363–368. DOI: 10.1021/ar00072a001.

[413] Kenichi Fukui. “Formulation of the reaction coordinate”. In: The Journal of Physical Chemistry 74.23 (1970), pp. 4161–4163. DOI: 10.1021/j100717a029.

[414] G. Kresse and J. Hafner. “Ab initio molecular dynamics for liquid metals”. In: Phys. Rev. B 47 (1 1993), pp. 558–561. DOI: 10.1103/PhysRevB.47.558.

[415] G. Kresse and J. Furthmüller. “Efficient iterative schemes for ab initio total-energy calculations using a plane-wave basis set”. In: Phys. Rev. B 54 (16 1996), pp. 11169–11186. DOI: 10.1103/PhysRevB.54.11169.

[416] G. Kresse and J. Furthmüller. “Efficient iterative schemes for ab initio total-energy calculations using a plane-wave basis set”. In: Phys. Rev. B 54 (16 1996), pp. 11169–11186. DOI: 10.1103/PhysRevB.54.11169.

[417] G. Kresse and D. Joubert. “From ultrasoft pseudopotentials to the projector augmented-wave method”. In: Phys. Rev. B 59 (3 1999), pp. 1758–1775. DOI: 10.1103/PhysRevB.59.1758.

[418] Emmanuel Quemener and Marianne Corvellec. “SIDUS—the solution for extreme deduplication of an operating system”. In: Linux J. 2013.235 (2013). ISSN: 1075-3583.

[419] John W. Arblaster. “Crystallographic Properties of Ruthenium”. In: Platinum Metals Review 57.2 (2013), pp. 127–136. ISSN: 0032-1400. DOI: 10.1595/147106713X665030.

[420] Patanachai Janthon et al. “Bulk Properties of Transition Metals: A Challenge for the Design of Universal Density Functionals”. In: Journal of Chemical Theory and Computation 10.9 (2014), pp. 3832–3839. DOI: 10.1021/ct500532v.

[421] J. B. Yang et al. “Crystal and electronic structures of LiNH2”. In: Applied Physics Letters 88.4 (2006), pp. 041914–041914. DOI: 10.1063/1.2163258.

[422] Ping Chen et al. “Interaction of hydrogen with metal nitrides and imides”. In: Nature 420 (2002), pp. 302–304. DOI: 10.1038/nature01210.

[423] H. Jacobs and R. Juza. “Neubestimmung der Kristallstruktur des Lithiumamids”. In: Zeitschrift für anorganische und allgemeine Chemie 391.3 (1972), pp. 271–279. DOI: 10.1002/zaac.19723910308.

[424] Jianchuan Wang et al. “Native defects in $LiNH_2$: A first-principles study”. In: Phys. Rev. B 84 (2 2011), p. 024107. DOI: 10.1103/PhysRevB.84.024107.

[425] Khang Hoang, Anderson Janotti, and Chris G. Van de Walle. “Mechanisms for the decomposition and dehydrogenation of Li amide/imide”. In: Phys. Rev. B 85 (6 2012), p. 064115. DOI: 10.1103/PhysRevB.85.064115.

[426] Hua Ning et al. “Density function theory investigation on the thermodynamic properties of the Li–N–H system”. In: Materials Chemistry and Physics 144.3 (2014), pp. 484–490. ISSN: 0254-0584. DOI: 10.1016/j.matchemphys.2014.01.023.

[427] W. R. Tyson and W. A. Miller. “Surface free energies of solid metals: Estimation from liquid surface tension measurements”. In: Surface Science 62.1 (1977), pp. 267–276. ISSN: 0039-6028. DOI: 10.1016/0039-6028(77)90442-3.

[428] H.D. Ebinger et al. “Adsorption and diffusion of Li on an Ru(001) surface: an NMR study”. In: Surface Science 412-413 (1998), pp. 586–615. ISSN: 0039-6028. DOI: 10.1016/S0039-6028(98)00492-0.

[429] W. Mannstadt and A. J. Freeman. “LDA theory of the coverage dependence of the local density of states: Li adsorbed on Ru(001)”. In: Phys. Rev. B 57 (20 1998), pp. 13289–13294. DOI: 10.1103/PhysRevB.57.13289.

[430] W. Mannstadt. “Coverage dependence of the work function of Li adsorbed on Ru(001): ab initio studies within DFT”. In: Surface Science 525.1 (2003), pp. 119–125. ISSN: 0039-6028. DOI: 10.1016/S0039-6028(02)02548-7.

[431] C.J. Zhang, M. Lynch, and P. Hu. “A density functional theory study of stepwise addition reactions in ammonia synthesis on Ru(0001)”. In: Surface Science 496.3 (2002), pp. 221–230. ISSN: 0039-6028. DOI: 10.1016/S0039-6028(01)01621-1.

[432] Xiuyuan Lu et al. “Kinetic and mechanistic analysis of NH3 decomposition on Ru(0001), Ru(111) and Ir(111) surfaces”. In: Nanoscale Adv. 3 (6 2021), pp. 1624–1632. DOI: 10.1039/D1NA00015B.

[433] Graeme Henkelman, Andri Arnaldsson, and Hannes Jónsson. “A fast and robust algorithm for Bader decomposition of charge density”. In: Computational Materials Science 36.3 (2006), pp. 354–360. ISSN: 0927-0256. DOI: 10.1016/j.commatsci.2005.04.010.

[434] Edward Sanville et al. “Improved grid-based algorithm for Bader charge allocation”. In: Journal of Computational Chemistry 28.5 (2007), pp. 899–908. DOI: 10.1002/jcc.20575.

[435] W Tang, E Sanville, and G Henkelman. “A grid-based Bader analysis algorithm without lattice bias”. In: Journal of Physics: Condensed Matter 21.8 (2009), p. 084204. DOI: 10.1088/0953-8984/21/8/084204.

[436] J. J. Mortensen et al. “Density Functional Calculations of N_2 Adsorption and Dissociation on a Ru(0001) Surface”. In: Journal of Catalysis 169.1 (1997), pp. 85–92. ISSN: 0021-9517. DOI: https://doi.org/10.1006/jcat.1997.1661.

[437] Shulan Zhou, Sen Lin, and Hua Guo. “First-Principles Insights into Ammonia Decomposition Catalyzed by Ru Clusters Anchored on Carbon Nanotubes: Size Dependence and Interfacial Effects”. In: The Journal of Physical Chemistry C 122.16 (2018), pp. 9091–9100. DOI: 10.1021/acs.jpcc.8b01965.

[438] W. Tsai and W. H. Weinberg. “Steady-state decomposition of ammonia on the ruthenium(001) surface”. In: The Journal of Physical Chemistry 91.20 (1987), pp. 5302–5307. DOI: 10.1021/j100304a034.

[439] GiovanniMaria Piccini et al. “Ab initio molecular dynamics with enhanced sampling in heterogeneous catalysis”. In: Catal. Sci. Technol. 12 (1 2022), pp. 12–37. DOI: 10.1039/D1CY01329G.

[440] Giovanni Bussi, Davide Donadio, and Michele Parrinello. “Canonical sampling through velocity rescaling”. In: The Journal of Chemical Physics 126.1 (Jan. 2007), p. 014101. ISSN: 0021-9606. DOI: 10.1063/1.2408420.

[441] Giacomo Miceli. “First principles study of the LiNH2/Li2NH hydrogen storage system”. PhD thesis. Università degli Studi di Milano-Bicocca, 2011. URL: https://boa.unimib.it/handle/10281/19693#.

[442] Chidozie Onwudinanti et al. “Hydrogen diffusion out of ruthenium—an ab initio study of the role of adsorbates”. In: Phys. Chem. Chem. Phys. 22 (15 2020), pp. 7935–7941. DOI: 10.1039/D0CP00448K.

[443] Duncan H. Gregory. “Lithium nitrides, imides and amides as lightweight, reversible hydrogen stores”. In: J. Mater. Chem. 18 (20 2008), pp. 2321–2330. DOI: 10.1039/B801021H.

[444] Robert Juza and Karl Opp. “Metallamide und Metallnitride, 24. Mitteilung. Die Kristallstruktur des Lithiumamides”. In: Zeitschrift für anorganische und allgemeine Chemie 266.6 (1951), pp. 313–324. DOI: https://doi.org/10.1002/zaac.19512660606.

[445] Kenji Ohoyama et al. “Revised Crystal Structure Model of Li2NH by Neutron Powder Diffraction”. In: Journal of the Physical Society of Japan 74.1 (2005), pp. 483–487. DOI: 10.1143/JPSJ.74.483.

[446] T. Noritake et al. “Crystal structure and charge density analysis of Li2NH by synchrotron X-ray diffraction”. In: Journal of Alloys and Compounds 393.1 (2005), pp. 264–268. ISSN: 0925-8388. DOI: https://doi.org/10.1016/j.jallcom.2004.09.063.

[447] Marie-Laure Bonnet et al. “Local Disorder in Lithium Imide from Density Functional Simulation and NMR Spectroscopy”. In: The Journal of Physical Chemistry C 116.35 (2012), pp. 18577–18583. DOI: 10.1021/jp3004272.

[448] M. P. Balogh et al. “Crystal Structures and Phase Transformation of Deuterated Lithium Imide, Li2ND”. In: Journal of Alloys and Compounds 420 (2006), pp. 326–336. DOI: 10.1016/j.jallcom.2005.11.066.

[449] Guillermo A. Ludueña et al. “Local Disorder in Hydrogen Storage Compounds: The Case of Lithium Amide/Imide”. In: ChemPhysChem 11.11 (2010), pp. 2353–2360. DOI: https://doi.org/10.1002/cphc.201000156.

[450] Feng Zhang, Yan Wang, and M. Y. Chou. “Theoretical investigation of intermediate phases between Li_2NH and $LiNH_2$”. In: Phys. Rev. B 82 (9 2010), p. 094112. DOI: 10.1103/PhysRevB.82.094112.

[451] Jinbo Yang et al. “Study of the Crystal Structure and Phase Transition of Li2NH System”. In: MRS Proceedings 1098 (2008), 1098-HH03–06. DOI: 10.1557/PROC-1098-HH03-06.

[452] A. Lazicki et al. “New Cubic Phase of Li_3N: Stability of the N^{3-} Ion to 200 GPa”. In: Phys. Rev. Lett. 95 (16 2005), p. 165503. DOI: 10.1103/PhysRevLett.95.165503.

[453] Allen C. Ho et al. “Experimental and theoretical study of Li_3N at high pressure”. In: Phys. Rev. B 59 (9 1999), pp. 6083–6086. DOI: 10.1103/PhysRevB.59.6083.

[454] E. Döneges. “Lithium Nitride”. In: Handbook of Preparative Inorganic Chemistry. Ed. by G. Brauer. 2nd. Vol. 1. New York: Academic Press, 1963, p. 984.

[455] Wen Li et al. “Li+ ion conductivity and diffusion mechanism in α-Li3N and β-Li3N”. In: Energy Environ. Sci. 3 (10 2010), pp. 1524–1530. DOI: 10.1039/C0EE00052C.

[456] Yanming Shen et al. “Novel lithium-nitrogen compounds at ambient and high pressures”. In: Scientific Reports 5 (2015), p. 14204. DOI: 10.1038/srep14204.

[457] H. Shi, K. Jacobi, and G. Ertl. “Dissociative chemisorption of nitrogen on Ru(0001)”. In: Journal of Chemical Physics 99.11 (1993), pp. 9248–9254. DOI: 10.1063/1.465541.

[458] S. Schwegmann et al. “The adsorption of atomic nitrogen on Ru(0001): geometry and energetics”. In: Chemical Physics Letters 264.6 (1997), pp. 680–686. DOI: 10.1016/s0009-2614(96)01394-2.

[459] B. Hammer. “Coverage dependence of N_2 dissociation at an N, O, or H precovered Ru(0001) surface investigated with density functional theory”. In: Phys. Rev. B 63 (20 2001), p. 205423. DOI: 10.1103/PhysRevB.63.205423.

[460] H. Bludau et al. “A low-energy electron diffraction analysis of the R30° structure of molecular nitrogen adsorbed on Ru(0001)”. In: Chemical Physics Letters 219.5 (1994), pp. 452–456. ISSN: 0009-2614. DOI: https://doi.org/10.1016/0009-2614(94)00101-4.

[461] Kenichi Fukui. “Formulation of the reaction coordinate”. In: The Journal of Physical Chemistry 74.23 (1970), pp. 4161–4163. DOI: 10.1021/j100717a029.

[462] Kenichi Fukui. “The path of chemical reactions - the IRC approach”. In: Accounts of Chemical Research 14.12 (1981), pp. 363–368. DOI: 10.1021/ar00072a001.

[463] H. P. Hratchian and H. B. Schlegel. “Following Reaction Pathways Using a Damped Classical Trajectory Algorithm”. In: The Journal of Physical Chemistry A 106.1 (2002), pp. 165–169. DOI: 10.1021/jp012125b.

[464] Søren Dahl et al. “Electronic factors in catalysis: the volcano curve and the effect of promotion in catalytic ammonia synthesis”. English. In: Applied Catalysis A-general 222.1-2 (2001), pp. 19–29. ISSN: 0926-860X.

[465] H. Dietrich, K. Jacobi, and G. Ertl. “Coverage, lateral order, and vibrations of atomic nitrogen on Ru(0001)”. In: The Journal of Chemical Physics 105.19 (1996), pp. 8944–8950. ISSN: 0021-9606. DOI: 10.1063/1.472624.

[466] H. Rauscher, K. L. Kostov, and D. Menzel. “Adsorption and decomposition of hydrazine on Ru(001)”. In: Chemical Physics 177.2 (1993), pp. 473–496. ISSN: 0301-0104. DOI: 10.1016/0301-0104(93)80027-7.

[467] L. Diekhöner et al. “Observation of metastable atomic nitrogen adsorbed on Ru(0001)”. In: The Journal of Chemical Physics 112.5 (2000), pp. 2507–2515. ISSN: 0021-9606. DOI: 10.1063/1.480817.

[468] K. Jacobi. “Nitrogen on Ruthenium Single-Crystal Surfaces”. In: physica status solidi (a) 177.1 (2000), pp. 37–51. DOI: 10.1002/(SICI)1521-396X(200001)177:1<37::AID-PSSA37>3.0.CO;2-Y.

[469] S. Dahl, E. Törnqvist, and I. Chorkendorff. “Dissociative adsorption of N_2 on Ru(0001): A surface reaction totally dominated by steps”. In: Journal of Catalysis 192.2 (2000), pp. 381–390. ISSN: 0021-9517. DOI: 10.1006/jcat.2000.2858.

[470] O. Hinrichsen et al. “The Kinetics of Ammonia Synthesis over Ru-Based Catalysts: 1. The Dissociative Chemisorption and Associative Desorption of N_2”. In: Journal of Catalysis 165.1 (1997), pp. 33–44. ISSN: 0021-9517. DOI: 10.1006/jcat.1997.1447.